

Roger LeB. Hooke

# PRINCIPLES OF GLACIER MECHANICS

THIRD EDITION





# Principles of Glacier Mechanics

The third edition of this successful textbook will supply advanced undergraduate and graduate students with the tools they need to understand modern glaciological research. Practicing glacial geologists and glaciologists will also find the volume useful as a reference book. Since the second edition, three-quarters of the chapters have been updated, and two new chapters have been added. Included in this edition are noteworthy new contributions to our understanding of important concepts, with over 170 references to papers published since the second edition went to press. The book develops concepts from the bottom up: a working knowledge of calculus is assumed, but, beyond that, the important physical concepts are developed from elementary principles. Emphasis is placed on connections between modern research in glaciology and the origin of features of glacial landscapes. Student exercises are included.

**Roger LeB. Hooke** is Research Professor in the School of Earth and Climate Sciences and the Climate Change Institute at the University of Maine. He has been involved in glaciological research for over 30 years, focusing on processes relevant to the origin of glacial landforms. In addition to the first and second editions of *Principles of Glacier Mechanics*, he has published over 100 research papers in journals such as the *Geological Society of America Bulletin*, *Geology*, the *Journal of Glaciology*, *Quaternary Research*, and the *Journal of Geology*.

*“Principles of Glacier Mechanics* by Roger Le B. Hooke is a must-have for anyone seriously interested in glaciers and ice sheets. This 3rd edition provides a compact, accessible, rigorous perspective on the last few decades of evolution in our understanding of glacier mechanics, and connects the reader from basic, fundamental principles to the most recent research.”

– Eric Rignot, University of California–Irvine

“This is the first book I’d recommend to a student or colleague who wants to understand the fundamentals of how glaciers work. It’s a fantastic textbook for teaching glaciology to senior undergraduate and graduate students in the geosciences. Painstaking efforts are made to instill conceptual understanding of processes before developing mathematical understanding. The book is truly aimed at teaching, rather than simply informing, and it succeeds admirably. More so than any other text, it lucidly establishes connections between the mechanics of glaciers and the spectacular landforms they create. The third edition of the book is more comprehensive than the first two editions, with additional chapters on ice streams/shelves and ice cores – two of the most topical and important subjects in glaciology. These additional chapters add significantly to its great value as an authoritative reference book. The lean, crisp writing and emphasis on building understanding from the bottom up make this an unusually readable introduction to a subject with increasing societal relevance as the climate warms.”

– Neal Iverson, Iowa State University

“Today, glaciology is one of the cornerstones of the Earth sciences. The book *Principles of Glacier Mechanics* provides an excellent overview of the subject and can be recommended for both students and professionals wanting to gain insight into this rapidly growing field. The book strikes a nice balance between the quantitative and qualitative aspects of glacier mechanics. The reader is provided with an excellent summary of observations of glaciers and ice sheets from around the world, and all the key physical principles and governing equations of glacier mechanics are presented and explained in a very accessible fashion. In short, this is a well-written and concise text on glacier mechanics and an excellent book for teaching and learning the mechanics of glacier flow.”

– G. Hilmar Gudmundsson, Northumbria University

# **Principles of Glacier Mechanics**

**THIRD EDITION**

**Roger LeB. Hooke**

University of Maine



**CAMBRIDGE**  
UNIVERSITY PRESS

**CAMBRIDGE**  
UNIVERSITY PRESS

University Printing House, Cambridge CB2 8BS, United Kingdom  
One Liberty Plaza, 20th Floor, New York, NY 10006, USA  
477 Williamstown Road, Port Melbourne, VIC 3207, Australia  
314–321, 3rd Floor, Plot 3, Splendor Forum, Jasola District Centre, New Delhi – 110025, India  
79 Anson Road, #06–04/06, Singapore 079906

Cambridge University Press is part of the University of Cambridge.

It furthers the University's mission by disseminating knowledge in the pursuit of education, learning, and research at the highest international levels of excellence.

[www.cambridge.org](http://www.cambridge.org)

Information on this title: [www.cambridge.org/9781108427340](http://www.cambridge.org/9781108427340)

DOI: 10.1017/9781108698207

Second edition © R. LeB. Hooke 2005

Third edition © Roger LeB. Hooke 2020

This publication is in copyright. Subject to statutory exception and to the provisions of relevant collective licensing agreements, no reproduction of any part may take place without the written permission of Cambridge University Press.

First edition 1997 by Pearson Education, Inc.

Second edition 2005 by Cambridge University Press

Third edition 2020

Printed in the United Kingdom by TJ International Ltd. Padstow Cornwall

*A catalogue record for this publication is available from the British Library.*

*Library of Congress Cataloging-in-Publication Data*

Names: Hooke, Roger LeB., author.

Title: Principles of glacier mechanics / Roger LeB. Hooke, University of Maine.

Description: Third Edition. | New York : Cambridge University Press, 2020. | Second edition: 2005. |

Includes bibliographical references and index.

Identifiers: LCCN 2019021512 | ISBN 9781108427340 (Hardback : alk. paper) |

ISBN 9781108446075 (Paperback : alk. paper)

Subjects: LCSH: Glaciers. | Glacial landforms. | Ice mechanics.

Classification: LCC GB2403.2 .H66 2019 | DDC 551.31–dc23

LC record available at <https://lccn.loc.gov/2019021512>

ISBN 978-1-108-42734-0 Hardback

ISBN 978-1-108-44607-5 Paperback

Cambridge University Press has no responsibility for the persistence or accuracy of URLs for external or third-party internet websites referred to in this publication, and does not guarantee that any content on such websites is, or will remain, accurate or appropriate.

It is with a deep sense of gratitude that I dedicate this book to those who, at various times through the formative stages of my life, guided me into the most exciting and rewarding career I can imagine: the study of our Earth.

To my parents, who opened many doors for me;

to my older brother, Richard, who led me through a door leading to the wilderness;

to John Muir, who opened my eyes to the spirituality in wilderness;

to my wife, Ann, who introduced me to Geology;

to John P. Miller, who focused my attention on processes at the Earth's surface; and

to Robert P. Sharp, who taught me that basic physical principles could be used to understand these processes.



# Contents

Preface to the third edition	<i>page</i> xiii
Preface to the second edition	xv
Preface to the first edition	xvii
Physical constants relevant to ice	xix
Derived SI units and conversion factors	xxi
<b>1 Why study glaciers?</b>	1
<b>2 Some basic concepts</b>	5
A note on units and coordinate axes	5
Glacier size, shape, and temperature	5
The condition of incompressibility	8
Stresses, strains, and strain rates	10
<b>3 Mass balance</b>	17
The transformation of snow to ice	18
Snow stratigraphy	20
Mass balance principles	22
Mass balance of polar ice sheets	26
Effect of albedo on mass balance	26
Climatic causes of fluctuations in the meteorological component, $B_m$	28
Loss of ice by calving ( $\dot{B}_L$ )	34
Bottom melting	39
Effect of atmospheric circulation patterns on mass balance	40
Global mass balance and sea level	43
Summary	44
<b>4 Flow and fracture of a crystalline material</b>	46
Crystal structure of ice	47
Dislocations	49
Activation energy	52
Premelting	53
Deformation mechanisms	55
Rate-limiting processes	56
Recrystallization	60

Summary of ice deformation	68
Deformation mechanism maps	68
A flow law for glacier ice	70
Fracture and crevassing	73
Summary	79
<b>5 The velocity field in a glacier</b>	81
Measurement of velocity	82
Balance velocity	83
Shear stress	84
Horizontal velocity at depth in an ice sheet	86
Horizontal velocity in a valley glacier	88
Mean horizontal velocity and ice flux	92
Vertical velocity	93
Submergence and emergence velocities	96
Flow field	97
Transverse profiles of surface elevation on a valley glacier	99
Radar stratigraphy	101
Effect of drifting snow on the velocity field	105
Ice streams	112
Summary	113
<b>6 Temperature distribution in polar ice sheets</b>	115
Energy balance in an ice sheet	115
Dependence of $K$ on temperature	120
The steady-state temperature profile at the center of an ice sheet	120
Temperature profiles in the ablation zone	129
Temperature profiles near the surface of an ice sheet	130
Temperature profiles far from a divide	131
Englacial and basal temperatures along a flowline calculated using the column model	135
Basal temperatures in Antarctica – comparison of solutions using the column model and a numerical model	138
Climate change	143
Geomorphic implications	143
Summary	147
<b>7 The coupling between a glacier and its bed</b>	149
Sliding	149
Deformation of subglacial till	166

Abrasion	191
Drumlins and flutes	194
Summary	197
<b>8 Water flow in and under glaciers: Geomorphic implications</b>	<b>199</b>
The englacial hydraulic system	199
Equipotential surfaces in a glacier	205
Types of subglacial drainage system	208
Melt rates in conduits	209
Water pressures in subglacial conduits on hard beds	213
Surges	232
Jökulhlaups	236
Subglacial drainage and the formation of eskers	238
Tunnel valleys	247
Water pressure and glacier quarrying	248
Origin of cirques and overdeepenings	252
Summary	254
<b>9 Stress and deformation</b>	<b>256</b>
Stress	256
Momentum balance	265
Deformation	266
Condition that principal axes of stress and strain rate coincide	271
Summary	273
<b>10 Stress and velocity distribution in an idealized glacier</b>	<b>274</b>
Solutions for stresses and velocities in plane strain	274
Comparison with real glaciers	289
Summary	290
<b>11 Numerical modeling</b>	<b>291</b>
Goals of modeling	291
Numerical integration	292
Finite-difference models	294
Finite-element models	300
Finite-volume models	302
Coupling thermal and mechanical models	302
Initial conditions and forcing	303
Validation	304
Sensitivity testing and tuning	304

Intercomparison of models	305
Non-deterministic models	306
Examples	307
Summary	318
<b>12 Applications of stress and deformation principles to classical problems</b>	320
Collapse of a cylindrical hole	320
Calculating basal shear stresses using a force balance	332
Longitudinal coupling	338
Analysis of borehole-deformation data	342
Summary	349
<b>13 Ice streams and ice shelves</b>	350
The grounding zone	350
Ice streams	352
Ice shelves	366
Summary	385
<b>14 Finite strain and the origin of foliation</b>	387
The strain ellipse	387
Simple and pure shear	389
Parameters describing cumulative deformation	390
Calculating cumulative strain	391
Components of foliation	393
Summary	406
<b>15 Response of glaciers to climate change</b>	408
Feedback processes	409
Pleistocene climate	410
Response of a temperate glacier	411
Elementary kinematic wave theory	413
Analysis of the effect of a small change in mass balance using a perturbation approach	416
Effect of diffusion	420
A novel approach to response times	420
Numerical modeling of glacier responses	425
Comparison with observation	429
Summary	431

<b>16 Ice core studies</b>	<b>433</b>
Laboratory techniques	434
Establishing a time scale for a core	436
The fruits of ice core studies	446
Summary	453
Problems	455
References	465
Index	506



## Preface to the third edition

Eleven years after publication of the second edition of *Principles*, our understanding of glaciers and ice sheets had advanced to the point that a third edition seemed warranted. It has taken 3 years to bring this to fruition. As before, I thank my Cambridge editor, Matt Lloyd, for his patience.

My objectives in writing this book are detailed in the prefaces to the first and second editions: namely to introduce upper division and graduate students to the fundamentals of glaciology, and in so doing to perhaps provide a reference book of use to practicing glaciologists and to glacial geologists seeking to understand the formation of diverse glacial landforms. These objectives have not changed. In keeping with that goal, many advanced topics are left to more specialized works.

New in this edition are chapters on ice streams and ice shelves and on ice-core studies. These are areas of glaciology that are particularly topical today, as we worry about the effects of climate warming on ice sheets, and try to understand the past climate system.

In addition to those acknowledged for their help and encouragement in previous prefaces, I'd like to express my appreciation for assistance provided by David Bahr, Carolyn Begeman, Allison Banwell, David Goldsby, Hilmar Gudmundsson, Brian Hanson, Neal Iverson, Doug MacAyeal, Keith Makinson, Paul Mayewski, Stephen Price, Eric Rignot, Sharon Sneed, Dominique Reynaud, Gerard Roe, and Sebastian Rosier in the course of preparing this edition.

June 7, 2019



## Preface to the second edition

When I wrote the preface to the first edition of this book 7 years ago, nothing was further from my mind than a second edition. The first edition was well received, however, and on numerous occasions colleagues have lamented the fact that it was no longer available. When Cambridge University Press agreed that a new edition was desirable, little did I realize what I had gotten into.

When I told Matt Lloyd (my editor at Cambridge) that my goal was to have the text ready by a certain time, he graciously gave me a target date that was nearly double that time. I told him that his time schedule was fine, but that I did not want to be held too strictly to it. As it happens, I had an unrealistic view of the volume of new material that needed to be sifted through, absorbed, and translated into language appropriate for the upper-division undergraduate and graduate-level students for whom this book is written. As with the first edition, my goal is not to provide an encyclopedia of research in glaciology, as other books do that well, but rather to give students the basic background they will need to understand the modern literature. At the same time, the book has proven to be a useful reference for professionals who don't keep all of the equations and conversion factors stored for instant recall. I myself use it for that purpose frequently.

I am indebted to many who have encouraged me in this undertaking, and especially to those who have generously given their time to review new sections or entire chapters, who have resurrected archived computer files to provide images or data files from which new figures were produced, or who have made new calculations especially for this volume. The following have assisted me in this effort: Richard Alley, Bob Bindshadler, Ginny Catania, Chris Clark, Lee Clayton, Paul Cutler, Gordon Hamilton, Brian Hanson, Bruce Hooke, Peter Hudleston, Kolumbian Hutter, Philippe Huybrechts, Neal Iverson, Peter Jansson, Susan Kaspari, Katie Leonard, Paul Mayewski, Shawn Marshall, Howard Mooers, Nadine Nereson, Felix Ng, Charlie Raymond, Vandy Spikes, Slawek Tulaczyk, and Joe Walder.

March 15, 2004



## Preface to the first edition

One might well ask why one should write a book about so specialized a subject as glacier mechanics when there are already other good books on this subject written by eminent glaciologists. This book is an outgrowth of a course that I teach to students who, in many cases, do not have any background in continuum mechanics. Consequently, it was necessary to start at a level considerably less advanced than that at which other similar books begin, and to develop the theoretical principles one step at a time. Thus, unlike other books on the subject and the general scientific literature, in which space is at a premium, the steps leading from one equation to another are, in most cases, easily seen. In addition, qualitative interpretations of the equations are often provided to clarify the physics behind the mathematics. Capable students with a solid background in basic physics and in differential and integral calculus, and with some modest exposure to differential equations, will have little difficulty understanding the concepts and derivations presented.

My goal in writing this book was not to produce a comprehensive treatise on glacier mechanics, but rather to develop the basic foundation upon which the modern literature on this subject rests. Thus, many topics are not covered, or are treated in less detail than some readers might wish. However, students who have a full appreciation for the concepts in this book will have the background they need to understand most of the current literature.

Beginning students in glaciology will find that this book will save them many long hours of searching through the background literature to clarify basic concepts. Glacial geologists and geomorphologists will also find much of value, including applications of glacier physics to the origin of some glacial landforms. Structural geologists and others with interest in stress and deformation will likewise discover that glaciers are, in fact, monomineralic rock masses that are deforming at the Earth's surface where they can be observed in detail. The book is, thus, appropriate for upper division and graduate level courses in glaciology, and as a supplementary text for courses in glacial geology and in structural geology.

In the preliminary pages, readers will find a compilation of physical constants relevant to ice, and a list of SI units and conversion factors. A series of problems keyed to individual chapters is also included.

The encouragement I have received in this undertaking from many present and former students, as well as from other glaciologists, has been a major stimulus in bringing it to completion. I trust the final product is worthy of their confidence. The book has benefited from the critical comments of R. W. Baker at the University of

Wisconsin, River Falls; C. R. Bentley at the University of Wisconsin, Madison; G. K. C. Clarke at the University of British Columbia; E. M. Grace and B. Hanson at the University of Delaware; N. R. Iverson at the University of Minnesota; T. Jóhannesson at the Icelandic Meteorological Office; M. Kuhn at the University of Innsbruck, Austria; M. F. Meier at the University of Colorado; J. F. Nye at the University of Bristol, England; C. F. Raymond at the University of Washington; R. L. Shreve at the University of California, Los Angeles; J. Weertman at Northwestern University, and especially I. Whillans at Ohio State University.

June 25, 1996

# Physical constants relevant to ice

Symbol	Parameter	Value
a	Coefficient of linear thermal expansion of: ordinary water at 0°C ice at -10°C	$-22.3 \times 10^{-6} \text{ K}^{-1}$ $51.6 \times 10^6 \text{ K}^{-1}$
b	Burgers vector	$4.5 \times 10^{-10} \text{ m}$
C	Heat capacity of pure ice at 0°C  C varies with temperature, approximately thus: $C = 152.5 + 7.1220$ , where θ is in Kelvins (Cuffey and Paterson, 2010, p. 400). For more detailed data see Yen (1981)	$2096 \text{ J kg}^{-1} \text{ K}^{-1}$
$C_w$	Heat capacity of air-free water at constant pressure and 0°C	$4184 \text{ J kg}^{-1} \text{ K}^{-1}$
c	Depression of the melting point  Pure ice and air-free water Pure ice and air-saturated water (Harrison, 1972)	$0.074 \text{ K MPa}^{-1}$ $0.098 \text{ K MPa}^{-1}$
E	Young's modulus  (Gold, 1958) [The ratio of axial stress to elastic axial strain in a test in uniaxial tension. $E = 2\mu(1 + v)$ ]	$8.3 \times 10^3 \text{ MPa}^*$
g	Acceleration of gravity	$9.81 \text{ m s}^{-2}$
K	Thermal conductivity at -1°C  K varies with temperature, thus: $K = 7.10 \times 10^7 - 0.0195 \times 10^7 \theta + 0.000363 \times 10^7 \theta^2$ where θ is the temperature in °C (a negative number) (Ratcliffe, 1962)	$7.1 \times 10^7 \text{ J m}^{-1} \text{ a}^{-1} \text{ K}^{-1}$
K	Bulk modulus (at -5°C) (Gold, 1958)  (Ratio of applied pressure to fractional change in volume)	$8.7 \times 10^3 \text{ MPa}^*$
$K_{Ic}$	Fracture toughness (Rist <i>et al.</i> , 1999)	$0.05\text{--}0.15 \text{ MPa m}^{1/2}$
L	Heat of Fusion	$3.34 \times 10^5 \text{ J kg}^{-1}$
Q	Activation energy for creep below -10°C  Q appears to vary with stress (Goldsby and Kohlstedt, 1997), with 60 kJ mol <sup>-1</sup> being a good average value at stresses commonly found in glaciers. Above -10°C, Q is presumably the same but the $\dot{\epsilon}$ vs 1/θ curve steepens due to the presence of a liquid phase on grain boundaries	$60 \pm 10 \text{ kJ mol}^{-1}$
V	Activation volume (Kirby <i>et al.</i> , 1987)	$-13 \times 10^{-6} \text{ m}^3 \text{ mol}^{-1}$
R	Gas constant	$8.314 \text{ J mol}^{-1} \text{ K}^{-1}$
S <sub>cr</sub>	Crushing strength of natural snow ice.	1.8 MPa at 0°C

(cont.)

Symbol	Parameter	Value
	The strength increases substantially with decreasing temperature. Hobbs (1974, p. 331) gives a graph from Butkovitch (1954) that can be approximated by: $S_{cr} = 1.8 - 0.266\theta - 0.0202\theta^2 - 7.72 \times 10^{-4}\theta^3 - 1.39 \times 10^{-5}\theta^4 - 9.37 \times 10^{-8}\theta^5$ where $\theta$ is the temperature in $^{\circ}\text{C}$ (a negative number) There is considerable variability depending on the type of ice tested and its orientation.	
$\beta$	Dihedral angle ( $\cos \beta = \gamma_{gb}/2\gamma_{SL}$ ) (Nye and Mae, 1972)	$2\beta = 32 \pm 3^{\circ}$
$\gamma_{SL}$	Specific surface energy of liquid–solid interface (Ketcham and Hobbs, 1969)	$0.034 \text{ J m}^{-2}$
$\gamma_{gb}$	Specific surface energy of grain boundary	$0.065 \text{ J m}^{-2}$
$\theta_m$	Melting point at atmospheric pressure	$0.0^{\circ}\text{C}$ $273.15 \text{ K}$
$\theta_{TP}$	Triple point temperature	$+0.0098^{\circ}\text{C}$
$P_{TP}$	Triple point pressure	$600 \text{ Pa}$
$\kappa$	Thermal diffusivity at $-1^{\circ}\text{C}$  [Below $-0.5^{\circ}\text{C}$ , $\kappa$ varies with temperature due to the variation in $K$ (see above). Above $-0.5^{\circ}\text{C}$ , $\kappa$ decreases due to the increase in effective $C$ (see above). Paterson (1971) estimates that, at $-0.1^{\circ}\text{C}$ , $\kappa$ is half its value for pure ice, and at $-0.01^{\circ}\text{C}$ it is 1% of the value for pure ice. These estimates assume a salinity of $10^{-6}$ ]	$37.2 \text{ m}^2 \text{ a}^{-1}$
$\mu$	Shear modulus (at $-5^{\circ}\text{C}$ )  (Gold, 1958) [The ratio of shear stress to elastic shear strain in a test in simple shear]	$3.8 \times 10^3 \text{ MPa}^*$
$v$	Poisson's ratio for polycrystalline ice  (Gold, 1958) [The ratio of the transverse strain (contraction) to the axial strain (extension) of a bar in a uniaxial tensile test]	$0.31^*$
$\rho_i$	Density of bubble-free ice	$916 \text{ kg m}^{-3}$
$\rho_w$	Density of water at $0^{\circ}\text{C}$	$999.84 \text{ kg m}^{-3}$
$\zeta$	Depression of melting point due to solutes	$1.86 \text{ }^{\circ}\text{C kg mol}^{-1}$

\* Values given for  $E$ ,  $K$ ,  $\mu$ , and  $v$  are based on the work of Gold (1958), as reported by Hobbs (1974, pp. 255–258). Hobbs also reports other values based on the work of other (earlier) investigators.

## Derived SI units and conversion factors

$1 \text{ N} = 1 \text{ kg m s}^{-2}$	Force (mass · acceleration)
$1 \text{ Pa} = 1 \text{ N m}^{-2} = 1 \text{ kg m}^{-1} \text{s}^{-2}$	Stress
$1 \text{ J} = 1 \text{ N m} = 1 \text{ kg m}^2 \text{s}^{-2}$	Work or energy
$1 \text{ W} = 1 \text{ Js}^{-1} = \text{N m s}^{-1}$	Power
$1 \text{ bar} = 0.1 \text{ MN m}^{-2} = 0.1 \text{ MPa} = 0.9868 \text{ atm}$	Stress
$1 \text{ cal} = 4.18 \text{ J}$	
$1 \text{ a} = 3.15569 \times 10^7 \text{ s}$	
$0^\circ\text{C} = 273.15 \text{ K}$	



# 1

## Why study glaciers?

Before delving into the mathematical intricacies with which much of this book is concerned, one might well ask why we are pursuing this topic – glacier mechanics? For many people who would like to understand how glaciers move, how they sculpt the landscape, how they respond to climatic change, mathematics does not come easily. I assure you that all of us have to think carefully about the meaning of the expressions that seem so simple to write down but so difficult to understand. Only then do they become part of our vocabulary. Only then can we make use of the added precision which mathematical analysis, properly formulated, is able to bring. Is it worth the effort? That depends upon your objectives; on why you chose to study glaciers.

There are many reasons, of course. Some are personal, some academic, and some socially significant. To me, the personal reasons are among the most important: glaciers occur in spectacular areas, often remote, that have not been scarred by human activities. Through glaciology, I have had the opportunity to live in these areas; to drift silently in a kayak on an ice-dammed lake in front of our camp as sunset gradually merged with sunrise on an August evening; to marvel at the northern lights while out on a short ski tour before bedtime on a December night; and to reflect on the meaning of life and of our place in nature. Maybe some of you will share these needs, and will choose to study glaciers for this reason. I have found that many glaciologists do share them, and this leads to a comradeship that is rewarding in itself.

Academic reasons for studying glaciers are perhaps difficult to separate from socially significant ones. However, in three academic disciplines, the application of glaciology to immediate social problems is at least one step removed from the initial research. The first of these is glacial geology. Glaciers once covered 30% of the land area of Earth, and left deposits of diverse shape and composition. How were these deposits formed, and what can they tell us about the glaciers that made them? The second discipline is structural geology; glacier ice is a metamorphic rock that can be observed in the process of deformation at temperatures close to the melting point. From study of this deformation, both in the laboratory and in the field, much has been learned about the origin of metamorphic structures in other crystalline rocks that were deformed deep within the Earth. The final discipline is paleoclimatology.

Glaciers record climatic fluctuations in two ways: the deposits left during successive advances and retreats provide a coarse record of climatic change which, with careful study, a little luck, and a good deal of skill, can be placed in correct chronological order and dated. A more detailed record is contained in ice cores from polar glaciers such as the Antarctic and Greenland ice sheets. Isotopic and other chemical variations in these cores reflect past atmospheric circulation patterns, changes in temperature, and changes in the composition of the atmosphere. Changes during the past several centuries to several millennia can be quite precisely dated using core stratigraphy. Those further back in time are dated less precisely using flow models and proxy measures of other well-dated phenomena such as Earth's orbital variations.

Relatively recent changes in climate and in concentrations of certain anthropogenic substances in the atmosphere are attracting increasing attention as humans struggle with problems of maintaining a healthy living environment in the face of overpopulation and the resulting demands on natural resources. Studies of ice cores and other dated ice samples provide a baseline from which to measure these anthropogenic changes. For example, levels of lead in the Greenland ice sheet increased about 4-fold when Greeks and Romans began extracting silver from lead sulfides in ~500 BCE (Hong *et al.*, 1994). Then, after dropping slightly in the first millennium AD, they increased to more than 80 times natural levels during the industrial revolution and to more than 200 times natural levels when lead additives became common in gasoline in ~1940 (Murozumi *et al.*, 1969). These studies are largely responsible for the fact that lead is no longer used in gasoline. Similarly, measurements of CO<sub>2</sub> and CH<sub>4</sub> in ice cores have documented levels of these greenhouse gases in pre-industrial times.

Other applications of glaciology are not hard to find. Some people in northern and mountainous lands live so close to glaciers that their lives would be severely altered by significant ice advances. Tales from the seventeenth and eighteenth centuries, a period of ice advance as the world entered the Little Ice Age, tell of glaciers gobbling up farms and farm buildings. Buildings were crushed into small pieces and mixed with "soil, grit, and great rocks" (Grove, 1988, p. 72). The Mer de Glace in France presented a particular problem, and several times during the seventeenth century exorcists were sent out to deal with the "spirits" responsible for its advance. They appeared to have been successful, as the glaciers were then near their Little Ice Age maxima and beginning to retreat. Increasing amounts of industrial black carbon, an aerosol, were falling on glacier surfaces then, absorbing solar radiation and increasing melt rates (Painter *et al.*, 2013).

Retreat may also present a problem. In many places, melting glacier ice provides a steady source of water for irrigation and other uses during the summer months. Glacier retreat reduces this flow and may divert it to a different valley. In the

western Himalaya, such a diversion forced the inhabitants of Kumik to move their village to a new location and dig a 7 km canal to provide water (Mingle, 2015).

Retreat of the Greenland and Antarctic Ice Sheets, together with that of numerous mountain glaciers world-wide, is also raising sea level. This retreat is expected to continue and to accelerate (Straneo and Heimbach, 2013) as global warming, exacerbated by black carbon from forest fires and burning of fossil fuels, increases melting. In the Admunsen Sea sector of West Antarctica, retreat of Thwaites and Pine Island glaciers could trigger collapse of the West Antarctic Ice Sheet, raising sea level ~3 m during the coming centuries to millennia (Park *et al.*, 2013; Feldmann and Levermann, 2015). In short, sea-level rise will increasingly impact our coastal infrastructure. Some political jurisdictions have had the foresight to begin planning for this eventuality.

Other people live in proximity to rivers draining lakes dammed by glaciers. Some of the biggest floods known from the geologic record resulted from the failure of such ice dams, and smaller floods of the same origin have devastated communities in the Alps and Himalayas. Somewhat further from human living environments, glaciologists may study the possibility of extracting economically valuable deposits from beneath glaciers, or how to curb the discharge of icebergs into shipping lanes.

Glacier ice itself is an economically valuable deposit; glaciers contain 60% of the world's fresh water, and peoples in arid lands have seriously studied the possibility of towing icebergs from Antarctica to serve as a source of water. People in mountainous countries use glacier meltwater not only for drinking, but also as a source of hydroelectric power. By tunneling through the rock under a glacier and thence up to the ice-rock interface, they trap water at a higher elevation than would be possible otherwise, and thus increase the energy yield. Glaciologists provide advice on the activity of the glaciers and where to find streams beneath them.

Lastly, we should mention a proposal to dispose of radioactive waste by letting it melt its way to the base of the Antarctic Ice Sheet. How long would such waste remain isolated from the biologic environment? How would the heat released affect the flow of the ice sheet? Might it cause a surge. In the end, this project was abandoned, not on glaciological grounds but, rather, because there seemed to be no risk-free way to transport the waste to Antarctica.

A good quantitative understanding of the physics of glaciers is essential for rigorous treatment of many of these academic problems, as well as for accurate analysis of various engineering and environmental problems involving glaciers and of concern to humans. The fundamental principles upon which this understanding is based are those of physics and, to a lesser extent, chemistry. Application of these principles to glacier dynamics is initially straightforward, but, as with many problems, the better we seek to understand the behavior of glaciers, the more involved, and often the more interesting the applications become.

So we have answered our first question; we study glaciers for the same reasons that we study many other features of the natural landscape, but also for a special reason which I will try to impart to you, wordlessly, if you will stand with me looking over a glacier covered with a thick blanket of fresh powder snow to distant peaks, bathed in alpine glow, breathless from a quick climb up a steep slope after a day of work, but with skis ready for the telemark run back to camp. “Mäktig,” my companion said – powerful.

# 2

## Some basic concepts

In this chapter, I'll introduce some basic concepts that will be used frequently throughout this book. First, we'll review some commonly used classifications of glaciers by shape and thermal characteristics. Then we consider the mathematical formulation of the concept of conservation of mass and, associated with it, the condition of incompressibility. This will appear again in Chapters 6 and 9. Finally, we discuss stress and strain rate, and lay the foundation for understanding the most commonly used flow laws for ice. Although a complete consideration of these latter concepts is deferred to Chapter 9, a modest understanding of them is essential for a fuller appreciation of some concepts presented in earlier chapters.

### A note on units and coordinate axes

SI (Système International) units are used in this book. The basic units of length, mass, and time are the meter (m), kilogram (kg), and second (s) (MKS). Temperatures are measured in Kelvins (K) or in the derived unit, degrees Celsius ( $^{\circ}\text{C}$ ). Some other derived units and useful conversion factors are given on p. *xvi*.

In most developments herein, I'll use a rectangular coordinate system with the  $x$ -axis horizontal or subhorizontal and in the direction of flow, the  $y$ -axis horizontal and transverse, and the  $z$ -axis normal to the other two and thus vertical or slightly inclined to the vertical. Some derivations are easier to approach with the  $z$ -axis directed upward, while in others it is simpler to have the  $z$ -axis directed downward.

### Glacier size, shape, and temperature

As humans, one way in which we try to organize knowledge and enhance communication is by classifying objects into neat compartments, each with its own label. The natural world persistently upsets these schemes by presenting us with particular items that fit neither in one such pigeonhole nor the next, but rather have

characteristics of both; continua are the rule rather than the exception. This is as true of glaciers as it is of other natural systems.

One way of classifying glaciers is by shape. Herein, we will be concerned with only two basic shapes. Glaciers that are long and comparatively narrow, and that flow in basically one direction, down a valley, are called *valley glaciers*. When a valley glacier reaches the coast and interacts with the sea, it is called a *tidewater glacier*. (I suppose this name is appropriate even in circumstances in which the tides are negligible.) Valley glaciers that are very short, occupying perhaps only a small basin in the mountains, are called *cirque glaciers*. In contrast to these forms are glaciers that spread out in all directions from a central dome. These are called either *ice caps*, or, if they are large enough, *ice sheets*.

There is, of course, a continuum between valley glaciers and ice caps or ice sheets. For example, one commonly finds valley glaciers flowing outward from ice caps or ice sheets; this kind of valley glacier is usually referred to as an *outlet glacier*. However, the end members, valley glaciers and ice sheets, typically differ in other significant ways (see, for example, Figure 3.1). Thus, a classification focusing on these two end members is useful.

Glaciers are also classified by their thermal characteristics, although once again a continuum exists between end members. We normally think of water as freezing at 0°C, but may overlook the fact that, once all the water in a space is frozen, the temperature of the resulting ice can be lowered below 0°C as long as heat can be removed from it. Thus, the temperature of ice in glaciers in especially cold climates can be well below 0°C. We call such glaciers *polar glaciers*. More specifically, polar glaciers are glaciers in which the temperature is below the melting temperature of ice everywhere above the bed. Parts of the bed may be at the melting point, and parts below it. The presence of meltwater at the bed has dramatic consequences, both for glacier kinematics and for landform development. In Chapter 6, we will investigate the temperature distribution in such glaciers in some detail.

Glaciers that are not polar are either *polythermal* or *temperate*. Polythermal glaciers contain large volumes of ice that are cold, but also large volumes that are at the melting temperature. Most commonly, the cold ice is present as a surface layer, tens of meters in thickness, on the lower part of the glacier (the ablation area).

In simplest terms, a temperate glacier is one that is at the melting temperature throughout. However, the melting temperature,  $\theta_m$ , is not easily defined. As the temperature of an ice mass is increased toward the melting point, veins of water form along lines where three ice crystals meet (Figure 8.1). At the wall of such a vein:

$$\theta_m = \theta_{TP} - \mathbf{C}P - \frac{\theta_{mK}\gamma_{SL}}{L\rho_i r_p} - \zeta \frac{s}{W} \quad (2.1)$$

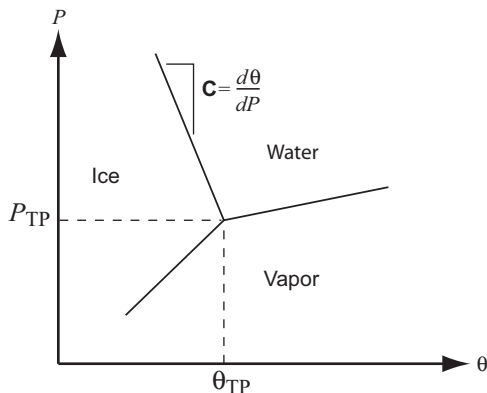


**Figure 2.1** Schematic phase diagram for  $\text{H}_2\text{O}$  near the triple point, TP. At the triple point, liquid, solid, and vapor phases are in equilibrium. As long as all three phases are present, neither the pressure nor the temperature can depart from their triple point values.

(Raymond and Harrison, 1975; Lliboutry, 1976). Here,  $\theta_{TP}$  is the triple point temperature,  $0.0098^\circ\text{C}$ , and  $\mathbf{C}$  is the depression of the melting point with increased pressure,  $P$  (Figure 2.1);  $\theta_{\text{mK}}$  is the melting point temperature in Kelvins,  $273.15\text{ K}$ ;  $\gamma_{SL}$  is the liquid–solid surface energy,  $0.034\text{ J m}^{-2}$ ;  $L$  is the latent heat of fusion,  $3.34 \times 10^5\text{ J kg}^{-1}$ ;  $\rho_i$  is the density of ice;  $r_p$  is the radius of curvature of liquid–solid interfaces;  $s$  is the solute content of the ice in mols  $\text{kg}^{-1}$ ,  $W$  is the fractional water content of the ice by weight ( $\text{kg/kg}$ ), and  $\zeta$  is the depression of the melting point resulting from solutes in the ice,  $1.86^\circ\text{C kg mol}^{-1}$ . The third term on the right in Equation (2.1) represents a change in melting temperature in the immediate vicinity of veins. In the second term,  $\mathbf{C}$  is the Clausius–Clapeyron slope:

$$\mathbf{C} = \frac{d\theta}{dP} = \left( \frac{1}{\rho_i} - \frac{1}{\rho_w} \right) \frac{\theta_{\text{TPK}}}{L}. \quad (2.2)$$

Here,  $\rho_w$  is the density of water and  $\theta_{\text{TPK}}$  is the triple point temperature in Kelvins.  $\mathbf{C}$  is  $0.0742\text{ K MPa}^{-1}$  in pure water, but rises to  $0.098\text{ K MPa}^{-1}$  in air-saturated water. As glacier ice normally contains air bubbles, the water is likely to contain air, even if it is not saturated with air. Thus, under most circumstances it is probably appropriate to use a value higher than  $0.0742\text{ K MPa}^{-1}$  (Lliboutry, 1976).

Clearly, the melting temperature varies on many length scales (Equation 2.1). On the smallest scales, it varies within veins that occur along crystal boundaries. On a slightly larger scale, it varies from the interiors of crystals to the boundaries because solutes become concentrated on the boundaries during crystal growth. On the largest scale, it varies with depth due to the change in pressure.

As a result of these variations, small amounts of liquid are present on grain boundaries at temperatures as low as about  $-35^\circ\text{C}$ , and the amount of liquid increases as the temperature increases. This phenomenon, known as *premelting*,

led Harrison (1972) to propose a more rigorous definition of a temperate glacier. He suggested that a glacier be considered temperate if its heat capacity is greater than twice the heat capacity of pure ice. This occurs when the temperature and liquid content of the ice are such that of any energy put into the ice, half is used to warm the ice (and existing liquid) and half is used to melt ice in places where the local melting temperature is depressed.

Harrison's definition, while offering the benefit of rigor, is not easily applied in the field. However, as we shall see in Chapter 4, relatively small variations in the liquid content of ice can have a major influence on its viscosity and crystal structure, among other things. Thus, this discussion serves to emphasize that the class of glaciers which we loosely refer to as temperate may include ice masses with a range of physical properties that are as wide as, or wider than, those of glaciers which we refer to as polar.

Ice sheets are commonly polar, while valley glaciers and small ice caps are more often temperate. However, there is nothing in the respective classification schemes that requires this. In fact, many valley glaciers in high Arctic areas and in Antarctica are at least polythermal, and some are undoubtedly polar.

## The condition of incompressibility

Let us next examine the consequences of the requirement that mass be conserved in a glacier. In Figure 2.2, a control volume of size  $dx \cdot dy \cdot dz$  is shown. The velocities into the volume in the  $x$ ,  $y$ , and  $z$  directions are  $u$ ,  $v$ , and  $w$ , respectively. The velocity out in the  $x$ -direction is:

$$u + \frac{\partial u}{\partial x} dx.$$

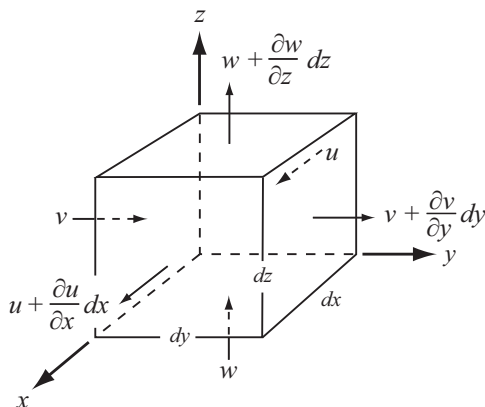


**Figure 2.2** Derivation of the condition of incompressibility.

Here,  $\partial u / \partial x$  is the velocity gradient through the volume, which, when multiplied by the length of the volume,  $dx$ , gives the change in velocity through the volume in the  $x$ -direction. The mass fluxes into and out of the volume in the  $x$ -direction are:

$$\begin{array}{lll} \rho & u & dy \ dz \text{ and} \\ \frac{\text{kg}}{\text{m}^3} & \frac{\text{m}}{\text{a}} & \text{m} = \frac{\text{kg}}{\text{a}} \end{array} \left( \rho u + \frac{\partial \rho u}{\partial x} dx \right) dy \ dz$$

Here,  $\rho$  is the density of ice. (The dimensions of the various parameters are shown beneath the left-hand term to clarify the physics. This is a procedure that I will use frequently in this book, and that the reader is likely to find useful, as errors in equations can often be detected in this way.) Similar relations may be written for the mass fluxes into and out of the volume in the  $y$ - and  $z$ -directions. Summing these fluxes, we find that the change in mass with time,  $\partial m / \partial t$ , in the control volume is:

$$\begin{aligned} \frac{\partial m}{\partial t} = & \rho u \ dy \ dz - \left( \rho u + \frac{\partial \rho u}{\partial x} dx \right) dy \ dz + \rho v \ dx \ dz - \left( \rho v + \frac{\partial \rho v}{\partial y} dy \right) dx \ dz + \rho w \ dx \ dy \\ & - \left( \rho w + \frac{\partial \rho w}{\partial z} dz \right) dx \ dy. \end{aligned}$$

Note that each term on the right-hand side has the dimensions  $\text{M} \cdot \text{T}^{-1}$ , or in the units which we will use most commonly herein,  $\text{kg a}^{-1}$ . Simplifying by canceling like terms of opposite sign and dividing by  $dx \cdot dy \cdot dz$  yields:

$$-\frac{1}{dx \ dy \ dz} \frac{\partial m}{\partial t} = \frac{\partial \rho u}{\partial x} + \frac{\partial \rho v}{\partial y} + \frac{\partial \rho w}{\partial z}. \quad (2.3)$$

Ice is normally considered to be incompressible, which means that  $\rho$  is constant. This is not true near the surface of a glacier, where snow and firn are undergoing compaction, but to a good approximation it is valid throughout the bulk of most ice masses. In this case, Equation (2.3) becomes:

$$-\frac{1}{\rho dx \ dy \ dz} \frac{\partial m}{\partial t} = \frac{\partial u}{\partial x} + \frac{\partial v}{\partial y} + \frac{\partial w}{\partial z}. \quad (2.4)$$

The mass of ice in the control volume can change if the control volume is not full initially. When it is full of incompressible ice, however,  $\partial m / \partial t = 0$ , and Equation (2.4) becomes:

$$\frac{\partial u}{\partial x} + \frac{\partial v}{\partial y} + \frac{\partial w}{\partial z} = 0. \quad (2.5)$$

This is the condition of incompressibility; it describes the situation in which neither mass nor density are changing in the control volume.

## Stresses, strains, and strain rates

A stress is a force per unit area, and has the dimensions  $\text{N m}^{-2}$ , or  $\text{Pa}$ . Stresses are vector quantities in that they have a magnitude and direction. Stresses that are directed normal to the surface on which they are acting are called normal stresses, while those that are parallel to the surface are shear stresses. A force applied to a surface at an oblique angle results in both shear and normal stresses on the surface.

### Notation

Referring to Figure 2.3,  $\sigma_{xz}$  is the shear stress in the  $z$ -direction on the plane normal to the  $x$ -axis. Thus, the first subscript in a pair is the orientation of the normal to the plane on which the stress acts, and the second gives the direction of the stress. (Some authors reverse this order.)

The sign convention used in such situations is as follows: Let  $\hat{n}$  be the outwardly directed normal to a surface.  $\hat{n}$  is positive if it is directed in the positive direction and conversely. If a normal stress is in the positive direction and  $\hat{n}$  is also positive on this face, the stress is defined as positive; conversely, if one is positive and the other negative, the stress is negative. Thus, both  $\sigma_{zz}$ 's in Figure 2.3 are positive and both  $\sigma_{xx}$ 's are negative. In other words, *tension is positive and compression is negative*.

Similarly, if a shear stress,  $\sigma_{zx}$ , is in the positive  $x$ -direction on a plane on which  $\hat{n}$  is positive, that shear stress is considered to be positive, and conversely. Thus, both shear stresses,  $\sigma_{xz}$  and  $\sigma_{zx}$ , in the diagram are positive.

As an example, consider the variation of  $u$  with depth in a glacier (Figure 2.4). As depicted by the arrows around the box in Figure 2.4,  $\sigma_{zx}$  is negative in the coordinate system shown. The velocity derivative,  $du/dz$ , is also negative ( $u$  decreases with increasing  $z$ ). Thus, the negative shear stress results in a negative velocity derivative, as one would expect.

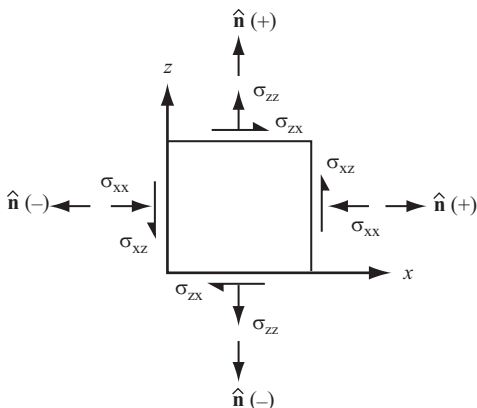


Figure 2.3 Sign convention for stresses in plane strain.

As may be evident from the discussion so far, Roman letters in equations will be italicized only when they represent a variable. Thus, because  $\sigma_{xx}$  is a specific stress,  $xx$  is not italicized, whereas in  $\sigma_{ij}$ , where  $i$  and  $j$  can take on values of  $x$ ,  $y$ , or  $z$ ,  $i$  and  $j$  are italicized. Greek symbols are not italicized.

## Tensors

The three-dimensional diagram in Figure 2.5 shows stress vectors on three faces of a cube. Similar stresses occur on the concealed faces, but they are in the opposite directions. The cube is considered to be infinitesimal, representing, say, a point in a glacier. Thus, stresses on any given face can be regarded as uniformly distributed and constant.

To completely describe the state of stress at this point, we need nine stress components; thus:

$$\begin{array}{lll} \sigma_{xx} & \sigma_{xy} & \sigma_{xz} \\ \sigma_{yx} & \sigma_{yy} & \sigma_{yz} \\ \sigma_{zx} & \sigma_{zy} & \sigma_{zz}. \end{array}$$

This assemblage of stress vectors is called a *second-rank tensor*. For comparison, a vector, like velocity, is a first rank tensor; to describe it we need its components along three coordinate axes, so we need three numbers. Similarly, pressure, a scalar, is a zero-rank tensor; it can be described with only one number, the magnitude of the pressure.

For steady (non-accelerating) uniform motion, forces must be balanced. Thus, to ensure that there is no tendency for the cube in Figure 2.5 to rotate, it is necessary that  $\sigma_{xy} = \sigma_{yx}$ ,  $\sigma_{xz} = \sigma_{zx}$ , and  $\sigma_{yz} = \sigma_{zy}$ . Such tensors are called *symmetric*.

When a tensor is symmetric, it is common to see, for example,  $xy$  used where, rigorously,  $yx$  might be more correct. Another common abbreviation that is often encountered is  $\sigma_x$  instead of  $\sigma_{xx}$ .

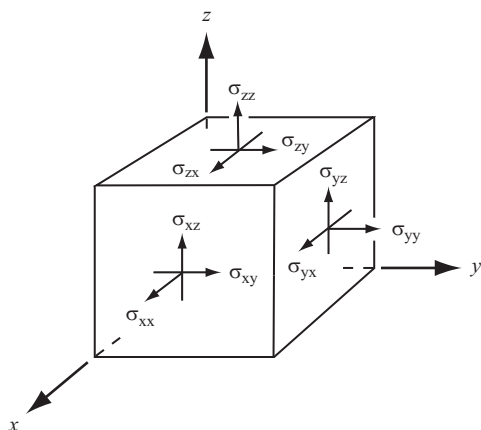


Figure 2.5 Stresses on a cube.

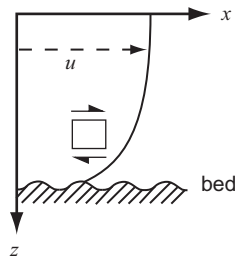


Figure 2.4 Vertical profile of horizontal velocity,  $u$ . Sense of shear stress,  $\sigma_{zx}$  is shown by arrows above and below the box.

## Strains and strain rates

In a deformable medium, stresses induce deformation or strain. Strain is defined as the change,  $\Delta\ell$ , in length of a line divided by the line's initial length,  $\ell_0$ , thus:  $\Delta\ell/\ell_0$ . The symbol  $\epsilon$  is commonly used to denote strain. The rate at which strain occurs, or the strain rate,  $d\epsilon/dt$ , is denoted by  $\dot{\epsilon}$ . The dot superscript is frequently used to denote a time derivative. As nine separate stress vectors are needed to fully describe the state of stress at a point, so also are nine strains or strain rates needed to describe the state of straining at that point. Thus, these assemblages of strains and strain rates are also second rank tensors, the strain and strain-rate tensors. As was the case with the stress tensor, these tensors, too, are symmetric, so  $\epsilon_{xy} = \epsilon_{yx}$ ,  $\dot{\epsilon}_{xz} = \dot{\epsilon}_{zx}$ , and so forth.

In Chapter 9, we will show that:

$$\dot{\epsilon}_{xy} = \frac{1}{2} \left( \frac{\partial u}{\partial y} + \frac{\partial v}{\partial x} \right) \quad (2.6a)$$

and similarly for the other shear strain rates. When  $x=y$ , this becomes:

$$\dot{\epsilon}_{xx} = \frac{\partial u}{\partial x} \quad (2.6b)$$

and so forth. Note that when the incompressibility condition, Equation (2.5), is written in terms of expressions like Equation (2.6b), it becomes:

$$\dot{\epsilon}_{xx} + \dot{\epsilon}_{yy} + \dot{\epsilon}_{zz} = 0. \quad (2.7)$$

Equations (2.6a) and (2.6b) define strain rates in terms of differences in velocity between points that are an infinitesimal distance (for example,  $dx$ ) apart. However, when measuring strains or strain rates in the laboratory or field, it is technically impossible to resolve differences in velocity over "infinitesimal" distances. Thus, we make measurements over longer distances and use what is called *logarithmic strain*. The quantity measured is the change in distance between two points over a time interval,  $\Delta t$ . If the initial distance is  $\ell_0$  and the final distance is  $\ell$ ,  $\dot{\epsilon}$  is defined as:

$$\dot{\epsilon} = \frac{1}{\Delta t} \ln \frac{\ell}{\ell_0}.$$

This relation will be derived in Chapter 9.

## Yield stress

In some materials there is no deformation at stresses below a certain stress, called the *yield stress*. The yield stress is a property of that particular material. In other materials, deformation rates are so low at low stresses that theoretical models sometimes assume the existence of a yield stress, even though there may not actually be one. Ice is such a material.

## Deviatoric stresses

Ice does not deform significantly in response to hydrostatic pressure alone. In other words, in a topographic depression containing ice (Figure 2.6), the hydrostatic (or cryostatic) pressure increases linearly with depth,  $z$ , at a rate  $\rho g z$ , where  $g$  is the acceleration due to gravity. As a rule of thumb, the pressure increases at a rate of 0.1 MPa for every 11 m of depth. Thus, it becomes quite high at large depths. However, if the surface of the ice in the depression is horizontal, as in a lake, the only deformation that would occur would be a relatively insignificant elastic compression.

On the other hand, if the ice surface were to slope gently (dashed line in Figure 2.6), and if points A and B are on a horizontal plane, then the pressure at A would be greater than the pressure at B. This pressure difference would result in a compressive strain between A and B. The strain rate would depend upon the small pressure difference, and not, in any significant way, on the much larger hydrostatic pressure at depth  $z$ . In other words, deformation is a result of the *non-hydrostatic stresses*.

It is convenient to define a stress, called the *deviatoric stress* or *stress deviator*, which reflects this principle. The deviatoric normal stress in the  $x$ -direction is:

$$\sigma'_{xx} = \sigma_{xx} - P \quad (2.8)$$

where  $P$  is the mean normal stress:

$$P = -\frac{1}{3}(\sigma_{xx} + \sigma_{yy} + \sigma_{zz}). \quad (2.9)$$

When all three normal stresses are equal, the stress is said to be isotropic and  $P$  is hydrostatic. This is the case in an incompressible material. As ice is nearly incompressible,  $P$  is approximately hydrostatic. As  $P$  is a normal stress, it contributes only to the normal stresses, and not to the shear stresses in Figure 2.5. In other words, the deviatoric shear stresses are the same as their non-deviatoric or total counterparts, but the deviatoric normal stresses are quite different from the total normal stresses.

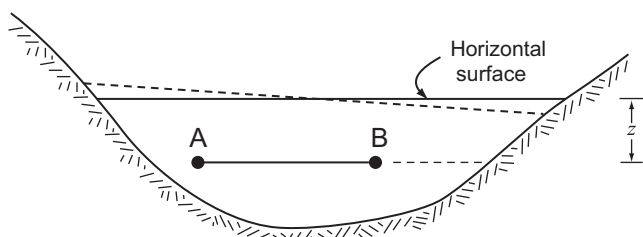


Figure 2.6 Sketch to illustrate non-hydrostatic pressure.

### Effective and octahedral shear stresses

Theoretical studies and a limited amount of experimental data suggest that the strain rate in a given direction in ice depends not only on the stress in that direction, but also on all of the other stresses acting on the medium. To take this into account, we define an *effective shear stress*,  $\sigma_e$ , and *effective strain rate*,  $\dot{\varepsilon}_e$ , by:

$$\sigma_e = \frac{1}{\sqrt{2}} \left( \sigma'_{xx}^2 + \sigma'_{yy}^2 + \sigma'_{zz}^2 + \sigma'_{xy}^2 + \sigma'_{yx}^2 + \sigma'_{xz}^2 + \sigma'_{zx}^2 + \sigma'_{yz}^2 + \sigma'_{zy}^2 \right)^{1/2} \quad (2.10)$$

and

$$\dot{\varepsilon}_e = \frac{1}{\sqrt{2}} \left( \dot{\varepsilon}_{xx}^2 + \dot{\varepsilon}_{yy}^2 + \dot{\varepsilon}_{zz}^2 + \dot{\varepsilon}_{xy}^2 + \dot{\varepsilon}_{yx}^2 + \dot{\varepsilon}_{xz}^2 + \dot{\varepsilon}_{zx}^2 + \dot{\varepsilon}_{yz}^2 + \dot{\varepsilon}_{zy}^2 \right)^{1/2}. \quad (2.11)$$

Alternatively, some glaciologists use the *octahedral shear stress*,  $\sigma_o$ , and *octahedral shear strain rate*,  $\dot{\varepsilon}_o$ , defined by:

$$\sigma_o = \frac{\sqrt{2}}{\sqrt{3}} \sigma_e \quad \text{and} \quad \dot{\varepsilon}_o = \frac{\sqrt{2}}{\sqrt{3}} \dot{\varepsilon}_e, \quad (2.12)$$

respectively.

### Principal stresses and strain rates

In Chapter 9 we will show that at any point in a medium it is always possible to orient a rectangular coordinate system in such a way that shear stresses vanish. Equation (2.10) then becomes:

$$\sigma_e = \left( \frac{\sigma'_{xx}^2 + \sigma'_{yy}^2 + \sigma'_{zz}^2}{2} \right)^{1/2}. \quad (2.13)$$

We give the name *principal stresses* to the remaining normal stresses; the axes in this coordinate system are called the *principal axes of stress*. Similarly, if the coordinate system is oriented such that shear strain rates vanish, the remaining strain rates are called the *principal strain rates* and the axes are the *principal axes of strain rate*.

By using Equation (2.13) to eliminate  $\sigma_e$  from the first of Equations (2.12), you will see that the octahedral shear stress is the root-mean-square of the principal stress deviators. Thus, when the coordinate axes are aligned parallel to the principal stresses, the octahedral shear stress is the resolved shear stress on the octahedral plane, a plane that intersects the three axes at points equidistant from the origin (Figure 2.7). Hence the name: octahedral shear stress.

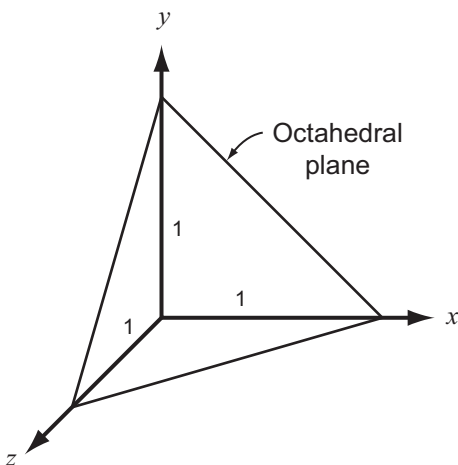


**Figure 2.7** A plane that intersects the  $x$ -,  $y$ -, and  $z$ -axes at points equidistant from the origin, in this case a unit distance, is called the octahedral plane. If similar planes are drawn involving the negative directions along the axes, the solid figure formed is a regular octahedron.

## The flow law

The most commonly used flow law for ice is Glen's flow law, named after John W. Glen upon whose experiments it is based (Glen, 1955). Glen originally wrote the flow law in the form:

$$\dot{\varepsilon}_e = \left( \frac{\sigma_e}{B} \right)^n \quad (2.14)$$

where  $B$  is a viscosity parameter that increases as the ice becomes stiffer, and  $n$  is an empirically determined constant. Most studies have found that  $n \approx 3$ . At low stresses, however,  $n$  appears to decrease to  $\sim 1.8$ , and at high stresses it rises to 4 (Goldsby, 2009). An alternative form of the flow law that is commonly used, and that we will use, is:

$$\dot{\varepsilon}_e = A\sigma_e^n. \quad (2.15)$$

$A$  is called the rate factor.  $B$  is normally given in  $\text{MPa yr}^{1/n}$ , while  $A$  is in  $\text{MPa}^{-n} \text{yr}^{-1}$  or  $\text{MPa}^{-n} \text{s}^{-1}$ . If the octahedral shear stress and strain rate are used, the numerical values of  $B$  and  $A$  must be adjusted accordingly, but the units stay the same.

Both forms of the flow law have their advantages, and as  $A = (1/B)^n$ , it is easy to convert between the two forms as long as  $n$  is known. The form  $\dot{\varepsilon}_e = A\sigma_e^n$  resembles conventional constitutive relations in rheology, and is also easier to generalize if greater precision is needed in situations involving complicated stress configurations (Glen, 1958). For example, some materials, when subjected to a shear stress, swell or contract perpendicular to the plane of shear. In other words, deformation occurs in

directions in which the stress is zero. Such rheologies require an extra term in the flow law, and this is more readily accommodated with a flow law of the form  $\dot{\epsilon}_e = A\sigma_e^n$ . So far, however, the forms presented in Equations (2.14) and (2.15) seem adequate to represent phenomena observed in studies of ice deformation, both in the laboratory and on glaciers, so the additional term is not needed.

In Chapter 9, we will show that if the principle axes of stress and strain rate coincide, as is normally the case, the flow law can be written as:

$$\dot{\epsilon}_{ij} = A\sigma_e^{n-1}\sigma'_{ij} \quad (2.16)$$

where  $i$  and  $j$  can represent  $x$  or  $y$  or  $z$ . Eliminating  $\sigma_e$  from Equations (2.15) and (2.16) yields:

$$\dot{\epsilon}_{ij} = A^{\frac{1}{n}}\dot{\epsilon}_e^{\frac{n-1}{n}}\sigma'_{ij}. \quad (2.17)$$

Equation (2.16) re-emphasizes a fundamental tenet of Glen's flow law mentioned earlier: namely that *the strain rate in a given direction is a function not only of the stress in that direction, but also of all of the other stresses acting on the medium*. Equation (2.17) shows that we can express this concept in terms of strain rates, which are generally easier to measure than stresses.

In the next several chapters we will be dealing with situations in which it is feasible to assume that one stress so dominates all of the others that the others can be neglected. However, the reader needs to be aware of the implications of this assumption.

# 3

## Mass balance

Glaciers exist because there are areas, generally at high elevations or in polar latitudes, where snow fall during the winter exceeds melt (and other losses) during the summer. This results in net accumulation, so this part of the glacier is called the *accumulation area* (Figure 3.1). As each snow layer is buried, the pressure of the overlying snow causes compaction, and movement of molecules in the liquid and vapor phases results in snow metamorphism. Snow that is more than a year old, and has thus been altered by these processes, is called *firn*. The end result of the firnification process, normally after several years, is solid ice.

Where there are lower elevations to which this ice can move, gravitational forces drive it toward these areas. In most cases, Antarctica being the principal exception, this eventually brings the ice into places where annual melt exceeds snow fall. Here, all of the winter snow and some of the underlying ice melts during the summer. This is called the *ablation area*. The line separating the accumulation and the ablation areas at the end of a melt season is called the *equilibrium line*. Along the equilibrium line, melt during the just-completed summer exactly equaled net snow accumulation during the previous winter.

Ice may also be lost by subaqueous melting and by calving. Both occur where glaciers terminate in water bodies, particularly marine ones. Subaqueous melting is especially important where seawater has access to the bottoms of floating ice tongues or shelves. Calving is a process in which blocks of ice, ranging in size from single ice crystals to thousands of cubic meters, break off of an ice cliff into a water body and float away to melt in more distant places. Calving is an important mode of ice loss from glaciers ending in the sea, and is the primary mode of ice loss from such glaciers in Antarctica.

In this chapter, we first discuss the transformation of snow to ice, and show how the processes involved result in a physical and chemical stratigraphy that, under the right circumstances, can be used to date ice that is thousands of years old. We then explore climatic factors that result in changes in the altitude of the equilibrium line or rate of calving, and hence in advance and retreat of glaciers. Finally, we discuss atmospheric circulation patterns that affect mass balance, and present estimates of global mass balance.

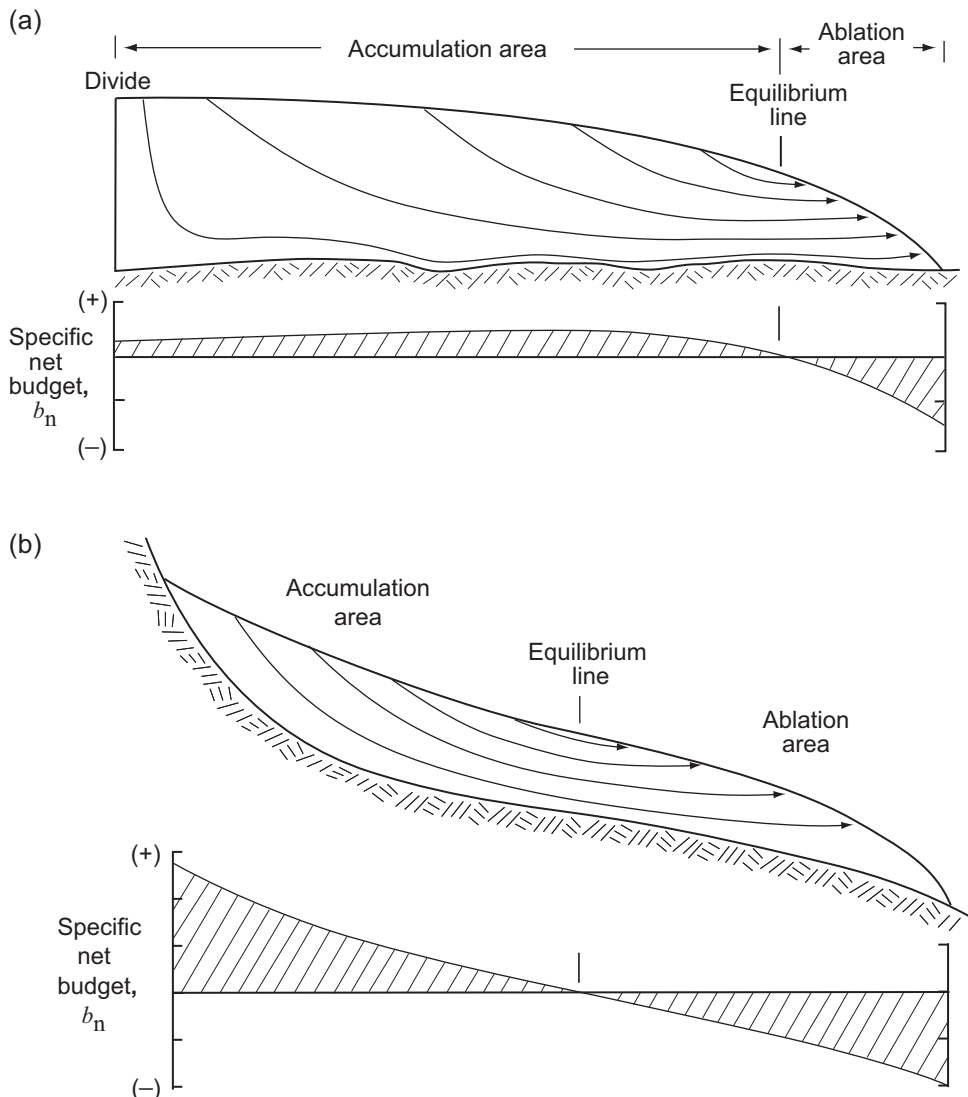


**Figure 3.1** Cross sections of: (a) a typical polar ice cap or ice sheet and (b) a typical valley glacier, showing the relation between equilibrium line and flow lines. Sketches are schematic, but relative proportions are realistic.

## The transformation of snow to ice

The first phase of the transformation of snow into ice involves diffusion of water molecules from the points of snowflakes toward their centers. This occurs because the vapor pressure is inversely proportional to the radius of curvature – the *Kelvin effect* (Legrand and Mayewski, 1997). The flakes thus tend to become rounded, or

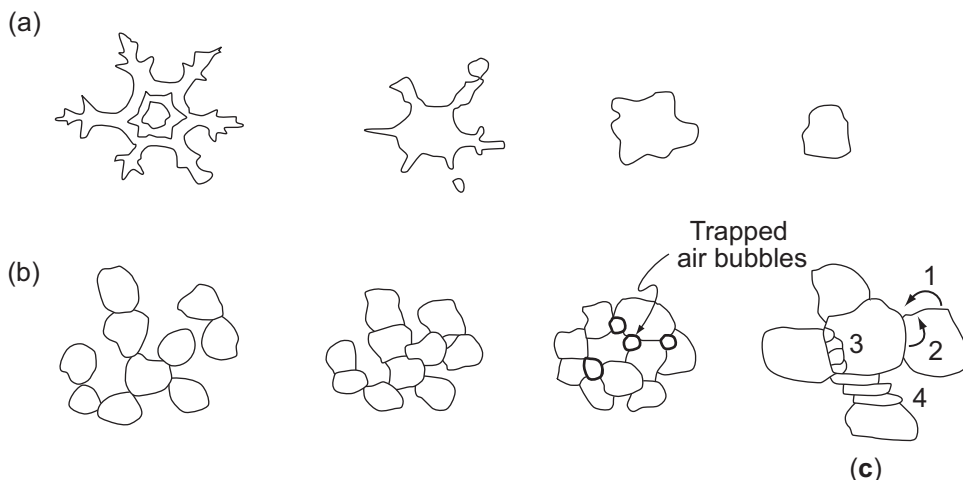


**Figure 3.2** Transformation of snow to ice. (a) Modification of snowflakes to a subspherical form. (b) Sintering. (c) Processes during sintering: 1 = sublimation, 2 = molecular diffusion within grains, 3 = nucleation and growth of new grains, and 4 = internal deformation of grains. (Based on Sommerfeld and LaChapelle, 1970, Figures 2, 16, and 17; and on Kinoshita, 1962, as reported by Lliboutry, 1964, Figure 1.14)

spherical (Figure 3.2a), reducing their surface area and, consequently, their surface free energy, which always tends toward a minimum. (The energy of a surface is higher than that of the bulk material owing to the presence of unsatisfied chemical bonds at the surface.) The surface free energy is also lower on larger grains because they have a lower ratio of surface area to volume, and thus lower radius of curvature. So grains tend to become larger.

The closest possible packing of spherical particles would be one with a porosity of about 26%, the so called *rhombohedral packing*. However, in natural aggregates of spheres of uniform diameter, the pore space is usually closer to 40%. In the case of firn, this corresponds to a density of  $\sim 550 \text{ kg m}^{-3}$ .

Further densification involves a process called *sintering* (Figure 3.2b), which involves transfer of material by sublimation and by molecular diffusion within grains, nucleation and growth of new grains, and internal deformation of the grains (Figure 3.2c). Sublimation is more important early in the transformation process when pore spaces are still large. Internal deformation increases in importance as the snow is buried deeper and pressures increase. In warm areas, the densification process is accelerated, both because grains may be drawn together by surface tension when water films form around them, and because percolating melt water may fill air spaces and refreeze.

An important transition in the transformation process occurs at a density of  $\sim 830 \text{ kg m}^{-3}$ . At about this density, pores become closed, preventing further air movement through the ice. Studies of the air thus trapped provide information on

the composition of the atmosphere at the time of close off (e.g. Raynaud *et al.*, 1993). Such studies, for example, have demonstrated that, over the past 400,000 years, atmospheric temperature and the volume of ice in glaciers and ice sheets are both closely related to the concentration of CO<sub>2</sub> in the atmosphere (Petit *et al.*, 1999). It takes longer for pores to close at colder temperatures. Thus, pore close off can occur at depths of tens to over a hundred meters and in ice over 2000 years old (Cuffey and Paterson, 2010, Table 2.2).

## Snow stratigraphy

At high elevations on polar glaciers, such as the Antarctic or Greenland ice sheets, there are areas where no melting occurs during the summer. At somewhat lower elevations, some melting does occur, and the meltwater thus formed percolates downward into the cold snow where it refreezes, forming lenses or gland-like structures. The higher of these two zones is called the *dry-snow zone* and the lower is the *percolation zone* (Figure 3.3) (Benson, 1961; Müller, 1962). In keeping with stratigraphic terminology in geology, parts of the annual snow pack on an ice sheet that have distinctive properties are referred to as *facies* – in this case the *dry-snow facies* and the *percolation facies*, respectively. The boundary between these two zones or facies, the *dry-snow line*, lies roughly at the elevation where the mean temperature of the warmest month is -6°C (Benson, 1962, cited by Loewe, 1970, p. 263).

At lower elevations, summer melting is sufficient to wet the entire snow pack. This is called the *wet-snow zone* (Figure 3.3). When this snow refreezes, a firm porous layer is formed. In downglacier parts of this zone, the basal layers of the

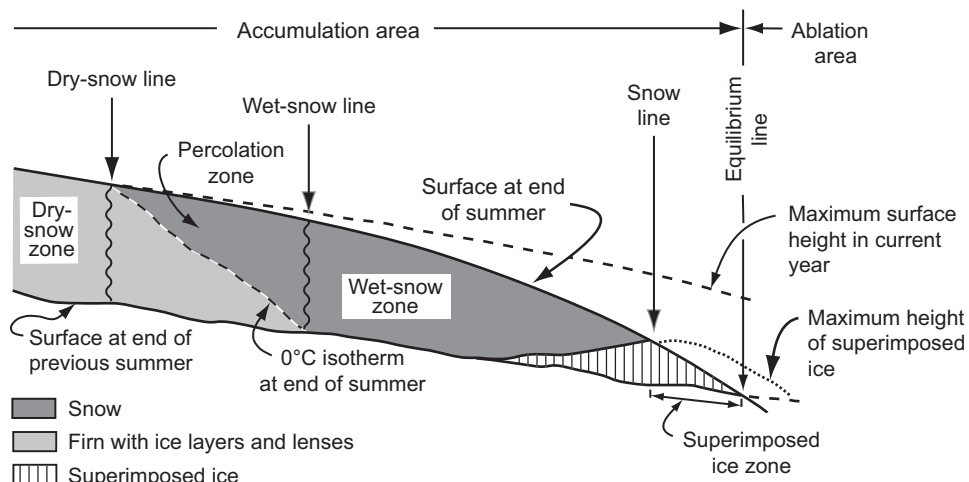


**Figure 3.3** Variation in snow facies with altitude (after Benson, 1962). The horizontal distance from the equilibrium line to dry-snow line is tens to hundreds of kilometers.

snow pack can become saturated with water. If the underlying ice is cold, this water-saturated snow may refreeze, forming ice that is called *superimposed ice*. As long as it is still undeformed, superimposed ice is readily recognized by its large and often highly irregular air bubbles.

At still lower elevations, only superimposed ice is present at the end of the melt season, and this is thus called the *superimposed ice zone*. The lower boundary of the superimposed ice zone at the end of the melt season is the equilibrium line.

On typical alpine glaciers, the first water percolating into cold snow at the beginning of the melt season may refreeze to form glands and lenses, as on polar ice sheets. However, by the end of the melt season, the entire snow pack will have been warmed to the melting point. Thus, neither the dry-snow nor the percolation facies are present on these glaciers. Furthermore, on a temperate glacier, heat conduction downward into the glacier beneath the snow pack is minimal, so little superimposed ice is formed.

Most of the warming of alpine snow packs is a result of the release of latent heat during refreezing of the first water to infiltrate. Freezing of 1 kg of water can warm 160 kg of snow 1°C. Conduction of heat from the surface is insignificant by comparison.

A distinct vertical zonation develops in annual layers of snow. The autumn snow is warmer than the overlying winter snow, so the vapor pressure is higher in the former. The resulting vapor-pressure gradient drives diffusion of molecules from autumn to winter snow. The autumn snow thus becomes coarser, and its density may decrease. These layers of coarse autumn snow are called *depth hoar*. Tabular crystals are the norm in depth hoar, but in extreme cases, large prism-shaped, pyramidal, or hollow hexagonal crystals develop.

### Dating ice using preserved snow stratigraphy

Depth hoar layers can be recognized in snow pits and at considerable depths in ice cores. Using such stratigraphic markers, glaciologists working in Antarctica and Greenland have been able to determine accumulation rates averaged over years or decades, and in deep cores, over millennia. In one deep core in central Greenland, the Greenland Ice Sheet Project 2 (GISP2) core, such physical stratigraphy, together with other annual markers, was used to date ice several thousand years old (Alley *et al.*, 1993; Meese *et al.*, 1997). It turned out that, at the end of the Younger Dryas, at ~11.7 ka, the accumulation rate increased by approximately a factor of two in a time span of only 3 or 4 years! The increase in the accumulation rate was attributed to a warming of the climate; this warming caused retreat of the ice margin and led, eventually, to the demise of the Laurentide Ice Sheet.

Visual stratigraphy, supplemented with measurements of chemical parameters that vary annually, is now used routinely to date the upper parts of cores. We will explore this further in Chapter 16.

## Mass balance principles

Broadly speaking, the change in mass of a glacier or ice sheet is:

$$\dot{B} = \dot{B}_m + \dot{B}_h + \dot{B}_L \quad (3.1)$$

where the dot represents a time derivative ( $dB/dt$ ) and the subscripts m, h, and L refer to meteorological effects, dynamic thickening or thinning, and terminus advance or retreat, respectively (Meier *et al.*, 2007). Let us discuss these in order.

The meteorological component of the mass balance,  $\dot{B}_m$ , is that due to winter snow fall and summer melt. A number of terms are used to describe different aspects of this part of the mass balance. The *winter balance* is the amount of snow that accumulates during the winter months, and the *summer balance*, a negative quantity, is the amount of snow and ice lost by melt. Over the course of a balance year, which is commonly taken to extend from the end of one melt season to the end of the next, the sum of the winter and summer balances is the *net balance*. Normally, these balances are expressed in terms of the thickness of a layer of water, or in *water equivalents*. When referred to a specific place on the glacier, they are expressed in  $m\text{ a}^{-1}$ , or  $\text{kg}\text{ a}^{-1}\text{m}^{-2}$ , and are called *specific balances*. Sometimes the word *budget* is used instead of balance, particularly when referring to the net balance. Traditionally, the health of a glacier has been assessed by measuring the summer and winter balances and subtracting them to obtain the net balance.

Significant amounts of accumulation may occur during the summer in the accumulation areas of polar glaciers, and conversely melt may occur throughout the winter in the ablation areas of some temperate glaciers. The terms summer and winter balance are applied with some poetic license in these instances. The most extreme example of this is on tropical glaciers where accumulation and melt may alternate on a time scale of hours to days. Despite these complications, the basic principles are still applicable.

Dynamic thickening (positive  $\dot{B}_h$ ) may occur when a kinematic wave resulting from a sustained positive meteorological mass balance moves from the accumulation area into the ablation area. We will discuss such waves further in Chapter 15. Dynamic thinning (negative  $\dot{B}_h$ ) occurs when forces resisting motion decrease, leading to acceleration and hence in stretching and thinning over and above that which occurs when the meteorological mass balance is negative. Terminus advance or retreat ( $\dot{B}_L$ ) occurs in a variety of ways. Slow advances or retreats may simply be consequences of a positive or negative meteorological mass balance, respectively. More rapid advances occur during surging, and retreats during calving and sometimes as a result of glacier lake outbursts, or jökulhlaups, that erode the terminus. If a negative  $\dot{B}_h$  resulting from stretching consists simply of an advance of the terminus, as in a surge, the ice “loss” through thinning is exactly compensated by

the “gain” through lengthening ( $\dot{B}_L = -\dot{B}_h$ ), so  $\dot{B} = 0$ . However, such stretching is commonly accompanied by strong melting or calving of the extended terminus, in which case  $\dot{B}_L < |\dot{B}_h|$ , leading to a negative mass balance.

We will see later in this chapter that a negative perturbation in  $\dot{B}_m$  can initiate dramatic retreat of the terminus of a tidewater glacier from its moraine, and in Chapter 13 that increased melting on ice shelves can lead to their collapse, and warming of ocean currents circulating beneath ice shelves can initiate irreversible retreat of the grounding line. Such changes have been dubbed *rapid dynamical change*. In our broad definition of mass balance (Equation 3.1) they are included in the terms  $\dot{B}_h$  and  $\dot{B}_L$ .

### Measuring the meteorological component of mass balance

Field-based measurements of  $B_m$  are made in a number of ways, and we will not go into them all here. Perhaps the most common method, and the one that is easiest to visualize, is to measure the height of the snow or ice surface on stakes that are placed in holes drilled in the glacier. The measurements are made first at the end of one melt season, then at the end of the following winter to obtain the winter balance, and finally at the end of the next melt season to obtain both the summer and the net balances. Snow density measurements must also be made in order to convert the winter accumulation and summer snow melt to water equivalents.

We define  $b_s(x,y,z)$  as the specific summer balance,  $b_w(x,y,z)$  as the specific winter balance, and  $b_n(x,y,z)$  as the specific net balance. Clearly,

$$b_n = b_s + b_w \quad (3.2)$$

and the overall state of health of the glacier can be evaluated from:

$$B_{bn} = \int_A (b_s + b_w) dA \quad (3.3)$$

where  $A$  is the area of the glacier and  $B_{bn}$  is the net balance due to meteorological processes. We commonly normalize  $B_{bn}$  to the area of the glacier, thus:  $\bar{b}_n = B_{bn}/A$ . When  $B_{bn}$  or  $\bar{b}_n$  are positive, the glacier is said to have a positive mass balance; if this condition persists for some years, the glacier advances, and conversely. Thus  $B_{bn}$  is an important parameter to measure and to understand.

It is convenient to restrict our discussion to variations in  $b_s$  and  $b_w$  with elevation,  $z$ . This is normally not valid in practice because of the effects of drifting and shading, which result in lateral variations in both accumulation and melt. The variation of  $b_n$  with elevation,  $b_n(z)$ , on a valley glacier in the Austrian Alps, Hintereisferner, is plotted in Figure 3.4. The curve labeled “o” in this figure represents the situation during a year in which the mass budget is balanced, or  $B_{bn} = 0$ . (Despite the low values of  $b_n$  at higher elevations,  $\int_A b_n dA = 0$  in this instance because, as is true of most valley glaciers, the width of Hintereisferner increases

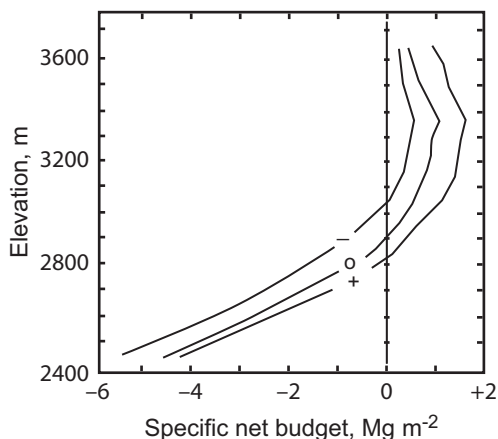


**Figure 3.4** Specific net budget,  $b_n$  plotted against elevation for Hintereisferner. Curve "o" is for a year of balanced mass budget, while curves “-” and “+” are for years of exceptionally negative or positive budget, respectively. (After Kuhn, 1981, Figure 1. Reproduced with permission of the author and the International Association of Hydrological Sciences)

with elevation.) Curves labeled “+” and “-” represent years of exceptionally positive or negative mass balance, respectively. Note that melting normally decreases nearly linearly with increasing elevation, so the lower parts of the curves in Figure 3.4 are relatively straight. However, at higher elevations in this particular case, snow fall decreases with elevation, resulting in curvature in the upper parts of the plot.

Programs of mass balance measurements normally continue for several years. Cumulative mass balances can then be calculated by summing the annual values of  $B_n$ . There are two ways of doing this, however. In the *conventional* approach,  $A$  in Equation (3.3) should be adjusted annually to reflect expansion or shrinkage of the glacier. (In practice, new maps of the glacier are not prepared every year, and as  $A$  varies slowly it is more common to use the same value of  $A$  for several years and then adjust it when a new map is made.) In the *reference-surface* approach (Elsberg *et al.*, 2001), on the other hand,  $A$  is the area of the glacier surface at a particular time, such as the time of the first mass balance survey if a good map exists for that time, and is not changed during the course of the program. The annual measurements are then adjusted to the level of the reference surface with the use of measured or estimated values of  $dB_n/dz$ . The conventional approach is better for hydrological forecasting and other applications when the actual change in glacier volume is desired. However, for studies of climate, the reference-surface approach is more useful because it provides a measure of climate change at a fixed reference elevation.

Mass balance is measured in this or similar ways on many valley glaciers and small ice caps, but such methods are clearly impractical on large ice sheets. During

much of the twentieth century this was a problem, as we knew the climate was warming but did not know how this was affecting the Greenland and Antarctic ice sheets, and thus what their contribution to sea level might be. Since the 1990s, however, satellites have revolutionized the measurement of mass balance on both valley glaciers and ice sheets.

### Satellite-based estimates of mass balance

Three types of satellite data are used to estimate mass balance. In what is referred to as the *input–output method*, the input, which includes both winter accumulation and summer runoff, is calculated with the use of a global climate model. The output is the flux of ice through a cross section of the glacier, close to the margin, where the ice thickness is known from radar or other data. The ice velocity through the cross section is determined with the use of Satellite-based interferometric synthetic aperture radar (InSAR). The radar data are used to generate high-resolution three dimensional images of a glacier surface from nearly the same point in space at two different times. Suitable images can be acquired by any of several different satellites. If the amount of movement between the times of acquisition of the images is less than a few meters, and changes in character of the ice surface due to melting or precipitation are minimal, superposition of the images reveals phase differences between the radar waves returned at the two different times. These phase shifts can be used to determine the velocity (Massonnet and Feigl, 1998).

The second approach utilizes two satellites of the Gravity Recovery And Climate Experiment (GRACE), launched in 2002. The GRACE satellites orbit in the same vertical plane and ~220 km apart. As the lead satellite passes over a place with slightly higher gravitational pull, it accelerates away from the trailing satellite. The change in distance between the two is used to determine  $g$ , the acceleration due to gravity. The change in  $g$  from one pass of the satellites to another over a glacier or ice sheet is used to calculate the change in mass of the ice body.

The third method utilizes either radar or laser altimetry to measure changes in ice-surface elevation through time. The European Remote-Sensing (ERS) satellites launched in the early 1990s use radar, and the Ice, Cloud, and land Elevation Satellite (ICESat) launched in 2003 uses a laser.

These satellite data require sophisticated processing (Velicogna, 2009; Arendt *et al.*, 2013) which we will not discuss in detail. InSAR images must be co-registered, the signal averaged and condensed, and a correction applied to the phase shift at each pixel to adjust for the difference in position of the satellite at the times of acquisition of the images (Goldstein *et al.*, 1993). GRACE, ERS, and ICESat data must be corrected for on-going glacio-isostatic adjustments resulting from Pleistocene deglaciation. GRACE data need to be adjusted for so-called leakage – the effect of distant changes in  $g$  on the local signal – and for any changes in groundwater levels in areas outside the permafrost zone. ICESat elevations are sensitive to the

slope of the topography, and estimates of changes in elevation between repeated passes of the satellite are affected by offsets between the satellite tracks. Corrections for any changes in the rate of firn compaction are also necessary (Zwally *et al.*, 2015). Despite these complications, GRACE and ICESat produced quite comparable results in a study of mass balances of glaciers in the Gulf of Alaska (Arendt *et al.*, 2013), and estimates of the mass balance of the Greenland and Antarctic ice sheets derived from GRACE and from an InSAR-based input–output model were found to agree within the limits of uncertainty of the two methods (Rignot *et al.*, 2011).

## Mass balance of polar ice sheets

Owing to their size, the accumulation pattern on polar ice sheets reflects both elevation and degree of continentality. If there is significant melting near the margin of a continental ice sheet, as is the case in Greenland but not Antarctica,  $b_n$  increases with elevation because the temperature decreases and the melt season becomes shorter. However, due to orographic effects storms also lose much of their moisture within a few hundred kilometers of the coast. Thus, in the interior of the Greenland and Antarctic ice sheets,  $b_n$  decreases with distance from the moisture source (and hence with increasing elevation). For example, in Antarctica accumulation rates are typically  $0.3\text{--}0.6 \text{ m a}^{-1}$  (water equivalent) around the perimeter of the continent, but decrease to  $<0.1 \text{ m a}^{-1}$  at the South Pole (Figure 3.5) (Giovinetto and Zwally, 2000). Thus, along the margins of ice sheets, accumulation patterns resemble those of maritime glaciers, while between the margins and the interiors the pattern reflects the change from a maritime to a continental environment.

## Effect of albedo on mass balance

The albedo is the fraction of the incoming shortwave (ultraviolet) radiation reaching Earth's surface that is reflected as longwave (infrared) radiation. Fresh snow reflects 80–90% of the incoming radiation, so it has an albedo of 0.80–0.90. As snow matures and snowflakes become rounded and larger, the albedo decreases. Both rounding and grain growth occur faster at warmer temperatures (Wiscombe and Warren, 1981). Since the mid 1990s the mean summer (June, July, August) albedo of the Greenland ice sheet has decreased  $0.02 \pm 0.004$  per decade, a trend which Tedesco *et al.* (2016) attribute to such an increase in grain size due to climate warming.

Further decreases in albedo occur if and when the snow pack becomes saturated with water, and then when bare ice is exposed in the superimposed ice and ablation

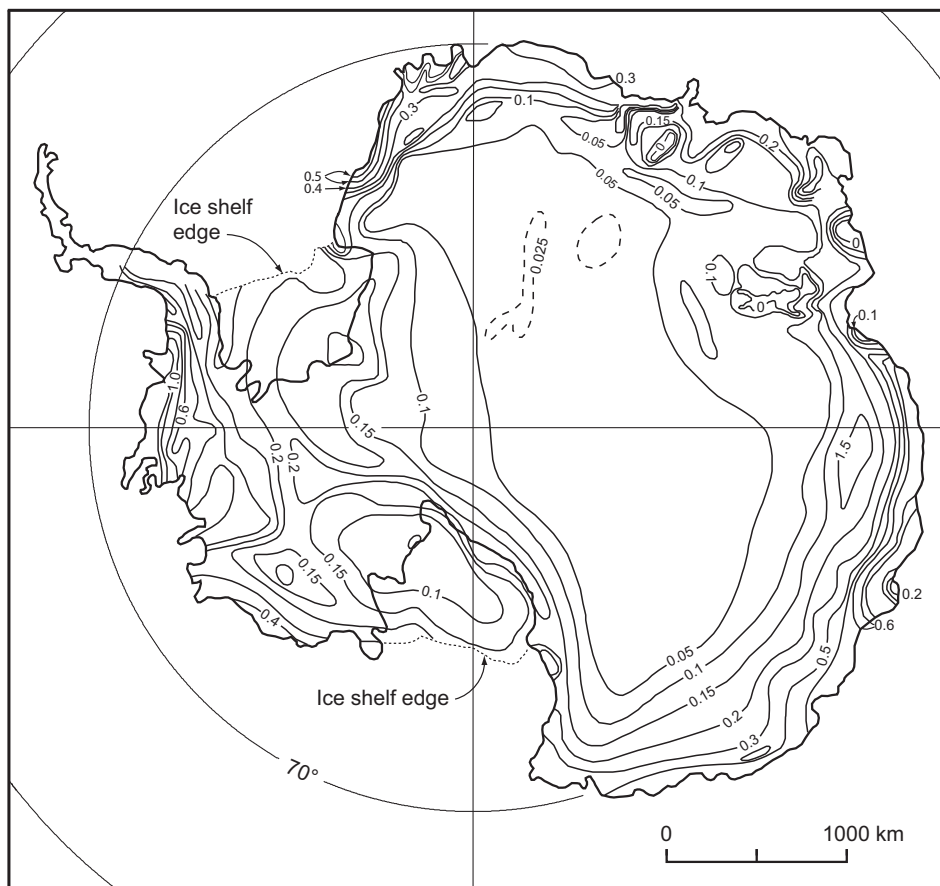


**Figure 3.5** Mass balance pattern in Antarctica. Contours at 0.025 (dashed), 0.05, 0.1, 0.15, 0.2, 0.3, 0.4, 0.5, 0.6, 0.8, 1.0, and 1.2 m a<sup>-1</sup> (water equivalent). (After Giovinetto and Zwally, 2000. Reproduced with permission of the authors and the International Glaciological Society)

zones. Bare ice typically has an albedo of ~0.5 (NSIDC, 2017; Warren *et al.*, 2012). If the ice contains dirt, a thin layer of which has accumulated on the ice surface during previous melt seasons, the albedo can be as low as 0.1 (Adhikari *et al.*, 2000). Dust and aerosols deposited from the atmosphere have the same effect.

Where dirt-bearing ice becomes exposed in the lower part of an ablation area, multiple years of ablation can result in the accumulation of a layer of low-albedo debris on the ice surface. While the layer is thin, heat absorbed by it increases the rate of melting of the underlying ice. The maximum rate occurs under layers ~10 mm thick, and can be as much as 70% greater than the melt rate of clean ice (Nakawo and Rana, 1999). Once the thickness of the layer exceeds ~20 mm, however, it acts as an insulator, reducing melt. The effectiveness of the insulation depends on the grain size and moisture content of the till, the orientation of the

surface with respect to insolation, and other meteorological variables. Moist till is a more effective insulator because some of the incident radiation is used to evaporate the moisture rather than penetrating to the ice–till interface (Östrem, 1959). The melt rate decreases asymptotically with increasing debris thickness: a 100 mm layer can reduce melt by 60% and a 500 mm layer by 90% (Kirkbride, 2011).

### Effect of black carbon on albedo

Black carbon, or soot, is produced by combustion of wood, biomass, and fossil fuels, and consists of small spheres of insoluble pure carbon,  $<2.5\text{ }\mu\text{m}$  in diameter, that are harmful to human health. Black carbon absorbs solar radiation strongly, so when it lands on a glacier or ice sheet it reduces the albedo and enhances melting.

In two high-elevation ice cores from the Alps the amount of black carbon began to increase in  $\sim 1860$ , coincident with an increase in industrialization in Europe (Painter *et al.*, 2013). At this time the climate was getting colder and winter precipitation was apparently unchanged. Despite this, some glaciers in the Alps were retreating. Numerical modeling suggested that something other than climate was driving the retreat (Huybrechts *et al.*, 1989). Calculations confirmed that the black carbon emanating from industrial sites could have increased melting by  $\sim 0.9\text{ m (w.e.) per year}$ , and that this would have resulted in glacier retreats comparable in magnitude to those observed (Painter *et al.*, 2013). Sigl *et al.* (2018), on the other hand, argue that most of the retreat occurred in the two decades before black carbon began to increase.

Most black carbon is washed out of the atmosphere by precipitation fairly close to its source, but significant amounts reach altitudes of 3–5 km, forming plumes that drift thousands of kilometers (Ramanathan and Carmichael, 2008). Thus, black carbon is likely playing a role in the disappearance of sea ice from the Arctic and in the mass balance of the Greenland Ice Sheet. It appears to have been a factor in an extreme event in Greenland in 2012, when melting extended over the entire ice sheet (Keegan *et al.*, 2014).

### Climatic causes of fluctuations in the meteorological component, $B_m$

Let us explore quantitatively how changes in winter precipitation, summer temperature, and radiation balance affect a glacier's mass balance. We simplify the analysis by letting  $b_w$  be composed of precipitation and drifting alone, thus ignoring mass additions by condensation and avalanching. Likewise, we take  $b_s$  to be a function only of surface melt, ignoring mass losses by evaporation, calving, bottom melting, and so forth. Although we assume that mass additions and losses by condensation

and evaporation, respectively, are negligible, the energy involved in these phase change processes is taken into consideration in the following analysis.

Surface melting is controlled by the available energy,  $Q$  ( $\text{kJ m}^{-2}\text{d}^{-1}$ ), thus:

$$\sum Q = R + H + V \quad (3.4)$$

in which  $R$  is the net radiation (the difference between the incoming, predominantly short wave radiation and the outgoing, predominantly long wave radiation);  $H$  is the sensible heat input; and  $V$  is the latent heat input due to condensation, or loss due to evaporation (Kuhn, 1981). Then, neglecting any summer snow fall:

$$-b_s = \frac{T}{L} \sum Q \quad (3.5)$$

where  $T$  is the length of the melt season in days,  $L$  is the latent heat of fusion,  $334 \text{ kJ kg}^{-1}$ , and the summation is over the melt season. (In the remainder of this discussion it will be convenient to use  $\text{kg m}^{-2} \text{a}^{-1}$  for the units of mass balance.)

Assume further that the transfer of sensible and latent heat to the glacier surface is proportional to the temperature difference between the air and the glacier surface, thus:

$$H + V = \gamma(T_a - T_s) \quad (3.6)$$

where  $T_a$  and  $T_s$  are the temperatures of the air and the glacier surface, respectively, and  $\gamma$  is a constant of proportionality. Kuhn (1989) suggests that  $\gamma$  lies between 0.5 and  $2.7 \text{ MJ m}^{-2} \text{ d}^{-1} \text{ K}^{-1}$ ; a value frequently found for firn is  $1.0 \text{ MJ m}^{-2} \text{ d}^{-1} \text{ K}^{-1}$ , while a reasonable mean value for glacier ice is  $\sim 1.7 \text{ MJ m}^{-2} \text{ d}^{-1} \text{ K}^{-1}$ . The range of values reflects the fact that the actual heat transfer is strongly influenced by such factors as the wind speed and the roughness and albedo of the glacier surface.

Combining Equations (3.2), (3.4), (3.5), and (3.6), rearranging terms, and writing all of the parameters as functions of elevation,  $z$ , yields:

$$b_w(z) = \frac{T}{L} [R(z) + \gamma(T_a(z) - T_s)] + b_n(z) \quad (3.7)$$

in which  $R$ ,  $T_a$ , and  $T_s$  are mean daily values over the melt season. As we are dealing with melting conditions,  $T_s = 0$ , and does not vary with  $z$ .

Curves “–,” “o,” and “+” in Figure 3.4 are nearly parallel to one another, suggesting that one may be “derived” from another simply by a lateral translation. Such a translation, however, results in a change in the equilibrium line altitude (ELA), represented in Figure 3.4 by the point where the curves cross the 0 specific net balance line. This suggests that changes in equilibrium line altitude may be a fairly good measure of the impact of climate variations. The effects of changes in the principle measures of climate, namely precipitation and temperature, on the ELA are best studied with the use of perturbation theory, a mathematical technique with many applications. We adopt the approach used by Kuhn (1981).

At the equilibrium line,  $b_n(z) = 0$  by definition. Thus if  $h_o$  is the elevation of the equilibrium line in a year of balanced mass budget:

$$b_w(h_o) = \frac{T}{L} [R(h_o) + \gamma(T_a(h_o) - T_s)]. \quad (3.8)$$

The standard approach in perturbation theory is to now rewrite Equation (3.8) for a situation in which the equilibrium line, in a perturbed state, is at an elevation,  $h$ , which is slightly higher or lower than in the “o” state. Thus, letting primed values represent the perturbed state, we have:

$$b'_w(h) = \frac{T}{L} [R'(h) + \gamma(T'_a(h) - T_s)].$$

Now subtract Equation (3.8) from this new relation:

$$b'_w(h) - b_w(h_o) = \frac{T}{L} [R'(h) - R(h_o) + \gamma(T'_a(h) - T_a(h_o))]. \quad (3.9)$$

Any of the primed parameters in Equation (3.9) that vary with  $z$  can be represented by perturbation equations of the form, using  $T_a$  as an example:

$$T'_a(h) = T_a(h_o) + \frac{\partial T_a}{\partial z} \Delta h + \delta T_a. \quad (3.10)$$

Figure 3.6 is a graphical representation of Equation (3.10). The lapse rate,  $\partial T_a / \partial z$ , during a year of balanced mass budget is represented by the slope of the slanting solid line;  $\Delta h$  represents a change in altitude of the equilibrium line. Thus,  $\frac{\partial T_a}{\partial z} \Delta h$  represents the change in temperature that would be expected simply because the ELA changed. However, the mean summer air temperature at this elevation may have been  $\delta T_a$  higher than it would have been during a year of balanced mass budget. So, to obtain the mean air temperature,  $T'_a$ , at elevation  $h$  during a summer during which the ELA was  $\Delta h$  higher than usual, start with  $T_a(h_o)$  and, following the arrows in Figure 3.6, add  $\frac{\partial T_a}{\partial z} \Delta h$ , keeping in mind that  $\partial T_a / \partial z$  is negative so this is a negative number, and then add  $\delta T_a$ .

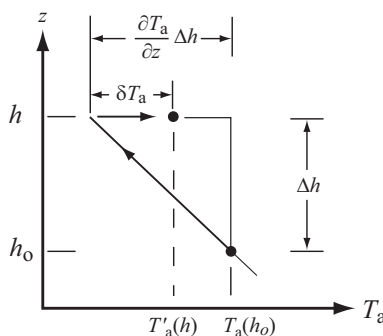


**Figure 3.6** Sketch illustrating parameters in Equation (3.10).

Writing Equations similar to (3.10) for  $b_w$  and  $R$ , rearranging them, and substituting into Equation (3.9) yields:

$$\frac{\partial b_w}{\partial z} \Delta h + \delta b_w = \frac{\mathbf{T}}{L} \left[ \frac{\partial R}{\partial z} \Delta h + \delta R + \gamma \left( \frac{\partial T_a}{\partial z} \Delta h + \delta T_a \right) \right]. \quad (3.11)$$

The significance of this relation can be elucidated with the use of a numerical example. Suppose  $\partial b_w/\partial z = 1 \text{ kg m}^{-2} \text{ m}^{-1}$ ,  $\mathbf{T} = 100 \text{ d}$ ,  $\gamma = 1.7 \text{ MJ m}^{-2} \text{ d}^{-1} \text{ K}^{-1}$ , and  $\partial T_a/\partial z$  is  $-0.006 \text{ K m}^{-1}$ . Suppose further, for the purposes of this example, that  $\partial R/\partial z = 0$ , as the radiation input does not vary significantly with elevation. Now consider a 100 m ( $= \Delta h$ ) increase in the ELA in a particular year. The changes  $\delta b_w$ ,  $\delta R$ , and  $\delta T_a$  that would be sufficient, if they occurred alone, to cause this change in ELA are given in Table 3.1. However, to gain familiarity with this relation, the reader is encouraged to carry out this calculation on his or her own.

To place these results in perspective, at 3050 m on Hintereisferner in the Austrian Alps, an elevation that is slightly above the normal position of the equilibrium line, the mean winter snow fall,  $b_w$ , is  $1620 \text{ kg m}^{-2}$  and its standard deviation is  $540 \text{ kg m}^{-2}$ . Likewise, the mean summer temperature,  $T_a$ , is  $+0.4^\circ\text{C}$ , and its standard deviation is  $0.8^\circ\text{C}$ . Comparing these standard deviations with the values of  $\delta b_w$  and  $\delta T_a$  in Table 3.1, it is clear that a 100 m change in the ELA could result, with nearly equal likelihood, either from a change in  $b_w$  or from a change in  $T_a$ . Similarly, the total radiation input is  $\sim 46 \text{ MJ m}^{-2} \text{ d}^{-1}$ , while the loss is  $\sim 40 \text{ MJ m}^{-2} \text{ d}^{-1}$ , leaving a mean radiation balance,  $R$ , of  $\sim 6 \text{ MJ m}^{-2} \text{ d}^{-1}$ . Changes of  $1.35 \text{ MJ m}^{-2} \text{ d}^{-1}$ , due to changes in cloud cover for example, are small compared with the total radiation budget, and thus are not unreasonable.

For comparison, the mean winter balance on Barnes Ice Cap on Baffin Island is  $\sim 400 \text{ kg m}^{-2}$  (Hooke *et al.*, 1987). Here, a  $\delta b_w$  of  $-400 \text{ kg m}^{-2}$  is highly improbable, as this would mean virtually no accumulation. Thus in this case, a 100 m change in the ELA would most likely be a result of a change in  $T_a$ . This is consistent with a study by Sneed *et al.* (2008), which found that, on the south dome of the ice cap, thinning rates of  $0.76 \pm 0.35 \text{ m a}^{-1}$  between 1984 and 2005 and of  $1.0 \pm 0.07 \text{ m a}^{-1}$  between 2004 and 2006 were well correlated with the summer temperature anomalies during those years.

This comparison illustrates a fundamental difference between glaciers in relatively dry but cold areas, areas that we refer to as having a *continental* climate, and

**Table 3.1** Possible causes of a 100 m increase in ELA

$\delta b_w = -400 \text{ kg m}^{-2}$	if $\delta T_a = \delta R = 0$
$\delta R = +1.35 \text{ MJ m}^{-2} \text{ d}^{-1}$	if $\delta b_w = \delta T_a = 0$
$\delta T_a = + 0.8^\circ\text{C}$	if $\delta b_w = \delta R = 0$

glaciers in warmer wetter *maritime* climates. Glaciers in continental settings owe their existence to low temperatures, and fluctuations in their mass budgets are strongly (inversely) correlated with mean summer temperature. Conversely, glaciers in maritime settings form in response to high winter snow fall; on such glaciers, the mass balance is less well correlated with  $T_a$  alone, and correlations can be improved significantly by adding winter precipitation to the regression. In fact, on some maritime glaciers the correlation of net balance with  $b_w$  alone is quite good (Walters and Meier, 1989, p. 371).

In the above analysis,  $T_a$  and  $R$  have been treated as independent variables. This is not strictly correct because an increase in the near-surface air temperature,  $T_a$ , of 1°C increases downward longwave radiation flux (Kruk *et al.*, 2010), and hence  $R$ , by about 0.3 MJ m<sup>-2</sup>d<sup>-1</sup> (Kuhn, 1981). This is a result of the increase in “black body” radiation, which varies as  $T^4$ . Incorporating this effect into the above calculation (Table 3.1) reduces  $\delta T_a$  to +0.7°C.

### The budget gradient

The rate of increase in  $b_n$  with height,  $z$ , at the elevation of the equilibrium line during a year of balanced mass budget,  $\left(\frac{db_{no}}{dz}\right)_{h_0}$ , is called the *budget gradient* (Figure 3.7 (or 3.4)). The budget gradient tends to be high on glaciers in maritime settings and low in continental settings. Typical values might be 10 kg m<sup>-2</sup> m<sup>-1</sup> a<sup>-1</sup> in the former and 3 kg m<sup>-2</sup> m<sup>-1</sup> a<sup>-1</sup> in the latter (Haefeli, 1962). High budget gradients represent situations in which there is a lot of accumulation above the equilibrium line and a lot of ablation below it, and conversely. High budget gradients are thus indicative of high flow rates, as a lot of ice must be transferred from the accumulation area to the ablation area in order to maintain a steady state profile, and this suggests high subglacial erosion rates. For these reasons, Shumskii (1964, p. 442) referred to  $db_{no}/dz$  as the energy of glaciation, and Meier (1961) called it the activity index.

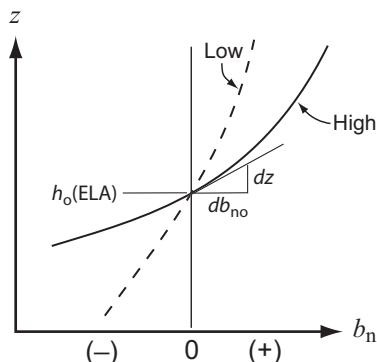


**Figure 3.7** Sketch illustrating the budget gradient.

To explore factors controlling the budget gradient, rearrange Equation (3.7) and take its derivative, noting again that  $T_s = 0$  on a melting glacier surface:

$$\frac{\partial b_{no}}{\partial z} = \frac{\partial b_w}{\partial z} - \frac{\mathbf{T}}{L} \left[ \frac{\partial R}{\partial z} + \gamma \frac{\partial T_a}{\partial z} \right]. \quad (3.12)$$

(Here, and in the next part of this discussion, all derivatives should be understood as being evaluated at the elevation of the equilibrium line during a year of balanced budget.)

On valley glaciers, the precipitation gradient,  $\partial b_w/\partial z$ , is commonly almost negligible. It may become significant if snow drift is important at higher elevations, and is also larger in areas where a significant amount of the summer precipitation occurs as snow at high elevations and rain at low elevations. In the Alps, where this is frequently the case, Kuhn (1981) suggests that a value of  $0.5 \text{ kg m}^{-2} \text{ m}^{-1} \text{ a}^{-1}$  is reasonable.

The net radiation gradient,  $\partial R/\partial z$ , is small as long as snow covers the ablation area. However, once ice is exposed, particularly if it has a thin dirt cover, the albedo drops and there is a significant change in  $R$  across the firn edge, or boundary between firn and ice. The first ice to become exposed is normally near the snout of the glacier or the margin of an ice cap, and the firn edge rises as the melt season progresses. Taking this into consideration,  $\frac{\mathbf{T}}{L} \left( \frac{\partial R}{\partial z} \right)$  may be as high as  $\sim 7 \text{ kg m}^{-2} \text{ m}^{-1}$  over a 120-day melt season (Kuhn, 1981).

The lapse rate,  $\partial T_a/\partial z$ , is limited by the dry adiabatic rate,  $\sim 0.010^\circ\text{C m}^{-1}$ , but a more realistic free air lapse rate along a glacier surface is  $\sim 0.007^\circ\text{C m}^{-1}$ . Thus, for a 120-day melt season,  $\frac{\mathbf{T}\gamma}{L} \left( \frac{\partial T_a}{\partial z} \right)$  is  $\sim 4.3 \text{ kg m}^{-2} \text{ m}^{-1}$ .

So, to explain the differences in  $\partial b_{no}/\partial z$  between maritime and continental climates, the dominant terms are those involving the lapse rate and, below the equilibrium line, the radiation balance. As  $\partial T_a/\partial z$  is likely to be comparable in maritime and continental settings, differences between the two settings are largely due to differences in  $\mathbf{T}$  and  $\partial R/\partial z$ . Melt seasons in high arctic continental settings may be a half to a third as long as those in, say, the Alps. Similarly, glaciers in continental settings also tend to be cleaner, thus reducing the albedo contrast across the firn edge, and hence the effective  $\partial R/\partial z$ . Differences in  $\partial b_w/\partial z$  may contribute some, as summer rain is less likely to be a factor in arctic continental areas.

During a year of balanced mass budget, the ratio of the area of the accumulation zone to that of the entire glacier, the *accumulation-area ratio*, is typically  $\sim 0.7$  (Glen, 1963). Using terminal and recessional moraines, one can use this ratio to estimate the change in size of an accumulation area, and hence the change,  $\Delta h$ , in ELA during a glacier retreat. Then the imbalance,  $b_{ni}$  (the difference between the “o”: curve and either the “+” or the “-” curves in Figure 3.4) is:

$$b_{ni}(h) = - \left( \frac{\partial b_{no}}{\partial z} \right)_{h_0} \Delta h. \quad (3.13)$$

Thus, if moraines suggest that an equilibrium line rose by an amount  $\Delta h$ , and if  $(\partial b_{no}/\partial z)_{ho}$  can be estimated,  $b_{ni}(h)$  can be calculated. To a good approximation,  $b_{ni}(h)$  is equal to the average of  $b_{ni}(z)$  over the glacier. In this way, one can estimate the change in climate that produced an observed change in glacier area.

## Loss of ice by calving ( $\dot{B}_L$ )

Over the last few decades, in an effort to better quantify mass balances and, thus, predict the response of glaciers to climate warming, the process of calving has attracted considerable attention. Calving occurs at the termini of valley glaciers ending in lakes or the ocean, at the edges of ice shelves, and from glaciers ending in cliffs where hanging valleys join deeper trunk valleys. The latter can pose a serious hazard for communities in the trunk valleys (Röthlisberger, 1974). Here we focus on the first three situations.

Over 38% of the world's glaciers end in the sea (Vaughan *et al.*, 2013), and are therefore called *tidewater glaciers*. A much smaller but unknown percentage end in freshwater lakes. Most tidewater glaciers are in polar regions. Calving is commonly the dominant mode of mass loss from these glaciers. It has been estimated, for example, that in 2001 over 40% of the ice loss from Greenland was through calving from tidewater outlet glaciers, and over 80% of that from Antarctica was by calving, largely from ice shelves (Table 3.2a). It is also widely believed that the demise of the Late Pleistocene Northern Hemisphere ice sheets was facilitated by loss of ice in calving bays that formed at the ends of outlet glaciers and migrated rapidly headward. Such calving would resemble that in grounded tidewater glaciers.

The terminal regions of tidewater glaciers are commonly intensely crevassed, and this affects the size of the blocks released. Those calving from the subaerial part of the face range in size from fractions of a cubic meter to  $\sim 10^4 \text{ m}^3$ . Others, commonly larger, break off below the water surface and float upward. There is also a constant flux of smaller fragments from both subaerial and submarine sections of the calving face. Most of these are probably released by melting along grain boundaries. In contrast, ice shelves are not as intensely crevassed as tidewater glaciers, so blocks calving from them commonly range from  $10^5$  to  $10^{11} \text{ m}^3$ .

While the processes of calving from grounded tidewater glaciers and floating ice shelves both involve propagation of fractures (Chapter 4), it seems likely that the origin of the stresses is substantively different in the two cases.

### Calving from tidewater glaciers

Calving from tidewater glaciers is multifaceted and poorly understood. The calving rate depends on the shape of the submerged part of the calving face and on the strength of the ice. The face shape is affected by drag at the bed and by melting on

**Table 3.2** Estimates of mass balance of the Greenland and Antarctic ice sheets and of smaller glaciers and ice caps in (a) 2001 and (b) 2010.a. Estimates for 2001<sup>a</sup>

Location	Accumulation, Gt a <sup>-1</sup>	Runoff, Gt a <sup>-1</sup>	Calving, Gt a <sup>-1</sup>	Bottom melting, Gt a <sup>-1</sup>	Net balance, Gt a <sup>-1</sup>	Equivalent sea-level rise, mm a <sup>-1</sup>
Greenland	520 ± 26	297 ± 32	235 ± 33	32 ± 3	-44 ± 53	0.12 ± 0.15
Antarctica	2246 ± 86	10 ± 10	2072 ± 304	540 ± 26	-376 ± 384	1.03 ± 1.06
Glaciers <sup>b</sup>	688 ± 109	778 ± 114			-91 ± 36	0.25 ± 0.10
Total					-511 ± 389	1.41 ± 1.07

b. Estimates for 2010<sup>c</sup>

Location	Net balance, Gt a <sup>-1</sup>			Acceleration, Gt a <sup>-2</sup>	Equivalent sea-level rise, mm a <sup>-1</sup>
	MB	GRACE	Mean		
Greenland	-350 ± 51	-286 ± 33	-318 ± 30	-19.5 ± 8	0.88 ± 0.08
Antarctica	-265 ± 150	-150 ± 75	-207 ± 84	-13.9 ± 10	0.57 ± 0.23
Glaciers <sup>b</sup>			-449 ± 95	-11.8 ± 6	1.24 ± 0.26
Total			-974 ± 130	-45.1 ± 7	2.68 ± 0.36

<sup>a</sup> Data from Church *et al.* (2001, p. 651 and Tables 11.3 and 11.4).<sup>b</sup> Ice caps and valley glaciers in Antarctica, Greenland, and elsewhere.<sup>c</sup> Data from Rignot *et al.* (2011). Mean of values from mass balance (MB) and GRACE methods. Glacier data from paragraph 16.

the submerged part of the face. The ice strength is affected by the extent of pre-existing crevassing resulting from extending longitudinal strain in the last several kilometers of the glacier. Ice near the termini of tidewater glaciers is also commonly temperate, so water along crystal boundaries weakens it.

Some crevasses penetrate the full thickness of a glacier. When this happens, blocks of ice hundreds of meters in length, width, and height are dislodged. They normally topple backwards, with the submerged foot moving outward and upward, resulting in mayhem at the water surface. More commonly, crevasses are closely spaced and only a few tens of meters deep, forming serac fields. This crevassing is intensified by additional longitudinal tensile stresses near the calving face, resulting from an imbalance of forces normal to the subaerial part of the face. These tensile stresses increase rapidly with height of the subaerial part of a calving face (Hanson and Hooke, 2000).

Vertical compressive stresses also increase rapidly with height of the subaerial calving face. Near the base of a 60–80 m face, they reach 0.55–0.70 MPa. At these stresses, the compressive strength of ice is commonly exceeded (S. Jones, 1982;

Moore *et al.*, 2010). A serac, unsupported by shear stresses on its up-ice side and unconfined on its down-ice side, is then likely to collapse. This is probably why subaerial parts of calving faces rarely exceed 60 m to 80 m in height (Brown *et al.*, 1982). Laboratory experiments suggest that failure probably occurs by slip on shear planes dipping  $\sim 30^\circ$  with respect to the axis of compression (Schulson, 1999). This likely explains why many subaerial calving events appear to consist of vertical collapse of large columns and slabs of ice (Williams, 2017 (youtube video)).

Submerged parts of calving faces may extend to depths of a few hundred meters. Ice blocks also become detached from these faces and float upward to the surface, creating dramatic disturbances as they emerge. This is particularly likely when melting near the water line results in a submerged ice foot extending outward from the glacier. Careful observations of calving events on San Rafael Glacier in Chile suggest, however, that the volume of ice released by such submarine events is way too small to account for the observed rate of retreat of the subaerial part of the terminus (Warren *et al.*, 1995). This suggests that melting below the water surface may be an important part of the process we call calving. This suspicion is reinforced by the observation that, in Alaska, calving rates are highest in October (Meier *et al.*, 1985), when the water is warmest (Matthews, 1981; Walters *et al.*, 1988); by observations in Svalbard showing that the calving rate is well correlated with ocean temperatures in the upper 60 m of the water column (Luckman *et al.*, 2015); by detailed measurements of water, heat, and salinity balance in a fjord in front of a calving glacier in Alaska, implying melt rates of meters per day on the calving face (Motyka *et al.*, 2003, 2013); and by sonar observations showing that submerged parts of calving faces of some outlet glaciers in Greenland are undercut (Rignot *et al.*, 2015).

Undercutting appears to be concentrated in areas where freshwater is emerging from tunnels at the base of a calving face (Fried *et al.*, 2015). The water, being less dense than seawater, rises in plumes across the face, resulting in strong free convection that draws in warm far-field water (Jenkins, 2011). This enhances heat transfer to the face. Recent climate warming has increased ocean temperatures and also increased the amount of surface meltwater percolating to the beds of tidewater glaciers, thus increasing subglacial discharge. These trends are likely responsible for recent rapid retreats of some tidewater glaciers in Greenland (Straneo and Heimbach, 2013).

## Calving rates

To determine the mean calving rate,  $\bar{u}_c$ , one usually measures the width-averaged ice velocity toward the calving face,  $\bar{u}_f$ , and the change in the mean position of the calving face,  $\Delta x$ , over a time interval,  $\Delta t$ . Then  $\bar{u}_c = \bar{u}_f + \frac{\Delta x}{\Delta t}$ , with  $\Delta x$  being taken as positive if the ice front retreats. To exclude seasonal variations,  $\Delta t$  is typically taken to be a year.

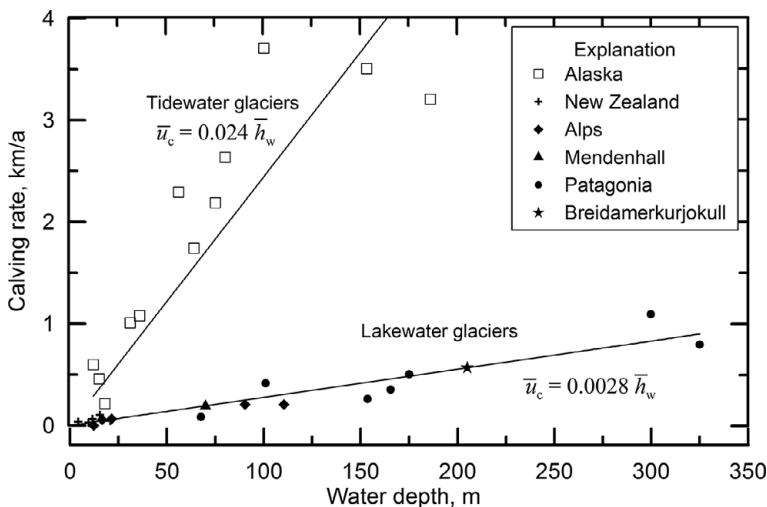


**Figure 3.8** Relation between calving rate and water depth. Alaskan data are from Brown *et al.* (1982) and lake data are from a compilation by Dykes and Brook (2010) and from Benn *et al.* (2007)

On grounded calving glaciers,  $\bar{u}_c$  ( $\text{m a}^{-1}$ ) tends to be roughly proportional to the mean water depth,  $\bar{h}_w$  (m), thus:

$$\bar{u}_c = c\bar{h}_w. \quad (3.14)$$

The empirical coefficient,  $c$ , is a function of the temperature and density of the far-field water and of the volume of freshwater emerging from beneath the glacier. Summer far-field water temperatures off southern Alaska (Walters *et al.*, 1988) are 3–4°C warmer than in West Greenland (Hanna *et al.*, 2009). This is likely largely responsible for  $c \approx 0.024 \text{ a}^{-1}$  in the former (Figure 3.8) and  $\approx 0.007 \text{ a}^{-1}$  in the latter (Pelto and Warren, 1991). In freshwater environments ( $c \approx 0.003 \text{ a}^{-1}$ , Figure 3.8) meltwater emerging from beneath a glacier is likely denser than the warmer lake water, in which case plumes would not develop so sub-lacustrine melting would be reduced.

Modeling has hinted at a possible physical explanation for the relation in Equation (3.14). The velocity gradient in the ice below the water line increases with water depth (Hanson and Hooke, 2003), so the submerged part of a calving face likely becomes overhanging more rapidly in deeper water. O’Leary and Christoffersen (2013) found that, because such overhangs increased the torque exerted on the subaerial part of the calving face, they could increase  $\bar{u}_c$  by as much as a factor of 2–4, with greater effect where the glacier is closer to floatation. If we conservatively take  $\bar{u}_c \propto 2.4 \frac{du}{dz}$ , then  $c = 0.024$  as found for Alaskan tidewater glaciers. In other words, the apparent dependence of  $\bar{u}_c$  on water depth is likely a consequence of an increase with depth in the rate of development of tensile stresses in the subaerial part of the calving face as ice near the waterline bulges out over that below the waterline.

Several other factors may influence  $\bar{u}_c$ . Extending longitudinal strain in the last several kilometers of the glacier typically results in extensive crevassing, so the ice arrives at the calving face in a weakened condition. Longitudinal strain rates up-ice from a calving face vary with geometry of the valley and this influences the density of crevassing. Water ponding in crevasses increases their depth. High concentrations of floating ice can exert a backpressure on the calving face (Nick *et al.*, 2010). Some or all of these likely also control  $\bar{u}_c$  on polar tidewater glaciers that, rather than being grounded, have floating termini. A robust physical relation between  $\bar{u}_c$  and these and potentially other parameters of the physical environment around a calving face is, thus, understandably elusive.

### Unstable retreat of tidewater glaciers by calving

The apparent dependence of  $\bar{u}_c$  on water depth results in an unusual cycle of advance and retreat of tidewater glaciers (Meier and Post, 1987). As is the case with normal valley glaciers, tidewater glaciers advance during periods when the climate is cool and accumulation exceeds surface melting. During the advance they build a submerged moraine and slowly push it down the fjord (Figure 3.9). This process can take hundreds of years, so the climate may become warm again long before the terminus reaches a stable position. As long as the terminus rests on the terminal moraine and  $\dot{B}$  is neutral or positive, this situation is stable. Once  $\dot{B}$  finally turns sufficiently negative for the terminus to withdraw from its moraine bank into deeper water, however, the calving rate increases. This results in an excess of ice loss over accumulation and the retreat accelerates unstably. In terms of Equation (3.1),  $\dot{B}_L$  becomes negative and, because the moraine is no longer exerting a back stress on the glacier,  $\bar{u}_f$  increases, stretching and thinning the glacier, so  $\dot{B}_h$  also becomes negative. The retreat typically continues until the terminus reaches shallow water near the head of the fjord.

Since the end of the Little Ice Age, all glaciers in coastal Alaska have retreated dramatically in this way. However, the retreats have not been synchronous, and

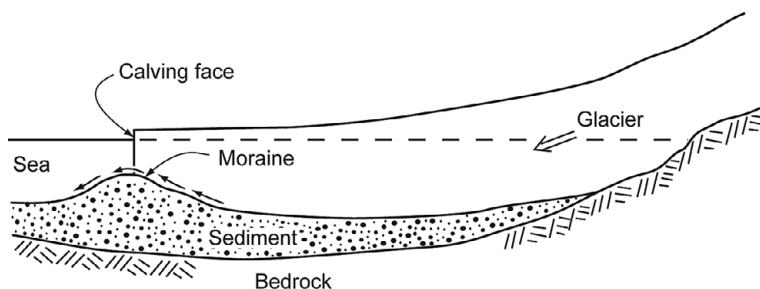


**Figure 3.9** Schematic diagram showing how calving tidewater glaciers advance by rolling over their moraines. Arrows show how sediment is washed and dragged up the proximal slope of the moraine and slumps down the distal slope, resulting in migration of the moraine.

have not been in response to identifiable climatic changes. Some glaciers reached their maximum extent and began to retreat in the late 1700s, but Columbia Glacier, the last of these glaciers to begin retreating, did not back off its moraine until the late 1970s (Meier and Post, 1987). There is considerable concern that some outlet glaciers in Greenland and Antarctica are currently undergoing or about to undergo such dramatic retreats, triggered by our warming climate.

### Calving of ice shelves

Over 90% of the ice loss from Antarctica is through calving, and most of this is from ice shelves. Calving from ice shelves is significantly different from that from grounded tidewater glaciers. Most notably, the ice blocks released from ice shelves may be much larger than those from tidewater glaciers. Iceberg B-15, which broke off from the Ross Ice Shelf in Antarctica on March 17, 2000, measured  $37 \times 295$  km with an area of  $10,915 \text{ km}^2$  (Lazzara *et al.*, 1999). A  $\sim 6000 \text{ km}^2$  slab separated from Larsen C ice shelf on 12 July 2017 (Hogg and Gudmundsson, 2017). These large sizes may reflect colder temperatures and less extensive crevassing of ice shelves, both of which would increase their strength. However, processes producing bergs of this size are still poorly understood. Surface and bottom crevasses initiated at the grounding line and extended as they are advected across the ice shelf may play a role (Kenneally and Hughes, 2006), as may rates of longitudinal extension (Levermann *et al.*, 2012).

Polar ice shelves can also break up exceedingly rapidly. The  $1600 \text{ km}^2$  Larsen A ice shelf disintegrated in 39 days in 1995; the  $3250 \text{ km}^2$  Larsen B shelf collapsed in only 41 days in February 2002. In these cases, it appears that climate warming resulted in extensive melting on the shelf surfaces. The water collected in lakes that depressed the ice surface, resulting in concentric ring fractures around the lake (Beltaos, 2002; Banwell *et al.*, 2013). Water percolated into these crevasses, generating high stresses at the crevasse tips (Weertman, 1973), and the crevasses apparently propagated through the shelf, leading to collapse (Scambos *et al.*, 2000).

We will explore these latter processes in greater detail in Chapter 13.

## Bottom melting

If the base of a glacier is at the pressure melting point and the glacier is sliding over its bed, frictional heating associated with the sliding and with deformation in the basal ice can melt significant quantities of ice. On the lower part of Columbia Glacier in the late 1970s, for example, the specific net balance at an elevation of  $\sim 400$  m was  $\sim -4.5 \text{ m a}^{-1}$  (Rasmussen and Meier, 1982, p. A7). The glacier was  $\sim 600$  m thick at this elevation, its surface slope was  $\sim 0.032$ , and the depth-averaged velocity was  $\sim 1.3 \text{ km a}^{-1}$  (Meier *et al.*, 1994). Thus, a column of ice of unit cross

sectional area would drop ~40 m in a year, releasing  $\sim 2.2 \times 10^8$  J of potential energy, which is sufficient to melt ~0.7 m of ice. Some of this melting will be internal, but much of it will occur near or at the bed. Thus, bottom melting may have been as much as 15% of the total ice loss at this elevation on Columbia Glacier. On most glaciers, however, the amount of such melting is a much smaller fraction of the total, and can be neglected in mass balance studies.

Bottom melting also occurs beneath floating ice shelves and ice tongues. Ocean currents penetrate beneath these, and the saline water mixes with fresh water draining subglacially. It thus becomes less dense and flows outward along the upward-sloping base of the ice shelf or tongue. As it rises, either melting or freezing can take place depending on the temperature and salinity of the mixture, the pressure, and the temperature gradient in the basal ice. Melting can occur in one place and freezing in another. Beneath ice shelves in Antarctica, it is estimated that such bottom melting may have accounted for as much as 20% of the mass loss in the early twenty-first century (Table 3.2a). We'll look at this process also in greater detail in Chapter 13.

### Effect of atmospheric circulation patterns on mass balance

Owing to changes in global climate, simultaneous major ice advances occurred during the Pleistocene and minor advances during the Little Ice Age. On shorter time scales, however, glaciers only a few hundred kilometers apart have behaved quite differently. For example, between the mid 1960s and the late 1980s, when maritime glaciers in Alaska had a relatively good balance year, those in southwestern Canada and adjacent areas in the United States had a bad year, and conversely (Walters and Meier, 1989; Hodge *et al.*, 1998). Walters and Meier found that this was related to the *Aleutian Low*, a semi-permanent, winter-time atmospheric low pressure region that lies off the Aleutian Islands (Figure 3.10). When the Aleutian Low is strong, storms are deflected into Alaska, resulting in high winter balances there (Osterberg *et al.*, 2017). When it is weak, storm tracks remain further south and accumulation rates are high in Washington and British Columbia. Stronger Aleutian Lows are associated with a deepening of a low pressure cell over the southeastern United States, and conversely. This is known as the Pacific North American teleconnection, or PNA.

The strength of the Aleutian low is affected by two oscillations, the *El Niño-Southern Oscillation*, or ENSO and the *Pacific Decadal Oscillation* or PDO.

### ENSO

Two circulations, one in the ocean and one in the atmosphere, are involved in ENSO. Under “normal” conditions trade winds, forced by Earth’s rotation, blow westward

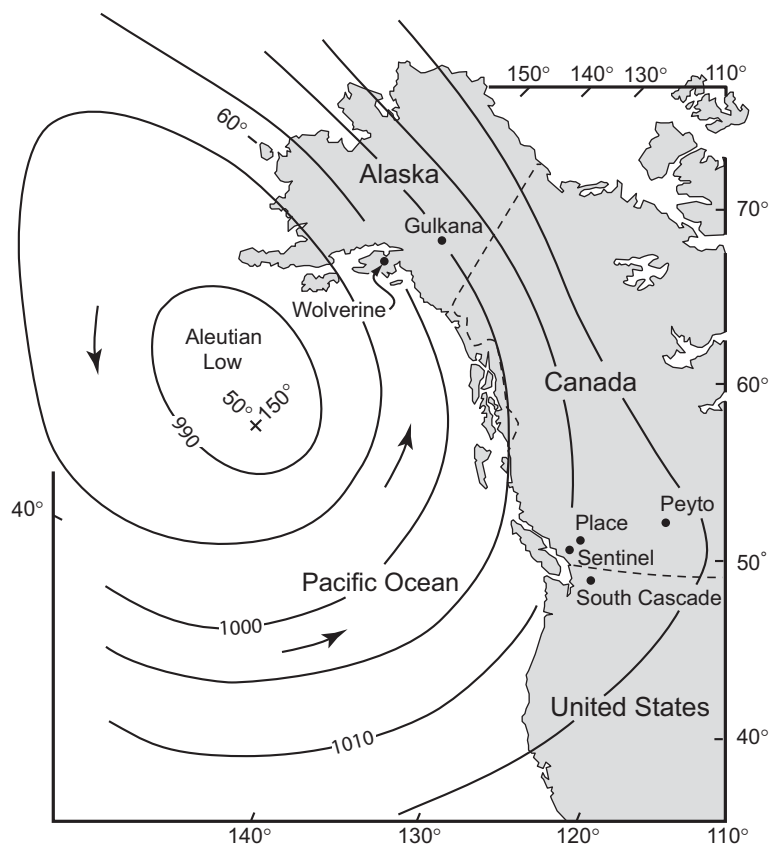


**Figure 3.10** Map of the west coast of North America showing the Aleutian Low and locations of some glaciers for which there are good mass balance records. Arrows show the direction of wind circulation. (Based on Walters and Meier, 1989, Figures 1 and 9)

in the equatorial Pacific. This drives a westerly surface current in the ocean which causes a ~0.6 m increase in elevation of the sea surface in the western Pacific relative to that off Peru. As it moves westward, the water absorbs heat from the atmosphere. By the time it reaches the western Pacific, it may have become as much as 8–10°C warmer. This water accumulates in what is known as the *Western Pacific Warm Pool*. The westward surface current and the resulting super-elevation propel an eastward return current at depth, beneath the thermocline, culminating in upwelling of cold water off Peru.

In the atmosphere, the air above the Warm Pool absorbs heat from the water and thus rises, driving an easterly flow in the mid to upper troposphere (the layer of air between the Earth's surface and, in the tropics, ~18 km above sea level). Moisture in the rising air condenses, resulting in heavy precipitation in the lower troposphere. After losing its moisture the air, now dry, descends off Peru, completing the loop. This is the *Walker circulation*.

At intervals of 2 to 6 or 7 years, for reasons that are not well understood, these circulations weaken. The ocean off Peru, and hence also the overlying air, become warmer. The lower density of the warmer air decreases the potential gradient between Peru and the western Pacific. This weakens the westerly trade winds, and the Pacific Warm Pool shifts eastward, bringing with it the region of heavy rainfall. This is an El Niño. The eastward movement of the Pacific Warm Pool alters the Walker circulation and this shifts the position of the jet stream, weakening the Aleutian Low and causing storms to enter North America hundreds of kilometers south of their normal entry points (Rasmusson, 1984). Eventually, the stronger circulation patterns return and the El Niño event is over. If the returning circulation is stronger than normal, the pattern is called a *La Niña*.

Although global in its effect owing to its impact on the jet stream, ENSO is generated by ocean-atmosphere interactions that are internal to the tropical Pacific and overlying atmosphere (Houghton *et al.*, 2001, p. 454).

## PDO

The PDO is predominantly a temperature oscillation. It is apparently driven by variations in the Aleutian Low, by ENSO, and by fluctuations in the *Kuroshio current*, a Gulf-Stream-like current in the western Pacific (Schneider and Cornuelle, 2005).

During the warm phase of the PDO, the Aleutian Low shifts southeastward and strengthens, sea surface temperatures in the eastern Pacific are somewhat warmer than normal, and those in the northwest Pacific are significantly cooler. The strengthened Aleutian Low deflects storm tracks into Alaska, as noted. El Niños also tend to be strengthened during the warm phase of the PDO, and moderated during the cool phase (Maxwell, 2002), but it is not clear whether a cause and effect relation is involved.

The PDO seems to have two dominant periodicities, 15–25 years and 50–70 years (Mantua and Hare, 2002). Transitions between the warm and cool phases are abrupt: a warm phase began in 1977, and appears to have ended in 1998. During this time storm tracks were directed into Alaska and  $B_w$  was low on Peyto Glacier (Figure 3.10) (Watson and Luckman, 2004).

The consequences of ENSO and the PDO are far reaching, affecting not only glaciers along the northwest coast but also weather patterns around the Pacific, throughout North America, and even globally. In El Niño years during the twentieth century, for example, accumulation was consistently higher in parts of West Antarctica, and there is a hint that it was lower at the South Pole (Kaspari *et al.*, 2004). This appears to be related to clockwise shifting of a low pressure cell in the Admundsen Sea during El Niño events (Cullather *et al.*, 1996). Over longer time periods, a study of the size distribution of dust particles in an ice core from the West Antarctic Ice Sheet suggests that a period of stronger El Niños between ~950 and ~1350 C.E. was

accompanied by a southward displacement of westerly winds in the southern hemisphere (Kaufman *et al.*, 2014). This was also a period of unusual warmth worldwide, called the Medieval Climate Anomaly (Fagan, 2008). Additional studies of the chemistry of ice cores from Mt. Logan in the Yukon and Mt. Denali in Alaska suggest that the Aleutian Low weakened at 877 C.E. and did not strengthen again until 1741 (Osterberg *et al.*, 2017). Since this last strengthening, accumulation on Mt. Denali has doubled, a change that is nearly synchronous with warming of western tropical Pacific and Indian Ocean sea surface temperatures (Winski *et al.*, 2017).

### The North Atlantic Oscillation

Another recently-discovered oscillation is the North Atlantic Oscillation or NAO. During the positive phase of this oscillation, there is a strong low pressure region over southern Greenland and Iceland during the winter, and the jet stream is further north. Northern Europe is thus wetter than normal in winter and cooler than normal in summer. The abnormally wet winters and cool summers result in glacier mass balances in Scandinavia that are either more positive or less negative than normal (Pohjola and Rogers, 1997). Cook *et al.* (1998) have identified periodicities in the north Atlantic oscillation of 2, 8, 24, and 70 years.

### Closing

Clearly, atmospheric circulation patterns that we are just beginning to understand result in regional variations in mass balance on a variety of spatial and temporal scales. The data base necessary for identifying and studying these circulation patterns is expanding rapidly, and much will be learned as glaciologists and meteorologists begin to extend and exploit it. Particularly intriguing are the remarkable teleconnections observed. Beyond this, however, is the question of what controls variations in atmospheric and oceanic circulation on time scales of decades to centuries.

## Global mass balance and sea level

Satellites are now providing far better estimates of mass balance than we have had heretofore. This is particularly true in Antarctica. However, estimated uncertainties are appreciable, and independent assessments still differ significantly (Table 3.2b; Shepherd *et al.*, 2012). This is not surprising given the cutting-edge processing necessary to obtain meaningful values from satellite data. Since 2001, mean net balances appear to have become increasingly negative in Greenland and on smaller glaciers (Table 3.2). This may also be the case in Antarctica, but the uncertainties make comparison difficult. The steady acceleration in the rate of ice loss (Table 3.2b) is cause for concern.

Of considerable interest currently is the rate of rise in global sea level and the contribution of melting glaciers and ice sheets thereto. The mean rate over the period 1993–2010, based on satellite altimetry, was  $3.2 \pm 0.4 \text{ mm a}^{-1}$  (Church *et al.*, 2013, p. 1139 and Table 13.1). The three principal contributors, averaged over 1993–2010, were melting of glaciers and ice sheets ( $1.36 \pm 0.39 \text{ mm a}^{-1}$ ), thermal expansion of the oceans ( $1.1 \pm 0.3 \text{ mm a}^{-1}$ ), and a decrease in terrestrial storage in lakes and groundwater reservoirs ( $0.38 \pm 0.12 \text{ mm a}^{-1}$ ). Changes due to melting of permafrost, sedimentation in the oceans, and changes in atmospheric moisture content were considered to be negligible in comparison (Church *et al.*, 2013, p. 1157). The total,  $2.84 \pm 0.51 \text{ mm a}^{-1}$ , was in agreement with the altimetry data within limits of uncertainty. Most of the discrepancy was likely in the estimates of contributions from glaciers and ice sheets. Significantly, their contribution appears to have nearly doubled since 2001 (Table 3.2).

---

## SUMMARY

In this chapter we have discussed snow accumulation and the transformation of snow to ice. We found that in polar environments, where little if any melting occurs, the physical and chemical stratigraphy in an annual layer of snow persists for many thousands of years and can be used to date the ice by counting annual layers.

We then explored the change in mass of a glacier or ice sheet: the sum of changes due to meteorological effects, to dynamic thickening or thinning, and to terminus advance or retreat. We defined some terms used to discuss meteorological effects, particularly summer, winter, and net balance, and summarized satellite techniques for measuring mass balance. We then used a perturbation approach to study the influence of temperature, radiation, and precipitation on net balance. It turned out that the net balance of glaciers in continental environments was sensitive, primarily, to summer temperature, while that of glaciers in maritime areas was sensitive to both winter balance and summer temperature. Radiation balance, principally due to differences in cloud cover, could play a role in either environment. The lower budget gradient and consequent more sluggish behavior of polar glaciers compared with their temperate counterparts turned out to be largely related to the shorter melt season in polar environments. We also saw that dynamic thickening or thinning, and terminus advance or retreat are closely linked. If a rapid glacier advance is accompanied by a commensurate amount of thinning, the mass does not change. However, such an advance may result in rapid melting of the terminus and hence retreat.

We then discussed the rolls of calving and bottom melting in mass balance, and discovered that, on tidewater glaciers, calving can lead to retreats that are, at best,

only weakly related to climate. On ice sheets, calving turns out to be a dominant but poorly understood process of mass loss. Bottom melting can be an important component of mass balance on fast-moving valley glaciers and beneath ice shelves.

We also found that as yet enigmatic variations in intermediate and large scale atmospheric circulation patterns complicate the picture, sometimes resulting in asynchronous mass-balance patterns on glaciers only a few hundred kilometers apart. Finally, we summarized some estimates of global mass balance, and the contribution of presently-negative mass balances to sea level rise.

# 4

## Flow and fracture of a crystalline material

In this chapter you will be introduced to the voluminous literature on deformation or *creep* of ice. We begin by looking at deformation processes on an atomic scale, and then introduce empirical and semi-empirical relations that provide a macroscopic description of the deformation. Finally, we briefly consider crevassing, using principles of linear fracture mechanics.

First, let's introduce (Figure 4.1) some experimental data on the dependence of strain rate,  $\dot{\epsilon}$ , on stress,  $\sigma$ , as this will form a useful background for discussion of creep mechanisms. Starting with John Glen's (1955) pioneering uniaxial-compression experiments, data like those in Figure 4.1 have been used to establish the form of the flow law presented in Equation (2.15):

$$\dot{\epsilon}_e = A\sigma_e^n. \quad (4.1)$$

The slopes of the lines in Figure 4.1 reflect the exponent,  $n$ . Despite the fact that in real glaciers and ice sheets,  $\sigma_e$  is generally  $<0.1$  MPa, there are few data points at such low stresses. This is because creep rates are then so low that experiments must be continued for days to weeks or months to yield useful results, and holding stresses and temperatures constant over such long time periods is challenging. However, at stresses less than  $\sim 0.2$  MPa (depending on grain size), the data suggest that  $n \approx 1.8$ , while at stresses greater than  $\sim 2$  MPa,  $n \approx 4$  (Goldsby and Kohlstedt, 1997, 2001). In the former regime,  $\dot{\epsilon}$  decreases with increasing grain size, but in the latter it is independent of grain size. At still lower stresses, Goldsby and Kohlstedt (2001) found that  $d\dot{\epsilon}_e/d\sigma_e$  increased again ( $n \approx 2.4$ ), and that the rate was again independent of grain size.

A large volume of experimental data on ice deformed in the laboratory and on natural ice in glaciers and ice shelves at stresses between  $\sim 0.02$  and  $\sim 10$  MPa (see Hooke (1981) and Goldsby and Kohlstedt (2001) for references) suggests that  $n \approx 3$ , a value that has been adopted in many numerical calculations. From Figure 4.1, it appears that this value reflects averaging of data spanning the transition from the  $n = 1.8$  to the  $n = 4$  regime, and that use of it may underestimate  $\dot{\epsilon}_e$  if the value of  $A$  is based on experiments at higher stresses.

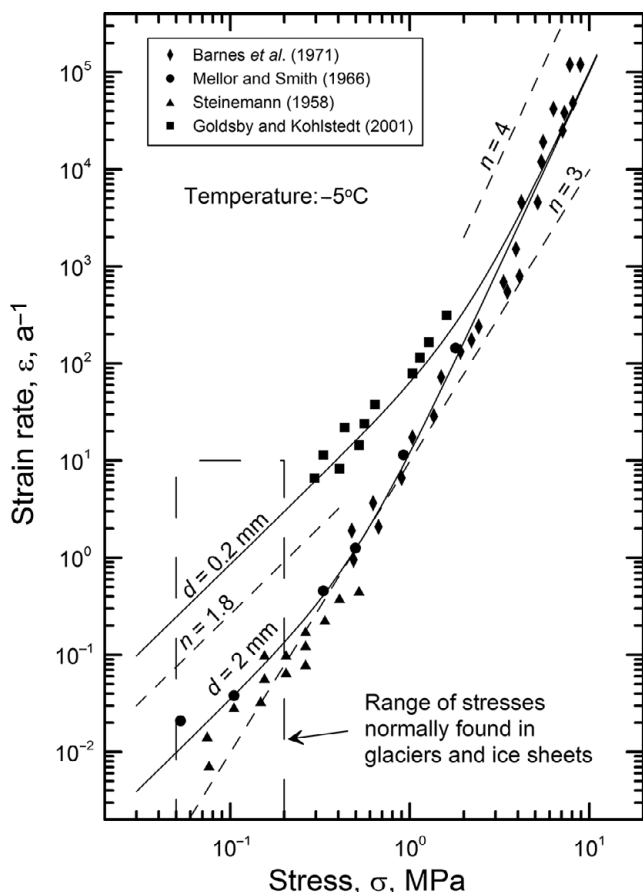


**Figure 4.1** Laboratory measurements of strain rate at various stresses for 0.2 mm and 2 mm ice at  $-5^{\circ}\text{C}$ . All tests were run to  $\dot{\varepsilon}_{\min}$ . Slopes corresponding to  $n = 1.8, 3.0$ , and  $4.0$  are shown by dashed lines. Experiments were conducted at temperatures between  $-4$  and  $-9^{\circ}\text{C}$ , and are adjusted to  $-5^{\circ}\text{C}$ . (Based on Goldsby, 2009, Figure 60.2. Reproduced with the permission of the authors and the American Geophysical Union)

## Crystal structure of ice

There are nine known crystalline forms of ice, but seven of them are stable only at pressures in excess of about 200 MPa, and the eighth, a cubic form, ice Ic, is stable only at temperatures below about  $-100^{\circ}\text{C}$  (Figure 4.2). As the highest pressures and lowest temperatures in glaciers on Earth are about 40 MPa and  $-60^{\circ}\text{C}$ , respectively, these eight forms need not concern us. We, thus, restrict our attention to the common form of terrestrial ice, ice Ih.

The structure of ice Ih is shown in stereoscopic view in Figure 4.3a. It is a hexagonal mineral (hence the “h”) with a rather open structure in which every

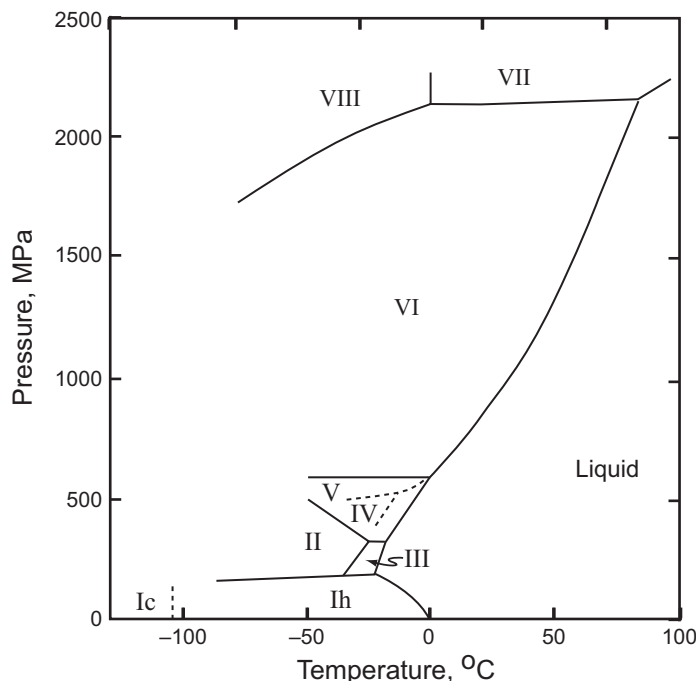


**Figure 4.2** Part of the phase diagram of water (after Kamb, 1965, Figure 1). The various polymorphs of ice are designated by roman numerals. Ice IV is a metastable phase, unstable everywhere with respect to ice V. Ice Ic is also metastable with respect to ice Ih.

oxygen atom, represented by the large circles in Figure 4.3a, is bonded to four additional oxygen atoms at the corners of a tetrahedron. The tetrahedra are joined together in such a way that the oxygens form hexagonal rings, with the O=O bonds zigzagging slightly up and down as one progresses around the ring (Figure 4.3b); three of the oxygens thus lie 0.09 nm above the other three. The plane of these rings is called the *basal plane* of the crystal structure.

The fourth oxygen atom in the tetrahedron is ~0.28 nm above or below that in the center of the tetrahedron. A line parallel to this bond, and hence normal to the basal plane, is called the *c-axis*.

Around each oxygen atom there are, of course, two hydrogen atoms. The hydrogen atoms, represented by the small circles in Figure 4.3a, lie on the bonds between the oxygen atoms. They are situated close to the oxygen to which they are bonded. As each oxygen atom is bonded to four other oxygens, only two of these hydrogen sites, selected at random, are occupied.

Along each O=O bond there are two hydrogen sites. Normally only one of these is occupied. Situations in which neither site is occupied are called *Bjerrum L defects*, and situations in which both sites are occupied are called *Bjerrum D defects*, or just *L* and *D* defects, respectively.

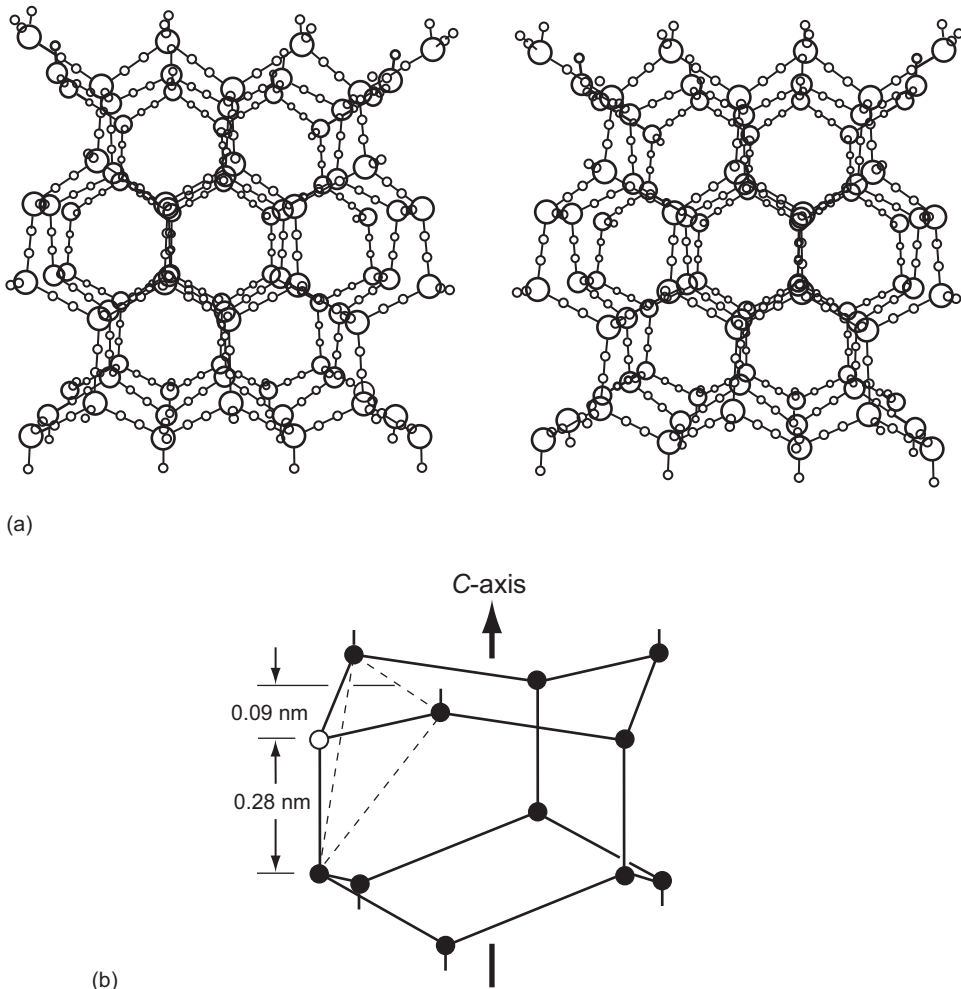


**Figure 4.3** (a) Stereographic view of the structure of ice Ih, viewed down the *c*-axis. Only half of the possible hydrogen sites, indicated by small circles, are occupied (after Hamilton and Ibers, 1968). (b) Structure of ice 1h viewed normal to the *c*-axis. Two of the hexagonal rings are shown. Short lines leading upward and downward from these rings are bonds to rings above and below. The oxygen shown with an open circle is the center of a tetrahedron, part of which is shown by the light dashed lines. (Modified from Hobbs, 1974, Figure 1.7)

## Dislocations

*Dislocations* are another type of defect in crystals. They are places where the crystal lattice is discontinuous or offset in some way. Virtually all crystalline materials contain dislocations. The two basic types of dislocation, the *edge dislocation* and the *screw dislocation*, are illustrated in Figure 4.4.

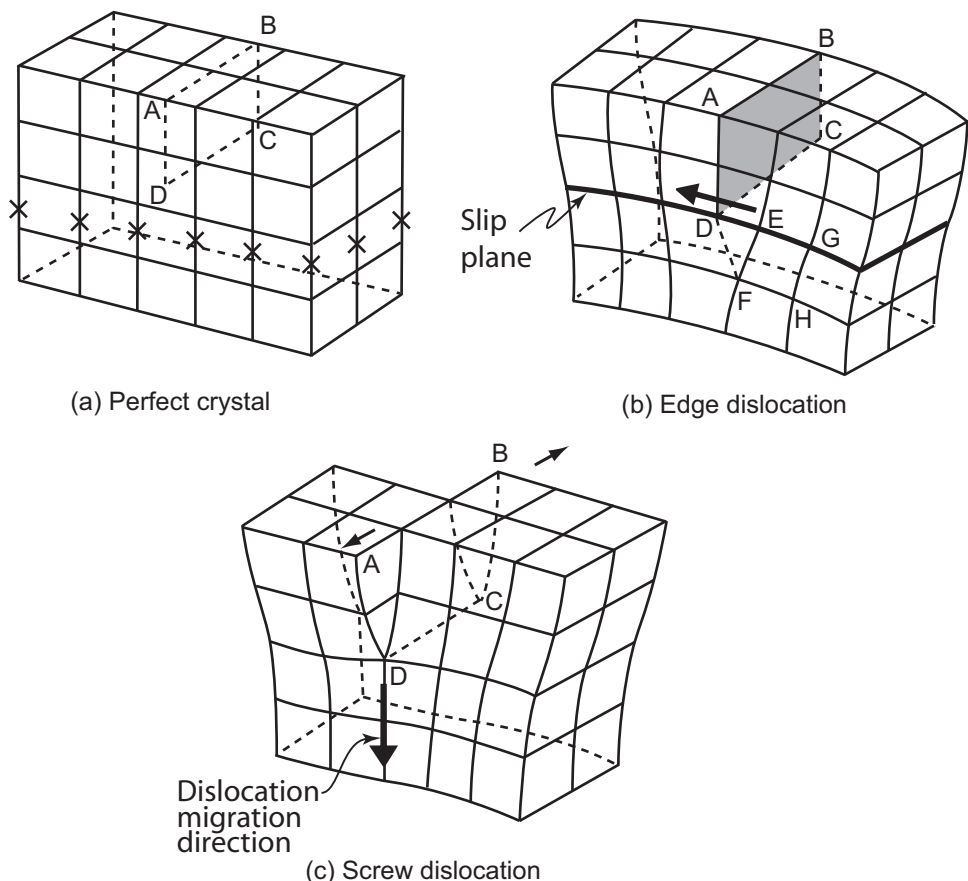


**Figure 4.4** (a) A perfect crystal. (b) An edge dislocation. (c) A screw dislocation. Heavy arrows in (b) and (c) show the direction of dislocation movement. Light arrows in (c) show a sense of offset across dislocation. (Modified from Hull, 1969, p. 17)

Dislocations play a vital role in the deformation or creep of crystalline materials. If one tried to deform the perfect crystal in Figure 4.4a by shearing the top three layers of atoms over the bottom two, the stress required would be enormous, as every one of the bonds indicated by an “x” would have to be broken *simultaneously*. In contrast, the crystal in Figure 4.4b, in which there is a dislocation, would deform much more easily because the bonds could be broken sequentially, one at a time. The bond between E and F would be broken first, and a new bond formed between D and F. Then the bond between G and H would be broken and a new one formed between E and H. This breaking and reforming of bonds results in movement of the dislocation. Calculations show that, in the absence of dislocations, crystalline materials could not possibly deform under the stresses at which they are observed to deform. In fact, it was through such theoretical studies that the existence of dislocations was first inferred.

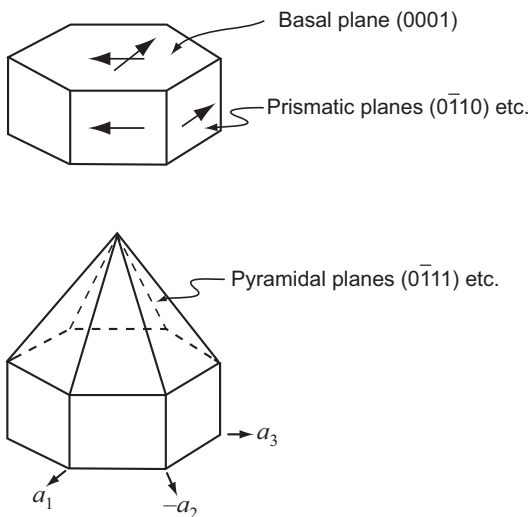


**Figure 4.5** Crystallographic planes in a hexagonal crystal.

Movement of dislocations takes place along planes defined by the crystal structure. These planes are called *slip planes* or *glide planes* (Figure 4.4b). The dominant glide plane in ice is the basal plane, as there are fewer O=O bonds between basal planes than there are within a basal plane (Figure 4.3b). Other possible glide planes are the prismatic and the pyramidal planes (Figure 4.5). Laboratory experiments have shown that the resistance to shear on basal planes is much less than that on the other crystallographic planes.

If strain in ice were homogeneous, deformation of one crystal in a polycrystalline aggregate would necessitate deformation of neighboring crystals to preserve continuity of the medium. Because basal planes in many crystals will not be oriented parallel to the maximum resolved shear stress, deformation along these planes will be slower than in planes that are better oriented. Crystals thus transmit stress nonuniformly (Duval *et al.*, 1983). Within such a polycrystalline sample, the *local* stress may vary over two orders of magnitude and strain is not homogeneous

If a surface is cut through a crystal of unstressed ice the density of dislocations on the surface is likely to be  $<10 \text{ mm}^{-2}$ . Upon application of a stress, the number of dislocations increases rapidly to  $>10^3 \text{ mm}^{-2}$  (Montagnat and Duval, 2004). The new dislocations may be generated at points where shear along a discrete atomic plane in one crystal or slip along grain boundaries between two crystals (Figure 4.6) focuses stress at a boundary of a neighboring crystal. Dislocations are formed at this boundary and move into the neighboring crystal. New dislocations may also be generated at *Frank–Read sources*. A Frank–Read source consists of a dislocation lying between two points at which the dislocation is fixed, called *pinning points*. Impurities or immobile tangles of dislocations may serve as

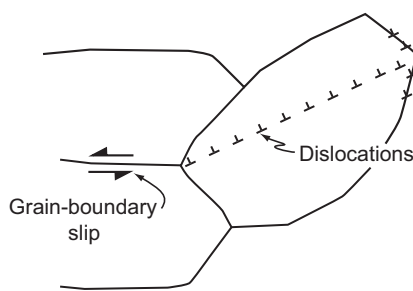


**Figure 4.6** Generation of dislocations at a three-grain intersection due to grain-boundary slip. The mismatch at the intersection may also be accommodated by diffusion or grain rotation.

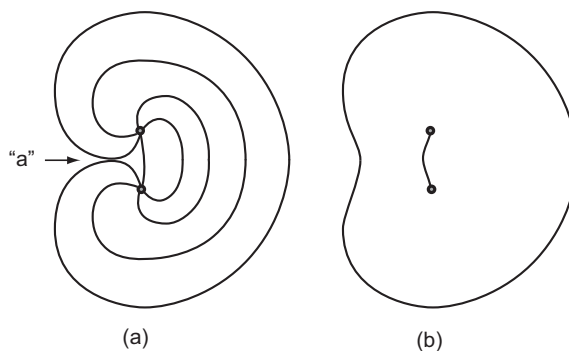


**Figure 4.7** Generation of dislocations at a Frank–Read source. Each line in (a) represents a successive position of a dislocation as it is bowed out between two pinning points. (b) The final stage with the new dislocation expanding outward and another dislocation between the pinning points.

pinning points. When a stress is applied, this dislocation is bowed out until it meets itself (at “a” in Figure 4.7a). At this point, the dislocations coming from opposite directions are of opposite sign, and the dislocation is locally annihilated. This leaves a dislocation in a ring and a new dislocation between the pinning points (Figure 4.7b). The new dislocation can then repeat the process, so this is a continuous source of dislocations. Dislocations generated by a Frank–Read source may multiply by spreading to neighboring planes, a process called *multiple cross glide* (Hull, 1969, pp. 165–167).

## Activation energy

The activation energy is the magnitude of an energy barrier that must be overcome for a kinematic process, such as movement of a dislocation, to occur. Each kinematic process has its own activation energy, and for a given process activation energies are different in different materials.

To determine the activation energy for a process, we need to introduce an expression for the rate factor,  $A$ , in Equation (4.1), namely:

$$A = A_0 e^{-\frac{Q}{R\theta}} \quad (4.2)$$

in which  $Q$  is the activation energy,  $R$  is the universal gas constant, and  $\theta$  is the Kelvin temperature. This equation was proposed by Svante Arrhenius in 1889 and bears his name. It is widely used in the study of thermally-activated processes and reactions.  $A_0$  is a reference parameter that is independent of temperature; literally, it is the viscosity at  $\theta = \infty$ , but this is physically meaningless.  $A_0$  is, however, a function of other parameters which we will discuss later.

Consider two tests run at the same stress,  $\sigma_e$ , but at different temperatures,  $\theta_1$  and  $\theta_2$ . Owing to the difference in temperature, the tests will yield two different strain rates,  $\dot{\epsilon}_1$  and  $\dot{\epsilon}_2$ . Combining Equations (4.1) and (4.2), writing the resulting equation separately for each of the two tests, and dividing one by the other yields:

$$\frac{\dot{\epsilon}_1}{\dot{\epsilon}_2} = e^{-\frac{Q}{R}\left(\frac{1}{\theta_1} - \frac{1}{\theta_2}\right)}. \quad (4.3)$$

As the strain rates, temperatures, and gas constant are all known, the only unknown in Equation (4.3) is  $Q$ , so we can solve for it. To reduce experimental uncertainty, it is normal to run a series of tests at different temperatures and to plot the results on a graph of  $\ln(\dot{\epsilon})$  versus  $1/\theta$  (Figure 4.8).  $Q$  is then obtained from the slope of a line through the data points.

## Premelting

The data points at lower temperatures in Figure 4.8 fall on a straight line with slope  $-Q/R$ . However, at temperatures above  $-15^\circ\text{C}$ , the points deviate from a straight line in a direction implying a higher activation energy; in other words, the increase in creep rate with temperature is greater than expected. At these temperatures, there is also a rapid increase in the electrical conductivity of ice (Mellor and Testa, 1969), and a less striking but still significant increase in the heat capacity (Harrison, 1972). These phenomena are attributable to development of a “layer” with a liquid-like structure on grain boundaries – a layer that allows ice skates to slide – and particularly at multiple grain junctions (Duval *et al.*, 1983; de La Chapelle *et al.*, 1995; Rosenberg, 2005). This is a process known as *premelting*. The layer is *liquid-like* inasmuch as it has a short-range hexagonal structure close to the ice interface, but becomes fully disordered, like water, further from the interface. The intermolecular distance close to the ice surface is smaller than in water, and that in water is, of course, less than in ice (which is why icebergs float)(Rosenberg, 2005). The lack of order is due to the discontinuity in crystal structure at the grain boundary, resulting

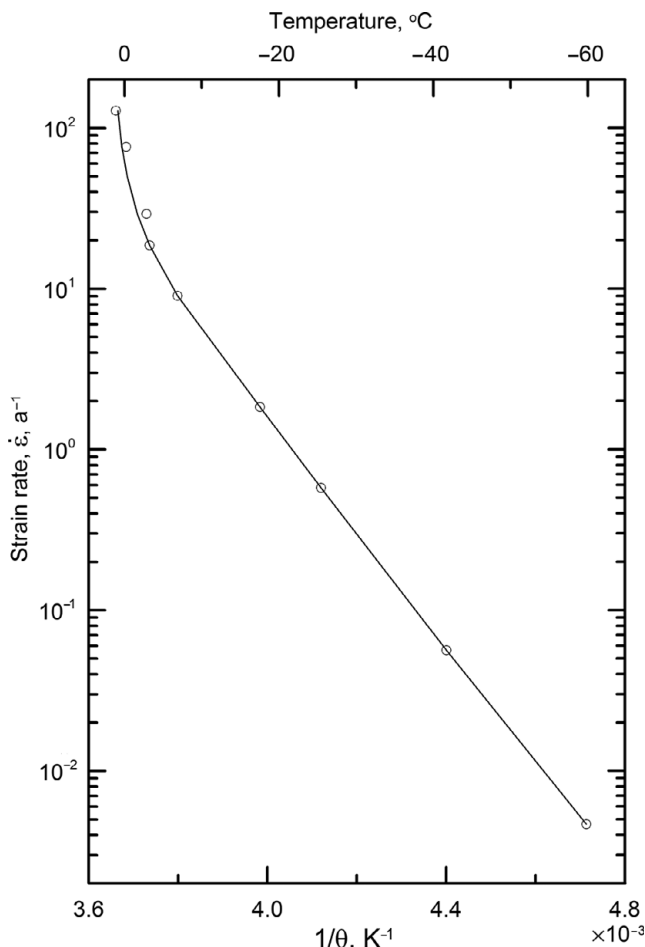


**Figure 4.8** Results of a laboratory experiment on the variation of strain rate with temperature. All experiments were run at the same stress. The slope of the straight part of the curve is proportional to the activation energy. (After Mellor and Testa, 1969, Figure 3. Reproduced with permission of the International Glaciological Society)

in incomplete, and thus weaker molecular bonds. This layer explains the increase in creep rate (because grain-boundaries become glissile), the increase in electrical conductivity (as impurities, if present, are concentrated at grain boundaries and impure water has a higher conductivity than the ice that was melted to form the layer), and the increase in heat capacity (because, of any heat added, some is used to melt ice rather than to increase the temperature). The effect of the liquid-like layer increases as the temperature increases, resulting in an apparent activation energy substantially higher than at lower temperatures. In the  $n = 4$  regime, Goldsby (2009) suggests using  $60 \text{ kJ mol}^{-1}$  at temperatures below  $-15^{\circ}\text{C}$  and  $181 \text{ kJ mol}^{-1}$  at temperatures above  $-18^{\circ}\text{C}$ . The overlap is intentional.

Various experiments have shown that premelting actually begins at temperatures as low as  $-35^{\circ}\text{C}$ , that the thickness of the liquid-like layer is then between 1 and 10 nm, and that grain-boundary sliding likely occurs at these and even lower

temperatures (D. Goldsby, written communication, March 2019). The thickness begins to increase at  $\sim -15^{\circ}\text{C}$ , and thereafter increases exponentially with increasing temperature (Rosenberg, 2005).

## Deformation mechanisms

Deformation mechanisms are mechanisms that produce strain. The literature on these mechanisms in ice is confusing, because a substantial amount of new terminology must be introduced, and processes may be described in different ways by different authors. An important distinction must be made between these mechanisms that produce strain and others that limit the strain rate but may not produce strain. These rate-limiting mechanisms are discussed later.

Three important mechanisms are diffusion, dislocation creep, and grain boundary sliding.

### Diffusion

Atoms migrate through solid materials by a process called *diffusion*. When the diffusion occurs in the absence of a gradient in chemical potential, it is referred to as *self-diffusion*. Diffusion along grain boundaries is *grain boundary diffusion* or simply *boundary diffusion*; the resulting deformation is *Coble creep* (Figure 4.9). Diffusion through a crystal lattice is called *volume diffusion*, and the deformation is *Nabarro-Herring creep*. The activation energy for grain growth in polar firn, a process likely dominated by grain boundary diffusion, is  $\sim 49 \text{ kJ mol}^{-1}$  (Gow, 1969; Goldsby and Kohlstedt, 2001), while that for volume self-diffusion of hydrogen and oxygen in ice is  $\sim 60 \text{ kJ mol}^{-1}$  (Ramseier, 1967). In addition to producing deformation, diffusion may result in movement of dislocations.

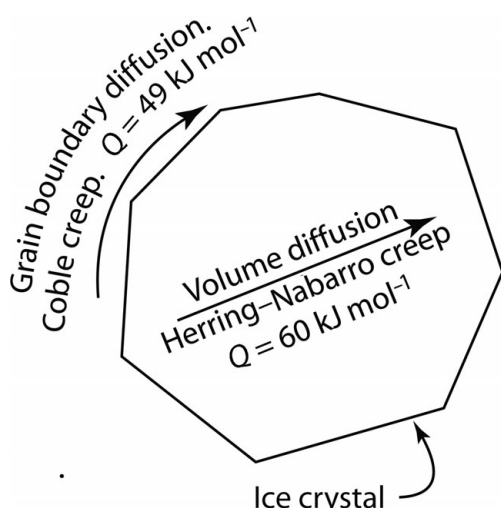


Figure 4.9 Self-diffusion mechanisms.

At very low stresses and small grain sizes, ice may deform entirely by diffusional creep. According to classical diffusion theory, and in contrast to the situation with power-law creep, the strain rate is then linearly proportional to stress. In addition, the deformation rate increases with decreasing grain size because diffusion paths are shorter. Because pure diffusional flow occurs at such low stresses, and hence strain rates, laboratory experiments to study it have yet to be successful. However, large fractions of ice sheets and ice shelves are deforming at stresses under which diffusional flow could predominate.

### Dislocation creep

When a sufficient number of dislocations move, crystals become distorted. This is referred to as *dislocation creep*.

Dislocations, as noted, move along glide planes defined by crystallographic structure. If the slip plane is the basal plane of the crystal, the deformation is called *basal slip*. Because the bonds between basal planes are relatively weak, basal slip is undoubtedly the most important slip system in ice. However, basal slip alone cannot explain deformation of a polycrystalline aggregate; at least three independent slip systems are required, but more on this later.

Dislocation creep produces flattened grains and irregular, sutured grain boundaries; it only rarely produces intersections at which four grains meet (Goldsby and Kohlstedt, 2002).

### Grain boundary sliding

In experiments at relatively low stresses, Goldsby and Kohlstedt (1997, 2001) found that  $n \approx 1.8$ , the activation energy was  $\sim 49 \text{ kJ mol}^{-1}$ , and  $\dot{\epsilon}$  depended on grain size (Figure 4.1). In thin sections, they noted that grain boundaries were relatively straight, grains were not flattened, and four-grain junctions were common, characteristics that are distinctly different from those produced by dislocation creep but that are commonly associated with another deformation mechanism: slip along boundaries between grains, or *grain boundary sliding*. Similar characteristics are observed in ice near the margin of Barnes Ice Cap, where deformation measurements yielded  $n \approx 1.65$  (Hooke, 1973b), and in the upper 2000 m or so of the Greenland and Antarctic ice sheets (Goldsby and Kohlstedt, 2002).

As sliding along a grain boundary invariably results in stresses on the boundary of another grain, thus initiating dislocation motion in that grain (Figure 4.6), grain boundary sliding and dislocation motion are intimately connected.

### Rate-limiting processes

The rate of deformation of a crystal or of a polycrystalline aggregate by dislocation creep depends on how rapidly dislocations can move. This, in turn, depends upon

factors such as the effectiveness of the mechanisms resisting motion, the ability of a dislocation to move from one atomic plane to another, and the orientation of the plane with respect to the stress. One process is usually significantly more important than the others because it is more effective than the others in *retarding* motion. This process is called the *rate-controlling* or *rate-limiting* process. Rate-limiting processes vary among materials, and within any one material they are likely to vary with temperature and stress, and possibly also with impurity content. Furthermore, among students of ice deformation, there is no broad agreement on which processes are most important under different conditions.

In the next few paragraphs, some possible rate-limiting processes in ice are described and evidence for them presented.

### Drag as the rate-limiting process

Dislocations moving in a crystallographic plane are restrained in their motion by a number of atomic-scale mechanisms collectively referred to as *drag*. The velocity of such a dislocation is proportional to the applied stress,  $\sigma$ , and the steady state dislocation density is proportional to  $\sigma^2$  (Weertman, 1983; Alley, 1992). The creep rate,  $\dot{\varepsilon}$ , is proportional to the product of the dislocation velocity and density, so  $\dot{\varepsilon} \propto \sigma^3$ . Thus, laboratory and field data yielding such a cubic dependence could suggest that drag mechanisms are rate limiting.

### Climb as the rate-limiting process

There is, however, an additional dislocation process that must be considered. Samples of previously-unstrained polycrystalline ice deformed in compression in the laboratory invariably go through a transient phase of decelerating creep and then a period of nearly constant creep rate (Figure 4.10a). The decelerating phase is inferred to be due to interference among dislocations as they multiply. The interference results in clusters of dislocations, called *dislocation tangles*, that inhibit deformation. This process is called *work hardening*.

The period of constant creep rate is attributed to *recovery processes* that eventually come into play at temperatures prevalent in glaciers. One such process involves diffusion of atoms away from (or vacancies toward) dislocations, resulting in movement of the dislocation from one crystallographic plane to another. If the atom at D in Figure 4.4b diffused away, for example, the dislocation would move upward. This is a process involving volume self-diffusion. It is called *dislocation climb* if the dislocations are of the edge type, and *cross slip* if they are of the screw type. Both climb and cross slip relieve tangles, allowing deformation to continue at a more-or-less steady rate (central part of curve in Figure 4.10a). As climb is the recovery process requiring more energy, it would be rate controlling. The observation that the activation energies for dislocation creep and for volume self-diffusion are identical ( $60\text{ kJ mol}^{-1}$ ), within limits of experimental uncertainty, supports the suggestion that

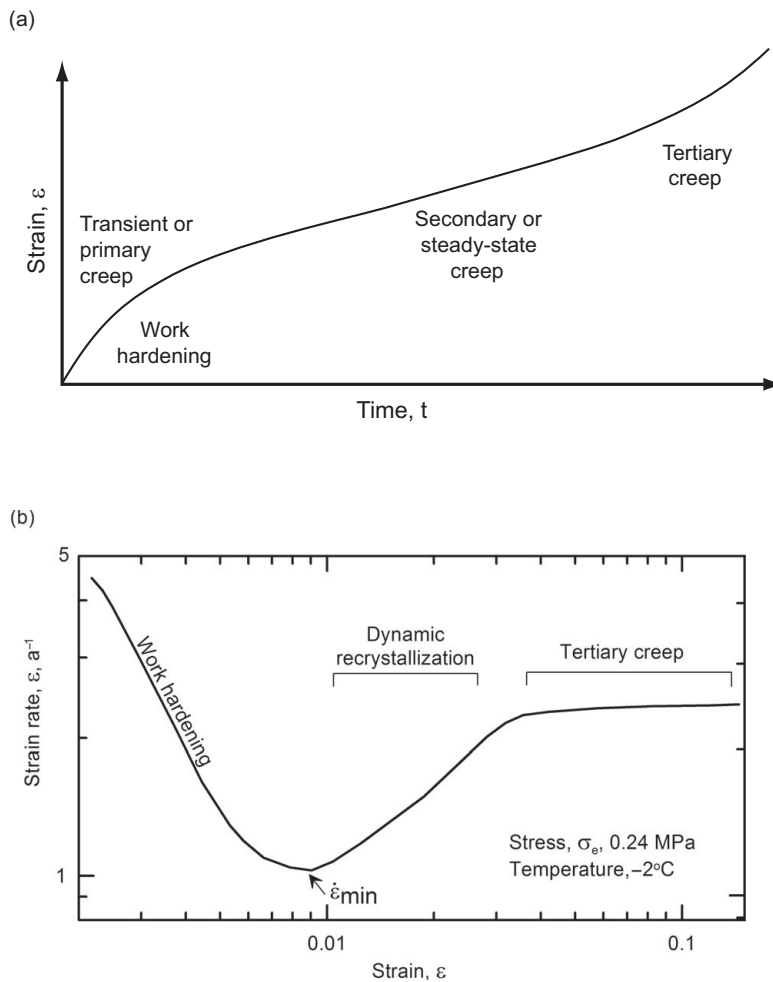


**Figure 4.10** (a) A typical strain-time curve for a sample of polycrystalline ice loaded in uniaxial compression. In early experiments, plots like this were used to identify the time span over which steady-state creep appeared to prevail. (b) As laboratory precision improved, it became possible to plot cumulative strain against strain rate, and thus more accurately identify the minimum strain rate. Note the increase in strain rate after about 1% strain and the constant strain rate in the tertiary creep phase. (Part (b) is adapted with permission from Treverrow *et al.*, 2012, Figure 4. Copyright: International Glaciological Society)

climb is the rate-limiting process (Weertman, 1983). Goldsby and Kohlstedt (2001) think this is the case in the  $n = 4$  regime, but not in the  $n = 1.8$  regime. Note that because these diffusion paths are within grains rather than being from one grain boundary to another, the deformation should be independent of grain size.

In their experiments at the lowest stresses, the  $n = 2.4$  regime, Goldsby and Kohlstedt again found  $Q = 58.5 \pm 3.5 \text{ kJ mol}^{-1}$ , and that the rate was independent of grain size. They interpret this as indicating that climb is also rate-limiting in this regime.

## Slip on other crystallographic planes

Von Mises (1928) showed that five independent systems are required for homogeneous deformation of a polycrystalline aggregate without opening voids. If deformation is inhomogeneous, however, four systems suffice (Hutchinson, 1976), and if dislocation climb operates, three systems are adequate (Groves and Kelly, 1969). Slip on the basal plane can occur in any of three directions, corresponding to the three *a*-axes of the hexagonal crystal, but only two of these are independent. Slip on either the prismatic or pyramidal planes (Figure 4.5) could provide a third system. On prismatic planes, however, the slip would probably be parallel to the basal plane, and so would not accommodate stresses normal to that plane. Thus, slip on pyramidal planes is likely necessary. As slip on pyramidal planes is much harder than slip on the basal plane at the same stress, slip on the pyramidal plane could be rate limiting.

## Dynamic recrystallization and grain boundary migration

*Dynamic recrystallization* is the continuous, or ongoing, nucleation and growth of new, unstrained grains at the expense of older strained ones. These processes are discussed in greater detail later; for now the important point is that growth of grains involves migration of grain boundaries. At stresses typical of those found in glaciers, migration rates range from  $\sim 3 \text{ mm a}^{-1}$  at  $-30^\circ\text{C}$  to  $\sim 30 \text{ mm a}^{-1}$  at  $-10^\circ\text{C}$  (Duval *et al.*, 1983).

The migration is a result of relatively slow diffusional processes that decrease the free energy of a system. The free energy is lower in unstrained grains. Thus, free energy is reduced by diffusion of atoms from strained ice ahead of a moving boundary to unstrained “new” ice behind it (Alley, 1992). Free energy is also lower in larger grains with lower grain boundary curvature. As grain growth lowers the curvature of grain boundaries, larger grains grow at the expense of smaller ones. The smaller grains are “consumed” by the larger ones (Montagnat and Duval, 2000).

Grain boundary migration does not result in deformation, so it is not a deformation process. It is, however, an efficient recovery process. By relieving internal stresses it could be a rate controlling mechanism, particularly in the  $n = 1.8$  regime where it counteracts any tendency for grains to become flattened (Goldsby and Kohlstedt, 2002).

## Grain boundary sliding

Dislocations generated at grain boundaries (Figure 4.6) migrate into the adjacent grain and eventually pile up at an opposite boundary. They can be removed from this pile up by climb into and along the grain boundary (Langdon, 1991). Langdon considered the rate of removal to be the rate-controlling process in some metals that he studied, but this is a process dominated by climb. If it were rate-limiting in ice in the  $n = 1.8$  regime, the activation energy should approximate that for volume

self-diffusion ( $60 \text{ kJ mol}^{-1}$ ), not that for boundary self-diffusion ( $49 \text{ kJ mol}^{-1}$ ) as found by Goldsby and Kohlstedt (1997, 2001). Goldsby and Kohlstedt think dislocation movement through crystals occurs relatively easily, so they argue that the rate-controlling mechanism in the  $n = 1.8$  regime is grain boundary sliding.

### Review of deformation mechanisms

Deformation of ice at the modest stresses and temperatures that occur in glaciers appears to be due to a combination of dislocation creep and grain-boundary sliding. Both basal and nonbasal slip systems contribute to the deformation. At high stresses, in the  $n = 4$  regime, dislocation creep is likely the primary deformation mechanism. The activation energy in this regime is  $\sim 60 \text{ kJ mol}^{-1}$ . The similarity of this activation energy with that for volume self-diffusion suggests that dislocation climb is the rate limiting process. At somewhat lower stresses,  $n \approx 1.8$  and  $\dot{\epsilon}$  depends on grain size. This and some textural characteristics suggest that, while glide and climb are occurring on basal and likely also nonbasal planes, grain boundary sliding is the rate-controlling mechanism. At still lower stresses,  $n \approx 2.4$  and dislocation slip on the basal plane may replace grain boundary sliding as the rate-limiting creep mechanism. Below  $\sim 0.05 \text{ MPa}$ , however, theoretical considerations suggest that pure diffusional flow may dominate.

In glaciers and ice sheets, it seems likely that dislocation slip on basal planes, rate-limited by grain boundary sliding ( $n \approx 1.8$ ) dominates *throughout much of the ice mass*, with dislocation creep ( $n \approx 4$ ) becoming important only near the bed. The commonly cited value of 3 for  $n$  likely reflects an averaging of experimental data across these two deformation regimes.

## Recrystallization

Crystals of glacier ice vary in size and in the degree to which they are interlocked. If there were no bonding across grain boundaries, for example, some polycrystalline ice samples would fall apart into a pile of roughly equant grains, up to a few millimeters in maximum dimension, while others would hang together like a three-dimensional jigsaw puzzle. We'll use the term *texture* to refer to these characteristics of crystal size and shape. In addition, under prolonged strain the *c*-axes of the crystals develop a variety of preferred orientations, or *fabrics*. Both texture and fabric, jointly referred to as the *microfabric*, affect the rheology of ice.

In order to study these processes, glaciologists, like petrologists, have traditionally used thin sections. The thin sections are typically somewhat less than a millimeter thick and 60–80 mm across. When polarized light is passed through a thin section and then observed through another polarizing filter oriented at right angles to the first, the individual crystals can be seen because the crystal structure

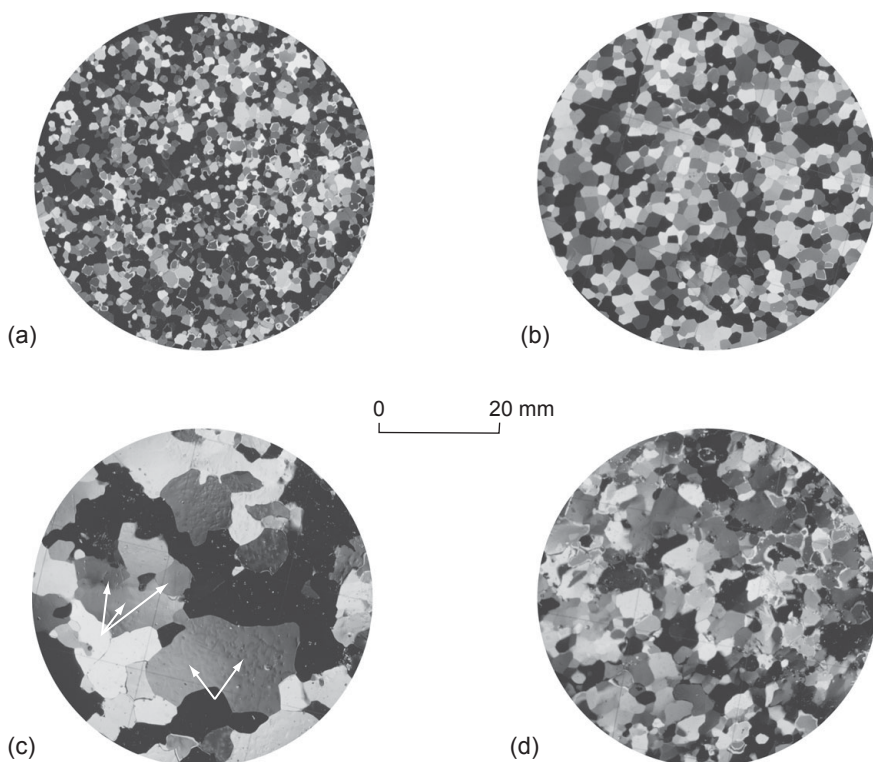


**Figure 4.11** Photographs, taken under crossed polarizers, of thin sections of ice from the Greenland ice sheet near Thule. The different grayscale tones of the grains reflect different orientations of the  $c$ -axes. (a) Initial texture formed by compaction of snow with addition of small amounts of melt water. The  $c$ -axes have a weak preferred orientation, with a preference for vertical orientations. (b) Texture resulting from grain growth with little or no deformation. The  $c$ -axes still have a weak vertical preferred orientation. (c) Texture resulting from polygonization. Adjacent grains with nearly the same grayscale tone (arrows) have  $c$ -axes that are nearly parallel to one another. The grain in the lower center is bent; in the one to left of center, distinct boundaries have formed between parts with slightly different orientations. (d) Texture following significant deformation. Grains are interlocked, and  $c$ -axes have a strong preferred orientation. (From Hooke, 1970)

rotates the light as it passes through the crystal, and the amount of rotation depends on the orientation of the crystal. When thus viewed, the different crystals have different colors (or grayscale tones in a black and white image – Figure 4.11). With the use of a universal stage on which a thin section can be rotated around a vertical axis and tilted about either of two mutually-perpendicular horizontal axes, crystals can be oriented so their  $c$ -axes are vertical. In this orientation, the crystal remains black as the stage is rotated around its vertical axis. The orientation of the crystal is then noted and plotted on an equal area net (Figure 4.12). To interpret such a plot, visualize a hemisphere with its flat “base” upward and its convex side down, and with a crystal in its center. The  $c$ -axis of the crystal intersects the hemisphere.

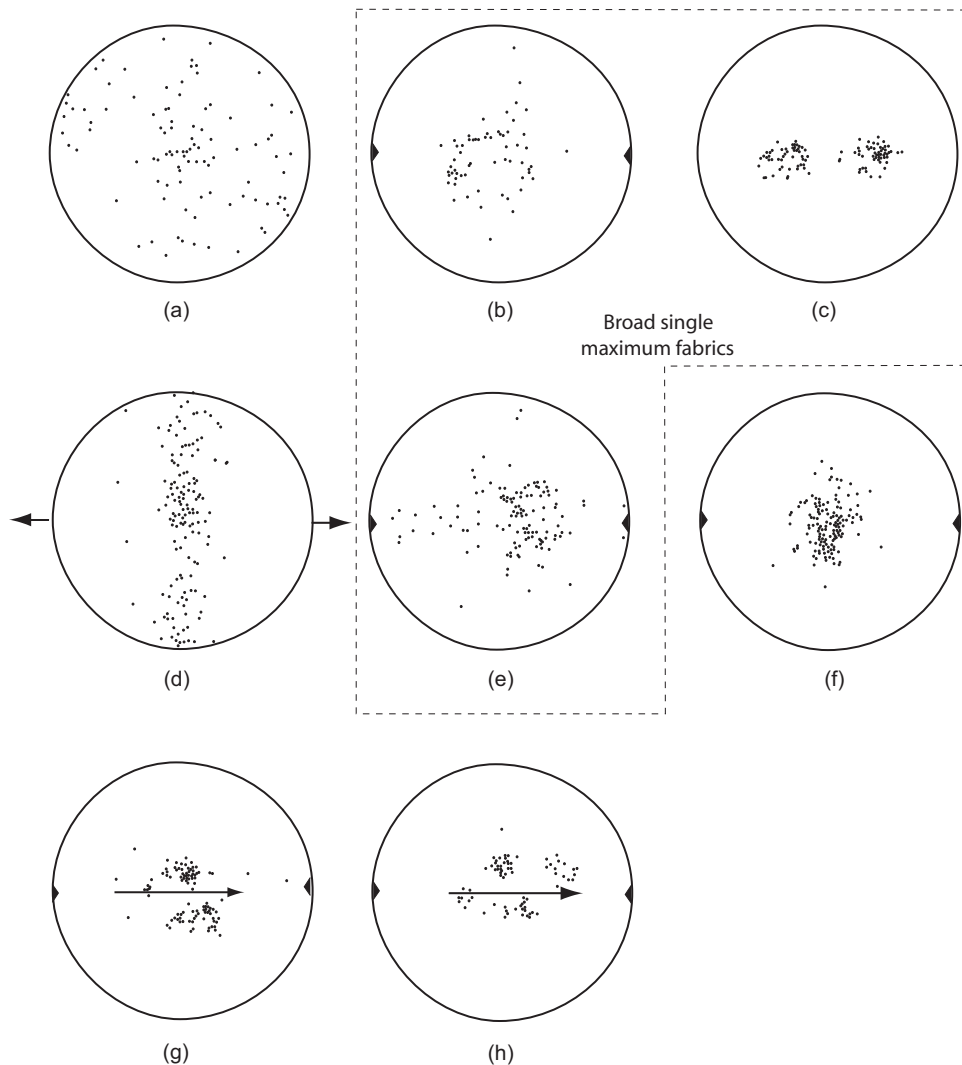


**Figure 4.12** Examples of crystallographic fabrics observed in ice. Plots are projections on the lower hemisphere of an equal-area net. Triangles on edges show the direction of bubble elongation which is presumed to be parallel to the direction of simple shear. (a) Fabric with weak preferred orientation of c-axes in superimposed ice. (b) Fabric resulting from uniaxial compression normal to the plane of the diagram. (c) Fabric that might be formed in pure shear. (d) Fabric produced by uniaxial tension; arrows show direction of tensile stress. (e) Broad single maximum fabric. (f, g, h) Fabrics resulting from simple shear in plane of diagram. Fabrics in (g) and (h) were produced by simple shear in the direction shown by arrows. (Sources: (a), (b) and (e-h) were measured on cores from boreholes in the Barnes Ice Cap (Figure 4.12) ( $T > -10^{\circ}\text{C}$ ); (c) is schematic; (d) is from a depth of 2020 m in the Vostok (Antarctica) core ( $T < -37^{\circ}\text{C}$ ). (a) and (e-h) from Hooke and Hudleston, 1980; (b) from Hooke and Hudleston, 1981; (d) from Lipenkov *et al.*, 1989)

A point on a fabric diagram like those in Figure 4.12 is the projection of this point of intersection onto the base of the hemisphere. Thus, a vertical *c*-axis plots at the center of the circle, and a *c*-axis dipping “south” plots between the center and the bottom of the circle. The points are normally plotted on a *Schmidt equal-area* net; this net is designed so that a unit area on the hemisphere plots into a unit area on the net. Consequently, a *c*-axis dipping at 45° actually plots about 55% of the distance from the center of the net to the boundary.

More recently, automated techniques have been developed to measure crystal orientations (e.g. Wilen *et al.*, 2003). Multiple cameras are used to image a thin section through crossed polarizers as the thin section is rotated or translated beneath a light source. Algorithms then determine extinction angles and solve for the *c*-axis orientations. While considerably faster than the universal stage, these automated procedures are not as fruitful as the newest approach – Electron backscatter diffraction (EBSD) – which utilizes an electron beam in a scanning electron microscope (Prior *et al.*, 2015). This is because EBSD, while time-consuming, also yields *a*-axis orientations, and can measure orientations of very small crystals.

Ice that forms from compaction of snow, perhaps with some addition of percolating meltwater, usually consists of crystals that are 2–4 mm in diameter (Figure 4.11a). During deformation, the texture and fabric of this ice are altered by dynamic recrystallization. Dynamic recrystallization, or simply recrystallization, is driven by the high local internal stresses characteristic of crystals that are poorly oriented with respect to the applied stresses, and the resulting widely differing internal energies in adjacent grains (Duval *et al.*, 1983). These are thus the sites where recrystallization is initiated.

One or more of three processes may be involved in recrystallization. In order of increasing energy difference between adjacent grains, these are *grain growth*, *polygonization*, and *nucleation of new grains* (Duval and Castelnau, 1995). Grain growth results from migration of grain boundaries and the absorption of smaller crystals. The result is a characteristic texture with equant crystals of relatively uniform size (Figure 4.11b). Because temperatures in the accumulation zones of polar ice sheets are relatively constant to depths of a few hundred meters (see Figure 6.6a), grain boundary migration occurs at relatively constant rates. Thus, initially, grain size increases nearly linearly with depth.

When migrating dislocations interfere with one another and pile up, *dislocation walls* may form. The orientation of the crystal lattice is slightly different on opposite sides of a wall, and this distortion increases as the wall develops, eventually leading to the formation of subgrains when the dislocation density on a surface is  $>\sim 10^4 \text{ mm}^2$  (Montagnat and Duval, 2004). The crystal is thus divided into two grains with nearly the same orientation (Figure 4.11c, arrows to left of center). This is *polygonization*. Under relatively high strain rates, polygonization begins at strains

of ~1% (Duval and Castelnau, 1995), but at the much lower strain rates found in the central regions of continental ice sheets, cumulative strains can approach 100% without causing polygonization (Alley, 1992). Thus, polygonization occurs at relatively shallow depths in temperate glaciers, but is normally found only at depths greater than a few hundred meters in polar ice sheets. Where polygonization occurs, it may balance grain growth so grain size remains relatively constant with increasing depth (Alley *et al.*, 1995).

Nucleation of new grains entails the appearance of small grains with basal planes parallel to the maximum resolved shear stress. The grains are thus oriented for easy glide. When they first appear, such grains are relatively unstrained in comparison with adjacent older deformed grains. The new grains grow at the expense of the older ones, thus lowering the free energy as noted. This is probably partly responsible for the interlocking textures seen in highly deformed ice (Figure 4.11d).

Nucleation and grain growth, combined, are sometimes referred to as *migration recrystallization*.

### Development of fabrics with preferred orientations of c-axes

Newly-nucleated, optimally-oriented crystals grow at the expense of older deformed ones, and continued straining gradually rotates them into orientations that are no longer optimal, so they begin to accumulate strain energy. The tendency for systems to minimize free energy then leads, once again, to nucleation of new grains at the sites of high strain energy. This continuous rotation and recrystallization results in a tendency for c-axes to be oriented normal to the maximum resolved shear stress.

Let us illustrate these processes by tracing the development of such fabrics, starting with ice near the surface in the accumulation area (Figure 4.11a). The c-axes of the crystals are either uniformly distributed or have a weak preference for vertical orientations (Figure 4.12a). The latter probably results from the orientation of snowflakes that have thin disk-like shapes, and thus, like a pile of poker chips, tend to lie flat as they accumulate. In addition, the vertical temperature gradient may have some influence during sintering.

As the ice becomes buried, it is compressed vertically and stretched longitudinally and sometimes also laterally. Where longitudinal and lateral strain rates are comparable in magnitude, the stress field is referred to as *uniaxial compression* (Figure 4.13a), whereas if lateral strain rates are negligible it is *pure shear* (Figure 4.13b). In both of these stress configurations, slip occurs most readily on the basal planes of crystals whose c-axes are inclined at ~45° to the compression axis (Figure 4.13d). Thus crystals are nucleated in this orientation, and these crystals grow at the expense of adjacent more highly-stressed ones, leading to a conical distribution of c-axes in uniaxial compression (a *small circle fabric*: Figure 4.12b) and to two maxima aligned in the direction of extension in pure shear (Figure 4.12c). (Small circle fabrics are also commonly referred to as *girdle fabrics*,

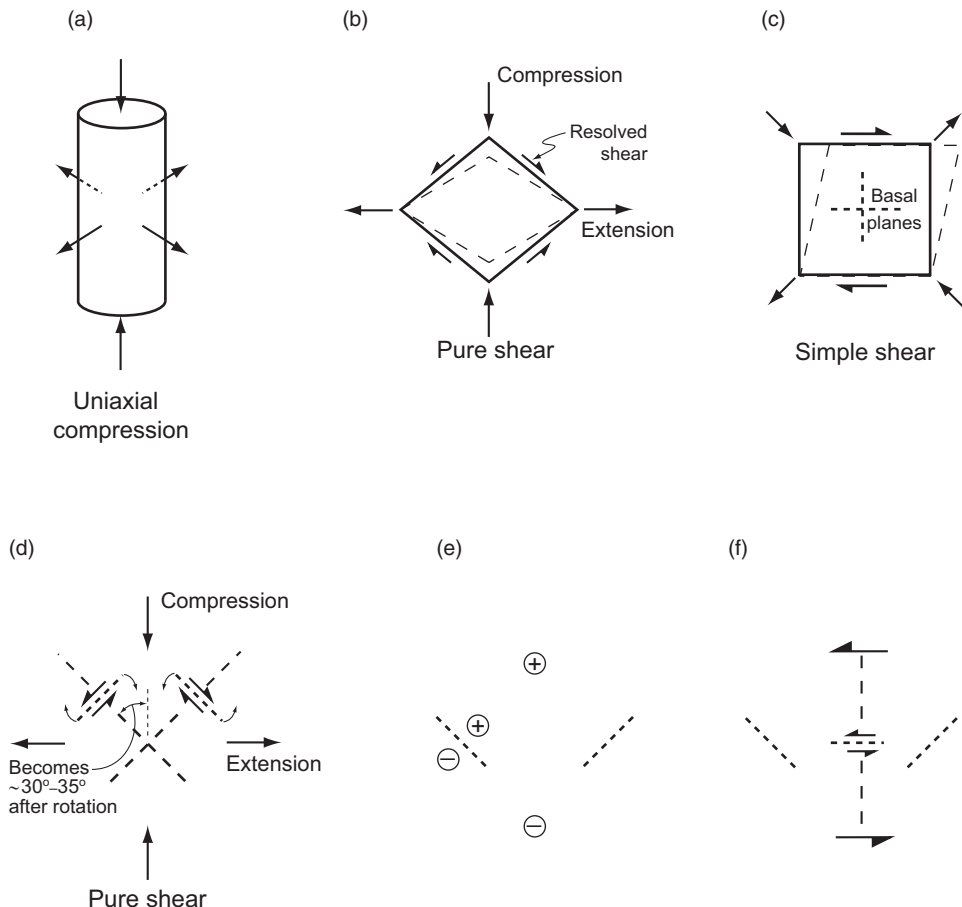


**Figure 4.13** Stress configurations and their relation to orientations of  $c$ -axes. Short-dashed lines show orientations of basal planes. (a) Uniaxial compression. (b) Pure shear; there is no strain normal to the plane of the diagram; dashed lines show shape after some deformation. (c) Simple shear; half arrows show direction of shear and dashed lines show shape after some deformation; full arrows show shear resolved into compression and tension; basal planes shown are those on which resolved shear stresses due to the compression are maximized (see d). (d)  $c$ -axes and basal planes in a newly nucleated crystal in uniaxial compression or pure shear; with continued compression, the  $c$ -axes rotate toward the axis of compression. (e) Simple shear viewed parallel to the shear direction with basal planes also parallel to the shear direction as in the fabric of Figure 4.12g;  $\oplus$  and  $\ominus$  signify stress vectors directed into and out of the page, respectively. (f) Simple shear viewed normal to the shear direction with basal planes of the two weak maxima in Figure 4.12h inclined to the shear direction.

although “girdle” implies a great circle.) The vertical compression and lateral extension, however, have the effect of rotating basal planes. In Figure 4.13d, the rotation is clockwise on the left and counterclockwise on the right. Thus, as the crystals grow, the  $c$ -axes rotate toward the compression axis (Alley, 1992), with the result that the mean angle between the compression axis and the  $c$ -axes is typically only  $\sim 30\text{--}35^\circ$ , not  $45^\circ$  (Kamb, 1972; Hooke and Hudleston, 1980).

The rotation rate decreases as the *c*-axes approach the compression axis (Alley, 1988). In addition, crystals that have been rotated too far, and thus become highly stressed, are replaced by new, strain-free, ones nucleated with more favorable orientations. These two factors lead to a paucity of crystal axes parallel to the compression axis, and hence to a small circle fabric rather than a single maximum fabric.

At Vostok station in Antarctica, transverse and vertical strain rates are compressive and are thought to be of comparable magnitude (Lipenkov *et al.*, 1989). Longitudinal extension thus results in a uniaxial *tensile* stress regime, which tends to rotate *c*-axes toward the compressive axes (Figure 4.13d). Temperatures at Vostok are  $<-37^{\circ}\text{C}$ , so recrystallization is suppressed. Thus, *c*-axes tend to accumulate parallel to the compressive axes. In this case, with roughly equal compressive stresses in the vertical and transverse direction, *c*-axes can lie anywhere on a great circle<sup>1</sup> normal to the tensile axis (Figure 4.12d).

Close to the bed, drag results in a stress configuration approximating *simple shear* parallel to the bed. In simple shear, planes parallel to the bed remain so, and the spacing between planes does not change. The stresses resulting in simple shear can be resolved into compressive and tensile stresses at  $45^{\circ}$  to the direction of shear (Figure 4.13c). As before, crystals tend to nucleate with basal planes at  $45^{\circ}$  to the compressive axis, parallel to the direction of maximum resolved shear stress. In one of these directions, basal planes are normal to the direction of shear, and in the other they are parallel to it. Crystals nucleated in the former orientation quickly accumulate large strain energies and are resorbed, while those in the latter orientation, with vertical *c*-axes, deform easily by slip on basal planes and are thus favored. The resulting fabrics, which are common in ice sheets (Gow and Williamson, 1976; Hooke and Hudleston, 1980), have single maxima that are quite tight near the bed (Figure 4.12f). The ratio of simple shear to pure shear decreases with height above the bed, leading to broader single maxima higher in the ice sheet (Figure 4.12e).

The fabrics in Figure 4.12b, c, and e all seem to form under roughly equivalent cumulative strain. The differences among them are primarily due to stress configuration. As a class, we will refer to them as *broad single maximum* fabrics.

Although the increase in creep rate associated with recrystallization usually begins at an cumulative effective strain,  $\varepsilon_e$  (Equation 2.11) of  $\sim 0.01$  in the laboratory (Figure 4.10b), broad single maximum fabrics are not particularly evident until  $\varepsilon_e \cong 0.04$  and only become well developed at  $\varepsilon_e = 0.4$  (Kamb, 1972; Jacka and Maccagnan, 1984). In the field, Hooke and Hudleston (1980) found that such fabrics first appeared at  $\varepsilon_e \cong 0.52$ . For reference, circles that have been deformed into ellipses by strains of these magnitudes have axial ratios of 1.03, 1.12, 3.10, and

---

<sup>1</sup> Whereas a small circle fabric represents *c*-axes distributed on the surface of a cone, a great circle represents a radial distribution of *c*-axis, as in spokes of a wheel.

4.35, respectively. Thus, dynamic recrystallization increases creep rates long before a detectable preferred *c*-axis orientation develops.

In simple shear at cold temperatures or high strain rates (or high cumulative strains), the single maximum fabric strengthens (Figure 4.12f). However, at lower strain rates and at temperatures above about  $-15^{\circ}\text{C}$ , an unexpected fabric appears. First, the single maximum splits in two, with a maximum on either side of the shear direction (Figure 4.12g). The basal planes corresponding to these *c*-axis orientations are still parallel to the shear direction, but the orientations of the planes are not optimal (Figure 4.13e). Then, with increased cumulative strain, strain rate, or temperature, first one and then a second maximum appears inclined to the direction of shear (Figure 4.12h). These planes are definitely not well oriented for slip (Figure 4.13f), and thus must stiffen the ice, at least slightly. These *multiple maximum* fabrics appear at  $\varepsilon_e \cong 1.3 \pm 0.3$  (Hooke and Hudleston, 1980). The corresponding axial ratio of the strain ellipse is  $\sim 40$ .

These multiple maximum fabrics are fairly common in glacier ice at temperatures above  $-15^{\circ}\text{C}$ , but rare or absent in colder ice (e.g. Kamb, 1959; Gow and Williamson, 1976). Their origin is not well understood. Shear deformation for an extended period of time at effective stresses of 0.03 (Barnes Ice Cap) to 0.04 (Matsuda and Wakahama, 1978) MPa and temperatures ( $>\sim -15^{\circ}\text{C}$ ) seem to be required for their formation.

By observing etch pits in thin sections of ice with such fabrics, Matsuda and Wakahama (1978) measured the orientations of *a*-axes as well as *c*-axes. In ice with 4-maximum fabrics, they found that the *a*-axes were clustered, and that *a*-axes of adjacent crystals were systematically aligned in a way that suggested mechanical twinning. The angle between the *c*-axes of the respective twin lattices was  $\sim 45^{\circ}$ , which is the same as the angle between the two maxima of Figure 4.12g. Twinning can be produced mechanically by applying a shear stress to a crystal, causing the lattice of part of the crystal to shift (as in shifting each of the layers of cylinders in the upper half of a pile, one cylinder to the right relative to the layer beneath it) (Bell, 1941).

Because the various fabrics appear to form under fairly specific conditions of cumulative strain, strain rate, and temperature, and because these parameters all tend to increase systematically with depth in the accumulation area of a glacier, fabric type also varies with depth. For example, near the divide in Barnes Ice Cap, the transition from weakly oriented to broad single maximum (or equivalent) fabric occurs at a depth  $\sim 140$  m, and the broad single maximum gives way to a multiple maximum fabric at  $\sim 200$  m (Figure 4.14). As the ice is advected outward, the transitions occur at shallower depths, and in the ablation area these fabrics are exposed at the surface. At Byrd Station in Antarctica, the transition to broad single maximum fabrics (small circle variety) occurs at a depth of  $\sim 350$  m. Then, a strong single maximum fabric appears at  $\sim 1200$  m and multiple maximum fabrics show up

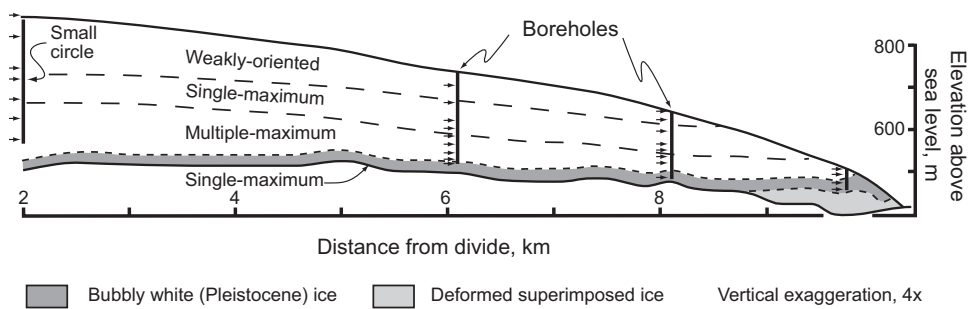


**Figure 4.14** Vertical cross section along a flow line on Barnes Ice Cap showing zones characterized by particular fabrics. Arrows show locations of samples used to determine fabric type. (After Hooke and Hudleston, 1980)

at  $\sim 1830$  m. Differences in temperature are probably largely responsible for the difference in depths to the transitions, although stress and cumulative strain may also play a role; Barnes Ice Cap is above  $-15^{\circ}\text{C}$  throughout, whereas at Byrd Station the temperature exceeds  $-15^{\circ}\text{C}$  only below 1750 m.

## Summary of ice deformation

Given these various processes of recrystallization and crystal deformation, one may well ask how we should visualize the deformation of polycrystalline ice on a granular scale. Available evidence suggests that internal stresses are heterogeneous, that slip takes place largely on basal planes within individual grains although some other slip systems must also operate, that this slip results in rotation of the crystal structure, that slip also takes place on grain boundaries, and that nucleation of grains with basal planes parallel to the maximum resolved shear stress and resorption of grains that have rotated out of this orientation results in the development of fabrics with preferred orientations. Mismatches at three-grain intersections due to differential slip may be accommodated by initiation and migration of dislocations into the adjacent grain, by diffusion, by grain rotation, or by some combination of these processes. The rate limiting processes appear to be grain boundary slip at low stresses and dislocation climb at higher stresses. Computer models incorporating these principles successfully simulate many characteristics of fabric evolution in ice sheets (Etchecopar, 1977; Van der Veen and Whillans, 1994).

## Deformation mechanism maps

Scientists working on the deformation of crystalline materials have found it useful to plot “maps” showing the deformation mechanisms operating at different

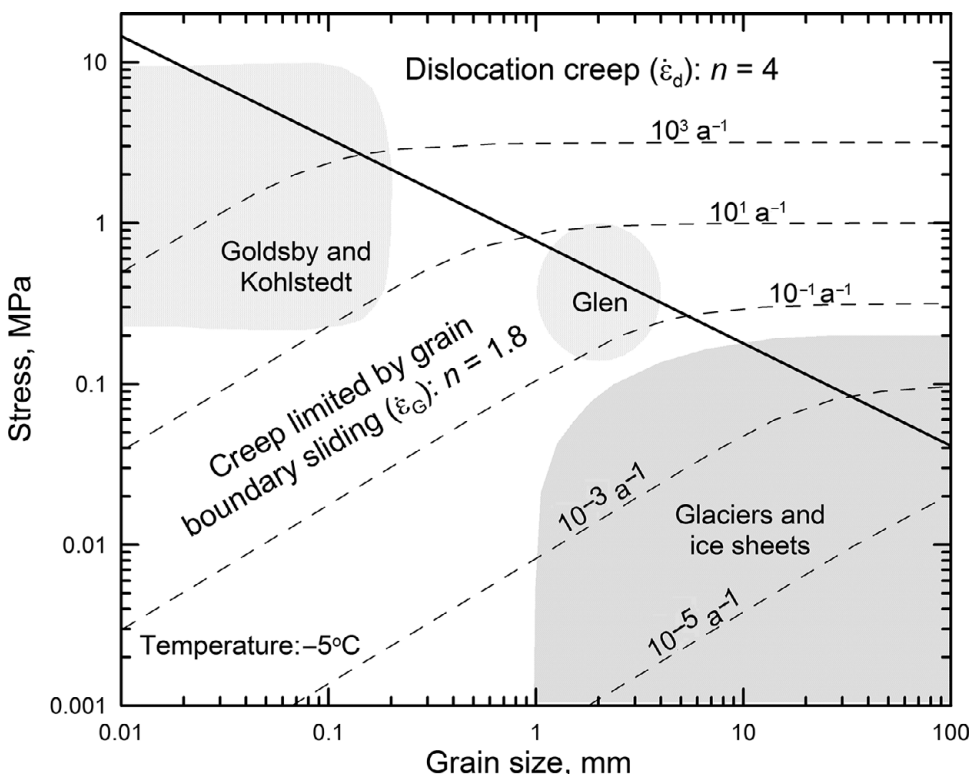


**Figure 4.15** Deformation mechanism map in  $\sigma - d$  space for ice at  $-5^\circ\text{C}$ , calculated with the use of Equation (4.4) with the constants in Table 4.1. Dashed lines are lines of equal strain rate. Along the heavy diagonal line the contributions of  $\dot{\epsilon}_G$  and  $\dot{\epsilon}_d$  to the deformation are equal. (Fields showing the range of stresses and strain rates in the Glen and the Goldsby and Kohlstedt experiments are adapted from Goldsby, 2009, Figure 60.3)

temperatures,  $\theta$ , stresses,  $\sigma$ , or grain sizes,  $d$ . Such a map in  $\sigma - d$  space, calculated for a temperature of  $-5^\circ\text{C}$ , is shown in Figure 4.15. At lower stresses, as we have discussed, deformation is likely dominated by dislocation slip on basal planes and rate-limited by grain boundary sliding (GBS). At higher stresses dislocation creep limited by climb is the dominant mechanism. The heavy diagonal line separates the two fields. Although both mechanisms may contribute to the deformation at all stresses and grain sizes, along this line the two mechanisms contribute equally.

Also shown in Figure 4.15 are contours (dashed) of strain rate. Strain rate is independent of grain size in the dislocation creep field. Curvature of the contours as they approach the diagonal reflects the gradually increasing influence of the process on the opposite side of the diagonal.

Note the range of stresses and grain sizes in the experiments of Glen (1955) and of Goldsby and Kohlstedt (1997, 2001), and their approximate range in glaciers and ice sheets. The range of Glen's experiments is typical of those done over the years; they lie on the boundary between the two creep regimes which, as noted, is probably

responsible for the value of  $n$  ( $\sim 3$ ), midway between the values for GBS limited creep ( $n = 1.8$ ) and dislocation creep ( $n = 4$ ). In contrast, the range of stresses and grain sizes in glaciers and ice sheets appears to fall almost entirely within the GBS-limited field. This suggests that models using  $n = 3$  are likely to overestimate strain rates. A major contribution of Goldsby and Kohlstedt was the development of techniques for making samples with grain sizes small enough to deform in the GBS-limited regime at stresses high enough to yield results on a laboratory time scale.

## A flow law for glacier ice

In the preceding sections of this chapter we have looked at details of the deformation process. In the remainder of this book, we will frequently need a simple yet reasonably accurate expression relating stress and strain rate in ice. In general, we will use Glen's flow law:  $\dot{\varepsilon}_e = A\sigma_e^n$  (Equation 4.1) with  $n = 3$  and  $A$  given by Equation (4.2).

As noted, however, the exponent,  $n$ , depends on the creep mechanism operating. Owing to early experiments on laboratory ice and on glaciers, glaciologists have usually adopted a value of 3 for  $n$  (Hooke, 1981), although some data suggested a lower value at low stresses. These latter experiments were often questioned because tests were not continued long enough to ensure that the transient phase of creep (Figure 4.10a) was complete and the minimum creep rate (Figure 4.10b) reached. However, experiments by Pimienta and Duval (1987) and studies by Alley (1992) and Montagnat and Duval (2000) did raise the possibility of values between 1 and 2 for deformation at low stresses, temperatures, and cumulative strains, and Goldsby and Kohlstedt's experiments seem to confirm this. Montagnat and Duval argue that grain boundary migration is particularly efficient under these conditions, so internal strain energy is small, and the density of dislocations does not increase as rapidly with stress as suggested by the arguments for drag being rate-limiting. Healing of dislocations by diffusional processes may also limit the density (Alley, 1992). Goldsby and Kohlstedt (1997, 2001), on the other hand, think that grain boundary sliding is the rate-limiting process at these low stresses.

To incorporate lower values of  $n$  at lower stresses, Goldsby and Kohlstedt suggest using:

$$\dot{\varepsilon}_e = \dot{\varepsilon}_G + \dot{\varepsilon}_d \quad (4.4)$$

where  $\dot{\varepsilon}_G$  and  $\dot{\varepsilon}_d$  are the strain rates resulting from deformation limited by grain boundary slip ( $n = 1.8$  regime) and dislocation climb ( $n = 4$  regime), respectively. These strain rates are given by Arrhenius-like relations:

$$\dot{\varepsilon} = A_0 \frac{1}{d^p} \sigma^n e^{-\frac{Q}{RT}} \quad (4.5)$$

**Table 4.1** Flow law constants (from Goldsby, 2009)

	Dislocation creep				Creep limited by grain-boundary sliding			
	$A$ , MPa $^{-4}$ a $^{-1}$	$n$	$p$	$Q$ , kJ mol $^{-1}$	$A$ , MPa $^{-1.8}$ m $^{1.4}$ a $^{-1}$	$n$	$p$	$Q$ , kJ mol $^{-1}$
$T > -15^\circ\text{C}$	$1.89 \times 10^{36}$	4.0	0	181	$9.47 \times 10^{33}$	1.8	1.4	192
$T < -15^\circ\text{C}$	$3.79 \times 10^{13}$	4.0	0	60	$1.23 \times 10^{05}$	1.8	1.4	49

in which  $d$  is the grain diameter. The values of  $A_0$ ,  $p$ , and  $Q$  depend on the deformation mechanism and whether the temperature is above or below  $-15^\circ\text{C}$ . Values of these parameters suggested by Goldsby (2009) are given in Table 4.1. A flow law of this form results in  $\dot{\varepsilon}_e - \sigma_e$  curves like that in Figure 4.1 and the dashed curves in Figure 4.15. In the  $n = 4$  regime, the strain rate is independent of grain size, so  $p = 0$ .

The strain rate may also be weakly dependent on hydrostatic pressure,  $P$ . This is formally incorporated by modifying the Arrhenius relation, thus:

$$A = A_0 e^{-\frac{Q+PV}{k\theta}} \quad (4.6)$$

where  $V$  is the *activation volume* for self-diffusion, and the quantity  $(Q + PV)$  is the *activation enthalpy*. In ice, it turns out that  $V$  is very low. Greve *et al.* (2014) estimated, theoretically, that  $V$  was between  $-3.2 \times 10^{-5}$  and  $-1.7 \times 10^{-5}$  m $^3$  mol $^{-1}$  with lower values for temperatures above  $-10^\circ\text{C}$ . They compared these values with experimental values of  $-1$  to  $-2 \times 10^{-5}$  m $^3$  mol $^{-1}$  and concluded that the agreement was satisfactory, given the difficulty of the experiments. As the highest pressures in ice sheets on Earth are  $\sim 40$  MPa,  $PV$  is  $\sim -1$  kJ mol $^{-1}$ , and is thus negligible in comparison with the values of  $Q$  in Table 4.1.

Lile (1978) and Russel-Head and Budd (1979) suggested that an *enhancement factor* could be introduced to incorporate the effect of crystal orientation into the flow law. This is now normally done by multiplying the right-hand side by a factor,  $E$ , thus:

$$\dot{\varepsilon}_e = EA_0 \frac{1}{d^p} \sigma_e^n e^{-\frac{Q-PV}{k\theta}}. \quad (4.7)$$

Rigorously, however, Glen's flow law is based on the assumption that the material is isotropic (see Chapter 9). Thus, adding an enhancement factor in this way to accommodate anisotropy is tacit admission of the failure of this assumption.

We do not yet have enough understanding of the recrystallization process to write an empirical relationship between  $E$  and the factors such as temperature, strain rate, and cumulative strain on which it depends. Selection of the appropriate values of  $E$  to use in any given situation is, therefore, largely subjective.

Laboratory experiments provide some basis for estimating  $E$ . Treverrow *et al.* (2012) ran some uniaxial compression tests at  $-2^\circ\text{C}$  on laboratory ice that was

initially-isotropic. They achieved total strains exceeding 10% (Figure 4.10b), resulting in small circle fabrics. They also did experiments in simple shear on laboratory ice and on samples with strong single-maximum fabrics from Law Dome in Antarctica. In the runs using isotropic laboratory ice the strain rate went through a minimum,  $\dot{\epsilon}_{\min}$  (Figure 4.10b), before accelerating into tertiary creep,  $\dot{\epsilon}_{ter}$ . The ratio  $\dot{\epsilon}_{\min}/\dot{\epsilon}_{ter}$  is their measure of  $E$ . Their results suggested an  $E$  for small circle fabrics of ~2.4, and for single maximum fabrics of ~5.5. The latter is reasonably consistent with the experiments of Russell-Head and Budd (1979) and Baker (1981, 1982), who sheared natural ice with a single-maximum fabric in the laboratory and obtained  $E \approx 4$ . Russell-Head and Budd also found that a section of a borehole in Law Dome, Antarctica, that passed through ice with a single-maximum fabric, deformed ~4 times faster than it would have in ice without such a fabric. Somewhat later, Budd and Jacka (1989) and Jacka and Maccagnan (1984) suggested that enhancement factors of ~3 are reasonable for ice in uniaxial compression once a small circle fabric has developed, and that factors of 8–10 may be appropriate for ice in simple shear.

In contrast to these studies suggesting values of  $E$  greater than 1,  $E$  for the great circle fabric in the Vostok core (Figure 4.12d) appears to decrease from ~0.16 at 1000 m to 0.07 at 2000 m (Pimienta *et al.*, 1988). This is consistent with Lipenkov *et al.*'s (1989) analysis of their fabric measurements. Their measure of the degree to which crystals are optimally aligned for creep in uniaxial tension showed a steady decline with depth from 0.22 to 0.15 over the same depth interval.

### Effect of water

Finally, we return to the effect of water on the creep rate. This was studied by Duval (1977) in a pioneering set of sophisticated experiments. His results, expressed in terms of the increase in  $A$  with increasing water content, are shown in Figure 4.16.

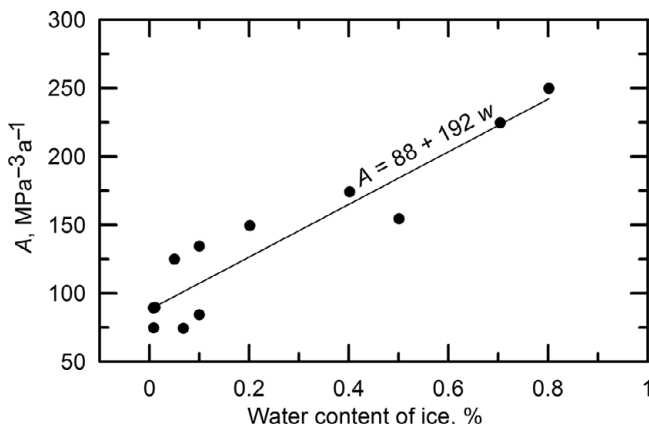


Figure 4.16 Variation in  $A$  with water content of polycrystalline ice. (Data reported by Duval, 1977)

With an increase in water content from 0.01% to 0.8%,  $A$  increases from ~90 to ~240 MPa $^{-3}$  a $^{-1}$ . Lliboutry (1983) reports that the water content of basal ice of temperate glaciers typically varies between 0.6% and 0.95%. Based on the line in Figure 4.16, this corresponds to a variation in  $A$  from 200 to 270 MPa $^{-3}$  a $^{-1}$ , and hence in  $\dot{\epsilon}$  of ~30%. Lower water contents, and hence lower values of  $A$ , are likely in temperate ice of polythermal glaciers.

## Fracture and crevassing

At sufficiently high stresses, ice fractures. Crevassing, resulting from high tensile stresses, is the type of fracturing with which people are most familiar. However, as noted in Chapter 3, fracturing near the base of the subaerial part of a calving face may be largely a consequence of crushing (compression).

Developing an understanding of the initiation and growth of fractures in ice has acquired a new urgency, owing to their importance in calving and the role of calving in the response of tidewater glaciers to climate warming. In addition, fracture propagation is now known to be important in introducing water to a glacier bed, where it increases the sliding speed.

In one of the earliest analytical studies of crevassing, Nye (1955) considered the balance between the rate at which a crevasse could be opened by a tensile stress and the rate at which it would close owing to the overburden pressure. As  $\dot{\epsilon} \propto \sigma^n$  and  $1.8 < n < 4$ , the closure rate increases non-linearly with depth. Nye considered a crevasse filled with air in a field of closely-spaced crevasses. If there is water in the crevasse, however, the water exerts an additional opening pressure and the crevasse can be much deeper. Weertman (1973) argued that if the water level were sufficiently high, a crevasse might well penetrate all the way through a glacier. Observations appear to confirm Weertman's conclusion. Zwally *et al.* (2002) attributed seasonal increases in speed at a site in Greenland to water reaching the bed through moulin, and suggested that the moulin were likely initiated by propagation of water-filled crevasses to the bed. Not long thereafter, Das *et al.* (2008) documented sudden drainage of a lake in Greenland and nearly simultaneous increases in surface speed, implying that the water had reached the bed. Boon and Sharp (2003) witnessed drainage of a lake on John Evans glacier on Ellesmere Island, followed 2 days later by emergence of turbid water at the glacier terminus. Finally, water in crevasses is believed to have played a significant role in the collapse of the Larsen B Ice Shelf mentioned in Chapter 3.

### Linear fracture mechanics

Flaws or microcracks exist in most if not all crystalline materials. At the tips of such cracks, stresses are greatly amplified over the far field state of stress, and these

amplified stresses act on single molecular bonds lacking neighbors capable of absorbing the stress. Thus, cracks may propagate at far-field stresses far below the strength of an unflawed specimen of the material. Such cracks can propagate unstably if more energy is released by a small increase in crack length than is absorbed by expansion of the crack (Griffith, 1921). Owing to the importance of fracture in the design of structures ranging from buildings to airplanes, the study of crack propagation is a well-developed discipline: *linear elastic fracture mechanics*. We will only skim the surface of this field herein.

Consider the elastic stress field around a vertical crack in the surface of a solid of infinite horizontal extent. Suppose the solid is subjected to a far field tensile stress,  $\sigma_{xx}$ , normal to the crack. Around the crack tip, stresses vary with the distance,  $r$ , and azimuth,  $\theta$ , from the tip (Figure 4.17), thus:

$$\begin{aligned}\sigma_{xx} &= \frac{K_I}{\sqrt{2\pi r}} \cos \frac{\theta}{2} \left( 1 + \sin \frac{\theta}{2} \sin \frac{3\theta}{2} \right) \\ \sigma_{zz} &= \frac{K_I}{\sqrt{2\pi r}} \cos \frac{\theta}{2} \left( 1 - \sin \frac{\theta}{2} \sin \frac{3\theta}{2} \right) . \\ \sigma_{xz} &= \frac{K_I}{\sqrt{2\pi r}} \sin \frac{\theta}{2} \cos \frac{\theta}{2} \cos \frac{3\theta}{2}\end{aligned}\quad (4.8)$$

(e.g. Lawn, 1993, p. 25).  $K_I$  is a parameter, known as the *stress intensity factor*, that applies to the crack tip. The subscript I is the mode of fracture. Mode I is opening (as in a crevasse), Mode II is sliding, and Mode III is tearing (van der Veen, 1998). We will restrict our discussion to Mode I fracture. In general,  $K_I = \beta \sigma \sqrt{a}$  where  $a$  is the crack length and  $\beta$  is a geometrical parameter that, in our case, depends upon factors such as the spacing of crevasses, the ice thickness, and the far field stress. Thus,  $K_I$  increases as either  $\sigma$  or  $a$  increase.  $K_I$ , and particularly  $\beta$ , describe how the far field stresses are amplified or intensified around a crack tip.

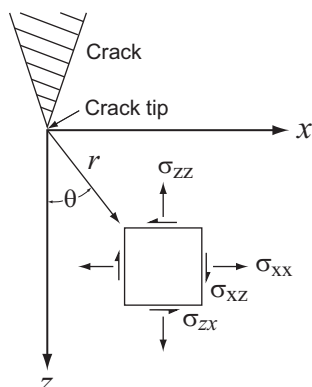


**Figure 4.17** Stress field on an infinitesimal element located a distance  $r$  from a crack tip. (Modified from Kenneally, 2003)

Clearly, high values of  $K_I$  translate into high stresses around the crack tip, and if the stresses become high enough the crack will propagate. Rather than express this critical value in terms of the stresses themselves, the standard procedure is to express it in terms of a value of  $K$  called the *fracture toughness*,  $K_{Ic}$ .  $K_{Ic}$  is a material property of the medium. If  $K_I$  exceeds  $K_{Ic}$ , the fracture will propagate unstably. Rist *et al.* (1999) have summarized their own measurements of  $K_{Ic}$  on ice cores from Antarctica and other worker's measurements on other types of samples, and find that it increases approximately linearly with ice density (Figure 4.18). The scatter in the data is large, however.

To determine a stress intensity factor, one needs a solution for the stresses in the vicinity of a crack tip. If one knows  $\sigma_{xx}$  at a location  $(r, \theta)$ , for example,  $K_I$  can be determined from the first of Equations (4.8). This is a *boundary value* problem; one needs to specify the stresses at the boundaries of a domain and solve for those in the interior of the domain. Analytical solutions are available for certain simple geometries, but numerical techniques are required for more complicated situations. Fortunately, one usually does not need to perform these calculations, as stress intensity factors are tabulated for many common situations in handbooks such as Sih (1973). Conveniently, they obey the principle of superposition; thus, in problems with a complex stress configuration, if one can obtain stress intensity factors for each of the stresses separately, they can be added to obtain the stress intensity factor

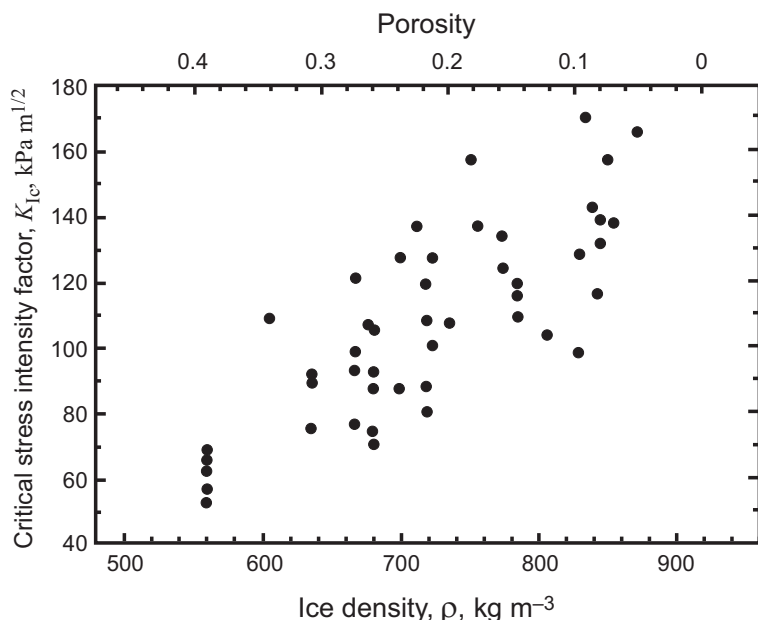


**Figure 4.18** Variation of  $K_{Ic}$  with density. Based on laboratory measurements on natural ice specimens from Ronne Ice Shelf. (After Rist *et al.*, 1999; reproduced with permission of the authors and the American Geophysical Union)

for the whole problem (Kanninen and Popelar, 1985, p. 27). We will illustrate this in the following paragraphs.

The alert reader may have noticed that the stresses in Equations (4.8) become infinite as  $r \rightarrow 0$ . However, deformation in a region immediately around the crack tip is plastic, and this keeps the stresses finite. To estimate the radius,  $r_p$ , of this plastic region, take  $\theta = 0$  in the first or second of Equations (4.8), assume that plastic behavior will occur once the stress exceeds 0.1 MPa (a commonly-cited plastic “yield strength” for ice), adopt a value for  $K_{Ic}$  of  $0.16 \text{ MPa m}^{-1/2}$ , and solve for  $r_p$ . The result is  $r_p \approx 0.4 \text{ m}$ . The principles of linear elastic fracture mechanics only apply if  $r_p$  is small compared with  $a$ . As we are concerned principally with crevasses, and as most crevasses reach depths of at least 10–20 m, this condition is satisfied. It also bears mentioning that, as  $r$  becomes large, additional terms must be added to Equations (4.8) so the right-hand sides conform with the far-field stresses rather than  $\rightarrow 0$  (van der Veen, 1998).

Let us consider the case of a single crevasse in a glacier of infinite horizontal extent subjected to a tensile stress,  $\sigma_{xx}$ . We need a stress intensity factor both for the tensile stress that tends to open the crack and for the compressive stress due to the overlying ice that tends to squeeze it closed. For the case of a crack of depth  $d$  in a medium of thickness  $H$  subjected to such a tensile stress,

$$K_{It} = \left[ 1.12 - 0.23 \frac{d}{H} + 10.55 \left( \frac{d}{H} \right)^2 - 21.72 \left( \frac{d}{H} \right)^3 + 30.39 \left( \frac{d}{H} \right)^4 \right] \sigma_{xx} \sqrt{\pi d} \quad (4.9)$$

(van der Veen, 1998). The subscript “t” signifies tension. If  $d \ll H$ , this reduces to:  $K_{It} = 1.12\sigma_{xx}\sqrt{\pi d}$ . The hydrostatic stress from the weight of the ice is  $-\rho_i g z$ , where  $\rho_i$  is the density of ice,  $g$  is the acceleration due to gravity, and  $z$  is the depth below the surface. The negative sign indicates that the stress is compressive. For a crack of depth  $d$  with a load varying from 0 at the surface to  $-\rho_i g d$  at the crack tip,  $K_{Io} = -0.683\rho_i g d \sqrt{\pi d}$  (van der Veen, 1998). The subscript “o” denotes overburden. The net stress intensity factor for the problem is then:  $K_{INet} = K_{It} + K_{Io}$ .

Let’s now explore the conditions under which a surface crack will propagate, and the depth to which it will extend. Vaughan (1993) found that tensile stresses between 0.09 and 0.32 MPa were necessary to open crevasses, so let’s assume  $\sigma_{xx} = 0.2 \text{ MPa}$ . If  $d \ll H$ ,  $K_{INet}$  varies with crevasse depth, as shown in Figure 4.19. From the enlargement in the lower left we see that once a crack  $\sim 0.16 \text{ m}$  long is formed,  $K_{INet} = K_{Ic}$ . Any further increase in crack depth will move the system into the field of unstable crack growth, and the crack will propagate unstably to a depth of  $\sim 35 \text{ m}$ . The depth, of course, depends on  $\sigma$ , but this is a realistic depth for air-filled crevasses.

We can use these principles to explore the question, raised earlier, of how high water levels must be maintained in a crevasse to potentially drive the crevasse

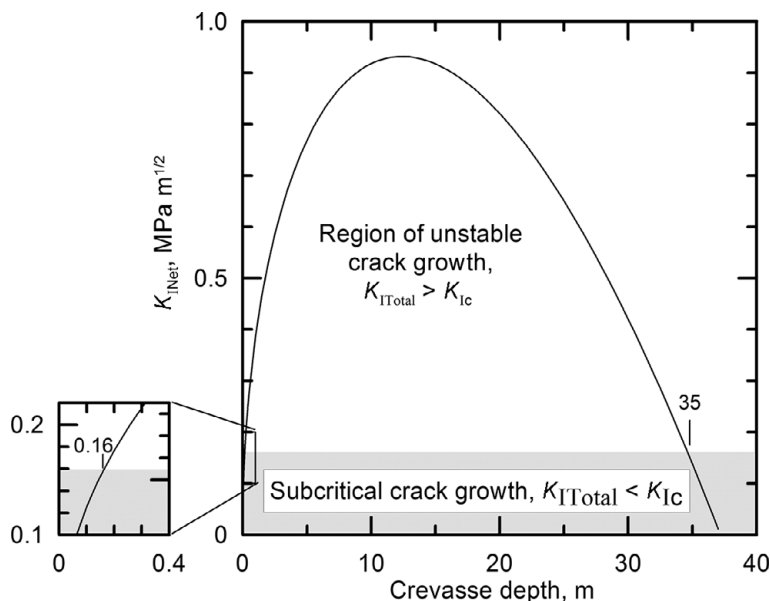


**Figure 4.19** Variation in stress intensity factor with crevasse depth for an air-filled crevasse formed by a tensile stress of 0.2 MPa. The crevasse would propagate to a depth of 35 m. If it got deeper,  $K_{I\text{Net}}$  would decrease below  $K_{Ic}$  and the crevasse would not propagate.

to the bed. By analogy with  $K_{I0}$  above, the stress intensity factor for this stress is  $K_{Iw} = 0.683\rho_w gd_w \sqrt{\pi d_w}$ , where  $\rho_w$  is the density of water and  $d_w$  is the depth of water in the crevasse.  $K_{Iw}$  is positive because the water pressure tends to open the crevasse. Now,  $K_{I\text{Net}} = K_{It} + K_{I0} + K_{Iw}$ , so once  $K_{I\text{Net}} > K_{Ic}$ , it will remain that way as long as  $K_{Iw} \geq |K_{I0}|$ . This will be the case as long as  $d_w \geq d(\rho_i/\rho_w)^{2/3}$ , or  $d_w \geq \approx 0.94d$ . If we let  $a = d - d_w$ , the distance from the glacier surface to the water surface, then the condition for crevasse propagation is  $a \leq \approx 0.06d$ , so as  $d$  increases, the water level can fall slightly and still drive the crevasse deeper. Note, however, that once  $d > \sim 0.25H$ , the value of  $K_{It}$  calculated from Equation (4.9) begins to differ significantly from the linear approximation, so calculations need to use Equation (4.9).

Two additional factors that need to be considered in calculations of crevasse depth are: (1) the presence of low density firn at the surface, and (2) the effect of other crevasses on  $\sigma_{xx}$ . In both cases, the consequences of taking these factors into consideration are fairly obvious. Low density firn reduces  $K_{I0}$  so crevasses penetrate deeper, and if there is a field of crevasses, the tensile stress will be relieved by adjacent crevasses,  $K_{It}$  will be lower (Equation 4.9), and no one crevasse will penetrate as deeply as would a single crevasse. Stress intensity factors can be obtained for these situations (van der Veen, 1998), but the algebra, while straightforward, becomes considerably more complicated.

### Effect of fracture on flow law

Cracks, even small ones that would not qualify as crevasses, weaken the ice. To quantify this, Borstad *et al.* (2016) define a damage parameter,  $D$ :

$$D = 1 - \left( \frac{A_o}{A_d} \right)^{1/n} \quad (4.10)$$

where  $A_d$  is the rate factor in the weakened ice. This is a standard approach in continuum damage mechanics (Pralong and Funk, 2005). Solving this for  $A_d$  and inserting the result in Equation (4.7) in place of  $A_o$  yields:

$$\dot{\epsilon}_e = EA_o \frac{1}{d^p} \left( \frac{\sigma_e}{1 - D} \right)^n e^{-\frac{Q-PV}{RT}}. \quad (4.11)$$

When there is no damage,  $A_d = A_o$  and  $D = 0$ . Conversely, if the damage is extreme,  $A_d$  becomes large,  $D \rightarrow 1$ , and  $\dot{\epsilon}_e$  becomes large. The challenge is to determine  $A_d$ . Note, also, that  $D$  could include softening due to development of an ice fabric with a preferred orientation of  $c$ -axes, thus replacing  $E$ .

A conceptual model of how a system might evolve is illustrated in Figure 4.20. As  $\tau_e$  increases,  $\dot{\epsilon}_e$  increases along the line labeled “ $D = 0$ .” Damage is presumed to occur once  $\tau_e$  exceeds a threshold value,  $\tau_o$  (taken here to be 0.0355 MPa), at which cracks propagate. Once damage has occurred at some location which we will call A, the ice there can no longer support the applied stress. Some of the resistance to flow

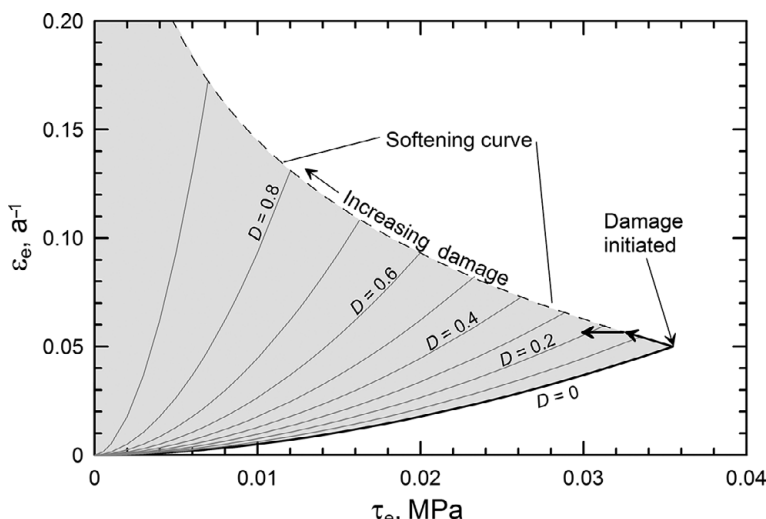


**Figure 4.20** Variation in  $\dot{\epsilon}_e$  with  $\tau_e$  in ice with varying degrees of damage,  $D$ . In undamaged ice,  $\dot{\epsilon}_e$  increases along the  $D = 0$  curve. Possible  $\dot{\epsilon}_e : \tau_e$  states are shaded. Outside the shaded region,  $\dot{\epsilon}_e$  is either too low for the given  $\tau_e$ , or the ice is too weak to support the given  $\tau_e$ . Curves of varying  $D$  are calculated using Equation (4.11) with the constants in Table 4.1 and with  $d = 4$  mm,  $E = 1$ , and  $PV \ll Q$ . Softening curve is calculated using Equation (4.12), with  $\kappa = 2.5$  and  $\tau_o = 0.0355$  MPa. The latter results in  $\dot{\epsilon}_e = 0.5$   $a^{-1}$  at failure.

is thus transferred elsewhere in the ice mass, and the stress at A is reduced to a level that the damaged ice can support. Let's suppose that, for a while, the stress continues to *try* to increase. This results in further damage, further weakening of the ice at A, further transfer of the resisting stresses elsewhere, and a further drop in stress at A; the system follows the heavy arrow extending away from the point of damage initiation in Figure 4.20. Eventually, enough stress has been transferred elsewhere so that the stress at A drops below that needed for further damage (second heavy arrow in Figure 4.20). Once this occurs, the damaged ice may begin to "heal" as crevasses close or are filled with water that then refreezes. Such healing is a result of different processes, so Borstad *et al.* (2016) do not try to analyze it.

Borstad *et al.* call the line of increasing damage in Figure 4.20 the "softening curve," and suggest that it may be described by:

$$\tau_e = \tau_0 e^{\left( -\frac{\dot{\epsilon}_e - \dot{\epsilon}_0}{\dot{\epsilon}_0(\kappa-1)} \right)}. \quad (4.12)$$

Here,  $\tau_0$  is the threshold stress for damage initiation,  $\dot{\epsilon}_0$  is the strain rate at that stress, and  $\kappa (> 1)$  is a ductility parameter that defines the initial downward slope of the softening curve. Thus  $\tau_0$  and  $\kappa$  are physically meaningful parameters that could presumably be established empirically.

To determine  $D$  at various times on the remnant Larsen B ice shelf, Borstad *et al.* (2016) compared strain rates calculated at grid points across the ice shelf using a numerical model with measured ones. The resulting values of  $D$ , together with the observed and modeled stresses and strain rates, yielded  $\kappa = 2.8 \pm 0.4$ .

Damage is clearly a factor that needs to be considered in modeling ice flow, particularly in outlet glaciers and ice shelves, so more work along these lines is warranted.

## SUMMARY

In this chapter, we first reviewed the crystal structure of ice, noting that there are imperfections in this structure, called dislocations, that allow ice (and other crystalline materials) to deform under stresses that are much lower than would be required in the absence of such imperfections. Processes that may limit the deformation rate are those which: (1) inhibit motion of a dislocation in a single crystallographic plane (drag), (2) prevent dislocations from climbing from one crystallographic plane to another to get around tangles, (3) impede motion on certain other crystallographic planes, and (4) inhibit slip between crystals.

Experimental data (Goldsby and Kohlstedt, 1997, 2001) suggest that climb limits dislocation creep at higher stresses (the  $n = 4$  regime) and grain-boundary slip limits

deformation by slip on basal crystallographic planes at intermediate stresses (the  $n = 1.8$  regime). At still lower stresses, diffusion and mechanisms that inhibit slip on basal planes are rate limiting.

When polycrystalline ice is subjected to a stress, some crystals will be oriented in a way that allows them to deform easily, and others will not. Stress concentrations thus develop, and drive recrystallization. Three distinct processes are involved in recrystallization: grain growth, polygonization, and nucleation of new grains. Recrystallization leads to preferred orientations of *c*-axes, and hence to more rapid deformation. The principal processes involved in the development of these fabrics appear to be nucleation of new grains and rotation of grains as slip occurs on their basal planes.

To place creep processes in ice in a more general framework, we introduced a deformation mechanism map in which we displayed deformation mechanisms and strain rates for a range of grain sizes and stresses. Prior to the studies of Goldsby and Kohlstedt (1997, 2001), most experiments were at stresses and grain sizes that spanned the boundary between dislocation creep and creep limited by grain boundary sliding. It now seems likely, however, that much of the deformation in natural ice masses occurs in the latter regime.

Next, we introduced Glen's flow law, and related the exponent,  $n$ , in the flow law to these creep mechanisms. We considered how temperature, pressure, texture, fabric, and water content affect the rate factor,  $A$ . Temperature and pressure effects may be incorporated into the flow law by rigorous, physically-based modifications, whereas *ad hoc* procedures based on empirical evidence are used to incorporate the other effects.

Finally, we introduced principles of linear elastic fracture mechanics and demonstrated that these principles can be used to estimate crevasse depths. Crevassing weakens ice, and a damage factor,  $D$ , may be used to incorporate this into the flow law.

# 4

## Flow and fracture of a crystalline material

In this chapter you will be introduced to the voluminous literature on deformation or *creep* of ice. We begin by looking at deformation processes on an atomic scale, and then introduce empirical and semi-empirical relations that provide a macroscopic description of the deformation. Finally, we briefly consider crevassing, using principles of linear fracture mechanics.

First, let's introduce (Figure 4.1) some experimental data on the dependence of strain rate,  $\dot{\epsilon}$ , on stress,  $\sigma$ , as this will form a useful background for discussion of creep mechanisms. Starting with John Glen's (1955) pioneering uniaxial-compression experiments, data like those in Figure 4.1 have been used to establish the form of the flow law presented in Equation (2.15):

$$\dot{\epsilon}_e = A\sigma_e^n. \quad (4.1)$$

The slopes of the lines in Figure 4.1 reflect the exponent,  $n$ . Despite the fact that in real glaciers and ice sheets,  $\sigma_e$  is generally  $<0.1$  MPa, there are few data points at such low stresses. This is because creep rates are then so low that experiments must be continued for days to weeks or months to yield useful results, and holding stresses and temperatures constant over such long time periods is challenging. However, at stresses less than  $\sim 0.2$  MPa (depending on grain size), the data suggest that  $n \approx 1.8$ , while at stresses greater than  $\sim 2$  MPa,  $n \approx 4$  (Goldsby and Kohlstedt, 1997, 2001). In the former regime,  $\dot{\epsilon}$  decreases with increasing grain size, but in the latter it is independent of grain size. At still lower stresses, Goldsby and Kohlstedt (2001) found that  $d\dot{\epsilon}_e/d\sigma_e$  increased again ( $n \approx 2.4$ ), and that the rate was again independent of grain size.

A large volume of experimental data on ice deformed in the laboratory and on natural ice in glaciers and ice shelves at stresses between  $\sim 0.02$  and  $\sim 10$  MPa (see Hooke (1981) and Goldsby and Kohlstedt (2001) for references) suggests that  $n \approx 3$ , a value that has been adopted in many numerical calculations. From Figure 4.1, it appears that this value reflects averaging of data spanning the transition from the  $n = 1.8$  to the  $n = 4$  regime, and that use of it may underestimate  $\dot{\epsilon}_e$  if the value of  $A$  is based on experiments at higher stresses.

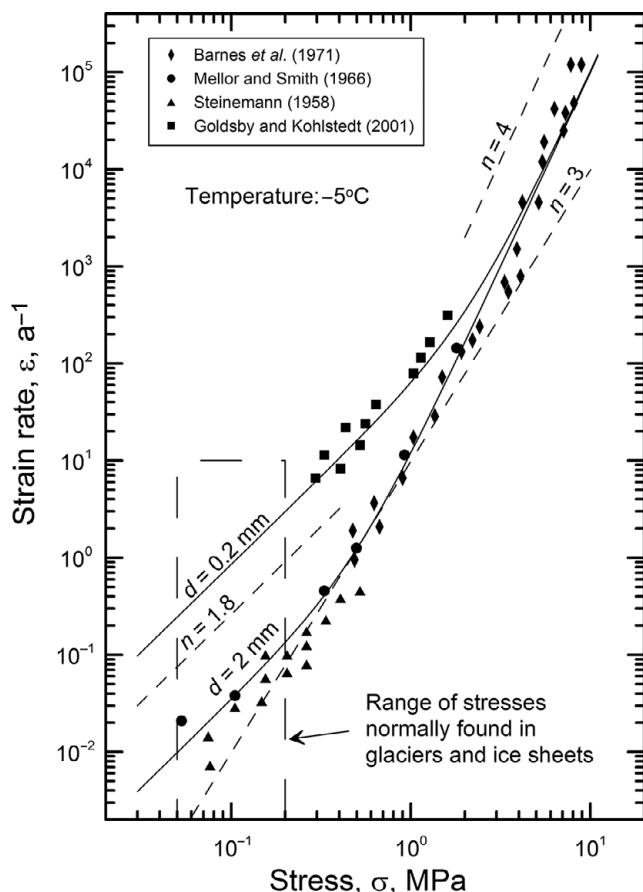


**Figure 4.1** Laboratory measurements of strain rate at various stresses for 0.2 mm and 2 mm ice at  $-5^{\circ}\text{C}$ . All tests were run to  $\dot{\varepsilon}_{\min}$ . Slopes corresponding to  $n = 1.8, 3.0$ , and  $4.0$  are shown by dashed lines. Experiments were conducted at temperatures between  $-4$  and  $-9^{\circ}\text{C}$ , and are adjusted to  $-5^{\circ}\text{C}$ . (Based on Goldsby, 2009, Figure 60.2. Reproduced with the permission of the authors and the American Geophysical Union)

## Crystal structure of ice

There are nine known crystalline forms of ice, but seven of them are stable only at pressures in excess of about 200 MPa, and the eighth, a cubic form, ice Ic, is stable only at temperatures below about  $-100^{\circ}\text{C}$  (Figure 4.2). As the highest pressures and lowest temperatures in glaciers on Earth are about 40 MPa and  $-60^{\circ}\text{C}$ , respectively, these eight forms need not concern us. We, thus, restrict our attention to the common form of terrestrial ice, ice Ih.

The structure of ice Ih is shown in stereoscopic view in Figure 4.3a. It is a hexagonal mineral (hence the “h”) with a rather open structure in which every

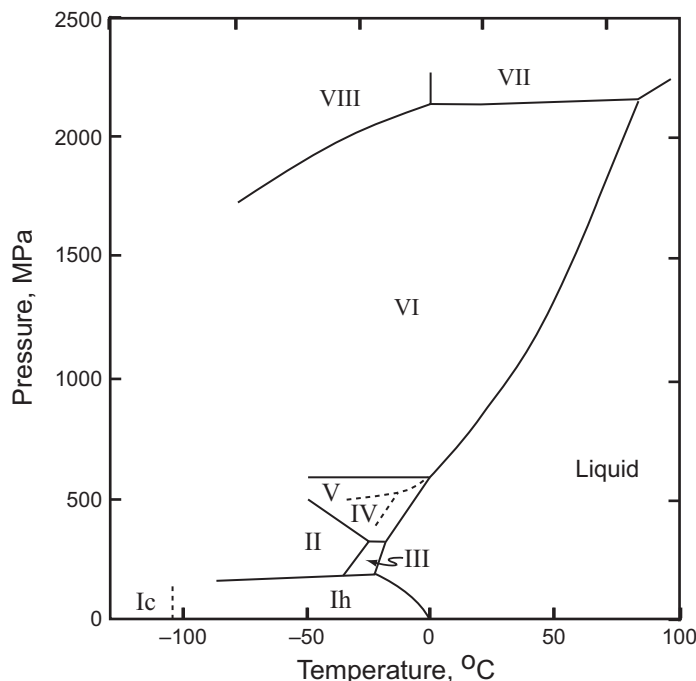


**Figure 4.2** Part of the phase diagram of water (after Kamb, 1965, Figure 1). The various polymorphs of ice are designated by roman numerals. Ice IV is a metastable phase, unstable everywhere with respect to ice V. Ice Ic is also metastable with respect to ice Ih.

oxygen atom, represented by the large circles in Figure 4.3a, is bonded to four additional oxygen atoms at the corners of a tetrahedron. The tetrahedra are joined together in such a way that the oxygens form hexagonal rings, with the O=O bonds zigzagging slightly up and down as one progresses around the ring (Figure 4.3b); three of the oxygens thus lie 0.09 nm above the other three. The plane of these rings is called the *basal plane* of the crystal structure.

The fourth oxygen atom in the tetrahedron is ~0.28 nm above or below that in the center of the tetrahedron. A line parallel to this bond, and hence normal to the basal plane, is called the *c-axis*.

Around each oxygen atom there are, of course, two hydrogen atoms. The hydrogen atoms, represented by the small circles in Figure 4.3a, lie on the bonds between the oxygen atoms. They are situated close to the oxygen to which they are bonded. As each oxygen atom is bonded to four other oxygens, only two of these hydrogen sites, selected at random, are occupied.

Along each O=O bond there are two hydrogen sites. Normally only one of these is occupied. Situations in which neither site is occupied are called *Bjerrum L defects*, and situations in which both sites are occupied are called *Bjerrum D defects*, or just *L* and *D* defects, respectively.

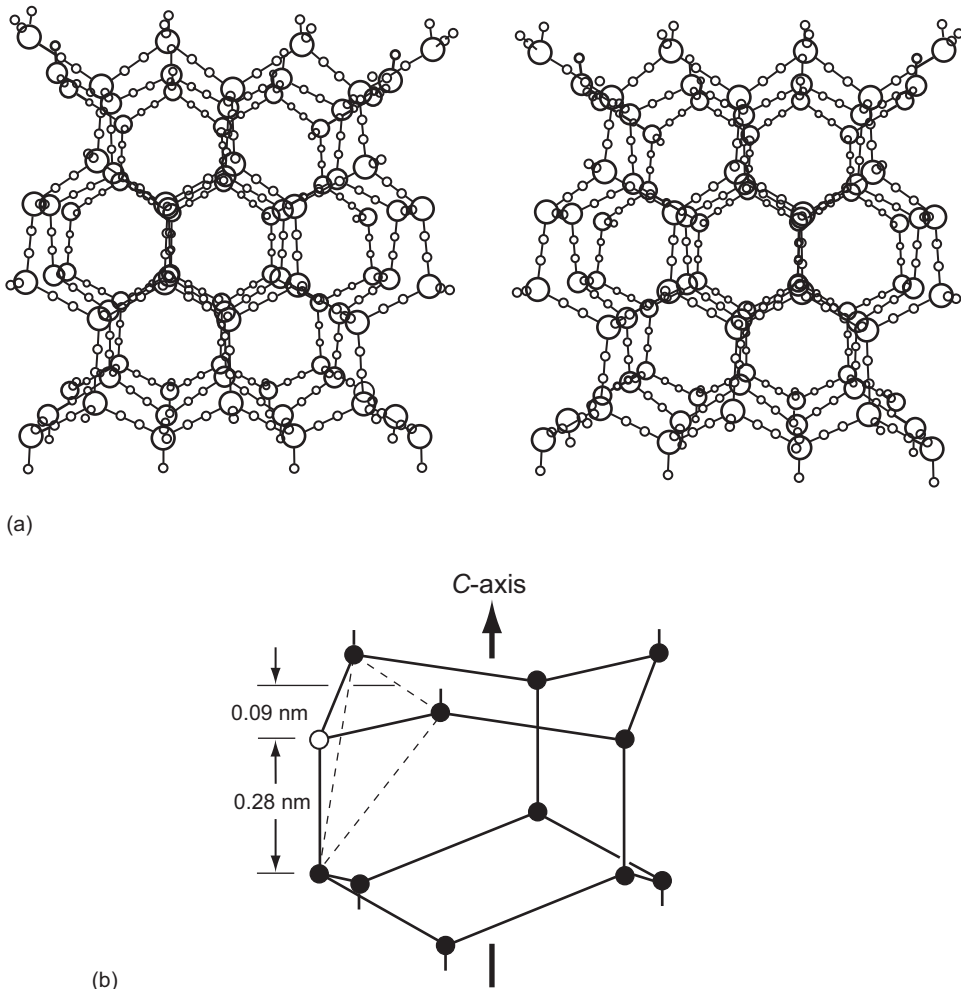


**Figure 4.3** (a) Stereographic view of the structure of ice Ih, viewed down the *c*-axis. Only half of the possible hydrogen sites, indicated by small circles, are occupied (after Hamilton and Ibers, 1968). (b) Structure of ice 1h viewed normal to the *c*-axis. Two of the hexagonal rings are shown. Short lines leading upward and downward from these rings are bonds to rings above and below. The oxygen shown with an open circle is the center of a tetrahedron, part of which is shown by the light dashed lines. (Modified from Hobbs, 1974, Figure 1.7)

## Dislocations

*Dislocations* are another type of defect in crystals. They are places where the crystal lattice is discontinuous or offset in some way. Virtually all crystalline materials contain dislocations. The two basic types of dislocation, the *edge dislocation* and the *screw dislocation*, are illustrated in Figure 4.4.

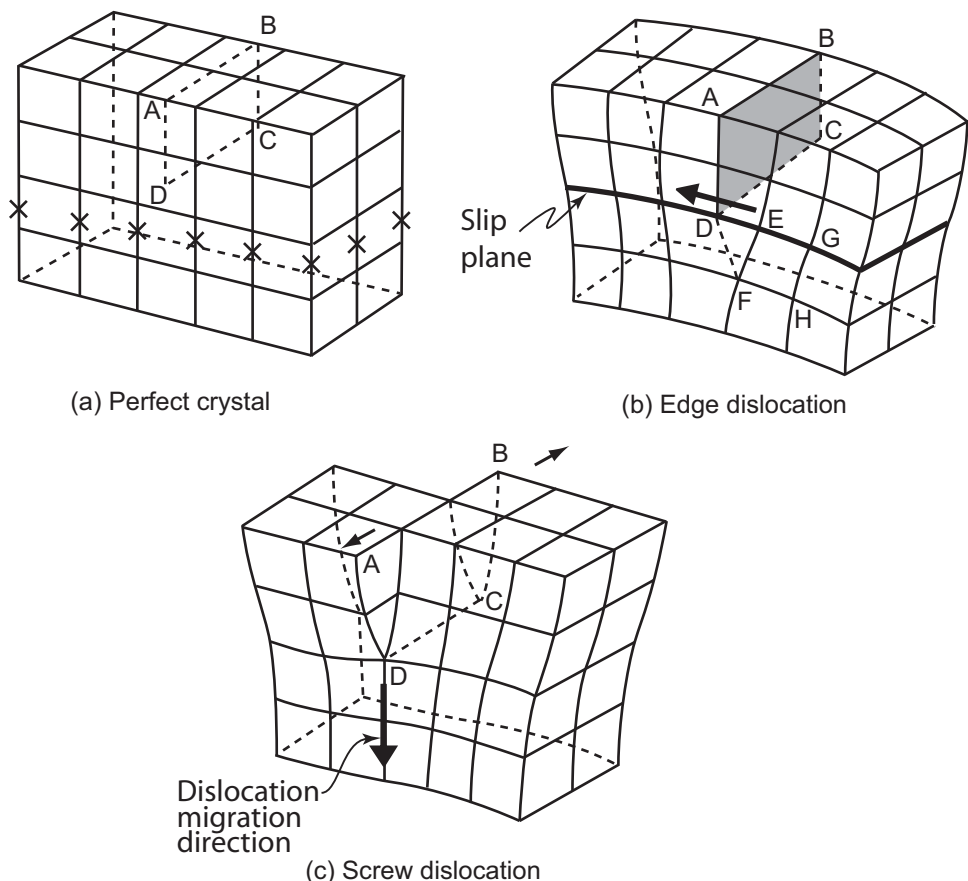


**Figure 4.4** (a) A perfect crystal. (b) An edge dislocation. (c) A screw dislocation. Heavy arrows in (b) and (c) show the direction of dislocation movement. Light arrows in (c) show a sense of offset across dislocation. (Modified from Hull, 1969, p. 17)

Dislocations play a vital role in the deformation or creep of crystalline materials. If one tried to deform the perfect crystal in Figure 4.4a by shearing the top three layers of atoms over the bottom two, the stress required would be enormous, as every one of the bonds indicated by an “x” would have to be broken *simultaneously*. In contrast, the crystal in Figure 4.4b, in which there is a dislocation, would deform much more easily because the bonds could be broken sequentially, one at a time. The bond between E and F would be broken first, and a new bond formed between D and F. Then the bond between G and H would be broken and a new one formed between E and H. This breaking and reforming of bonds results in movement of the dislocation. Calculations show that, in the absence of dislocations, crystalline materials could not possibly deform under the stresses at which they are observed to deform. In fact, it was through such theoretical studies that the existence of dislocations was first inferred.

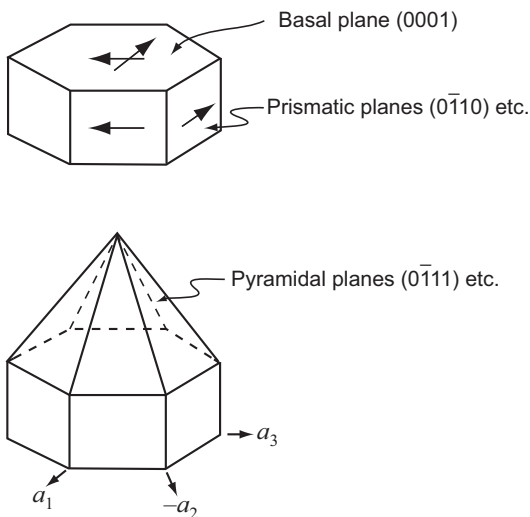


**Figure 4.5** Crystallographic planes in a hexagonal crystal.

Movement of dislocations takes place along planes defined by the crystal structure. These planes are called *slip planes* or *glide planes* (Figure 4.4b). The dominant glide plane in ice is the basal plane, as there are fewer O=O bonds between basal planes than there are within a basal plane (Figure 4.3b). Other possible glide planes are the prismatic and the pyramidal planes (Figure 4.5). Laboratory experiments have shown that the resistance to shear on basal planes is much less than that on the other crystallographic planes.

If strain in ice were homogeneous, deformation of one crystal in a polycrystalline aggregate would necessitate deformation of neighboring crystals to preserve continuity of the medium. Because basal planes in many crystals will not be oriented parallel to the maximum resolved shear stress, deformation along these planes will be slower than in planes that are better oriented. Crystals thus transmit stress nonuniformly (Duval *et al.*, 1983). Within such a polycrystalline sample, the *local* stress may vary over two orders of magnitude and strain is not homogeneous

If a surface is cut through a crystal of unstressed ice the density of dislocations on the surface is likely to be  $<10 \text{ mm}^{-2}$ . Upon application of a stress, the number of dislocations increases rapidly to  $>10^3 \text{ mm}^{-2}$  (Montagnat and Duval, 2004). The new dislocations may be generated at points where shear along a discrete atomic plane in one crystal or slip along grain boundaries between two crystals (Figure 4.6) focuses stress at a boundary of a neighboring crystal. Dislocations are formed at this boundary and move into the neighboring crystal. New dislocations may also be generated at *Frank–Read sources*. A Frank–Read source consists of a dislocation lying between two points at which the dislocation is fixed, called *pinning points*. Impurities or immobile tangles of dislocations may serve as

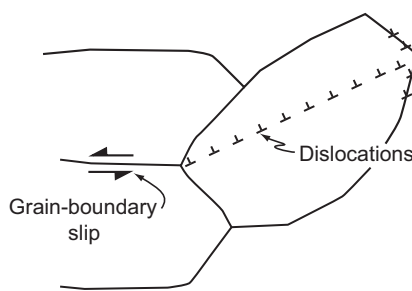


**Figure 4.6** Generation of dislocations at a three-grain intersection due to grain-boundary slip. The mismatch at the intersection may also be accommodated by diffusion or grain rotation.

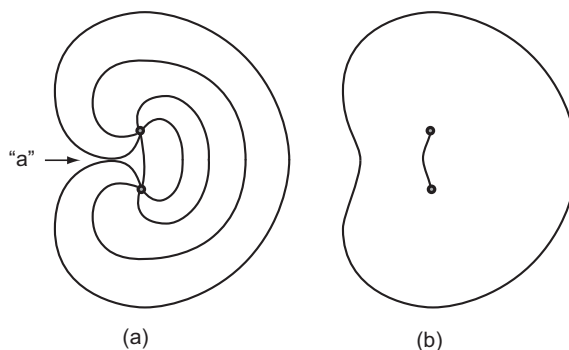


**Figure 4.7** Generation of dislocations at a Frank–Read source. Each line in (a) represents a successive position of a dislocation as it is bowed out between two pinning points. (b) The final stage with the new dislocation expanding outward and another dislocation between the pinning points.

pinning points. When a stress is applied, this dislocation is bowed out until it meets itself (at “a” in Figure 4.7a). At this point, the dislocations coming from opposite directions are of opposite sign, and the dislocation is locally annihilated. This leaves a dislocation in a ring and a new dislocation between the pinning points (Figure 4.7b). The new dislocation can then repeat the process, so this is a continuous source of dislocations. Dislocations generated by a Frank–Read source may multiply by spreading to neighboring planes, a process called *multiple cross glide* (Hull, 1969, pp. 165–167).

## Activation energy

The activation energy is the magnitude of an energy barrier that must be overcome for a kinematic process, such as movement of a dislocation, to occur. Each kinematic process has its own activation energy, and for a given process activation energies are different in different materials.

To determine the activation energy for a process, we need to introduce an expression for the rate factor,  $A$ , in Equation (4.1), namely:

$$A = A_0 e^{-\frac{Q}{R\theta}} \quad (4.2)$$

in which  $Q$  is the activation energy,  $R$  is the universal gas constant, and  $\theta$  is the Kelvin temperature. This equation was proposed by Svante Arrhenius in 1889 and bears his name. It is widely used in the study of thermally-activated processes and reactions.  $A_0$  is a reference parameter that is independent of temperature; literally, it is the viscosity at  $\theta = \infty$ , but this is physically meaningless.  $A_0$  is, however, a function of other parameters which we will discuss later.

Consider two tests run at the same stress,  $\sigma_e$ , but at different temperatures,  $\theta_1$  and  $\theta_2$ . Owing to the difference in temperature, the tests will yield two different strain rates,  $\dot{\epsilon}_1$  and  $\dot{\epsilon}_2$ . Combining Equations (4.1) and (4.2), writing the resulting equation separately for each of the two tests, and dividing one by the other yields:

$$\frac{\dot{\epsilon}_1}{\dot{\epsilon}_2} = e^{-\frac{Q}{R}\left(\frac{1}{\theta_1} - \frac{1}{\theta_2}\right)}. \quad (4.3)$$

As the strain rates, temperatures, and gas constant are all known, the only unknown in Equation (4.3) is  $Q$ , so we can solve for it. To reduce experimental uncertainty, it is normal to run a series of tests at different temperatures and to plot the results on a graph of  $\ln(\dot{\epsilon})$  versus  $1/\theta$  (Figure 4.8).  $Q$  is then obtained from the slope of a line through the data points.

## Premelting

The data points at lower temperatures in Figure 4.8 fall on a straight line with slope  $-Q/R$ . However, at temperatures above  $-15^\circ\text{C}$ , the points deviate from a straight line in a direction implying a higher activation energy; in other words, the increase in creep rate with temperature is greater than expected. At these temperatures, there is also a rapid increase in the electrical conductivity of ice (Mellor and Testa, 1969), and a less striking but still significant increase in the heat capacity (Harrison, 1972). These phenomena are attributable to development of a “layer” with a liquid-like structure on grain boundaries – a layer that allows ice skates to slide – and particularly at multiple grain junctions (Duval *et al.*, 1983; de La Chapelle *et al.*, 1995; Rosenberg, 2005). This is a process known as *premelting*. The layer is *liquid-like* inasmuch as it has a short-range hexagonal structure close to the ice interface, but becomes fully disordered, like water, further from the interface. The intermolecular distance close to the ice surface is smaller than in water, and that in water is, of course, less than in ice (which is why icebergs float)(Rosenberg, 2005). The lack of order is due to the discontinuity in crystal structure at the grain boundary, resulting

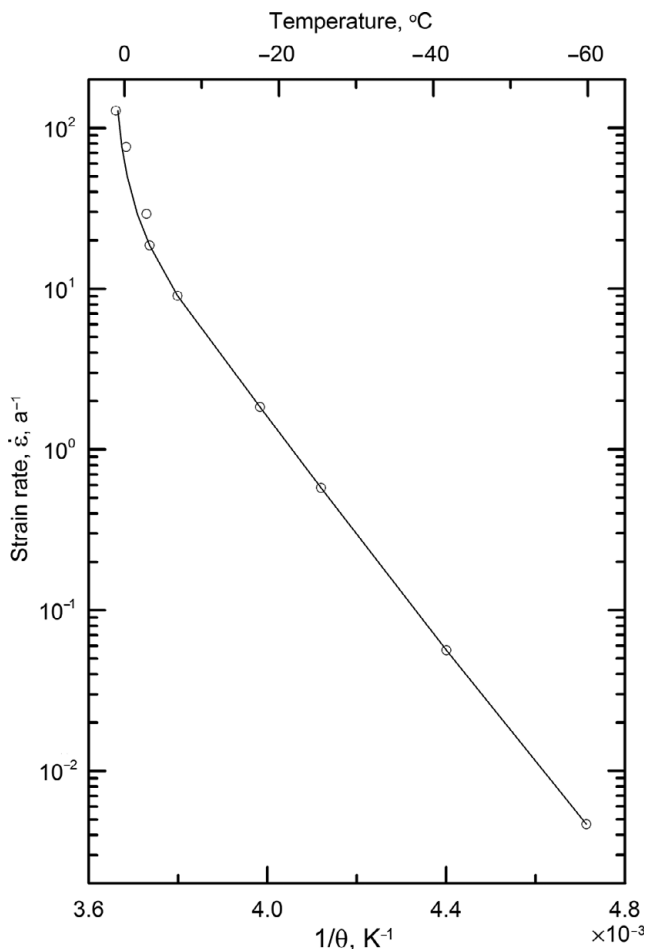


**Figure 4.8** Results of a laboratory experiment on the variation of strain rate with temperature. All experiments were run at the same stress. The slope of the straight part of the curve is proportional to the activation energy. (After Mellor and Testa, 1969, Figure 3. Reproduced with permission of the International Glaciological Society)

in incomplete, and thus weaker molecular bonds. This layer explains the increase in creep rate (because grain-boundaries become glissile), the increase in electrical conductivity (as impurities, if present, are concentrated at grain boundaries and impure water has a higher conductivity than the ice that was melted to form the layer), and the increase in heat capacity (because, of any heat added, some is used to melt ice rather than to increase the temperature). The effect of the liquid-like layer increases as the temperature increases, resulting in an apparent activation energy substantially higher than at lower temperatures. In the  $n = 4$  regime, Goldsby (2009) suggests using  $60 \text{ kJ mol}^{-1}$  at temperatures below  $-15^{\circ}\text{C}$  and  $181 \text{ kJ mol}^{-1}$  at temperatures above  $-18^{\circ}\text{C}$ . The overlap is intentional.

Various experiments have shown that premelting actually begins at temperatures as low as  $-35^{\circ}\text{C}$ , that the thickness of the liquid-like layer is then between 1 and 10 nm, and that grain-boundary sliding likely occurs at these and even lower

temperatures (D. Goldsby, written communication, March 2019). The thickness begins to increase at  $\sim -15^{\circ}\text{C}$ , and thereafter increases exponentially with increasing temperature (Rosenberg, 2005).

## Deformation mechanisms

Deformation mechanisms are mechanisms that produce strain. The literature on these mechanisms in ice is confusing, because a substantial amount of new terminology must be introduced, and processes may be described in different ways by different authors. An important distinction must be made between these mechanisms that produce strain and others that limit the strain rate but may not produce strain. These rate-limiting mechanisms are discussed later.

Three important mechanisms are diffusion, dislocation creep, and grain boundary sliding.

### Diffusion

Atoms migrate through solid materials by a process called *diffusion*. When the diffusion occurs in the absence of a gradient in chemical potential, it is referred to as *self-diffusion*. Diffusion along grain boundaries is *grain boundary diffusion* or simply *boundary diffusion*; the resulting deformation is *Coble creep* (Figure 4.9). Diffusion through a crystal lattice is called *volume diffusion*, and the deformation is *Nabarro-Herring creep*. The activation energy for grain growth in polar firn, a process likely dominated by grain boundary diffusion, is  $\sim 49 \text{ kJ mol}^{-1}$  (Gow, 1969; Goldsby and Kohlstedt, 2001), while that for volume self-diffusion of hydrogen and oxygen in ice is  $\sim 60 \text{ kJ mol}^{-1}$  (Ramseier, 1967). In addition to producing deformation, diffusion may result in movement of dislocations.

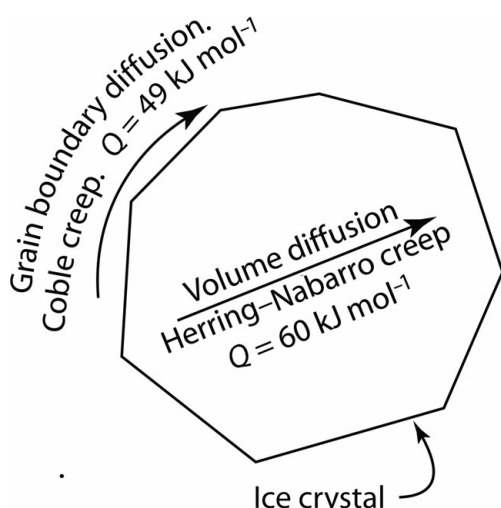


Figure 4.9 Self-diffusion mechanisms.

At very low stresses and small grain sizes, ice may deform entirely by diffusional creep. According to classical diffusion theory, and in contrast to the situation with power-law creep, the strain rate is then linearly proportional to stress. In addition, the deformation rate increases with decreasing grain size because diffusion paths are shorter. Because pure diffusional flow occurs at such low stresses, and hence strain rates, laboratory experiments to study it have yet to be successful. However, large fractions of ice sheets and ice shelves are deforming at stresses under which diffusional flow could predominate.

### Dislocation creep

When a sufficient number of dislocations move, crystals become distorted. This is referred to as *dislocation creep*.

Dislocations, as noted, move along glide planes defined by crystallographic structure. If the slip plane is the basal plane of the crystal, the deformation is called *basal slip*. Because the bonds between basal planes are relatively weak, basal slip is undoubtedly the most important slip system in ice. However, basal slip alone cannot explain deformation of a polycrystalline aggregate; at least three independent slip systems are required, but more on this later.

Dislocation creep produces flattened grains and irregular, sutured grain boundaries; it only rarely produces intersections at which four grains meet (Goldsby and Kohlstedt, 2002).

### Grain boundary sliding

In experiments at relatively low stresses, Goldsby and Kohlstedt (1997, 2001) found that  $n \approx 1.8$ , the activation energy was  $\sim 49 \text{ kJ mol}^{-1}$ , and  $\dot{\epsilon}$  depended on grain size (Figure 4.1). In thin sections, they noted that grain boundaries were relatively straight, grains were not flattened, and four-grain junctions were common, characteristics that are distinctly different from those produced by dislocation creep but that are commonly associated with another deformation mechanism: slip along boundaries between grains, or *grain boundary sliding*. Similar characteristics are observed in ice near the margin of Barnes Ice Cap, where deformation measurements yielded  $n \approx 1.65$  (Hooke, 1973b), and in the upper 2000 m or so of the Greenland and Antarctic ice sheets (Goldsby and Kohlstedt, 2002).

As sliding along a grain boundary invariably results in stresses on the boundary of another grain, thus initiating dislocation motion in that grain (Figure 4.6), grain boundary sliding and dislocation motion are intimately connected.

### Rate-limiting processes

The rate of deformation of a crystal or of a polycrystalline aggregate by dislocation creep depends on how rapidly dislocations can move. This, in turn, depends upon

factors such as the effectiveness of the mechanisms resisting motion, the ability of a dislocation to move from one atomic plane to another, and the orientation of the plane with respect to the stress. One process is usually significantly more important than the others because it is more effective than the others in *retarding* motion. This process is called the *rate-controlling* or *rate-limiting* process. Rate-limiting processes vary among materials, and within any one material they are likely to vary with temperature and stress, and possibly also with impurity content. Furthermore, among students of ice deformation, there is no broad agreement on which processes are most important under different conditions.

In the next few paragraphs, some possible rate-limiting processes in ice are described and evidence for them presented.

### Drag as the rate-limiting process

Dislocations moving in a crystallographic plane are restrained in their motion by a number of atomic-scale mechanisms collectively referred to as *drag*. The velocity of such a dislocation is proportional to the applied stress,  $\sigma$ , and the steady state dislocation density is proportional to  $\sigma^2$  (Weertman, 1983; Alley, 1992). The creep rate,  $\dot{\varepsilon}$ , is proportional to the product of the dislocation velocity and density, so  $\dot{\varepsilon} \propto \sigma^3$ . Thus, laboratory and field data yielding such a cubic dependence could suggest that drag mechanisms are rate limiting.

### Climb as the rate-limiting process

There is, however, an additional dislocation process that must be considered. Samples of previously-unstrained polycrystalline ice deformed in compression in the laboratory invariably go through a transient phase of decelerating creep and then a period of nearly constant creep rate (Figure 4.10a). The decelerating phase is inferred to be due to interference among dislocations as they multiply. The interference results in clusters of dislocations, called *dislocation tangles*, that inhibit deformation. This process is called *work hardening*.

The period of constant creep rate is attributed to *recovery processes* that eventually come into play at temperatures prevalent in glaciers. One such process involves diffusion of atoms away from (or vacancies toward) dislocations, resulting in movement of the dislocation from one crystallographic plane to another. If the atom at D in Figure 4.4b diffused away, for example, the dislocation would move upward. This is a process involving volume self-diffusion. It is called *dislocation climb* if the dislocations are of the edge type, and *cross slip* if they are of the screw type. Both climb and cross slip relieve tangles, allowing deformation to continue at a more-or-less steady rate (central part of curve in Figure 4.10a). As climb is the recovery process requiring more energy, it would be rate controlling. The observation that the activation energies for dislocation creep and for volume self-diffusion are identical ( $60\text{ kJ mol}^{-1}$ ), within limits of experimental uncertainty, supports the suggestion that

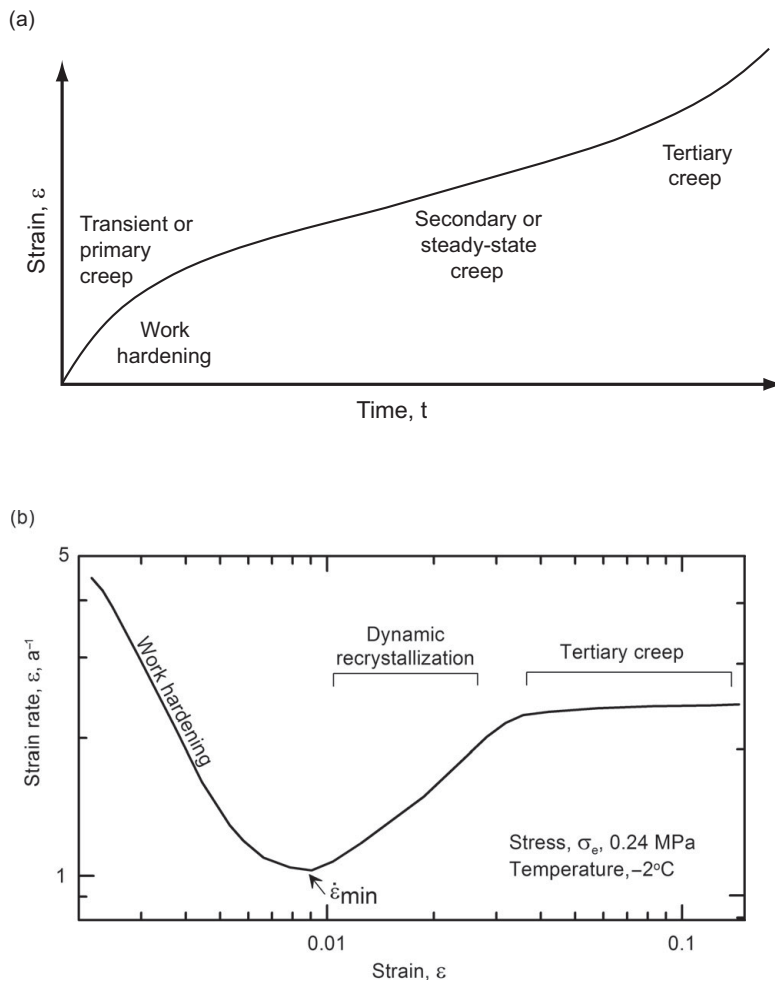


**Figure 4.10** (a) A typical strain-time curve for a sample of polycrystalline ice loaded in uniaxial compression. In early experiments, plots like this were used to identify the time span over which steady-state creep appeared to prevail. (b) As laboratory precision improved, it became possible to plot cumulative strain against strain rate, and thus more accurately identify the minimum strain rate. Note the increase in strain rate after about 1% strain and the constant strain rate in the tertiary creep phase. (Part (b) is adapted with permission from Treverrow *et al.*, 2012, Figure 4. Copyright: International Glaciological Society)

climb is the rate-limiting process (Weertman, 1983). Goldsby and Kohlstedt (2001) think this is the case in the  $n = 4$  regime, but not in the  $n = 1.8$  regime. Note that because these diffusion paths are within grains rather than being from one grain boundary to another, the deformation should be independent of grain size.

In their experiments at the lowest stresses, the  $n = 2.4$  regime, Goldsby and Kohlstedt again found  $Q = 58.5 \pm 3.5 \text{ kJ mol}^{-1}$ , and that the rate was independent of grain size. They interpret this as indicating that climb is also rate-limiting in this regime.

## Slip on other crystallographic planes

Von Mises (1928) showed that five independent systems are required for homogeneous deformation of a polycrystalline aggregate without opening voids. If deformation is inhomogeneous, however, four systems suffice (Hutchinson, 1976), and if dislocation climb operates, three systems are adequate (Groves and Kelly, 1969). Slip on the basal plane can occur in any of three directions, corresponding to the three *a*-axes of the hexagonal crystal, but only two of these are independent. Slip on either the prismatic or pyramidal planes (Figure 4.5) could provide a third system. On prismatic planes, however, the slip would probably be parallel to the basal plane, and so would not accommodate stresses normal to that plane. Thus, slip on pyramidal planes is likely necessary. As slip on pyramidal planes is much harder than slip on the basal plane at the same stress, slip on the pyramidal plane could be rate limiting.

## Dynamic recrystallization and grain boundary migration

*Dynamic recrystallization* is the continuous, or ongoing, nucleation and growth of new, unstrained grains at the expense of older strained ones. These processes are discussed in greater detail later; for now the important point is that growth of grains involves migration of grain boundaries. At stresses typical of those found in glaciers, migration rates range from  $\sim 3 \text{ mm a}^{-1}$  at  $-30^\circ\text{C}$  to  $\sim 30 \text{ mm a}^{-1}$  at  $-10^\circ\text{C}$  (Duval *et al.*, 1983).

The migration is a result of relatively slow diffusional processes that decrease the free energy of a system. The free energy is lower in unstrained grains. Thus, free energy is reduced by diffusion of atoms from strained ice ahead of a moving boundary to unstrained “new” ice behind it (Alley, 1992). Free energy is also lower in larger grains with lower grain boundary curvature. As grain growth lowers the curvature of grain boundaries, larger grains grow at the expense of smaller ones. The smaller grains are “consumed” by the larger ones (Montagnat and Duval, 2000).

Grain boundary migration does not result in deformation, so it is not a deformation process. It is, however, an efficient recovery process. By relieving internal stresses it could be a rate controlling mechanism, particularly in the  $n = 1.8$  regime where it counteracts any tendency for grains to become flattened (Goldsby and Kohlstedt, 2002).

## Grain boundary sliding

Dislocations generated at grain boundaries (Figure 4.6) migrate into the adjacent grain and eventually pile up at an opposite boundary. They can be removed from this pile up by climb into and along the grain boundary (Langdon, 1991). Langdon considered the rate of removal to be the rate-controlling process in some metals that he studied, but this is a process dominated by climb. If it were rate-limiting in ice in the  $n = 1.8$  regime, the activation energy should approximate that for volume

self-diffusion ( $60 \text{ kJ mol}^{-1}$ ), not that for boundary self-diffusion ( $49 \text{ kJ mol}^{-1}$ ) as found by Goldsby and Kohlstedt (1997, 2001). Goldsby and Kohlstedt think dislocation movement through crystals occurs relatively easily, so they argue that the rate-controlling mechanism in the  $n = 1.8$  regime is grain boundary sliding.

### Review of deformation mechanisms

Deformation of ice at the modest stresses and temperatures that occur in glaciers appears to be due to a combination of dislocation creep and grain-boundary sliding. Both basal and nonbasal slip systems contribute to the deformation. At high stresses, in the  $n = 4$  regime, dislocation creep is likely the primary deformation mechanism. The activation energy in this regime is  $\sim 60 \text{ kJ mol}^{-1}$ . The similarity of this activation energy with that for volume self-diffusion suggests that dislocation climb is the rate limiting process. At somewhat lower stresses,  $n \approx 1.8$  and  $\dot{\epsilon}$  depends on grain size. This and some textural characteristics suggest that, while glide and climb are occurring on basal and likely also nonbasal planes, grain boundary sliding is the rate-controlling mechanism. At still lower stresses,  $n \approx 2.4$  and dislocation slip on the basal plane may replace grain boundary sliding as the rate-limiting creep mechanism. Below  $\sim 0.05 \text{ MPa}$ , however, theoretical considerations suggest that pure diffusional flow may dominate.

In glaciers and ice sheets, it seems likely that dislocation slip on basal planes, rate-limited by grain boundary sliding ( $n \approx 1.8$ ) dominates *throughout much of the ice mass*, with dislocation creep ( $n \approx 4$ ) becoming important only near the bed. The commonly cited value of 3 for  $n$  likely reflects an averaging of experimental data across these two deformation regimes.

## Recrystallization

Crystals of glacier ice vary in size and in the degree to which they are interlocked. If there were no bonding across grain boundaries, for example, some polycrystalline ice samples would fall apart into a pile of roughly equant grains, up to a few millimeters in maximum dimension, while others would hang together like a three-dimensional jigsaw puzzle. We'll use the term *texture* to refer to these characteristics of crystal size and shape. In addition, under prolonged strain the *c*-axes of the crystals develop a variety of preferred orientations, or *fabrics*. Both texture and fabric, jointly referred to as the *microfabric*, affect the rheology of ice.

In order to study these processes, glaciologists, like petrologists, have traditionally used thin sections. The thin sections are typically somewhat less than a millimeter thick and 60–80 mm across. When polarized light is passed through a thin section and then observed through another polarizing filter oriented at right angles to the first, the individual crystals can be seen because the crystal structure

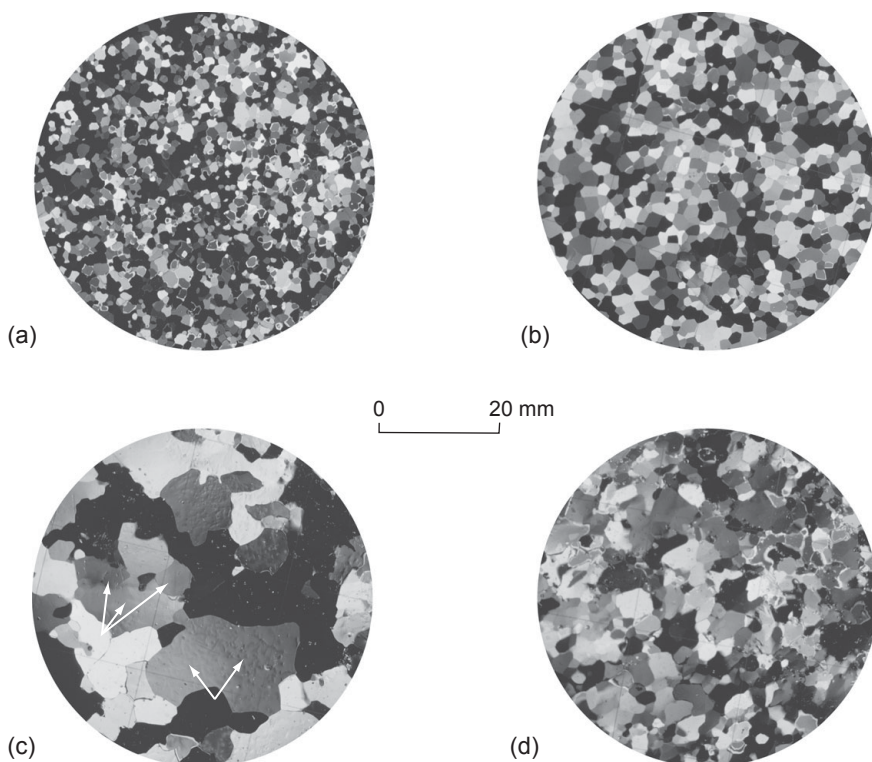


**Figure 4.11** Photographs, taken under crossed polarizers, of thin sections of ice from the Greenland ice sheet near Thule. The different grayscale tones of the grains reflect different orientations of the  $c$ -axes. (a) Initial texture formed by compaction of snow with addition of small amounts of melt water. The  $c$ -axes have a weak preferred orientation, with a preference for vertical orientations. (b) Texture resulting from grain growth with little or no deformation. The  $c$ -axes still have a weak vertical preferred orientation. (c) Texture resulting from polygonization. Adjacent grains with nearly the same grayscale tone (arrows) have  $c$ -axes that are nearly parallel to one another. The grain in the lower center is bent; in the one to left of center, distinct boundaries have formed between parts with slightly different orientations. (d) Texture following significant deformation. Grains are interlocked, and  $c$ -axes have a strong preferred orientation. (From Hooke, 1970)

rotates the light as it passes through the crystal, and the amount of rotation depends on the orientation of the crystal. When thus viewed, the different crystals have different colors (or grayscale tones in a black and white image – Figure 4.11). With the use of a universal stage on which a thin section can be rotated around a vertical axis and tilted about either of two mutually-perpendicular horizontal axes, crystals can be oriented so their  $c$ -axes are vertical. In this orientation, the crystal remains black as the stage is rotated around its vertical axis. The orientation of the crystal is then noted and plotted on an equal area net (Figure 4.12). To interpret such a plot, visualize a hemisphere with its flat “base” upward and its convex side down, and with a crystal in its center. The  $c$ -axis of the crystal intersects the hemisphere.

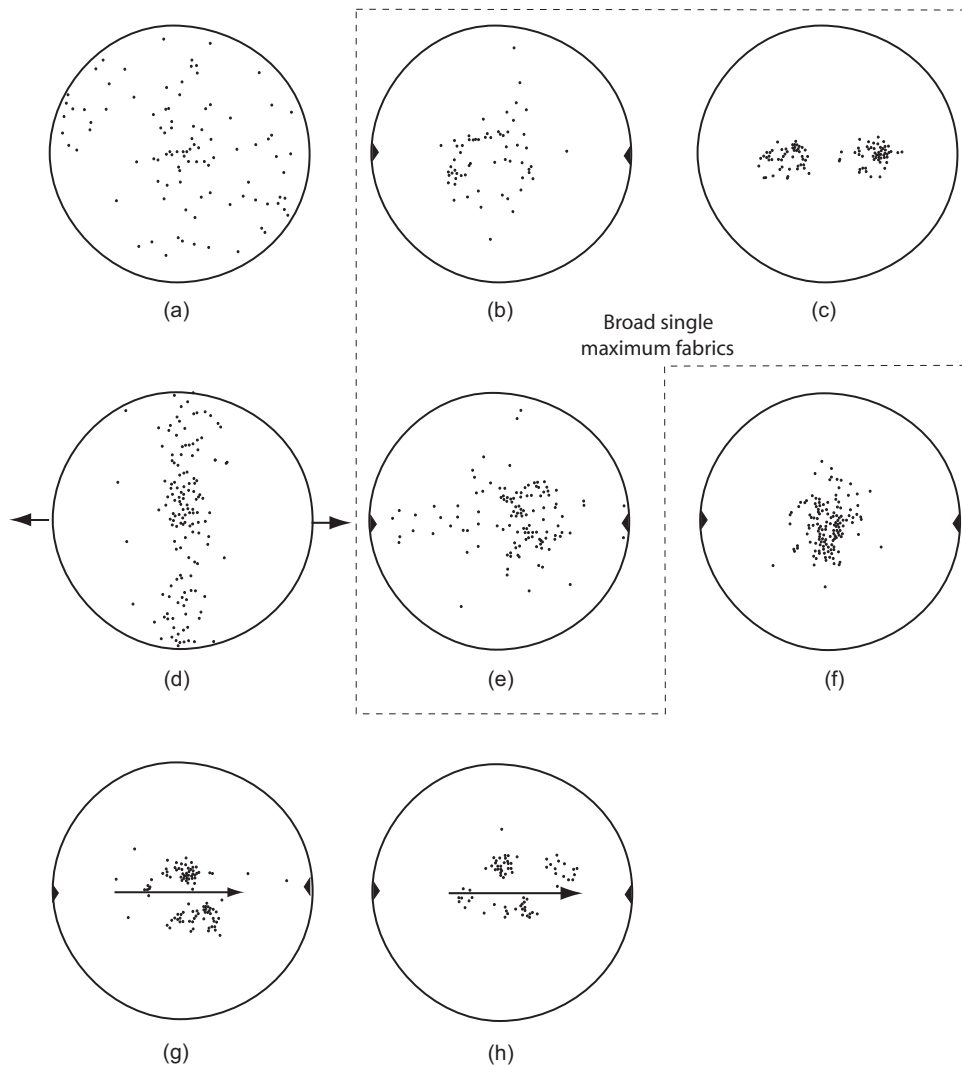


**Figure 4.12** Examples of crystallographic fabrics observed in ice. Plots are projections on the lower hemisphere of an equal-area net. Triangles on edges show the direction of bubble elongation which is presumed to be parallel to the direction of simple shear. (a) Fabric with weak preferred orientation of c-axes in superimposed ice. (b) Fabric resulting from uniaxial compression normal to the plane of the diagram. (c) Fabric that might be formed in pure shear. (d) Fabric produced by uniaxial tension; arrows show direction of tensile stress. (e) Broad single maximum fabric. (f, g, h) Fabrics resulting from simple shear in plane of diagram. Fabrics in (g) and (h) were produced by simple shear in the direction shown by arrows. (Sources: (a), (b) and (e-h) were measured on cores from boreholes in the Barnes Ice Cap (Figure 4.12) ( $T > -10^{\circ}\text{C}$ ); (c) is schematic; (d) is from a depth of 2020 m in the Vostok (Antarctica) core ( $T < -37^{\circ}\text{C}$ ). (a) and (e-h) from Hooke and Hudleston, 1980; (b) from Hooke and Hudleston, 1981; (d) from Lipenkov *et al.*, 1989)

A point on a fabric diagram like those in Figure 4.12 is the projection of this point of intersection onto the base of the hemisphere. Thus, a vertical *c*-axis plots at the center of the circle, and a *c*-axis dipping “south” plots between the center and the bottom of the circle. The points are normally plotted on a *Schmidt equal-area* net; this net is designed so that a unit area on the hemisphere plots into a unit area on the net. Consequently, a *c*-axis dipping at 45° actually plots about 55% of the distance from the center of the net to the boundary.

More recently, automated techniques have been developed to measure crystal orientations (e.g. Wilen *et al.*, 2003). Multiple cameras are used to image a thin section through crossed polarizers as the thin section is rotated or translated beneath a light source. Algorithms then determine extinction angles and solve for the *c*-axis orientations. While considerably faster than the universal stage, these automated procedures are not as fruitful as the newest approach – Electron backscatter diffraction (EBSD) – which utilizes an electron beam in a scanning electron microscope (Prior *et al.*, 2015). This is because EBSD, while time-consuming, also yields *a*-axis orientations, and can measure orientations of very small crystals.

Ice that forms from compaction of snow, perhaps with some addition of percolating meltwater, usually consists of crystals that are 2–4 mm in diameter (Figure 4.11a). During deformation, the texture and fabric of this ice are altered by dynamic recrystallization. Dynamic recrystallization, or simply recrystallization, is driven by the high local internal stresses characteristic of crystals that are poorly oriented with respect to the applied stresses, and the resulting widely differing internal energies in adjacent grains (Duval *et al.*, 1983). These are thus the sites where recrystallization is initiated.

One or more of three processes may be involved in recrystallization. In order of increasing energy difference between adjacent grains, these are *grain growth*, *polygonization*, and *nucleation of new grains* (Duval and Castelnau, 1995). Grain growth results from migration of grain boundaries and the absorption of smaller crystals. The result is a characteristic texture with equant crystals of relatively uniform size (Figure 4.11b). Because temperatures in the accumulation zones of polar ice sheets are relatively constant to depths of a few hundred meters (see Figure 6.6a), grain boundary migration occurs at relatively constant rates. Thus, initially, grain size increases nearly linearly with depth.

When migrating dislocations interfere with one another and pile up, *dislocation walls* may form. The orientation of the crystal lattice is slightly different on opposite sides of a wall, and this distortion increases as the wall develops, eventually leading to the formation of subgrains when the dislocation density on a surface is  $>\sim 10^4 \text{ mm}^2$  (Montagnat and Duval, 2004). The crystal is thus divided into two grains with nearly the same orientation (Figure 4.11c, arrows to left of center). This is *polygonization*. Under relatively high strain rates, polygonization begins at strains

of ~1% (Duval and Castelnau, 1995), but at the much lower strain rates found in the central regions of continental ice sheets, cumulative strains can approach 100% without causing polygonization (Alley, 1992). Thus, polygonization occurs at relatively shallow depths in temperate glaciers, but is normally found only at depths greater than a few hundred meters in polar ice sheets. Where polygonization occurs, it may balance grain growth so grain size remains relatively constant with increasing depth (Alley *et al.*, 1995).

Nucleation of new grains entails the appearance of small grains with basal planes parallel to the maximum resolved shear stress. The grains are thus oriented for easy glide. When they first appear, such grains are relatively unstrained in comparison with adjacent older deformed grains. The new grains grow at the expense of the older ones, thus lowering the free energy as noted. This is probably partly responsible for the interlocking textures seen in highly deformed ice (Figure 4.11d).

Nucleation and grain growth, combined, are sometimes referred to as *migration recrystallization*.

### Development of fabrics with preferred orientations of c-axes

Newly-nucleated, optimally-oriented crystals grow at the expense of older deformed ones, and continued straining gradually rotates them into orientations that are no longer optimal, so they begin to accumulate strain energy. The tendency for systems to minimize free energy then leads, once again, to nucleation of new grains at the sites of high strain energy. This continuous rotation and recrystallization results in a tendency for c-axes to be oriented normal to the maximum resolved shear stress.

Let us illustrate these processes by tracing the development of such fabrics, starting with ice near the surface in the accumulation area (Figure 4.11a). The c-axes of the crystals are either uniformly distributed or have a weak preference for vertical orientations (Figure 4.12a). The latter probably results from the orientation of snowflakes that have thin disk-like shapes, and thus, like a pile of poker chips, tend to lie flat as they accumulate. In addition, the vertical temperature gradient may have some influence during sintering.

As the ice becomes buried, it is compressed vertically and stretched longitudinally and sometimes also laterally. Where longitudinal and lateral strain rates are comparable in magnitude, the stress field is referred to as *uniaxial compression* (Figure 4.13a), whereas if lateral strain rates are negligible it is *pure shear* (Figure 4.13b). In both of these stress configurations, slip occurs most readily on the basal planes of crystals whose c-axes are inclined at ~45° to the compression axis (Figure 4.13d). Thus crystals are nucleated in this orientation, and these crystals grow at the expense of adjacent more highly-stressed ones, leading to a conical distribution of c-axes in uniaxial compression (a *small circle fabric*: Figure 4.12b) and to two maxima aligned in the direction of extension in pure shear (Figure 4.12c). (Small circle fabrics are also commonly referred to as *girdle fabrics*,

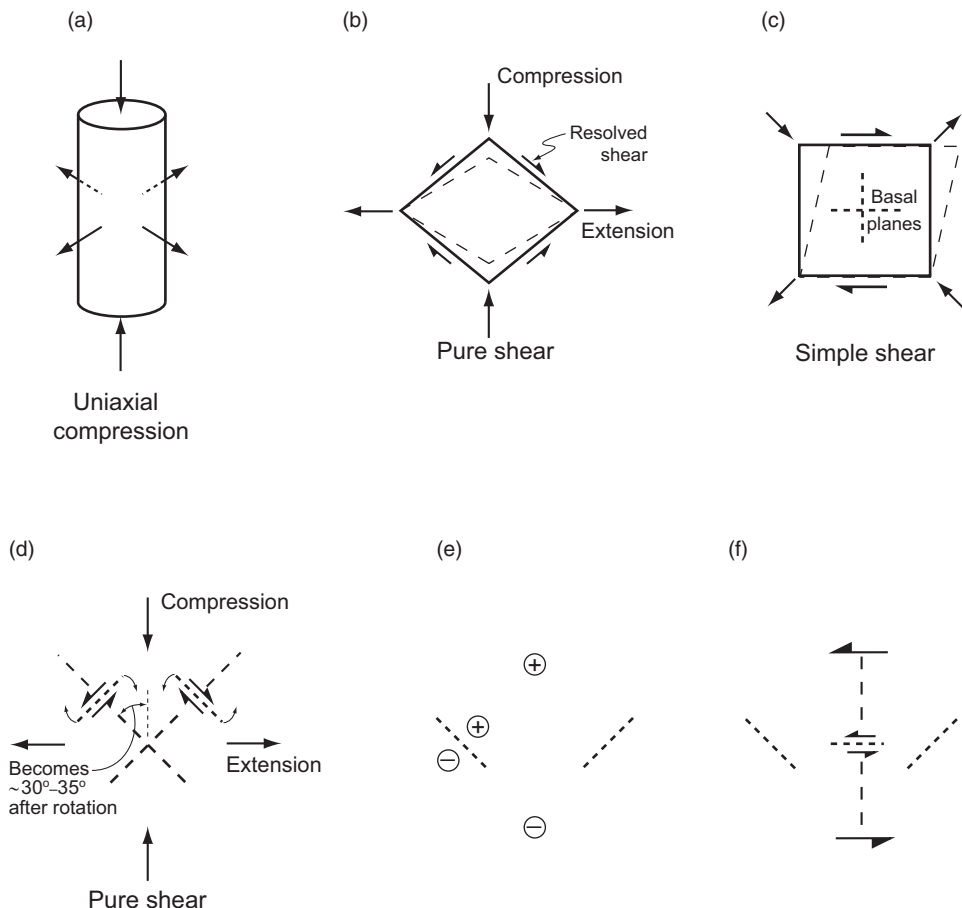


**Figure 4.13** Stress configurations and their relation to orientations of  $c$ -axes. Short-dashed lines show orientations of basal planes. (a) Uniaxial compression. (b) Pure shear; there is no strain normal to the plane of the diagram; dashed lines show shape after some deformation. (c) Simple shear; half arrows show direction of shear and dashed lines show shape after some deformation; full arrows show shear resolved into compression and tension; basal planes shown are those on which resolved shear stresses due to the compression are maximized (see d). (d)  $c$ -axes and basal planes in a newly nucleated crystal in uniaxial compression or pure shear; with continued compression, the  $c$ -axes rotate toward the axis of compression. (e) Simple shear viewed parallel to the shear direction with basal planes also parallel to the shear direction as in the fabric of Figure 4.12g;  $\oplus$  and  $\ominus$  signify stress vectors directed into and out of the page, respectively. (f) Simple shear viewed normal to the shear direction with basal planes of the two weak maxima in Figure 4.12h inclined to the shear direction.

although “girdle” implies a great circle.) The vertical compression and lateral extension, however, have the effect of rotating basal planes. In Figure 4.13d, the rotation is clockwise on the left and counterclockwise on the right. Thus, as the crystals grow, the  $c$ -axes rotate toward the compression axis (Alley, 1992), with the result that the mean angle between the compression axis and the  $c$ -axes is typically only  $\sim 30\text{--}35^\circ$ , not  $45^\circ$  (Kamb, 1972; Hooke and Hudleston, 1980).

The rotation rate decreases as the *c*-axes approach the compression axis (Alley, 1988). In addition, crystals that have been rotated too far, and thus become highly stressed, are replaced by new, strain-free, ones nucleated with more favorable orientations. These two factors lead to a paucity of crystal axes parallel to the compression axis, and hence to a small circle fabric rather than a single maximum fabric.

At Vostok station in Antarctica, transverse and vertical strain rates are compressive and are thought to be of comparable magnitude (Lipenkov *et al.*, 1989). Longitudinal extension thus results in a uniaxial *tensile* stress regime, which tends to rotate *c*-axes toward the compressive axes (Figure 4.13d). Temperatures at Vostok are  $<-37^{\circ}\text{C}$ , so recrystallization is suppressed. Thus, *c*-axes tend to accumulate parallel to the compressive axes. In this case, with roughly equal compressive stresses in the vertical and transverse direction, *c*-axes can lie anywhere on a great circle<sup>1</sup> normal to the tensile axis (Figure 4.12d).

Close to the bed, drag results in a stress configuration approximating *simple shear* parallel to the bed. In simple shear, planes parallel to the bed remain so, and the spacing between planes does not change. The stresses resulting in simple shear can be resolved into compressive and tensile stresses at  $45^{\circ}$  to the direction of shear (Figure 4.13c). As before, crystals tend to nucleate with basal planes at  $45^{\circ}$  to the compressive axis, parallel to the direction of maximum resolved shear stress. In one of these directions, basal planes are normal to the direction of shear, and in the other they are parallel to it. Crystals nucleated in the former orientation quickly accumulate large strain energies and are resorbed, while those in the latter orientation, with vertical *c*-axes, deform easily by slip on basal planes and are thus favored. The resulting fabrics, which are common in ice sheets (Gow and Williamson, 1976; Hooke and Hudleston, 1980), have single maxima that are quite tight near the bed (Figure 4.12f). The ratio of simple shear to pure shear decreases with height above the bed, leading to broader single maxima higher in the ice sheet (Figure 4.12e).

The fabrics in Figure 4.12b, c, and e all seem to form under roughly equivalent cumulative strain. The differences among them are primarily due to stress configuration. As a class, we will refer to them as *broad single maximum* fabrics.

Although the increase in creep rate associated with recrystallization usually begins at an cumulative effective strain,  $\varepsilon_e$  (Equation 2.11) of  $\sim 0.01$  in the laboratory (Figure 4.10b), broad single maximum fabrics are not particularly evident until  $\varepsilon_e \cong 0.04$  and only become well developed at  $\varepsilon_e = 0.4$  (Kamb, 1972; Jacka and Maccagnan, 1984). In the field, Hooke and Hudleston (1980) found that such fabrics first appeared at  $\varepsilon_e \cong 0.52$ . For reference, circles that have been deformed into ellipses by strains of these magnitudes have axial ratios of 1.03, 1.12, 3.10, and

---

<sup>1</sup> Whereas a small circle fabric represents *c*-axes distributed on the surface of a cone, a great circle represents a radial distribution of *c*-axis, as in spokes of a wheel.

4.35, respectively. Thus, dynamic recrystallization increases creep rates long before a detectable preferred *c*-axis orientation develops.

In simple shear at cold temperatures or high strain rates (or high cumulative strains), the single maximum fabric strengthens (Figure 4.12f). However, at lower strain rates and at temperatures above about  $-15^{\circ}\text{C}$ , an unexpected fabric appears. First, the single maximum splits in two, with a maximum on either side of the shear direction (Figure 4.12g). The basal planes corresponding to these *c*-axis orientations are still parallel to the shear direction, but the orientations of the planes are not optimal (Figure 4.13e). Then, with increased cumulative strain, strain rate, or temperature, first one and then a second maximum appears inclined to the direction of shear (Figure 4.12h). These planes are definitely not well oriented for slip (Figure 4.13f), and thus must stiffen the ice, at least slightly. These *multiple maximum* fabrics appear at  $\varepsilon_e \cong 1.3 \pm 0.3$  (Hooke and Hudleston, 1980). The corresponding axial ratio of the strain ellipse is  $\sim 40$ .

These multiple maximum fabrics are fairly common in glacier ice at temperatures above  $-15^{\circ}\text{C}$ , but rare or absent in colder ice (e.g. Kamb, 1959; Gow and Williamson, 1976). Their origin is not well understood. Shear deformation for an extended period of time at effective stresses of 0.03 (Barnes Ice Cap) to 0.04 (Matsuda and Wakahama, 1978) MPa and temperatures ( $>\sim -15^{\circ}\text{C}$ ) seem to be required for their formation.

By observing etch pits in thin sections of ice with such fabrics, Matsuda and Wakahama (1978) measured the orientations of *a*-axes as well as *c*-axes. In ice with 4-maximum fabrics, they found that the *a*-axes were clustered, and that *a*-axes of adjacent crystals were systematically aligned in a way that suggested mechanical twinning. The angle between the *c*-axes of the respective twin lattices was  $\sim 45^{\circ}$ , which is the same as the angle between the two maxima of Figure 4.12g. Twinning can be produced mechanically by applying a shear stress to a crystal, causing the lattice of part of the crystal to shift (as in shifting each of the layers of cylinders in the upper half of a pile, one cylinder to the right relative to the layer beneath it) (Bell, 1941).

Because the various fabrics appear to form under fairly specific conditions of cumulative strain, strain rate, and temperature, and because these parameters all tend to increase systematically with depth in the accumulation area of a glacier, fabric type also varies with depth. For example, near the divide in Barnes Ice Cap, the transition from weakly oriented to broad single maximum (or equivalent) fabric occurs at a depth  $\sim 140$  m, and the broad single maximum gives way to a multiple maximum fabric at  $\sim 200$  m (Figure 4.14). As the ice is advected outward, the transitions occur at shallower depths, and in the ablation area these fabrics are exposed at the surface. At Byrd Station in Antarctica, the transition to broad single maximum fabrics (small circle variety) occurs at a depth of  $\sim 350$  m. Then, a strong single maximum fabric appears at  $\sim 1200$  m and multiple maximum fabrics show up

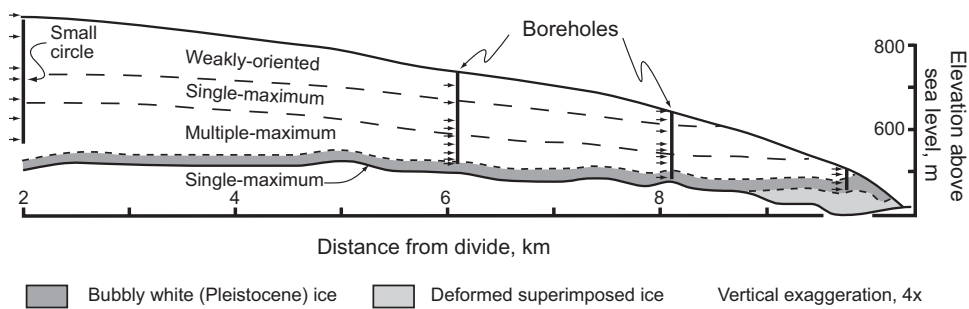


**Figure 4.14** Vertical cross section along a flow line on Barnes Ice Cap showing zones characterized by particular fabrics. Arrows show locations of samples used to determine fabric type. (After Hooke and Hudleston, 1980)

at  $\sim 1830$  m. Differences in temperature are probably largely responsible for the difference in depths to the transitions, although stress and cumulative strain may also play a role; Barnes Ice Cap is above  $-15^{\circ}\text{C}$  throughout, whereas at Byrd Station the temperature exceeds  $-15^{\circ}\text{C}$  only below 1750 m.

## Summary of ice deformation

Given these various processes of recrystallization and crystal deformation, one may well ask how we should visualize the deformation of polycrystalline ice on a granular scale. Available evidence suggests that internal stresses are heterogeneous, that slip takes place largely on basal planes within individual grains although some other slip systems must also operate, that this slip results in rotation of the crystal structure, that slip also takes place on grain boundaries, and that nucleation of grains with basal planes parallel to the maximum resolved shear stress and resorption of grains that have rotated out of this orientation results in the development of fabrics with preferred orientations. Mismatches at three-grain intersections due to differential slip may be accommodated by initiation and migration of dislocations into the adjacent grain, by diffusion, by grain rotation, or by some combination of these processes. The rate limiting processes appear to be grain boundary slip at low stresses and dislocation climb at higher stresses. Computer models incorporating these principles successfully simulate many characteristics of fabric evolution in ice sheets (Etchecopar, 1977; Van der Veen and Whillans, 1994).

## Deformation mechanism maps

Scientists working on the deformation of crystalline materials have found it useful to plot “maps” showing the deformation mechanisms operating at different

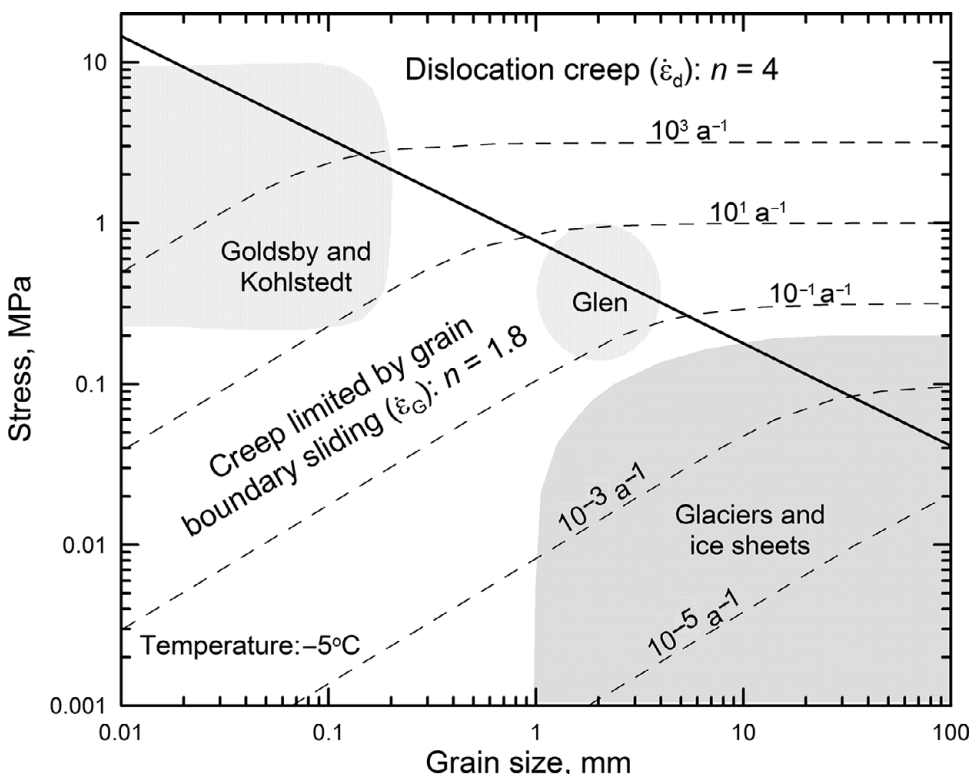


**Figure 4.15** Deformation mechanism map in  $\sigma - d$  space for ice at  $-5^\circ\text{C}$ , calculated with the use of Equation (4.4) with the constants in Table 4.1. Dashed lines are lines of equal strain rate. Along the heavy diagonal line the contributions of  $\dot{\epsilon}_G$  and  $\dot{\epsilon}_d$  to the deformation are equal. (Fields showing the range of stresses and strain rates in the Glen and the Goldsby and Kohlstedt experiments are adapted from Goldsby, 2009, Figure 60.3)

temperatures,  $\theta$ , stresses,  $\sigma$ , or grain sizes,  $d$ . Such a map in  $\sigma - d$  space, calculated for a temperature of  $-5^\circ\text{C}$ , is shown in Figure 4.15. At lower stresses, as we have discussed, deformation is likely dominated by dislocation slip on basal planes and rate-limited by grain boundary sliding (GBS). At higher stresses dislocation creep limited by climb is the dominant mechanism. The heavy diagonal line separates the two fields. Although both mechanisms may contribute to the deformation at all stresses and grain sizes, along this line the two mechanisms contribute equally.

Also shown in Figure 4.15 are contours (dashed) of strain rate. Strain rate is independent of grain size in the dislocation creep field. Curvature of the contours as they approach the diagonal reflects the gradually increasing influence of the process on the opposite side of the diagonal.

Note the range of stresses and grain sizes in the experiments of Glen (1955) and of Goldsby and Kohlstedt (1997, 2001), and their approximate range in glaciers and ice sheets. The range of Glen's experiments is typical of those done over the years; they lie on the boundary between the two creep regimes which, as noted, is probably

responsible for the value of  $n$  ( $\sim 3$ ), midway between the values for GBS limited creep ( $n = 1.8$ ) and dislocation creep ( $n = 4$ ). In contrast, the range of stresses and grain sizes in glaciers and ice sheets appears to fall almost entirely within the GBS-limited field. This suggests that models using  $n = 3$  are likely to overestimate strain rates. A major contribution of Goldsby and Kohlstedt was the development of techniques for making samples with grain sizes small enough to deform in the GBS-limited regime at stresses high enough to yield results on a laboratory time scale.

## A flow law for glacier ice

In the preceding sections of this chapter we have looked at details of the deformation process. In the remainder of this book, we will frequently need a simple yet reasonably accurate expression relating stress and strain rate in ice. In general, we will use Glen's flow law:  $\dot{\varepsilon}_e = A\sigma_e^n$  (Equation 4.1) with  $n = 3$  and  $A$  given by Equation (4.2).

As noted, however, the exponent,  $n$ , depends on the creep mechanism operating. Owing to early experiments on laboratory ice and on glaciers, glaciologists have usually adopted a value of 3 for  $n$  (Hooke, 1981), although some data suggested a lower value at low stresses. These latter experiments were often questioned because tests were not continued long enough to ensure that the transient phase of creep (Figure 4.10a) was complete and the minimum creep rate (Figure 4.10b) reached. However, experiments by Pimienta and Duval (1987) and studies by Alley (1992) and Montagnat and Duval (2000) did raise the possibility of values between 1 and 2 for deformation at low stresses, temperatures, and cumulative strains, and Goldsby and Kohlstedt's experiments seem to confirm this. Montagnat and Duval argue that grain boundary migration is particularly efficient under these conditions, so internal strain energy is small, and the density of dislocations does not increase as rapidly with stress as suggested by the arguments for drag being rate-limiting. Healing of dislocations by diffusional processes may also limit the density (Alley, 1992). Goldsby and Kohlstedt (1997, 2001), on the other hand, think that grain boundary sliding is the rate-limiting process at these low stresses.

To incorporate lower values of  $n$  at lower stresses, Goldsby and Kohlstedt suggest using:

$$\dot{\varepsilon}_e = \dot{\varepsilon}_G + \dot{\varepsilon}_d \quad (4.4)$$

where  $\dot{\varepsilon}_G$  and  $\dot{\varepsilon}_d$  are the strain rates resulting from deformation limited by grain boundary slip ( $n = 1.8$  regime) and dislocation climb ( $n = 4$  regime), respectively. These strain rates are given by Arrhenius-like relations:

$$\dot{\varepsilon} = A_0 \frac{1}{d^p} \sigma^n e^{-\frac{Q}{RT}} \quad (4.5)$$

**Table 4.1** Flow law constants (from Goldsby, 2009)

	Dislocation creep				Creep limited by grain-boundary sliding			
	$A$ , MPa $^{-4}$ a $^{-1}$	$n$	$p$	$Q$ , kJ mol $^{-1}$	$A$ , MPa $^{-1.8}$ m $^{1.4}$ a $^{-1}$	$n$	$p$	$Q$ , kJ mol $^{-1}$
$T > -15^{\circ}\text{C}$	$1.89 \times 10^{36}$	4.0	0	181	$9.47 \times 10^{33}$	1.8	1.4	192
$T < -15^{\circ}\text{C}$	$3.79 \times 10^{13}$	4.0	0	60	$1.23 \times 10^{05}$	1.8	1.4	49

in which  $d$  is the grain diameter. The values of  $A_0$ ,  $p$ , and  $Q$  depend on the deformation mechanism and whether the temperature is above or below  $-15^{\circ}\text{C}$ . Values of these parameters suggested by Goldsby (2009) are given in Table 4.1. A flow law of this form results in  $\dot{\varepsilon}_e - \sigma_e$  curves like that in Figure 4.1 and the dashed curves in Figure 4.15. In the  $n = 4$  regime, the strain rate is independent of grain size, so  $p = 0$ .

The strain rate may also be weakly dependent on hydrostatic pressure,  $P$ . This is formally incorporated by modifying the Arrhenius relation, thus:

$$A = A_0 e^{-\frac{Q+PV}{k\theta}} \quad (4.6)$$

where  $V$  is the *activation volume* for self-diffusion, and the quantity  $(Q + PV)$  is the *activation enthalpy*. In ice, it turns out that  $V$  is very low. Greve *et al.* (2014) estimated, theoretically, that  $V$  was between  $-3.2 \times 10^{-5}$  and  $-1.7 \times 10^{-5}$  m $^3$  mol $^{-1}$  with lower values for temperatures above  $-10^{\circ}\text{C}$ . They compared these values with experimental values of  $-1$  to  $-2 \times 10^{-5}$  m $^3$  mol $^{-1}$  and concluded that the agreement was satisfactory, given the difficulty of the experiments. As the highest pressures in ice sheets on Earth are  $\sim 40$  MPa,  $PV$  is  $\sim -1$  kJ mol $^{-1}$ , and is thus negligible in comparison with the values of  $Q$  in Table 4.1.

Lile (1978) and Russel-Head and Budd (1979) suggested that an *enhancement factor* could be introduced to incorporate the effect of crystal orientation into the flow law. This is now normally done by multiplying the right-hand side by a factor,  $E$ , thus:

$$\dot{\varepsilon}_e = EA_0 \frac{1}{d^p} \sigma_e^n e^{-\frac{Q-PV}{k\theta}}. \quad (4.7)$$

Rigorously, however, Glen's flow law is based on the assumption that the material is isotropic (see Chapter 9). Thus, adding an enhancement factor in this way to accommodate anisotropy is tacit admission of the failure of this assumption.

We do not yet have enough understanding of the recrystallization process to write an empirical relationship between  $E$  and the factors such as temperature, strain rate, and cumulative strain on which it depends. Selection of the appropriate values of  $E$  to use in any given situation is, therefore, largely subjective.

Laboratory experiments provide some basis for estimating  $E$ . Treverrow *et al.* (2012) ran some uniaxial compression tests at  $-2^{\circ}\text{C}$  on laboratory ice that was

initially-isotropic. They achieved total strains exceeding 10% (Figure 4.10b), resulting in small circle fabrics. They also did experiments in simple shear on laboratory ice and on samples with strong single-maximum fabrics from Law Dome in Antarctica. In the runs using isotropic laboratory ice the strain rate went through a minimum,  $\dot{\epsilon}_{\min}$  (Figure 4.10b), before accelerating into tertiary creep,  $\dot{\epsilon}_{ter}$ . The ratio  $\dot{\epsilon}_{\min}/\dot{\epsilon}_{ter}$  is their measure of  $E$ . Their results suggested an  $E$  for small circle fabrics of ~2.4, and for single maximum fabrics of ~5.5. The latter is reasonably consistent with the experiments of Russell-Head and Budd (1979) and Baker (1981, 1982), who sheared natural ice with a single-maximum fabric in the laboratory and obtained  $E \approx 4$ . Russell-Head and Budd also found that a section of a borehole in Law Dome, Antarctica, that passed through ice with a single-maximum fabric, deformed ~4 times faster than it would have in ice without such a fabric. Somewhat later, Budd and Jacka (1989) and Jacka and Maccagnan (1984) suggested that enhancement factors of ~3 are reasonable for ice in uniaxial compression once a small circle fabric has developed, and that factors of 8–10 may be appropriate for ice in simple shear.

In contrast to these studies suggesting values of  $E$  greater than 1,  $E$  for the great circle fabric in the Vostok core (Figure 4.12d) appears to decrease from ~0.16 at 1000 m to 0.07 at 2000 m (Pimienta *et al.*, 1988). This is consistent with Lipenkov *et al.*'s (1989) analysis of their fabric measurements. Their measure of the degree to which crystals are optimally aligned for creep in uniaxial tension showed a steady decline with depth from 0.22 to 0.15 over the same depth interval.

### Effect of water

Finally, we return to the effect of water on the creep rate. This was studied by Duval (1977) in a pioneering set of sophisticated experiments. His results, expressed in terms of the increase in  $A$  with increasing water content, are shown in Figure 4.16.

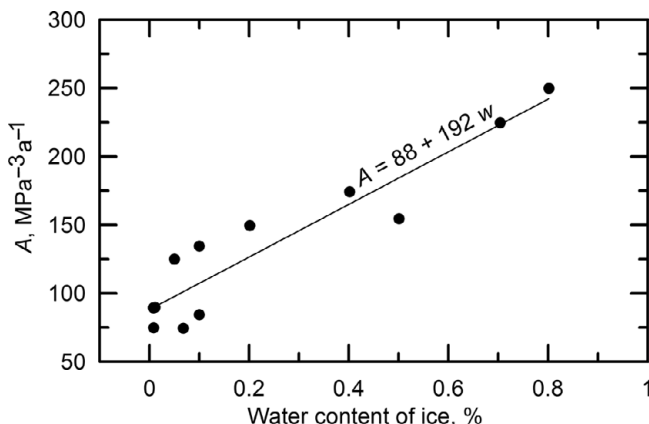


Figure 4.16 Variation in  $A$  with water content of polycrystalline ice. (Data reported by Duval, 1977)

With an increase in water content from 0.01% to 0.8%,  $A$  increases from ~90 to ~240 MPa $^{-3}$  a $^{-1}$ . Lliboutry (1983) reports that the water content of basal ice of temperate glaciers typically varies between 0.6% and 0.95%. Based on the line in Figure 4.16, this corresponds to a variation in  $A$  from 200 to 270 MPa $^{-3}$  a $^{-1}$ , and hence in  $\dot{\epsilon}$  of ~30%. Lower water contents, and hence lower values of  $A$ , are likely in temperate ice of polythermal glaciers.

## Fracture and crevassing

At sufficiently high stresses, ice fractures. Crevassing, resulting from high tensile stresses, is the type of fracturing with which people are most familiar. However, as noted in Chapter 3, fracturing near the base of the subaerial part of a calving face may be largely a consequence of crushing (compression).

Developing an understanding of the initiation and growth of fractures in ice has acquired a new urgency, owing to their importance in calving and the role of calving in the response of tidewater glaciers to climate warming. In addition, fracture propagation is now known to be important in introducing water to a glacier bed, where it increases the sliding speed.

In one of the earliest analytical studies of crevassing, Nye (1955) considered the balance between the rate at which a crevasse could be opened by a tensile stress and the rate at which it would close owing to the overburden pressure. As  $\dot{\epsilon} \propto \sigma^n$  and  $1.8 < n < 4$ , the closure rate increases non-linearly with depth. Nye considered a crevasse filled with air in a field of closely-spaced crevasses. If there is water in the crevasse, however, the water exerts an additional opening pressure and the crevasse can be much deeper. Weertman (1973) argued that if the water level were sufficiently high, a crevasse might well penetrate all the way through a glacier. Observations appear to confirm Weertman's conclusion. Zwally *et al.* (2002) attributed seasonal increases in speed at a site in Greenland to water reaching the bed through moulin, and suggested that the moulin were likely initiated by propagation of water-filled crevasses to the bed. Not long thereafter, Das *et al.* (2008) documented sudden drainage of a lake in Greenland and nearly simultaneous increases in surface speed, implying that the water had reached the bed. Boon and Sharp (2003) witnessed drainage of a lake on John Evans glacier on Ellesmere Island, followed 2 days later by emergence of turbid water at the glacier terminus. Finally, water in crevasses is believed to have played a significant role in the collapse of the Larsen B Ice Shelf mentioned in Chapter 3.

### Linear fracture mechanics

Flaws or microcracks exist in most if not all crystalline materials. At the tips of such cracks, stresses are greatly amplified over the far field state of stress, and these

amplified stresses act on single molecular bonds lacking neighbors capable of absorbing the stress. Thus, cracks may propagate at far-field stresses far below the strength of an unflawed specimen of the material. Such cracks can propagate unstably if more energy is released by a small increase in crack length than is absorbed by expansion of the crack (Griffith, 1921). Owing to the importance of fracture in the design of structures ranging from buildings to airplanes, the study of crack propagation is a well-developed discipline: *linear elastic fracture mechanics*. We will only skim the surface of this field herein.

Consider the elastic stress field around a vertical crack in the surface of a solid of infinite horizontal extent. Suppose the solid is subjected to a far field tensile stress,  $\sigma_{xx}$ , normal to the crack. Around the crack tip, stresses vary with the distance,  $r$ , and azimuth,  $\theta$ , from the tip (Figure 4.17), thus:

$$\begin{aligned}\sigma_{xx} &= \frac{K_I}{\sqrt{2\pi r}} \cos \frac{\theta}{2} \left( 1 + \sin \frac{\theta}{2} \sin \frac{3\theta}{2} \right) \\ \sigma_{zz} &= \frac{K_I}{\sqrt{2\pi r}} \cos \frac{\theta}{2} \left( 1 - \sin \frac{\theta}{2} \sin \frac{3\theta}{2} \right) . \\ \sigma_{xz} &= \frac{K_I}{\sqrt{2\pi r}} \sin \frac{\theta}{2} \cos \frac{\theta}{2} \cos \frac{3\theta}{2}\end{aligned}\quad (4.8)$$

(e.g. Lawn, 1993, p. 25).  $K_I$  is a parameter, known as the *stress intensity factor*, that applies to the crack tip. The subscript I is the mode of fracture. Mode I is opening (as in a crevasse), Mode II is sliding, and Mode III is tearing (van der Veen, 1998). We will restrict our discussion to Mode I fracture. In general,  $K_I = \beta \sigma \sqrt{a}$  where  $a$  is the crack length and  $\beta$  is a geometrical parameter that, in our case, depends upon factors such as the spacing of crevasses, the ice thickness, and the far field stress. Thus,  $K_I$  increases as either  $\sigma$  or  $a$  increase.  $K_I$ , and particularly  $\beta$ , describe how the far field stresses are amplified or intensified around a crack tip.

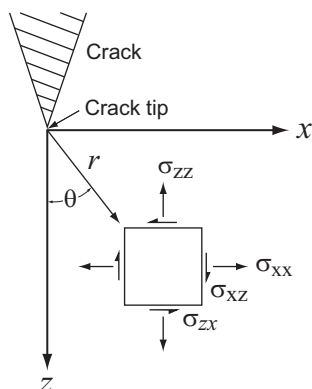


**Figure 4.17** Stress field on an infinitesimal element located a distance  $r$  from a crack tip. (Modified from Kenneally, 2003)

Clearly, high values of  $K_I$  translate into high stresses around the crack tip, and if the stresses become high enough the crack will propagate. Rather than express this critical value in terms of the stresses themselves, the standard procedure is to express it in terms of a value of  $K$  called the *fracture toughness*,  $K_{Ic}$ .  $K_{Ic}$  is a material property of the medium. If  $K_I$  exceeds  $K_{Ic}$ , the fracture will propagate unstably. Rist *et al.* (1999) have summarized their own measurements of  $K_{Ic}$  on ice cores from Antarctica and other worker's measurements on other types of samples, and find that it increases approximately linearly with ice density (Figure 4.18). The scatter in the data is large, however.

To determine a stress intensity factor, one needs a solution for the stresses in the vicinity of a crack tip. If one knows  $\sigma_{xx}$  at a location  $(r, \theta)$ , for example,  $K_I$  can be determined from the first of Equations (4.8). This is a *boundary value* problem; one needs to specify the stresses at the boundaries of a domain and solve for those in the interior of the domain. Analytical solutions are available for certain simple geometries, but numerical techniques are required for more complicated situations. Fortunately, one usually does not need to perform these calculations, as stress intensity factors are tabulated for many common situations in handbooks such as Sih (1973). Conveniently, they obey the principle of superposition; thus, in problems with a complex stress configuration, if one can obtain stress intensity factors for each of the stresses separately, they can be added to obtain the stress intensity factor

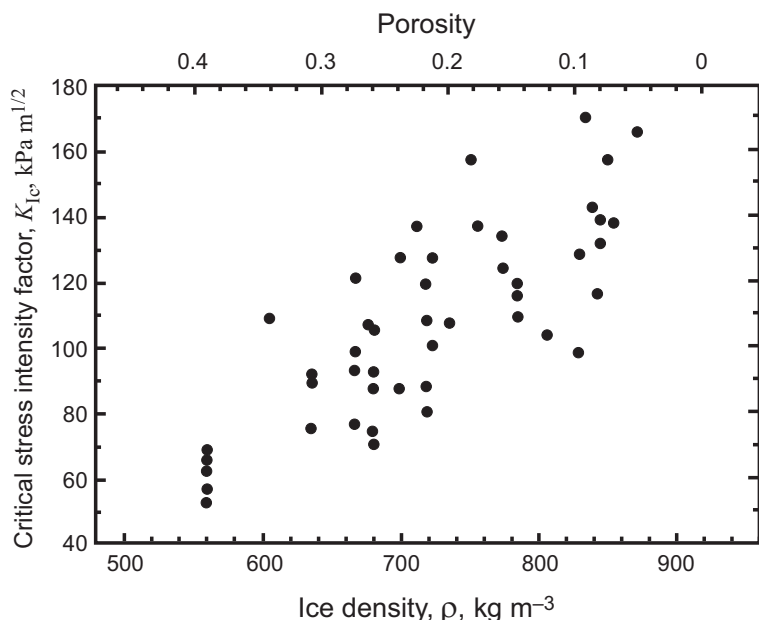


**Figure 4.18** Variation of  $K_{Ic}$  with density. Based on laboratory measurements on natural ice specimens from Ronne Ice Shelf. (After Rist *et al.*, 1999; reproduced with permission of the authors and the American Geophysical Union)

for the whole problem (Kanninen and Popelar, 1985, p. 27). We will illustrate this in the following paragraphs.

The alert reader may have noticed that the stresses in Equations (4.8) become infinite as  $r \rightarrow 0$ . However, deformation in a region immediately around the crack tip is plastic, and this keeps the stresses finite. To estimate the radius,  $r_p$ , of this plastic region, take  $\theta = 0$  in the first or second of Equations (4.8), assume that plastic behavior will occur once the stress exceeds 0.1 MPa (a commonly-cited plastic “yield strength” for ice), adopt a value for  $K_{Ic}$  of  $0.16 \text{ MPa m}^{-1/2}$ , and solve for  $r_p$ . The result is  $r_p \approx 0.4 \text{ m}$ . The principles of linear elastic fracture mechanics only apply if  $r_p$  is small compared with  $a$ . As we are concerned principally with crevasses, and as most crevasses reach depths of at least 10–20 m, this condition is satisfied. It also bears mentioning that, as  $r$  becomes large, additional terms must be added to Equations (4.8) so the right-hand sides conform with the far-field stresses rather than  $\rightarrow 0$  (van der Veen, 1998).

Let us consider the case of a single crevasse in a glacier of infinite horizontal extent subjected to a tensile stress,  $\sigma_{xx}$ . We need a stress intensity factor both for the tensile stress that tends to open the crack and for the compressive stress due to the overlying ice that tends to squeeze it closed. For the case of a crack of depth  $d$  in a medium of thickness  $H$  subjected to such a tensile stress,

$$K_{It} = \left[ 1.12 - 0.23 \frac{d}{H} + 10.55 \left( \frac{d}{H} \right)^2 - 21.72 \left( \frac{d}{H} \right)^3 + 30.39 \left( \frac{d}{H} \right)^4 \right] \sigma_{xx} \sqrt{\pi d} \quad (4.9)$$

(van der Veen, 1998). The subscript “t” signifies tension. If  $d \ll H$ , this reduces to:  $K_{It} = 1.12\sigma_{xx}\sqrt{\pi d}$ . The hydrostatic stress from the weight of the ice is  $-\rho_i g z$ , where  $\rho_i$  is the density of ice,  $g$  is the acceleration due to gravity, and  $z$  is the depth below the surface. The negative sign indicates that the stress is compressive. For a crack of depth  $d$  with a load varying from 0 at the surface to  $-\rho_i g d$  at the crack tip,  $K_{Io} = -0.683\rho_i g d \sqrt{\pi d}$  (van der Veen, 1998). The subscript “o” denotes overburden. The net stress intensity factor for the problem is then:  $K_{INet} = K_{It} + K_{Io}$ .

Let’s now explore the conditions under which a surface crack will propagate, and the depth to which it will extend. Vaughan (1993) found that tensile stresses between 0.09 and 0.32 MPa were necessary to open crevasses, so let’s assume  $\sigma_{xx} = 0.2 \text{ MPa}$ . If  $d \ll H$ ,  $K_{INet}$  varies with crevasse depth, as shown in Figure 4.19. From the enlargement in the lower left we see that once a crack  $\sim 0.16 \text{ m}$  long is formed,  $K_{INet} = K_{Ic}$ . Any further increase in crack depth will move the system into the field of unstable crack growth, and the crack will propagate unstably to a depth of  $\sim 35 \text{ m}$ . The depth, of course, depends on  $\sigma$ , but this is a realistic depth for air-filled crevasses.

We can use these principles to explore the question, raised earlier, of how high water levels must be maintained in a crevasse to potentially drive the crevasse

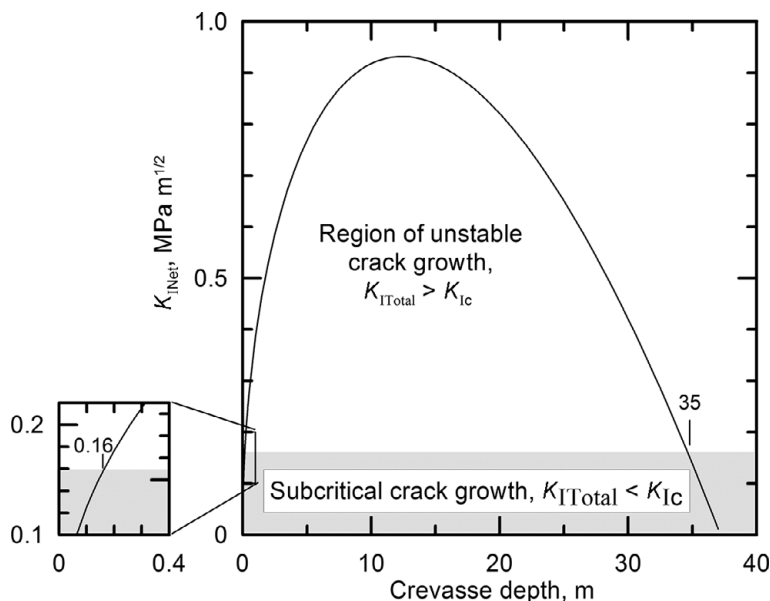


**Figure 4.19** Variation in stress intensity factor with crevasse depth for an air-filled crevasse formed by a tensile stress of 0.2 MPa. The crevasse would propagate to a depth of 35 m. If it got deeper,  $K_{I\text{Net}}$  would decrease below  $K_{Ic}$  and the crevasse would not propagate.

to the bed. By analogy with  $K_{I0}$  above, the stress intensity factor for this stress is  $K_{Iw} = 0.683\rho_w gd_w \sqrt{\pi d_w}$ , where  $\rho_w$  is the density of water and  $d_w$  is the depth of water in the crevasse.  $K_{Iw}$  is positive because the water pressure tends to open the crevasse. Now,  $K_{I\text{Net}} = K_{It} + K_{I0} + K_{Iw}$ , so once  $K_{I\text{Net}} > K_{Ic}$ , it will remain that way as long as  $K_{Iw} \geq |K_{I0}|$ . This will be the case as long as  $d_w \geq d(\rho_i/\rho_w)^{2/3}$ , or  $d_w \geq \approx 0.94d$ . If we let  $a = d - d_w$ , the distance from the glacier surface to the water surface, then the condition for crevasse propagation is  $a \leq \approx 0.06d$ , so as  $d$  increases, the water level can fall slightly and still drive the crevasse deeper. Note, however, that once  $d > \sim 0.25H$ , the value of  $K_{It}$  calculated from Equation (4.9) begins to differ significantly from the linear approximation, so calculations need to use Equation (4.9).

Two additional factors that need to be considered in calculations of crevasse depth are: (1) the presence of low density firn at the surface, and (2) the effect of other crevasses on  $\sigma_{xx}$ . In both cases, the consequences of taking these factors into consideration are fairly obvious. Low density firn reduces  $K_{I0}$  so crevasses penetrate deeper, and if there is a field of crevasses, the tensile stress will be relieved by adjacent crevasses,  $K_{It}$  will be lower (Equation 4.9), and no one crevasse will penetrate as deeply as would a single crevasse. Stress intensity factors can be obtained for these situations (van der Veen, 1998), but the algebra, while straightforward, becomes considerably more complicated.

### Effect of fracture on flow law

Cracks, even small ones that would not qualify as crevasses, weaken the ice. To quantify this, Borstad *et al.* (2016) define a damage parameter,  $D$ :

$$D = 1 - \left( \frac{A_o}{A_d} \right)^{1/n} \quad (4.10)$$

where  $A_d$  is the rate factor in the weakened ice. This is a standard approach in continuum damage mechanics (Pralong and Funk, 2005). Solving this for  $A_d$  and inserting the result in Equation (4.7) in place of  $A_o$  yields:

$$\dot{\epsilon}_e = EA_o \frac{1}{d^p} \left( \frac{\sigma_e}{1 - D} \right)^n e^{-\frac{Q-PV}{RT}}. \quad (4.11)$$

When there is no damage,  $A_d = A_o$  and  $D = 0$ . Conversely, if the damage is extreme,  $A_d$  becomes large,  $D \rightarrow 1$ , and  $\dot{\epsilon}_e$  becomes large. The challenge is to determine  $A_d$ . Note, also, that  $D$  could include softening due to development of an ice fabric with a preferred orientation of  $c$ -axes, thus replacing  $E$ .

A conceptual model of how a system might evolve is illustrated in Figure 4.20. As  $\tau_e$  increases,  $\dot{\epsilon}_e$  increases along the line labeled “ $D = 0$ .” Damage is presumed to occur once  $\tau_e$  exceeds a threshold value,  $\tau_o$  (taken here to be 0.0355 MPa), at which cracks propagate. Once damage has occurred at some location which we will call A, the ice there can no longer support the applied stress. Some of the resistance to flow

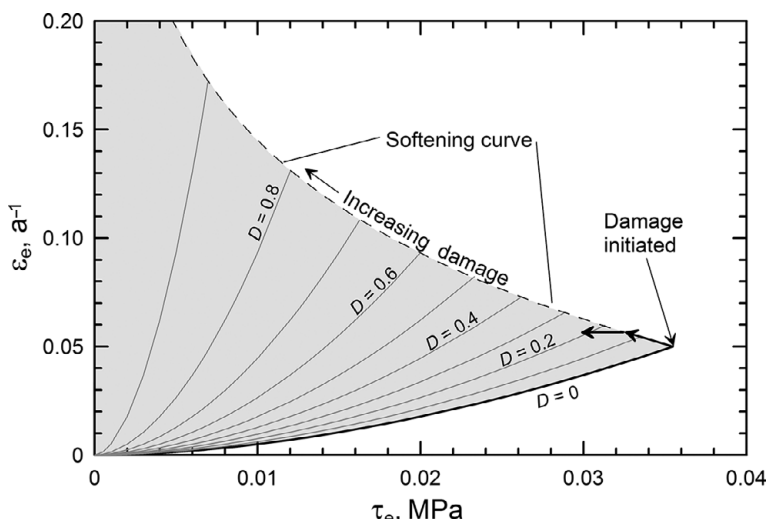


**Figure 4.20** Variation in  $\dot{\epsilon}_e$  with  $\tau_e$  in ice with varying degrees of damage,  $D$ . In undamaged ice,  $\dot{\epsilon}_e$  increases along the  $D = 0$  curve. Possible  $\dot{\epsilon}_e : \tau_e$  states are shaded. Outside the shaded region,  $\dot{\epsilon}_e$  is either too low for the given  $\tau_e$ , or the ice is too weak to support the given  $\tau_e$ . Curves of varying  $D$  are calculated using Equation (4.11) with the constants in Table 4.1 and with  $d = 4$  mm,  $E = 1$ , and  $PV \ll Q$ . Softening curve is calculated using Equation (4.12), with  $\kappa = 2.5$  and  $\tau_o = 0.0355$  MPa. The latter results in  $\dot{\epsilon}_e = 0.5$   $a^{-1}$  at failure.

is thus transferred elsewhere in the ice mass, and the stress at A is reduced to a level that the damaged ice can support. Let's suppose that, for a while, the stress continues to *try* to increase. This results in further damage, further weakening of the ice at A, further transfer of the resisting stresses elsewhere, and a further drop in stress at A; the system follows the heavy arrow extending away from the point of damage initiation in Figure 4.20. Eventually, enough stress has been transferred elsewhere so that the stress at A drops below that needed for further damage (second heavy arrow in Figure 4.20). Once this occurs, the damaged ice may begin to "heal" as crevasses close or are filled with water that then refreezes. Such healing is a result of different processes, so Borstad *et al.* (2016) do not try to analyze it.

Borstad *et al.* call the line of increasing damage in Figure 4.20 the "softening curve," and suggest that it may be described by:

$$\tau_e = \tau_0 e^{\left( -\frac{\dot{\epsilon}_e - \dot{\epsilon}_0}{\dot{\epsilon}_0(\kappa-1)} \right)}. \quad (4.12)$$

Here,  $\tau_0$  is the threshold stress for damage initiation,  $\dot{\epsilon}_0$  is the strain rate at that stress, and  $\kappa (> 1)$  is a ductility parameter that defines the initial downward slope of the softening curve. Thus  $\tau_0$  and  $\kappa$  are physically meaningful parameters that could presumably be established empirically.

To determine  $D$  at various times on the remnant Larsen B ice shelf, Borstad *et al.* (2016) compared strain rates calculated at grid points across the ice shelf using a numerical model with measured ones. The resulting values of  $D$ , together with the observed and modeled stresses and strain rates, yielded  $\kappa = 2.8 \pm 0.4$ .

Damage is clearly a factor that needs to be considered in modeling ice flow, particularly in outlet glaciers and ice shelves, so more work along these lines is warranted.

## SUMMARY

In this chapter, we first reviewed the crystal structure of ice, noting that there are imperfections in this structure, called dislocations, that allow ice (and other crystalline materials) to deform under stresses that are much lower than would be required in the absence of such imperfections. Processes that may limit the deformation rate are those which: (1) inhibit motion of a dislocation in a single crystallographic plane (drag), (2) prevent dislocations from climbing from one crystallographic plane to another to get around tangles, (3) impede motion on certain other crystallographic planes, and (4) inhibit slip between crystals.

Experimental data (Goldsby and Kohlstedt, 1997, 2001) suggest that climb limits dislocation creep at higher stresses (the  $n = 4$  regime) and grain-boundary slip limits

deformation by slip on basal crystallographic planes at intermediate stresses (the  $n = 1.8$  regime). At still lower stresses, diffusion and mechanisms that inhibit slip on basal planes are rate limiting.

When polycrystalline ice is subjected to a stress, some crystals will be oriented in a way that allows them to deform easily, and others will not. Stress concentrations thus develop, and drive recrystallization. Three distinct processes are involved in recrystallization: grain growth, polygonization, and nucleation of new grains. Recrystallization leads to preferred orientations of *c*-axes, and hence to more rapid deformation. The principal processes involved in the development of these fabrics appear to be nucleation of new grains and rotation of grains as slip occurs on their basal planes.

To place creep processes in ice in a more general framework, we introduced a deformation mechanism map in which we displayed deformation mechanisms and strain rates for a range of grain sizes and stresses. Prior to the studies of Goldsby and Kohlstedt (1997, 2001), most experiments were at stresses and grain sizes that spanned the boundary between dislocation creep and creep limited by grain boundary sliding. It now seems likely, however, that much of the deformation in natural ice masses occurs in the latter regime.

Next, we introduced Glen's flow law, and related the exponent,  $n$ , in the flow law to these creep mechanisms. We considered how temperature, pressure, texture, fabric, and water content affect the rate factor,  $A$ . Temperature and pressure effects may be incorporated into the flow law by rigorous, physically-based modifications, whereas *ad hoc* procedures based on empirical evidence are used to incorporate the other effects.

Finally, we introduced principles of linear elastic fracture mechanics and demonstrated that these principles can be used to estimate crevasse depths. Crevassing weakens ice, and a damage factor,  $D$ , may be used to incorporate this into the flow law.

# 6

# Temperature distribution in polar ice sheets

In this chapter, we will derive the energy balance equation for a polar ice sheet. Solutions to this equation yield the temperature distribution in an ice sheet and the rate of melting or refreezing at its base. We will study some analytical solutions of the equation for certain relatively simple situations. A solution of the full equation is possible, however, only with numerical models. This is because: (1) ice sheets have irregular top and bottom surfaces; (2) the boundary conditions – the temperature or temperature gradient at every place along the boundaries – vary in space and time; (3) longitudinal transport (*advection*) of heat by ice flow cannot be handled well with the analytical solutions; and (4) there may be extension or compression transverse to the flowline, which makes the problem three dimensional. Furthermore, because the temperature distribution is governed, in part, by ice flow, and conversely, because the flow rate is strongly temperature-dependent, a full solution requires coupling of the energy and momentum (ice flow) equations.

The thermal conditions in and at the base of an ice sheet are of interest not only to the glacier modeler concerned with flow rates and the possibility of sliding, but also to the glacial geologist with interest in the erosive potential of the ice and processes of subglacial deposition.

## Energy balance in an ice sheet

### Advection

Consider a control volume of length  $dx$ , width  $dy$ , and height  $dz$ , as shown in Figure 6.1. This volume represents an element of space within an ice sheet. Ice flows into the volume from the left with a velocity  $u$ , and out on the right with the same velocity. The temperature of the ice flowing into the volume is  $\theta$ , and that of the ice flowing out is  $\theta + (\partial\theta/\partial x) dx$ . The rate of energy transfer into the control volume, measured in joules per year, is:

$$(u \ dy \ dz) \rho C \theta$$
$$\frac{m^3}{a} \quad \frac{kg}{m^3} \quad \frac{J}{kgK} \quad K = \frac{J}{a}$$

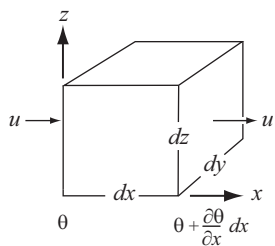


**Figure 6.1** Parameters used in derivation of the advection term in the energy balance equation.

where  $\rho$  is the density of ice and  $C$  is the heat capacity or specific heat. A similar expression can be written for the rate of energy transfer out of the volume at temperature  $\theta + (\partial\theta/\partial x) dx$ . The change in energy within the volume per unit time,  $\partial q/\partial t$ , is the difference between these two expressions, or:

$$\begin{aligned}\frac{\partial q}{\partial t} &= u dy dz \rho C \left[ \theta - \left( \theta + \frac{\partial\theta}{\partial x} dx \right) \right] \\ &= -u dx dy dz \rho C \frac{\partial\theta}{\partial x}\end{aligned}$$

To obtain the change of temperature in the volume per unit time, one can readily deduce from the dimensions of the terms that it is necessary to divide by  $\rho C dx dy dz$ , thus:

$$\frac{\partial\theta}{\partial t} = \frac{1}{\rho C dx dy dz} \frac{\partial q}{\partial t} = -u \frac{\partial\theta}{\partial x} \quad (6.1)$$

$$\frac{1}{\frac{\text{kg}}{\text{m}^3} \frac{\text{J}}{\text{kgK}}} \frac{\text{J}}{\text{m}^3} = \frac{\text{K}}{\text{a}}$$

Here,  $\partial\theta/\partial t$  is the rate of change of temperature with time in the volume as a result of ice being advected into it at a temperature that is different from that of ice leaving it. Similar equations may be written for the  $y$ - and  $z$ -directions, and the results summed to obtain the total change in temperature per unit time in the control volume.

Note that we have been careful to emphasize changes in a particular element of space, the control volume, as distinct from those in an element of ice moving through space. This is because we are using an Eulerian coordinate system, with the coordinate axes fixed in space. Sometimes it is more convenient to use a Lagrangian coordinate system in which an element of ice is followed as it moves through space.

## Conduction

The energy content of the control volume may also change as a result of conduction of heat. Consider the situation depicted in Figure 6.2, in which the temperature gradient across the left hand face,  $dy dz$ , is  $\partial\theta/\partial x$ , and that across the corresponding right hand face is:

$$\frac{\partial\theta}{\partial x} + \frac{\partial}{\partial x} \left( K \frac{\partial\theta}{\partial x} \right) dx.$$

The heat flux is proportional to the temperature gradient. The constant of proportionality is  $K$ , the thermal conductivity of ice. Thus, on the left-hand face there is a heat flux:

$$q = K \frac{\partial\theta}{\partial x} dy dz \quad (6.2)$$

$$\frac{J}{m \cdot K} \frac{K}{m} m \cdot m = \frac{J}{a}.$$

Heat flows from warm areas to cold areas, which means that, for positive  $\partial\theta/\partial x$ , the heat flux is to the left, or out of the left hand side of the control volume in Figure 6.2.

As before, we write a similar expression for the heat flux into the control volume, and subtract the flux out from the flux in, thus:

$$\begin{aligned} \frac{\partial q}{\partial t} &= \left[ K \frac{\partial\theta}{\partial x} + \frac{\partial}{\partial x} \left( K \frac{\partial\theta}{\partial x} \right) dx - K \frac{\partial\theta}{\partial x} \right] dy dz \\ &= \frac{\partial}{\partial x} \left( K \frac{\partial\theta}{\partial x} \right) dx dy dz \\ &= \left( K \frac{\partial^2\theta}{\partial x^2} + \frac{\partial K}{\partial x} \frac{\partial\theta}{\partial x} \right) dx dy dz. \end{aligned}$$

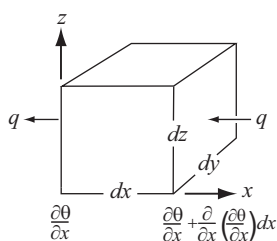


**Figure 6.2** Parameters used in derivation of the conduction term in the energy balance equation.

Dividing again by  $\rho C dx dy dz$ , the change in temperature in the control volume is:

$$\frac{\partial \theta}{\partial t} = \frac{K}{\rho C} \frac{\partial^2 \theta}{\partial x^2} + \frac{1}{\rho C} \frac{\partial K}{\partial x} \frac{\partial \theta}{\partial x}. \quad (6.3)$$

$K/\rho C$  is called the thermal diffusivity,  $\kappa$ , which has SI dimensions of  $\text{m}^2 \text{ a}^{-1}$ . Thus, Equation (6.3) becomes:

$$\frac{\partial \theta}{\partial t} = \kappa \frac{\partial^2 \theta}{\partial x^2} + \frac{1}{\rho C} \frac{\partial K}{\partial x} \frac{\partial \theta}{\partial x}. \quad (6.4)$$

So the change in temperature with time in the control volume due to conduction is related to the changes, as one moves from one side of the volume to the other, in the temperature gradient,  $\partial \theta / \partial x$ , and in  $K$ . Again, similar equations may be written in the  $y$ - and  $z$ -directions.

### Strain heating

Finally, a certain amount of heat is generated within the control volume due to straining of the ice. During deformation, the energy expenditure is the work done divided by the time required to do the work, and work is force times distance, thus:

$$\frac{\text{Work}}{\text{time}} = \frac{\text{Force} \times \text{distance}}{\text{time}}. \quad (6.5)$$

In simple shear (Figure 6.3), the average distance moved in a unit time is  $1/2$  the displacement of the top of the control volume with respect to the bottom, or  $1/2(\partial u / \partial z) dz$ , and the force exerted is  $\sigma_{zx} dx dy$ . In Chapter 2 (Equation 2.6a) we noted that strain rates may be defined in terms of velocity derivatives, thus:

$$\dot{\epsilon}_{zx} = \frac{1}{2} \left( \frac{\partial u}{\partial z} + \frac{\partial w}{\partial x} \right)$$

In simple shear  $\partial w / \partial x = 0$ , so the distance per unit time,  $1/2(\partial u / \partial z) dz$ , is  $\dot{\epsilon}_{zx} dz$  and Equation (6.5) becomes:

$$\frac{\text{Work}}{\text{time}} = \sigma_{zx} dx dy \dot{\epsilon}_{zx} dz$$

$$\frac{N}{m^2} m m \frac{1}{a} m = \frac{N - m}{a} = \frac{J}{a}.$$

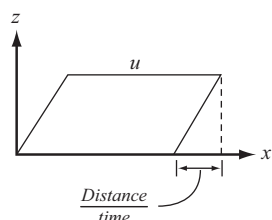


Figure 6.3 Work done in simple shear.

Dimensionally, this is seen to be a rate of energy expenditure, so again we divide by  $\rho C \, dx \, dy \, dz$  to obtain the rate of change of temperature per unit volume:

$$\frac{\partial \theta}{\partial t} = \frac{\sigma_{zx} \dot{\varepsilon}_{zx}}{\rho C}. \quad (6.6)$$

Equation (6.6) was derived for a situation in which deformation was restricted to simple shear in the  $x$ - $z$  plane. In the general case, other components of the stress tensor will be different from 0, so other deformations will be occurring. With a little more background, it is relatively easy to show that the general form of Equation (6.6) is:

$$\frac{\partial \theta}{\partial t} = \frac{\sigma_e \dot{\varepsilon}_e}{\rho C}. \quad (6.7)$$

For convenience,  $Q$  is commonly used to represent the heat production instead of  $\sigma_e \dot{\varepsilon}_e$ , so:

$$\frac{\partial \theta}{\partial t} = \frac{Q}{\rho C}. \quad (6.8)$$

### The generalized energy-balance equation

The rate of change of temperature in the control volume is the sum of the changes represented by Equations (6.1), (6.4), and (6.8), plus changes resulting from heat advection and conduction in the  $y$ - and  $z$ -directions, thus:

$$\frac{\partial \theta}{\partial t} = \kappa \left[ \frac{\partial^2 \theta}{\partial x^2} + \frac{\partial^2 \theta}{\partial y^2} + \frac{\partial^2 \theta}{\partial z^2} \right] + \frac{1}{\rho C} \left[ \frac{\partial K}{\partial x} \frac{\partial \theta}{\partial x} + \frac{\partial K}{\partial y} \frac{\partial \theta}{\partial y} + \frac{\partial K}{\partial z} \frac{\partial \theta}{\partial z} \right] - u \frac{\partial \theta}{\partial x} - v \frac{\partial \theta}{\partial y} - w \frac{\partial \theta}{\partial z} + \frac{Q}{\rho C}. \quad (6.9)$$

As Equation (6.9) is rather cumbersome, it is often convenient to simplify it by using the del operator, defined by:

$$\nabla = \frac{\partial}{\partial x} \hat{\mathbf{i}} + \frac{\partial}{\partial y} \hat{\mathbf{j}} + \frac{\partial}{\partial z} \hat{\mathbf{k}} \quad (6.10)$$

where  $\hat{\mathbf{i}}$ ,  $\hat{\mathbf{j}}$ , and  $\hat{\mathbf{k}}$  are unit vectors in the  $x$ -,  $y$ -, and  $z$ -directions, respectively. When applied to scalar quantities such as either  $\kappa$  or  $\theta$ , the del operator gives a gradient, which is a vector quantity. Accordingly, the fourth through sixth terms and the seventh through ninth terms on the right hand side in Equation (6.9) become scalar or dot products of two vectors, thus:

$$\frac{\partial \theta}{\partial t} = \kappa \nabla^2 \theta + \frac{1}{\rho C} \nabla K \cdot \nabla \theta - \vec{u} \cdot \nabla \theta + \frac{Q}{\rho C}. \quad (6.11)$$

Here,  $\vec{u}$  is the vector velocity. The first term on the right in Equation (6.11) also represents a scalar product:  $\nabla \cdot \nabla \theta$ .

It is sometimes convenient to define:

$$\frac{D\theta}{Dt} = \frac{\partial\theta}{\partial t} + \vec{u} \cdot \nabla\theta$$

in which case, Equation (6.11) becomes:

$$\frac{D\theta}{Dt} = \kappa \nabla^2\theta + \frac{1}{\rho C} \nabla K \cdot \nabla\theta + \frac{Q}{\rho C}. \quad (6.12)$$

Equation (6.11) is the Eulerian form of the equation, in which the coordinates are fixed in space, while Equation (6.12) is the Lagrangian form in which the coordinate system is moving with the ice.  $D\theta/Dt$  is known as the substantial or Lagrangian derivative.

## Dependence of $K$ on temperature

The thermal conductivity of ice is  $\sim 66 \text{ MJ m}^{-1} \text{ a}^{-1} \text{ K}^{-1}$  at  $0^\circ\text{C}$  and  $\sim 83 \text{ MJ m}^{-1} \text{ a}^{-1} \text{ K}^{-1}$  at  $-60^\circ\text{C}$ . Thus, to the extent that the temperature varies in any of the coordinate directions,  $K$  also varies. This effect is normally neglected except in numerical models, and we will follow this custom. Equation (6.9) thus becomes:

$$\frac{\partial\theta}{\partial t} = \kappa \left[ \frac{\partial^2\theta}{\partial x^2} + \frac{\partial^2\theta}{\partial y^2} + \frac{\partial^2\theta}{\partial z^2} \right] - u \frac{\partial\theta}{\partial x} - v \frac{\partial\theta}{\partial y} - w \frac{\partial\theta}{\partial z} + \frac{Q}{\rho C}. \quad (6.13)$$

Neglecting the temperature dependence of  $K$  is reasonable because the effect is relatively small, which, in combination with small temperature gradients, makes these terms negligible in comparison with the others in Equation (6.9).

## The steady-state temperature profile at the center of an ice sheet

Our next task is to solve Equation (6.13) for some relatively simple situations. The first is that at an ice divide, at the center of an ice sheet, a problem first investigated by Robin (1955). The following development follows his closely. The coordinate system we will use is shown in Figure 6.4:  $x$  is horizontal and directed down glacier, and  $z$  is vertical and positive upward;  $z=0$  is at the bed.

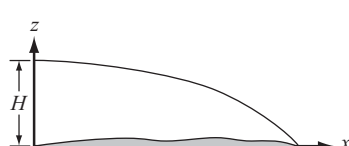


**Figure 6.4** Coordinate system used in calculating the steady-state temperature profile at the center of an ice sheet.

## Simplifying assumptions

At an ice divide, there is no flow in the horizontal directions, and the temperature field is assumed to be symmetrical about the divide. Thus,  $u$  and  $v$  are zero, as are any derivatives in the  $x$  and  $y$  directions. We further assume that strain rates are small, so strain heating can be neglected. Finally, we seek a steady state solution so  $\partial\theta/\partial t=0$ . Equation (6.13) now becomes:

$$0 = \kappa \frac{d^2\theta}{dz^2} - w \frac{d\theta}{dz}. \quad (6.14)$$

As  $\theta$  is now a function of  $z$  alone, this is an ordinary differential equation.

In order to integrate this,  $w$  must be expressed as a function of  $z$ . To do this we assume that ice is incompressible, that  $w=0$  on the bed, and, initially, that the longitudinal strain rate is independent of depth. These are the conditions used to derive Equation (5.21). In our present coordinate system with the origin on the bed and the  $z$ -axis positive upward, Equation (5.21) is:

$$w = \frac{z}{H} w_s. \quad (6.15)$$

We have not yet specified either the sign or the magnitude of  $w_s$ . At an ice divide, the vertical velocity is downward (Figure 3.1a), so the sign of  $w_s$  is negative in the coordinate system of Figure 6.4, and in the steady state  $|w_s| = b_n$ , the accumulation rate. Thus, replacing  $w_s$  with  $-b_n$  in Equation (6.15), combining it with (6.14), and rearranging, we obtain:

$$0 = \frac{d^2\theta}{dz^2} + \frac{b_n z}{\kappa H} \frac{d\theta}{dz}. \quad (6.16)$$

To calculate the temperature distribution, this equation must be integrated twice.

## The first integration

For the first integration, let  $2\zeta^2 = b_n/\kappa H$  and  $\beta = d\theta/dz$ . Equation (6.16) then becomes:

$$0 = \frac{d\beta}{dz} + 2\zeta^2 z \beta. \quad (6.17)$$

Separating variables, we obtain:

$$\int \frac{d\beta}{\beta} = -2\zeta^2 \int z dz$$

which may be integrated to yield:

$$\ln \beta = -\zeta^2 z^2 + c$$

or

$$\beta = e^c e^{-\zeta^2 z^2}. \quad (6.18)$$

The next task is to evaluate the constant of integration,  $e^c$ .

### The basal boundary condition

The constant of integration may be evaluated by using the boundary condition  $\beta = \beta_o$  on  $z=0$ . In other words, we presume that the temperature gradient in the basal ice,  $\beta_o$ , is known or can be estimated. This is known as a Neumann boundary condition. By specifying the gradient at the bed we are implicitly specifying the heat flux upward into the ice. Making these substitutions in Equation (6.18) yields  $e^c = \beta_o$ . Thus, replacing  $e^c$  with  $\beta_o$  and  $\beta$  with  $d\theta/dz$  in Equation (6.18) yields:

$$\frac{d\theta}{dz} = \beta_o e^{-\zeta^2 z^2}. \quad (6.19)$$

This is a solution for the temperature gradient as a function of elevation above the bed.

The requirement that the temperature gradient in the basal ice be known is fundamentally unavoidable. However, this is not as serious a problem as one might, at first, expect. In the steady state,  $\beta_o$  is adjusted so that all of the heat coming from within the earth, the geothermal flux, can be conducted upward into the ice. Thus, if the geothermal flux can be estimated,  $\beta_o$  can be calculated because the constant of proportionality between the two, the thermal conductivity of ice,  $K$ , is known.

To clarify the physical processes by which  $\beta_o$  is adjusted, consider a non-steady-state situation in which  $\beta_o$  is too low. Some of the geothermal heat would then remain at the ice–rock interface, where it would warm the ice. Because the temperature decreases upward in the glacier, the ice being colder than the Earth’s interior, such warming would increase  $\beta_o$  until all of the heat could be conducted upward into the ice, thus tending to re-establish the steady state. (For the moment, we neglect basal melting).

Geothermal heat is heat conducted from the gradually-cooling mantle and core, supplemented with heat produced by radioactive decay in the crust. Numerous measurements of the geothermal flux have been made, so we have a fair idea of its magnitude in different geological terranes. Geophysicists use the *heat flow unit*, or *HFU*, to describe this flux: 1 HFU is  $1 \mu\text{cal cm}^{-2} \text{ s}^{-1}$ . In glaciology, however, it is more common to use  $\text{W m}^{-2}$ . The world-wide average geothermal flux is 1.2 HFU, or  $50 \text{ mW m}^{-2}$ . This corresponds to a temperature gradient in basal ice of  $0.0226 \text{ K m}^{-1}$ . The gradient in the underlying rock is normally somewhat different as the thermal conductivity of the rock is not necessarily exactly the same as that of the ice. In general, geothermal fluxes are highest in volcanic terranes, high in geologically young terranes, and lowest in geologically ancient terranes. A few examples of geothermal fluxes in glaciated areas are given in Table 6.1.

In the discussion above, we asserted that knowledge of  $\beta_o$  was “fundamentally unavoidable.” It is true, of course, that a boundary value problem such as this could be solved with some other basal boundary condition, such as the basal temperature. (This will be left as an exercise for the reader.) However, as the basal temperature is

**Table 6.1** Geothermal fluxes in some geological terranes in which glaciers are or were found

Locality	Heat flux		Basal gradient K m <sup>-1</sup>	Reference
	HFU	mW m <sup>-2</sup>		
Antarctica (East)	1.2 <sup>1</sup>	50	0.0226	Budd <i>et al.</i> (1971)
Antarctica (West)	1.4 <sup>1</sup>	59	0.0264	Budd <i>et al.</i> (1971)
Baffin Bay	1.35	56	0.0255	
Canadian Shield	0.8	33	0.0151	
Greenland summit	1.2	51	0.0226	Dahl-Jensen <i>et al.</i> (1998)
World average	1.2	50	0.0226	

<sup>1</sup> Estimated.

one of the quantities that we are particularly eager to determine, and as basal temperatures are much harder to estimate from existing data than are basal temperature gradients, choosing  $\beta_o$  as the basal boundary condition is the only logical choice in most situations.

### The second integration

To obtain the actual temperature distribution, it is necessary to integrate Equation (6.19). Separating variables as before yields:

$$\int_{\theta(h)}^{\theta_s} d\theta = \beta_o \int_h^H e^{-\zeta^2 z^2} dz. \quad (6.20)$$

Here, the integration is from some level,  $z = h$ , in the glacier, where the temperature is  $\theta(h)$ , to the surface at  $z = H$ , where the temperature is  $\theta_s$ . [Note that, in this case, rather than solve Equation (6.19) as an indefinite integral and then evaluate a constant of integration by applying a boundary condition, it is more convenient to express the integrals as definite integrals. Thus the boundary condition,  $\theta = \theta_s$  on  $z = H$ , is incorporated into the limits of integration. Further discussion of this boundary condition is deferred for the moment.]

The integral on the right hand side of Equation (6.20) does not have a solution in closed form. However, it occurs frequently, and thus has been tabulated. In addition, many computer statistical packages have solutions. The challenge is to express it in the terms used in these tables.

We first express the integral on the right hand side as the difference between integrals over the range  $0 \rightarrow H$  and  $0 \rightarrow h$ , thus:

$$\theta_s - \theta(h) = \beta_o \left[ \int_0^H e^{-\zeta^2 z^2} dz - \int_0^h e^{-\zeta^2 z^2} dz \right] \quad (6.21)$$

and then make the substitution:  $\zeta z = t$ , whence  $dz = dt/\zeta$ , and  $t = \zeta h$  on  $z = h$ . We also multiply and divide by  $\sqrt{\pi}/2$ , thus:

$$\theta_s - \theta(h) = \frac{\sqrt{\pi} \beta_o}{2 \zeta} \left[ \frac{2}{\sqrt{\pi}} \int_0^{\zeta H} e^{-t^2} dt - \frac{2}{\sqrt{\pi}} \int_0^{\zeta h} e^{-t^2} dt \right]. \quad (6.22)$$

One definition of a tabulated function, called the error function, is:

$$\text{erf}(x) = \frac{2}{\sqrt{\pi}} \int_0^x e^{-t^2} dt \quad (6.23a)$$

Thus, our final solution for the temperature,  $\theta(h)$ , at depth  $h$  is:

$$\theta(h) = \theta_s - \frac{\sqrt{\pi} \beta_o}{2 \zeta} [\text{erf}(\zeta H) - \text{erf}(\zeta h)]. \quad (6.24)$$

Values of  $\text{erf}(x)$  can be looked up, much as can values of a sine or cosine. Caution is required, however, as some tables define  $\text{erf}(x)$  slightly differently than we have in Equation (6.23a), and thus require a different set of substitutions in Equation (6.21). A common alternative definition is:

$$\text{erf}(x) = \frac{1}{\sqrt{2\pi}} \int_0^x e^{-\frac{1}{2}t^2} dt \quad (6.23b)$$

which requires the substitution:  $\zeta z = t/\sqrt{2}$ . This leads to other changes in Equations (6.22) and (6.24). Budd (1969) uses a less common definition, namely:

$$\text{erf}(x) = \int_0^x e^{-t^2} dt \quad (6.23c)$$

and has plotted this (Figure 6.5) along with another function that arises in calculations of temperature distributions in ice sheets. With this definition, Equation (6.22) can be written:

$$\theta(h) = \theta_s - \frac{\beta_o}{\zeta} [\text{erf}(\zeta H) - \text{erf}(\zeta h)]. \quad (6.25)$$

In applying Equation (6.24) or (6.25), note that  $\beta_o$  is negative in the coordinate system of Figure 6.4.

### The boundary condition at the surface

As noted, the boundary condition at the surface,  $z = H$ , is the ice temperature,  $\theta_s$ , and this must be known in order to calculate a temperature profile from Equations (6.24) or (6.25). This is known as a Dirichlet boundary condition, one in which the state variable, in this case temperature, is specified. Below, we will show that the

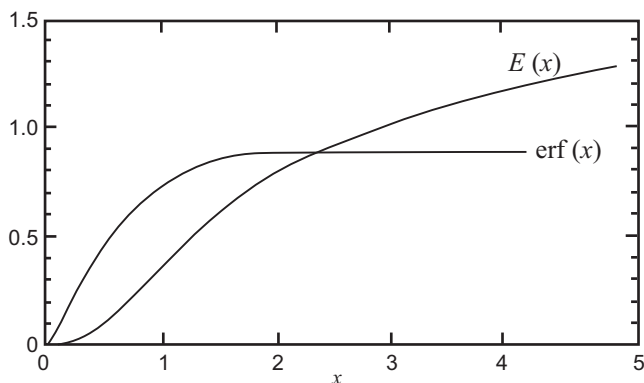


**Figure 6.5** Values of the error function,  $\text{erf}(x)$ , as defined by Equation (6.23c), and of Dawson's integral,  $E(x)$ , for a typical range of values of  $x = \zeta H$ . (Modified from Budd, 1969, Figure 4.10. Reproduced with permission of the Australian Antarctic Division)

temperature at a depth of about 10 m in a glacier is very close to the mean annual atmospheric temperature,  $\theta_a$ , so it is normally assumed that  $\theta_s = \theta_a$ . However, it may be well to note some situations in which this approximation is not very good.

Temperatures in the ablation zones of some glaciers may be somewhat warmer than the mean annual temperature. This is because snow insulates the ice during the winter, preventing cooling. In addition, percolating meltwater reaches the snow/ice interface soon after melting starts in the spring, thus warming the ice faster than would be the case with conduction alone. On Barnes Ice Cap, these two effects result in near-surface ice temperatures that are about 2°C above the mean annual temperature (Hooke *et al.*, 1983).

Somewhat higher on a glacier, near and above the equilibrium line, percolating meltwater can penetrate into the firn of prior years. When this water refreezes, the heat of fusion is released at a significant depth in the glacier, not just at the snow/ice interface. The warming effect is thus much enhanced, and ice temperatures in this zone may be several degrees warmer than the mean annual temperature.

At high latitudes and altitudes on polar ice sheets, the ice temperature may be slightly below the mean annual temperature because radiative cooling during the clear winter night is more effective than heating during the summer day (Hooke *et al.*, 1983).

### Melting and freezing at the bed

In our analysis so far, we have tacitly assumed that the temperature at the base of the glacier is below the melting point. However, this assumption has not been incorporated into Equations (6.24) or (6.25). To be specific, if the bed is at the pressure melting point and melting is occurring there, some of the geothermal heat is clearly being used for that purpose and is not being conducted upward into the

ice. Thus, our estimate of  $\beta_o$  is likely to be too high. If we inadvertently insert such a value of  $\beta_o$  into Equations (6.24) or (6.25), the calculated temperature at the bed,  $\theta_o$ , will turn out to be greater than the pressure melting temperature, which is clearly impossible.

To obtain a correct solution for the temperature profile in this case,  $\beta_o$  must be adjusted downward. The procedure is straightforward. Because  $\text{erf}(0) = 0$  and  $\theta(0) = \theta_{\text{pmp}}$ , the pressure melting point temperature, Equation (6.24) can be solved for  $\beta_o$ , thus:

$$\beta_o = \frac{2\zeta}{\sqrt{\pi}} \frac{(\theta_s - \theta_{\text{pmp}})}{\text{erf}(\zeta H)}. \quad (6.26)$$

The melting point is depressed approximately  $0.098 \text{ K MPa}^{-1}$  (if the water produced is saturated with air) so, for example,  $\theta_{\text{pmp}}$  under 500 m of ice would be  $\sim -0.4^\circ\text{C}$ . Inserting the value of  $\beta_o$  obtained from Equation (6.26) into Equation (6.24) and solving for temperatures at other depths in the glacier will give the desired temperature profile. [Note that this approach is equivalent to solving Equation (6.17) with a temperature (Dirichlet) boundary condition at the bed].

The basal melt rate,  $dm/dt$ , can also be calculated. The heat available for melting is the difference between the geothermal heat flux and the heat flux into the ice, or  $K(\beta_G - \beta_o)$ , where  $\beta_G$  is the gradient that would be required to conduct the geothermal flux upward into the ice. Thus, we obtain:

$$\frac{dm}{dt} = K \frac{(\beta_G - \beta_o)}{\rho L} \cong 0.23(\beta_G - \beta_o) \text{ m a}^{-1} \quad (6.27)$$

$$\begin{aligned} \frac{\text{J}}{\text{m a K}} & \quad \frac{\text{K/m}}{\frac{\text{kg J}}{\text{m}^3 \text{kg}}} \\ & \end{aligned}$$

where  $L$  is the latent heat of fusion, and the result is in  $\text{m a}^{-1}$  if the gradients are in  $\text{K m}^{-1}$ .

It is also possible that water formed by basal melting at some distant locality has moved along the bed to the site at which the temperature profile is to be calculated. Until all such water is refrozen, perhaps incorporating sediment into the ice in the process, it will keep the basal temperature at the pressure melting point. Again, Equation (6.24) does not know about this water, so the intelligent scientist must intervene. Presumably, he or she has calculated basal melt and freeze rates further upglacier, and has kept track of how much of the water produced has not refrozen or drained away in the substrate. In any case, the procedure is similar to that above, except that now the value of  $\beta_o$  calculated from Equation (6.26) will be greater than that necessary to conduct the geothermal heat upward into the ice, and  $dm/dt$  in Equation (6.27) will be negative, indicating freezing.

### Character of the temperature profile

Several temperature profiles calculated from Equation (6.24) are shown in Figure 6.6a. For the conditions assumed, the ice is nearly isothermal in the upper few hundred meters and then warms rapidly near the bed. Higher vertical velocities, resulting from higher accumulation rates at the surface, increase the thickness of the isothermal zone and decrease the basal temperature.

In essence, cold ice is advected downward from the surface, and the upward-moving geothermal heat warms this descending ice. With higher accumulation rates and, hence, higher vertical velocities, the heat supplied can warm a smaller fraction of the descending ice, so the ice column as a whole is colder.

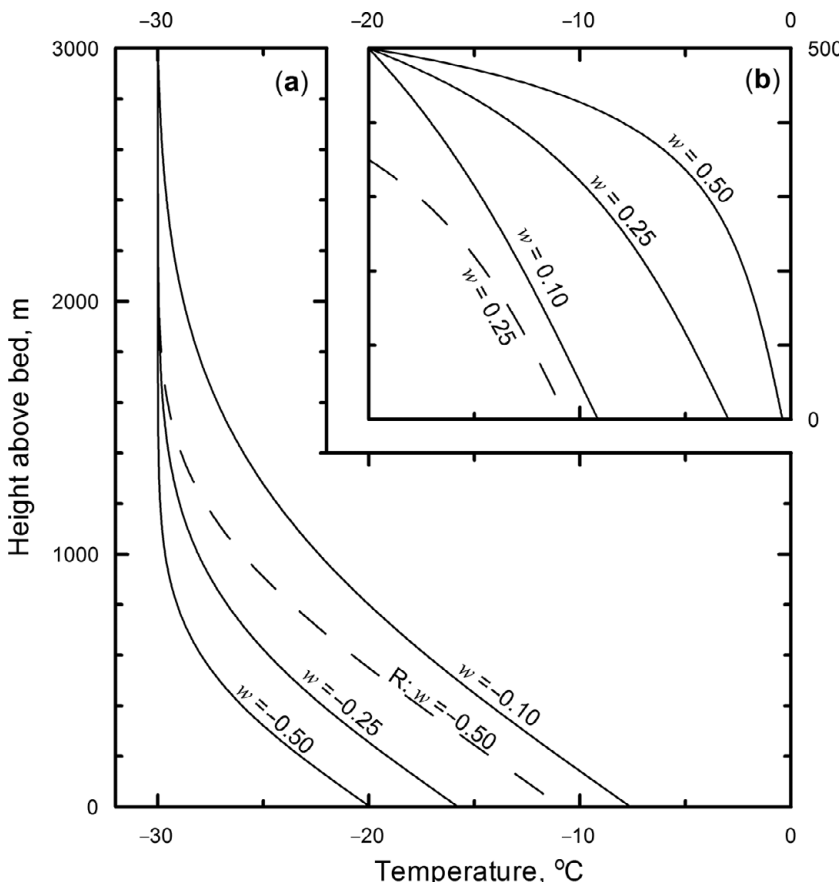


**Figure 6.6** Temperature profiles in polar ice sheets calculated using Equations (6.24) and (6.29), or, in the case of the dashed profiles, Equation (6.28). Positive vertical velocities are upward and conversely. (a) Accumulation zone. (b) Ablation zone. All calculations use  $\beta_0 = -0.017 \text{ K m}^{-1}$  except that for  $w = 0.5 \text{ m a}^{-1}$  in the ablation zone; there  $\beta_0$  is reduced to  $-0.007 \text{ K m}^{-1}$  in order to match the pressure melting temperature at the bed. The calculated melt rate (Equation 6.27) is then  $2.2 \text{ mm a}^{-1}$ .

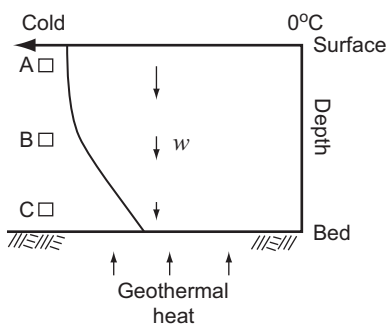


**Figure 6.7** Qualitative illustration of effect of downward vertical velocity on a temperature profile.

The shape of the temperature profile can be understood qualitatively in the following way. Consider the three elements of ice, labeled A, B, and C in Figure 6.7. All three are moving downward, but because  $w$  decreases with depth (Equation 6.15), element A will be moving fastest and element C slowest. As element C moves down, it must warm up, and this requires heat. Thus, the heat flux out of the top of this element will be less than that into the bottom, and the temperature gradient required to conduct this heat will be less at the top of the element than at the bottom. However,  $w$  is small in this part of the glacier, so despite the comparatively high temperature gradient here, this element does not have to warm up very much and the change in temperature gradient through it is small, as shown by the curve to the right in Figure 6.7. Element B has a higher velocity, and the temperature gradient is still comparatively high here, at mid-depth in the glacier, so this element must warm up a lot. Thus, here the change in temperature gradient through the element is rather large. Element A has the highest vertical velocity, but at this level in the glacier nearly all of the heat introduced at the base has been consumed in warming deeper ice. Thus, the temperature gradient here is quite low, and despite its high velocity, element A does not have to warm up very much. Thus, again, the change in temperature gradient through the element is small.

Later we will examine temperature profiles in the ablation area, where the vertical velocity is upward. However, the reader may find it both challenging and instructive to try to deduce the character of the profile there, using the logic just presented.

### Error introduced by the assumed vertical velocity distribution

One of the most tenuous assumptions we made in deriving Equation (6.24) was that the longitudinal strain rate,  $\partial u / \partial x$ , was independent of depth. This led to the use of a linear decrease in  $w$  with depth (Equation 6.15) in Equation (6.16). As discussed in Chapter 5, we know that  $\partial u / \partial x$  decreases with depth under most conditions. Early attempts to use a more realistic relation for  $w$  were made by Philberth and Federer

(1971) and Budd *et al.* (1971), but they relied on *ad hoc* relations without good theoretical basis.

It would be convenient if we could simply use either Equation (5.24) or Equation (5.25) for  $w$ , but this leads to solutions for  $\beta$  that cannot be integrated a second time. Thus, a numerical integration is necessary.

To illustrate the importance of this effect, let us use Equation (5.25) (modified for a coordinate system with the  $z$ -axis positive upward) in place of Equation (6.15) for  $w$ . The solution for the temperature gradient is then:

$$\frac{d\theta}{dz} = \beta_o e^{-\xi z^3} \quad (6.28)$$

where  $\xi = b_n / 3\kappa H^2$ . Integrating this numerically with  $w = b_n = -0.5 \text{ m a}^{-1}$  yields the dashed curve in Figure 6.6a. Thus, using this more realistic expression for  $w$  leads to basal temperatures that are nearly  $10^\circ\text{C}$  warmer than given by Equation (6.24) for otherwise similar conditions!

## Temperature profiles in the ablation zone

In the ablation area, except very near the equilibrium line,  $w$  is positive, or upward. In this case, the solution of Equation (6.16) for the temperature gradient becomes:

$$\frac{d\theta}{dz} = \beta_o e^{\zeta^2 z^2}. \quad (6.29)$$

This equation, again, cannot be integrated in closed form, and the integral has not been tabulated. Examples of profiles obtained by a numerical integration<sup>1</sup> are shown in Figure 6.6b. Of particular interest is the exponential increase in gradient near the surface, a result that is apparent from Equation (6.29). A consequence of this behavior is that basal temperatures must commonly reach the melting point in the ablation zone, even with modest ice thicknesses and vertical velocities. Furthermore, when basal temperatures do reach the melting point,  $\beta_o$  becomes small, so most of the geothermal heat is trapped at the bed, resulting in high basal melt rates.

---

<sup>1</sup> Various ways to perform a numerical integration are discussed in Chapter 11. The easiest approach, in this case, is to use a spreadsheet. Specify  $\beta_o$  and  $\zeta$ , make an initial guess for the temperature at the bed,  $\theta_b$ , and start with  $z = 0$ . Choose an increment  $dz$ , and calculate  $d\theta$  from  $\beta_o e^{\zeta^2 z^2} dz$ .  $\theta_b + d\theta$  is the temperature at  $z = dz$ . Now use this value of  $z$  and repeat the calculation to get  $\theta$  at successive heights above the bed. You have to start at the bed and integrate upward, and then adjust the temperature at the bed to get the observed surface temperature (the boundary condition).  $\beta_o$  is negative, so  $d\theta$  is negative.

## Temperature profiles near the surface of an ice sheet

Earlier (p. 124–125) we noted that, although the temperature at the surface,  $\theta_s$ , varies seasonally, the temperature at a depth of  $\sim 10$  m is very close to the mean annual temperature. Let us now verify this. We adopt a coordinate system with  $z = 0$  at the surface and the  $z$ -axis pointing downward. At the surface we assume that the seasonal variation can be described by  $\theta(z = 0, t) = \frac{1}{2}\theta_r \sin(\omega t)$ , where  $\theta_r$  is the annual temperature range (twice the amplitude) and  $\omega$  is the period of the oscillation, or  $2\pi$  radians/year. Beneath the surface, we expect the oscillations to be damped. The annual temperature range at depth,  $z$ , is  $\theta_{\max}(z) - \theta_{\min}(z)$ . Our goal is to calculate the depth at which this range decreases to an acceptably small fraction,  $\delta = [\theta_{\max}(z) - \theta_{\min}(z)]/\theta_r$ , of the variation in  $\theta_r$ . We can then measure the temperature at this depth and use it as our boundary condition at the surface.

Ignoring horizontal gradients, strain heating, and vertical advection (so there is no accumulation, ablation, or compaction), Equation (6.13) simplifies to:

$$\frac{\partial \theta}{\partial t} = \kappa \frac{\partial^2 \theta}{\partial z^2}. \quad (6.30)$$

The solution to this is:

$$\theta(z, t) = \frac{1}{2}\theta_r e^{-z\sqrt{\frac{\omega}{2\kappa}}} \sin\left(\omega t - z\sqrt{\frac{\omega}{2\kappa}}\right) \quad (6.31)$$

(Carslaw and Jaeger, 1959, p. 65). Thus, if the seasonal variation in temperature at the surface is sinusoidal, the temperature profile at any given time during the year can be calculated from Equation (6.31). Some profiles for representative times are shown in Figure 6.8.

At any given depth,  $h$ ,  $\theta_{\max}$  and  $\theta_{\min}$  occur when  $\sin(\omega t - h\sqrt{\omega/2\kappa}) = \pm 1$ , respectively. Thus, if we specify an acceptable value of  $\delta$ , Equation (6.31) can be used to calculate the depth,  $h$ , at which that  $\delta$  is reached:

$$h = \sqrt{\frac{2\kappa}{\omega}} \ln \frac{1}{\delta}. \quad (6.32)$$

Choosing  $\delta = 0.01$  (or 1%), we find that  $h = 10.4$  m if  $\kappa = 16 \text{ m}^2 \text{ a}^{-1}$ , a value appropriate for unpacked snow. In ice, with  $\kappa = 37.2 \text{ m}^2 \text{ a}^{-1}$ ,  $h = 15.9$  m. Thus, temperatures measured at a depth of 10 m in snow and firn or 16 m in ice should closely approximate the mean annual temperature.

The most serious assumption in this calculation is that accumulation and ablation can be ignored. In the accumulation area, accumulating snow insulates the surface, reducing  $\theta_r$ . This is probably not too serious a problem. However, in the ablation area, as noted earlier, there is not only the insulating effect of snow during the fall

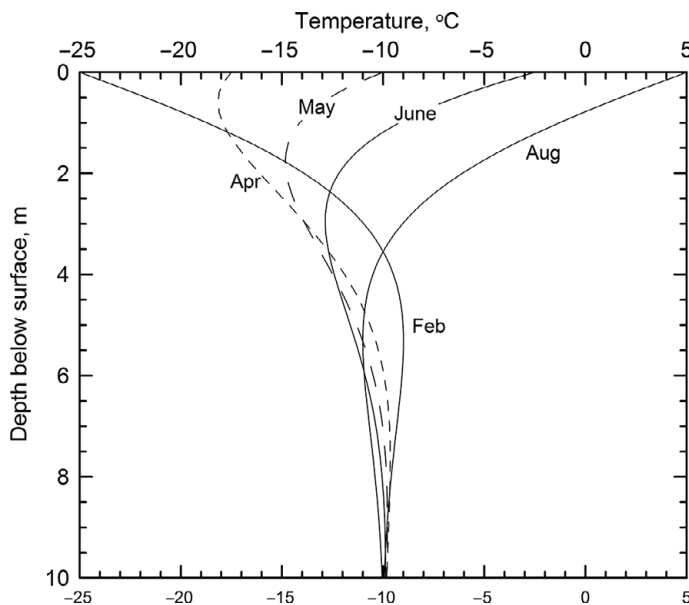


**Figure 6.8** Seasonal variation in near-surface temperature profiles in the dry-snow zone of an ice sheet.

and winter, but also warming by percolating meltwater in the late spring or early summer and then lowering of the ice surface later in the summer. Combined, these processes result in 15 m temperatures that are likely to be warmer than the mean annual temperature, as noted (p. 125).

## Temperature profiles far from a divide

### The column model

Budd (1969) and Budd *et al.* (1971) solved Equation (6.13) in a more general form than those we have considered so far. Calculations using their model, which they refer to as the *Column model*, can be done with a hand-held calculator or spreadsheet.

The coordinate system used is shown in Figure 6.9. The temperature profile is to be calculated at a point a distance  $\chi$  from the divide. Starting again with Equation (6.13), we restrict the model to two dimensions, thus eliminating derivatives in the  $y$ -direction; we assume that temperature gradients in the  $x$ -direction are sufficiently small that their derivative is negligible; and we assume a steady state. With these assumptions, Equation (6.13) becomes:

$$0 = \kappa \frac{\partial^2 \theta}{\partial z^2} - u \frac{\partial \theta}{\partial x} - w \frac{\partial \theta}{\partial z} + \frac{Q}{\rho C}. \quad (6.33)$$

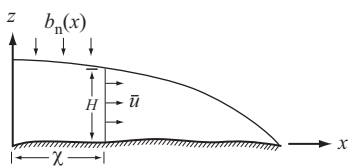


**Figure 6.9** Coordinate system and parameters involved in Column model calculations.

Consider, now, the strain heating term,  $Q/\rho C$ . Starting with Equation (6.8), substitute  $\sigma_e \dot{\varepsilon}_e$  for  $Q$ , and then  $A\sigma_e^3$  for  $\dot{\varepsilon}_e$ , and then, since  $\sigma_{zx}$  is likely the dominant term in  $\sigma_e$  over most of the ice thickness, approximate  $\sigma_e$  by  $\rho g d \alpha$ , where  $d$  is the depth below the surface, yielding  $\sigma_e \dot{\varepsilon}_e = A(\rho g d \alpha)^4$ . So  $Q/\rho C \propto d^4$ . In other words, because the strain rate increases rapidly near the bed, most of the strain heating occurs in the basal few meters of ice. [The student may find it interesting to study this effect by solving Problem 6.2.] Recognizing that most strain heating occurs *near* the bed, Budd (1969) approximated it as occurring entirely *at* the bed. Thus, he reasoned, this heat could simply be added to the geothermal flux. The basal boundary condition,  $\beta_o$ , then becomes:

$$\beta_o = \beta_G + \frac{\tau_b \bar{u}}{K} \quad (6.34)$$

$$\frac{K}{m} \quad \frac{K}{m} \quad \frac{\frac{N \cdot m}{m^2 \cdot a}}{\frac{J}{maK}} = \frac{K}{m} \quad 1 N \cdot m = 1 J$$

and  $Q/\rho C$  is set to zero. Here, as before,  $\beta_G$  is the gradient required to conduct the geothermal flux upward into the ice;  $\tau_b$  is the basal drag, approximated by  $\rho g H \alpha$ ; and  $\bar{u}$  is the mean horizontal velocity. For  $\bar{u}$  at  $\chi$  we use the balance velocity:

$$\bar{u} = \frac{1}{H} \int_0^\chi b_n(x) dx \quad (6.35)$$

(Equation 5.1). In calculations, care must be taken to ensure that the sign of the  $\frac{\tau_b \bar{u}}{K}$  term is the same as that of  $\beta_G$ ; this sign is determined by the choice of coordinate axes.

We turn now to the term  $u \cdot \partial \theta / \partial x$  in Equation (6.33). The rate at which the atmospheric temperature increases as one moves to lower elevations along the ice surface is  $\alpha \lambda$ , so let's set  $\partial \theta / \partial x = \alpha \lambda$ . This is the rate at which the upper few meters of the glacier warm as a result of horizontal advection. If  $\alpha$  is sufficiently small, the deeper ice will warm at *nearly* the same rate, with almost negligible lag. This led Budd (1969) to suggest that, to a reasonable first approximation,  $u \cdot \partial \theta / \partial x$  can be replaced with  $u \alpha \lambda$  in Equation (6.33). The consequences of this assumption are discussed later.

With the additional substitution of  $(w_s - w_b)z/H$  for  $w$ , Equation (6.33) becomes:

$$\kappa \frac{\partial^2 \theta}{\partial z^2} - (w_s - w_b) \frac{z}{H} \frac{\partial \theta}{\partial z} = u \alpha \lambda \quad (6.36)$$

in which  $w_s$  and  $w_b$  are the vertical velocities at the surface and bed, respectively. The former can be calculated from the submergence velocity (Equation 5.26) when  $b_n$ ,  $u_s$ , and  $\alpha$  are known. Equation (6.36) is to be solved using the boundary condition of Equation (6.34). If the velocity at the bed is assumed to be parallel to the bed,  $w_b$  can be estimated from knowledge of  $u_b$  and the bed slope, averaged over a horizontal distance of an ice thickness or so, and the basal melt rate (if any). Assuming that  $u_b = \bar{u} = u_s$  is probably a reasonable approximation in this calculation, but knowing  $\bar{u}$ , one could also calculate  $u_s$  and  $u_b$  from Equations (5.18) and (5.19). In our coordinate system,  $w_s$  is negative. Thus, as long as  $w_b$  does not become too positive (due, for example, to flow up an adverse bed slope or an exceptional amount of refreezing)  $(w_s - w_b)$  will be negative. Let us thus define  $\tilde{b}_n = -(w_s - w_b)$ . As  $w_b$  is normally small compared with  $w_s$ ,  $\tilde{b}_n \approx b_n$ . Equation (6.36) thus resembles Equation (6.16), but with the addition of the horizontal advection term on the righthand side.

Budd's solution to Equation (6.36) is:

$$\theta(h) = \theta_s - \frac{\beta_o}{\zeta} [\operatorname{erf}(\zeta H) - \operatorname{erf}(\zeta h)] - \frac{2\bar{u}\alpha\lambda H}{\tilde{b}_n} [E(\zeta H) - E(\zeta h)]. \quad (6.37)$$

where:

$$\operatorname{erf}(x) = \int_0^x e^{-t^2} dt$$

$$E(x) = \int_0^x \left[ e^{-y^2} \int_0^y e^{t^2} dt \right] dy$$

$$\zeta = \sqrt{\tilde{b}_n / 2\kappa H}$$

Note that this solution uses Budd's definition of the error function,  $\operatorname{erf}(x)$ .  $E(x)$  is the integral of a function known as Dawson's integral (the quantity in square brackets), and it too has been tabulated. A plot of  $E(x)$  for a reasonable range of  $x$  is shown in Figure 6.5.

Temperature profiles can be calculated readily using Equation (6.37) and Figure 6.5. Two are shown in Figure 6.10. The minimum temperature occurs at some depth below the glacier surface. This represents cold ice that is advected downward and laterally from some point further upglacier, where the surface is at a higher elevation and hence colder. However, the Column model does not include

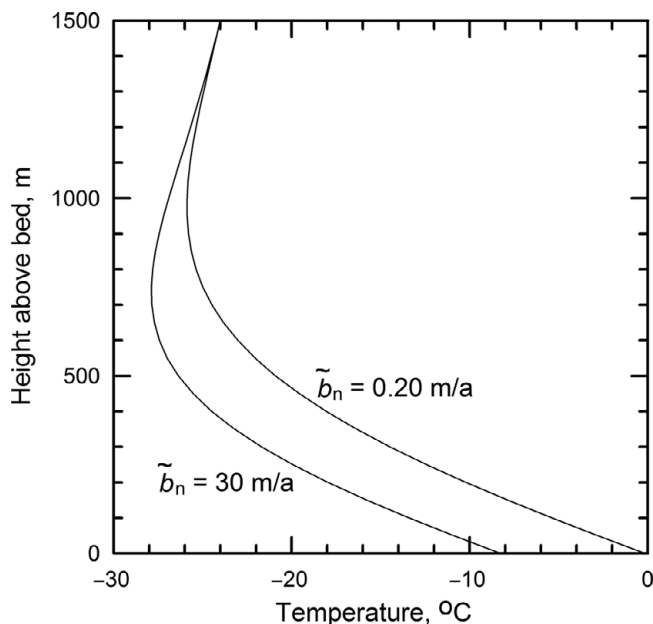


**Figure 6.10** Temperature profiles for two different values of  $\tilde{b}_n$  calculated from Equation (6.37). The following values of the parameters were used:  $\alpha = -0.01$ ,  $u = 15 \text{ m a}^{-1}$ ,  $\lambda = -0.01 \text{ K m}^{-1}$ ,  $K = 7.1 \times 10^7 \text{ J m}^{-1} \text{ a}^{-1} \text{ K}^{-1}$ ,  $\kappa = 37.2 \text{ m}^2 \text{ a}^{-1}$ ,  $H = 1500 \text{ m}$ ,  $\theta_s = -24^\circ\text{C}$ , and  $\beta_G = -0.020 \text{ K m}^{-1}$ .

this longitudinal advection rigorously; it simply specifies a warming rate. Thus, the temperature at depth is only an approximation that becomes better as the warming rate decreases. This approximation is best, therefore, where surface slopes ( $\alpha$ ) and lapse rates ( $\lambda$ ) are lowest.

The Column model yields a temperature profile in which the magnitude and the curvature of the positive temperature gradient near the surface are adjusted so that heat conducted downward from the surface, in combination with heat advected downward, is just sufficient to warm the ice above the point of minimum temperature at the rate  $u\alpha\lambda$ . Ice below this point is warmed at this rate by heat from the bed – both geothermal and frictional. When the warming rate at depth that is specified (by representing it by  $u\alpha\lambda$ ) is larger than that in a natural situation that the reader might wish to model, as is commonly the case, the positive temperature gradient at the surface becomes too high, and the temperatures at depth too cold. This can lead to physically impossible calculated temperature distributions, with pockets of cold ice surrounded by warmer ice but with no way for the ice to have cooled down (e.g. by heat loss to colder ice).

Despite these drawbacks, the Column model does illustrate the basic physical controls on the temperature distribution in ice sheets, and if the user recognizes its limitations, it can yield plausible estimates of temperatures. For geomorphologists wishing to test ideas on the origin of certain landforms, for example, the errors

introduced by the simplifying assumptions made in the Column model are probably no greater than the uncertainties in the ice age values of parameters like  $b_n$ ,  $H$ ,  $\beta_o$ , and  $\bar{u}$  that are used in it.

### Englacial and basal temperatures along a flowline calculated using the column model

Let us now consider the temperature distribution along a flowline calculated with the use of the Column model. The original objective of the modeling, shown in Figure 6.11, was to investigate the possibility that there could have been, along the margin of the Laurentide Ice Sheet in North Dakota, a ~2 km-wide zone in which the ice was frozen to the bed. Such a temperature distribution is implied by glacial landforms, as discussed further in the Geomorphic implications section below (Moran *et al.*, 1980). Thus, the modeled flowline was assumed to extend from Hudson Bay to North Dakota.

In the model, the accumulation rate was assumed to be  $0.20 \text{ m a}^{-1}$  65 km upglacier from the equilibrium line, and to decrease linearly to  $0.05 \text{ m a}^{-1}$  at the divide, and to 0 at the equilibrium line. The decrease in  $b_n$  toward the divide is consistent with the present accumulation pattern in Antarctica (Figure 3.5) and northern Greenland, although not southern Greenland (Zwally and Giovinetto, 2000). In the ablation area, the ablation rate increased linearly downglacier from the equilibrium line at a rate adjusted to provide a balanced mass budget. The horizontal velocity was approximated by the balance velocity (Equation (5.1)), modified to allow for divergence of the flowlines. The ice sheet profile was adjusted to provide the shear stress necessary to yield this horizontal velocity, using a relation similar to the first of Equations (5.19) with a sliding law to estimate  $u_b$ . Isostatic depression of the earth's crust was included. The vertical velocity was calculated from the submergence or emergence velocity relation (Equation (5.26)), and was assumed to decrease linearly with depth (Equation 6.15). The temperature at the margin was  $-7.5^\circ\text{C}$ . The temperature along the surface was calculated assuming a lapse rate of  $-0.01 \text{ K m}^{-1}$ , and making an empirical correction for warming effects of percolating melt water. The geothermal fluxes used were appropriate to the geologic terrane along the flowline. The warming rate was assumed to be  $\frac{1}{2} u \alpha \lambda$ .

Several features of the temperature distribution in Figure 6.11 merit comment:

- The outward and downward advection of cold ice is represented by the reversal in slope of the  $-20^\circ\text{C}$  and  $-25^\circ\text{C}$  isotherms ~900 km from the divide.
- The progressive compression of the isotherms near the bed downflow from the divide reflects the outward increase in basal temperature gradient as strain heating increases.

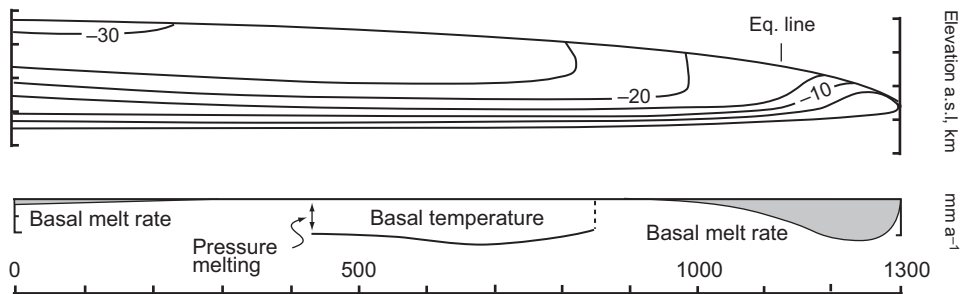


**Figure 6.11** Temperature distribution along a flowline calculated with the use of the Column model. The bed is at the pressure melting temperature except in the section labeled “Basal temperature.” (From Moran *et al.*, 1980, Figure 6. Reproduced with permission of the International Glaciological Society)

- Basal melting occurs over the first 250 km of the flowline because the accumulation rate here is low, so downward advection of cold ice is less important than it is further downglacier. A non-linear decrease in vertical velocity with depth (Equation 5.24) would lead to more melting here, while a higher accumulation rate would lead to less melting.
- Between ~250 and ~420 km from the divide, half of the meltwater formed in the first 250 km is refrozen to the base. This keeps the bed at the pressure melting temperature. The rest of the water was assumed to have drained away into the bedrock. Had it been assumed, instead, that more of the meltwater remained at the ice/bed interface, the zone of subfreezing temperatures between ~420 and ~840 km from the divide would be smaller or absent.
- The zone of subfreezing basal temperatures between ~420 and ~840 km owes its existence to increased downward advection of cold ice as the accumulation rate increases outward.
- Basal melting resumes downglacier from ~840 km as strain heating warms the basal ice. It becomes particularly important in the ablation area, where upward vertical velocities decrease the basal temperature gradient, thus trapping more heat at the bed.
- In the model, the basal frozen zone at the margin, barely visible at the scale of the figure, is a result of: (i) cold atmospheric temperatures at the margin; (ii) decreasing vertical velocity as the margin is approached; and (iii) the assumption that basal meltwater drains away as groundwater or in localized subglacial conduits. The vertical velocity decreases because, as the surface slope steepens, a greater fraction of the ablation rate is balanced by the  $u_s \tan \alpha$  term in the emergence velocity. In Nature, however, such frozen zones are more likely to occur as a result of ice advance over permafrost (Cutler *et al.*, 2000). Modeling suggests that such permafrost can persist for hundreds of years and extend tens of kilometers upglacier from the margin.

Even though the Column model is rudimentary in comparison with numerical models being used today, it does reproduce what are probably the essential features of the temperature distribution at the base of a continental-scale ice sheet with an ablation zone of significant width, namely: (1) melting beneath the divide if the accumulation rate is sufficiently low, and freezing otherwise; (2) in the former case, a zone of freeze-on in the lower part of the accumulation area followed by a possible zone in which the ice is frozen to the bed; (3) melting beneath the ablation area; and (4) a possible frozen toe in areas where marginal temperatures were relatively cold and permafrost likely present. The distribution of these zones depends on  $b_n$ ,  $\beta_G$ , and  $\theta_s$ . Temporal changes in  $b_n$  and  $\theta_s$  due to climate change will alter the basal temperature distribution, but, as discussed further below, there will be a lag of order  $10^3$  years between any change in climate and a response at the bed.

Transitions between zones are likely gradual. In a transition from a region of frozen bed to one of thawed bed, for example, hill tops and areas underlain by materials with lower thermal conductivity may remain frozen while intervening areas reach the pressure melting point (Figure 6.12), and conversely. Subtle topographic control of heat flow (Figure 6.13) reinforces this tendency by focusing geothermal heat away from higher areas into lower areas. In transitions from thawed to frozen bed, this keeps lower areas wet longer.

That water from melting basal ice flows downglacier along the bed and refreezes is consistent with observations of layers of dirty ice, several meters thick, that are encountered at the bottoms of core holes that reach the bed, like those at Byrd Station, Antarctica, and Camp Century, Greenland. The dirt is generally dispersed throughout the ice, and the dirty ice has fewer air bubbles than the overlying clean ice. In the Camp Century core, oxygen isotope ratios indicated that the basal dirty ice was formed from water that originally condensed at lower temperatures than the overlying ice. These observations are consistent with melting of ice that originally formed at a higher altitude than the overlying ice, downglacier flow of that water

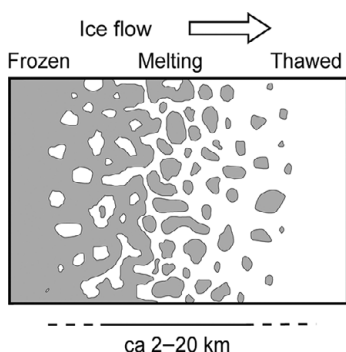


**Figure 6.12** Hypothetical distribution of frozen and thawed areas within a transition zone from a region of frozen bed to one of thawed bed. (Modified from Hughes, 1992, Figure 14)

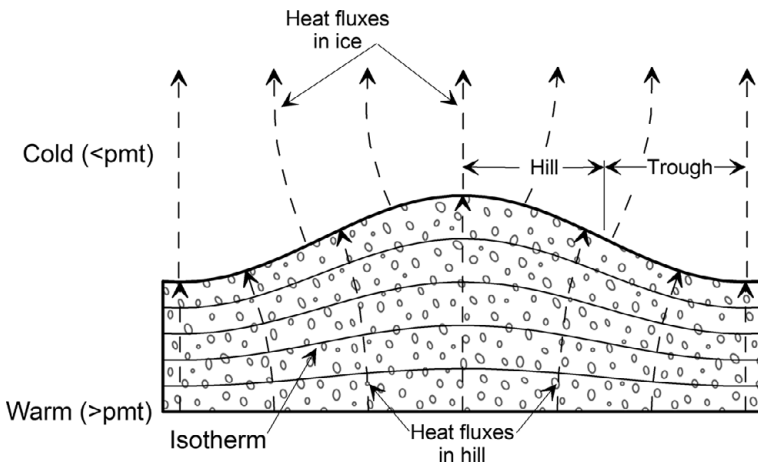


**Figure 6.13** Owing to topographic focusing, the heat flow in a "hill" in a glacier bed that is at the pressure melting temperature (pmt) is normal to isotherms and, thus, is toward lower parts of the bed and away from higher parts, resulting in more melting in low areas. (From Hooke and Medford, 2013, Figure 3. Reproduced with permission of Elsevier Science)

along the bed, and finally refreezing of the water, incorporating the dirt. It is difficult to account for meters-thick layers of basal ice with dispersed dirt in any other way, although regelation of ice downward into till is a possible way of entraining layers of dirt with higher debris content (Iverson, 1993).

If an ice sheet moves over an ore body in a zone in which water is refreezing to the base of the ice sheet, grains or clasts of the ore that become entrained are commonly surrounded by ice containing clasts only of the country rock (Figure 6.14b and c). When the ice finally melts and till is deposited, the ore particles form a "plume" encased in till composed only of country rock (Figure 6.14d). The ore-free till above the plume was entrained by freeze-on of basal water upglacier from the ore body, and that below the plume by freeze-on after ice had moved beyond the ore body (Figure 6.14c). Broadening of the plume down-flow occurred by diffusion. When ore clasts become exposed at the till surface, they can be traced up-flow on the surface and, with trenching or coring, still further up-flow at depth. Many valuable ore bodies have been found in this way over the past century, and even back to the mid-eighteenth century.

### Basal temperatures in Antarctica – comparison of solutions using the column model and a numerical model

The reliability and weaknesses of the Column model can be illustrated further by comparing basal temperatures in Antarctica calculated using it (Budd *et al.*, 1971)

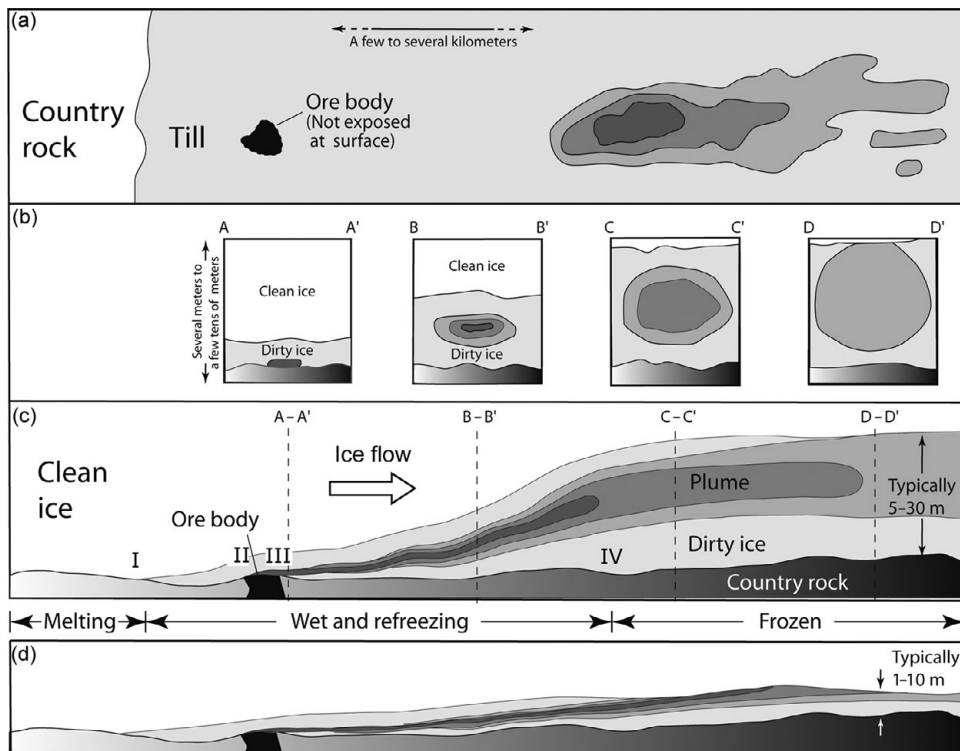


**Figure 6.14** Genesis of a 3-D plume. (a) Map view of the plume as exposed at the surface. b) Transverse cross sections through plume while still in ice. (c) Longitudinal section showing: (i) initiation of entrainment at I where water begins to refreeze to the glacier sole, (ii) initiation and end of dispersal train at II and III, respectively, and (iii) cessation of entrainment at IV where water supply is exhausted. (d) Plume after till is deposited; this geometry was obtained by compressing the geometry in (c) vertically and shearing it horizontally. Compare with (a) (modified from Miller 1984. Reproduced from Hooke *et al.* (2013), Figure 5, with permission of NRC Research Press)

with those calculated using a state-of-the-art numerical model (Huybrechts, 1990). First, however, it is instructive to discuss some general characteristics of the Antarctic ice sheet that affect the temperature distribution.

A digital elevation model (DEM) of the ice sheet is shown in Figure 6.15 (Liu *et al.*, 1999). By constructing this image with considerable vertical exaggeration, Liu *et al.* have emphasized intricate details of the surface topography, many of which would be difficult to discern were one standing on the surface of the ice sheet. Noteworthy is the apparent roughness of parts of the surface. This is caused by undulations with wavelengths of 4–10 km and amplitudes of only 5–10 m that result from flow over topography on the bed. Also of interest is the remarkably flat area labeled ‘Lake Vostok.’ As discussed previously (p. 106), this area is over a subglacial lake. With an area of 12,500 km<sup>2</sup>, and mean depth of 430 m, Lake

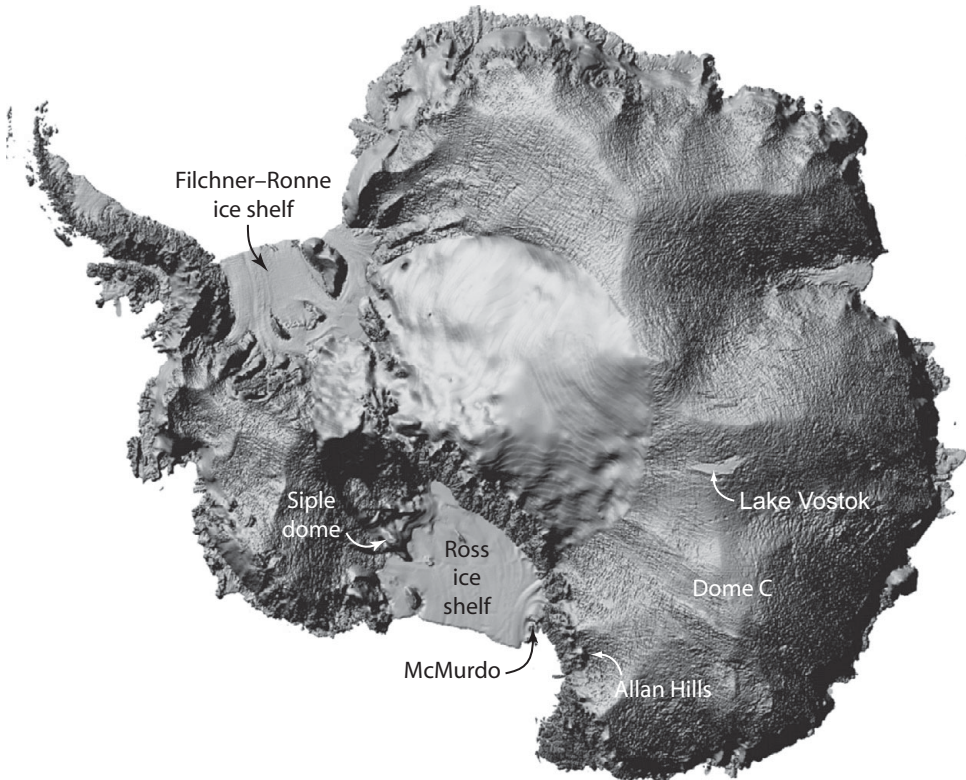


**Figure 6.15** Digital elevation model of Antarctica. (From Liu *et al.*, 1999. Courtesy of G. Hamilton)

Vostok is the largest of nearly 400 subglacial lakes that have been detected through radio-echo sounding.

The basal drag in Antarctica, calculated from the surface profile and ice thicknesses, is shown in Figure 6.16. In contrast to the situation on valley glaciers, where  $\tau_b$  is typically between 50 and 150 kPa (p. 90), the basal drag is below 80 kPa over most of Antarctica. Note also that  $\tau_b$  decreases inland. The low accumulation rates near the center of the ice sheet result in low balance velocities. Thus, the driving stresses required to provide those balance velocities are also low. Because both  $\tau_b$  and  $\bar{u}$  (Figure 5.2) increase toward the coast, the basal temperature gradient,  $\beta_o$ , also increases (Equation 6.34). The geothermal gradient,  $\beta_G$ , is estimated to be  $\sim 0.02 \text{ K m}^{-1}$  in East Antarctica, while, due to strain heating,  $\beta_o$  is nearly five times that near the coast.

Basal temperatures calculated with the use of the Column model and by Huybrechts (1990) are shown in Figure 6.17a and b, respectively. In both, one of the coldest spots is in central East Antarctica, over a mountain range where the ice is only 1.5–2 km thick. In nearby areas it is over 4 km thick. Both models also

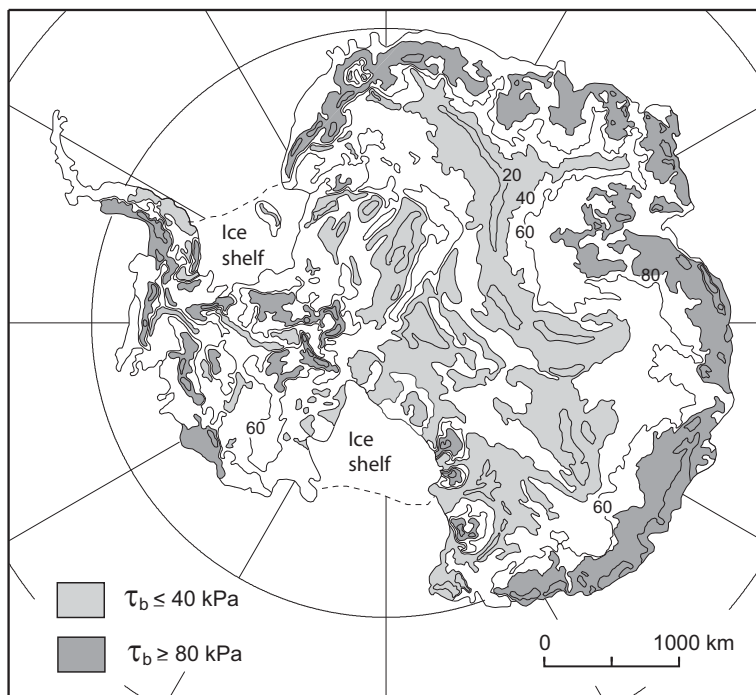
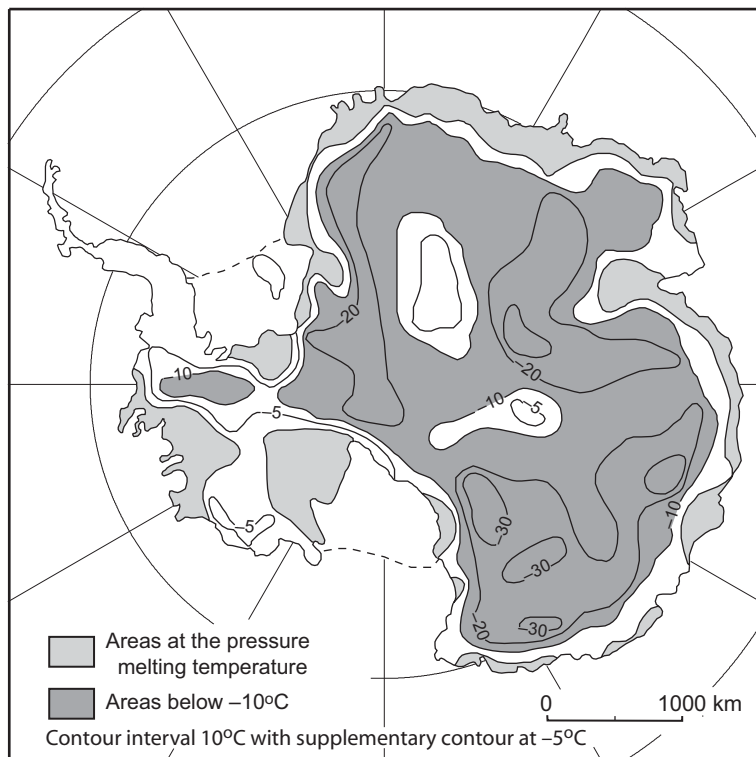


**Figure 6.16** Basal drag in Antarctica, calculated by Ph. Huybrechts, especially for this book, using the model described in Huybrechts (2002).

predict basal melting in the same areas in West Antarctica. However, there are important systematic differences between the maps. Most obvious is the large area of basal melting in East Antarctica in Huybrechts's map, in areas where the Column model predicts basal temperatures below  $-10^{\circ}\text{C}$ . This difference is, in part, because Huybrechts used an 8% higher geothermal flux, but this alone cannot account for so large a difference. Possible explanations for the remaining discrepancy are the use of an unrealistic linear decrease in  $w$  with depth in the Column model and the requirement in the Column model that the warming rate at depth equal that at the surface. As we have seen, the former can lead to basal temperatures that are too cold (Figure 6.6, Compare profiles for  $w = -0.50 \text{ m a}^{-1}$ ), and the latter can result in temperature gradients at the surface which are too high, thus also making deeper temperatures too cold. In contrast, Huybrechts's model predicts colder temperatures in Queen Maud Land. This appears to be because Budd *et al.* used balance velocities that were an order of magnitude higher than Huybrechts in this sector, thus overemphasizing strain heating. The differences between these modeled basal temperature distributions emphasize the need for caution in using the Column model, and also for accurate accumulation, ice thickness, and surface temperatures in both models.

(a)



(b)

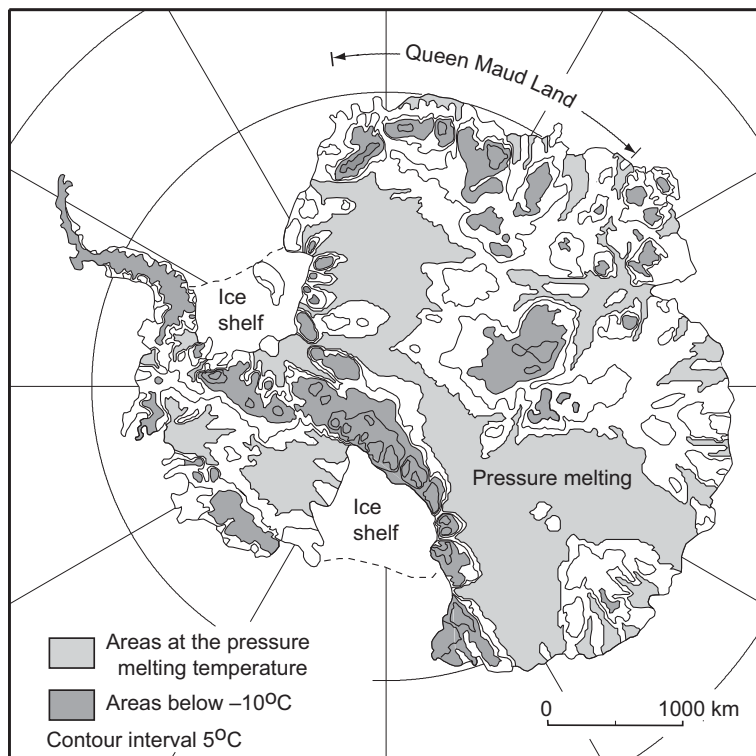


**Figure 6.17** Basal temperatures,  $^{\circ}\text{C}$ , from: (a) the Column model and (b) calculated by Ph. Huybrechts, especially for this book, using the model described in Huybrechts (2002). ((a) Modified from Budd *et al.*, 1971. Reproduced with permission of the Australian Antarctic Division)

## Climate change

When we think of climate change, changes in temperature are likely to be uppermost in our minds, and that is our concern in this discussion. However, it is well to keep in mind that changes in precipitation, wind speed and direction, and humidity are also components of climate change.

A change in mean annual temperature affects the boundary condition at the surface of an ice sheet. When such a change occurs, temperatures at depth are no longer in equilibrium with the climate and flow field. It is clear from Equations (6.25) and (6.37) that if  $\theta_s$  increases, the steady-state temperature throughout the ice sheet must increase by the same amount, and conversely. However, it takes time for a warming or cooling at the surface to affect the temperature of the deeper ice. Figure 6.8 shows, for example that a  $7.5^{\circ}\text{C}$  warming between May and June had a negligible effect on the temperature at a depth of 4 m.

A “permanent” change in temperature, like that which took place at the end of the Pleistocene, takes thousands of years to begin to affect the temperature at the bed of a thick ice sheet, and even longer to begin to re-establish something resembling a steady-state (Figure 6.18). Theoretically, the time to reestablish a steady-state is infinite, and the steady state is approached asymptotically because the temperature must also change in the underlying bedrock (Figure 6.18). Thus, an ice sheet has a very long memory. State-of-the-art models involving energy balance, ice flow, and oxygen isotope records can be used to simulate temperature profiles measured in deep boreholes, and from them extract information on climate change over centuries or millennia. With the use of such a model, Cuffey and Clow (1997) estimated that the mean temperature during the last glacial at the top of the Greenland Ice sheet was  $\sim 15^{\circ}\text{C}$  colder than at present, but there are many variables in the calculation that are not well constrained such as changes in  $b_n$ , the amount of isostatic uplift and its effect, and the amount of thinning due to retreat of the ice sheet margin.

## Geomorphic implications

The basal temperature distribution (Figure 6.11) has implications for glacial erosion and deposition and the origin of some glacial landforms. Erosion rates are likely to be highest where meltwater is refreezing to the glacier sole. Thus, we might expect to find that erosion was most intense some distance from the divide. Conversely, the formation of lodgment till by subglacial melting should be most prevalent beneath the ablation zone where melt rates are high. Both are consistent with observation.

In regions where mean annual temperatures are sufficiently low, marginal zones of frozen bed are likely, owing either to ice advance over permafrost or to loss of heat

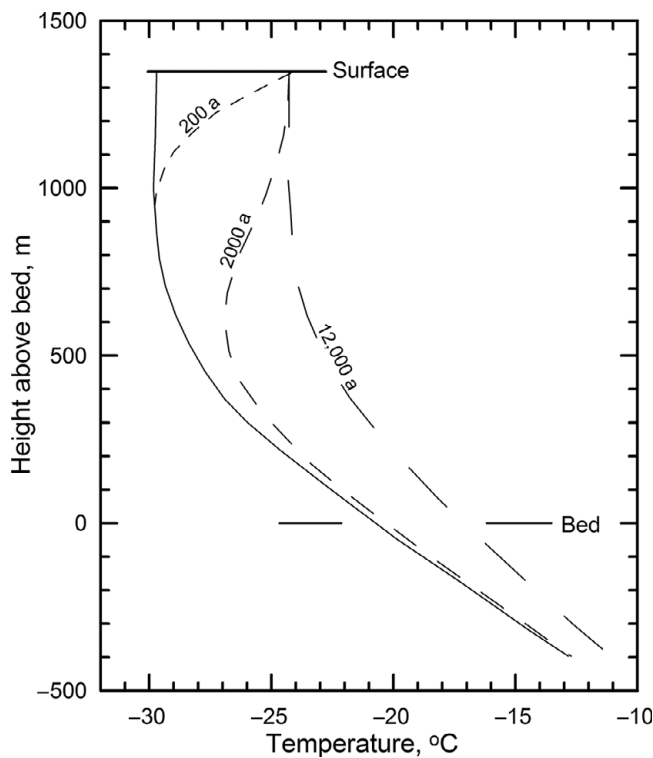


**Figure 6.18** Changes in a temperature profile through time after a  $5^{\circ}\text{C}$  increase in temperature at the surface, calculated with a time-dependent numerical model. Initial profiles based on Equation (6.25). Ice sheet thickness, vertical velocity at surface, and geothermal gradient are similar to those at Camp Century, Greenland. (Modified from Hooke *et al.*, 1980, Figure 6. Reproduced with permission of the Canadian Journal of Earth Sciences)

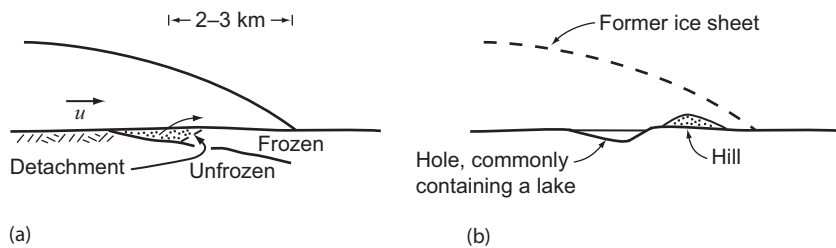


**Figure 6.19** Formation of a hill-hole pair by thrusting at a frozen margin.

through the surface of the down-flow thinning ice sheet. Such a zone, 2–3 km wide, seems to have been present in North Dakota and adjacent areas of Alberta and Saskatchewan during the Late Glacial Maximum. Here, blocks of bedrock, tens to hundreds of meters on a side, became frozen to the base of the glacier and were moved outward a kilometer or so (Figure 6.19). Detachment may have been facilitated by high pore water pressures in the unfrozen rock beneath the frozen zone. Upon

deposition, these blocks formed hills. When the ice eventually receded, the basins from which the blocks were plucked commonly became lakes (Moran *et al.*, 1980). Other megablocks of unconsolidated pre-Pleistocene strata, up to  $10 \text{ km}^2$  in area and 20 m thick, are found in western Canada and along the southern margin of the Weichselian Ice Sheet in Europe (Aber and Ber, 2007, pp. 101–110). These are presumed to have been entrained and transported in a similar manner. The nearest known sources for one in Alberta and another in Poland are more than 300 km away.

In some places, subglacial frozen bed conditions persisted throughout the last glacial period. The best studied such areas are in western Sweden, in the divide region of the Weichselian ice sheet. These cold zones were probably a consequence of a combination of high accumulation rates, cold temperatures, and thin ice in the topographically high divide region. Relict periglacial landforms like patterned ground (Kleman and Borgström, 1994) and weathering features such as tors (Kleman and Hättestrand, 1999) are found in these areas. These features developed under ice-free conditions during the last interstadial. At the edges of these zones of relict landscape, where the bed was transitioning from frozen to thawed (Figure 6.12), higher areas remained frozen while lower ones were at the pressure melting point. Kleman and Borgström (1994) have described a distinctive set of landforms in such situations (Figure 6.20). Up- and

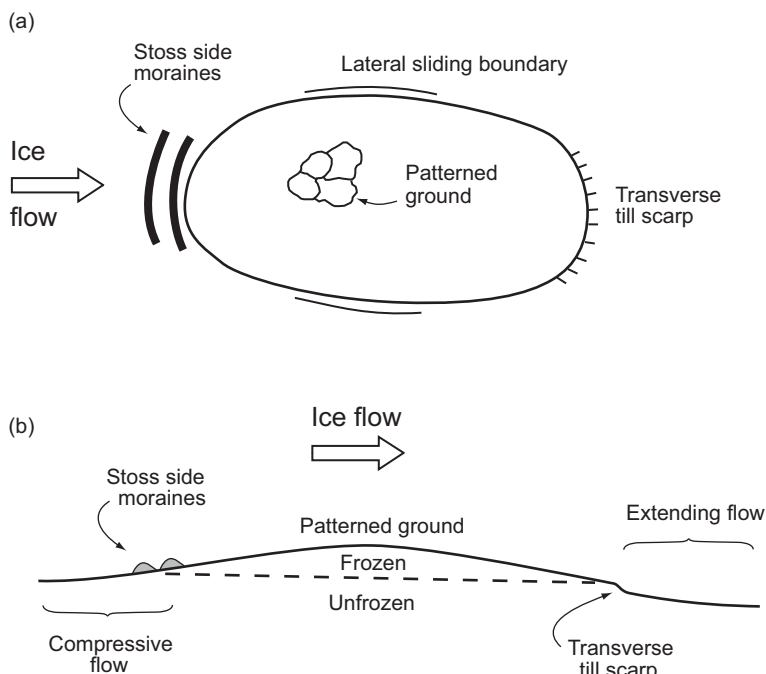


**Figure 6.20** Schematic map (a) and cross section (b) through a low hill that remained frozen throughout a glacial advance and on which periglacial landforms are thus preserved. Stoss side moraines were formed in the zone of compressive ice flow on the stoss side of hill, and transverse till scarps were formed on the lee side.

downglacier from the higher areas the ice was sliding, whereas it remained frozen to the substrate over the higher ground. This led to longitudinal compression on the stoss side of the high, and longitudinal extension in its lee. Till dragged by the ice became stacked in transverse moraines on the stoss side, while on the lee side it was pulled away, forming an abrupt scarp. Along the lateral boundaries, there is a narrow transition separating the relict surface from areas of glacially modified topography.

Ribbed moraines are another distinctive landform. They consist of rather evenly-spaced anastomosing, somewhat sinuous ridges (Figure 6.21a), a couple of tens of meters high, a few tens of meters in width, and a few hundred meters apart, oriented transverse to the direction of ice flow (Dunlop and Clark, 2006). They are generally believed to have developed subglacially. They commonly occur in fields that are elongated in the direction of ice flow.

One form of ribbed moraine, found in Sweden, occurs around the edges of areas where frozen bed conditions either persisted throughout a glaciation or perhaps developed during deglaciation (Hättestrand and Kleman, 1999). The ridges there

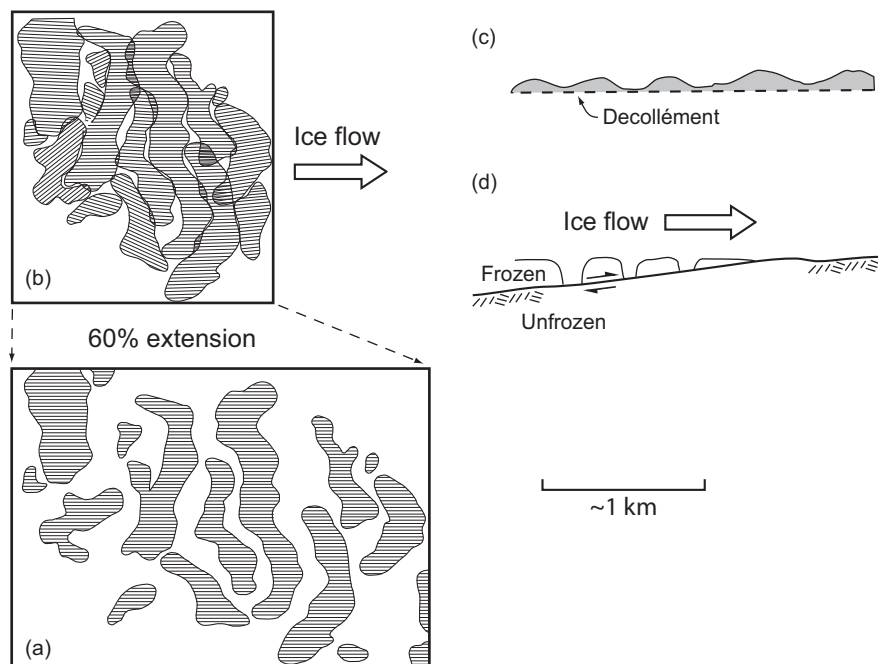


**Figure 6.21** Formation of ribbed moraine. (a) Map of ribbed moraine ridges near Lake Rogen in west-central Sweden. The line pattern on the ridges shows the direction of faint fluting. (b) Inferred original relative positions of ridges. Areas of overlap are attributed to streamlining after the ridges were pulled apart. (c) Schematic cross section through a series of ridges showing thickness of material above décollement. (d) Schematic diagram showing how a layer of frozen soil overlying thawed material could be pulled apart by extensional flow in the ice. (a and b from Hättestrand and Kleman, 1999. Reproduced with permission of the authors and Elsevier Science)

typically consist of glacial drift similar to that in adjacent areas without ridges. The drift is usually till, but may be glaciofluvial sediment or a combination of the two. In troughs between ridges, seismic investigations and limited exposures suggest that the drift sheet is thin or missing (Figure 6.21c). If one could decouple the ridges from the substrate and slide them together, they would fit remarkably well (Figure 6.21b). These characteristics suggest that the ridges were formed by pull-apart of a once continuous drift sheet at the boundary between zones of thawed and frozen bed (Figure 6.21d). Hättestrand and Kleman have argued convincingly that this is the case. They have shown that in Sweden, this type of ribbed moraine is confined almost exclusively to core areas of the late Pleistocene ice sheet. They find that the ridges are transverse to ice flow directions during deglaciation and not to flow directions during the Late Glacial Maximum, suggesting that they formed during deglaciation.

In many areas of ribbed moraine, the ridges do not fit together as well as those in Figure 6.21b, and the areas cannot be clearly associated with frozen bed conditions. Indeed, Stokes *et al.* (2008) have described ribbed moraine superimposed on mega-scale glacial lineations in the bed of a paleo ice stream. Thus, it seems clear that other mechanisms of formation were involved (Dunlop and Clark, 2006), and that the name should be considered descriptive, not genetic.

As our understanding of the origin and distribution of features such as hill-hole pairs, relict surfaces, and ribbed moraine improves, they will become increasing valuable in constraining numerical models of Pleistocene ice sheets. Some modeling studies have already used the distribution of these features for this purpose (e.g. Moran *et al.*, 1980; Fastook and Holmlund, 1994), but much remains to be done.

---

## SUMMARY

We began this chapter by deriving the energy balance equation. Given boundary conditions appropriate for a polar ice sheet, solutions to this equation yield the temperature distribution in the ice sheet. The boundary conditions most commonly used are: (1) the temperature at the surface (a Dirichlet condition), which is approximated by the mean annual temperature, perhaps with a correction for heating by percolating melt water; and (2) the temperature gradient in the ice at the bed (a Neumann condition). The latter is based on estimates of the geothermal flux. If calculations suggest that the bed is at the pressure melting point, the temperature gradient is adjusted to ensure that calculated basal temperatures do not exceed the melting point, thus effectively changing to a Dirichlet condition.

Using appropriate simplifications, we studied solutions to the energy balance equation for an ice divide, for seasonal variations in near-surface temperature, and

for a column of ice extending through an ice sheet some distance from the divide. Two key assumptions in the latter, the so-called Column model, are that  $w$  decreases linearly with depth and that longitudinal advection can be approximated by assuming a warming rate at depth that equals that at the surface. Both lead to basal temperatures that are too cold. With suitable caution, however, the Column model is useful for illustrating the various physical processes that affect the temperature distribution along a flowline of an ice sheet. Numerical models are able to incorporate more variables than are the analytical solutions we studied, and can be used to extract estimates of temporal changes in surface temperature and ice sheet thickness from measured temperature profiles.

Finally, we discussed some geomorphic features formed at boundaries between zones of thawed and frozen bed, and noted that these could be used to constrain numerical models of ice sheets.

# 7

## The coupling between a glacier and its bed

In Chapter 4 we saw that reasonable profiles of internal deformation could be calculated with the use of Glen's flow law:  $\dot{\varepsilon}_e = A\sigma_e^n$ . This is, in large part, because ice is a crystalline solid with relatively uniform properties. The principle causes of inaccuracy in such calculations are a consequence of impurities in the ice (including water), of anisotropy associated with the development of preferred crystal orientations, and of incomplete knowledge of the stress and temperature.

When the basal temperature is at the pressure melting point, glaciers also move readily over their beds (Figure 5.5). However, the rate at which this movement occurs is far more difficult to analyze. This is, in part, because the boundary conditions, principally the water pressure and the morphology of the bed, are not known. However, a more fundamental problem is the fact that granular rock debris is usually present, either between the ice and the bed or in the ice, or both. The processes involved in the deformation of these materials are reasonably well understood qualitatively, but a well-founded constitutive relation remains elusive. Furthermore, unlike the situation with pure ice, the properties and concentration of the rock debris vary, not only from glacier to glacier, but also from point to point beneath a single glacier. Although it may be impossible to know the rheology of this material and the boundary conditions well enough to accurately predict the rate of movement of a glacier over its bed, it is nevertheless important to understand the processes.

We'll start this discussion by looking at the movement of clean ice over an irregular hard bed – the traditional sliding problem – and then noting some of the principal shortcomings of this analysis. Finally, we'll study deformation of the granular materials over which many glaciers move. This inquiry has led to relations between the rate of movement and measurable quantities such as water pressure and driving stress that can be tested with field data. It has also led to better understanding of certain glacial landforms.

### Sliding

The basic processes by which ice moves past an obstacle on a rigid bed, regelation and plastic flow, were first discussed by Deeley and Parr (1914) and later quantified by

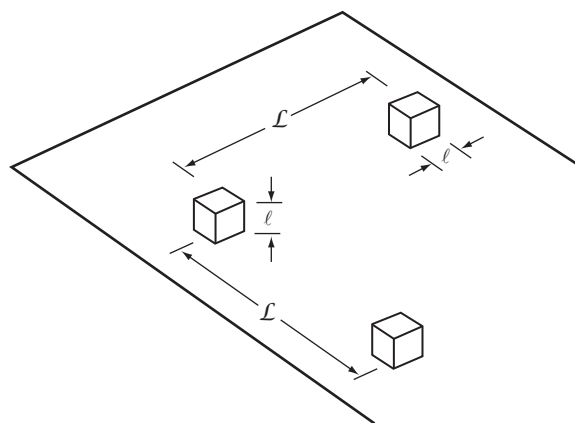


Figure 7.1 Bed geometry used in Weertman's (1964) analysis of basal sliding.

Weertman (1957a, 1964). *Regelation* involves melting of ice in the region of high pressure on the upglacier or stoss side of an obstacle and refreezing of that water in the region of lower pressure on its lee face. *Plastic flow* is simply deformation of ice in a three-dimensional flow field around the obstacle. In his analysis, Weertman used a simplified model of the bed geometry, sometimes called the tombstone model, consisting of uniformly-spaced rectangular blocks on a flat surface (Figure 7.1). This model has been roundly criticized as being unrealistic, and inappropriately defended by arguing that fudge factors can be inserted to make it applicable to real situations. The real value of the model is that the physical principles involved in the sliding process are illustrated without resorting to advanced mathematics.

Consider a bed consisting of a plane on which there is a regular array of cubical obstacles with sides of length,  $\ell$ , and mean spacing,  $L$  (Figure 7.1). We define the roughness of the bed,  $r$ , as  $\ell/L$ . The mean drag is  $\tau_b$ . The ice is at the pressure melting point, and is separated from the bed by a thin water film, so we assume that faces parallel to the flow cannot support a shear stress. Thus, the drag over an area  $L^2$  must be supported by a single obstacle. The total force on the obstacle is then  $F = \tau_b L^2$ , so the stress or pressure difference across the obstacle,  $\Delta P$ , is:

$$\Delta P = \sigma_{\text{stoss}} - \sigma_{\text{lee}} = \frac{\tau_b L^2}{\ell^2} = \frac{\tau_b}{r^2} \quad (7.1)$$

where the subscripts refer to stoss and lee sides of the obstacle, respectively, and  $\ell^2$  is the cross sectional area of the obstacle. It is important to recognize that  $\tau_b$  is a resisting stress, and, although it must equal the driving stress,  $\tau_d = S_f \rho g d \alpha$  (e.g. Equation 5.15), the two are products of different physical factors.

### Regelation

Let's deal with regelation first. The average temperature at the bed is constrained to be at the pressure melting point, which is determined by the average pressure in the

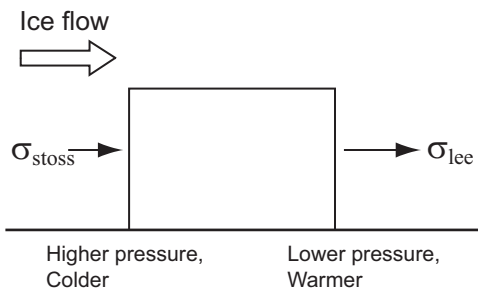


**Figure 7.2** Pressure and temperature on stoss and lee sides of a rectangular obstacle on a glacier bed.

water layer. The average pressure is a function of the local glacier thickness. The pressure in the water film on the stoss face of the obstacle is higher than the average, and the pressure on the lee face is lower (Figure 7.2). The pressure difference across the obstacle,  $\Delta P$ , results in a temperature difference,  $\Delta T = \mathbf{C} \Delta P$ , where  $\mathbf{C}$  is the change in melting temperature with pressure (Equation 2.2).

The temperature difference across the obstacle is thus (using Equation (7.1)):

$$\Delta T = \mathbf{C} \frac{\tau_b}{r^2} \quad (7.2)$$

and the temperature gradient through it is  $\Delta T/\ell$ . The heat flow through the obstacle,  $Q_h$ , is thus:

$$Q_h = \frac{\Delta T}{\ell} K_r \ell^2 = \Delta T K_r \ell \quad (7.3)$$

where  $K_r$  is the thermal conductivity of rock.  $K_r$  has the dimensions  $J \text{ m}^{-2} \text{ a}^{-1} (\text{K}/\text{m})^{-1}$ , or  $J \text{ m}^{-1} \text{ a}^{-1} \text{ K}^{-1}$ , so  $Q_h$  has the dimensions  $J \text{ a}^{-1}$ . A typical value of  $K_r$  for rock or ice near the pressure melting point is  $7.1 \times 10^7$ .

This heat flow can melt ice at a rate,  $Q_h/H\rho$ , where  $H$  is the heat of fusion,  $3.34 \times 10^5 \text{ J kg}^{-1}$ , and  $\rho$  is the density of ice,  $\sim 900 \text{ kg m}^{-3}$ . Thus, the melt rate is expressed in  $\text{m}^3 \text{ a}^{-1}$ . Dividing this rate by the cross sectional area of the obstacle,  $\ell^2$ , gives the speed with which ice can move past the obstacle by regelation,  $u_{br}$ . Thus, using Equations (7.2) and (7.3):

$$u_{br} = \frac{Q_h}{\ell^2 H \rho} = \frac{\mathbf{C} \tau_b K_r}{\ell H \rho r^2}. \quad (7.4)$$

In reality, some heat also flows from the low pressure region to the high pressure region through the ice above the obstacle and through the rock beneath it, so this relation somewhat underestimates  $u_{br}$ .

The water formed by melting in the high pressure area on the stoss side of the obstacle flows either upglacier or downglacier to areas of lower pressure. The area of low pressure in the lee of the obstacle we've been analyzing is one such sink. Because the temperature gradient conducts heat back through the obstacle, away from this area, this water refreezes. Thus, to complete the regelation cycle, the water

flux to the lee of the obstacle must equal the melt on the stoss side. We'll examine the consequences of a failure of this condition later, and consider plastic flow next.

### Plastic flow

Owing to the enhanced stresses on an obstacle, plastic flow (or creep) of ice past the obstacle is intensified. Weertman (1957a) thus assumed that the speed with which ice creeps past the obstacle,  $u_{bp}$ , was proportional to  $\ell$  and to the creep rate obtained by using the stress difference from Equation (7.1) in the flow law:

$$u_{bp} = b\dot{\varepsilon}\ell = bA \left( \frac{\tau_b}{r^2} \right)^n \ell \quad (7.5)$$

where  $b$  is a dimensionless constant of proportionality. Note that dimensionally  $\dot{\varepsilon}\ell$  is a speed.

### Sliding speed

Comparing Equations (7.4) and (7.5), you will note that as  $\ell$  increases,  $u_{br}$  decreases but  $u_{bp}$  increases (Figure 7.3);  $u_{br}$  decreases because the path that heat follows back through the obstacle increases with  $\ell$ , so the temperature gradient decreases, thus decreasing the heat flow. The reasons for the increase in  $u_{bp}$  are less obvious; dimensionally, it results from the fact that, to obtain a speed from a strain rate, one must multiply by a length scale, and the obvious length scale in the present situation is  $\ell$ . Physically, a larger obstacle blocks the path of more ice, so for this ice to get past the obstacle, one might expect the boundary layer (the zone of increased flow adjacent to the obstacle) to expand and the flow speed in it, increase. Both should scale (the factor  $b$ ) with the size of the obstacle.

The total sliding speed,  $u_b$ , is generally considered to be the sum of the contributions from regelation and plastic flow (Figure 7.3), so combining the physical constants by letting  $\Omega_r = CK_r/H\rho$  and  $\Omega_p = bA$ , we have:

$$u_b = u_{br} + u_{bp} = \Omega_r \frac{\tau_b}{\ell r^2} + \Omega_p \left( \frac{\tau_b}{r^2} \right)^n \ell. \quad (7.6)$$

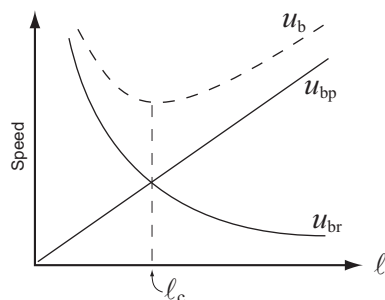


**Figure 7.3** Relation between obstacle size and sliding speed due to regelation,  $u_{br}$ , and to plastic flow,  $u_{bp}$ . The resulting sliding speed of the glacier,  $u_b$ , the sum of  $u_{br}$  and  $u_{bp}$ , is a minimum at  $\ell = \ell_c$ , implying that for any given roughness, obstacles of this size exert the maximum drag on the glacier.

We, also, will consider the contributions to be additive, but note that Nye (1969a, pp. 455–456) finds that this is not strictly correct because on real beds, consisting of roughness elements of many different sizes, the pressure distribution driving regelation is not the same as that driving plastic deformation. Remember, too, that  $u_b$  is determined by  $\tau_d$ , so  $u_b$  is the independent variable in Equation (7.6), and  $\tau_b$  is dependent.

Let's seek the obstacle size,  $\ell_c$ , for which  $u_b$  is a minimum (Figure 7.3). To do this we take the derivative of  $u_b$  with respect to  $\ell$ , thus:

$$\frac{du_b}{d\ell} = -\Omega_r \frac{\tau_b}{\ell^2 r^2} + \Omega_p \left( \frac{\tau_b}{r^2} \right)^n \quad (7.7)$$

set the result to 0, and solve for  $\ell_c$ :

$$\ell_c = \sqrt{\frac{\Omega_r}{\Omega_p}} \left( \frac{\tau_b}{r^2} \right)^{\frac{1-n}{2}}. \quad (7.8)$$

Inserting this back into the expressions for  $u_{br}$  and  $u_{bp}$  (Equations 7.4 and 7.5) yields:

$$u_{br} = \sqrt{\Omega_r \Omega_p} \left( \frac{\tau_b}{r^2} \right)^{\frac{n+1}{2}} \quad \text{and} \quad u_{bp} = \sqrt{\Omega_r \Omega_p} \left( \frac{\tau_b}{r^2} \right)^{\frac{n+1}{2}}, \quad (7.9)$$

respectively. Thus, when  $u_b$  is a minimum,  $u_{br} = u_{bp}$  and  $u_b = 2u_{br} = 2u_{bp}$ .

Low sliding speeds imply high drag, and conversely. Thus, although drag is exerted on the glacier by obstacles of all sizes, those of size  $\ell_c$  appear to have a disproportionate effect, exerting more drag on the base of the glacier than do obstacles of any other discrete size. Accordingly,  $\ell_c$  has come to be called the *controlling obstacle size*. As implied by  $u_{br} = u_{bp}$ , regelation and plastic flow contribute equally to motion of ice past roughness elements of this size.

When one considers a bed composed of a continuous spectrum of obstacles sizes, and particularly of roughnesses, the concept of a controlling size is no longer as relevant (Nye, 1969a, p. 459). Nevertheless, an obstacle size for which  $u_{br} = u_{bp}$  normally appears when bed geometry is simplified in order to make theoretical studies of sliding mathematically tractable. The name *controlling obstacle size* for this size is probably irrevocably ingrained in the literature.

For beds on which  $r$  is constant, we can add the relations in Equations (7.9), assume that  $n=3$ , set  $\tau_b = \tau_d$ , and combine the constant factors into a single constant,  $\Omega = \sqrt{\Omega_r \Omega_p}$ , to yield:

$$u_b = \Omega \frac{\tau_d^2}{r^4}. \quad (7.10)$$

Of particular interest is the quadratic dependence of  $u_b$  on  $\tau_d$ , and the strong inverse dependence on  $r$ .

With the use of elegant mathematical techniques that are beyond the scope of this book, Nye (1969a) and Kamb (1970) analyzed sliding of glaciers by regelation and plastic flow over a realistic bed consisting of superimposed sine waves. To obtain exact solutions, both Nye and Kamb had to assume a linear rheology ( $n = 1$ ) for ice. Kamb also obtained an approximate solution for a non-linear rheology. Both Kamb and Nye concluded that  $u_b \propto \tau_d/r^2$  in the linear theory. This is consistent with our Equations (7.9) with  $n = 1$ . In Kamb's nonlinear theory, the relation between  $\tau_b$  and  $\ell_c$  (Equation 7.8) also leads to  $u_b \propto \tau_d^2$ , at least for certain roughness spectra. The dependence of  $u_b$  on  $r$  in Kamb's nonlinear theory is more complicated, owing to the way in which roughness is defined. Let us now examine this in more detail.

### Roughness in the Nye-Kamb theory

In the Nye-Kamb theory the bed topography is modeled as superimposed sine waves, and the roughness,  $\varsigma$ , is defined as  $a/\lambda$ , where  $a$  and  $\lambda$  are the amplitude and length of a sine wave (Figure 7.4). Thus,  $\varsigma$  is a measure of steepness of the adverse slope that the bumps present to the glacier. The sliding speed,  $u_b$ , is considered to be inversely proportional to the square of the bed slope opposing the flow. As before, we can define a controlling wavelength,  $\lambda_c$ , for which  $u_{br} = u_{bp}$ .

When  $\varsigma$  is constant for all wavelengths, the spectrum is called *white*. This is one of the spectra for which  $u_b \propto \tau_d^2$  in Kamb's nonlinear theory. From casual observations of glacier beds, however, it is quickly clear that  $\varsigma$  is not constant; there is commonly, though not always (Benoist, 1979), a distinct absence of short wavelengths. In his field studies, Kamb found almost no obstacles with wavelengths less than 0.5 m in the direction of flow. He further observed that  $\varsigma$  was commonly  $\sim 0.05$ .

The frequent absence of short wavelengths is usually attributed to preferential abrasion of these features by regelating ice. As noted, regelation is most effective over small obstacles. During regelation, rock particles entrained in the basal ice and projecting down into the regelation layer are forced into strong contact with any obstacle upon the stoss side of which this ice melts. Thus, small obstacles are abraded away, while larger ones, accommodated principally by plastic flow, are not.

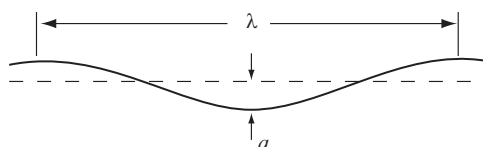


**Figure 7.4** Wavelength and amplitude of a sinusoidal wave on a glacier bed.

## Tests of sliding theories

The only sliding theory that can be reasonably tested with field data is Kamb's approximate nonlinear one. The sliding speed and other data used for the test were collected on Blue and Athabasca glaciers, using boreholes to the bed and tunnels along the bed. Because the area of the bed thus exposed was not large enough to permit direct measurement of the roughness, Kamb calculated  $\zeta$  and  $\lambda_c$  from the measured sliding speeds and known glacier geometry (Table 7.1). When he used a full white roughness spectrum in his calculations, the values of  $\zeta$  were about one-third those in the table. Thus, in accordance with his observations, he assumed that obstacles with short wavelengths had been abraded away, and he replaced the full white roughness spectrum with a truncated spectrum which did not have obstacles with those wavelengths. This yielded values of  $\zeta$  (Table 7.1) that are consistent with observations on exposed bedrock outcrops, thus providing support for the theory. In the absence of these shorter wavelengths, however, and with  $\tau_b \approx \tau_d$ ,  $u_b \propto \tau_d^3$  (Equation 7.5) instead of  $\tau_d^2$ .

Another test of the theory comes from observations of the thickness of the regelation layer at the base of a glacier. Regelation ice can be distinguished from more highly deformed ice by grain size and crystal orientation. Using thin sections of the ice, Kamb and LaChapelle (1964) measured thicknesses of the regelation layer in ice tunnels beneath Blue Glacier. They judged the average thickness to be about 5 mm, while the maximum was 29 mm. These values can be compared with those calculated from Kamb's theory. The calculation is based on the fact that the thickness of the regelation layer in a depression in the lee of a bump is proportional

**Table 7.1** Measured sliding speeds and corresponding calculated roughnesses and controlling wavelengths (from Kamb, 1970)

Location	Measured $u_b$ , m a <sup>-1</sup>	Calculated $\zeta$	Calculated $\lambda_c$ , m
Blue Glacier			
Borehole K	22	0.05	0.32–0.45
Borehole V	4	0.09	0.47–0.67
Western ice fall	6	0.02–0.04	0.62–1.12
Central ice fall			
On ridge	128	0.03	0.15–0.28
In trough	4	0.13	0.37–0.53
Athabasca Glacier			
Hole 1B	41	0.02	0.50–0.70
Hole 1A	42	0.02	0.33–0.47
Hole 209	3	0.06	0.59–0.84
Means		0.054	0.53

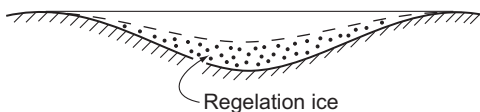


**Figure 7.5** In the lee of a bump of the controlling size, regelation ice should fill the lower half of the space between bumps.

to the degree to which the bump was accommodated by regelation. Thus, for obstacles of the controlling size, accommodated half by regelation and half by plastic flow, regelation ice should half fill the depression between bumps (Figure 7.5). The predicted thicknesses were 1–10 mm. The fact that observed thicknesses were greater than this suggests that regelation may be more important than predicted by the theory.

### Weaknesses of present sliding theory

There are a number of processes involved in sliding of ice over a hard bed that are not adequately described in the above theoretical models. An obvious example is the failure to consider frictional forces between rock particles in the basal ice and the underlying bedrock. To study this effect, Iverson *et al.* (2003) conducted an experiment at the Svartisen Subglacial Laboratory in Norway. The laboratory is situated in a tunnel system in the bedrock beneath Engabreen (Norwegian for *the Enga glacier*), an outlet glacier from the Svartisen ice cap. The tunnels were excavated for a hydroelectric power project. One inclined tunnel, excavated specifically for scientific studies, leads upward to the base of the glacier, giving access to the bed beneath 210 m of sliding temperate ice. Using this inclined tunnel, Iverson and his colleagues placed an instrumented panel at the base of the glacier. The upper surface of the panel consisted of a  $0.3 \times 0.3$  m smooth granite tablet. Debris-laden ice slid across the tablet, and the shear traction on it was recorded along with the sliding speed, water pressure, and temperature in the panel. Shear tractions on the tablet varied from 60 to 110 kPa, and at one point rose to 200 kPa. The spatially averaged driving stress is estimated to be between 150 and 300 kPa, so the measured shear tractions on the tablet were a significant fraction of the total drag. As the tablet was smooth and mounted flush with the fixed edges of the panel, shear tractions on it would presumably have been negligible if the ice had been free of sediment.

“Frictional” drag may also occur in areas where ice becomes temporarily frozen to the bed. Robin (1976) proposed two mechanisms for forming such *cold patches*. In the first, which he dubbed the “heat pump effect” (Figure 7.6a), melting occurs in ice just above the bed, in the zone of high pressure on the stoss side of a bump. This melting requires heat. The heat source is the surrounding ice, which is thus cooled to the local pressure melting point. The resulting water may be squeezed out of the ice through veins formed where three ice crystals abut one another (see Figure 8.1b). When the resulting “cold” ice is transported to the top of the bump, where the

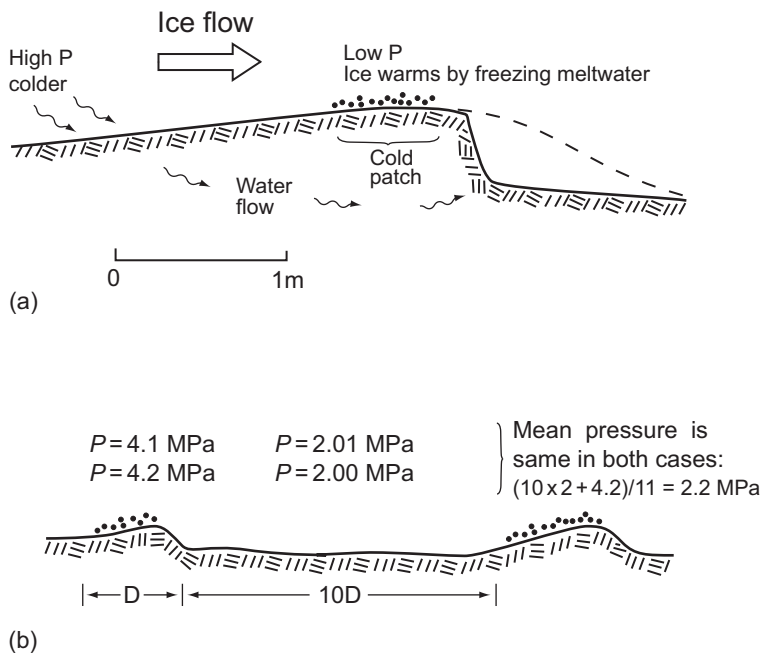


**Figure 7.6** Formation of cold patches (after Robin, 1976). (a) Water that is squeezed out of the ice on the stoss side of an obstacle may drain away and, thus, not be available to refreeze in the low pressure zone at the top of the obstacle. (b) Small changes in pressure between obstacles result in large changes on tops of obstacles.

pressure is less, any water remaining in the ice and along the ice–rock interface is refrozen, releasing the heat of fusion and thus warming the ice to the new pressure melting temperature. The water within the ice likely freezes first, followed by that at the interface. If the amount of water present is sufficient, enough heat will be released to warm the ice to the local pressure melting point without freezing all of the water at the interface. However, if some of the melt water has escaped around the bump, as shown in Figure 7.6a, *all* of the water at the interface may freeze, thus bonding the glacier to the bed.

The second mechanism discussed by Robin involves local increases in water pressure in areas between bumps. Because the weight of the glacier is constant, any such increase will decrease the pressure on the stoss sides of bumps, where the pressure is already higher than average. In the example shown in Figure 7.6b, the area between bumps is 10 times the area of the bumps. Thus, a 0.01 MPa increase in pressure between bumps reduces the pressure over the bumps by 0.1 MPa, resulting in a  $\sim 0.07^\circ\text{C}$  (Equation 2.2) increase in the pressure melting temperature. As the ice over the bumps was at the pressure melting temperature before the pressure change, it had to warm when the pressure decreased, and the heat required to warm it came from freezing of any water present, potentially including any at the ice–rock interface.

In addition to increasing the drag between the glacier and the bed, such cold patches may be an effective erosional mechanism. Rock fragments that have been loosened from the bed but do not project appreciably above it are separated from the ice by a melt film. As long as the melt film exists, they may be held in the bed by rock-to-rock frictional forces that exceed the drag exerted by the ice through the film. However, such fragments may be entrained if the melt film becomes frozen.

There are also a number of problems surrounding the use of the simple regelation theory presented above. Nye (1973a) notes, for example, that at any point on an obstacle, the melt rate (or freezing rate) required for movement of ice past that obstacle by regelation is completely determined by the geometry of the obstacle, and in particular by the inclination of the face relative to the direction of motion. The melt rate determines the heat sources and sinks, so the temperature distribution is known, and hence also the pressure distribution. The melting and freezing rates also determine the water fluxes required. The awkward fact is that, for normal bed geometries, the pressure distribution predicted by the simple theory commonly does not provide pressure gradients in the melt film that are consistent with the water fluxes required. To resolve this discrepancy, one has to take into consideration spatial variations in the thickness of the melt film and temperature gradients across it.

Impurities provide a second problem for regelation theory. Water moving in a melt film over an obstacle on the bed may absorb ions from the bed or from rock flour between the bed and the ice. Such impurities lower the freezing point. Thus, the temperature in the lee of the obstacle is lower than would be the case with pure water, and the temperature gradient through the obstacle is correspondingly reduced (Figure 7.2). This reduces the heat flux through the obstacle, and thus reduces  $u_{br}$ .

When impurities collect in a freezing water film in the lee of a bump, fractionation occurs; some of the impurities are carried away by the ice that forms, while the rest remain in the melt film. (In a steady-state the concentration of impurities in the film is such that the rate of removal of ions from the lee side during freezing equals the influx of ions in water coming from the stoss side of the bump.) The impure ice thus formed melts on the stoss side of the next suitable bump downglacier, and the resulting impure melt water will acquire more impurities as it flows past that bump. After several such cycles, the concentration of ions in water on the lee sides of obstacles becomes high enough to induce precipitation. The most common such precipitates are  $\text{CaCO}_3$  (Figure 7.7), but Fe/Mn coatings are also observed. Hallet (1976a, 1976b), Hallet *et al.* (1978), and Ng and Hallet (2002) have made detailed studies of the calcium carbonate precipitates, and Hallet (1976b) calculated the degree to which, during sliding over a hypothetical bed composed of sinusoidal waves of a single wavelength,  $u_{br}$  is reduced by various concentrations of  $\text{CaCO}_3$  in the melt film (Figure 7.8). Because solutes reduce the efficacy of the regelation



Figure 7.7  $\text{CaCO}_3$  precipitate in the forefield of Tsanfleuron Glacier, Switzerland. (Photograph by author)

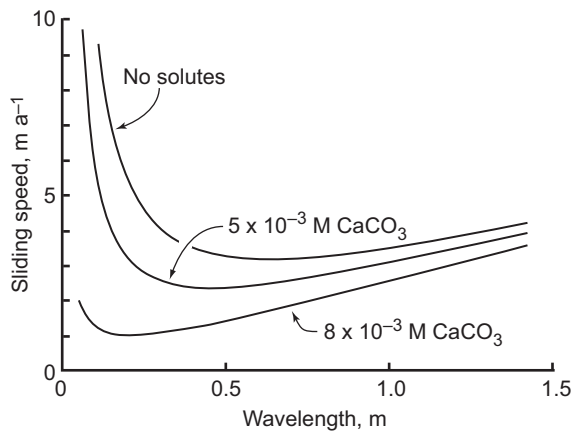


Figure 7.8 Effect of solutes on speed of sliding over a sinusoidal bump. (After Hallet, 1976b. Reproduced with permission of the author and the International Glaciological Society)

process, they effectively shift the  $u_{\text{br}}$  curve in Figure 7.3 downward. Thus, the wavelength for which  $u_b$  is a minimum, that is  $\lambda_c$ , is reduced. Hallet estimated that  $\lambda_c$  would drop from  $\sim 0.6$  m when no solutes are present to  $\sim 0.2$  m for the highest solute concentration (Figure 7.8).

Finally, the rheology of basal ice may be somewhat different from that of ice well above the bed, thus altering the role of plastic flow, and cavities may form in the lee of obstacles. These effects are discussed next.

### Rheology of basal ice

In comparison with most of the ice in a glacier, basal ice may have fewer bubbles, a different solute content, and more sediment. In addition, constant changes in stress field as the ice flows around successive bumps may result in zones of transient creep (Figure 4.10) as the crystal structure adjusts. Consequently, basal ice is likely to be rheologically significantly different from ice higher in the glacier, albeit with a gradational change from one rheology to the other.

The effect of sediment, in particular, is not well understood despite extensive research. Dirt particles can strengthen ice by inhibiting movement of dislocations and, as they occur on grain boundaries, by reducing grain-boundary sliding. In concentrations in excess of ~40% by volume, they may also interact with each other, increasing frictional forces. On the other hand, premelting layers of unbound water form at interfaces between ice and sediment particles. These layers, although only nanometers in thickness, weaken the ice. The presence of the layers implies that the free energy of the interface is lowered by converting a layer of the solid to liquid (Dash, 1995, p. 120). Sediment particles may also increase the deformation rate by acting as dislocation sources, by nucleating new grains, and by supplying solutes that increase premelting and the thickness of the interfacial water layers (see p. 53–55) (Moore, 2014). The extent of premelting also increases with the surface area of the sediment particles, so their size distribution likely affects the rheology.

These effects vary with temperature. In cold ice, grain boundary sliding is already suppressed and premelting is minimized, so sediment particles tend to strengthen ice. In a series of experiments at  $-9.1^{\circ}\text{C}$ , Hooke *et al.* (1972) found that  $A$  decreased exponentially with sand content; in ice with 20 volume percent dispersed fine sand, it was only 15% of that in clean ice. Hooke *et al.* inferred that sand particles inhibited movement of dislocations, and attributed the strengthening of the ice to development of dislocation tangles in the vicinity of particles. Closer to the melting point, however, the effect of premelting tends to dominate and ice is softened.

Cohen (2000), utilizing the facilities of the Svartisen Subglacial Laboratory, conducted a unique experiment to study the latter effects. He emplaced an instrumented 0.15 m high conical obstacle at the base of the glacier and measured forces on it, temperatures in it, and the speed with which ice flowed past it. He then modeled the flow with the use of a fully three-dimensional numerical model. With  $n = 3$  and with values of  $A$  ranging from 450 to 4500  $\text{MPa}^{-3} \text{ a}^{-1}$ , the model reproduced the observed forces and ice speeds. A normal value of  $A$  for temperate

ice with little or no interstitial water, however, would be  $\sim 250 \text{ MPa}^{-3} \text{ a}^{-1}$ . The increase in  $A$  thus implies a 2–20-fold increase in  $\dot{\varepsilon}$ .

The ice at the site of the experiment contained sediment-bearing lamellae, several millimeters thick, interlaminated with clean ice. This is typical of basal ice from both temperate and polar glaciers. At the level of the obstacle, the sediment-rich layers contained  $\sim 20\%$  debris by volume, the water content was  $\sim 2\%$ , and the cross sectional area of the crystals averaged  $\sim 7 \text{ mm}^2$  (compared with  $\sim 50 \text{ mm}^2$  in the overlying clean ice). There was no preferred orientation of  $c$ -axes. As none of these factors offered a satisfactory explanation for the high values of  $A$ , Cohen (2000) suggested that unbound water layers around the sediment acted as a lubricant, enhancing sliding between the sediment-rich layers and the lamellae of clean ice.

Echelmeyer and Wang (1987) also found that ice in the basal zone of Urumqi Glacier No. 1 in Tibet deformed much more readily than clean ice. In this case, the ice had a debris content of 30–40% by volume. The temperature was  $-2^\circ\text{C}$ . The measured deformation rate would correspond to a value of  $A$  of over 100 times that of clean ice. They, too, attributed the softness of the basal ice-sediment mixture to liquid-like interfacial water layers.

### Cavities and the effect of water pressure

Lliboutry (1968 and earlier) appears to have been the first to emphasize the now widely recognized role that water pressure,  $P_w$ , plays in sliding (e.g. Figure 7.9). When  $P_w$  exceeds the local ice pressure in the lee of a bump, a cavity forms. The elevated water pressure in the cavity can increase  $u_b$  in two ways: (i) if sustained, it increases the length of the cavity, thereby bridging over roughness elements that would otherwise exert drag on the ice; and (ii) it exerts a net downglacier force on ice bridging the cavity. In addition, an elevated water pressure weakens any deforming subglacial till over which the glacier is moving, thus increasing  $u_d$  (Figure 5.5). Here, we consider the first two of these effects. The third will be addressed in connection with our discussion of subglacial till deformation.

Let us briefly examine the conditions required for separation and cavity formation in an idealized situation. The pressure at the bed is:

$$P(x, y) = P_i + P_o(x, y)$$

where  $P_i$  is the ice overburden pressure and  $P_o(x, y)$  is a fluctuating contribution that is positive on the stoss sides of bumps and negative on lee sides (Iken and Bindschadler, 1986). On a bed consisting of sinusoidal waves of amplitude  $a$  and wavelength,  $\lambda$ ,  $P_o$  varies sinusoidally. The maximum and minimum pressures occur at inflection points on the up- and downglacier faces of the undulations, and are (Iken and Bindschadler, 1986):

$$P_o|_{\max, \min} = P_i \pm \frac{\lambda \tau_b}{a\pi}. \quad (7.11)$$

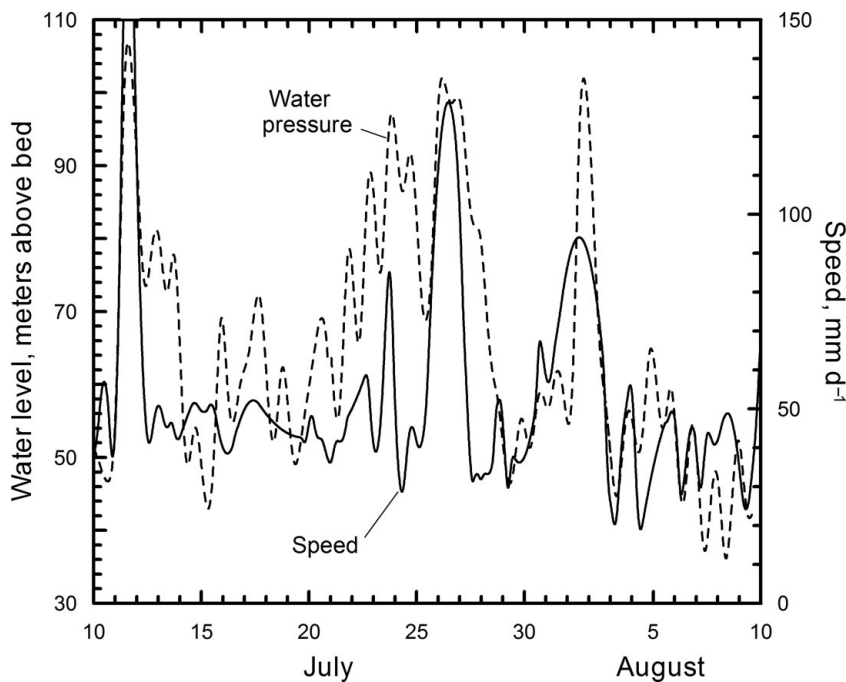


**Figure 7.9** Diurnal variations in surface speed on Storglaciären, Sweden, measured with the use of a computer-controlled laser distance meter. The distance from a point off the glacier to a stake on the glacier was determined every 10 minutes. The dashed line shows corresponding water pressures measured in nearby boreholes. Only the major peaks in speed are clearly related to water pressure peaks. (Modified from Hanson *et al.*, 1998. Reproduced with permission of the author and the International Glaciological Society)

If  $P_w > P_{o \text{ min}}$ , separation occurs and a cavity will form. If  $P_w$  remains elevated the cavity will eventually reach a final length determined by the degree to which  $P_w$  exceeds  $P_{o \text{ min}}$ , and the task of balancing  $\tau_d$  is shifted to places where the ice is still in contact with the bed. Because  $\tau_d$  is now (temporarily) greater than  $\tau_b$ ,  $u_b$  increases, and this results in the necessary increase in  $\tau_b$  to again balance  $\tau_d$ . Note, once again, that  $\tau_b$  is the dependent variable.

The second mechanism by which elevated water pressures lead to acceleration of a glacier is hydraulic jacking. An elevated water pressure in a cavity pushes upglacier against the bedrock and downglacier against ice. The result is an addition to  $\tau_d$ . Once again, drag forces on the bed must increase to balance this increased  $\tau_d$ , and an increase in  $u_b$  provides this increase in  $\tau_b$ .

Thus, separation reduces drag exerted by the bed on the ice, while hydraulic jacking increases the driving stress that must be balanced. In both cases,  $u_b$  increases, and this increases  $\tau_b$  to bring it back into balance with  $\tau_d$ .

Diurnal increases in water pressure due to input of meltwater or storm water don't last long enough to increase cavity size appreciably. Thus, in ice flow over bedrock beds, diurnal changes in speed resulting from fluctuations in  $P_w$  (Figure 7.9) must be a result, principally, of hydraulic jacking. Furthermore, for a high  $P_w$  to have a

significant effect on  $u_b$ , the subglacial drainage system must be reasonably well connected to cavities on the lee sides of bumps so that an increase in  $P_w$  in the englacial drainage system results in a comparable increase in  $P_w$  in a large number of cavities. [Pressures in water films on the stoss sides of bumps are always in excess of the overburden pressure, and thus are not affected appreciably by changes in the (lower) pressure in the drainage system.]

The effect of changing water pressure in a lee-side cavity is nicely illustrated by a numerical modeling study conducted by Röthlisberger and Iken (1981) (Figure 7.10). The authors first established the shape that a cavity would have under a water pressure of 2.41 MPa. When the pressure was then reduced to 2.36 MPa, velocity vectors in the ice turned toward the cavity (Figure 7.10a), tending to close it. Conversely, an increase in  $P_w$  to 2.43 MPa sufficed to start enlarging the cavity at a rate of about 10 mm d<sup>-1</sup> (Figure 7.10b).

The bold numbers in Figure 7.10b show the reduction in normal pressure on the bed due to the increase in  $P_w$  in the cavity. The decrease of over 1.2 MPa at the crest of the bump could easily have resulted in freezing there in a real situation, as suggested by Robin (Figure 7.6b).

The effect of  $P_w$  on sliding is usually incorporated by including the effective normal pressure,  $N_e$ , or normal pressure minus water pressure, in the denominator of equations like Equation (7.10), thus:

$$u_b = \Omega \frac{\tau_d^2}{N_e^p r^4}. \quad (7.12)$$

The exponent,  $p$ , is evaluated empirically. An increase in  $P_w$  thus decreases  $N_e$  and may also increase  $\tau_d$ , so  $u_b$  increases.

As  $N_e \rightarrow 0$ , Equation (7.12) implies that  $u_b$  increases without bound. Let's look at this in somewhat greater detail. Figure 7.11 shows a cavity in the lee of a sinusoidal bump on the bed of a glacier. The projected area of the cavity face, normal to the back slope of the bump, is  $\lambda \sin \beta$ . This is the area against which the pressure in the cavity,  $P_w$ , acts. Thus,  $P_w \lambda \sin \beta$  is the force trying to push the glacier up the back slope of the bump. The component of the body force acting parallel to the back slope of the bump and in the upglacier direction is  $\rho g d \lambda \sin (\beta - \alpha)$ . Thus, if  $P_w$  increases so that  $P_w \lambda \sin \beta > \rho g d \lambda \sin (\beta - \alpha)$ , and if this critical  $P_w$  is maintained as the cavity expands, the cavity would bridge the bump. If all bumps on the glacier bed were of the same size and shape, the glacier would then accelerate without bound (Iken, 1981). Using the expressions for  $P_i$  and  $\tau_b$  shown in Figure 7.11 and the trigonometric identity,  $\sin(\beta - \alpha) = \sin \beta \cos \alpha - \cos \beta \sin \alpha$ , we obtain:  $P_{w\ crit} = P_i - \frac{\tau_b}{\tan \beta}$ . Rewriting this in terms of a critical effective pressure,  $N_{e\ crit} = P_i - P_{w\ crit}$ , and rearranging yields:

$$\frac{\tau_b}{N_{e\ crit}} \leq \tan \beta \quad (7.13)$$

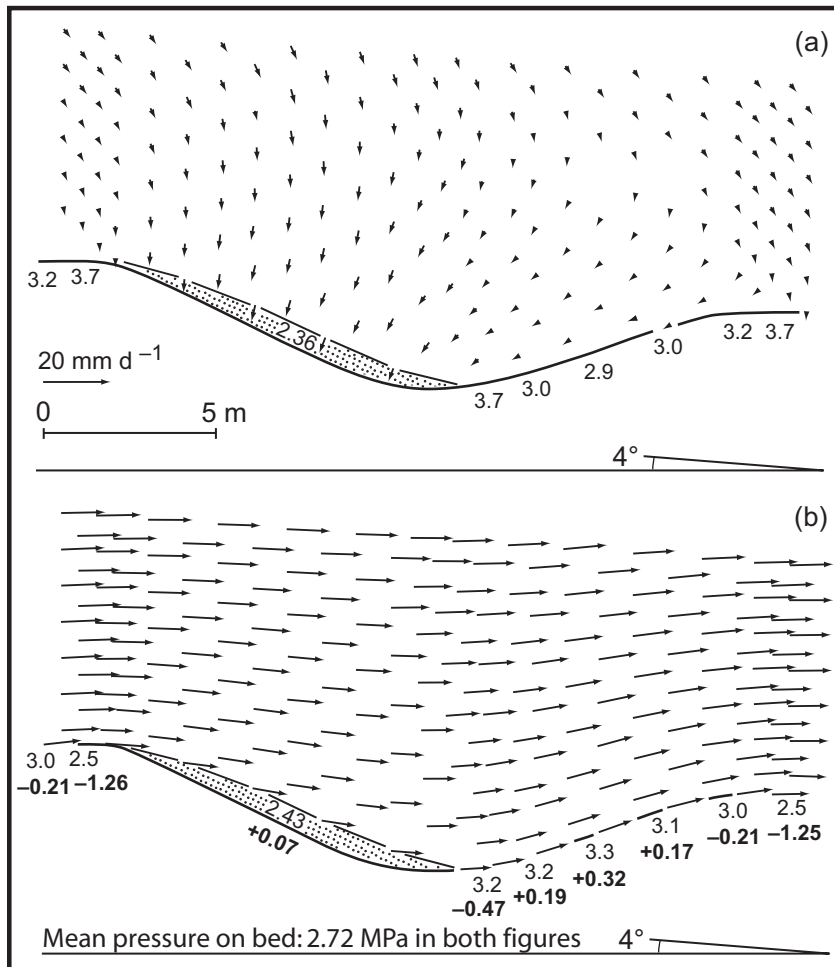


**Figure 7.10** Flow around a subglacial cavity in the lee of a sinusoidal bump based on a numerical model using the finite element method. (a) The water pressure in the cavity, 2.36 MPa, is too low so the cavity is shrinking. (b) The water pressure in the cavity is too large, so the cavity is expanding. Light-faced numbers show pressure at bed. Bold numbers show change in pressure following a 0.07 MPa change in water pressure in the cavity. The driving stress was 0.103 MPa in both experiments, and the mean pressure at the bed was 2.72 MPa. The cavity would be stable at a pressure of 2.41 MPa. (After Röthlisberger and Iken, 1981, Figure 3. Reproduced with permission of the authors and the International Glaciological Society)

as the condition for stability. Thus,  $P_{w\ crit}$  is actually somewhat less than  $P_i$ . This suggests that  $P_i$  in Equation (7.12) should probably be replaced with  $P_{w\ crit}$ , thus:

$$u_b = \Omega \frac{\tau_d^2}{(P_{w\ crit} - P_w)^p r^4} = \Omega \frac{\tau_d^2}{(N_e - N_{e\ crit})^p r^4}. \quad (7.14)$$

On an actual glacier bed consisting of a variety of sizes and shapes of obstacles, however,  $P_{w\ crit}$  would not be exceeded everywhere simultaneously. Thus, for most

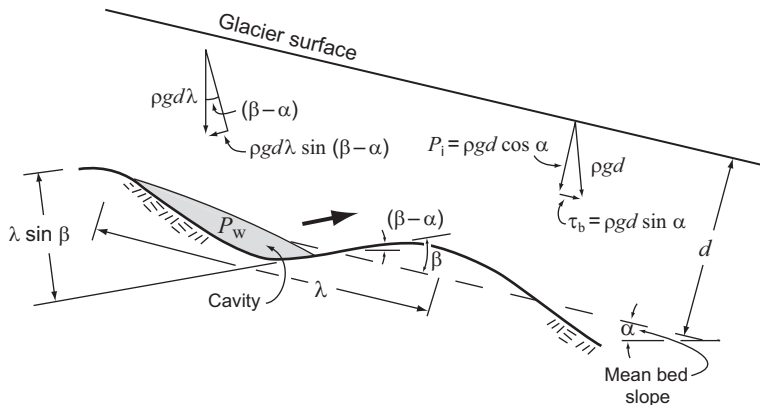


Figure 7.11 Diagram illustrating calculation of  $P_{\text{crit}}$ .

situations,  $P_{w \text{ crit}} \approx P_i$  is probably more realistic and more practical, as calculation of  $N_{e \text{ crit}}$  requires detailed knowledge of bed topography.

Iken and Bindschadler (1986) have collected an outstanding set of field data on the relation between water pressure and surface speed on Findelegletscher (Findelegen glacier) in the Swiss Alps (Figure 7.12). The data clearly show the expected exponential increase in speed with increased water pressure.

If the character of the bed in front of Findelegletscher is similar to that beneath the glacier, one can calculate sliding speeds using Kamb's (1970) theory. For wavelengths and roughnesses that Iken and Bindschadler believe to be appropriate, the theory gives sliding speeds that are too large, compared with the surface speed, to be realistic. Iken and Bindschadler attribute the discrepancy largely to failure of the theory to take rock-to-rock friction into consideration.

Jansson (1995) studied the relation between  $N_e$  and surface speed,  $u_s$ , on Findelegletscher and Storglaciären. He used Iken and Bindschadler's (1986) data (Figure 7.12) for Findelegletscher, and because  $\tau_b$  was nearly the same at the two sites and did not vary significantly within either of the data sets, he folded its effect, and that of bed roughness,  $r$ , into  $\Omega$ . He found that relations of the form:

$$u_s = \frac{\Omega}{N_e^{0.4}} \quad (7.15)$$

fit the data well (Figure 7.13), but  $\Omega$  was more than an order of magnitude higher on Findelegletscher. This discrepancy remained after subtracting the contribution of internal deformation, estimated with the use of Equation (5.16) (dashed lines in Figure 7.13). Such a difference in sliding speed implies a basal drag beneath Storglaciären that is about twice that beneath Findelegletscher (assuming

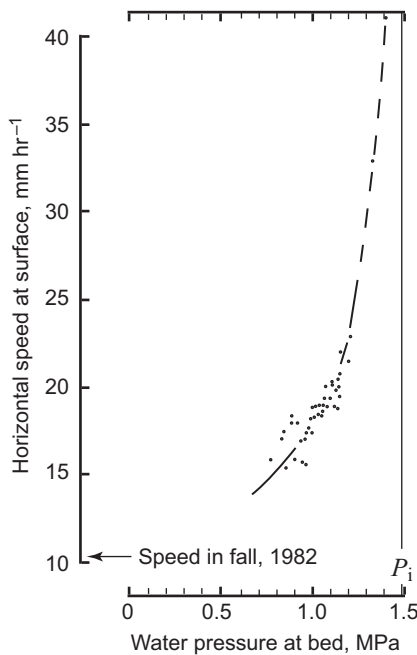


**Figure 7.12** Speed of a stake on the surface of Findelengletscher as a function of water pressure. (After Iken and Bindschadler, 1986, Figure 6. Reproduced with permission of the authors and the International Glaciological Society)

$u_b \propto r^{-4}$ , as in Equation 7.14). This likely reflects the presence of a till layer between the base of Storglaciären and the bedrock (Brand *et al.*, 1987).

More recent data from Findelengletscher (Iken and Truffer, 1997) serve only to further emphasize our lack of understanding of the effect of water pressure on sliding. By 1985, 3 years after the measurements shown in Figure 7.12, the surface speed had decreased 25% for comparable water pressures. By 1994 there had been an additional 35% decrease. There have not been any significant changes in the geometry of the glacier, and hence in  $\rho g d_a$ , that could explain this deceleration. Iken and Truffer suggest that the basal water system was better connected in 1982, so that high water pressures reached more subglacial cavities. Thus, in effect, there may have been more subglacial hydraulic jacks urging the glacier forward in earlier years. Alternatively, it is possible that more entrained particles have come in contact with the bed, leading to more rock-to-rock friction.

### Deformation of subglacial till

We have known for decades that ice moving over granular subglacial materials can deform these materials. (Herein, the term “granular material” should be understood to include materials with significant amounts of clay, although a distinction

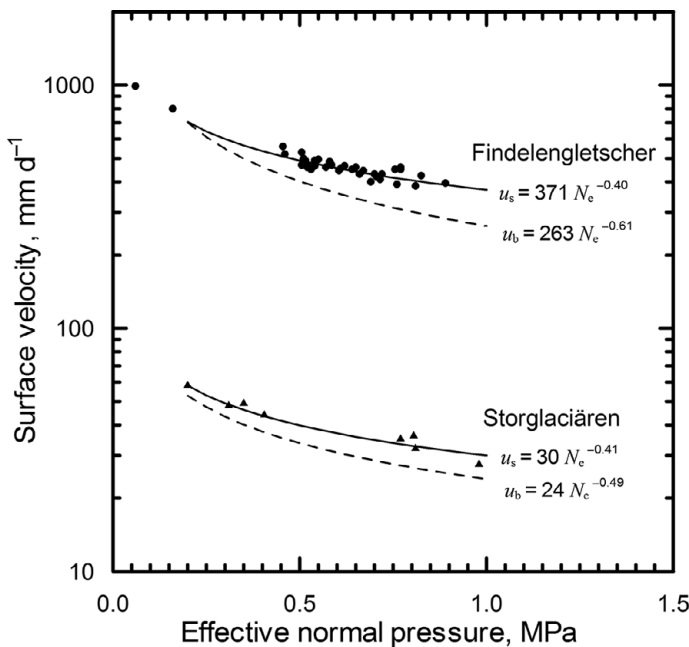


**Figure 7.13** Relation between surface speed,  $u_s$ , sliding speed,  $u_b$ , and effective pressure,  $N_e$ , on Findelengletscher and Storglaciären. Dashed lines show sliding speed estimated by subtracting internal deformation from  $u_s$ . (After Jansson, 1995. Reproduced with permission of the author and the International Glaciological Society)

between granular materials and clays is usually made in the soil mechanics literature.) Commonly, the granular material is till, either formed by erosion during the present glacial cycle, or left from a previous one. Recently it has become clear that a large fraction of the surface velocity of some glaciers may be a result of deformation of such till (Figure 5.5).

Intense interest in till rheology dates from work on Whillans Ice Stream in Antarctica, where studies of seismic velocities suggested that a 2–13 m thick layer of till with high porosity, saturated with water under high pressure, was present beneath the ice (Blankenship *et al.*, 1986). The high porosity suggested active deformation, facilitated by the high water pressure. As the driving stress was only 0.01–0.02 MPa, the high speed of the ice stream, about  $450 \text{ m a}^{-1}$ , was attributed to deformation of this presumed till. Subsequent drilling revealed that the ice stream was, indeed, underlain by till, and also confirmed that the water pressure was close to the overburden pressure (Engelhardt *et al.*, 1990). A key question, then, is whether the till is deforming, or alternatively whether the high water pressure has simply decoupled the ice stream from the till. Experiments addressing this question are described later in this chapter.

Subsequently, it was suggested that the large volumes of glacigenic material found in some till sheets in the midwestern United States and in some submarine

fans surrounding the Barents Sea could only have been transported to their present locations in deforming subglacial till layers (e.g. Alley, 1991; Hooke and Elverhøi, 1996). The amount of material that could be transported in basal ice or by subglacial melt streams is estimated to be too low to account for the volumes of these deposits in the time inferred to be available for their formation. In the Barents Sea case, calculated basal melt rates are so high that little material is likely to have been entrained by basal ice, and yet too low to provide the water volumes required for significant fluvial transport. On the other hand, contrary evidence, discussed later, raises the question of whether deformation extends to sufficient depths in subglacial till to result in large sediment fluxes.

Because glacial till is a granular material, its rheology is quite different from that of ice. Granular materials normally have a failure strength,  $s_f$ , below which deformation is largely elastic. The failure strength is related to two physical properties of the material, the cohesion,  $c$ , and the angle of internal friction,  $\varphi$ , by the classical Mohr–Coulomb relation:

$$s_f = c + N_e \tan \varphi. \quad (7.16)$$

To determine  $c$  and  $\varphi$ , laboratory tests are conducted in which the stress needed to shear a material is measured at various effective normal pressures. The stress normally varies linearly with  $N_e$  (Figure 7.14), so the slope of the line is  $\tan \varphi$ , and the intercept is the apparent cohesion.

The term *apparent* cohesion is used because detailed measurements often show that the variation of  $s_f$  with  $N_e$  is not linear at low effective normal pressures; rather it is as shown by the dashed line in the inset in Figure 7.14. The true cohesion is the

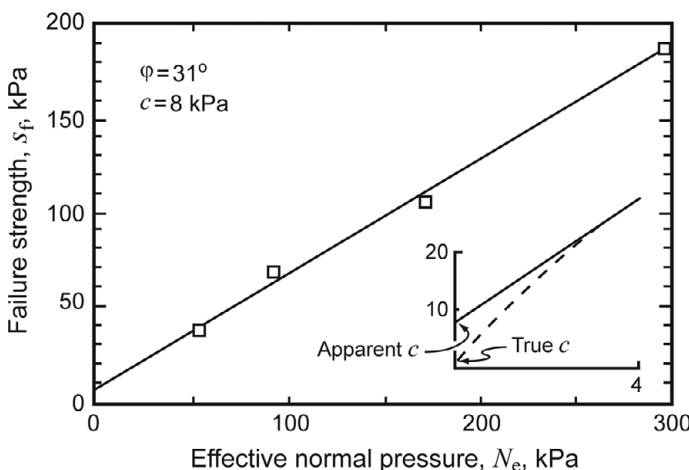


**Figure 7.14** Relation between shear strength,  $s_f$ , and  $N_e$  obtained from a laboratory test on a till sample from Storglaciären (Iverson, unpublished). Inset shows, schematically, how  $s_f$ , may actually vary with  $N_e$  at low effective pressures.

value of  $s_f$  at the intercept of this dashed line with the ordinate. Because the apparent cohesion normally varies directly with the true cohesion, however, we normally will not draw a distinction between the two quantities.

Let's now examine the physics involved in cohesion, and the physical significance of  $\varphi$ .

## Cohesion

True cohesion in soils is a consequence of cementation, of electromagnetic forces between clay particles, and of electrostatic forces resulting from charge imbalances among ions absorbed on clay minerals (Mitchell, 1993, pp. 125, 373–374). Cementation is the major source of cohesion in subaerial soils, but would not be significant in continuously-deforming subglacial tills. Thus, the magnitude of  $c$  in such tills is determined primarily by the amount and species of clay minerals present.

*In situ* deforming subglacial tills formed by erosion in the current cycle of glaciation do not seem to have much clay-sized material unless the glacier has moved over a bed containing such material. Furthermore, most of the clay-sized particles that are present in these clay-poor tills are not clay minerals. Thus,  $c$  may be small in such tills. For example, in silty and clayey sands,  $c$  is typically between 20 and 75 kPa (Hausmann, 1990), but in samples of till collected from beneath Whillans ice stream and containing ~35% clay minerals derived from Tertiary glaciomarine sediments (Tulaczyk *et al.*, 1998; Kamb, 2001),  $c = 3 \pm 1.3$  kPa (Tulaczyk *et al.*, 2000a).

The absence of clay-sized material in deforming tills is likely to be largely a consequence of flushing by subglacial streams. In addition, however, it is noteworthy that the deviatoric stress required to fracture a grain increases as the particle size decreases, and that in the limit very fine grains deform plastically rather than fracture into still smaller particles (Kendall, 1978). That the clay-sized particles present in such tills tend not to be clay minerals is due to the absence of subaerial weathering processes. Higher concentrations of clay-sized particles and of clay minerals in Pleistocene tills may be a consequence either of subaerial weathering after retreat of the ice, or of incorporation of previously-weathered material over which the ice moved.

Cohesion is not increased by saturation by water unless clay minerals are present. The well-known fact that the walls of wet sand castles stand up better than dry ones is, rather, due to surface tension. Because surface tension, in this case, is a result of stresses associated with the air–water interface, it arises only when the sand is wet but pore spaces still contain air.

## Consolidation

When a granular material accumulates gradually, it compacts under its own weight. Such a material is called *normally consolidated*. If an additional load, such as a shear

stress less than  $s_f$ , is then placed on the material, particles adjust, reducing void space, and the material becomes *overconsolidated*. The term overconsolidated is also used to describe a granular material which, after being normally consolidated, experiences a reduction in overburden pressure due to erosion or, perhaps, to melting of an overlying glacier. A reduction in  $N_e$  may also lead to overconsolidation. The highest past effective stress to which a sample has been subjected is called the *preconsolidation stress*.

The state of consolidation is altered whenever a granular material is sheared. Thus, for example, if a subglacial till, previously consolidated by an effective pressure of 100 kPa, is later sheared at an effective pressure of 30 kPa, the preconsolidation stress is reset to the lower value (Tulaczyk *et al.*, 2001).

### Angle of internal friction

When the shear stress applied to an overconsolidated granular material is sufficient to cause it to deform, it must *dilate* so that individual grains can move over one another (Figure 7.15a). [A normally consolidated material may either dilate or compact slightly, depending on the granulometry (size distribution of particles) and the conditions under which it accumulated.] Dilation increases pore space, which is why the high porosity of the till beneath Whillans ice stream suggests deformation.

Grains in such a deforming material must also *slide* past one another locally (Figure 7.15b). The forces resisting this sliding motion are frictional. Frictional forces are a consequence of the interlocking of microscopic asperities on the surfaces of the materials (Mitchell, 1993, p. 362). The strength of the frictional surface between two particles,  $s_p$ , is proportional to the effective normal pressure,  $N_e$ :  $s_p = \mu N_e$ . The constant of proportionality,  $\mu$ , is called the coefficient of friction.

Let's define  $\beta$  as the angle, relative to the shear plane, that particles must ascend during dilation from an overconsolidated state (Figure 7.15a) and also define  $\omega = \tan^{-1} \mu$ . Then  $\varphi = \beta + \omega$  (Iverson *et al.*, 1996). In granular materials that do not have much clay,  $\omega$  is typically 20–25°, and  $\varphi$  is typically between 25 and 40° (Mitchell, 1993, pp. 343, 366). Thus, more than half of the resistance to deformation of such a

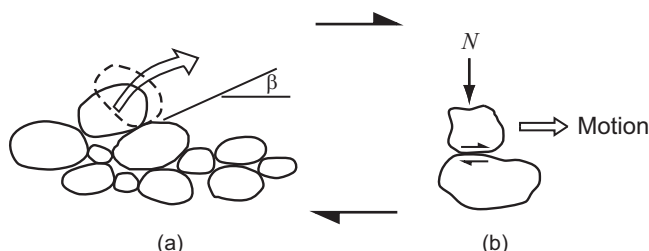


**Figure 7.15** Deformation of a granular medium involves both: (a) dilation as grains move apart in order to pass over one-another; and (b) friction between grains that are constrained to slide past one-another.

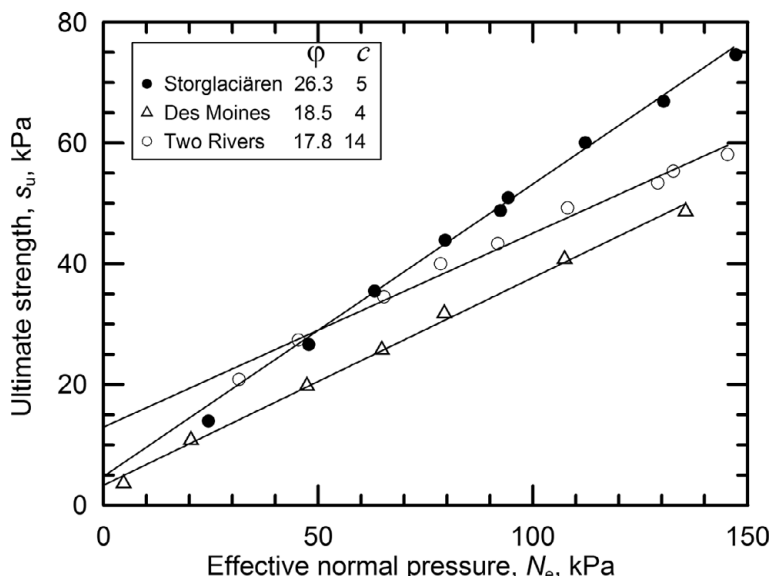


**Figure 7.16** Variation in ultimate strength with  $N_e$  for three tills, based on laboratory experiments, similar to that shown in Figure 7.14, using a ring shear apparatus. (Iverson *et al.*, 1998 and written communication. Reproduced with permission of the author and the International Glaciological Society)

material is a consequence of frictional forces, while the remainder is due to processes such as dilation and crushing (Mitchell, 1993, p. 401).

Because  $\varphi$  depends on  $\beta$ , it also depends on the granulometry of the material. If spaces between particles in Figure 7.15a were filled with finer material, for example, a particle could not settle down into the gap between subjacent particles, and thus would not have to rise so much to move over its neighbor;  $\beta$  would then be lower, and hence so would  $\varphi$ . Thus, in the sandy Storglaciären till,  $\varphi$  is  $26^\circ$ , but in two clay-rich tills it is only  $18^\circ$  (Figure 7.16).

Normal pressures suppress dilation and also force particles into firmer contact, thus increasing  $s_p$ . These two factors account for the dependence of  $s_f$  on  $N_e$ .

Let's now consider an experiment in which a granular material under a prescribed effective pressure is deformed at a constant strain rate with the shear stress required to achieve that strain rate,  $\tau$ , being measured as a function of time or displacement. Initially,  $\tau$  increases linearly (Figure 7.17). This reflects elastic (recoverable) deformation. The point at which the rise begins to deviate from linearity is the *fundamental strength* (Terzaghi, 1950) or *yield strength*. Subsequent strain reflects irrecoverable visco-plastic deformation. The peak of the curve is the *failure strength*,  $s_f$ . It is  $s_f$  that is measured in experiments like that in Figure 7.14. If the material was initially overconsolidated,  $\tau$  then commonly declines somewhat before reaching a constant value at the *residual* or *ultimate strength*,  $s_u$ , of the material. The decrease varies from 0 to  $\sim 25\%$ , depending largely on the granulometry of the material (Iverson

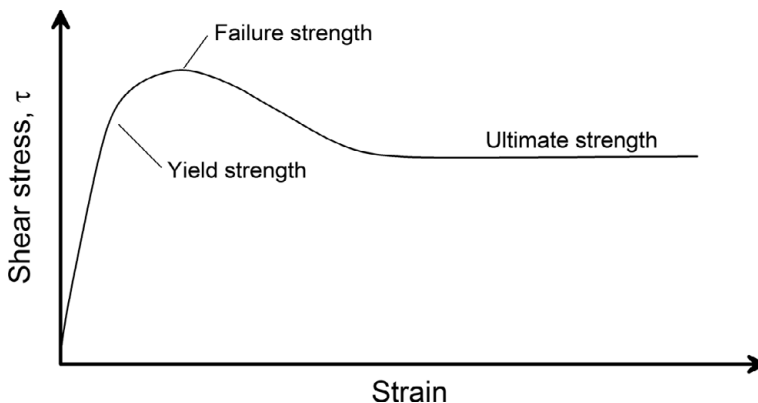


**Figure 7.17** Schematic illustration of the variation of shear stress with time (or displacement) in a granular medium that is sheared at a constant rate.

*et al.*, 1997; Tulaczyk *et al.*, 2000a; Sane *et al.*, 2008). The final value is normally reached after a shear strain of the order of 10–30%. As was the case with  $s_f$  (Figure 7.14),  $s_u$  also normally varies linearly with  $N_e$  (Figure 7.16) (Iverson, 2010, and references therein).

The ultimate strength is commonly somewhat less than the failure strength because a sediment, once dilated, remains dilated, so the fraction of  $\tau$  needed to induce dilation is no longer needed. The decrease from  $s_f$  to  $s_u$  thus reflects a decrease in  $\beta$  and hence in  $\varphi$  (compare the Storglaciären data in Figures 7.14 and 7.16). [In materials in which clay-sized particles are abundant (>20%) and are predominantly clay minerals, a further decline in strength may occur as platy clay particles become aligned parallel to the direction of shear.]

Desai (2000; see also Sane *et al.*, 2008) has developed an analytical model of this process in which deformation begins in isolated mesoscopic elements within the material and, with increasing strain, these disturbed zones expand to eventually encompass the entire volume. In their model,  $s_f$  and  $s_u$  are reached after only 10–20% and 85%, respectively, of the material has begun to deform.

### Void ratio

The void ratio,  $e$ , is the ratio of the volume of pores,  $V_p$ , to the volume of solids,  $V_s$ :  $e = V_p/V_s$ . (Note that this is not the same as porosity; porosity is the percentage of voids in the total volume.) The void ratio varies with  $N_e$ , thus:

$$e = e_0 - C_p \log \frac{N_e}{N_{eo}} \quad (7.17)$$

(Figure 7.18), where  $e_0$  is the void ratio at a reference effective normal pressure of  $N_{eo}$ , and  $C_p$  is a dimensionless coefficient of compressibility (e.g. Tulaczyk *et al.*, 2000a).

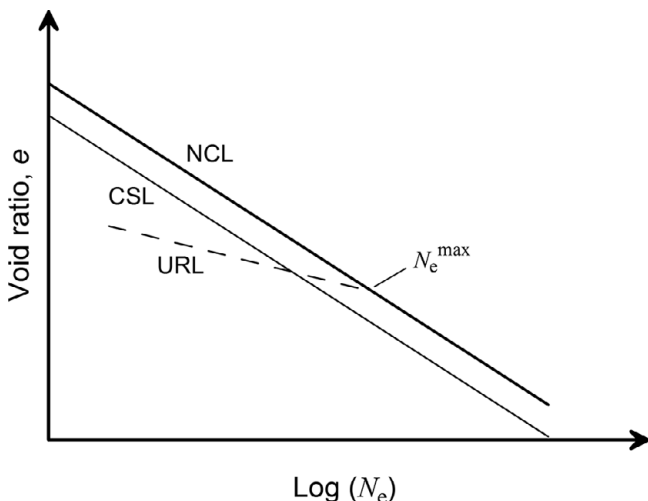


**Figure 7.18** Schematic diagram showing variation of void ratio with effective normal pressure. See text for explanation.

As a normally consolidated material is buried by continued accumulation,  $e$  decreases as shown, schematically, by the line labeled NCL (*normal consolidation line*) with slope  $-C_p$  in Figure 7.18. In an overconsolidated material,  $e$  is below the NCL. If such a material is then sheared,  $e$  will adjust to a steady value shown by the line labeled CSL (*critical state line*). If the initial overconsolidated state is below the CSL the material will dilate; if the initial state is between the NCL and CSL lines, it will compact. When deformation stops, the material will not consolidate unless  $N_e$  is increased by more than the amount indicated by the horizontal spacing between the two lines.

If the normal load on a material increases to, say,  $N_e^{\max}$  (Figure 7.18), and is then relaxed, the material will expand elastically along a path like the one labeled URL (*unloading-reloading line*). Upon reloading, it will follow this URL path back to  $N_e^{\max}$ , and then begin to consolidate further along the NCL line. This property can be exploited to determine  $N_e^{\max}$ . One collects an undisturbed sample in the field and subjects it to a gradually increasing load in the laboratory, in what is called a *preconsolidation test*. The maximum  $N_e$  to which the sample had previously been subjected is that at which the slope of the resulting  $e$  vs  $\ln(N_e)$  line increases abruptly.

This fact was first exploited by Harrison (1958), who used preconsolidation tests to estimate the profile of the Champaign Lobe of the Laurentide Ice Sheet in central Indiana. His values of  $N_e^{\max}$  were lower than he expected. More recently, Hooyer and Iverson (2002) conducted such tests on several samples of till deposited by the Des Moines Lobe which advanced out of North Dakota into Minnesota and Iowa about 16,700 years ago. Their values of  $N_e^{\max}$  ranged from 120 to 300 kPa. These

values are also quite low, considering the probable ice thickness. This suggests that pore water pressures beneath both lobes were high, which, in turn, implies that the motion of both lobes may have been dominated by a combination of sliding over the underlying till and deformation of that till. In the case of the Des Moines Lobe, this provides an explanation for the considerable extent of the lobe despite other evidence suggesting that driving stresses were quite low.

### Grain fracture and the granulometry of deforming subglacial till

If a granular medium is sheared at a constant rate between moving platens, in one of which there is a pressure sensor that is many times the diameter of individual grains but much smaller than the platen itself, the pressure recorded by this sensor varies with time (Figure 7.19) (Mandl *et al.*, 1977; Iverson *et al.*, 1996). Sometimes it exceeds the mean normal load on the sample by as much as 25%, while at other times it is significantly less than the mean. One logical explanation for this is that grains in the medium become aligned to form bridges such as that shown in Figure 7.20a. When traced through a granular material of significant thickness, these bridges are much more complicated than suggested by the simple sketch in Figure 7.20a; high contact stresses are distributed along a three-dimensional array of routes, forming what could be called a grain-bridge network (Iverson *et al.*, 1996). The complexity of a two-dimensional network can be studied by shearing an array of photoelastic disks and viewing them in transmitted polarized light (Figure 7.21). Changes in the optical properties of disks under stress makes them appear lighter. Thus, the bridges show up as chains of lighter disks in Figure 7.21.

For deformation to occur, grain bridges must fail. Failure may be a consequence either of fracture of a grain (Figure 7.20b) or of slippage between grains

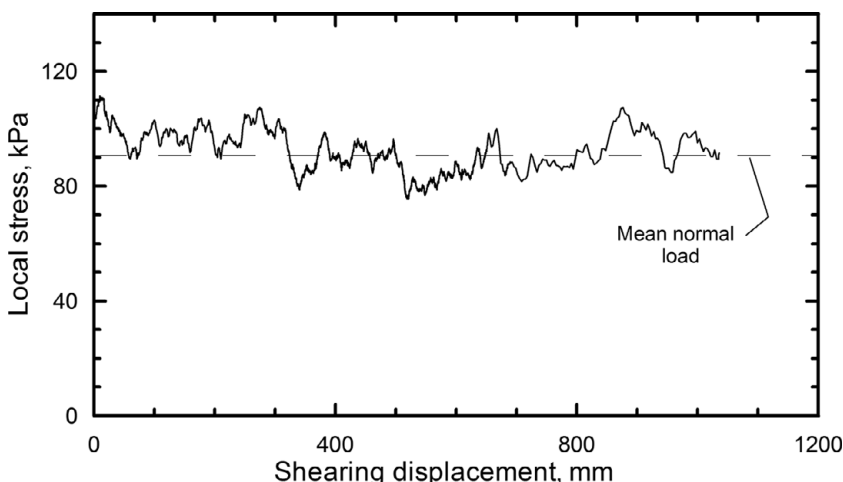


**Figure 7.19** Variation in local pressure with time in a granular medium, ~55 mm thick, as it is deformed in a ring shear experiment. (Data courtesy of N. R. Iverson and T. S. Hooyer)

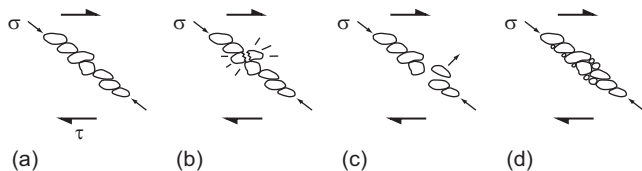


**Figure 7.20** (a) A grain bridge, formed by nearly coaxial alignment of several grains in a deforming granular medium, may fail by: (b) fracture of a grain; or (c) slip between grains. (d) Stresses at contacts between grains are reduced when additional particles occupy pore space. Heavy arrows show shear stress applied to material,  $\tau$ , and the component of this stress along grain bridge,  $\sigma$ . (Modified from Hooke and Iverson, 1995, Figure 1)



**Figure 7.21** Grain bridges in a two-dimensional array of photoelastic disks under shear. Each white dot is a disk that has been stressed, making it appear lighter. Unstressed discs are black. (Adapted from Howell *et al.*, 1999)

(Figure 7.20c). Fracture is most likely when two adjacent grains are of roughly equal size and when the space between them is not filled with smaller grains that absorb some of the stress. Slip between grains occurs when resolved stresses parallel to contacts between particles are greater than  $s_p$ . Such slip may be due to fracture of interlocked asperities on the contact surfaces or to dislocation creep within the asperities. In the latter case, a frictional interface that initially appears to be stable may, in time, slip. Because the deviatoric stress required to fracture a grain varies with particle size, and because contacts between grains may have different orientations leading to different resolved stresses, there must be a wide range of bridge strengths.

Grain fracture alters the granulometry of a material. Biegel *et al.* (1989) argue that the end product of this process is a granulometry that maximizes the support that each particle receives, and thus minimizes stress concentrations capable of causing fracture. For example, forces between particles in Figure 7.20d are distributed over several contact points, so local stresses are less likely to reach a level that will cause fracture. The granulometry which provides maximum support, according to

Biegel *et al.*, is one in which no two particles of the same size are in contact. Such a material has a fractal particle-size distribution with a fractal dimension of  $\sim 2.6$ . That is, if  $N_o$  is the number of particles of a reference size,  $d_o$ , then the number of particles of size  $d$ ,  $N(d)$ , is:

$$N(d) = N_o \left( \frac{d}{d_o} \right)^{-m}. \quad (7.18)$$

The exponent,  $m$ , is the fractal dimension. [As should be evident from Equation (7.18), fractal size distributions appear to be the same at all scales. Thus, if there is one particle of unit size in a field of view, there will be  $10^m$  particles that are 1/10th this size, regardless of the units used in making the measurement.] Sammis *et al.* (1987) have shown that gouge from the Lopez Canyon Fault in California has such a particle-size distribution.

Deforming subglacial tills also have a fractal granulometry, with a fractal dimension close to 2.9 (Figure 7.22). This suggests that grain fracture may play an important role in till deformation. That the fractal dimension is larger than the ideal of 2.6 is attributed to the production of fine material by abrasion, a process that would be inhibited by the higher effective normal pressures characteristic of deformation in active faults (Hooke and Iverson, 1995). However, more work is needed to fully understand the processes that give rise to size distributions with different fractal dimensions in granular materials.

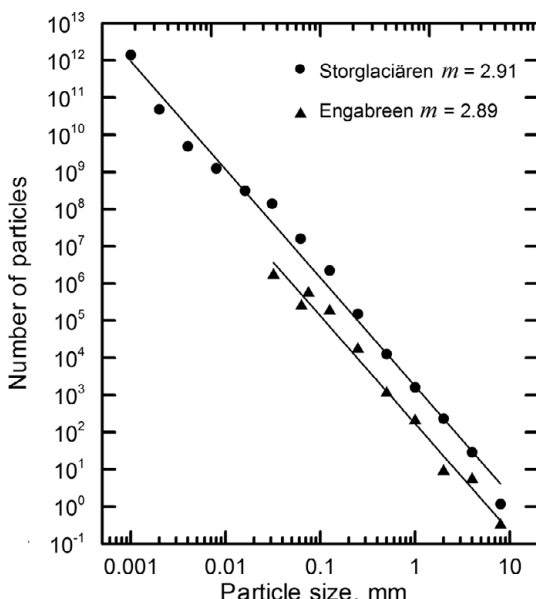


**Figure 7.22** Grain-size distributions in two subglacial tills that were deforming. Fractal dimension of each till is shown. (Modified from Hooke and Iverson, 1995, Figure 2)

## The roles of pore water and permeability

If the base of a glacier is at the pressure melting point, any till present will be effectively saturated. In contrast to the situation in a dry granular medium, this pore water plays a fundamental role. When till tries to dilate, for example, pores must increase in size, reducing the pore-water pressure. This increases  $N_e$  while also setting up a potential gradient (commonly loosely referred to as a pressure gradient) driving water into the dilating zone. The latter flow forces grains together, increasing frictional forces. The increases in  $N_e$  and in frictional forces combine to strengthen the till – a process known as *dilatant hardening* (e.g. Lambe and Whitman, 1969, p. 445; Tulaczyk *et al.*, 2000a). The increase is temporary because eventually enough water flows into the pores to allow the till to dilate to the critical state void ratio. The time required for this depends on the permeability of the till. The most likely source of the water is a water layer at the ice/till interface.

Conversely, if movement of grains alters the grain network in such a way as to allow the till to collapse, water will be forced out of the pores back to the ice/till interface. In tills with low permeability, this delays collapse of the pore space, decreasing  $N_e$ , and weakening the till.

## Till rheology

There is a considerable volume of literature on the failure strength of granular materials because slope failures, leading, for example, to collapse of highway embankments or to landslides, are inconvenient. We, however, are interested in the *time-dependent* behavior of deforming granular materials because we want to know how they affect glacier motion. Thus, we need to understand deformation processes at stresses between the yield strength and the failure strength, and also those related to the ultimate strength.

Previously, we used the term “creep” to describe the visco-plastic deformation of ice. Deformation of granular materials at stresses between the yield strength and the failure strength is also commonly referred to as creep, as those familiar with the slow downslope movement of soil on slopes will recognize. Creep consists of “... intricate deformations, revealing and accentuating the resistance patterns ...” of the material (Terzaghi, 1950, p. 87), a description that could apply equally well to movement of dislocations in ice and to adjustments of the structure in a granular medium. In the latter case, creep results from perturbations that are effectively random and that cause alterations in soil structure. On a subaerial slope, burrowing organisms, frost action, and raindrop impact are examples. In subglacial till, stick-slip behavior of the ice or changes in  $N_e$  are the most likely sources of perturbations. Changes in  $N_e$  may be due to fluctuating water input from the surface or to adjustments in the subglacial hydraulic system. Because the maximum compressive stress in the till,  $\sigma_{\max}$ , is the vector sum of the bed-parallel driving stress and  $N_e$ , changes in  $N_e$  both reorient  $\sigma_{\max}$  and alter its magnitude. This leads to

reorganization of the grain structure, resulting in deformation (Damsgaard *et al.*, 2016). In numerical modeling experiments, Damsgaard found that this could lead to till deformation at rates of  $1\text{--}10 \text{ m a}^{-1}$ . In the absence of such random perturbations,  $\dot{\varepsilon}$  would decrease logarithmically with time (Nguyen *et al.*, 2011).

The fundamental question is whether  $s_u$  increases with strain rate, other factors such as effective pressure, granulometry, mineralogy, and so forth, remaining constant. If such an increase occurs, the strain rate may be a unique function of the applied stress, and a “flow law” for till may exist. If  $s_u$  does not increase, or possibly even decreases with increased strain rate, the till may be behaving as a perfectly plastic substance; one in which, once  $s_u$  is reached, the stress on the material cannot increase further. In this case, any further increases in the driving stress must be balanced by resistance elsewhere.

We've seen that  $s_u$  increases linearly with  $N_e$  (Figure 7.16), but how does  $s_u$  vary as the strain rate is increased? Tests to study this have now been done on a number of tills. Because  $s_u$  is known to increase with  $N_e$ , and because  $N_e$  varied among the experiments,  $s_u$  is first normalized by dividing by  $N_e$ . It turns out that  $s_u/N_e$  actually decreases with increasing strain rate in four of the seven tills for which data are available, a phenomenon sometimes referred to as *velocity weakening* (Biegel *et al.*, 1989; Iverson *et al.*, 1998), and  $s_u/N_e$  is essentially independent of  $\dot{\varepsilon}$  in two others (Figure 7.23). Thus, once  $s_u$  is reached, any further increase in the driving stress must be balanced by increases in resistance elsewhere.

There are two likely sites for this increased resistance: glacier margins and so-called *sticky spots*, or local areas of enhanced resistance (Alley, 1993). A prerequisite for a site to qualify as a sticky spot is that the resisting stress must increase with  $\dot{\varepsilon}$ . One likely candidate is bedrock highs that either penetrate through the subglacial till layer or cause it to thin enough to reduce the strain rate in it. Another is patches till that are more resistant owing to random spatial variations in either granulometry or  $N_e$ .

### Toward a physical model of till rheology

The principal processes leading to till deformation are dilation and failure of grain bridges. Dilation occurs early in the deformation process, and once the medium is dilated it remains so. Thus, dilation should not be rate controlling, and in the absence of repeated formation and failure of grain bridges, we might expect the material to deform steadily and homogeneously, once  $s_u$  is reached. Grain bridges form, however, and deformation proceeds only when a bridge fails. This suggests that failure of grain bridges may be the rate-controlling process in till deformation. If this is the case, and if the formation of grain bridges is effectively stochastic in time and space, then a mechanistic rheological model for till deformation should be based on these processes. Analysis should focus on the frequency of failure of grain bridges and on the amount of deformation, or *step length*, resulting from each failure.

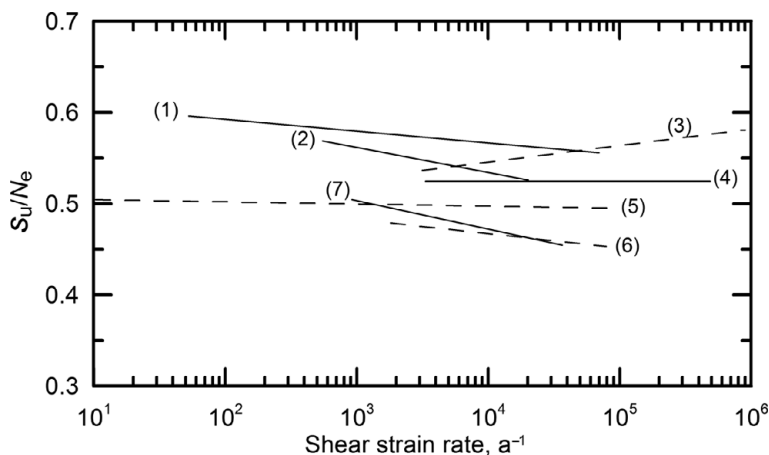


**Figure 7.23** Relation between ultimate strength normalized by the effective pressure and shear strain rate for seven different tills (modified from Iverson, 2010, Figure 2a). The tills and original data sources are:

- (1) Lower Cromer till, British Isles (Tika *et al.*, 1996),
- (2) Storglaciären till, Sweden (Iverson *et al.*, 1998),
- (3) Ceaser till, Ohio (Rathbun *et al.*, 2008),
- (4) Cowden till, British Isles (Tika *et al.*, 1996),
- (5) Whillans Ice Stream till, Antarctica (Tulaczyk *et al.*, 2000a),
- (6) Two rivers till, Illinois (Iverson *et al.*, 1998),
- (7) Des Moines Lobe till, Iowa (Iverson, 2010).

(Used with permission of the author and the International Glaciological Society)

Studies of processes that are thermally activated, such as the creep of ice (Equation 4.5), provide a conceptual framework for such a model. In thermally activated processes, the process operates or proceeds when a certain energy barrier is exceeded. In the creep of ice, the barrier is the energy needed to break an atomic bond, thus allowing movement of a dislocation (Figure 4.4), and the step length is determined by the crystal structure. Fundamental to the theory of thermally activated processes is a premise, based on principles of statistical mechanics, that the probability distribution,  $p(f)$ , of energy levels,  $f$ , in atomic bonds is given by:

$$p(f) \propto e^{-\alpha f} \quad (7.19)$$

where  $\alpha$  is a constant (Glasstone *et al.*, 1941, p. 159). In containers filled with beads and subjected to a normal load, the distribution of force levels at intergranular contacts is, indeed, given by Equation (7.19), with  $f$  now defined as the force at such contacts (Liu *et al.*, 1995). Thus, it seems plausible that the theory of thermally activated processes can be adapted to the analysis of deformation of granular materials. Mitchell *et al.* (1968) and Mitchell and Soga (2005, pp. 478–480) have used this approach, and conclude that a relation of the form:

$$\dot{\varepsilon} = \Gamma e^{\gamma \tau} \quad (7.20)$$

should describe the steady strain rate in a granular material. Here,  $\tau$  is a mean shear stress sufficient to cause deformation and thus maintain dilation, and  $\Gamma$  and  $\gamma$  are constants, presumably dependent upon the strength and granulometry of the material.

A flow law for till that is of this form is:

$$\dot{\varepsilon} = \dot{\varepsilon}_o e^{\left(\frac{\tau - \tau_o}{b\tau_o}\right)} \quad \tau, \tau_o \geq s_u \quad (7.21)$$

(e.g. Mitchell and Soga, 2005, Figure 12.9), where  $\dot{\varepsilon}_o$  is a reference strain rate greater than 0, and  $\tau_o$  is the stress yielding that strain rate. This relation is consistent with laboratory data. Because increases in  $N_e$  suppress  $\dot{\varepsilon}$ ,  $\tau_o$  must increase with  $N_e$ .

In engineering tests on sandy materials preconsolidated to 392 kPa,  $b \approx 0.013$  (Nakase and Kamei, 1986, Figure 14), whereas for materials with significant quantities of clay, it is  $\sim 0.043$  (Mitchell and Soga, 2005, Figure 12.9). Tests on till from beneath Whillans ice stream yielded values that ranged from 0.10 for samples preconsolidated at 35 kPa to 0.002 for samples preconsolidated at 343 kPa (Figure 7.24) (S. Tulaczyk, written communication, August 19, 2003). Nakase and Kamei's value is broadly consistent with the latter (Figure 7.24). Tulaczyk *et al.* (2001) found that the preconsolidation stresses of samples from beneath Whillans ice stream were typically 10–20 kPa, so a value of  $b$  of  $\sim 0.1$  is probably appropriate, at least for these fine-grained tills.

These low values of  $b$  magnify any small increase in  $\tau$ . Thus, Equation (7.21) suggests that strain rates increase substantially with only a small increase in  $\tau$ . In

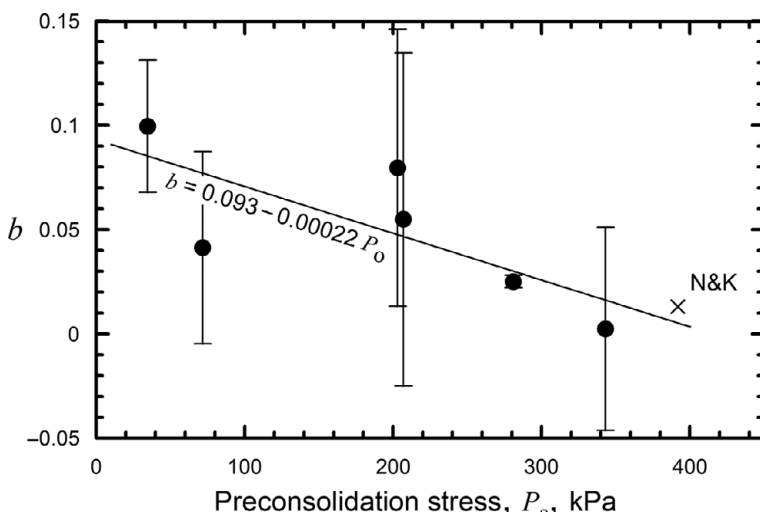


**Figure 7.24** Effect of preconsolidation stress on  $b$ . Data are based on undrained triaxial tests on samples of till from beneath Whillans ice stream (Tulaczyk *et al.*, 2000a). Values of  $b$  were kindly calculated by Tulaczyk (written communication, August 19, 2003). Error bars are estimated from plots supplied by Tulaczyk. N&K = Nakase and Kamei (1986).

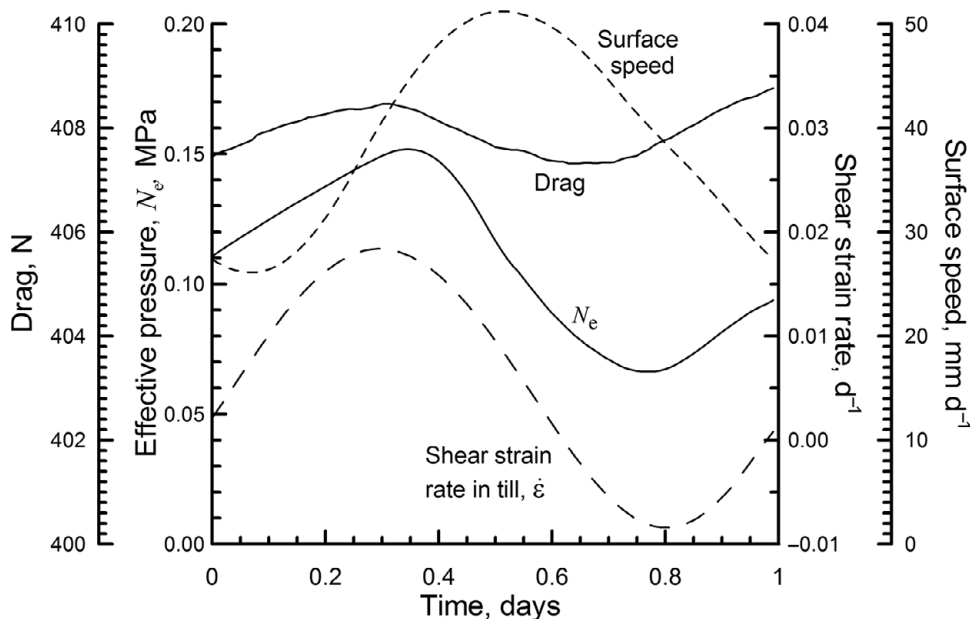


**Figure 7.25** Relation among drag on a cylinder pulled through subglacial till beneath about 120 m of ice, glacier surface speed, water pressure in a nearby borehole, and shear strain rate in the till. Data are from a period of about 10 days in August 1992, at a time when all parameters were varying diurnally, and are “stacked” by averaging values obtained at the same time of day each day. (After Hooke *et al.*, 1997. Reproduced with permission of the International Glaciological Society)

recognition of the quasi-plastic nature of this behavior, this rheology is referred to as *Coulomb plastic*.

Such a dependence of  $\dot{\epsilon}$  on  $\tau$  in till is consistent with field measurements on Storglaciären (Hooke *et al.*, 1997). The measurements were made by inserting instruments into till beneath  $\sim 120$  m of ice, using boreholes through the glacier to gain access to the till. One instrument consisted of a cylinder with conical ends (the “fish”), which was dragged through the till by a wire connected to a load cell. Another was a tiltmeter with which the strain rate,  $\dot{\epsilon}$ , in the till was measured. The force required to drag the fish varied between about 407.4 N and 408.6 N during a period of several days when the speed of the glacier varied diurnally (Figure 7.25). The variations in drag were basically in phase with those in  $N_e$ , which is consistent with a Mohr–Coulomb behavior (Equation 7.16). However, variations in  $\dot{\epsilon}$  with  $N_e$  are in phase, whereas in a Mohr–Coulomb material they would be out of phase because increases in  $N_e$  would strengthen the material and thus decrease  $\dot{\epsilon}$ , and conversely. Furthermore, if we assume that the speed with which the fish was pulled through the till varied in phase with the surface speed and that the variations were of comparable amplitude, one would expect the drag to be in phase with the surface speed, which it is not. Thus, it appears that the force on the fish was only weakly

dependent on its speed through the till, and hence on the strain rate in the till immediately adjacent to it. This is consistent with a Coulomb-plastic rheology and a constitutive relation of the form of Equation (7.21).

Note also, in Figure 7.25, that the shear strain rate becomes negative when the water pressure is high (low  $N_e$ ). It seems that in this case, the high water pressure decouples the glacier from the bed, permitting the ice to slide over the bed. The negative shear strain rate is attributed to reverse creep (elastic recovery) as ice is gradually decoupled from the bed. Possibly also involved is vertical expansion of the till as the ice is lifted. The latter would tend to straighten up the tiltmeter, which was then inclined downflow. An expansion of the till of only 0.7 mm would be sufficient to produce this backward tilt. The in-phase variations of  $\dot{\epsilon}$  with  $N_e$  are attributed to such partial decoupling.

Positive values of  $b$  (Figure 7.24) represent velocity strengthening, whereas negative values represent velocity weakening (Figure 7.23). Low positive values of  $b$  suggest that the probability distribution of forces between contacts in grain bridges is relatively narrow, as Liu *et al.* (1995) found to be the case, so once one bridge fails, it does not take long for stresses on another to rise to failure level. Velocity weakening, on the other hand, suggests that, following failure of a grain bridge, either: (i) others do not form readily to absorb the applied stress, or (ii) the step length increases with stress, or both. This suggests that our analysis needs to be expanded to consider not only the probability of failure of a bridge, but also probability of formation of new ones and controls on the step length. This is left as an exercise for a capable PhD student.

### Coupling between a glacier and a till bed: plowing

At an interface between a glacier and a till bed there will be clasts imbedded partially in ice and partially in the till. Ice may move past these clasts by a combination of regelation and plastic flow, much as it moves past bedrock bumps. Clasts gripped firmly in the ice may also plow through the till, causing local bed deformation. Evidence for such plowing is occasionally preserved in tills in deglaciated areas (Westgate, 1968; Ehlers and Stephan, 1979; Clark and Hansel, 1989; Iverson and Hooyer, 2004).

Water pressure is again key. When  $P_w$  is low, ice-till coupling is increased and till is strengthened. As  $P_w$  rises, the till weakens, promoting plowing. At high enough  $P_w$ , a water layer likely develops between the ice and the bed, submerging some of the smaller particles. This decouples the ice from the bed locally, but elsewhere clasts will continue to plow through the bed.

A clast plows when the drag force exerted on it by the glacier exceeds the resisting force supplied by the till. This is easily said, but not so easily quantified. By analogy with Equation (7.6), the mean shear stress over a bed consisting of isolated hemispheres may be approximated by:

$$u_b \approx \Omega_r \frac{\tau_{pi}}{d} + \Omega_p \tau_{pi}^n d \quad (7.22)$$

where  $\tau_{pi}$  is now the stress exerted on the clast by the ice (rather than the mean shear traction on the bed),  $u_b$  is the speed with which ice moves past the clast, and the clast diameter,  $d$ , has been substituted for  $\ell$  (e.g. Lliboutry, 1979, Equations 40 and 41; Iverson, 1999, Equation 7). As with ice flow past obstacles on a glacier bed, the stress that the ice exerts on a clast is a maximum for clasts of some critical size,  $d_c$ , accommodated roughly equally by regelation and by plastic deformation. Thus, noting that  $\tau_{pi}$  is now the dependent variable, the drag force [which is proportional to  $\tau_{pi}(d/2)^2$ ] depends on the speed with which the ice moves past the clast and on the clast size. If the water pressure is high enough to open a cavity in the lee of the clast, it will exert an additional downflow force on the ice, thus increasing  $\tau_{pi}$ . So  $\tau_{pi}$  also depends inversely on  $N_e$ .

Whether a clast plows or not will depend upon the strength of the till, which is also controlled by  $N_e$ . Iverson (1999) has adapted analyses of pile driving studies to this problem, and found that the stress resisting movement of the clast,  $\tau_{pt}$ , is well approximated by:

$$\tau_{pt} = \frac{1}{2 + kN_F} \left[ N_F \left( N_e + \frac{c}{\tan \varphi} \right) - \frac{c}{\tan \varphi} \right] \quad (7.23)$$

in which  $N_F$  is a dimensionless bearing-capacity factor that varies directly with  $\varphi$  and likely ranges from  $\sim 10$  to  $\sim 40$  in tills, and  $k$  is a pressure shadow factor, reflecting the fact that the value of  $N_e$  in the lee of an obstacle will be lower than the farfield value. The value of  $k$  varies from  $\sim 0.1$  when regelation is the dominant mechanism of ice flow past the clast to  $\sim 0.45$  when plastic flow dominates.

When  $\tau_{pi} > \tau_{pt}$ , a clast will plow. The pore-water pressure in front of a plowing clast is then increased, however, reducing  $N_e$ , and thus weakening the till. This, in turn, increases the plowing speed. Thomason and Iverson (2008) have studied this effect; with the use of Iverson's ring shear apparatus, they dragged till past a hemisphere at different speeds,  $u_c$ , and measured the difference,  $\Delta P_w$ , between the pore-water pressure in front of the hemisphere and that some distance away from it. As  $u_c$  increases, the  $\Delta P_w$  increases rapidly at first, and then becomes constant.

The constant  $\Delta P_w$  reflects a balance between the rate of increase in  $P_w$  in front of the clast and dissipation of this high pressure by flow of water through the till. The former can be characterized by  $u_c d$ , a measure of the rate of till compaction, while the latter is characterized by the diffusivity,  $D$ , of the till. Thus,  $\Delta P_w$  increases as the dimensionless ratio,  $\mathbb{R} = u_c d / D$ , approaches and then exceeds unity (Figure 7.26). In the Engabreen till, with  $D \approx 11 \text{ m}^2 \text{ a}^{-1}$ ,  $\mathbb{R} < 1$  as long as  $u_c < \sim 300 \text{ m a}^{-1}$  ( $\blacktriangle, \nabla$  in Figure 7.26) whereas, for Des Moines lobe till, with  $D \approx 0.3 \text{ m}^2 \text{ a}^{-1}$ ,  $\mathbb{R} > 1$  when  $u_c > \sim 10 \text{ m a}^{-1}$  ( $\bullet, \circ$  in Figure 7.26). The sliding speed at Engabreen is  $\sim 60 \text{ m a}^{-1}$  (Iverson *et al.*, 2003), so  $\Delta P_w$  is unlikely to become elevated. However, in

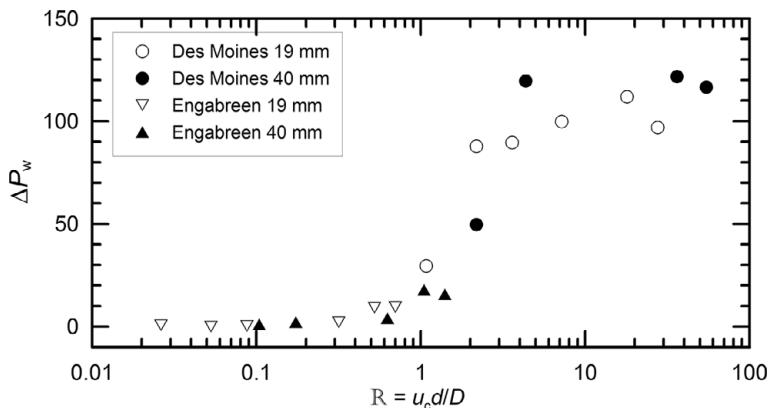


**Figure 7.26**  $\Delta P_w$  generated by hemispherical clasts, 19 and 40 mm in diameter, plowing through till as a function of the dimensionless ratio,  $R = u_c d/D$ , for tills from the Pleistocene Des Moines lobe ( $D = 0.3 \text{ m}^2 \text{ a}^{-1}$ ) and the modern Norwegian valley glacier Engabreen ( $D = 11 \text{ m}^2 \text{ a}^{-1}$ ). (After Thomason and Iverson, 2008, Figure 13. Reproduced with permission of the authors and the International Glaciological Society)

fine-grained Pleistocene tills like that of the Des Moines lobe and those beneath ice streams in Antarctica, relatively modest sliding speeds can lead to an elevated  $\Delta P_w$ . Because the elevated  $\Delta P_w$  weakens the till,  $u_c$  increases further in a positive feedback, resulting in velocity weakening. Thus, the preferred mode of basal motion is likely to be sliding with plowing in fine-grained tills, and coupling with more pervasive deformation in tills with coarser grain sizes. Extensive sliding would limit sediment transfer in deforming till sheets, so this again raises the question of how the large volumes of fine-grained till deposited by the Pleistocene ice sheets were moved. Regelation of ice into till and concentration of deformation in shear zones at depth in the till, discussed below, may provide an answer.

### Regelation of ice into till

When the temperature at the base of a glacier is at the pressure melting point and the pore-water pressure in subglacial till is less than the ice pressure, ice can penetrate into the bed, much as it moves laterally past bumps on the bed, by regelation. The process is illustrated schematically in Figure 7.27. The pressure at the top of the till is  $P_i$ , the ice pressure. Ice has regelated downward into the till, forming a frozen fringe of thickness  $h$ . At the base of the fringe, the pressure in the water is  $P_w$ . The potential gradient driving regelation is, thus:  $(P_i - P_w)/h = N_e/h$ . The speed,  $v_r$ , with which the ice penetrates into the till is:

$$v_r = K_t \frac{N_e}{h} \quad (7.24)$$

where  $K_t$ , the apparent conductivity of the till to ice, is determined by the porosity and thermal properties of the till (Philip, 1980; Iverson, 2000). As the ice works its

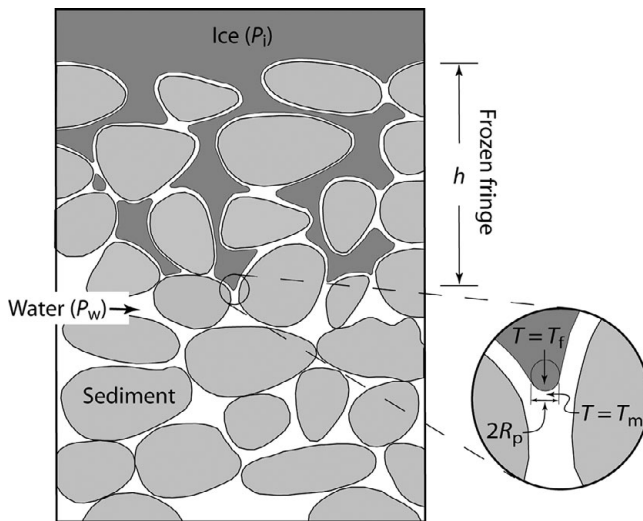


**Figure 7.27** Schematic diagram showing penetration of ice into a granular medium. Inset shows detail of temperatures at the point of deepest penetration. (Adapted from Rempel, 2008, Figure 1b)

way into the till,  $h$  increases, decreasing  $v_r$ . Penetration stops when  $v_r$  equals the melt rate at the base of the fringe,  $m$ . As we saw in Chapter 6,  $m$  depends on the heat balance at the bed – the difference between the input of geothermal and frictional heat on the one hand and loss of heat to the overlying ice on the other. Our next goal is to estimate the value of  $h$  when  $v_r = m$ , as this level then becomes the effective base of the glacier.

The rate-limiting process in regelation into till is the heat flow driven by the difference in temperature between the colder (higher pressure) top of the frozen fringe and the warmer (lower pressure) base. The latter temperature merits further comment. The melting temperature at the base of the fringe,  $T_m$ , depends on  $P_w$ . However, owing to the curvature of the ice/water interface the temperature,  $T_f$ , within the fringe at the farthest extent of the pore ice is:

$$T_f = T_m \left( 1 - \frac{2\gamma_{SL}}{r_p \rho_i L} \right)$$

where  $\gamma_{SL}$  is the liquid/solid interface energy,  $0.034 \text{ J m}^{-2}$ ,  $r_p$  is the radius of curvature of the interface,  $L$  is the latent heat of fusion,  $3.34 \times 10^5 \text{ J kg}^{-1}$ , and the temperatures are in Kelvins (Rempel, 2008; see also Equation 2.1). Thus, say the temperature at the top of the fringe is  $272.5 \text{ K} (= -0.65^\circ\text{C})$ , the pressure melting temperature under  $\sim 1000 \text{ m}$  of ice, and that at its base,  $T_m$ , is  $272.6 \text{ K} (= -0.55^\circ\text{C})$ . Then if  $r_p$  is  $\sim 6 \mu\text{m}$ , a value perhaps typical of fine-grained till with small passages between pores,  $T_f$  is  $272.49 \text{ K} (= -0.66^\circ\text{C})$ , and the temperature difference driving regelation is only  $0.09^\circ\text{C}$  rather than  $0.10^\circ\text{C}$ , a reduction of 10%.

Four complicating factors bear mentioning. First, as discussed earlier, premelt liquid-like films increase the deformation rate in the fringe, leading to increased frictional heating. Secondly, solutes leached from the till may depress the melting temperature and slow regelation. Thirdly, the curvature of the ice/water interface at the base of the fringe also leads to surface-tension effects which, in silt-sized sediment, can partially or completely balance the potential gradient driving regelation (Alley *et al.*, 1997). Finally, It is not clear how regelation would proceed if there were also ice flow parallel to the bed.

Despite these complications, laboratory and field experiments demonstrate that till can be entrained by regelation. Iverson and Slemmons (1995) conducted some of the first laboratory experiments designed to test this. They found that ice penetrated up to 85 mm into a sample of basal till from Storglaciären, and that, except at the lowest driving stresses during which temperature control was a problem,  $v_r$  was generally within a factor of 2 of that predicted by Equation (7.24). Iverson and Souchez (1996) measured  $\delta^{18}\text{O}$ ,  $\delta\text{D}$ , and deuterium excess, in samples of ice collected from the fringe in one of these experiments and found that they varied with depth in a way suggesting fractionation. The fractionation was attributed to loss of water during incomplete regelation, a loss that is also likely to occur in Nature. They then compared these trends with analyses from ice-cemented sediment layers collected from the base of the Greenland Ice Sheet at its western margin, and found the same trends, consistent with the hypothesis that these sediment layers, also, were entrained by regelation. Finally, Iverson *et al.* (2007) emplaced an instrumented prism of till-like sediment, 1.8 m long (in the direction of ice flow), 1.6 m wide, and 0.45 m deep, beneath Engabreen at a place where the ice was 213 m thick. After several days, ice had penetrated 50–80 mm into the till, presumably by regelation, as there is no other viable explanation for the penetration. Calculations based on Equation (7.24) were, again, consistent with this depth of penetration.

### Depth of deformation in a subglacial till

Let's now address two questions, to which there are currently no firm answers: (1) What controls the thickness of the layer of subglacial till that can be mobilized by an overriding glacier; and (2) what is the shape of the velocity profile through this layer?

Evidence for thick layers of deforming till is ambiguous. As noted, Alley (1991) and Hooke and Elverhøi (1996) have suggested that, during the Pleistocene, huge amounts of sediment must have been moved long distances in deforming subglacial layers of till. This would seem to require pervasive simple shear in layers at least a few meters thick. Similarly, Anandakrishnan *et al.* (2007) find that a till wedge deposited at the grounding line of Whillans Ice Stream likely required advection of a deforming layer of till “tens of centimeters” in thickness, and Nygård *et al.* (2007)

document a till flux of  $\sim 8000 \text{ m}^3 \text{ m}^{-1} \text{ a}^{-1}$  from the Norwegian Channel Ice Stream and attribute it to advection in a  $\sim 6 \text{ m}$  thick till layer that is “only slightly over-consolidated.” However, Piotrowski *et al.* (2001) argue that features observed in many Pleistocene tills are inconsistent with pervasive deep shear strain. Likewise, Thomason and Iverson (2009) and Shumway and Iverson (2009) made detailed measurements of clast fabrics and strain magnitude in two till sheets in the mid-western United States, using the orientation of elongate sand grains and, separately, magnetic techniques. They find that the till likely accreted over time, rather than being moved into place in one event, and that both the magnitude of strain,  $< 30$ , and the depth in the till to which deformation occurred at any one time, only a few decimeters, are too low to account for the volume of till in the sheets in the times available for their accretion. This is consistent with the experiments of Thomason and Iverson (2008) showing that velocity-weakening by plowing clasts likely limits the depth of till deformation in fine-grained tills. In addition, studies of cores of subglacial till obtained through boreholes that penetrated the kilometer-thick Whillans ice stream revealed little evidence for deformation (Tulaczyk *et al.*, 1998; Kamb, 2001, p. 172). Clasts were not striated, and there were no distinct shears or other visible macroscopic or microscopic fabrics or textures suggestive of deformation. On the other hand, diatoms of different ages were mixed together in the Whillans till, requiring some sort of deep deformation process. Cushioning by soft clay minerals, which comprise  $\sim 35\%$  of the matrix, may have inhibited formation of striations and other deformation structures.

Analysis of the variation of  $\tau$  and  $N_e$ , with depth provides a basis for calculating the thicknesses of deforming layers and velocity profiles in them. Consider a till layer of bulk density,  $\rho_t$ , beneath a glacier of thickness,  $h$ , and surface slope,  $\alpha$ . Let the origin of the coordinate system be at the ice/till interface with the  $z$ -axis directed downward, and let subscript b refer to the conditions at the interface. Then within the till layer:

$$\tau = \rho_i g h \alpha + \rho_t g z \alpha$$

and

$$N_e = N_{eb} + (\rho_t - \rho_w) g z \quad (7.25)$$

(Alley, 1989b). Taking derivatives with respect to  $z$  and adopting  $\rho_t = 2000 \text{ kg m}^{-3}$  then yields:

$$\begin{aligned} \frac{d\tau}{dz} &= \rho_t g \alpha \approx 20 \alpha \text{ kPa m}^{-1} \\ \frac{dN_e}{dz} &= (\rho_t - \rho_w) g \approx 10 \text{ kPa m}^{-1}. \end{aligned} \quad (7.26)$$

For typical ice surface slopes,  $< 0.01$ , the rate of increase of  $N_e$  with depth clearly exceeds that of  $\tau$ , so the strength of the till should increase faster than the applied

stress. Thus, the decrease in  $\dot{\varepsilon}$  in the till is likely to be nonlinear, and deformation will cease at the depth at which the ultimate strength exceeds  $\tau$ .

In situations in which water is produced by melting at the ice-till interface and is lost downward by flow through a permeable substrate, the hydraulic head must decrease downward through the till. Then  $dN_z/dz$  will be higher than in the purely hydrostatic case represented by the second of Equations (7.26), and the deforming layer should be thinner than otherwise (Alley, 1989b).

On the other hand, Tulaczyk *et al.* (2001) found that, in sediment cores up to 3 m long, obtained from beneath Whillans Ice Stream, the void ratio did not vary with depth as it would if the till were allowed to consolidate normally (Figure 7.18). They suggested that the till must have undergone deformation to a depth of at least 3 m, thus dilating it, and that, owing to the low permeability of the till, reconsolidation was delayed. Continuous deformation would not have been necessary; a deformation recurrence interval that was short in comparison with the characteristic diffusive time scale, ~25 years, would suffice to delay reconsolidation.

To actually measure the ratio of till deformation to sliding at an ice/till interface, Engelhardt and Kamb (1998) implanted stakes in the till beneath Whillans Ice Stream, using boreholes to gain access to the till. As the ice moved away from a stake, a wire attached to it was pulled off of a spool anchored in the basal ice and the rate of rotation of the spool was measured. In one such “tethered-stake” experiment, the top of the stake was believed to be about 30 mm below the base of the ice, and the rate of relative motion between the spool and the stake was  $\sim 1.0 \text{ m d}^{-1}$ , or 83% of the surface speed. Thus, sliding and deformation in the top 30 mm of the till accounted for most of the ice movement. The remaining 17% could have been either internal deformation of the ice or deformation deeper in the till layer.

In a similar tethered-stake experiment on Bindschadler Ice Stream, however, the sliding speed, including deformation in the upper 0.34 m of the till, was only 10–20% of the  $1 \text{ m d}^{-1}$  surface speed (Kamb, 2001). As the driving stress was too low to cause significant internal ice deformation, Kamb attributed the remaining 80–90% of the motion to deformation below the level of emplacement of the stake.

Whillans and Bindschadler ice streams rest on fine-grained tills. The next two experiments involve coarse-grained tills. Observations in a shaft excavated downward from a tunnel beneath the glacier Breiðamerkurjökull in Iceland demonstrated that, within about  $1/2$  m of the glacier sole, deformation of the till was pervasive, while at greater depths it was localized in shear zones (Boulton and Hindmarsh, 1987). Such shear zones are characteristic of virtually all laboratory experiments on granular materials, and similar zones are a well-known characteristic of granular materials that have been overridden by glaciers (Brown *et al.*, 1987; Menzies and Shilts, 1996, pp. 48–49).

Evidence for still deeper deformation comes from an experiment on Black Rapids Glacier in Alaska. Truffer *et al.* (2000) emplaced tiltmeters at depths of  $\sim 0.1$ , 1, and

2 m in a 7-m thick till layer beneath the glacier. The tiltmeters recorded little deformation of the till in 410 days, despite the fact that the base of the glacier and the 2 m of till containing the tiltmeters moved 35–45 m during that time interval. They concluded that the motion must be along one or more shear zones at greater depths in the till, yet Equations (7.26) suggest that deformation should be concentrated toward the top of the till.

Iverson *et al.* (1998) proposed a mechanism for distributing deformation through a significant thickness of till, as observed at Breiðamerkurjökull. They suggest that an increase in  $P_w$  initiates deformation in a thin shear zone which then dilates. Dilatant hardening strengthens the zone, causing the locus of deformation to shift. During a subsequent drop in  $P_w$ , the dilated zone will begin to consolidate back to its ambient porosity. The next episode of deformation may then initiate a shear zone in a quite different place. Thus frequent water pressure fluctuations may facilitate distribution of shear throughout the till.

Iverson and Iverson (2001) developed another, somewhat similar, model that could explain modest depths of deformation. They thought that displacements likely occurred across shear zones several millimeters thick when grain bridges failed, and assumed that: (i) the deforming part of the till could be viewed as consisting of a stack of shear zones, (ii) fluctuations in  $N_e$  cause slip on any given shear zone to occur intermittently, (iii) the frequency of slip was the same on all shear zones, and (iv) the amount of slip on a shear zone during a given event decreased with depth owing to the relative rates of change of  $N_e$  and  $\tau$  with depth. By varying some of their less well constrained parameters within reasonable limits, they were able to match the measured profile in the coarse-grained till beneath Breiðamerkurjökull quite well (Figure 7.28).

Tulaczyk (1999) suggested two more possible mechanisms for distributing deformation through moderately thick layers of till:

- (1) During fluctuations in basal water pressure, alternating waves of high and low pressure will penetrate into the till, much as seasonal temperature waves penetrate into the surface of a glacier (see Figure 6.8). The rate at which these waves penetrate depends on the hydraulic diffusivity of the till. If the till is homogeneous and if deformation occurs in a relatively narrow shear zone at the weakest point in it – namely the point where the water pressure is highest – then this shear zone will migrate downward through the till with the pressure wave. According to Tulaczyk *et al.*'s (2000a) calculations, diurnal pressure fluctuations could distribute shear through ~0.07 m of fine-grained till like that beneath Whillans Ice Stream and through over a meter of coarser tills typical of valley glaciers.
- (2) Alternatively, because the peak strength of a non-deforming till is greater than the ultimate strength (Figure 7.17), shear zones may not migrate readily. In this

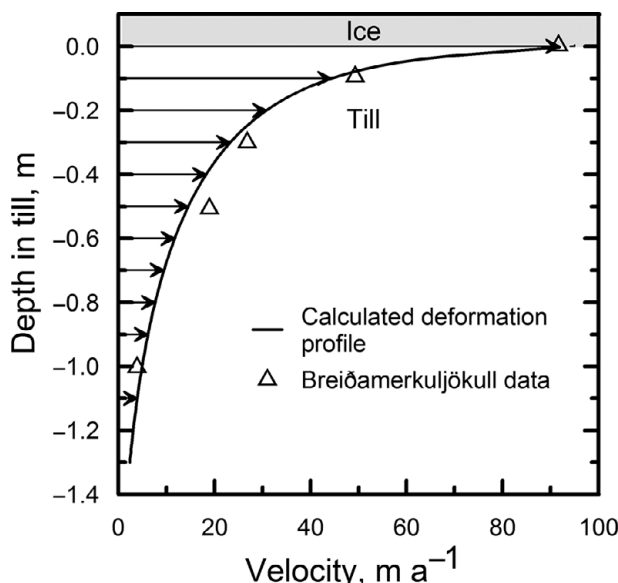


**Figure 7.28** Comparison of a calculated velocity profile in a deforming subglacial till and a measured profile beneath Breiðamerkurjökull. (Modified from Iverson and Iverson, 2001, Figure 3. Reproduced with permission of the authors and the International Glaciological Society)

case, the strength of the till may be determined by the maximum effective pressure that the material experiences during a water pressure cycle. A shear zone could develop and persist at the depth of the minimum  $N_e$ . Till above this level would move as a plug without significant internal deformation.

In the case of Black Rapids Glacier, calculations suggested that the minimum  $N_e$  in an annual cycle would be between 3.5 and 4.6 m below the ice/till interface (Truffer *et al.*, 2000). Thus, Tulaczyk's second explanation could explain the lack of deformation in the uppermost 2 m of this till.

In summary, first order models suggest that layers of deforming till should be relatively thin, particularly in fine-grained tills, and some measurements support this interpretation. However, other observations suggest that layers may be meters thick in certain situations, and more complex models are emerging that explain such layers.

Meanwhile, two alternative modes of moving large volumes of till emerge from the discussion earlier in this chapter and in Chapter 6. First, a considerable thickness of till may be entrained by regelation. Secondly, and perhaps more significantly, enormous slabs of material can be entrained, particularly at places where ice advances over thin permafrost. High water pressures develop beneath the permafrost as subglacial meltwater from upglacier tries to escape. This facilitates detachment of substantial slabs of subglacial material (see p. 143–145). As subsequent

subglacial melting gradually deposits this material, it may be deformed and homogenized, thus obscuring the mode of entrainment and transport.

## Abrasion

The bedrock beneath glaciers is striated and abraded. Abrasion occurs when a clast entrained in either ice or till is forced against the bedrock and dragged across it. Let's first consider the case of an isolated clast surrounded by ice, as first analyzed quantitatively by Hallet (1979a). The abrasion rate,  $A_b$ , is:

$$A_b = kF_N v_p. \quad (7.27)$$

Here,  $F_N$  is the contact force,  $v_p$  is the particle velocity parallel to the bed, and  $k$  is an attritivity coefficient that depends on the relative hardness of the bed and the striator.

Ice is relatively soft, so one might imagine that a particle imbedded in basal ice would simply be pushed up into the ice rather than exert a sustained high contact force against the bed, so  $F_N$  merits further comment. Ice at the base of a temperate glacier is melted by both geothermal and frictional heat, and this meltwater drains away along the bed or percolates into the bed. To replace this loss, and also to compensate for any thinning due to longitudinal stretching, ice must flow toward the bed, moving past any rocks resting on the bed. As first recognized by Hallet (1979a), it is this convergence of ice with the bed that forces clasts against the bed, maintaining an appreciable  $F_N$ . As with ice flow past bedrock bumps and plowing clasts, the ice moves past clasts resting on the bed by a combination of regelation and plastic flow (Figure 7.29). Accordingly, there is a critical clast size,  $\sim 200$  mm (diameter), that is pushed against the bed more vigorously than smaller or larger particles.

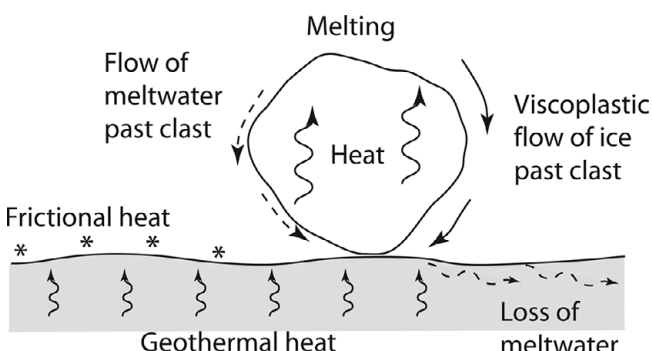


**Figure 7.29** Schematic diagram showing ice flowing around a clast toward the bed to replace ice melted at the bed. Ice moves past the clast by regelation and visco-plastic deformation. Clasts may be of any size, but the maximum force against the bed occurs when clasts are  $\sim 200$  mm in diameter.

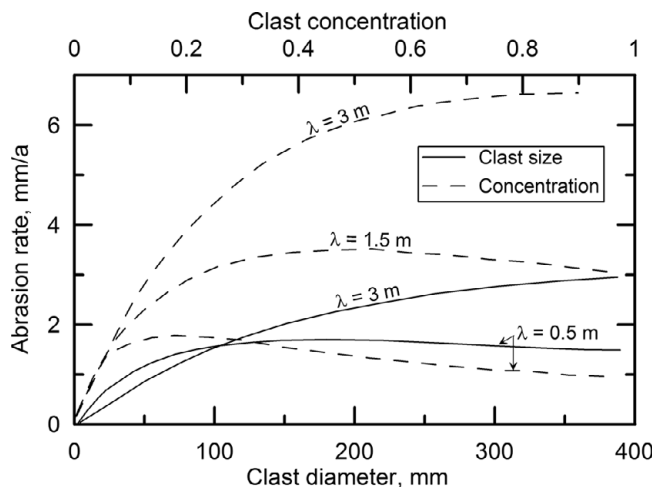


**Figure 7.30** Calculated rates of erosion of sinusoidal undulations ( $a/\lambda = 0.05$ ) by limestone clasts abrading a limestone bed. Solid curves show rate as a function of clast diameter and  $\lambda$  when basal ice contains 10% clasts (by volume). Dashed curves show rate of erosion by 200 mm clasts as a function of  $\lambda$  and clast concentration. (Modified from Hallet, 1981, Figures 3 and 4. Reproduced with permission of the author and the International Glaciological Society)

If one wished to estimate the actual rate at which a bed is eroded by abrasion, one would have to: (i) sum over all clasts in contact with the bed, (ii) take into consideration spatial variations in the rate at which ice converges with the bed, and hence in  $F_N$ , as the ice flows over bed undulations, (iii) deal with interactions between adjacent clasts that could affect  $F_N$ , and (iv) include changes in  $v_p$  as the number of clasts in frictional contact with the bed changes. By limiting consideration to the first two of these, Hallet (1981) was able to calculate rates of abrasion of sinusoidal undulations of different wavelengths by limestone clasts of different sizes dragged over a limestone bed (Figure 7.30, solid curves). The roughness of the bed,  $a/\lambda$ , was 0.05 in all cases. As might be expected, the calculations suggested that some bed undulations, those with short wavelengths, would be eroded fastest by 200 mm clasts. However, owing to the variation with  $\lambda$  in the rate of convergence of ice with the bed and the fact that fragments of different sizes are subjected to different effective rates of convergence, the erosion rate increases with both  $\lambda$  and particle size. Hallet also calculated the abrasion rate by varying concentrations of 200 mm clasts (Figure 7.30, dashed curves). The rate first increases with clast concentration, but then declines as interaction of clasts with the bed reduces  $v_p$ .

Iverson (1991a) studied striations on recently exposed limestone in the Canadian Rocky Mountains and in laboratory experiments. He identified two important processes affecting the character of the resulting striations: comminution of the striator tip and rotation of the striator. A striator tip with a leading edge that is normal to the bed ( $\omega = 90^\circ$  in Figure 7.31a) tends to gouge a groove ever deeper into the bed as it is dragged along. This produces a striation that begins as a faint, thin

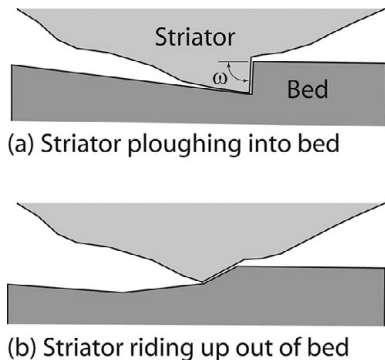


**Figure 7.31** Longitudinal section of an idealized striator tip:  
 (a) with  $\omega = 90^\circ$  plowing a striation. (b) with  $\omega \ll 90^\circ$   
 (due to wear) riding up out of striation.

trace and deepens down flow. If forces on the striator tip eventually exceed its strength and it fails, or if torque on the clast rotates it out of the groove, the striation ends abruptly, often in a deep, steep-walled gouge. If the tip fails gradually, on the other hand, reducing  $\omega$  to  $\leq 45^\circ$ , the striator may ride up out of the groove (Figure 7.31b), leaving a striation that gradually diminishes in size downflow and finally disappears. He also described some striations that began abruptly as deep gouges and then became progressively narrower and shallower downflow. The initial deep gouge was presumably made by a striator that rather abruptly impacted the bed, perhaps by rotation.

Glacial abrasion produces nicely polished bedrock surfaces. Siman-Tov *et al.* (2017) have examined cross sections of these surfaces with transmission electron microscopy, and find that the polish consists of a largely amorphous coating, 1–4  $\mu\text{m}$  thick, within which there are commonly recognizable sub-micron scale mineral fragments broken from underlying grains. Some of the underlying grains are also bent in the direction of glacier movement. The coating fills hollows in and smooths over the rough abraded surface. Blackburn *et al.* (2019) have analyzed the chemical composition of the coating and find that it is enriched in Si and depleted in base cations relative to the bulk chemistry of the underlying rock. They argue that comminution of particles during abrasion increases their surface area, leading to extensive dissolution, and that refreezing of meltwater (in the regelation process) concentrates the Si so that it precipitates. The base cations are carried away in the meltwater. The process is very much like that responsible for  $\text{CaCO}_3$  precipitates (Figure 7.7), except that the amorphous Si is smeared out over the abraded surface, while the  $\text{CaCO}_3$  is concentrated in thicker deposits in the lee of bumps.

### Abrasion of a frozen bed

When the temperature at the base of a glacier is below the pressure melting temperature and the ice is frozen to the bed, it is usually assumed that sliding

cannot take place. For most purposes, this is a reasonable assumption. Shreve (1984), however, showed that, even at subfreezing temperatures, the liquid-like layer at interfaces between ice and foreign particles (including a bedrock bed), could result in regelation of ice past bumps on the bed. For a driving stress of 0.1 MPa and a bed roughness spectrum measured by Nye (1970, pp. 386–387), Shreve calculated sliding rates ranging from  $3.5 \text{ mm a}^{-1}$  at  $-20^\circ\text{C}$  to  $35 \text{ mm a}^{-1}$  at  $-5^\circ\text{C}$ . Echelmeyer and Wang (1987) measured a sliding speed of  $180 \text{ mm a}^{-1}$  at  $-4.6^\circ\text{C}$  under Urumqi Glacier No. 1 in Tibet. After adjusting for differences in driving stress and bed roughness, this speed was consistent with Shreve's theory. These sliding speeds are too low to be of significance glaciologically. However, over a period of years they could result in striations, a possibility which should give nightmares to glacial geologists who commonly interpret striations to be evidence of a thawed bed.

## Drumlins and flutes

Drumlins and flutes are two remarkable, yet poorly understood bedforms that likely involve some combination of erosion, deposition, and till deformation. Drumlin fields are typically located within a few tens of kilometers of moraines marking the ice margin at the time of drumlin formation. This suggests that the drumlins formed beneath the ablation zone or near the transition from the accumulation to the ablation area, a place where basal temperatures are likely to transition from frozen to thawed (Figure 6.12). Downflow, drumlins may become increasingly elongate, eventually grading into flutes. Flutes may occur in the absence of drumlins as, for example, in the beds of former ice streams.

### Drumlins

Streamlined bedforms like drumlins can undoubtedly be formed in a variety of ways, but the existence of fields of several tens or even hundreds of drumlins argues convincingly for an explanation involving an instability (Patterson and Hooke, 1995). A state of unstable equilibrium is one in which a system will remain in equilibrium as long as it is not perturbed. A marble balanced on top of an inverted bowl is an example (Figure 7.32b). If the marble is nudged, it will roll down the side of the bowl. In contrast, a marble inside an upright bowl would be in stable equilibrium, as any perturbation displacing it from the bottom of the bowl would set up (gravitational) forces tending to return it to the bottom (Figure 7.32a). In the case of drumlins, it is possible that, under certain conditions, ice flow past a low hill could set up a flow field leading to erosion on either side of the hill or deposition on top of it, or both. We know from exposures of drumlin interiors that both erosion and deposition can be involved in drumlin formation, albeit in different proportions in different drumlins (Patterson and Hooke, 1995).

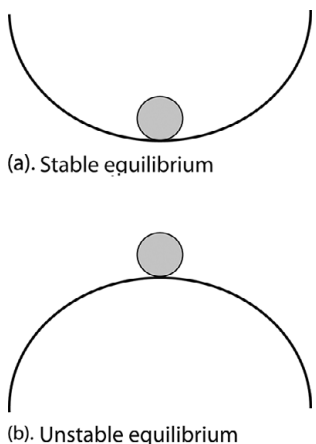


**Figure 7.32** Examples of (a) stable equilibrium, and (b) unstable equilibrium.

Patchy areas of frozen bed in low hills, such as might occur at a transition from a frozen to a thawed bed (Figure 6.12), are one possible perturbation. The geothermal heat flux in such a hill would be focused on thawed areas between frozen patches, keeping them wet and the frozen patch cold (Figure 6.13). A frozen patch strong enough to resist entrainment by the glacier would increase drag on the glacier sole relative to that in adjacent thawed zones. Conservation of mass then requires that a slight dimple develop in the glacier surface. (Depressions in the lees nunataks are an extreme form of this dimpling.) Bedrock hills or patches of well-drained, and thus relatively strong sediment could have the same effect (Boulton, 1987). Surface slopes into the dimple from either side would drive downflow-converging lateral flows near the bed, similar to that measured by Raymond (1971) on Athabasca glacier (Figure 5.12). Schoof and Clarke (2008) show theoretically that such spiral flow may occur in basal ice, and Gudmundsson *et al.* (1998) think that such dimples, seeded by bed perturbations, spawn the low flow-parallel ridges characteristic of the surfaces of ice streams.

In the case of the hill in Figure 6.13, Hooke and Medford (2013) argued that lateral flow would drag material from the thawed areas diagonally up onto the cold hill. They showed that, at the top of the hill, heat flow upward into the ice from the ice/bed interface should exceed the geothermal flux to the interface, so freezing would be likely there. They thought this would lead to deposition of till dragged from the flanks. Iverson (written communication, April 19, 2013), however, suggested that the till might instead be frozen to the base of the glacier and carried away. Many drumlins have only a thin carapace of till deposited by the drumlin-forming ice sheet, so the latter may be common. In either case, erosion of the thawed areas would increase the relief.

In a series of papers Hindmarsh (1998), Fowler (2000), and most recently Stokes *et al.* (2013) have argued for an alternative instability – one that involves shear in

ice flowing over a deformable till. They assume: (i) a sliding law relating  $\tau$ ,  $u_b$ , and  $N_e$ , (ii) that the sediment flux in the deforming till layer scales with  $\tau$  and  $N_e$ , resulting in a deforming layer tens of centimeters to a meter or so in thickness, and (iii) that ice is Newtonian viscous ( $n = 1$ ). The instability occurs because when ice flows over a low bump, compressive stresses are higher on the stoss side of the bump. If the effective viscosity of the till is low compared with that of the ice, however, the interfacial velocity will remain approximately constant. This results in more till flowing into the bump than out of it, causing it to grow.

## Flutes

Flutes range in height from a few centimeters to many meters, and in length from a meter or so to several kilometers. Wavelengths (the transverse distance between ridge crests) of large flutes may reach tens to hundreds of meters. Very large ones may reach heights of 40–50 m.

As with drumlins, both erosional and depositional processes are likely involved in the formation of flutes. Till fabric measurements on the flanks of some flutes display a herringbone pattern with long axes on opposite flanks converging downflow, suggesting that the flute-forming material was either dragged diagonally up their flanks or squeezed in from below (Figure 7.33) (Shaw and Freschauf, 1973; N. Jones, 1982). Backhoe trenches across a long, 10–15 m high flute in North Dakota revealed highly-contorted laminated lake beds, gravelly sandy silty till, and sandstone blocks derived from the bedrock, suggesting viscoplastic flow of till into the flute (Bluemle *et al.*, 1993). Individual flutes are also commonly flanked by troughs (Figure 7.33)(e.g. Rose, 1989; Benn, 1994); it is generally inferred that these are erosional, and that the material eroded from them was either squeezed laterally into the flute or dragged diagonally up onto it. In a flute in Saskatchewan, however, till fabrics 3–4 m below the crest indicated ice flow at  $\sim 45^\circ$  to the crest, reflecting an earlier ice advance for which there was

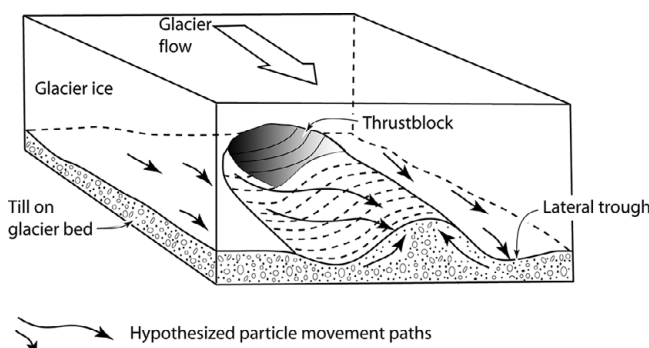


**Figure 7.33** Sketch showing possible movement of deforming till into a flute forming in lee of a thrust block.

independent evidence (Gravenor and Meneley, 1958). In this case lateral viscoplastic flow of till into the flute is less likely.

Some flutes, like drumlins, may be seeded by frozen patches or low hills. However, Bluemle *et al.* (1993) found that the stoss ends of many flutes began at small thrust blocks which rose to the same height or slightly higher than the flute (Figure 7.33). The thrust blocks may be a few tens of meters long and 2–4 m thick.

At the distal end of a developing flute there is likely to be a zone of low pressure, much as there is in the lee of a roche moutonnée. A cavity formed here is a possible sink for material dragged or squeezed from bordering troughs. This would lengthen the flute. Relatively thin ice beneath the lower part of the ablation zone, or relatively fast ice flow as at the base of an ice stream would facilitate formation and maintenance of such a cavity, and once the till was deposited, overconsolidation might make it resistant to erosion.

---

## SUMMARY

In this chapter we have explored the coupling between glaciers and both rigid and deformable beds. In the former, the dominant processes by which ice moves past irregularities on the bed are regelation and plastic flow. As small obstacles are accommodated more readily by regelation and larger obstacles by plastic flow, there are, theoretically, obstacles of intermediate size which exert more drag on a glacier than do larger or smaller ones, at least if the roughness is constant. This intermediate size has come to be called the controlling obstacle size, although on a glacier bed with a continuum of obstacle sizes and roughnesses, the concept of a “controlling” size becomes less relevant.

Theoretically, the speed with which ice moves past obstacles by regelation is proportional to  $\tau_b$ , whereas in plastic flow it is proportional to  $\tau_b^3$ . When both processes are involved,  $u_b \propto \tau_b^2$ . However,  $\tau_b$  is a dependent variable; the independent variable is  $\tau_d$ . If  $\tau_d$  changes, say due to a change in  $P_w$ ,  $u_b$  changes and this changes  $\tau_b$ . The equilibrium condition is  $\tau_b = \tau_d$ .

The theory of sliding over rigid beds is imperfect because it does not take into account friction resulting from rock fragments entrained in the basal ice and dragged over the bed, local freezing of the ice to the bed, certain complications in the regelation theory for obstacles of irregular geometry, impurities in the melt water formed during regelation, and effects of changing water pressure. A good deal of recent research has been focused on the last of these effects. Increases in water pressure can increase sliding speed by hydraulic jacking and, over somewhat longer time spans, by increasing the degree of separation of the glacier from the bed.

Our understanding of movement of glaciers over soft beds is still modest. It is well known that the strength of granular materials depends on cohesion, on friction between individual grains, and on the need for such materials to dilate before appreciable deformation can occur. Once the strength is exceeded, however, we wish to know the relation between the stress and the strain rate. Theoretical considerations, geotechnical studies, and field measurements suggest that  $\dot{\varepsilon} \propto e^{\gamma\tau}$ , with  $\gamma$  fairly large and either positive or negative.

Factors controlling the velocity profile in deforming subglacial till and the depth to which deformation extends are still elusive, complicating our efforts to account for the accumulation of large volumes of till during the Pleistocene. A glacier may become decoupled from a soft bed so that it glides over it without deforming it significantly. Plowing, on the other hand, may increase the coupling, but it also increases the pore water pressure in the till, thus concentrating deformation near the interface. When the subglacial water pressure is low, ice can regelate into the bed, increasing coupling. Random activation of shear zones at different depths may distribute deformation over some depth. Fluctuating water pressures could result in shear zones developing at different and greater depths in the till, facilitating sediment transfer.

Geothermal and frictional heat melt basal ice, resulting in ice flow toward the bed. As this ice regelates and flows past clasts resting on the bed, it forces the clasts against the bed. These clasts abrade the bed when dragged across it. Rotation of the clasts results in different types of striation.

Irregularities in the bed likely result in ice flow patterns that redistribute till, forming drumlins and flutes. Drumlin fields undoubtedly reflect some kind of instability. Flutes appear to form under ice that is thinner or moving faster, perhaps reflecting deposition in a low pressure zone at the downflow end of the flute.

# 8

# Water flow in and under glaciers: Geomorphic implications

A great deal has been learned about water flow through and beneath glaciers in the past four decades. Much of the progress has been theoretical, as experimental techniques for studying the englacial and subglacial hydraulic systems are few and not yet fully exploited, and observational evidence is difficult to obtain for obvious reasons. An added benefit of the recent progress is that we have gained a much better understanding of glacial erosional processes and of the origin of certain glacial landforms that owe their existence to the interaction between water and ice.

We begin this chapter with a discussion of the development and geometry of englacial water conduits in temperate glaciers. Then, the subglacial part of the system is examined. Finally, we consider geomorphic implications of some of the recent research.

## The englacial hydraulic system

### Veins and the initial development of passages in the upper part of the system

Nye and Frank (1973) argued that veins should be present along boundaries where three ice crystals meet, and that, at four-grain intersections, these veins should join to form a network of capillary-sized tubes through which water can move. They, thus, concluded that temperate ice should be permeable.

Such veins and capillary passages have been observed in ice cores obtained from depths of up to 60 m on Blue Glacier, Washington (Figure 8.1a) (Raymond and Harrison, 1975). The veins are triangular in shape (Figure 8.1b) and roughly 25  $\mu\text{m}$  across.

Estimates of the permeability of glacier ice resulting from this vein system vary widely. Expressed in terms of the thickness of a water layer that would be transmitted downward into the ice, values range from  $\sim 1 \text{ mm a}^{-1}$  in coarse-grained ice with relatively few crystal boundaries per unit volume (Raymond and Harrison, 1975) to  $1 \text{ m a}^{-1}$  in fine-grained ice (Nye and Frank, 1973). One source of uncertainty is the likelihood that air bubbles located on veins would block water movement. Lliboutry (1996) estimated that the probability,  $P_b$ , of a vein being blocked is:

(a)

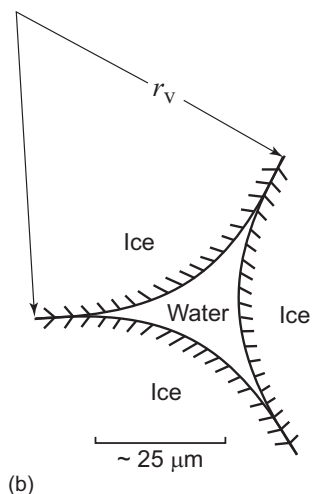
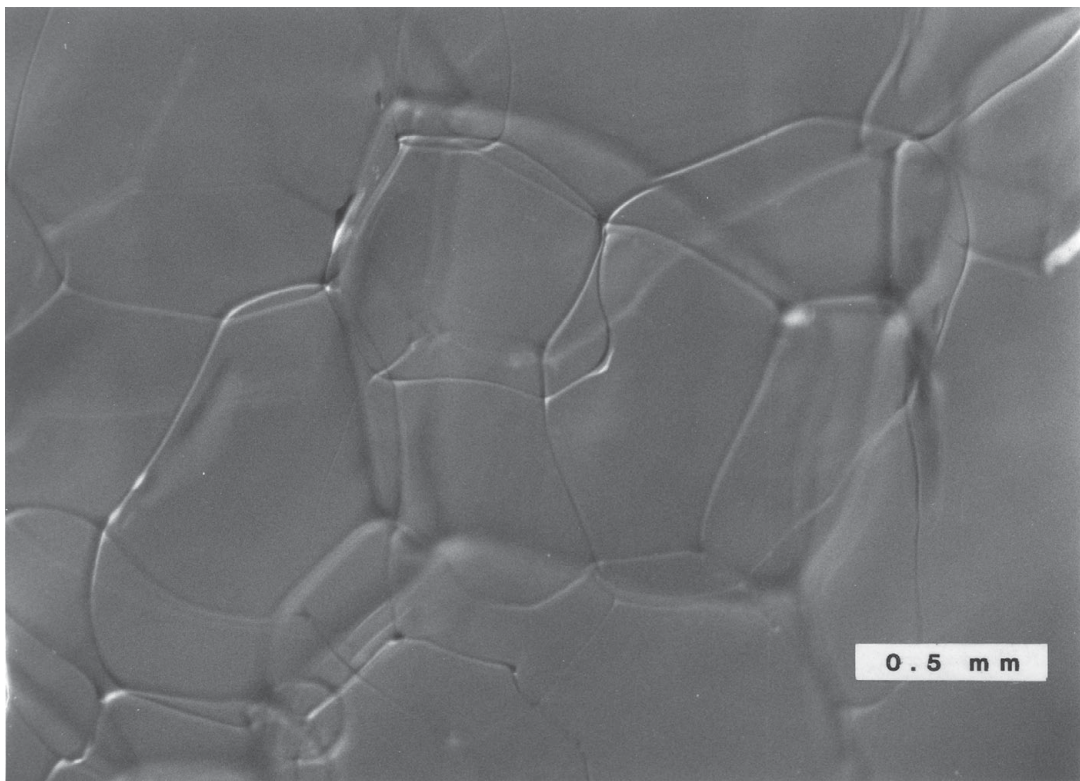


**Figure 8.1** (a) Veins in ice from Blue Glacier. (b) Cross section of a vein with approximate scale. (c) Millimeter-sized tubes from a depth of 20 m in Blue Glacier (White marks are 100 mm apart). (a and c from Raymond and Harrison, 1975. Reproduced with permission of the authors and the International Glaciological Society)

(c)

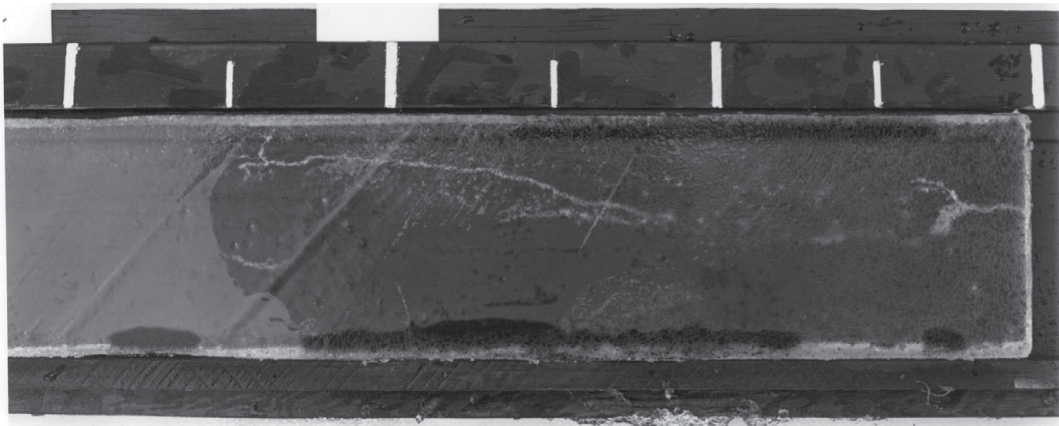


**Figure 8.1 (cont.)**

$$P_b = \frac{3\sqrt{v_a}}{4d_b} \left( 1 - \frac{\rho_{bi}}{\rho_i} \right)$$

where  $v_a$  is the cross sectional area of veins per unit area,  $d_b$  is the bubble diameter, and  $\rho_{bi}$  and  $\rho_i$  are the densities of bubbly and bubble-free ice respectively. As  $\rho_{bi}/\rho_i$  is normally close to unity, the probability of a vein being blocked is low. The inverse dependence on  $d_b$  may seem odd, but it arises because, for a given  $\rho_{bi}$ , there are fewer bubbles when they are large. Bubbles, however, may occur preferentially on grain boundaries, in which case this analysis underestimates  $P_b$ .

Water moving through such a vein system dissipates viscous energy in the form of heat. The amount of heat produced is proportional to the water flux. To a first approximation, the ice is already isothermal and at the pressure melting point. Thus, the heat cannot be conducted away from the veins, but instead must be consumed by melting ice. In this way, passages could be enlarged. Shreve (1972) and Röhlisberger (1972) argued that, when two such passages of unequal size separate and rejoin, the larger passage would carry more flow per unit of wall area and thus would be enlarged at the expense of the smaller passage. They suspected that some veins would become enlarged to millimeter-scale tubes a short distance below the surface.

Raymond and Harrison confirmed the existence of such tubes in ice from a depth of 20 m in Blue Glacier (Figure 8.1c). The tubes formed an upward-branching arborescent network, as expected. Because the Shreve-Röhlisberger argument applies equally well to larger anastomosing passages, we may imagine that, at greater depths, the arborescent network would continue to evolve, with ever larger conduits developing. These conduits would drain water produced by strain heating in the deforming ice in addition to that from the surface.

Water movement through a vein system in ice is not Darcian, however, because ice deforms. Lliboutry (1996) studied this. Near the glacier surface he considered the water pressure in the vein system,  $P_w$ , to be only slightly less than the ice pressure,  $P_i = \rho_i gh + \sigma_e$ , where  $h$  is the depth below the surface and  $\sigma_e$  is a pressure due to longitudinal and other stresses (e.g. Equation 2.10). Owing to the contribution of  $\sigma_e$ , he thought  $P_w$  would commonly exceed the hydrostatic pressure,  $\rho_w gh$ , near the glacier surface, and water flow thus would be *upward* in a surface boundary layer a couple of meters thick. This would preclude percolation of surface water.

Lliboutry (1996) further thought that changes in cross sectional area of a vein by plastic deformation or by dissipation of viscous energy would be negligible in comparison with changes due to heat flow to veins from the surrounding ice. The ice temperature in a vein wall,  $\theta_{mv}$ , is given by Equation (2.1):

$$\theta_{mv} = \theta_{TP} - \frac{\mathbf{C}P_v}{L\rho_i r_v} - \zeta \frac{s}{W} \quad (8.1a)$$

in which  $r_v$  is the radius of curvature of the vein wall (Figure 8.1b),  $P_v$  is the pressure in the ice near the interface,  $\gamma_{SL}$  is the liquid–solid interface energy ( $0.34 \text{ N m}^{-1}$ ) and the other symbols are as defined in Chapter 2. (Note that  $\gamma_{SL}/r_v$  is a pressure,  $\text{N m}^{-2}$ .) Owing to the curvature of the vein wall, the pressure in the ice is  $\gamma_{SL}/r_v$  higher than that in the water, thus:  $P_v = P_w + (\gamma_{SL}/r_v)$ .

A lens, on the other hand, has two convex sides with radii  $r_L$ , and the ice is on the convex side. The third term on the right in Equation 8.1a is thus positive, and multiplied by 2:

$$\theta_{mL} = \theta_{TP} - \mathbf{C}P_L + \frac{2\theta_{mK}\gamma_{SL}}{L\rho_i r_L} - \zeta \frac{s}{W}, \quad (8.1b)$$

and the pressure in the ice near the lens,  $P_L$ , is  $2r_v/\gamma_{SL}$  lower than that in the water, thus:  $P_L = P_w - (2\gamma_{SL}/r_L)$ .

In the short distance between a lens and a vein,  $\theta_{TP}$  won't change, so if  $P_w$  and the solute content,  $s$ , are the same in the lens and the vein, as might be expected, and noting that  $2/r_L \ll 1/r_v$ , the temperature difference is:

$$\theta_{mL} - \theta_{mv} = \frac{\gamma_{SL}}{r_v} \left( \mathbf{C} + \frac{\theta_{mK}}{L\rho_i} \right).$$

This temperature difference drives heat flow from the lens to the vein, reducing the size of the lens and increasing that of the vein. As the size of the vein increases, however,  $r_v$  decreases. Thus, eventually, the heat flow is reduced to the point where it simply keeps the water in the vein at the pressure melting temperature which, owing to the slightly lower pressure in the water, is higher than that in the ice by an amount  $C(P_i - P_w)$ . Lliboutry argues that this heat flow is the primary factor controlling vein size.

Once a depth is reached where  $P_w > P_i$ , Lliboutry thought veins could become enlarged, forming the millimeter-scale tubes observed by Raymond and Harrison.

## Connections to the surface

In the accumulation area, one can visualize continuous connections between a vein system and the overlying porous firn. As the veins do not necessarily transmit downward all of the percolating meltwater, and may not transmit any of it, a local water table commonly forms in the firn (Vallon *et al.*, 1976; Fountain, 1989). Measurements of the slope of this water table in the vicinity of crevasses demonstrate that the latter are the principal conduits for movement of water deeper into the glacier (Fountain, 1989).

In the ablation area there may be a surface layer of cold ice, several meters thick. This cold layer forms on glaciers in continental climates where snowfall is low enough to allow appreciable cooling of the ice by conduction during the winter. It is less likely to form in more maritime climates where larger snowfalls form an effective insulating layer. When present, it is likely to persist well into the melt season, if not entirely through it, and thus forms an effective barrier to penetration of surface meltwater by veins. So it is, again, principally by way of crevasses that surface water reaches the interior of the glacier.

When a crevasse first forms, it may fill with water and overflow. In larger crevasses, however, this situation normally does not persist for long. It seems probable that, once a crevasse penetrates deep enough to intersect the millimeter-scale conduit system, increasing the water supply to these conduits dramatically, the conduits are quickly enlarged until they can transmit all of the incoming water downward into the glacier.

In the ablation area of the Greenland Ice Sheet, 30 km from the ice sheet margin, surface streams draining into crevasses have, in some cases, kept them filled with meltwater. This apparently allowed them to propagate (Chapter 4) through over 1000 m of ice to the glacier bed (Zwally *et al.*, 2002; Stevens *et al.*, 2015). In one case, water reaching the bed through nearby moulin ponds there over a period of 6–12 hours, lifting the ice and stretching the glacier surface, thus causing a tensile fracture at the surface. The fracture occurred under a lake, and the lake drained in 1–2 hours (Stevens *et al.*, 2015). The same sequence of uplift, fracture, and drainage occurred in three successive years, 2011–2013.

Crevasses may close as they are moved into an area, or are rotated into an orientation such that stresses across them are compressive. However, where melt streams in the ablation area pour into such a crevasse, the viscous and potential energy dissipated maintains a connection to the englacial conduit system. The hole thus formed in the glacier surface is called a *moulin*.

When a new crevasse opens across a melt stream upglacier from a moulin, it cuts off the water supply to the moulin. Lacking an energy source, the moulin is constricted by inward flow of ice, and during the winter its upper part fills with

snow. In due course, the snow becomes saturated with water which eventually freezes. These processes result in distinctive structures in the ice.

Over a period of several years, Holmlund (1988) carefully mapped such structures on Storglaciären as ablation exposed ever deeper levels in the glacier. He also descended into some of the moulin during the winter. He found that moulins there are typically 30–40 m deep, although deeper ones occur on other glaciers, that channels leading from the bottoms of moulins typically meander and trend in the direction of the initiating crevasse, and that after some distance the channel ends in a conduit leading downward into the glacier.

Our task now is to consider the geometry of the englacial drainage system deeper in the glacier, below the level of Holmlund's mapping.

### The englacial drainage system at depth

Field studies have yielded some insights into the nature of the englacial drainage system below the depths reached by moulins. In tunnels melted along the bed of Bondhusbreen, a glacier in Norway, cylindrical englacial conduits were encountered a couple of meters above the glacier bed on three occasions (Hooke *et al.*, 1985). One was ~100 mm in diameter and had a bed of well-rounded 50–100 mm diameter stones, partly embedded in the ice. Another was ~30 mm in diameter and actively discharging water. Similar englacial conduits have been observed emerging in ice cliffs at glacier margins.

Boreholes in Storglaciären have intersected englacial conduits on numerous occasions. From such data, Hooke and Pohjola (1994) estimated that there were likely about five conduits in every 100 m<sup>2</sup> of glacier cross section, of which only one or two were active. Active conduits were encountered only at depths >50 m, presumably reflecting the cold surface layer in the ablation area of this glacier. In video images, most conduits appeared to be either irregular or oval, though some seemed to be horizontal cracks. Estimated flow velocities in the conduits, based on dye trace tests, were 0.02–0.08 m s<sup>-1</sup>.

Subsequently, also on Storglaciären, Fountain *et al.* (2005) encountered a slightly lower density of conduits, but a similar fraction were active. Their imaging suggested that most of the conduits were steeply-dipping fractures, with orientations reflecting the stress regime in the glacier. The median fracture width was 40 mm. They also encountered a cylindrical conduit, 0.1 m in diameter, at a depth of 42 m. The conduit paralleled surface crevasses and was normal to the flow direction. Such an orientation is consistent with Holmlund's observations. Flow speeds in the passages ranged from 0.005 to 0.04 m s<sup>-1</sup>. Fountain *et al.* view fracturing as an on-going process, continually reorganizing and refreshing the englacial drainage system. They believe that such fracture-dominated systems are likely characteristic of all temperate glaciers.

## Equipotential surfaces in a glacier

In a permeable medium, water flows in the direction of the negative of the maximum gradient of the potential,  $\Phi$ , where  $\Phi$  is defined by:

$$\Phi = \Phi_0 + P_w + \rho_w g z. \quad (8.2)$$

Here,  $\Phi_0$  is a reference potential,  $P_w$  is the pressure in the water,  $\rho_w$  is the density of water,  $g$  is the acceleration due to gravity, and  $z$  is the elevation above some datum level such as sea level.

To gain some appreciation for this concept, consider the situation in a lake (Figure 8.2). Let  $\Phi = \Phi_1$  at point 1 on the lake surface. At point 2 at depth  $\Delta z$ ,  $P_w$  is  $\rho_w g \Delta z$  higher, but the third term on the right in Equation (8.2) is lower by the same amount. Therefore,  $\Phi_2 = \Phi_1$  and there is no flow between points 1 and 2. However, if the lake surface slopes gently toward the outlet, moving horizontally at constant  $z = z_2$  from point 2 to point 3 will result in a decrease in  $P_w$ , and hence in  $\Phi$ . Flow will then be toward the position of lower  $P_w$ , which is also a position of lower  $\Phi$ . In other words, it is not the gradient in  $P_w$  that controls the direction of flow, but the gradient in  $\Phi$ . (Remember this whenever you hear about flow being driven by a pressure gradient!)

To determine the potential field in a glacier from Equation (8.2), we must determine  $\Phi$ , and hence  $P_w$ , everywhere.  $P_w$  is not hydrostatic because the water is moving, and most of it is a long way from the surface through many small passages.

In an englacial system of cylindrical conduits or in conduits at the glacier bed, the pressure in the ice,  $P_i$ , differs from that in the water, and the ice deforms as a result.  $P_w$  rarely exceeds  $P_i$  significantly, but it can be much less than  $P_i$ . Passages may thus expand slightly at very high water pressures, and they close rapidly at low pressures. In addition, as noted, viscous heat melts conduit walls, enlarging passages. In a steady state, the rate of closure of passages,  $u_c$ , equals the melt rate,  $m$  (Figure 8.3), so the net rate of increase in passage size,  $\dot{r}$  ( $= m - u_c$ ), is 0. (Although mathematically untidy, note that we have defined positive  $u_c$  as being inward, while

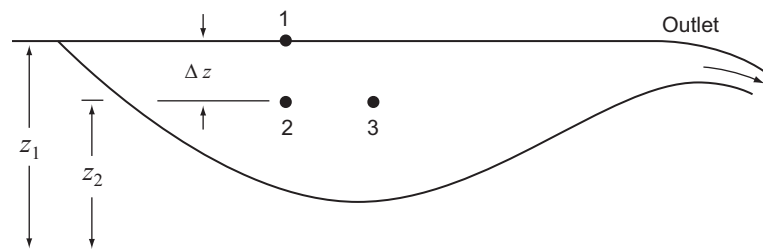


**Figure 8.2** Illustration of difference between pressure field and potential field.

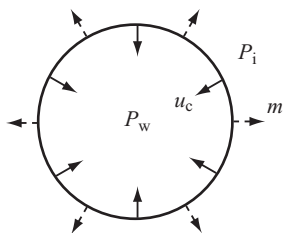


**Figure 8.3** In a steady state, closure of a cylindrical conduit,  $u_c$ , is balanced by melt,  $m$ .

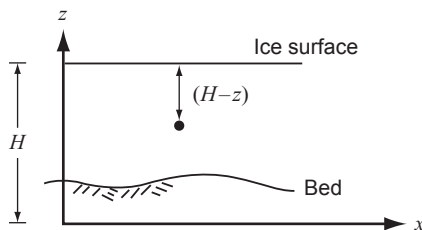


**Figure 8.4** Coordinate axes used in discussion of conduit closure.

positive  $m$  is outward. This simplifies some of the later equations.) In a fracture-dominated englacial system, water flow is so slow that  $m$  is negligible, but in passages carrying higher discharges this effect cannot be neglected.

As usual, we'll assume that the flow of ice can be represented by Glen's flow law,  $\dot{\varepsilon}_e = A\sigma_e^{-n}$ , and that ice is incompressible and isotropic. The pressure causing creep closure of the passages,  $P_c$ , is:

$$P_c = P_i - P_w. \quad (8.3)$$

To a good approximation,  $P_i = \rho_i g (H - z)$ , where  $H$  is the elevation of the ice surface above the datum level (Figure 8.4). Then:

$$\frac{u_c}{r} = A \left( \frac{P_c}{n} \right)^{\frac{1}{n}} \quad (8.4)$$

(Nye, 1953). This relation will be derived in Chapter 12 (Equation 12.21). In the derivation it is assumed that  $\sigma_e = \sigma'_{rr}/\sqrt{2}$ , where  $\sigma'_{rr}$  is the radial stress deviator, so other components of the deviatoric stress tensor, and hence of the strain rate tensor, are assumed to be negligible (see Equation 2.10). Thus, deformation of the ice, other than that resulting from the presence of the passage, is neglected. In the present application, in which this assumption is clearly violated, we add a multiplying factor,  $K$ , which is  $\sim 1$ .  $K$  equals 1 if  $\sigma_e = \sigma'_{rr}/\sqrt{2}$ . Rearranging and substituting for  $P_c$  and  $P_i$ , we can rewrite Equation (8.3) as:

$$P_w = \rho_i g (H - z) - K n \left( \frac{u_c}{A r} \right)^{\frac{1}{n}} \quad u_c \geq 0. \quad (8.5)$$

(If  $u_c < 0$ , implying that the passage is opening as a result of water pressures in excess of the ice pressure,  $|u_c|$  must be used, and the sign of the second term adjusted accordingly, but  $u_c < 0$  is rare in nature.) In a fracture-dominated system in which  $u_c$  is negligible, the last term on the right can be neglected. In a conduit system, in excess of a couple of kilometers from the glacier terminus, changes in  $K$ ,  $u_c$ , and  $r$  with distance along a tunnel are small, so this term can be taken to be constant. Thus, combining Equations (8.2) and (8.5) and taking the derivative with respect to an arbitrary direction,  $s$ , yields:

$$\frac{\partial \Phi}{\partial s} = \rho_i g \frac{\partial(H - z)}{\partial s} + \rho_w g \frac{\partial z}{\partial s}. \quad (8.6)$$

To determine the orientations of equipotential planes in the glacier, we make use of the fact that, if  $s$  lies in such a plane,  $\partial\Phi/\partial s = 0$ , so:

$$-(\rho_w - \rho_i) \frac{\partial z}{\partial s} = \rho_i \frac{\partial H}{\partial s}. \quad (8.7)$$

Our objective is to define the dip of this plane,  $\varphi$ . The dip in some horizontal direction,  $x$ , will be  $dz/dx$  (Figure 8.5). Therefore, multiplying Equation (8.7) by  $\partial s/\partial x$  and rearranging gives:

$$\frac{\partial z}{\partial s} \frac{\partial s}{\partial x} = -\frac{\rho_i}{\rho_w - \rho_i} \frac{\partial H}{\partial s} \frac{\partial s}{\partial x}$$

or, inserting numerical values for the respective densities, letting  $\alpha = dH/dx$ , the slope of the glacier surface, and noting that  $\tan \varphi = dz/dx$ :

$$\varphi \approx -\tan^{-1}(11 \tan \alpha). \quad (8.8)$$

Thus, the equipotential planes dip upglacier (note the minus sign) with a slope of about 11-times the slope of the glacier surface (Figure 8.6), a result first obtained by Shreve (1972). Water entering the glacier from the surface thus should reach the bed some distance downglacier from the entry point. In support of this, Iken and Bindschadler (1986) found that pressure fluctuations in boreholes drilled to the bed of Findelengletscher, just below the firn edge, did not correlate with marked variations in stream flow entering nearby moulin. Rather, the pressure fluctuations seemed to reflect a slower delayed input of water through the snow cover above the firn edge.

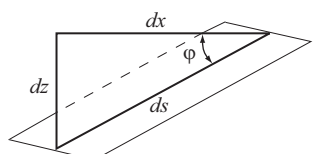


**Figure 8.5** Sloping conduit, showing relation between  $dx$ ,  $dz$ ,  $\varphi$ , and  $ds$ .

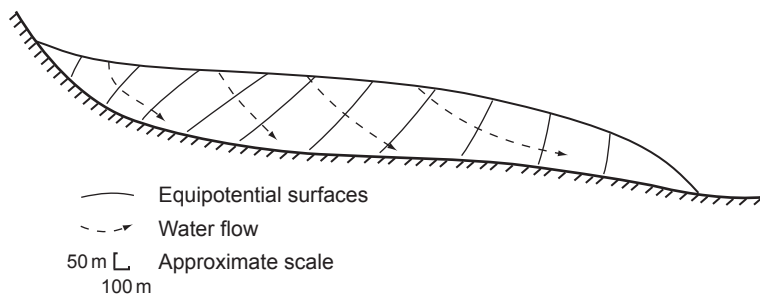


**Figure 8.6** Longitudinal section of a glacier showing up-glacier-dipping equipotential surfaces and the theoretical directions of englacial water flow. (After Hooke, 1989, Figure 1)

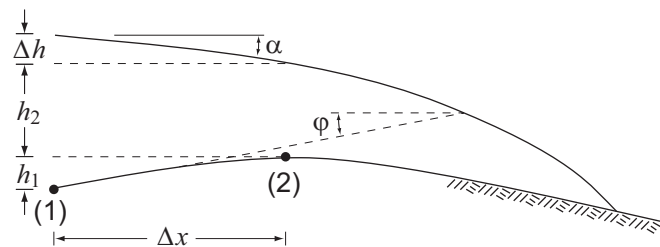


**Figure 8.7** Sketch illustrating alternative derivation of dip of equipotential planes in a glacier.

### Alternative derivation of equipotential-plane dip

Consider the situation in Figure 8.7. There is a conduit along the bed between points 1 and 2. We wish to determine under what conditions the upglacier slope of the hill will be parallel to an equipotential plane so that water in the conduit will not flow. The ice pressure at (1) is  $P_{i1} = \rho_i g(h_1 + h_2 + \Delta h)$ , and that at (2) is  $P_{i2} = \rho_i g h_2$ . In the absence of water flow and conduit closure, the pressure in the water at (1),  $P_{w1}$ , would be the sum of  $P_{i2}$  plus the hydrostatic head in the conduit,  $\rho_w g h_1$ . If  $P_{i1} > P_{w1}$ , the conduit will begin to close and water will be forced out over the hill. Thus, the condition we seek is  $P_{i1} = P_{w1}$ , or:

$$\rho_i g(h_1 + h_2 + \Delta h) = \rho_i g h_2 + \rho_w g h_1. \quad (8.9)$$

Solving this for  $h_1$ , dividing by  $\Delta x$ , noting that  $\alpha = -\Delta h/\Delta x$  and  $\tan \varphi = h_1/\Delta x$ , and inserting numerical values for the densities leads directly to Equation (8.8) Q.E.D.

### Types of subglacial drainage system

Subglacial drainage systems that transfer water quickly are commonly referred to as *channelized* or *efficient*. Systems through which water moves slowly are called *distributed* or *inefficient*.

Röthlisberger (1972) analyzed an efficient system consisting of a straight, cylindrical conduit in ice at the glacier bed. His theoretical development can easily be modified to apply to a slightly more realistic semicircular conduit, melted upward into the ice. Such conduits have come to be called *R channels*. Some tunnels emerging at glacier margins are roughly semicircular, while others are wide and not so high.

Nye (1973b) suggested, alternatively, that channels might be incised into the bedrock bed of a glacier. Such channels, frequently called *Nye* or *N channels*, have also been described (Walder and Hallet, 1979; Hallet and Anderson, 1980). They are typically 0.1–0.2 m deep and 0.2–0.5 m wide, although some reach widths and depths of several meters. Nye channels are not common, perhaps because changes in ice surface profile, movement of the ice, and melting of the conduit walls can all displace streams laterally, so they do not stay in one place long enough to erode a channel.

Kamb (1987) described and analyzed a distributed, hard-bed drainage system that he called a linked cavity system, consisting of cavities in the lees of steps in the bed, linked together by orifices that retard the flow. The orifices make the system inefficient.

Finally, there are drainage systems on soft beds. These are substantially more complicated to analyze, as sediment transport and creep of the sedimentary bed must be included (Ng, 2000a).

We'll begin by considering melt rates in conduits and then use that analysis in the Röthlisberger model.

## Melt rates in conduits

### Temperate ice

Let's consider the rate of melting of the walls of a conduit at the bed of a temperate glacier (Shreve, 1972). The total amount of energy available per unit length of conduit,  $\Delta s$ , per unit time is:

$$\frac{Q}{\text{m}^3/\text{s}} \cdot \frac{\partial \Phi}{\partial s} \cdot \Delta s = \frac{N - m}{\text{m}/\text{s}} = \frac{\text{J}}{\text{s}} \quad (8.10)$$

Some of this energy must be used to warm the water to keep it at the pressure melting point as ice thins in the downglacier direction. The rest is available to melt ice, thus:

$$\frac{m}{s} (\pi r \Delta s) \rho_i L + \rho_w Q C_w \mathbf{C} \frac{\partial(H - z)}{\partial s} \rho_i g \Delta s = Q \frac{\partial\Phi}{\partial s} \Delta s \quad (8.11)$$

$\frac{m}{s}$     $m$     $m$     $\frac{kg}{m^3}$     $\frac{J}{kg}$     $\frac{kg}{m^3}$     $\frac{m^3}{s}$     $\frac{J}{kgK}$     $\frac{K}{N/m^2}$     $\frac{m}{m}$     $\frac{kg}{m^3}$     $\frac{m}{s^2}$     $m$ .

Here,  $r$  is the radius of a semicircular conduit,  $L$  is the latent heat of fusion,  $C_w$  is the heat capacity of water,  $\mathbf{C}$  is the change in the melting point per unit of pressure ( $K Pa^{-1}$ ), and  $Q$  is the discharge (not the activation energy as in Chapter 4). As you will see from inspection of the terms and the dimensions of the various quantities in them, the first term on the left is the energy available to melt tunnel walls. In the second,  $\rho_w Q C_w$  is the energy needed per unit time to warm the water  $1^\circ C$  and  $(\partial(H - z)/\partial s) \cdot \rho_i g \Delta s$  is the pressure change over the distance  $\Delta s$ . The latter times  $\mathbf{C}$  is the number of degrees the water must warm to keep it at the pressure melting point. Here, we have implicitly taken the positive  $s$ -direction to be upglacier, in the direction opposite to that of the water flow. Thus, both  $\partial\Phi/\partial s$  and  $\partial(H - z)/\partial s$  are positive.

It is common to define  $k = \rho_w C_w \mathbf{C}$ . Inserting numerical values [ $\rho_w = 1000 kg m^{-3}$ ,  $C_w = 4218 J kg^{-1} K^{-1}$  at  $0^\circ C$ , and  $\mathbf{C} = 0.098 \times 10^{-6} K Pa^{-1}$ ] we find that  $k = 0.413$  and that it is dimensionless. Here, we've assumed that the water is saturated with air, as glacier ice normally contains air bubbles.

Then, using Equation (8.6) and dividing by  $\Delta s$  yields:

$$m\pi r \rho_i L + k \left( \frac{\partial\Phi}{\partial s} - \rho_w g \frac{\partial z}{\partial s} \right) Q = Q \frac{\partial\Phi}{\partial s}$$

or, solving for  $m$ :

$$m = \frac{Q \left[ (1 - k) \frac{\partial\Phi}{\partial s} + k \rho_w g \frac{\partial z}{\partial s} \right]}{\pi r \rho_i L}. \quad (8.12)$$

It is interesting to insert some numbers into this Equation to get a sense of the magnitude of  $m$ . Consider a horizontal tunnel so  $\partial z/\partial s = 0$ . Suppose the tunnel has a radius of 0.25 m and that it is under a glacier with a surface slope of 0.01. To determine  $Q$  we now need a relation between the mean velocity over the tunnel cross section,  $\bar{v}$ , and the tunnel roughness. The Gaukler-Manning-Strickler equation is one of two that is commonly used for such calculations. It is:

$$\bar{v} = \frac{Q}{\frac{1}{2} \pi r^2} = \frac{R^{2/3} S^{1/2}}{\tilde{n}} \quad (8.13)$$

where  $R$  is the hydraulic radius of the tunnel, or the cross-sectional area divided by the wetted perimeter (so  $R = \pi r / 2(\pi + 2)$  in a semicircular tunnel),  $S$  is the non-dimensional headloss:

$$S = \frac{1}{\rho_w g} \frac{\partial \Phi}{\partial s} \quad (8.14)$$

which is approximately equal to the glacier surface slope, and  $\tilde{n}$  is known as the Manning roughness coefficient. For smooth channels,  $\tilde{n}$  may be as low as  $0.005 \text{ m}^{-1/3} \text{ s}$ , but studies of floods, called *jökulhlaups*, resulting from drainage of ice-dammed lakes through subglacial conduits, yield values ranging from  $0.08\text{--}0.12 \text{ m}^{-1/3} \text{ s}$  (Björnsson, 1992). Choosing an intermediate value of  $0.1 \text{ m}^{-1/3} \text{ s}$ , Equation (8.13) gives a mean velocity of about  $0.18 \text{ m s}^{-1}$ , or  $Q \approx 0.018 \text{ m}^3 \text{ s}^{-1}$ , and Equation (8.14) gives  $\partial \Phi / \partial s \approx 98 \text{ N m}^{-3}$ . Whence  $m \approx 0.13 \text{ m a}^{-1}$ . This may not seem like a lot, but, volumetrically, the amount of ice melted in a year is  $\sim 1.1$ -times the size of the original semicircular conduit.

Owing to this melting and the resulting inward flow of ice toward the conduit, structures such as foliation in the ice are also bent inward. A beautiful example of this is shown in Figure 8.8.



**Figure 8.8** Foliation deflected into a conduit by inward flow of ice in response to melting of conduit walls. (From Taylor, 1963, Figure 11. Reproduced with permission of the author and the International Glaciological Society)

Some heat may also be advected into the glacier in water originating at the glacier surface and entering the englacial conduit system by way of moulin. The melt rate from such water,  $m_s$ , in a *circular englacial* conduit is:

$$m_s = \frac{Q\rho_w C_w \frac{\partial\theta}{\partial s}}{2\pi r_p L} \quad (8.15)$$

(Shreve, 1972). Here,  $\partial\theta/\partial s$  is the rate at which the water cools as it flows through the conduit. If we assume that  $\partial\theta/\partial s \approx 0.1 \text{ K km}^{-1}$  and use the discharge in the previous example,  $m_s \approx 0.5 \text{ m a}^{-1}$ . Thus, this is a heat source that cannot be neglected. Furthermore, it will be augmented by heat from conversion of potential energy of the falling water. A cubic meter of water falling 100 m releases enough heat to melt 2.9 kg of ice. A possible mitigating factor, however, is that ice crystals are often carried in streams on a glacier surface. Thus, some of this heat would be used to melt these crystals rather than conduit walls. It is not clear how the energy will be partitioned in this situation. One would also expect most of this heat to be consumed in the moulin itself or in the first few hundred meters of flow in an englacial passage.

### Conduits under cold ice

In a polar ice sheet, the base of which is at the pressure melting point, heat is normally conducted upward into the ice from the bed. (In rare instances, the ice some distance above the bed may be as warm as or warmer than that at the bed, but still colder than the pressure melting point, in which case this heat loss will not occur.) If a conduit begins to develop at the base of such an ice sheet, temperature contours are deflected upward and compressed as shown in Figure 8.9. The temperature gradient above the conduit is thus increased; above a semicircular conduit, once the temperature has time to adjust to the presence of the conduit, the gradient is twice that in the absence of the conduit. During development of the conduit, the

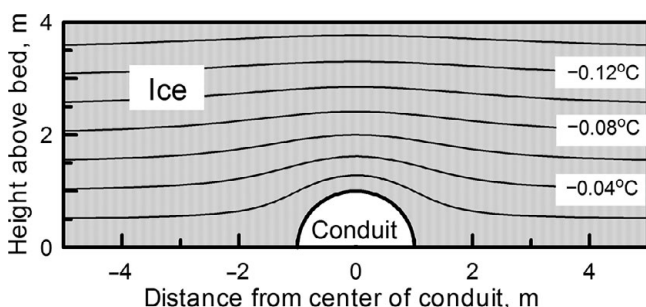


**Figure 8.9** Temperature above a semi-circular conduit at the bed of a cold glacier that is at the pressure melting point at the bed. Temperatures are relative to the pressure melting temperature. (From Hooke and Fastook, 2007, Figure 11. Reproduced with permission of the International Glaciological Society)

gradient is even larger. Under suitable conditions this increase is likely to be sufficient to conduct upward into the ice all of the viscous heat dissipated by the flowing water. In this case, no heat is available to enlarge the conduit.

## Water pressures in subglacial conduits on hard beds

Our next task is to determine the water pressure in conduits. Our discussion focuses on subglacial conduits on hard beds, but much of the development is equally applicable to englacial ones that are deep enough that  $P_w$  is greater than atmospheric pressure. As we've seen (Chapter 7), the water pressure in subglacial conduits is of considerable interest owing to its effect on the sliding speed.

Qualitatively, we expect  $P_w$  in subglacial conduits to increase upglacier because the ice thickness increases, but  $P_c$  must remain relatively constant so that  $u_c = m$ . Furthermore, an increase in  $P_w$ , or more rigorously in  $\Phi$ , is necessary to provide the potential gradient driving water toward the terminus. Less obvious is the way in which  $P_w$  should vary with  $Q$ , yet this is quite important because, if  $P_w$  decreases as  $Q$  increases, water will be drawn from smaller conduits toward larger ones, leading to the development of an arborescent drainage network. Conversely, if  $P_w$  increases as  $Q$  increases, the conduit system will tend to remain braided or *distributed*. In the type of system that we have been discussing, consisting of conduits that may vary in size but not in shape in the longitudinal direction, it turns out that  $P_w$  decreases as  $Q$  increases. However, in subglacial drainage systems in which conduits locally lie in the lee of bedrock steps, so that conduit geometry is controlled by the steps, the reverse may be true. Let's defer further discussion of these phenomena, and turn to a quantitative analysis, following closely the work of Röthlisberger (1972).

We start with the steady-state condition,  $u_c = m$ , and obtain an expression representing this condition by combining Equations (8.4) and (8.12), thus:

$$rA\left(\frac{P_c}{n}\right)^n = \frac{Q\left[(1-k)\frac{\partial\Phi}{\partial s} + k\rho_w g\frac{\partial z}{\partial s}\right]}{\pi r\rho_i L}. \quad (8.16)$$

Rigorously, Equation (8.4) applies only to cylindrical tubes on which the only stress is  $\sigma_{rr}$ . Here, for want of a better alternative, and with some misgivings, we apply it to a semicircular conduit at the glacier bed where other stresses are clearly present. The most important of these is  $\tau_{\theta r}$ , the friction between the ice and the bed (Figure 8.10);  $\tau_{\theta r}$  clearly restrains closure along the bed. Noting that  $R = \pi r/2(\pi + 2) = 0.306r$  in semicircular conduits and solving Equations (8.13) and (8.14) for  $r$  yields:

$$r = 1.136(\tilde{n}Q)^{\frac{3}{8}}\left(\frac{\rho_w g}{\partial\Phi/\partial s}\right)^{\frac{3}{16}}. \quad (8.17)$$

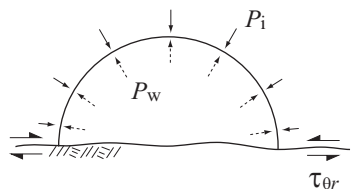


**Figure 8.10** Some of the stresses around a semicircular conduit at the bed.

Combining Equations (8.16) and (8.17) to eliminate  $r$ , letting:

$$D = 1.136^2 (\rho_w g)^{3/8} \pi \rho_i L = 3.90 \times 10^{10} \left( \frac{N}{m^2} \right)^{\frac{11}{8}} m^{-\frac{3}{8}}$$

and simplifying, we obtain:

$$(1 - k) \left( \frac{\partial \Phi}{\partial s} \right)^{\frac{11}{8}} + k \rho_w g \frac{\partial z}{\partial s} \left( \frac{\partial \Phi}{\partial s} \right)^{\frac{3}{8}} = \frac{AD \tilde{n}^{\frac{3}{4}} P_c^n}{Q^{\frac{1}{4}} n^n}. \quad (8.18)$$

We now need to relate  $\partial \Phi / \partial s$  to  $P_w$  and to the geometry of the tunnel system. Differentiating Equation (8.2) with respect to  $s$  yields:

$$\frac{\partial \Phi}{\partial s} = \frac{\partial P_w}{\partial s} + \rho_w g \frac{\partial z}{\partial s}. \quad (8.19)$$

Referring to Figure 8.5, we see that:

$$ds = \frac{dx}{\cos \beta} \quad (8.20)$$

so, noting again that  $dz/dx = \tan \beta$ , Equation (8.19) becomes:

$$\frac{\partial \Phi}{\partial s} = \left[ \frac{dP_w}{dx} + \rho_w g \tan \beta \right] \cos \beta. \quad (8.21)$$

Letting:

$$G = \left[ \frac{dP_w}{dx} + \rho_w g \tan \beta \right] \quad (8.22)$$

and using Equations (8.21) and (8.22) in Equation (8.18) yields:

$$G^{\frac{11}{8}} - kG^{\frac{11}{8}} + k \left( G - \frac{dP_w}{dx} \right) G^{\frac{3}{8}} = \frac{AD \tilde{n}^{\frac{3}{4}} P_c^n}{Q^{\frac{1}{4}} n^n \cos^{\frac{11}{8}} \beta}. \quad (8.23)$$

Cancelling the two terms in  $kG^{11/8}$  and replacing  $P_c$  and  $G$  by their equivalents from Equations (8.3) and (8.22) results in the relation we've been seeking:

$$\left[ \frac{dP_w}{dx} + \rho_w g \tan \beta \right]^{\frac{11}{8}} - k \left[ \frac{dP_w}{dx} + \rho_w g \tan \beta \right]^{\frac{3}{8}} \frac{dP_w}{dx} = \frac{AD \tilde{n}^{\frac{3}{4}} (P_i - P_w)^n}{Q^{\frac{1}{4}} n^n \cos^{\frac{11}{8}} \beta}. \quad (8.24)$$

Equation (8.24) is a non-linear differential equation that can be integrated numerically to obtain the water pressure,  $P_w$ , in a conduit as a function of distance,  $x$ , from the terminus (where  $x=0$ ), subject to the boundary condition that  $P_w=0$  at the terminus. (Atmospheric pressure is ignored, as it is approximately uniform over the glacier.) If the conduit is not full of water at the terminus, the boundary condition applies some distance upglacier from the terminus, where the conduit first becomes full, and the integration must start at this point. To carry out the integration, one uses the surface and bed topography along the course of the conduit to calculate  $P_i$  and  $\beta$  at each step,  $dx$ .

Some solutions for a semicircular tunnel at the base of an ice sheet with a parabolic surface profile and resting on a horizontal bed are shown in Figure 8.11.

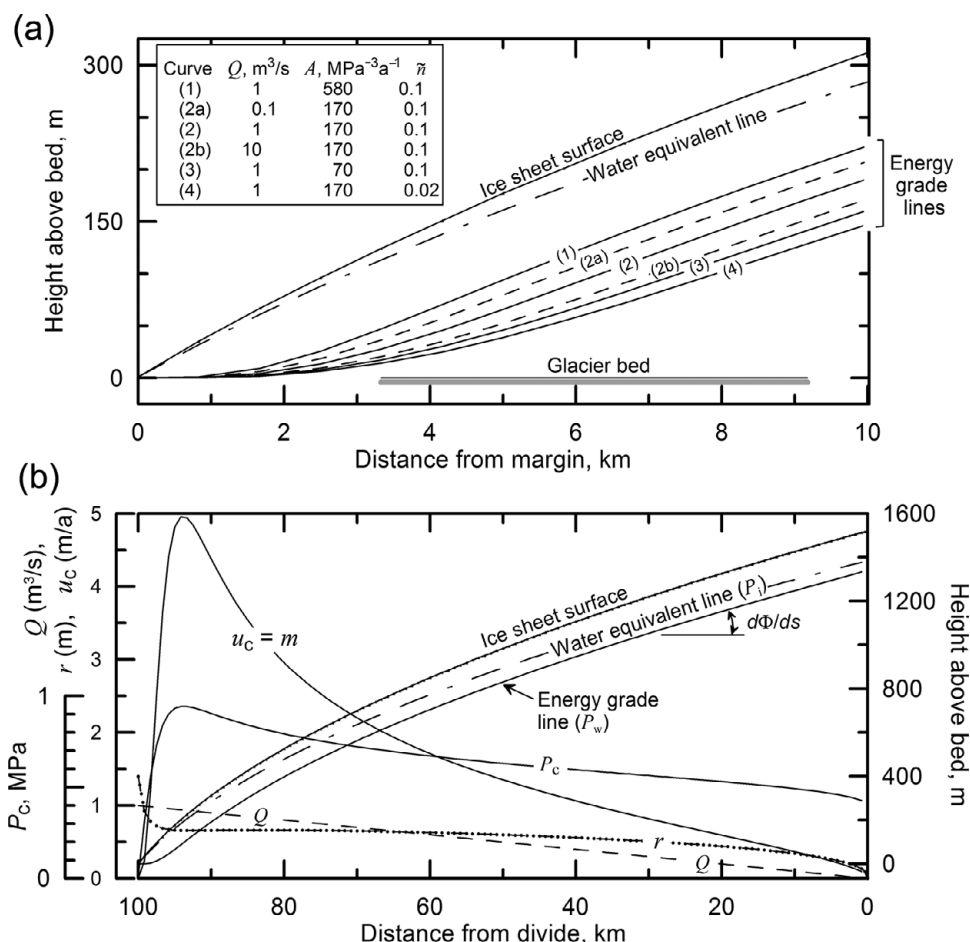


**Figure 8.11** Hydrology beneath a 100 km flowline in an ice sheet with a parabolic surface profile. Discharge is 0 at 100 km and increases linearly to the margin. (a) Energy grade lines for various conditions in the last 10 km of the 100 km tunnel. (b) Energy grade line and associated conduit parameters for conditions of Curve (2) in (a) over full length of tunnel. (Note change in direction of x-axis.)

The water is assumed to have been derived entirely from subglacial melt. The discharge shown is that at the margin, having increased linearly from zero 100 km from the margin (Figure 8.11b). The water pressure is represented on the ordinate by the height to which water would rise in a vertical borehole that intersects the tunnel, or the *piezometric head*. A line connecting these water levels in a series of boreholes along a tunnel is called the *energy grade line* or *hydraulic grade line*, and its slope is  $\partial\Phi/\partial s$ . The *water equivalent line* in Figure 8.11 is the piezometric head at which the glacier would float.

Aside from the obvious increase in the energy grade line ( $P_w$ ) in the upglacier direction, thus providing the hydraulic head gradient necessary to drive the flow, there are some characteristics of the patterns in Figure 8.11 that merit comment:

1. Water pressure increases as  $A$  increases [compare curves (1), (2), and (3) in Figure 8.11a]. This is because higher values of  $A$  imply softer ice and, hence, higher tunnel closure rates. Thus, higher water pressures are necessary to keep  $u_c = m$ .
2. Water pressure decreases as  $Q$  increases [curves (2a), (2), and (2b) in Figure 8.11a]. Although obvious from inspection of Equation (8.24), this may seem counterintuitive. Consider the consequences of reducing  $Q$ , holding, for the moment,  $P_w$  and hence  $\partial\Phi/\partial s$ , constant:  $m$  will decrease (Equation 8.12) so  $u_c > m$  and the conduit will start to close. The conduit cross sectional area,  $\mathcal{A}$ , varies as  $r^2$  but  $u_c$  varies as  $r$  (Equation 8.4), so  $\mathcal{A}$  decreases faster than  $u_c$ . Thus, once  $u_c$  has decreased enough to match the new  $m$ ,  $\mathcal{A}$  will have decreased so much that  $P_w$  is forced to increase to continue to drive the flow. Note that there is a negative feedback in this process inasmuch as the increase in  $P_w$  reduces  $u_c$ , restoring equilibrium.

Numerically, halving  $Q$  would result in a  $(1 - 0.5^{0.375}) \cdot 100 = 23\%$  decrease in  $r$  (Equation 8.17), and hence also in  $u_c$  (Equation 8.4) as  $P_c$  hasn't changed yet, and a 50% decrease in  $mr$  (Equation 8.12). The latter implies a  $\left(1 - \frac{1}{2} \frac{1}{(1-0.23)}\right) \cdot 100 = 35\%$  decrease in  $m$ , so  $m$  is now less than  $u_c$ . The tunnel will thus close, constricting the flow and raising  $P_w$ .

3. In an ice sheet, far from the margin, both  $Q$  and the surface slope are low. Owing to the latter,  $\partial\Phi/\partial s$ , is also low, so  $m$  is small (Equation 8.12), and hence so also is  $P_c$  (so that  $u_c = m$ ). Outward, both  $Q$  and  $\partial\Phi/\partial s$  increase (Figure 8.11b), however, resulting in an accelerating increase in  $m$ . In the first 15 km this results in an increase in  $r$  and hence in  $P_c$ . Between 15 and 95 km, however,  $r$  increases quite slowly, so the increase in  $m$  is balanced almost entirely by the increase in  $P_c$ . ( $P_c = P_i - P_w$ , and  $P_w$  decreases slightly faster than  $P_i$ ). Within a few kilometers of the margin,  $P_c$  plummets as the ice thickness decreases, so  $P_w \rightarrow P_i$ , and  $\partial\Phi/\partial s$  decreases to nearly 0 (Figure 8.11a). The latter reduces  $m$ .

The low  $\partial\Phi/\partial s$ , and hence  $m$ , far from the margin, in combination with the likely presence of cold ice above the bed, thus reducing both  $m$  and  $P_c$ , likely limits conduit growth, resulting in a distributed (or braided) drainage system lacking conduits cut upward into the ice (Meierbach et al., 2013). Thus, in Nature, the nearly constant  $r$  between 15 and 95 km probably results in a braided, distributed drainage system rather than a single tunnel.

Röthlisberger presented solutions of Equation (8.24) for some other idealized situations (Figure 8.12). Three interesting points merit discussion.

1. In Figure 8.12a the negative  $P_w$  near the margin implies that, for  $u_c$  to equal  $m$ , there must be suction. In other words, the  $u_c$  provided by the pressure of the overlying ice, alone, is not adequate to match  $m$ , even with  $P_w=0$ . Suction is necessary to increase  $u_c$ . In reality, air is likely to enter the tunnel from the terminus, resulting in open channel flow.

In this case,  $u_c$  is low because the ice is thin, and  $m$  is high because the bed slopes downward in the direction of flow, thus increasing the contribution of the second term on the right in Equation (8.6) to the energy dissipation. It is, in fact, easy to show that, unless the ice is more than a couple of hundred meters thick, even slight positive bed slopes increase the energy dissipation sufficiently to lead to open channel flow in semicircular conduits (Hooke, 1984). The additional energy thus available is readily calculated from the decrease in potential energy,  $mgh$ .

2. In Figure 8.12b,  $P_w > P_i$  some distance from the terminus. In this situation, the tunnel, if it existed, would be expanding and the tunnel size would be

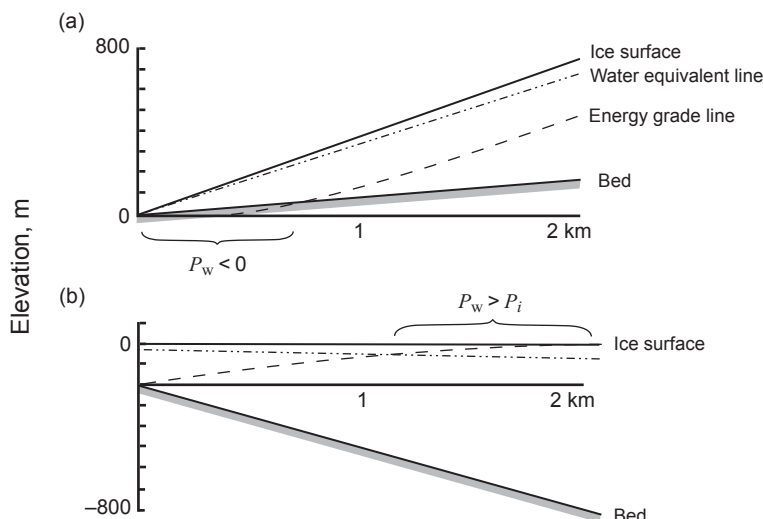


**Figure 8.12** Hydraulic grade lines for discharges of  $10 \text{ m}^3 \text{ s}^{-1}$  in circular conduits in two idealized situations. (Modified from Röthlisberger, 1972, Figure 5. Reproduced with permission of the International Glaciological Society)

maintained by freezing of ice to the walls. In Nature, in these situations, water likely leaks out along the bed, effectively floating the glacier.

This condition arises when, as in Figure 8.12b, the bed has an adverse slope that is so steep that water flowing up it does not dissipate enough energy to remain warmed to the pressure melting point. Mathematically, the second term on the left in Equation (8.11) exceeds the term on the right, forcing  $m$  to become negative. Physically, the water becomes supercooled, leading to freezing. The latent heat released warms the rest of the water to keep it at the pressure melting point. We'll discuss this further below, in connection with the origin and shape of overdeepenings in glacier beds.

3. Finally, it will be noted that, with increasing distance from the terminus, the energy grade lines in both Figures 8.11 and 8.12 become nearly parallel to the water equivalent lines. As the slopes of the energy grade and water equivalent lines represent, respectively, the gradients in  $P_w$  and  $P_i$  at the bed, this means that  $P_c$ , and hence also  $u_c$ , are nearly constant. Inspection of Equations (8.17) and (8.19) will show that  $r$  is also nearly constant. This justifies ignoring the  $Kn(u_c/Ar)^{1/n}$  term in Equation (8.5) when differentiating to obtain  $\partial\Phi/\partial s$  (Equation 8.6).

Our analysis so far has treated  $Q$  as being bounded, with water being supplied to the conduit by melt at the glacier bed or through a moulin. The hydraulic head (e.g. the level of water in the moulin) adjusts so  $P_w$ ,  $r$ , and  $m$  ( $= u_c$ ) satisfy Equations (8.5), (8.17), and (8.12), respectively. Suppose our subglacial conduit heads, instead, in a large lake in a tributary valley dammed by a trunk glacier. As Nye (1976) pointed out,  $P_w$  is then effectively constant and  $Q$  is unbounded. A conduit size *could* exist such that  $P_w$ ,  $m$ ,  $u_c$ , and  $r$  satisfy the above equations. However, if  $m$  were then to increase slightly, the conduit would expand, increasing  $Q$ , and hence also  $m$ , unstably, leading to a jökulhlaup. Conversely, if  $m$  were to decrease slightly, the conduit would contract, decreasing  $Q$  and hence also  $m$ ; the conduit would collapse. In other words, the conduit would be unstable to small perturbations in  $m$ .

### Comparison with observations

Equation (8.24) makes specific predictions about basal water pressures. These predictions have been tested in the field. Water pressures are significantly higher than expected. There are four possible reasons for this discrepancy.

- (i) Röthlisberger (1972) and Iken and Bindschadler (1986) suspected that  $A$  might be higher in basal ice, as suggested by Cohen's (2000) study at Engabreen (Chapter 7). However, to obtain agreement between measurement and theory they had to use values of  $A$  ranging from  $\sim 1000$  to  $\sim 37,000 \text{ MPa}^{-3} \text{ a}^{-1}$ . Typical values for temperate ice are  $\sim 250 \text{ MPa}^{-3} \text{ a}^{-1}$ . Cohen's study would support values only at the lower end of this range.

- (ii) Basal conduits are unlikely to be semicircular for two reasons: (a) drag on the bed ( $\tau_0$ , in Figure 8.10) inhibits closure low on conduit walls, and (b) when water is derived from the glacier surface, water fluxes vary diurnally; during periods of low flow when water doesn't fill the tunnel, melting may be concentrated low on the walls. Both of these would tend to widen conduits.

In conduits that are wide and low, the conduit roof receives less support from the walls, so closure is faster than in a semicircular one with the same cross sectional area. The higher closure rate can be approximated by calculating the closure rate for a much larger circular conduit, but restricting the channel cross section to the area between a chord and the top of the cylinder (Figure 8.13). Rather good agreement between theory and field measurements can be obtained in this way (e.g. Figure 8.14), but in some cases with a conduit geometry (e.g. ~5.6 m wide and only 0.02 m high in the case of Figure 8.14) that is probably unrealistic.

- (iii) Because  $dP/dr$  is calculated along a flow path, the pressure at a point a given straight line distance from a glacier margin will be higher if the flow path is sinuous. Extreme sinuosity, however, is required to achieve the agreement between the measured and calculated pressures shown in Figure 8.14 with a semicircular conduit and modest value of  $A$  (Hooke *et al.*, 1990).
- (iv) Equation (8.24) ignores the effect that stresses parallel to the conduit axis have on the closure rate. As noted previously (Equation 2.10), such stresses increase the rate of tunnel closure even though not acting in the direction of closure. However, these additional stresses are normally small compared with  $P_c$  so including them has a negligible effect on  $\sigma_e$ .

In conclusion, observed water pressures in glaciers can be modeled well with the use of a modified version of Equation (8.24) in which conduits are broad, low, and

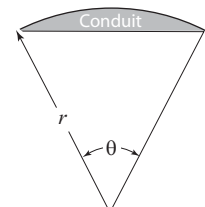


**Figure 8.13** Broad low conduit modeled by choosing a large radius,  $r$  (Equation 8.4), but restricting the conduit to the space between a chord and the top of the circle of that radius.

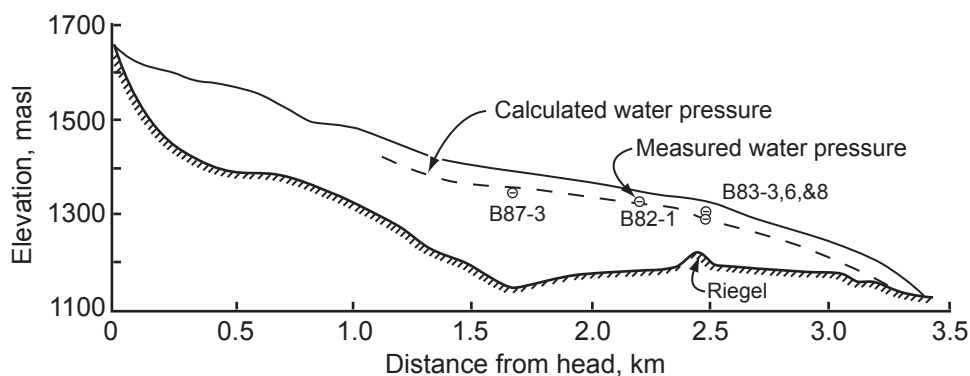


**Figure 8.14** Longitudinal section of Storglaciären showing locations of boreholes, mean winter water levels in holes, and calculated hydraulic grade line. (From Hooke *et al.*, 1990, Figure 3. Reproduced with permission of the International Glaciological Society)

sinuous, and  $A$  is higher. How the modifications should be distributed among these possible factors is not clear.

### The linked cavity system

On Variegated Glacier, Alaska, it was found that, despite a water discharge,  $Q$ , of  $5 \text{ m}^3 \text{s}^{-1}$ , dye moved through the subglacial drainage system with a speed,  $v$ , of only  $0.025 \text{ m s}^{-1}$ , implying a channel cross sectional area,  $\mathcal{A}$  ( $=Q/v$ ), of  $\sim 200 \text{ m}^2$ . If the flow were in a single conduit with a reasonable roughness,  $\tilde{n}$ , Equation (8.13) would predict velocities that were one to two orders of magnitude higher than those observed.

Kamb (1987) suggested that the flow, rather than being in a single conduit, was in a network of cavities (Figure 8.15a) formed in the lees of steps in the bed (Figure 8.15b). That such cavities exist is demonstrated by precipitates (p. 158–159), by the lack of striations in such locations on deglaciated bedrock surfaces, and by observations during subglacial exploration (Vivian and Bocquet, 1973). Kamb thought the cavities would be linked together by orifices that were much smaller in cross sectional area than the cavities (Figure 8.15b, B-B'). The cavities provide the large  $A$  required, and the orifices throttle the flow, reducing the velocity.

In analyzing the stability of such linked cavity systems, Kamb focused on the orifices, and on the heat released by viscous dissipation in them. If the heat released is small compared with the sliding speed, the roof of the orifice will be

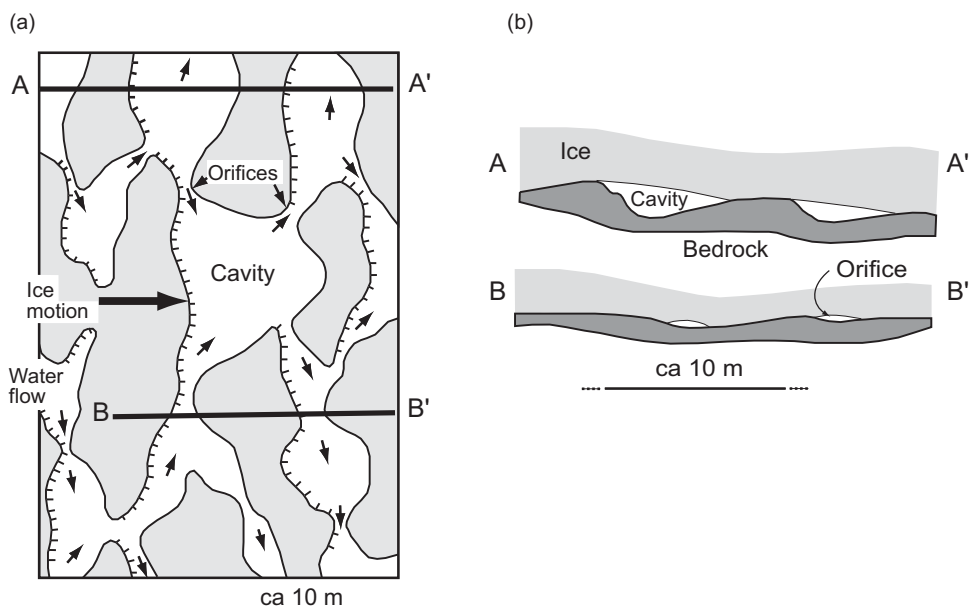


**Figure 8.15** (a) Schematic map of a linked-cavity basal water system. (b) Cross sections through the linked-cavity system of (a). (After Kamb, 1987, Figures 1 and 2)

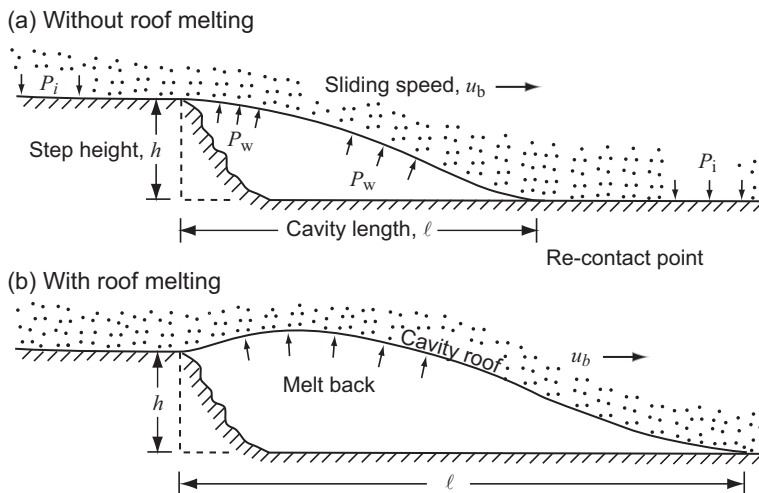


**Figure 8.16** Geometry of ideal orifice in lee of a step in the bed: (a) without roof melting, (b) with roof melting. The figures could represent a cavity equally well. (Modified from Kamb, 1987, Figure 5)

as shown in Figure 8.16a. With more energy dissipation, lower  $u_b$ , or higher  $P_w$ , however, the orifice becomes longer and more arched, owing to melting of its roof (Figure 8.16b). Kamb found, theoretically, that if  $P_w$  is increased enough, the length of an orifice would increase without bound. This could lead to a transition to a tunnel system.

If  $u_b > 0$ , orifices can exist with  $P_w = 0$ . Owing to this, and to the contrasting ways in which orifices and cylindrical conduits are closed, Kamb's theory predicts that discharge should vary directly with piezometric head in a linked cavity system, and that  $P_w$  should be higher in such a system than in a tunnel system, once the orifices are filled with water (Figure 8.17). This contrasts with the situation in a tunnel system, in which, as noted, Röthlisberger's theory predicts an inverse dependence of  $P_w$  on  $Q$  (Figures 8.11a and 8.17). A consequence of the direct dependence of  $P_w$  on  $Q$  in the linked cavity system is that a stable system of many interconnected cavities can exist. In a tunnel system, on the other hand, lower pressures in larger tunnels would result in diversion of the flow in smaller ones toward the larger ones, leading to an arborescent network.

### Conduits on deforming till

Hitherto, our discussion of subglacial conduits has focused on situations in which the bed is comparatively rigid. Many glaciers, however, move over beds of deformable till. In Chapter 7 we found that the deformability of till and the nature of the coupling between it and the glacier sole are both strongly dependent upon the effective pressure,  $N_e$ . The effective pressure, in turn, depends, through  $P_w$ , on the nature of the drainage system at the ice–till interface. As  $P_w$  at such an interface is

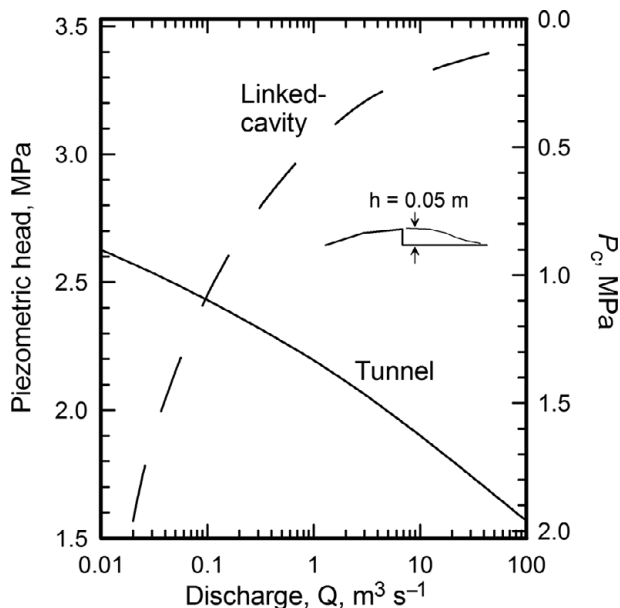


**Figure 8.17** Variation of  $P_c$  with  $Q$  for tunnel and linked-cavity systems. Glacier is 400-m thick and has a surface slope of 0.1. Step height is 0.05 m. Other parameters used in calculating the curves are given by Kamb (1987, p. 9094). (After Kamb, 1987, Figure 12. Reproduced with permission of the author. Copyright by the American Geophysical Union)

clearly of prime importance in the development of ice streams and perhaps also in surging (Truffer *et al.*, 2000), a quantitative understanding of conduits on deformable substrates is clearly needed.

As with a conduit at an ice–rock interface, the roof of one at an ice–till interface tends to close when  $P_w < P_i$ , and in the steady state this tendency is balanced by melting. In addition, however, creep of till into the conduit tends to constrict it, and in the steady state any such flow must be balanced by erosion of the till by the flowing water (Alley, 1989a; Walder and Fowler, 1994; Ng, 2000a, b). The physics of the latter processes are still poorly understood, as neither the rheology of till nor the mechanics of sediment transport are known well enough. Nevertheless, we can make some predictions about the nature of the drainage system.

Consider the channel shown in Figure 8.18. If any sediment on the sloping “bank” of the channel, as at A, can be moved downstream by the current, gravitational forces will tend to move it, also, toward the middle of the channel. Consequently, channels should become wider and shallower until the velocity and shear stress on the banks are too low to move sediment. Parker (1979) has proposed that, in the transition zone between the bed and the bank, lateral diffusion of downstream momentum results in a gradual outward decrease in the shear stress,  $\tau_w$ , exerted by the water on the bed, so that movement of bed material decreases gradually toward the banks rather than ceasing abruptly at some particular threshold depth.

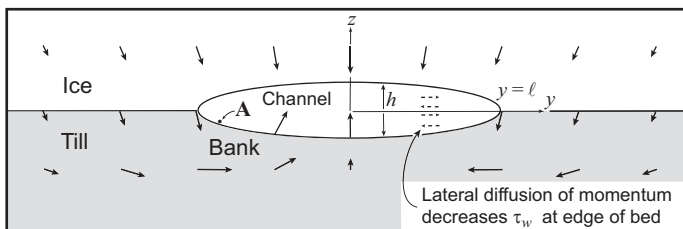


**Figure 8.18.** Flow of ice and sediment around a subglacial conduit incised into till. In this example the effective viscosity of the till is substantially less than that of the ice (see text). Vectors are based on Ng (2000b, Figure 9).

Although Parker's model was developed for subaerial gravel-bedded rivers, there is no obvious reason why it should not also apply to subglacial conduits in noncohesive till, even if the till is fine grained, so long as there is an inward-sloping bank region. Channels in till are thus likely to be wide and shallow, as illustrated in Figure 8.18, a conclusion shared by Alley (1989a), Walder and Fowler (1994), and Ng (2000a, b).

Ng (1999) has suggested that, in such a conduit, the vertical closure rate,  $w$ , due to flow of ice should be given approximately by:

$$w(y) = A \left( \frac{P_c}{2} \right)^n \sqrt{\ell^2 - y^2} \quad (8.25)$$

where  $\ell$  is the half width of the conduit,  $y$  is the distance from its center, and the appropriate value for  $A$  is  $\sim 250 \text{ MPa}^{-3} \text{ a}^{-1}$ . (Compare this with Equation 8.4.) Thus,  $w$  is highest in the middle of the channel, at  $y = 0$ , and decreases toward the bank,  $y = \ell$ . This would be consistent with the suggestion that melt rates should be higher where the water is deeper, and the energy dissipation thus greater (Shreve, 1985a). Ng also proposes a similar relation for creep of till into the conduit, with  $A(P_c/2)^n$  in Equation (8.25) replaced with an appropriate relation for till.

The vectors in Figure 8.18 reflect a situation in which the effective viscosity of the till is substantially less than that of the ice. If the effective viscosities are roughly equal, flow of the till is much slower, owing, in part, to the limited thickness of the till (Ng, 2000b).

Let's now consider the water pressure in such a conduit. Walder and Fowler (1994) note that low water pressure promotes flow of ice toward a conduit but strengthens the till. Under these conditions, their calculations suggest that the channel bed should be relatively flat, and the roof arched upward into the ice – a Röthlisberger channel. Conversely, a high water pressure promotes flow of till into a conduit but inhibits inward flow of ice. In this case, the channel is likely cut downward into the till. The effective pressure at which the transition between these two regimes occurs depends on the granulometry of the till.

Far from the margin of an ice sheet, the low surface slope and, in the absence of moulins, low discharge, require that the conduit system adjust to provide a high  $P_w$ . Closure by ice flow is thus inhibited, and deformation of till into conduits enhanced. Conversely, valley glaciers normally have higher surface slopes and discharges, so  $P_w$  is lower and  $m$  is higher, leading to conduit geometries controlled by the inward flux of ice.

We have seen that  $P_w$  decreases as  $Q$  increases in conduits on hard beds, so water is diverted from smaller conduits to larger ones, leading to an arborescent drainage network. Of interest, then, is the question of whether this relation also holds for conduits on deforming till.

Let's leave this question for the moment to describe an elegant analysis by Ng (2000a), in which he derived three coupled ordinary differential equations that can be solved numerically for the water and sediment discharges,  $Q$  and  $Q_s$ , conduit geometry, and  $P_c$ , all as functions of distance along a conduit from its source. The principle independent variables in the analysis are the fluxes of water and sediment into the conduit. The water flux is from basal melting over some distance on either side of the conduit, and the sediment flux is from small tributaries along the conduit. The coupling among these variables occurs because  $P_c$  controls: (1) the flux of ice toward the conduit, and thus the contribution of melting of the conduit roof to  $Q$ , and (2) the strength of the till and hence the flux of till into the bottom of the conduit, the primary source of  $Q_s$ . Given the independent boundary conditions  $P_c$ ,  $Q$ ,  $Q_s$ ,  $\tilde{n}$ , and the granulometry of the sediment, Ng calculates  $\ell$ ,  $\tau_w$ ,  $m$ ,  $d\Phi/ds$ , conduit height,  $h$  (Figure 8.18), mean water velocity,  $\bar{u}$ , and mean sediment concentration,  $\bar{c}$ . These seven unknowns are connected through seven equations, which we can express qualitatively as follows:

- $Q_s$  is related, non-linearly, to  $\tau_w$  and  $h$  because they determine the intensity of turbulence;
- $\bar{c} (= Q_s/Q)$ ;
- $\tau_w$  is related to  $\bar{u}$  and the hydraulic roughness of the conduit;
- $\bar{u}$  times the cross sectional area of the conduit must equal  $Q$ ;
- $w$ , integrated across the conduit, must equal  $m\ell$  (Equation 8.25);
- $d\Phi/ds$  is related to the slope of the bed and to  $dP_w/ds$  (Equation 8.19); and
- $m$  is related to  $d\Phi/ds$  and  $Q$  (Equation 8.12).

The energy used to keep the water at the pressure melting point (Equation 8.11) is neglected, so the solution applies, rigorously, only to an ice sheet of uniform thickness. Note that conduit geometry and the rate of erosion of the bed are all determined solely by the independent variables – the water and the sediment fluxes from basal melting and small tributaries – together with three parameters (ice sheet thickness, conduit roughness, and grain size) that are specified and held constant.

In an illustrative calculation based on this model, Ng assumed that a small amount of water was seeping through the till and along the ice/till interface upstream from the head of the conduit. This water entered the conduit without transporting any sediment, so  $Q > 0$  but  $Q_s = 0$  here.  $P_c$  was taken to be 0.1 MPa at the head, well below any likely transition to Röthlisberger channels, so we may expect the conduit to be incised into the sediment. Along the conduit, basal melting was presumed to supply water at a constant rate of  $0.01 \text{ m}^3 \text{ s}^{-1} \text{ km}^{-1}$ , and the sediment flux from tributaries was taken to be  $265 \text{ g s}^{-1} \text{ km}^{-1}$ .

Downstream changes in several key variables are shown in Figure 8.19. At the upstream end of the conduit there is a boundary zone about 30 km long in which  $dP_c/ds \neq 0$  (Figure 8.19b), and  $\ell$  and  $h$  vary somewhat erratically (Figure 8.19d); downstream from this zone,  $P_c = Q_s^{1/2} Q^{-5/6}$ , which turns out to be essentially constant. The contribution of roof melting (Figure 8.19e) to  $Q$  is negligible in comparison with the total  $Q$  so the discharge increases nearly linearly (Figure 8.19a). To accommodate the increase in  $Q$ ,  $\bar{u}$ ,  $h$ , and  $\ell$  all increase (Figure 8.19d). The increases in  $\bar{u}$  and  $h$  increase  $\tau_w$  (not shown).  $Q_s$  increases non-linearly (Figure 8.19a), reflecting its non-linear dependence on  $\bar{u}$  and  $\tau_w$ . Thus  $\bar{c}$  also increases (Figure 8.19c). As expected,  $h \ll \ell$  (Figure 8.19d) so the conduit is wide and low. Generally,  $dQ_s/ds$  is substantially more than the  $265 \text{ g s}^{-1} \text{ km}^{-1}$  supplied by tributaries. For example, 70 km from the head of the conduit  $dQ_s/ds \approx 1800 \text{ g s}^{-1} \text{ km}^{-1}$ . Till creeping into the conduit is eroded at a rate of  $\sim 2 \text{ m a}^{-1}$  to nearly  $7 \text{ m a}^{-1}$ , thus supplying the bulk of the sediment load (Figure 8.19e). This is substantially higher than the melt rate of  $\sim 0.17 \text{ m a}^{-1}$  on the conduit roof.

Returning to the question of the nature of the drainage system, note that  $P_c \propto Q^{-5/6}$  so  $P_w$  increases as  $Q$  increases. A distributed drainage system is thus to be expected.

Field evidence from Whillans Ice Stream appears to support this conclusion. With the use of a hot water drill, Engelhardt and Kamb (1997) drilled 27 holes to the bed there. Upon reaching the bed, water levels in the holes fell rapidly, suggesting the presence of a preexisting gap between the ice and the bed. In some instances the falling water level resulted in pressure pulses in nearby holes. By measuring the rates at which water levels fell, Engelhardt and Kamb calculated that the presumed gaps were  $\sim 2 \text{ mm}$  high. Analysis of oscillations in water pressure in nearby holes, interpreted as indicating seiche-like flow back and forth between the holes when the second hole reached the bed, also suggested a gap of about this size (Kamb, 2001, p. 187). In other cases, Engelhardt and Kamb inferred that the water was forcing its way outward from the hole along the ice-bed interface. In these cases, they calculated that a gap, 3 mm to 4 mm high, was likely opening along the interface. Subsequent monitoring established that most of the holes eventually connected with a subglacial drainage system of some kind.

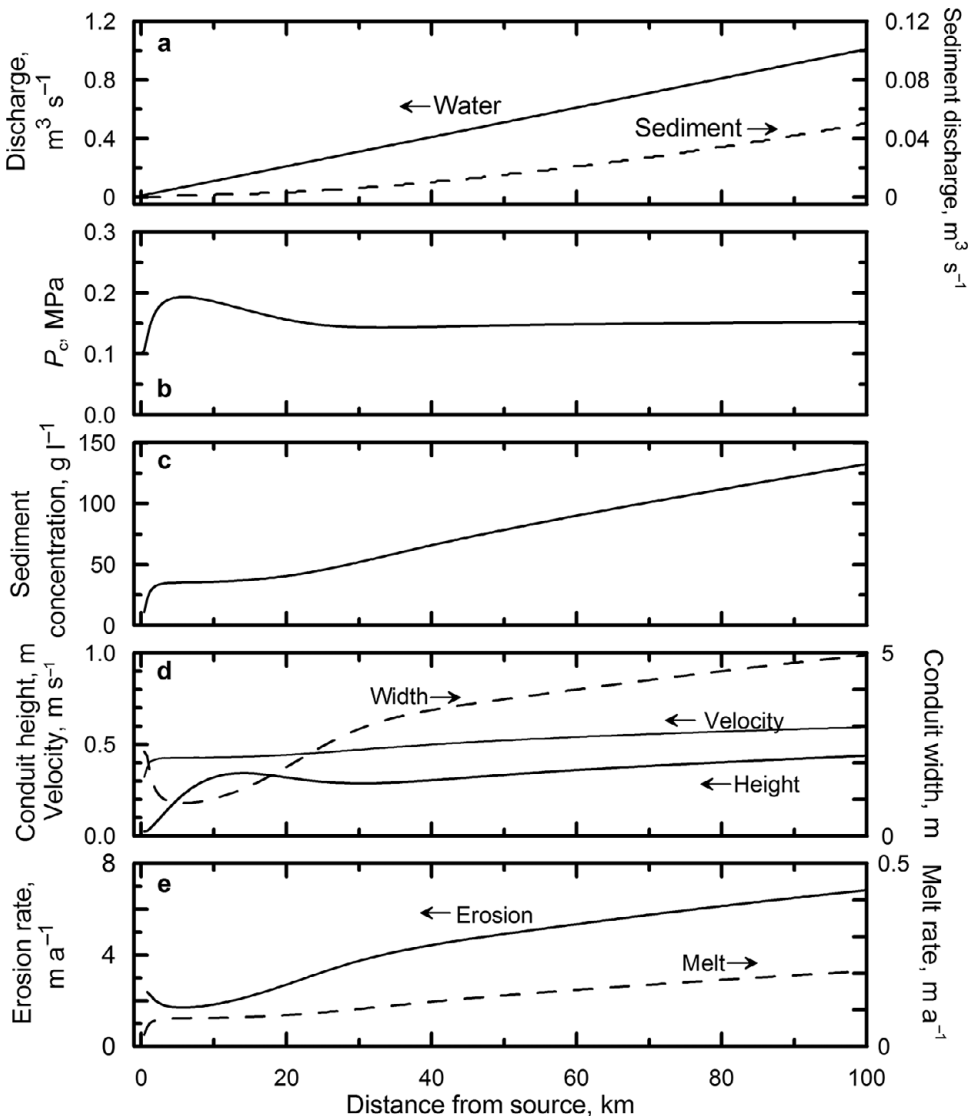


**Figure 8.19** (a) Discharge and sediment load in a stream 100 km long beneath an ice sheet of uniform thickness. (b) Effective pressure and (c) sediment concentration in the stream, (d) width and height of the conduit, and mean velocity in it, and (e) rate of melting of conduit roof and of erosion of till creeping into conduit. Arrows indicate relevant ordinate. (Plotted from data kindly supplied by Felix Ng, some of which were used in his 2000a paper)

Over time spans of several months, Engelhardt and Kamb found that water levels fluctuated and that the fluctuations in some holes were well correlated, while those in others showed no correlation whatsoever. Holes that showed good correlation over some time periods showed no correlation over others. Water levels in holes within  $\sim 10^2$  m of one another were often, but not always comparable, but levels in

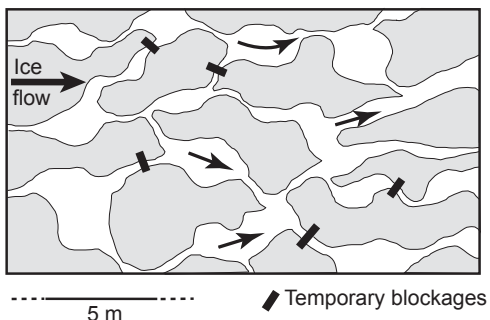


**Figure 8.20** Possible geometry of a linked water pocket drainage system on till at the base of an ice sheet.

more distant holes commonly differed by several meters. Pressures in some holes even rose above the estimated overburden pressure on occasion.

A system of wide shallow linked water pockets (Figure 8.20) with links periodically blocked by deformation of till or ice, would be compatible with these observations. Individual pockets might be meters across and millimeters to tens of millimeters deep, and links might be 1/10<sup>th</sup> to 1/100<sup>th</sup> this size. In such a system, one can readily imagine that some boreholes might bottom in areas between pockets and have difficulty forcing a connection to one, that a pressure wave initiated at one hole might have to travel a long distance down one tortuous waterway and then up another in order to reach a nearby hole, that when a conduit became blocked the water pressure in it might rise temporarily and be out of phase with pressure variations in other holes, and even that pressures might rise above the overburden pressure in waterways that were blocked downstream but remained connected upstream.

Through-going channels like those in Figure 8.18 are likely also present. Such conduits are necessary to carry flow from basal melting upglacier from the site of the boreholes. Iverson (2000), using his theory of regelation into till (p. 184–186) and the basal water pressures measured by Englehardt and Kamb, calculated that such channels would be 100 m to 200 m apart beneath Whillans Ice Stream. In exposures of fine-grained till deposited by continental ice sheets, evidence for such channels is preserved in the form of gravel lenses a few decimeters to some meters wide and about 1/10th as thick. Some of these are known to be ribbon-like, elongated in the direction of ice flow (Eyles *et al.*, 1982; Brown *et al.*, 1987).

## So what does the subglacial drainage system look like?

### Data

Let's first establish what we know. Natural subglacial conduits have been observed in artificially-melted subglacial passages (Hooke *et al.*, 1985) and are commonly observed emerging from the margins of glaciers (e.g. Fountain and Walder, 1998,

Figure 13). The heights of these conduits are typically less than half their widths; most are not semicircular. We also know, as noted, that cavities form. As long as part of a glacier's movement is by sliding, cavities will certainly be present, and orifices in the lee of smaller obstacles will provide links between at least some cavities.

Dye trace studies have yielded a wealth of information. In such studies, a slug of fluorescent dye is introduced into a subglacial stream, commonly through a moulin or borehole, and the concentration of dye in a stream at the glacier terminus is monitored with a fluorometer, a device capable of measuring very small concentrations of dye. The dye concentration is plotted versus time, yielding what has become known as a *breakthrough curve* (Figure 8.21). The time required for the dye to reach the sampling site is a measure of the flow velocity. Some breakthrough curves have multiple peaks (Figure 8.21b). The width of a breakthrough curve is a measure of dispersion. Dispersion is low in relatively straight flows with low width/depth ratios, and high in braided flows.

Basal water pressures, measured with pressure transducers submerged in boreholes or moulin, also yield valuable data. In at least some instances, water pressures have been found to increase gradually during the winter, when discharges were low (Figure 8.22). On Storglaciären this increase was accompanied by a decrease in surface velocity,  $u_s$  (Hooke *et al.*, 1989, 1990), but at one site in Greenland  $u_s$  increased as  $P_w$  increased during the winter (van de Wal *et al.*, 2015).

When surface meltwater begins to reach the glacier bed in the spring, surface velocities commonly increase abruptly (Figure 8.22). On Storglaciären, these initial velocity increases usually don't last long, but later in the melt season additional periods of increased velocity are likely to occur. These latter are associated with high water pressures resulting either from air temperatures significantly higher than those during the first velocity increase (Figure 8.22), or from rain, or both. Not all high  $P_w$  events result in high surface velocities, however (Figure 7.9). In southwest Greenland, too, in the ablation area, van de Wal *et al.* (2015) found that  $u_s$  could more than double during the summer, with higher velocities continuing until the end of August. Annual velocities, however, were not strongly correlated with total melt, and indeed in some places they decreased slightly with increased melt. Sundal *et al.* (2011) also documented significantly higher summer velocities in Greenland, with the speed up lasting longer during summers with *lower* total melt.

At sites more than a few kilometers from the margin, van de Wal *et al.* (2015) commonly saw a brief early-September dip in  $u_s$  below its mean winter value.

In dye-trace tests elsewhere in west Greenland, Chandler *et al.* (2013) found that, as the melt season progressed, water velocities increased and dispersion decreased. The change occurred later and more slowly in moulins further from the margin. The changes were detected in trials from moulins up to and including one that was 41 km from the margin, but not from one 57 km from the margin.

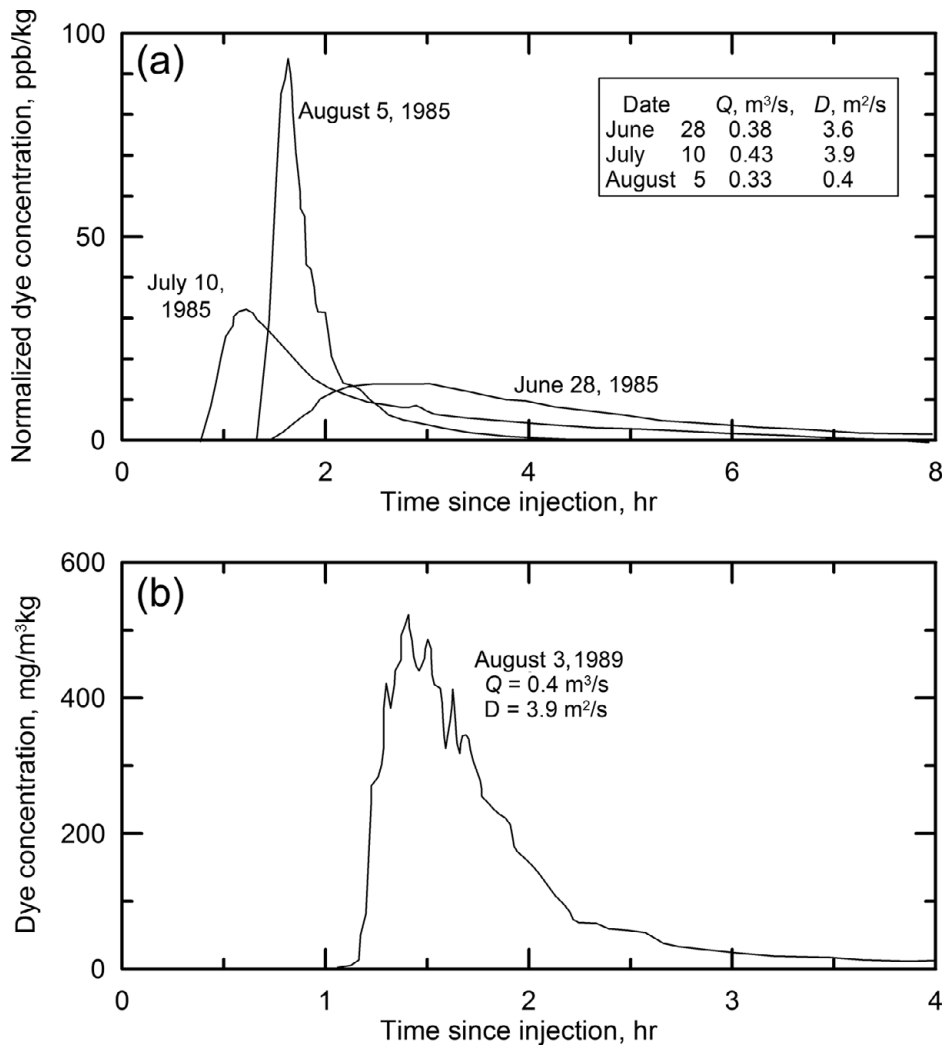


**Figure 8.21** Typical breakthrough curves from dye-trace experiments on Storglaciären. (a) Three curves from the summer of 1985. Injections were all in the same moulin. (b) A curve from August 1989.  $D$  = dispersion. ((a) is from Seaberg *et al.*, 1988, Figure 2b. (b) is from Hock and Hooke, 1993, Figure 3. Reproduced with permission of the International Glaciological Society (a) and the Geological Society of America (b))

At another site in west Greenland, ~25 km from the margin, where the ice was ~620 m thick, Andrews *et al.* (2014) found that water pressures in boreholes that were not connected to a channelized drainage system tended to be high, approaching or locally exceeding the overburden pressure. Pressure variations in these holes were both small and out-of-phase with those in moulin. (This out-of-phase behavior is seen elsewhere, and is attributed to a cantilever effect whereby high  $P_w$  in the connected moulin lifts the glacier, taking weight off of unconnected areas sampled

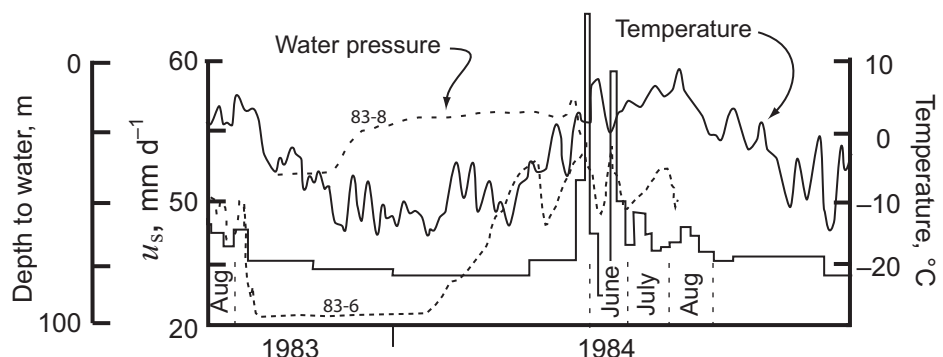


**Figure 8.22** Surface speed of a strain diamond on Storglaciären in 1983–1984, water pressure in nearby boreholes 83-6 and 83-8 (see Figure 8.14) expressed as depth to water surface from glacier surface, and mean daily temperature, smoothed using a five-day running mean. (Modified from Hooke *et al.*, 1989, Figure 3a. Reproduced with permission of the International Glaciological Society)

by the boreholes.) In moulin,  $P_w$  correlated well with  $u_s$  early in the melt season, but remained high as  $u_s$  decreased in the late summer.

Finally, we know that there can be appreciable differences among nearby glaciers. Iken and Bindschadler (1986, p. 110), for example, studied differences between the subglacial drainage of Findelengletscher and Gornergletscher, two glaciers of comparable size near Zermatt in the Swiss Alps. They concluded that the drainage of Gornergletscher was in a few large tunnels, whereas that of Findelengletscher was in numerous smaller conduits. They did not propose an explanation for this difference.

### Interpretation

A model for the seasonal evolution of a drainage system that is consistent with these observations and interpretations is as follows: During the winter, roofs of broad low conduits settle down on higher areas in the bed, leading to decreased water flow speeds and braiding. Cavities in the lees of bedrock steps shrink, although kept open by the steps. The drainage system becomes less efficient. Under thicker glaciers, local collapse of the conduit part of the system is possible. More commonly, however, remnants of the previous year's tunnels likely survive, maintained by the small winter discharge provided by subglacial melt and by groundwater seepage. As surface water inputs then increase in the spring and water backs up in the undersized system,  $P_w$  and  $\partial\Phi/\partial s$  increase, and hence so also does  $m$ . The increased  $P_w$  inhibits closure and increases  $u_b$ , and is thus responsible for the observed increases in  $u_s$  (Figure 8.22). Subsequent rather abrupt drops in  $P_w$  and  $u_s$  suggest that remnant cavities and tunnels increase in size rapidly as the tunnel system is re-established and the drainage becomes more efficient. That the drops in  $u_s$  in Greenland occurred during warm summers but not during cooler ones (Sundal *et al.*, 2011) is attributed to the higher water input in warm summers, accelerating

the development of an efficient drainage. That it occurred later in the season at sites farther from the margin is attributed to lower surface slopes there, resulting in lower  $m$  and delaying the transition to a more efficient system (Chandler *et al.*, 2013).

High dispersion and the multiple peaks in some breakthrough curves suggest braiding: packages of dye apparently followed different anabranches of a braided subglacial stream, moving at different rates and thus reaching the terminus at slightly different times. A decrease in dispersion as the melt season progresses is generally interpreted, again, as indicating that the drainage system became more efficient. (In Figure 8.21a, the higher velocity during the July 10 test is likely a consequence of the higher discharge on that day.) Streams may remain braided as the tunnel system develops, however, with gravel bars or bedrock knobs separating anabranches (Figure 8.21b).

The tendency for  $P_w$  to increase in winter when  $Q$  is low (Figure 8.22) is consistent with Röthlisberger's theory (Figure 8.11a), and suggests the presence of an efficient conduit-type drainage system. Water velocities obtained from tracer studies, however, are commonly too low to be consistent with flow in a single straight conduit extending from the input point to the terminus. On the other hand, the water velocities (as well as winter water pressures) can be modeled rather well with Equation (8.24) by including one or more of the following modifications: (i) a drainage system that bifurcates several times between the terminus and the injection point, with smaller tributaries carrying lower discharges at lower velocities, (ii) a sinuous conduit, (iii) broad, low conduits, in which the hydraulic radius,  $R$ , is lower and  $\bar{n}$  likely higher (Equation 8.13), and (iv) a higher value of  $A$  in basal ice.

The brief early September dip in  $u_s$  observed by van de Wal *et al.* (2015) likely reflects a decrease in  $P_w$  when the decrease in  $Q$  occurred faster than conduits could close. This dip may be equivalent to the much longer period of decreased  $P_w$  during the early winter at Storglaciären (Figure 8.22). Under Storglaciären's thinner ice it would take longer for the conduits to close. This likely also explains the observation that  $u_s$  decreased during the early winter at Storglaciären (Figure 8.22), before conduits closed enough to increase  $P_w$ , but increased during this time period in Greenland.

These observations and interpretations lead one to suspect that a typical drainage system likely consists of a continuous gradation between more efficient parts, probably represented by an arborescent system of broad, low, perhaps individually-braided conduits, and less efficient parts characterized by a non-arborescent network of water-filled cavities, some of which are linked, albeit in some cases only weakly, while others are isolated (see also Hoffman *et al.*, 2016). In the latter,  $P_w$  can approach the overburden pressure as Andrews *et al.* (2014) found. As diurnal changes in  $P_w$  can produce widely variable responses in  $u_s$  (Figure 7.9), it seems that the number and size of connections to subglacial cavities varies appreciably from one high  $P_w$  event to another, thus affecting the number, distribution, and strength of hydraulic jacks operating. Seasonal changes in water input, and

hence in  $u_b$ , alter the efficiency of different parts of the system, changing linkages, and perhaps leading to changes in  $P_w$  that are out of phase in nearby locations.

### Spatial and temporal distribution of drainage system types

Although we have been treating drainage systems on hard beds and soft beds separately, most glaciers rest on bedrock in some areas and on loose material in others. The character of the loose material is also quite variable. Till beneath valley glaciers commonly contains substantial amounts of sand and gravel, while that beneath Antarctic ice streams and that overridden by the Laurentide Ice Sheet in the midwestern United States is much finer. This is probably largely a consequence of the nature of the bedrock supplying the debris: resistant mountain ranges on the one hand and large areas of weak sedimentary rock on the other. The angle of internal friction is typically higher in coarse materials (Chapter 7), so till beneath mountain glaciers is likely to be stronger. In addition,  $N_e$  is typically higher beneath mountain glaciers because distances to the margin are shorter and fluctuations in  $P_w$  much larger, particularly during the summer. Although till beneath mountain glaciers is known to deform (Figure 7.25), these two factors combined make till deformation more likely beneath ice sheets. The analysis of Walder and Fowler (1994) thus predicts that conduits will be eroded downward into the till, and distributed drainage networks more common beneath ice sheets, and conversely. From the point of view of a valley glacier, coarse till that is not deforming may look very much like rough bedrock, so the drainage system developed on it may have characteristics of a system on a hard bed.

The nature of the drainage system must thus vary from place to place beneath a glacier and from one glacier to another. Where basal melting occurs, the melting is distributed, so some parts of any subglacial drainage system must be distributed. Some systems may be almost entirely distributed, while others may have an arborescent component, particularly near the margin. On short time scales, both types of system are likely to be altered or disrupted by flow of the ice, though the linked cavity system, stabilized by the location of cavities on the lee sides of bedrock obstacles, is less subject to such change. On longer time scales, the drainage system at a particular place must vary as the glacier profile changes, the bed is eroded, and subglacial materials are rearranged. The challenge, therefore, may be to determine not what type of drainage system is present beneath a particular glacier, but rather the spatial distribution of the different types of system beneath that glacier.

## Surges

A surge is a rapid advance of a glacier, unrelated to changes in mass balance, that lasts a few months to a couple of years. During a surge, the terminus may advance

as much as a few kilometers at speeds of  $10^1 - 10^2 \text{ m d}^{-1}$ , and relatively stagnant ice in the terminus region may be reactivated or overridden. Owing to high strain rates, surges are accompanied by dramatic crevassing.

During a surge, a large amount of ice is transferred from a *reservoir area*, which is usually, though not always, in the accumulation area, to a *receiving area* in the terminus region. Accordingly, the surface elevation in the reservoir area is drawn down and the receiving area thickens. Changes in thickness of tens of meters are common.

Surges are followed by periods of quiescence lasting on the order of decades. During quiescence, ice speeds are less than the balance velocity so the glacier thickens in the reservoir area and thins in the receiving area, thus becoming steeper. Before the resulting increase in driving stress can raise speeds to equal the balance velocity, however, another surge occurs, so the process is commonly periodic.

Surges may occur on glaciers resting on either hard beds composed mainly of bedrock, or on soft beds composed of till. Surges may also occur on glaciers that are, at least in part, frozen to their beds. In either case, it is likely that high basal water pressures play a central role.

Kamb (1987) has developed a model for surging of temperate glaciers on hard beds. He postulates that cavity enlargement is inhibited during build up to a surge, owing to the increase in thickness, and hence  $P_i$ . Water pressures must thus rise higher before the limits of stability of the linked cavity system are exceeded and a transition to a tunnel system initiated. Linked cavities are thus more likely to persist beneath the upper, thicker part of the glacier. As  $P_w$  rises in the late winter or spring,  $u_b$  increases, inhibiting melt back (Figure 8.16) and decreasing the size of orifices. This further increases  $P_w$  and hence  $u_b$  in a positive feedback process. According to this model, surging occurs when the glacier geometry is such that the linked cavity system can persist for several weeks or months beneath the upper part of the glacier, the destabilizing effect of increases in  $P_w$  being exceeded by the stabilizing effect of the increase in  $u_b$  in the developing surge. As the surge front moves downglacier, the tunnel system beneath the lower part of the glacier is disrupted and transformed into a linked cavity system behind the front (Humphrey and Raymond, 1994). Eventually, however, due either to further increases in  $P_w$  or to changes in glacier geometry or both, the tunnel system is finally re-established under the bulk of the glacier, water drains efficiently,  $P_w$  decreases, and the surge ends.

This model is consistent with observations leading up to and during the 1982–1983 surge of Variegated Glacier, Alaska, one of the best studied examples of a surging glacier in the world (Kamb *et al.*, 1985; Kamb, 1987). Variegated Glacier surges every 20 years or so (Kamb *et al.*, 1985). During the decade leading up to the 1982–1983 surge, the glacier became thicker and steeper, and on its upper part  $u_s$  increased during the winter (Figure 8.23a and b) (Raymond and

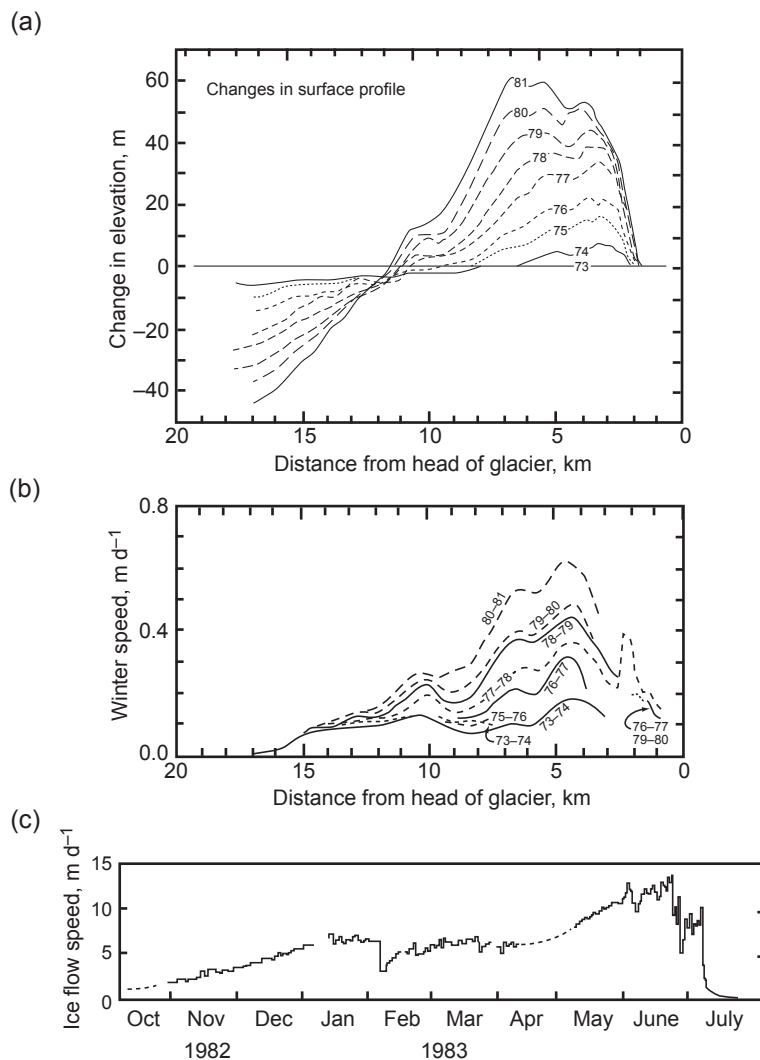


**Figure 8.23** Evolution of the: (a) surface profile, and (b) speed of Variegated Glacier during its build up to a surge. (c) Surface speed of the upper part of Variegated Glacier during its surge in 1982–1983. ((a) and (b) from Raymond and Harrison, 1988, Figures 4 and 5b; (c) from Kamb *et al.*, 1985, Figure 2b. Reproduced with permission of the authors, the International Glaciological Society, and the American Association for the Advancement of Science)

Harrison, 1988). Calculated and measured rates of internal deformation indicate that the increase in  $u_s$  was largely a result of an increase in  $u_b$ . In 1983, the acceleration to surge speeds started in the early winter on the upper part of the glacier (Figure 8.23c) when decreasing water input is likely to have led to increasing  $P_w$ , and the increase in  $u_b$  may have resulted in destruction of a tunnel system. Dye-trace data, mentioned earlier (p. 220), suggest that the drainage system was distributed at this time. The dye moved slowly and emerged at a number of points

across the width of the glacier terminus, and the water was extremely turbid. As the surge progressed, the glacier's speed gradually increased (Figure 8.23c), presumably in the positive feedback process mentioned above. Eventually, large floods of dirty water emerged at the terminus, the glacier surface dropped abruptly, indicating that a lot of water had been in subglacial storage reservoirs, and the surge ended. A dye trace following the surge suggested that the drainage system had reverted to a tunnel configuration; the dye moved quickly and appeared in only one stream, and the sediment concentration was lower. Measurements in a borehole confirmed that  $P_w$  was within 0.5 MPa of the overburden pressure during the surge, with frequent fluctuations to within 0.15 MPa of overburden, and occasionally above it. Before and after the surge,  $P_w$  was typically 0.8–1.6 MPa below the overburden pressure, which was 3.6 MPa at the site of the hole.

Presenting a possible alternative model for some other surges, Truffer *et al.*, (2000) suggest that, if a glacier is underlain by till, a surge could be initiated when water pressures and shear stresses become large enough to mobilize the till. Any efficient tunnel drainage would then be disrupted, to be replaced by an inefficient distributed drainage. A substantial amount of water can be stored in such a drainage system, and  $P_w$  will be high, thus sustaining the fast motion. A sudden release of the stored water would end the surge, as on Variegated Glacier.

Surging of polythermal glaciers, on the other hand, may involve thermal mechanisms. Clarke (1976) thought that a surge might be initiated once enough of the bed of such a glacier warmed to the pressure melting point and sliding began. Frictional heating would then increase the area of the thawed bed in a positive feedback. As the surge progressed and the glacier thinned, the temperature gradient at the bed would increase until all of the frictional and geothermal heat could be conducted upward into the ice. The bed would then refreeze, the surge would end, and a period of quiescence would follow. Eventually the thickness of the glacier would increase enough to warm the bed and initiate a new surge. Such surges last several years. This model has been analyzed in greater detail by Fowler *et al.* (2001).

A somewhat different thermal mechanism is apparently responsible for surging of a polythermal outlet glacier draining Austfonna Ice Cap on Svalbard (Dunse *et al.*, 2015). This glacier, which is frozen to its bed at the margin, last surged in the 1870s. A new surge began in the autumn of 2012, a recurrence interval of ~140 years. During 4 years leading up to the initiation of the 2012 surge, and likely for some years before that, prior to the initiation of measurements, there was a step-like increase in  $u_s$  on the lower part of the glacier each summer. The velocity would roughly double in July and then give back only part of that increase over the next few months. These accelerations resulted in extensional flow, crevassing, and some drawdown in the reservoir area. The increases in  $u_s$  are attributed to

increases in  $u_b$  and in till deformation as input of surface meltwater increased  $P_w$  at the bed. Once this process was initiated, the crevassing increased the input of surface water in a positive feedback. Dunse *et al.* think that sensible and latent heat transferred to the bed by this water gradually increased the area of the bed that was at the pressure melting point. This would account for the observation that, following each summer's acceleration,  $u_s$  did not drop back all the way to its value the previous winter. Eventually the thawed area increased enough to destabilize the glacier and it surged. The glacier was still surging as of July 2018 (Schellenberger *et al.*, 2017; T. Dunse, written communication), but the surge was expected to end once thinning of the ice had reduced the driving stress sufficiently. Thereafter gradual cooling of the bed, likely combined with a change in drainage structure, would stabilize the glacier, accounting for the long interval between surges.

In short, there appear to be several sources of instability that can lead to surging. Their common denominator is a mechanism that increases  $u_b$ .

## Jökulhlaups

Icelanders have been particularly interested in understanding jökulhlaups because they occur frequently there, causing extensive damage to infrastructure and leaving distinctive scars on the landscape. The largest of these jökulhlaups have estimated peak discharges of order  $10^5 \text{ m}^3 \text{ s}^{-1}$  and total volumes of  $\sim 1 \text{ km}^3$  (Björnsson, 1992). The water sources are either subglacial lakes, formed over geothermal hot spots, or ice-marginal lakes (see p. 218). Many of the Icelandic jökulhlaups originate beneath the ice cap Vatnajökull. Those draining Vatnajökull's subglacial lake Grímsvötn have occurred every 4–6 years since the 1940s, and are among the best studied.

One might expect that a jökulhlaup would be initiated once the level of a subglacial lake had risen high enough to float the enclosing ice. This, however, is not the case. The ice seals tend to fail when  $P_w$  is as much as 0.2–0.6 MPa less than  $P_i$  (Björnsson, 1992). Nye (1976) explains this in the following way: The lake water is warmed by the geothermal heat. The warmed water continually melts ice surrounding and covering the lake. As the transition from ice to water involves an increase in volume, the lake exerts an upward force on the ice covering it. Because the ice cannot respond fast enough by flow, this force acts as a cantilever, tending to lift the ice at the seal, reducing the water pressure at which the seal fails.

Once the seal is broken and water starts to flow, it may either melt a tunnel upward into the ice – a Röthlisberger channel – or spread out in a sheet. Most jökulhlaups appear to involve tunnel flow, though some of the largest apparently

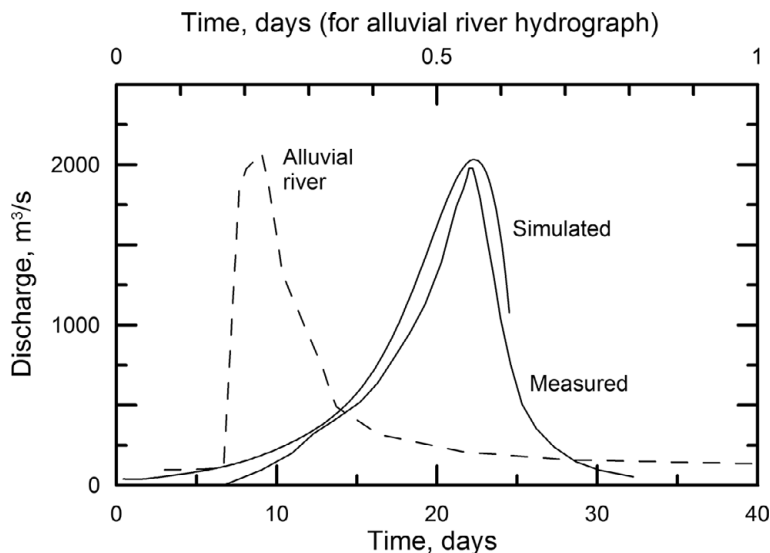


**Figure 8.24** Theoretical and observed hydrographs from a jökulhlaup from Grímsvötn, Iceland, and a hydrograph from a small alluvial river for comparison. Theoretical hydrograph calculated using  $\bar{n} = 0.8 \text{ m}^{-1/3} \text{ s}$ . (Jökulhlaup hydrographs from Björnsson, 1992, Figure 9. Reproduced with permission of author and the International Glaciological Society)

involved sheet flow. Here, we will consider only the former. As earlier, viscous heat and heat stored in the lake water tend to enlarge the tunnel, and ice creep tends to close it. At first,  $\partial\Phi/\partial s$ ,  $Q$ , and  $P_w$  are high so the melt rate exceeds the closure rate, and the tunnel grows larger, increasing  $Q$  in a positive feedback as discussed above (p. 218). This causes a catastrophic flood. However, as the lake drains and its level subsides,  $\partial\Phi/\partial s$ ,  $Q$ , and  $P_w$  all decrease and closure exceeds melt by a substantial margin, leading to collapse of the tunnel and a precipitous decrease in flow. The flow is commonly shut off before the lake has drained completely (Nye, 1976; Clarke, 1982).

A hydrograph from a Grímsvötn jökulhlaup is shown in Figure 8.24, together with one calculated using parameters relevant to that particular flood. A typical hydrograph from a flood on an alluvial river is also shown for comparison. The river hydrograph rises sharply and then falls gradually as delayed surface runoff and groundwater find their way to the channel. The jökulhlaup hydrograph rises slowly as the conduit is opened, and then falls rapidly as the conduit collapses. The shape of the rising limb of the actual hydrograph is captured fairly well by the simulation, but then the hydrograph takes too long to peak, so simulation of the descending limb is unsatisfactory. (The theoretical model terminates when the calculations predict that the conduit is closed.) A likely explanation for this failure is that the numerical model assumes a cylindrical conduit (Björnsson, 1992). A broad low conduit would close faster.

## Subglacial drainage and the formation of eskers

### Esker paths

Traces of subglacial drainage paths are often preserved in the landscape. Eskers are one of the more common geomorphological features marking these paths. Eskers are sinuous ridges of gravel, typically with undulating crests, deposited by streams flowing in subglacial tunnels. They are largest and best developed in areas that were once covered by late Pleistocene continental ice sheets moving over hard beds with minimal till cover (Walder and Fowler, 1994). They can be tens of meters in height and tens or hundreds of kilometers in length.

Eskers often appear to follow bizarre paths when viewed from the perspective of people accustomed to the courses of subaerial streams. Eskers may climb hills, trend diagonally down valley sides, and run along valley sides instead of in valley bottoms. Shreve (1972, 1985a, 1985b) has shown that these characteristics can be readily understood from consideration of the hydraulic potential field beneath an ice sheet.

We've noted (Figure 8.6) that englacial water is expected to move in directions that are normal to equipotential planes in a glacier. Similarly, along the bed of a glacier water flow should be normal to the intersections of these equipotential planes with the bed. This is equivalent to saying that water flow down a valley side should be normal to topographic contours, as topographic contours are the intersections of surfaces that are a constant height above sea level ( $\equiv$  surfaces of equipotential) with the topography.

Let's consider a couple of examples. The solid lines on the map in Figure 8.25a are topographic contours. They depict a gentle slope leading down to a valley that drains to the south. East of the valley there is a ridge that varies in elevation. Now, visualize the situation when an ice sheet covered the landscape, as shown in Figure 8.25b. The surface of the ice sheet sloped to the east, so the equipotential planes dipped westward. The dashed contours show the intersections of these planes with the landscape. These intersections are precisely analogous to the outcrop pattern that would be formed on the landscape by a westward-dipping sedimentary rock unit.

Under subaerial conditions, creeks would run down the gentle topographic slope on the west side of the valley, and then turn south. However, when ice covered the area, subglacial water would not have turned south. Instead, flowing normal to the contours of equipotential, it would have been deflected toward the low point in the ridge. If such a subglacial stream could not carry all of the sediment delivered to it, we might now find an esker crossing the ridge at its lowest point. This is commonly observed in situations in which ridges cross the paths of eskers.

In Figure 8.25b the equipotential planes are distorted in the vicinity of the ridge. This is because the ice is flowing and the pressure is thus higher on the stoss side of

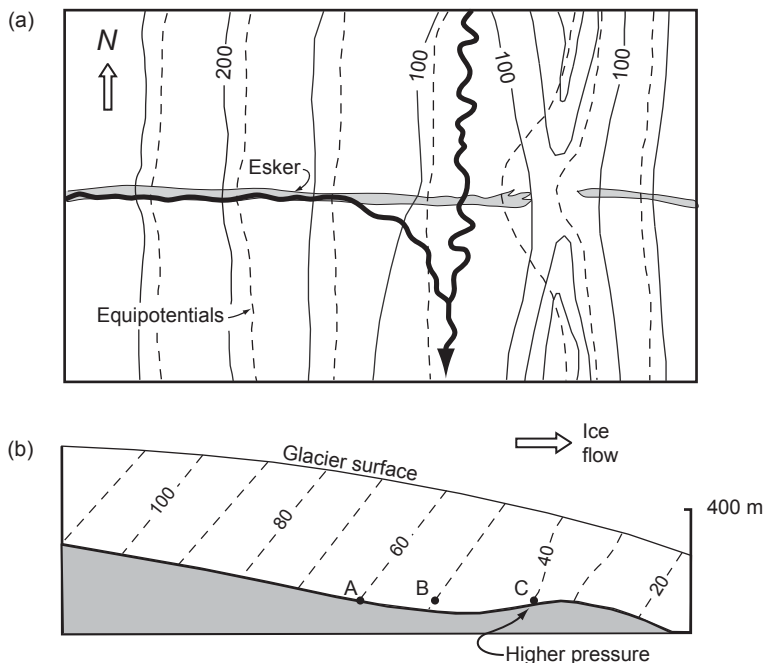


**Figure 8.25** (a) Contour map of a landscape on which are superimposed contours (dashed) of equipotential from a time when an ice sheet covered the landscape. (b) Topographic cross section from a time when ice was present, showing the equipotential surfaces in the ice sheet.

the ridge than in its lee. To understand why the planes are distorted as shown, remember that at a *constant elevation* the decrease in potential from A through B to C is due solely to a decrease in  $P_w$  (Equation 8.2). Some distance away from the ridge a potential drop of 10 units occurs over a horizontal distance  $\overline{AB}$ . Near the stoss side of the ridge, however, where the pressure is elevated, a longer distance,  $\overline{BC}$ , is required for the same drop. In the lee of the ridge, the distortion is in the opposite sense. Because the velocity of water in a tunnel is proportional to  $\partial\Phi/\partial s$  (Equations 8.13 and 8.14), this distortion of the potential field affects the velocity. In particular, where  $\partial\Phi/\partial s$  is higher over the crest of the ridge, the velocity would be higher. This is consistent with the observation that eskers are commonly discontinuous across the crests of such ridges; the higher velocity flow there presumably inhibited deposition.

Another hypothetical situation is shown in Figure 8.26. Here, a topographic valley drains southeastward, diagonally across the direction of glacier flow. Consequently, the trough in the equipotential contours is on the valley side rather than in the valley bottom, and this is where an esker would be found if conditions were otherwise suitable for its formation. Again, eskers are commonly found in such positions under these circumstances.

With an understanding of the physical processes that determine the locations of eskers in situations such as those in Figures 8.25 and 8.26, it is sometimes

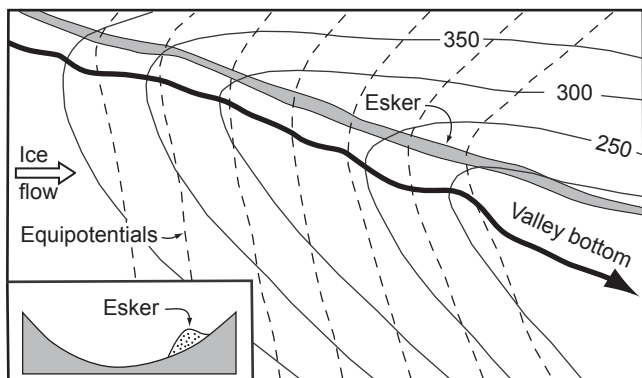


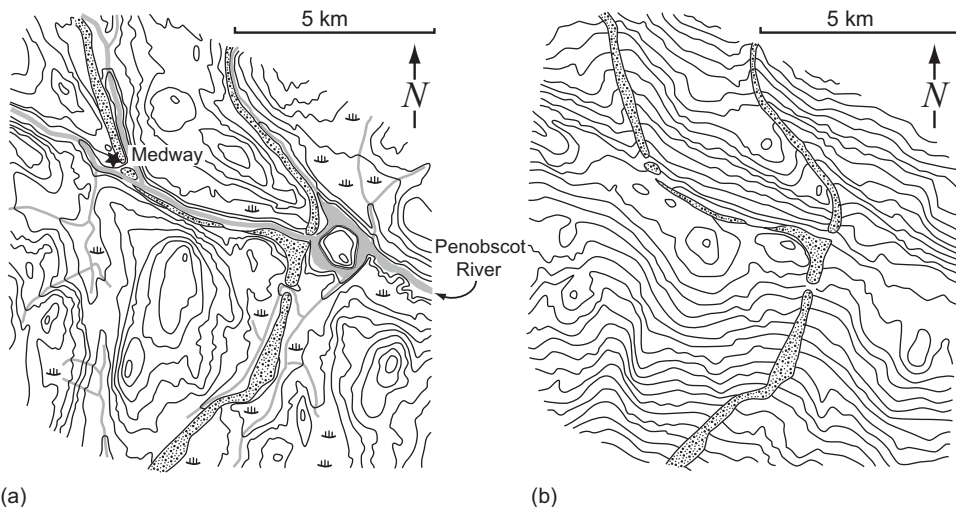
**Figure 8.26** Topographic map of a valley trending diagonally across the direction of ice flow, showing how an esker formed in such a situation would be on the side of the valley.

possible to determine the surface slope of the glacier beneath which the esker formed. As an example of this, consider the section of the Katahdin esker near the town of Medway in Maine shown in Figure 8.27a. Ice flow was roughly from north to south in this area. In the northern part of the map, two branches of the esker follow respective southeast-trending branches of the Penobscot River, but are slightly offset from the river, up onto the valley sides in the downglacier direction, as in Figure 8.26. However, south of the junction between the two branches, the esker departs from the valley of the Penobscot to run *up* the valley of a small tributary and then across the divide between this tributary and another small southward-flowing creek. Shreve (1985a) found that the course of the esker was more consistent with the potential field beneath an ice sheet with a surface slope of 0.005 (Figure 8.27b) than with ice sheets with higher or lower surface slopes.

### Sediment supply to eskers

Eskers form where the sediment load delivered to a subglacial stream exceeds the transport capacity of the stream. The debris-laden basal ice of the glacier is the primary source of such sediment. As the energy dissipated by the flowing water melts this ice, debris is released and an inward flow of ice toward the tunnel is induced.

A nice demonstration of this process is provided by lithologic pebble counts from the Great Pond section of the Katahdin esker, down-flow from a point where the esker crosses bedrock units of distinctive lithology (Van Beaver, 1971). The concentration of pebbles of these lithologies in the esker reaches a maximum about 3 km down-flow from the point where the esker crosses the units (Figure 8.28). Had the stream been acquiring the pebbles directly from the bedrock, a difficult task at best once the esker began to develop on top of the rock, the concentration should have peaked at the down-flow edge of the unit. Actually, however, it was the glacier that



(a)

(b)

**Figure 8.27** (a) Map of the Penobscot River and a section of the Katahdin esker near Medway, Maine. Near the middle of the map, the esker leaves the valley of the river and trends south-southwestward up a small tributary valley. (b) Map of equipotential contours beneath an ice sheet with a southward surface slope of 0.005. The esker generally follows a trough in the potential surface. (After Shreve, 1985a. Reproduced with permission of the author and the Geological Society of America)

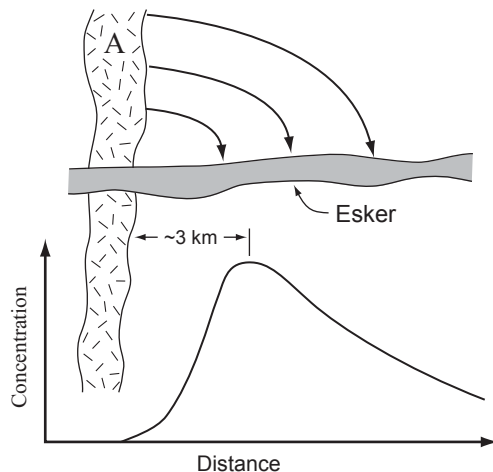


**Figure 8.28** Schematic sketch showing variation in concentration of lithology A in an esker down-flow from the point where the esker crosses the outcrop of this lithology. Rocks eroded by the glacier are carried along arcuate paths downglacier and inward toward tunnel.

eroded the pebbles from the bed. It then carried them along arcuate paths (Figure 8.28) until they were released into the stream (Shreve, 1985a).

This source of sediment is quite adequate to overload a subglacial stream, leading to deposition. For example, suppose an esker formed beneath an ice sheet with a surface slope of 0.025. Numerical modeling suggests that this is a reasonable surface

slope within a few kilometers of the margin. Suppose further that the geometric mean diameter,  $d_{50}$ , of the coarsest sample was 46 mm. This is the coarsest of three analyses made by Hooke and Fastook (2007). The flow velocity under which such sediment would be in general motion in a semicircular conduit with a gravel bed is:

$$v = \frac{2.731 d_{50}^{0.486}}{S^{0.182}} = 1.2 \text{ ms}^{-1} \quad (8.26)$$

Parker (1979). In a conduit with a roughness,  $\tilde{n}$ , of  $0.1 \text{ m}^{-1/3} \text{ s}$ , such a velocity would be attained if the conduit diameter were  $\geq 4.4 \text{ m}$ , in which case the discharge would be  $\geq 9.6 \text{ m}^3 \text{ s}^{-1}$ . Parker's regime equations then yield a sediment flux of  $\sim 0.13 \text{ m}^3 \text{ d}^{-1}$  per meter width. The energy available for melting would thus be  $\sim 90 \text{ J m}^{-2} \text{ s}^{-1}$ , which would melt  $\sim 0.026 \text{ m}$  of ice per day. If the basal ice contained 10% debris by volume, the debris released by this melting would overload the stream after it flowed along the conduit for only 49 m ( $0.026 \times 0.10 \times 49 = 0.13 \text{ m}^3 \text{ d}^{-1}$  per meter width).

### Size and location of water conduits on eskers

It is natural to assume, as a first approximation, that the tunnel within which an esker formed was comparable in size to the esker (Figure 8.29a). This is consistent with the observation that some eskers are composed of coarse gravel, commonly containing meter-scale rounded boulders, with a dearth of sedimentary structures. This, however, may be a poor assumption, as the flux of water implied by a tunnel of this size would be horrendous.

In the calculation above we found that gravel with a  $d_{50}$  of 46 mm would be in general motion in a semicircular conduit with a diameter  $\geq 4.4 \text{ m}$ , which is small in comparison with the size of many eskers.

In a gravel with a  $d_{50}$  of 46 mm, 50% of the gravel, by weight, is larger than 46 mm, so a  $d_{50}$  of 46 mm does not ignore the larger clasts that are commonly present. However, many of the largest boulders in eskers may have simply dropped from the tunnel roof and been rounded by impact with smaller material in transport; they may not have moved significantly. Furthermore, the fluid velocity needed to move a 1 m boulder is somewhat over  $5 \text{ m s}^{-1}$  (Costa, 1983, Figure 4). While this is not an unreasonable velocity, Equation (8.26) is then not suitable for estimating a corresponding conduit size because: (i) 1 m is a maximum size and not  $d_{50}$ , and (ii) the effective roughness decreases as the conduit size increases.

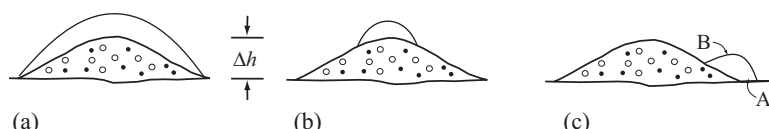


**Figure 8.29** Esker of height  $\Delta h$  with: (a) conduit comparable in size to esker; (b) small conduit on top of esker; and (c) small conduit low on side of esker.

If the tunnel is relatively small compared with the size of the esker, it is also of interest to determine whether it is on top of the esker (Figure 8.29b) or low on the side (Figure 8.29c). The intersections of upglacier-dipping equipotential planes with an esker will be convex downflow, as in a sloping ridge, and streams are not noted for flowing along ridge crests. This suggests that the conduits should be low on the side of the esker. However, one might then expect eskers to be broad-crested and low rather than sharp-crested and high, as is commonly the case.

This problem can be addressed using the following argument, adapted from Lliboutry (1983). If the height of the esker is  $\Delta h$  (Figure 8.29), and there are two channels that are connected hydraulically, one on top of the esker and one on the side, then:

$$\begin{aligned} P_w^{\text{side}} &= P_w^{\text{top}} + \rho_w g \Delta h \\ P_i^{\text{side}} &= P_i^{\text{top}} + \rho_i g \Delta h. \end{aligned} \quad (8.27)$$

The pressure causing tunnel closure is  $P_c = P_i - P_w$ , so subtracting the first of Equations (8.27) from the second:

$$P_c^{\text{side}} = P_c^{\text{top}} - (\rho_w - \rho_i) g \Delta h$$

Now, from Equation (8.18), holding factors other than  $Q$  and  $P_c$  constant and using  $n = 3$ , we find that  $Q \propto P_c^{12}$ . Thus:

$$\frac{Q^{\text{top}}}{Q^{\text{side}}} = \left[ \frac{P_c^{\text{top}}}{P_c^{\text{side}}} \right]^{12} = \left[ 1 + \frac{(\rho_w - \rho_i) g \Delta h}{P_c^{\text{side}}} \right]^{12}. \quad (8.28)$$

So  $Q^{\text{top}} > Q^{\text{side}}$  and the conduit on top of the esker will expand at the expense of that on the side. Phrased differently, owing to the nonlinearity of the flow law, the increase in  $P_w$  as one moves down off the esker is easily offset by the increase in potential closure rate, so water is forced up onto the top of the esker.

In summary, although questions remain, these calculations and the shapes of sharp-crested eskers suggest that esker-forming flows were small compared with the size of many eskers, and that the non-linearity of Glen's flow law results in a tendency for conduits to be on tops of eskers, despite the potential gradient favoring positions on the flanks.

### Esker heads, nets, and segments

Following an esker downflow in the valley Antedalen, in Norway, one first encounters several situations in which a small esker drops down off the side of the parent, parallels it for a short distance, and then climbs back up onto it again (Figure 8.30). These small daughter eskers form because the ice was getting thin, reducing  $u_c$  and invalidating the analysis leading to Equation (8.28) which applies only when  $u_c = m$ . Further downflow, where the ice was still thinner, the parent esker was larger and

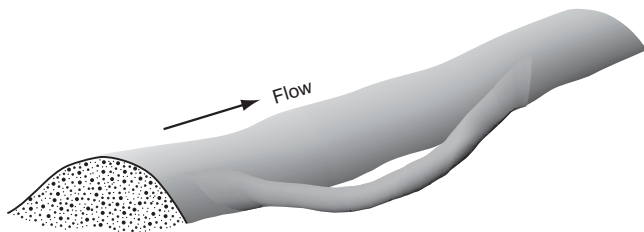


**Figure 8.30** Sketch of small daughter esker diverging from and later rejoining parent esker. This occurs near the ice margin where the ice is thin and  $u_c$  is low (Bruce Hooke assisted with artwork).

the daughters grew to nearly the same size as the parent, forming an anastomosing pattern of ridges – an *esker net*. Esker nets are common (Figure 8.31). They were apparently first described by Stone (1899, p. 448ff), who called them reticulated eskers. The downflow increase in size occurs because, with  $m > u_c$ , the conduit expands, reducing the water velocity so coarser sediment is deposited, forming a massive wedge-shaped deposit – an *esker head* (Figure 8.31). During deposition of the Katahdin esker, the ice margin was in the sea. Thus, one typically finds that esker heads give way downstream to steep slopes leading down to submarine fans or to deltas. The fans are composed of sand and fine gravel that was flushed through the enlarged conduit where coarser material was being deposited. In Antedalen, in contrast, the ridge character becomes indistinct downflow, and the system merges into a kettled outwash plain.

Many eskers were deposited in segments as the ice retreated (e.g. Donner 1965; Banerjee and McDonald, 1975; Hebrand and Åmark, 1989; Ashley *et al.*, 1991; Bolduc, 1992, p. 115; Hooke and Fastook, 2007). In the Katahdin esker, a typical segment begins as a relatively small, sharp-crested ridge. Downflow the ridge increases in size, at first gradually, but nearer the margin more rapidly (Figure 8.32), ending in an esker head or net, or in a combination of the two forms (Figure 8.31). The next segment downflow may develop from a continuation of one of the branches of an esker net (Figure 8.31), emerge from a fan or delta, or pick up after a short gap (Figure 8.32).

The Katahdin esker was deposited in ~2000 years as the ice retreated ~150 km from the coast to northern Maine. There are roughly 30 segments in this distance, so their mean length is ~5 km, and the mean length of time to deposit a segment was ~70 years.

Based on their modeling, Hooke and Fastook (2007) estimated that subglacial melting could provide a discharge of  $\sim 2 \text{ m}^3 \text{ s}^{-1}$  at the margin of the ice sheet at the location of the Katahdin esker. The calculations above suggest that  $2 \text{ m}^3 \text{ s}^{-1}$  would not move the material found in the esker. Perhaps more critically, the melt rate on the conduit walls was too low to supply enough material to build a segment in the time available. Thus surface water, reaching the bed through moulin, was apparently required.

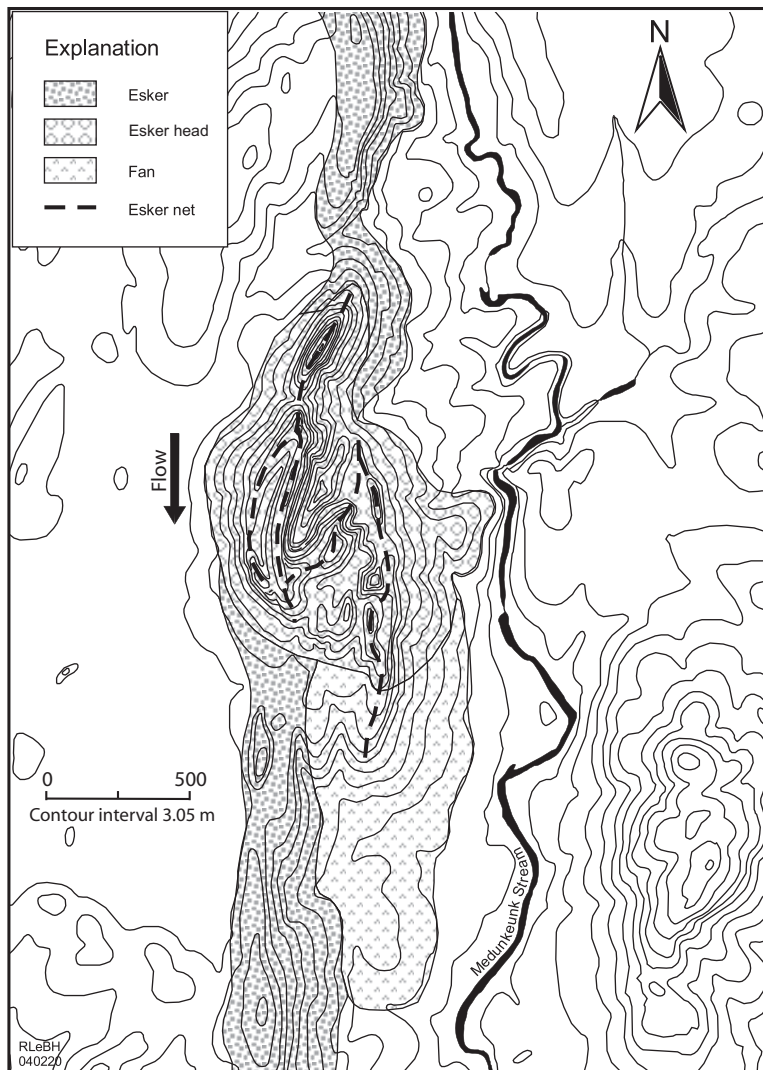


**Figure 8.31** Map of a section of the Katahdin esker showing an esker head and net. There is a fan downflow from the head (the site is 4½ km NNE of Lincoln Center, Maine).

Eskers, however, tend to consist of a single, albeit discontinuous, ridge, and they follow “valleys” in the equipotential contours. Moulins, on the other hand, occur in places where bed topography results in local areas of extending flow or in depressions in the surface in which lakes can form. There is no physical reason why moulins should occur over equipotential valleys. Yet, one seldom finds tributary eskers that might represent pathways from moulins to

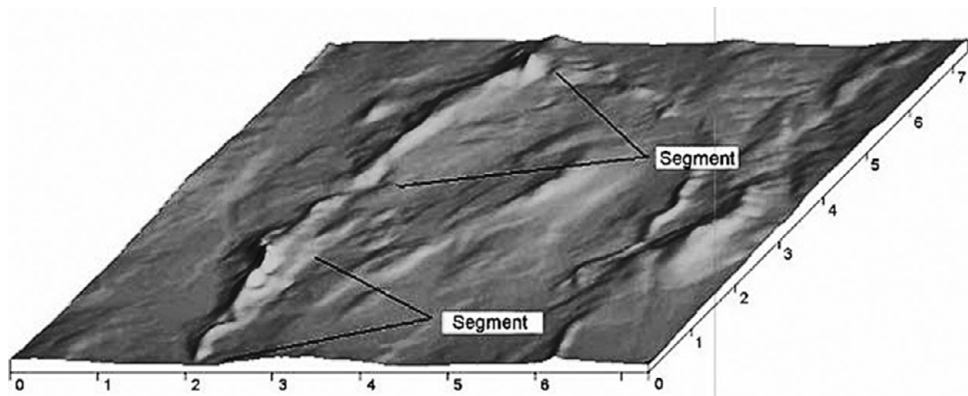


**Figure 8.32** Oblique view, looking downflow, of two segments on the Katahdin esker southeast of Olamon, Maine. Based on a 30 m digital elevation model; scale in kilometers. (From Hooke and Fastook, 2007, Figure 9. Reproduced with permission of the International Glaciological Society)

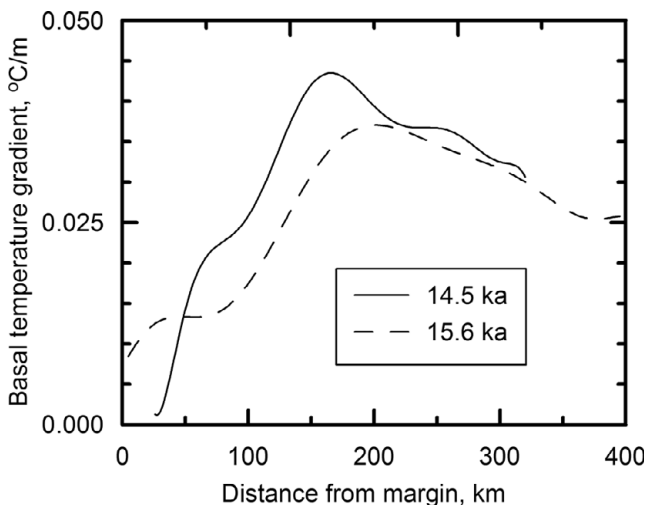


**Figure 8.33** Basal temperature gradients in the Laurentide Ice Sheet in Maine at two different times during deglaciation. Based on a numerical model. (Modified from Hooke and Fastook, 2007, Figure 7. Reproduced with permission of the International Glaciological Society)

equipotential valleys. So why do esker segments line up as consistently as they do?

Hooke and Fastook thought that subglacial drainage systems leading away from moulin might be distributed. Their modeling suggested that at distances greater than  $\sim 5\text{--}10$  km from the margin, high temperature gradients in the basal ice could conduct upward into the ice so much of the viscous heat dissipated by the flowing water, that none would be left to melt an arched conduit in which an esker could form (Figure 8.33). According to this hypothesis, deposition of an esker segment did not start until the water had reached the equipotential valley and flowed some

distance toward the margin. Further from the margin, the decreasing glacier surface slope results in lower  $\partial\Phi/\partial s$  and hence lower  $m$ , further inhibiting development of arched Röthlisberger conduits in which eskers could form.

## Tunnel valleys

*Tunnel valleys* are another geomorphic feature formed by subglacial water flow. These valleys are broad and relatively straight, are oriented normal to former ice margins, and end at these margins. Some ascend adverse gradients near their termini (Mooers, 1989; Cutler *et al.*, 2002), so they must have been eroded by “pressurized” water. Thus, they were clearly formed subglacially. The lack of evidence for modification by overriding ice, however, implies that any subsequent ice movement was sluggish or short lived.

Tunnel valleys were apparently first described by Ussing (1903) from Jylland in Denmark. They occur along the margins of many lobes of the Laurentide Ice Sheet in midwestern USA, where they are typically 10–20 km long, 200–500 m wide, and 5–30 m deep (Hooke and Jennings, 2006). Some, however, reach depths in excess of 200 m, and the depth of fill, if any, is generally not known. Some have tributaries or distributaries. Tunnel valleys are rare or absent along the most southerly margin of the Laurentide Ice Sheet, implying that they are a characteristic of colder environments where frozen bed conditions were likely present along the ice margin (Cutler *et al.*, 2000).

Tunnel valleys commonly debouch onto proglacial gravel fans. In some cases there are distinct but overlapping fans at the end of a single tunnel valley (Attig *et al.*, 1989; Patterson, 1994), suggesting that flows coursed through the same valley more than once, but not continuously.

The origin of the water and the nature of the flows that cut the tunnel valleys are actively debated. Was the water from basal melt alone, or was there a contribution from the surface? Was the water flow continuous over a period of decades or centuries, or was it released catastrophically? Boulton and Hindmarsh (1987) and Mooers (1989) have discussed the possibility that they were eroded by relatively modest discharges maintained for long periods of time. The former think that subglacial melt could provide these flows, but Mooers appeals to large sustained discharges from superglacial meltwater delivered to the bed through moulin.

Cutler *et al.* (2002) found that some fans at the ends of tunnel valleys consisted of tens of meters of sand and gravel overlain by a bed, 3–5 m thick, containing boulders up to 2 m in diameter. The boulder bed seemed to require a water flux greater than could be supplied by superglacial water or by steady-state basal melt. They suggested that it was deposited by subglacial water that was released catastrophically when a seal was breached. The seal, they thought, was a marginal

zone in which the ice was frozen to the bed. Relict permafrost features, pollen evidence, and numerical modeling all suggest that a wedge of frozen ground might well have extended several kilometers in under the ice sheet at this time (as in Figure 6.19a).

Hooke and Jennings (2006) also appeal to a seal formed by a frozen margin, and suggest that sapping, driven by the high gradient in hydraulic head across such a seal, could initiate an outburst, or jökulhlaup, from a subglacial lake. In a rough calculation, they found that the pressure tending to force water up through the proglacial permafrost could be many times the overburden pressure. This ratio increases rapidly as the permafrost thins, suggesting that outbursts would be most likely during climatic warming. Once the subglacial lake had drained, the valley would again fill with ice, the seal would reform, and over a period of years the lake would refill, setting the stage for another outburst. Based on the size of the valleys and the volume of material in a typical deposit from a single flood, they suggested that the number of floods involved in cutting a valley was of order  $10^1$ , and that floods of order  $10^8 \text{ m}^3$  were necessary to transport the volume of material in the deposit. Given the likely size of the area drained by a tunnel valley and typical subglacial melt rates, they thought the time necessary to accumulate this amount of water by subglacial melting would be on the order of  $10^1$  years.

## Water pressure and glacier quarrying

Quarrying is the principal process of glacier erosion. In quarrying, blocks of bedrock must first be loosened, either along pre-existing joints or along fractures formed by subglacial processes. Then they must be entrained by the glacier. Because rock fragments that have been loosened but not removed are uncommon on deglaciated bedrock surfaces, Hallet (1996) argues that loosened blocks are readily entrained. He thus concludes that fracture must be the rate-limiting process.

All rocks contain microcracks, fractions of a millimeter to a few millimeters in length. When cracks are favorably-oriented, pressure fluctuations on bedrock bumps, amplified by changes in  $P_w$  in adjacent cavities (See Figure 7.10), can cause propagation of crack tips (Griffith, 1924), even at stresses well below the experimentally-determined tensile strength of the rock (Atkinson and Rawlings, 1981; Atkinson, 1984; Segall, 1984), much as a crack initiated at a stone bruise on your windshield eventually propagates across the windshield. The likelihood of crack growth increases when the water pressure in the cracks remains elevated while that in an adjacent cavity drops, or when *stress corrosion*, the weakening of strained bonds by an environmental agent, in this case water, reduces the rock's strength (Atkinson, 1984; Iverson, 1991b). Even higher and more concentrated stress differences can result when ice drags a cobble or boulder across a bump.

Boulders with smooth stoss faces and plucked lee faces that are embedded in till, called *bullet boulders*, provide convincing field evidence for subglacial fracture (e.g. Sharp, 1982). These boulders were transported by the ice and became lodged in the till as the basal ice melted. They would not have had their characteristic shape prior to lodgement, nor could they have been transported to their present location, intact, if they had pre-existing fractures. Thus their shape, including the plucked lee face, must have been produced by the overriding glacier after they became lodged.

Once a block of rock is isolated by fractures, bed-parallel forces tending to slide it out of position must exceed frictional forces tending to hold it in place in order for entrainment to occur (Iverson, 1989). Both bed-parallel and the frictional forces are affected by fluctuations in  $P_w$ . As noted earlier (Figure 7.6), pressure-release freezing may occur on tops of bumps when increases in water pressure in cavities transfer part of the weight of a glacier away from the bumps (Robin, 1976), and similar cold patches can also develop due to simple flow of ice from the stoss side of a bump to its crest. Both processes increase the drag exerted by the ice on the block.

Increases in  $P_w$  also reduce frictional forces resisting dislodgement of loosened blocks (Iverson, 1989). This is because the increases in  $P_w$  reduce the normal pressure on bedrock surfaces upglacier from cavities, thus decreasing the friction along fractures that bound loosened blocks. In addition, once fractures are well-developed and in hydraulic communication with cavities, increases in  $P_w$  in the fractures themselves reduce the effective pressure across fracture surfaces.

Iverson (2012) has developed a model of glacier erosion by quarrying based on these ideas. He thought that any volume of rock should contain many fractures of varying strength, and that larger volumes would have a greater probability of containing a large flaw. Thus, the likelihood of entrainment of a fragment should depend, in part, on the volume of rock under attack. In a two-dimensional glacier bed with steps of length,  $L$ , and height,  $h$ , and cavities of length,  $S$  (Figure 8.34), the volume of rock subject to intense stress,  $\sigma_n$ , is  $h(L - S)$ . Iverson suggested that a

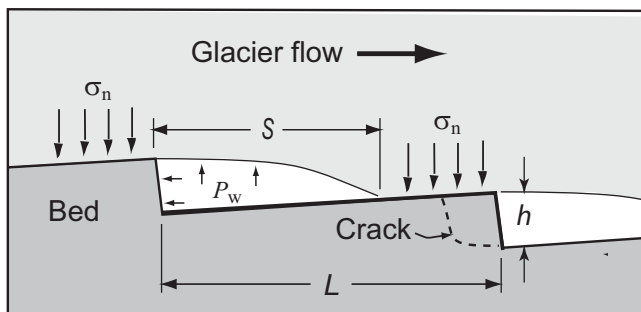


Figure 8.34 Bed geometry and parameters used in Iverson's (2012) analysis of glacier quarrying.

reasonable estimate of the mean size,  $V_e$ , of fragments dislodged would be half this, so the mean amount of erosion of a step by removal of such a fragment would be (in units of meters per step):

$$\frac{V_e}{L} = \frac{1}{2}h\left(1 - \frac{S}{L}\right).$$

In a year a glacier slides a distance,  $u_b$ , and thus exerts stress on  $u_b/L$  steps per year, so the erosion rate,  $E$  (m a<sup>-1</sup>), is:

$$E = \frac{u_b V_e}{L^2} = \frac{u_b kh}{2L} \left(1 - \frac{S}{L}\right)$$

where  $k$  is the probability that a step will fail under the applied stress.

To estimate  $S$ , note that the time required for the ice to move from the top of a step to the point where it again contacts the bed,  $S/u_b$ , equals the time required for the ice to sink a distance  $h$ , or  $h/u_c$ , where  $u_c$  is the cavity closure rate. The latter can be estimated with the use of Equation (8.4) with  $S$  substituted for  $r$ . The result is:

$$S = 0.31 \left(\frac{u_b h}{A}\right)^{\frac{1}{2}} \left(\frac{n}{P_c}\right)^{\frac{h}{2}} \quad (8.29)$$

in which 0.31 is a correction factor, based on an exact solution to this problem for ice with a linear ( $n = 1$ ) rheology. This correction factor adjusts for the fact that in the present case the ice is supported by the bed at the point of separation, thus reducing  $u_c$  (Iverson and Petersen, 2011).

For  $k$ , the probability of failure of a step under a deviatoric stress,  $\sigma'$ , Iverson uses a Weibull probability distribution of rock strength:

$$k = 1 - e^{-\frac{h(L-S)}{V_o} \left(\frac{\sigma'}{\sigma_0}\right)^m}$$

in which  $V_o$  is a characteristic rock volume large enough to contain the largest cracks,  $\sigma_0$  is the mean strength of the rock under conditions of slow subcritical crack growth, and  $m$  is a modulus which ranges from ~1.5 in rocks with a heterogeneous distribution of flaw strengths to ~5 in fairly homogeneous rocks.

To obtain  $\sigma'$ , note that the glacier is supported in part by water in the cavity and in part by the vertical pressure,  $\sigma_n$ , on the crest of a step, so summing forces:

$$P_i L = P_w S + \sigma_n (L - S). \quad (8.30)$$

Fracture is promoted by  $\sigma_n$  acting on the crest of the step, but resisted by  $P_w$  supporting the rock face. Thus the stress tending to fracture the rock is  $\sigma_n - P_w$  ( $\equiv \sigma'$  (Equation 2.8)), so we can write:

$$\sigma' = \sigma_n - P_w \frac{(L - S)}{(L - S)} = \sigma_n + \frac{P_w S}{(L - S)} - \frac{P_w L}{(L - S)}.$$

Then using Equation (8.30) and remembering that the effective stress,  $N_e (= P_c)$ , is  $P_i - P_w$ , we see that:

$$\sigma' = P_c \left( \frac{L}{L - S} \right). \quad (8.31)$$

Iverson has calculated  $E$  as a function of  $u_b$  for a number of bed configurations. One was a bed consisting of a random distribution of step sizes ranging from 0–2 m in height and arranged randomly on the bed. He used  $\sigma_0 = 3.3$  MPa and a variety of values of  $m$  (Figure 8.35a). Three points merit comment:

- (i) Ice-bed separation increases rapidly at first, but then levels out at ~80% at a sliding speed of ~300 m a<sup>-1</sup>. This is because separation is limited by the crushing strength of ice, ~6 MPa (Hallet, 1996).
- (ii)  $E$  increases rapidly with  $u_b$ , reflecting the fact that cavities are longer when  $u_b$  is higher, and this concentrates stress on smaller segments of the bed. A corollary is that, as  $P_w$  increases, holding  $u_b$  constant,  $E$  decreases because

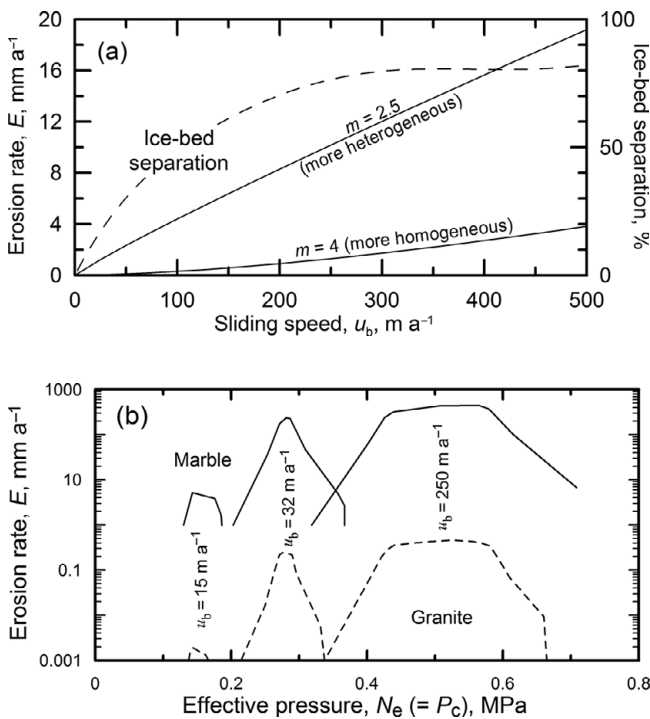


**Figure 8.35** Theoretical rates of quarrying on a bed like that shown in Figure 8.34: (a) for two different values of the Weibull modulus,  $m$ , and (b) for a granite and a marble. Ice-bed separation is also shown in (a). ((a) is based on linear interpolations of parameters in Iverson, 2012, Figure 3. (b) is based on Hallet, 1996, Figure 2. Reproduced with permission of the authors, the Geological Society of America, and the International Glaciological Society)

$\sigma_n$  decreases and because, as the cavity lengthens,  $\sigma_n$  is concentrated on a smaller volume of rock with less probability of harboring the weakest cracks.

- (iii)  $E$  increases as the rock strength becomes increasingly heterogeneous (as  $m$  decreases).

Figure 8.35a captures the effects of  $u_b$  and of the heterogeneity of rock strength,  $m$ , but not of mean strength,  $\sigma_o$ , or of  $P_c$ . Hallet (1996) developed a theory based on the principles of fracture mechanics, and calculated  $E$  for a granite and a marble (Figure 8.35b). The marble, being considerably weaker, eroded ~1000-times faster! In addition,  $E$  initially increases as  $P_c$  increases, but then goes through a maximum and decreases. This can be understood in the following way: At constant  $P_i$  (glacier thickness), increasing  $P_c$  implies decreasing  $P_w$ . At high  $P_w$ ,  $S \rightarrow L$  and  $\sigma_n$  is concentrated on a smaller area, but the high  $P_w$  supports the step, decreasing  $\sigma'$ . (In the Iverson model, this would also focus the stress on a potentially less heterogeneous, and hence stronger volume of rock.) At low  $P_w$ ,  $S$  is small but  $\sigma_n$  is distributed over a larger surface area. Thus, there is a maximum in  $E$  under a narrow range of high, but not extreme  $P_w$ 's. For example, under 450 m of ice,  $P_i \approx 4$  MPa, but at  $u_b = 250$  m  $a^{-1}$ , granite is eroded most effectively when  $0.4 < N_e < 0.6$ , which is when  $3.4 < P_w < 3.6$ .

Hallet's model also predicts that maximum quarrying rates will occur at higher effective pressures as  $u_b$  increases. This appears to be because, as  $u_b$  increases,  $P_c$  must also increase to maintain contact of ice with the bed; otherwise separation would effectively limit  $E$ .

In summary, it appears that steady flow and low effective pressures can fracture weaker rocks or rocks with macroscopic flaws. However, fluctuations in subglacial water pressure and associated transient changes in glacier sliding speed facilitate quarrying, particularly of more resistant lithologies. Abrupt reductions in water pressure promote fracture while increases, whether rapid or more gradual, promote the dislodgement and entrainment of loosened blocks.

## Origin of cirques and overdeepenings

Cirques and overdeepened basins in glacier beds are familiar landforms in glaciated mountain terrain (Figure 8.36). Both cirques and overdeepenings have steep headwalls and both commonly have beds with adverse slopes. Let's discuss the headwalls first.

Headwalls have ragged surfaces, apparently resulting from fracture and removal of blocks of rock. This morphology suggests that they are eroded by glacial quarrying. As we have just discussed, quarrying appears to be a result of water-pressure fluctuations on time scales of hours to days. These fluctuations seem to be most

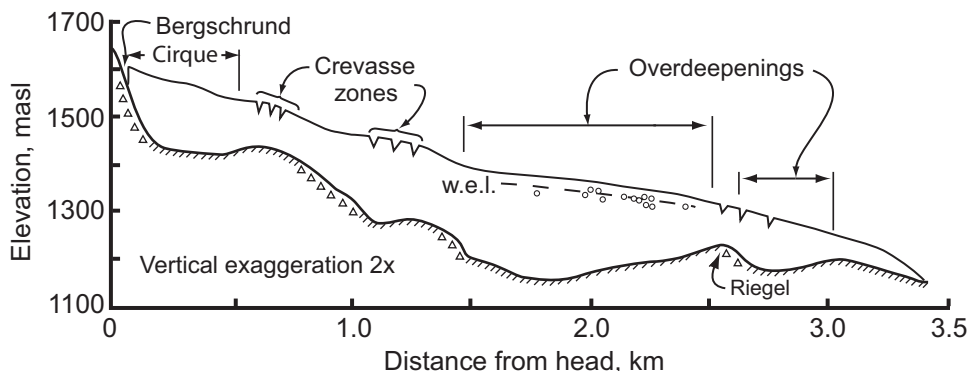


**Figure 8.36** Longitudinal section of Storglaciären, Sweden, approximately along a flowline, showing cirque, overdeepened basins, water-input points (crevasse zones and bergschrund), and inferred locations of quarrying (indicated by  $\Delta\Delta\Delta$ ). w.e.l. = water equivalent line; circles (o) show heights of water in boreholes. (Modified from Hooke, 1991, Figure 2)

pronounced close to areas of water input (Hooke, 1991). In the case of cirques, the water input is localized by the bergschrund, and in the case of overdeepenings, by crevasses that form over the convexities at their heads (Figure 8.36). Thus, these water inputs and resulting pressure fluctuations occur at precisely the points where erosion is necessary to maintain the headwalls.

In the case of the headwall of an overdeepening, a positive feedback process appears to be operating. Crevassing over a minor convexity in the bed, an initial perturbation, localizes water input and hence erosion. The erosion is concentrated on the downglacier side of the convexity. Thus, as erosion progresses, the convexity is amplified, resulting in further crevassing.

The other defining characteristic of cirques and overdeepenings is the adverse slope of their beds. The steepness of this slope appears to be limited by the ability of water to flow along an upward-sloping bed without freezing. If  $k = 0.413$  and  $\rho = 916 \text{ kg m}^{-3}$  in Equation (8.12), for example, it is easy to show (using Equation (8.6)) that  $m = 0$  when  $dz/ds = -1.2 dH/ds$ . In other words, when the adverse bed slope,  $dz/ds$ , is  $\sim 1.2$ -times the surface slope, all of the energy dissipated in the flowing water is needed to warm the water to keep it at the pressure melting point as the ice thins in the downglacier direction. Where the adverse slope is steeper, Equation (8.12) predicts that  $m$  will become negative. In Nature, water in the conduit freezes, forming *frazil ice* (platelets of ice that form in the flowing water) which further retards the flow. Equation (8.24) then predicts that  $P_w > P_i$ , as in Figure 8.12b. This is consistent with measured water pressures in the main overdeepening of Storglaciären which scatter around the overburden pressure (Figure 8.36). Field data suggest that the water, rather than remaining in a conduit, either spreads out over the bed in a maze of linked water pockets with flow velocities

that are too low to move significant amounts of sediment or is forced into englacial conduits (Hooke and Pohjola, 1994).

Where subglacial streams are not available to flush out the products of erosion, a layer of till likely accumulates. Substantial amounts of this sediment can be entrained if frazil ice forms and is eventually incorporated into the glacier sole (Lawson *et al.*, 1998). Continuity considerations suggest that the till layer will increase in thickness until the downglacier mass transfer by deformation within it and entrainment by frazil ice at its surface equals production of sediment by erosion further upglacier. Such a sediment layer would protect the bed throughout the downglacier reaches of an overdeepening, thus concentrating erosion at its head. This is probably why overdeepenings exist, and why their longitudinal profiles are characteristically asymmetrical with the deepest point at their upglacier ends (Hooke, 1991).

---

## SUMMARY

In this chapter we have investigated the glacier hydraulic system, starting with the network of veins along lines of intersection among three ice crystals, and progressing through the englacial to the subglacial system. We found that, theoretically, water flow in the englacial system should be normal to equipotential surfaces that dip upglacier at an angle roughly 11-times the slope of the glacier surface. Along the bed, water flow is normal to the intersections of these equipotential surfaces with the bed.

Water moving through conduit systems in or beneath glaciers releases viscous energy. This energy melts ice on conduit walls. The pressure in the water, however, is generally less than that in the surrounding ice, so the conduits close by creep. In the steady state, the water pressure is everywhere adjusted so that  $u_c = m$ . Along the bed  $u_c$  is inhibited by drag. In addition, melting is concentrated low on the walls when tunnels are not full of water. Thus, the steady-state conduit shape is likely to be broad and low.

The water pressure in conduits increases upglacier, approximately in proportion to the increase in thickness of ice over the conduit. In conduit systems consisting of tunnels,  $P_w$  decreases as  $Q$  increases, but in systems consisting of cavities in the lee of bedrock steps linked by orifices,  $P_w$  increases as  $Q$  increases. Thus, tunnel systems are likely arboreal, while linked-cavity systems are distributed. In all probability, these are end members of a continuum of drainage system types.

Tunnel systems may collapse when discharges are low, tunnels are shrinking, and water pressures are increasing. If the tunnel system cannot regenerate when discharges increase again, water pressures may rise high enough to initiate a surge.

In conduits between a glacier and a deformable bed, the steady state condition is one in which, in addition to  $u_c = m$ , erosion of sediment by the flowing water must balance the flux of sediment into the conduit. Under these conditions, conduit systems are likely to be distributed. Analysis suggests that this condition is most likely when glacier surface slopes are low and water pressures high, as is commonly the case beneath ice sheets.

In the last part of the chapter, we investigated four problems of geomorphic interest: the formation and courses of eskers, the origin of tunnel valleys, quarrying, and the erosion of cirques and overdeepenings. Many esker characteristics can be understood in terms of gradients of hydraulic potential at the base of an ice sheet. The source of the water that carved tunnel valleys is unclear, but indications are that repeated large discharges were likely involved. Erosion of hard bedrock by glaciers is greatly facilitated by fluctuations in water pressure at the bed. Cirques and overdeepenings appear to be products of enhanced quarrying where water has easy access to the bed and lack of erosion where till accumulates, protecting adverse bed slopes.

# 9

## Stress and deformation

In this chapter we will derive general equations for calculating the force per unit area, or traction, on a plane that is not parallel to the coordinate axes, and then use these equations to determine the orientation of the plane on which tractions are a maximum. We will see how this leads to the concept of the *invariant* of a tensor, and show that this provides the fundamental basis for Glen's flow law. Then we'll derive the stress equilibrium equations.

In the second half of the chapter we'll derive expressions for strain rates in terms of velocity derivatives, and develop some relations based on these expressions and some other basic equations. This will set the stage for calculating stresses and velocities in a very simple ice sheet, consisting of a slab of ice of uniform thickness on a uniform slope (Chapter 10) and for investigating some more realistic problems (Chapter 12).

### Stress

While we've been referring to stresses and strain rates throughout the last few chapters, we will now enter into a much more detailed discussion, involving the tensor properties of these quantities. The reader may find it helpful, therefore, to review the section on stresses and strain rates in Chapter 2.

The rank of a tensor is the number of parameters, excluding magnitude, needed to describe a component of the tensor. For example, a velocity is a vector with a magnitude and direction. It is a first-rank tensor. To describe a component of a stress tensor, one must specify its magnitude, its direction, and the orientation of the plane on which it operates. Thus, it is a second rank tensor. Alternatively, one can consider a tensor of rank  $n$  to be a quantity uniquely specified by  $3^n$  real numbers. In a vector, these would be a magnitude and the two angles describing the direction.

#### General equations for transformation of stress in two dimensions

Consider a domain in a slab of material of unit thickness (measured normal to the page), as shown in Figure 9.1. Stresses are uniformly distributed over the domain; in terms of the  $x$ - $z$  coordinate system shown, they are  $\sigma_{xx}$  and  $\sigma_{zx}$  in the  $x$ -direction,

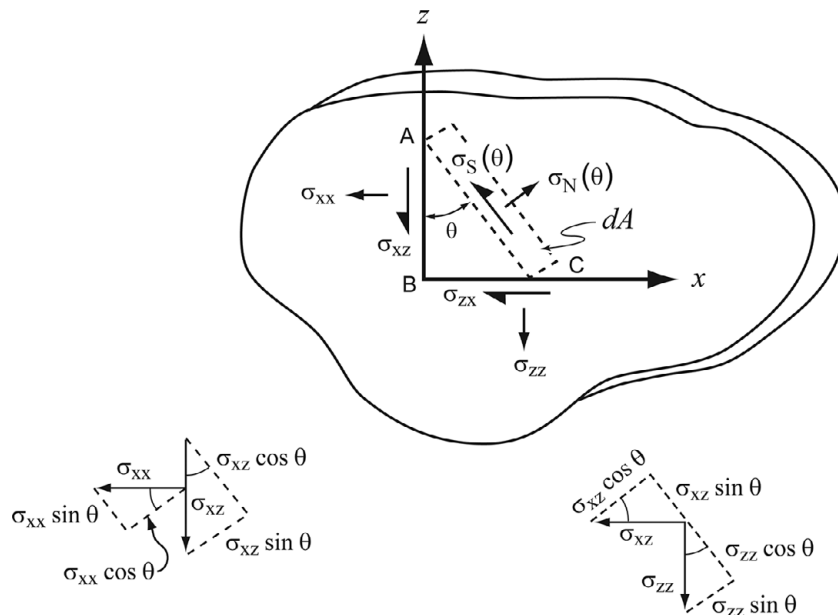


Figure 9.1 Stresses on a triangular prism of material isolated from a domain.

and  $\sigma_{zz}$  and  $\sigma_{xz}$  in the  $z$ -direction. Shear forces on any small element of the domain of unit size in the  $x$ - and  $z$ -directions must be in equilibrium if there is to be no tendency for the element to rotate. Thus,  $\sigma_{xz} = \sigma_{zx}$ , so we will use  $\sigma_{xz}$  to represent both. Now cut the domain along plane  $\overline{AC}$ , which makes an angle  $\theta$  with the  $z$ -axis. This plane has an area which we designate  $dA$ . As a consequence of the stress field in the slab, the edges of the cut will have a tendency to move with respect to one another. We will ignore the part of the domain to the right of the cut, and ask what forces must be applied on  $dA$  to balance this tendency. Specifically, we wish to find the stress vectors  $\sigma_N(\theta)$  and  $\sigma_S(\theta)$  on this plane, where the subscripts N and S refer to normal and shear, respectively.

To do this, consider the prism ABC, and sum forces on it that act normal ( $F_N$ ) and parallel ( $F_S$ ) to  $dA$ , remembering that a force is a stress times an area, and set the sums equal to 0, the condition for static equilibrium. Note that surface  $\overline{AB}$  has area  $dA \cos \theta$  and surface  $\overline{BC}$  has area  $dA \sin \theta$ . The components of  $\sigma_{xx}$ ,  $\sigma_{zz}$ , and  $\sigma_{xz}$  parallel and perpendicular to the plane  $dA$  are shown in the diagrams at the bottom of Figure 9.1. The force summation yields:

$$\begin{aligned}\Sigma F_N &= \sigma_N(\theta)dA - \sigma_{xx} \cos^2 \theta dA - \sigma_{xz} \sin \theta \cos \theta dA \\ &\quad - \sigma_{xz} \cos \theta \sin \theta dA - \sigma_{zz} \sin^2 \theta dA = 0\end{aligned}$$

and:

$$\begin{aligned}\Sigma F_S &= \sigma_S(\theta)dA + \sigma_{xx} \sin \theta \cos \theta dA - \sigma_{xz} \cos^2 \theta dA \\ &\quad + \sigma_{xz} \sin^2 \theta dA - \sigma_{zz} \cos \theta \sin \theta dA = 0.\end{aligned}$$

Simplifying results in:

$$\sigma_N = \sigma_{xx} \cos^2 \theta + \sigma_{zz} \sin^2 \theta + \sigma_{xz}(2 \sin \theta \cos \theta)$$

and

$$\sigma_S = -(\sigma_{xx} - \sigma_{zz})(\sin \theta \cos \theta) + \sigma_{xz}(\cos^2 \theta - \sin^2 \theta).$$

These relations may be further simplified with the use of the trigonometric identities:

$$\frac{1}{2} \sin 2\theta = \sin \theta \cos \theta$$

and

$$\cos 2\theta = \cos^2 \theta - \sin^2 \theta = 2 \cos^2 \theta - 1 = 1 - 2 \sin^2 \theta$$

to yield:

$$\sigma_N = \sigma_{xx} \frac{(1 + \cos 2\theta)}{2} + \sigma_{zz} \frac{(1 - \cos 2\theta)}{2} + \sigma_{xz} \sin 2\theta$$

or

$$\sigma_N = \frac{\sigma_{xx} + \sigma_{zz}}{2} + \frac{\sigma_{xx} - \sigma_{zz}}{2} \cos 2\theta + \sigma_{xz} \sin 2\theta \quad (9.1)$$

and

$$\sigma_S = -\frac{\sigma_{xx} - \sigma_{zz}}{2} \sin 2\theta + \sigma_{xz} \cos 2\theta. \quad (9.2)$$

These are the desired relations for  $\sigma_N(\theta)$  and  $\sigma_S(\theta)$ .

### Principal stresses

We now wish to find the orientation,  $\theta$ , of the plane on which  $\sigma_N(\theta)$  is either a maximum or minimum. Take the derivative of Equation (9.1) with respect to  $\theta$  and set the result equal to 0, thus:

$$\frac{\partial \sigma_N}{\partial \theta} = -2 \frac{\sigma_{xx} - \sigma_{zz}}{2} \sin 2\theta + 2\sigma_{xz} \cos 2\theta = 0 \quad (9.3a)$$

or

$$\tan 2\theta = \frac{2\sigma_{xz}}{(\sigma_{xx} - \sigma_{zz})}. \quad (9.3b)$$

This equation may be satisfied by either of two values of  $2\theta$ ,  $180^\circ$  apart. Thus, there are two solutions for  $\theta$  that are  $90^\circ$  apart. One is the plane of maximum  $\sigma_N(\theta)$ , and the other is the plane of minimum  $\sigma_N(\theta)$ . We call the stresses acting in these directions the *principal stresses*. This is an important concept to understand, and we will return to it frequently.

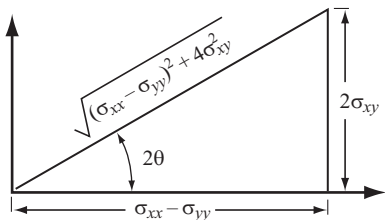


**Figure 9.2** Illustration of relation among  $(\sigma_{xx} - \sigma_{zz})$ ,  $\sigma_{xz}$ , and  $2\theta$  in Equation (9.3b).

The magnitude of the principal stresses is obtained by substituting for  $2\theta$  in Equation (9.1). Equation (9.3b) and the diagram in Figure 9.2 are used to get expressions for  $\cos 2\theta$  and  $\sin 2\theta$ . The result is:

$$\sigma_{1,2} = \frac{\sigma_{xx} + \sigma_{zz}}{2} + \frac{\sigma_{xx} - \sigma_{zz}}{2} \frac{\sigma_{xx} - \sigma_{zz}}{\sqrt{(\sigma_{xx} - \sigma_{zz})^2 + 4\sigma_{xz}^2}} + \sigma_{xz} \frac{2\sigma_{xz}}{\sqrt{(\sigma_{xx} - \sigma_{zz})^2 + 4\sigma_{xz}^2}}$$

or

$$\sigma_{1,2} = \frac{\sigma_{xx} + \sigma_{zz}}{2} \pm \frac{1}{2} \sqrt{(\sigma_{xx} - \sigma_{zz})^2 + 4\sigma_{xz}^2} \quad (9.4)$$

where  $\sigma_1$  is  $\sigma_N$  max and  $\sigma_2$  is  $\sigma_N$  min. Thus,  $(\sigma_1 + \sigma_2) = (\sigma_{xx} + \sigma_{zz})$ .

Comparing Equations (9.2) and (9.3a), it will be seen that  $\frac{\partial \sigma_N}{\partial \theta} = 2\sigma_S$ . Thus, when  $\frac{\partial \sigma_N}{\partial \theta} = 0$ ,  $\sigma_S = 0$ . This is an important principle: *Shear stresses vanish on planes on which the normal stresses are a maximum or minimum.*

The orientations and magnitudes of the maximum shear stresses can be obtained in a similar manner. This is left as an exercise for the reader.

### Mohr's circle

A convenient way to illustrate the dependence of  $\sigma_{xx}$ ,  $\sigma_{zz}$ , and  $\sigma_{xz}$  on  $2\theta$  is to use a graphical construction known as Mohr's circle (Figure 9.3). To construct the figure:

1. Draw a rectangular coordinate system with normal stresses ( $\sigma_N$ ) on the abscissa and shear stresses ( $\sigma_S$ ) on the ordinate, and plot points A and A' at  $(\sigma_{xx}, \sigma_{xz})$  and  $(\sigma_{zz}, -\sigma_{xz})$ , respectively.
2. Connect points A and A' with a straight line, and draw a circle with B as the center and passing through A and A'.

In this figure,  $\overline{BE} = \frac{1}{2}(\sigma_{xx} - \sigma_{zz})$ , so the radius of the circle is:

$$\sqrt{\left(\frac{1}{2}(\sigma_{xx} - \sigma_{zz})\right)^2 + \sigma_{xz}^2} = \frac{1}{2} \sqrt{(\sigma_{xx} - \sigma_{zz})^2 + 4\sigma_{xz}^2}.$$

Thus, from Equation (9.4), the magnitudes of  $\sigma_1$  and  $\sigma_2$  are represented by the lengths of lines  $\overline{OD}$  and  $\overline{OC}$ , respectively, and from Equation (9.3b), angle ABD is

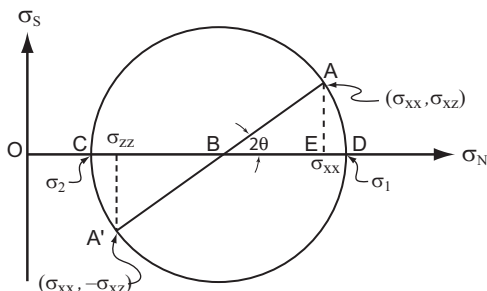


Figure 9.3 Mohr's circle.

2θ. So if one knows the normal and shear stresses at a point, one can use Mohr's circle to determine the principal stresses and their orientation relative to the known stresses.

### Invariants of a tensor

Regardless of the orientation of the axes in Figure 9.1, the magnitudes and orientations of  $\sigma_1$  and  $\sigma_2$  cannot change as long as the overall stress field does not change. This is because  $\sigma_1$  and  $\sigma_2$  are functions of the state of stress in the domain and not of  $\theta$ . We now use this fact and Mohr's circle to illustrate another fundamental principle.

Because the magnitudes of  $\sigma_1$  and  $\sigma_2$ , as represented by  $\overline{OD}$  and  $\overline{OC}$ , respectively, determine the size of the circle and its position on the  $\sigma_N$ -axis, the size and position do not change as  $\theta$  varies. Thus:

$$\frac{1}{2}(\sigma_{xx} + \sigma_{zz}) \quad (9.5a)$$

and

$$\frac{1}{2} \left[ (\sigma_{xx} - \sigma_{zz})^2 + 4\sigma_{xz}^2 \right]^{1/2} \quad (9.5b)$$

(represented by  $\overline{OB}$  and the radius of the circle, respectively) remain constant. These two quantities are thus independent of the orientation of the axes, or  $\theta$ ; they are known as the *invariants* of the tensor. On the other hand,  $\sigma_{xx}$ ,  $\sigma_{zz}$ , and  $\sigma_{xz}$  do vary as  $\theta$  varies. This variation is represented by movement of points A and A' around the circle.

Phrased in terms of Equation (9.4),  $\sigma_1$  and  $\sigma_2$  will remain constant and independent of  $\theta$  only if the quantities  $\frac{1}{2}(\sigma_{xx} + \sigma_{zz})$  and  $\frac{1}{2}[(\sigma_{xx} - \sigma_{zz})^2 + 4\sigma_{xz}^2]^{1/2}$  are independent of  $\theta$ . Thus, these two quantities must be invariant.

### Extension to three dimensions and introduction of deviatoric stresses

It has been found empirically that, to a first approximation, deformation of ice subjected to a normal stress is independent of the hydrostatic pressure or mean stress,  $P$  (see discussion of Equation 4.6). This might well be anticipated from the

observation that ice is (nearly) incompressible. In three dimensions, the mean stress is given by:

$$P = \frac{1}{3} (\sigma_{xx} + \sigma_{yy} + \sigma_{zz}). \quad (9.6)$$

Because deformation is independent of  $P$ , we define a new set of stresses, denoted by primes, by  $\sigma'_{xx} = \sigma_{xx} - P$ ,  $\sigma'_{yy} = \sigma_{yy} - P$ , and  $\sigma'_{zz} = \sigma_{zz} - P$ . These stresses are variously known as *deviatoric stresses*, *stress deviators*, or *non-hydrostatic stresses*. “Deviator” refers to the fact that they are deviations from the mean stress.

A more compact relation for the deviatoric stresses is:

$$\sigma'_{ij} = \sigma_{ij} - \frac{1}{3} \delta_{ij} \sigma_{kk} \quad i, j, k = x, y, z. \quad (9.7)$$

Here, we have introduced the Kronecker  $\delta$ ;  $\delta_{ij}$  takes the values:

$$\delta_{ij} = 1 \quad i = j$$

$$\delta_{ij} = 0 \quad i \neq j.$$

We have also introduced the Einstein summation convention, introduced by Albert Einstein in 1916. Whenever two subscripts are repeated in the same term, as in  $\sigma_{kk}$ , that term is summed over all possible combinations of the subscripts. Equation (9.7), therefore, represents nine equations, of which three are identical due to the symmetry of the tensor. Two of the nine are:

$$\begin{aligned} \sigma'_{xx} &= \sigma_{xx} - \frac{1}{3} (\sigma_{xx} + \sigma_{yy} + \sigma_{zz}) \\ \sigma'_{xz} &= \sigma_{xz}. \end{aligned}$$

As you see, deviatoric shear stresses are identical to their non-deviatoric (or total) counterparts. Only the normal stresses are different. In general, deformation depends only on these non-hydrostatic components of the stress field.

If we were to go through a derivation similar to that above (Equations 9.1–9.5) in three dimensions (Johnson and Mellor, 1962, pp. 23–25), we would find that there were three invariants having the form:

$$\begin{aligned} J_1 &= \sigma'_{xx} + \sigma'_{yy} + \sigma'_{zz} \\ J_2 &= \sigma'_{xy}^2 + \sigma'_{yz}^2 + \sigma'_{zx}^2 - \sigma'_{xx} \sigma'_{yy} - \sigma'_{yy} \sigma'_{zz} - \sigma'_{zz} \sigma'_{xx} \\ J_3 &= \sigma'_{xx} \sigma'_{yy} \sigma'_{zz} + 2\sigma'_{xy} \sigma'_{yz} \sigma'_{zx} - \sigma'_{xx} \sigma'_{yz}^2 - \sigma'_{yy} \sigma'_{xz}^2 - \sigma'_{zz} \sigma'_{xy}^2. \end{aligned} \quad (9.8a)$$

If total stresses were used instead of deviatoric stresses, the right hand sides of Equations (9.8a) would be the same, except for the primes, but on the left, by convention, we would use  $I$  rather than  $J$ , thus:

$$\begin{aligned} I_1 &= \sigma_{xx} + \sigma_{yy} + \sigma_{zz} \\ I_2 &= \sigma_{xy}^2 + \sigma_{yz}^2 + \sigma_{zx}^2 - \sigma_{xx}\sigma_{yy} - \sigma_{yy}\sigma_{zz} - \sigma_{zz}\sigma_{xx} \\ I_3 &= \sigma_{xx}\sigma_{yy}\sigma_{zz} + 2\sigma_{xy}\sigma_{yz}\sigma_{zx} - \sigma_{xx}\sigma_{yz}^2 - \sigma_{yy}\sigma_{xz}^2 - \sigma_{zz}\sigma_{xy}^2. \end{aligned} \quad (9.8b)$$

It is easy to show that  $J_1$  is 0. Just use Equation (9.7) to express the deviatoric stresses in terms of their total counterparts, and simplify. Note also that;

$$\frac{1}{3}I_1 = P. \quad (9.9)$$

Let us now derive an alternative expression for  $J_2$ . To do this, square the first of Equations (9.8a), thus:

$$J_1^2 = \sigma'_{xx}^2 + \sigma'_{yy}^2 + \sigma'_{zz}^2 + 2(\sigma'_{xx}\sigma'_{yy} + \sigma'_{yy}\sigma'_{zz} + \sigma'_{zz}\sigma'_{xx}) = 0.$$

This expression equals zero because  $J_1 = 0$ , so we have:

$$\sigma'_{xx}^2 + \sigma'_{yy}^2 + \sigma'_{zz}^2 = -2(\sigma'_{xx}\sigma'_{yy} + \sigma'_{yy}\sigma'_{zz} + \sigma'_{zz}\sigma'_{xx}).$$

Substituting this into the expression for  $J_2$  yields:

$$2J_2 = \sigma'_{xx}^2 + \sigma'_{yy}^2 + \sigma'_{zz}^2 + 2\sigma'_{xy}^2 + 2\sigma'_{yz}^2 + 2\sigma'_{zx}^2 \quad (9.10)$$

or, using the summation convention:

$$J_2 = \frac{1}{2}\sigma'_{ij}\sigma'_{ij} \quad i, j = x, y, z.$$

The reader will recognize the right hand side of Equation (9.10) as  $2\sigma_e^2$  (Equation 2.10). Thus, the effective shear stress that we have mentioned several times previously is, in fact, the square root of the second invariant of the stress tensor:

$$\sigma_e = \sqrt{J_2} = \left[ \frac{1}{2}\sigma'_{ij}\sigma'_{ij} \right]^{1/2}.$$

Using the summation convention, the effective strain rate (Equation 2.11) can also be written more compactly as  $\dot{\epsilon}_e = \left[ \frac{1}{2}\dot{\epsilon}_{ij}\dot{\epsilon}_{ij} \right]^{1/2}$ .

### A yield criterion

A yield criterion is a statement of the conditions under which deformation will occur. If the condition is not met, there is no deformation, and conversely. The simplest imaginable yield criterion is that of Tresca (1864):

$$|\sigma_\ell - \sigma_m| \geq k \quad \ell, m = 1, 2, 3$$

or when the difference between any two principal stresses exceeds a material constant,  $k$ , determined experimentally for any given material, yielding will occur. An alternative, the von Mises (1928) yield criterion, is:

$$(\sigma_1 - \sigma_2)^2 + (\sigma_2 - \sigma_3)^2 + (\sigma_3 - \sigma_1)^2 \geq k.$$

In this case, each of the three principal stresses contributes.

Let us investigate the relation between the von Mises criterion and  $J_2$ . After some manipulation we can obtain:

$$(\sigma_1 - \sigma_2)^2 + (\sigma_2 - \sigma_3)^2 + (\sigma_3 - \sigma_1)^2 = 2(\sigma'_1{}^2 + \sigma'_2{}^2 + \sigma'_3{}^2) + 2J_2 \quad (9.11)$$

where the primes denote deviatoric stresses as before. Note that we started with total stresses on the left side. Had we started with deviatoric stresses, we would have obtained the same result, as  $P$  drops out. Thus, *the yield criterion is unchanged if we use deviatoric stress instead of total stress*. From Equation (9.10), noting that the shear stresses vanish because we are here dealing with principal stresses, we find that the term in brackets on the right hand side of Equation (9.11) is equal to  $2J_2$ . Thus, the von Mises yield criterion reduces to  $6J_2 \geq k$ , or, since  $J_2 = \sigma_e^2$ , we have  $\sigma_e \geq \sqrt{k/6}$ . In other words, when  $\sigma_e$  equals or exceeds  $\sqrt{k/6}$ , yielding will occur.

Yield criteria are often associated with perfect plasticity. A perfectly plastic material does not deform at stresses below its yield strength,  $k$ . However, once the applied stress reaches  $k$ , the material begins to deform, and it deforms at a rate such that the stress does not exceed  $k$  (Figure 9.4). In terms of Glen's flow law, a perfectly plastic material would be represented by  $n \rightarrow \infty$ , so there would be no strain until  $\sigma_e$  equaled  $A^{-1/n}$  where  $A^{-1/n}$  would be the equivalent of  $\sqrt{k/6}$ . *Viscoplastic* or *Bingham* materials also exhibit a yield stress but once the yield stress is reached, the material deforms at a rate that depends on the amount by which the applied stress exceeds the yield stress (Figure 9.4). Inasmuch as there may, indeed, be a stress below which ice does not deform, it resembles a nonlinear viscoplastic material. Glen's flow law does not recognize this yield stress, however, but approximates it by predicting very small strain rates at low stresses.

Thus, by using  $\sigma_e$  in the flow law, we are not incorporating a yield stress per se. Rather, we are simply saying that the strain rate in any given direction is likely to be a function of all of the stresses acting on the material, not just the stresses in that

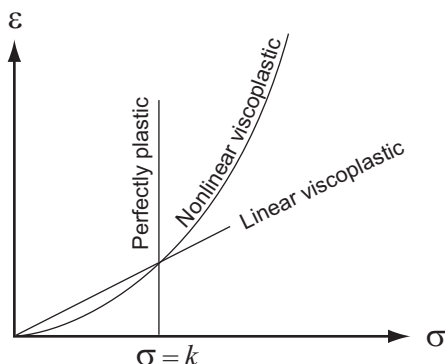


**Figure 9.4** Variation of strain rate,  $\dot{\varepsilon}$ , with applied stress,  $\sigma$ , in perfectly plastic and viscoplastic materials.

direction. For example, the flow law states that ice will shear faster under a stress  $\sigma_{xy}$  if there is also a deviatoric normal stress,  $\sigma'_{xx}$ , on it. Experiments by Li *et al.* (1996) firmly support this concept.

### The invariants in plane strain

Let us now examine the relation between the invariants in plane strain (Equations 9.5) and those in Equations (9.8). By *plane strain* we mean that there is no deformation in one of the coordinate directions, in this case the  $y$ -direction. As deformation is caused by deviatoric stresses, this implies that  $\sigma'_{yx}$ ,  $\sigma'_{yy}$ , and  $\sigma'_{yz}$  are all 0. From Equation (9.7) we thus have:

$$\sigma'_{yy} = \sigma_{yy} - P = 0 \quad (9.12)$$

so  $\sigma_{yy} = P$ , and then from Equation (9.6):

$$P = \frac{1}{2}(\sigma_{xx} + \sigma_{zz}). \quad (9.13)$$

(Note that since  $\sigma_{yy} = P$ ,  $\sigma_{yy}$  does *not* equal 0 even though  $\sigma'_{yy}$  does.) With  $\sigma'_{yy} = 0$ ,  $J_1 = (\sigma'_{xx} + \sigma'_{zz})$ . Using Equations (9.7) and (9.13), it is then easy to show that, as in three dimensions,  $J_1$  also equals 0 in plane strain.

Then, from Equation (9.10), adding and subtracting  $2\sigma'_{xx}\sigma'_{zz}$  to complete the square:

$$J_2 = \frac{1}{2}(\sigma'_{xx}^2 + \sigma'_{xz}^2 + \sigma'_{zz}^2 + 2\sigma'_{xx}\sigma'_{zz} - 2\sigma'_{xx}\sigma'_{zz}).$$

So:

$$J_2 = \frac{1}{2}[(\sigma'_{xx} - \sigma'_{zz})^2 + 2\sigma'_{xz}^2 + 2\sigma'_{xx}\sigma'_{zz}].$$

Changing to total stress by substituting Equation (9.7) then yields:

$$J_2 = \frac{1}{2}[(\sigma_{xx} - \sigma_{zz})^2 + 2\sigma_{xz}^2 + 2(\sigma_{xx}\sigma_{zz} - \sigma_{xx}P - \sigma_{zz}P + P^2)].$$

After some manipulation using Equation (9.13), we then obtain:

$$J_2 = \left\{ \frac{1}{2}[(\sigma_{xx} - \sigma_{zz})^2 + 4\sigma_{xz}^2]^{1/2} \right\}^2. \quad (9.14)$$

(It can then be shown that the  $J_3 = J_2$  in two dimensions, but we will not do this here.)

You will recognize the right hand sides of Equations (9.13) and (9.14) as being the invariants in Equations (9.5a) and (9.5b), respectively. Using Equation (9.9), you will see that  $\frac{1}{2}(\sigma_{xx} + \sigma_{zz}) = \frac{1}{3}I_1$  and, from Equation (9.14):  $\frac{1}{2}[(\sigma_{xx} - \sigma_{zz})^2 + 4\sigma_{xz}^2]^{1/2} = \sqrt{J_2} = \sigma_e$ . So the invariants we first identified in Equations (9.5) in two dimensions are functions of  $I_1$  and  $J_2$ .

The right hand side of Equation (9.14) turns out to be the maximum shear stress in plane strain. You can show this by setting the derivative of Equation (9.2) equal to 0. If the axes were, in addition, chosen to be parallel to the principal stresses,  $\sigma_{xz}$  would vanish, leaving:

$$\sigma_e = \pm \frac{1}{2}(\sigma_1 - \sigma_2).$$

The directions of the maximum shear stresses would then be  $45^\circ$  and  $135^\circ$  to the principal axes. [To show this, determine the orientation of the planes on which  $\sigma_s$  is a maximum, using a procedure similar to that which we used to obtain Equations (9.3), and compare these planes with the orientations of the planes on which  $\sigma_N$  is a maximum].

## Momentum balance

The stress equilibrium equations are derived by balancing forces in the directions of the coordinate axes. Consider forces in the  $x$ -direction on a block of size  $dx dy dz$ , as shown in Figure (9.5):

$$\begin{aligned}\Sigma F_x = & -\sigma_{xx} dy dz + \left( \sigma_{xx} + \frac{\partial \sigma_{xx}}{\partial x} dx \right) dy dz - \sigma_{yx} dx dz + \left( \sigma_{yx} + \frac{\partial \sigma_{yx}}{\partial y} dy \right) dx dz \\ & - \sigma_{zx} dx dy + \left( \sigma_{zx} + \frac{\partial \sigma_{zx}}{\partial z} dz \right) dx dy + \rho g_x dx dy dz = 0\end{aligned}$$

The first two terms on the right are the normal forces on the faces of the block that are normal to the  $x$ -axis. Note that, in each case, the stress (shown in Figure 9.5) is multiplied by the area of the face, in this case  $dy dz$ , to obtain a force. The next four terms are the shear forces in the  $x$ -direction on faces normal to the  $y$ - and  $z$ -axes, respectively. The last term is the body force;  $g_x$  in this term represents the component of the gravitational acceleration that is parallel to the  $x$ -axis. Canceling like terms of opposite sign and dividing by  $dx dy dz$  yields:

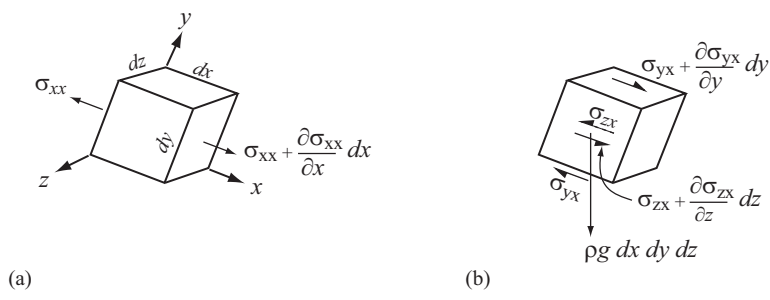


**Figure 9.5** Stresses in the  $x$ -direction on a block of size  $dx dy dz$ . (a) Normal stresses.  
(b) Shear stresses.

$$\frac{\partial \sigma_{xx}}{\partial x} + \frac{\partial \sigma_{yx}}{\partial y} + \frac{\partial \sigma_{zx}}{\partial z} + \rho g_x = 0.$$

Similar expressions are readily obtained in the  $y$ - and  $z$ -directions. Using the summation convention, these become:

$$\frac{\partial \sigma_{ij}}{\partial x_i} + \rho g_j = 0. \quad (9.15)$$

As  $i$  is repeated in the first term, this represents three terms. However,  $j$  is not repeated, so we can write separate equations for  $j = x, y$ , and  $z$ . Thus Equation (9.15) represents three equations.

Because Equations (9.15) represent the summation of forces in a particular direction, and because  $F = ma = m\frac{dv}{dt} = \frac{d}{dt}mv$  where  $m$  is mass,  $a$  is acceleration,  $v$  is velocity, and  $mv$  is momentum, Equations (9.15) represent conservation (e.g.  $d/dt = 0$ ) of linear momentum.

## Deformation

Having applied a stress to a medium, we expect strain or deformation to occur. Suppose  $\bar{x}$ ,  $\bar{y}$ , and  $\bar{z}$  (Figure 9.6) represent the displacement of a particle from  $P$  to  $P'$  in the directions of the coordinate axes, respectively. We will consider infinitesimal displacements so the time required for the deformation  $\rightarrow 0$ .

Normal strain in the  $x$ -direction at  $P$  is defined as:

$$\varepsilon_{xx} = \lim_{\ell \rightarrow 0} \frac{\Delta\ell}{\ell} \quad (9.16)$$

where  $\ell$  is the length of a line drawn in the  $x$ -direction, and  $\Delta\ell$  is the elongation of that line, so  $\Delta\ell/\ell$  is the elongation of the line per unit length. Referring to Figure 9.7,

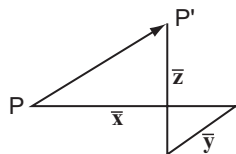


**Figure 9.6** Components of a displacement from  $P$  to  $P'$ .

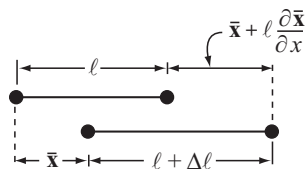


**Figure 9.7** Elongation of a line during deformation.

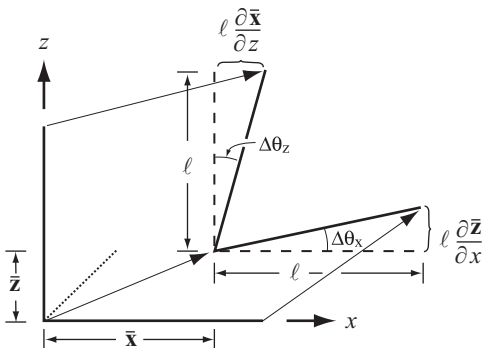


**Figure 9.8** Change in a right angle during deformation.

if a line, initially of length  $\ell$ , is translated such that its left end moves a distance  $\bar{x}$  in the  $x$ -direction, its right end moves a distance  $\bar{x} + \ell \frac{\partial \bar{x}}{\partial x}$  in this direction, and the  $x$ -component of its new length is  $\ell + \Delta\ell$ , then substituting into Equation (9.16) yields:

$$\varepsilon_{xx} = \text{Lim}_{\ell \rightarrow 0} \frac{\bar{x} + \ell \frac{\partial \bar{x}}{\partial x} - \bar{x}}{\ell} = \frac{\partial \bar{x}}{\partial x}. \quad (9.17)$$

By taking the limit as  $\ell \rightarrow 0$  we eliminate the variation with  $x$ , thus obtaining  $\varepsilon_{xx}$  at point  $\mathbf{P}$ . Similarly:  $\varepsilon_{yy} = \frac{\partial \bar{y}}{\partial y}$  and  $\varepsilon_{zz} = \frac{\partial \bar{z}}{\partial z}$ .

Shear strain is defined as one half the decrease in an initially right angle. Referring to Figure 9.8, this can be expressed as:

$$\varepsilon_{xz} = \frac{\Delta\theta}{2} = \frac{\Delta\theta_x + \Delta\theta_z}{2} = \frac{1}{2} \text{Lim}_{\ell \rightarrow 0} \left[ \tan^{-1} \frac{\ell(\partial \bar{x}/\partial z)}{\ell} + \tan^{-1} \frac{\ell(\partial \bar{z}/\partial x)}{\ell} \right].$$

For infinitesimal changes,  $\theta \approx \tan \theta$  so:

$$\varepsilon_{xz} = \frac{1}{2} \left( \frac{\partial \bar{x}}{\partial z} + \frac{\partial \bar{z}}{\partial x} \right) \quad (9.18a)$$

and similarly:

$$\varepsilon_{yz} = \frac{1}{2} \left( \frac{\partial \bar{y}}{\partial z} + \frac{\partial \bar{z}}{\partial y} \right) \quad (9.18b)$$

and

$$\varepsilon_{xy} = \frac{1}{2} \left( \frac{\partial \bar{x}}{\partial y} + \frac{\partial \bar{y}}{\partial x} \right). \quad (9.18c)$$

As before (Chapter 2), there are nine components of strain. Thus, this is another second rank tensor, the *strain tensor*. It, too, is symmetric because  $\varepsilon_{xz} = \varepsilon_{zx}$  and so forth.

In general, shear results in rotation as well as distortion. For example, if  $\partial \bar{x}/\partial z \neq \partial \bar{z}/\partial x$  in Figure 9.8, the dotted line inclined at  $45^\circ$  to the  $x$ -axis will be rotated through an angle:

$$\omega_{xz} = \frac{1}{2} \left( \frac{\partial \bar{x}}{\partial z} - \frac{\partial \bar{z}}{\partial x} \right).$$

Similar expressions may be written for other rotations.

To obtain rates, which are normally of greater interest in a deforming ice mass, we differentiate with respect to time. Thus, the normal strain rate in the  $x$ -direction,  $\dot{\varepsilon}_{xx}$ , is:

$$\dot{\varepsilon}_{xx} = \frac{d\varepsilon_{xx}}{dt} = \frac{d}{dt} \frac{\partial \bar{x}}{\partial x}.$$

Velocity is defined as a change in distance with time, or if  $u$  is the velocity in the  $x$ -direction,  $u = d\bar{x}/dt$ . Thus, we obtain:

$$\dot{\varepsilon}_{xx} = \frac{\partial u}{\partial x}. \quad (9.19)$$

Similarly, shear strain rates become:

$$\dot{\varepsilon}_{xz} = \frac{1}{2} \left( \frac{\partial u}{\partial z} + \frac{\partial w}{\partial x} \right) \quad (9.20)$$

and so forth.

The symmetry of Equation (9.20) suggests the possibility of again using the summation convention to write expressions for the strain rates, thus:

$$\dot{\varepsilon}_{ij} = \frac{1}{2} \left( \frac{\partial u_i}{\partial x_j} + \frac{\partial u_j}{\partial x_i} \right). \quad (9.21)$$

If  $i=j$  in this expression, it reduces to Equation (9.19), so this formulation represents both shear and normal strain rates.

Similarly, the *rotation rate tensor* is:

$$\dot{\omega}_{ij} = \frac{1}{2} \left( \frac{\partial u_i}{\partial x_j} - \frac{\partial u_j}{\partial x_i} \right). \quad (9.22)$$

The rotation rate tensor is antisymmetric because  $\dot{\omega}_{ij} = -\dot{\omega}_{ji}$ . Note also that  $\dot{\omega}_{ii} = 0$  when  $i=j$ . In other words, pure stretching does not result in rotation of an element. However, a line within the element that is not parallel to an axis may rotate. If  $\dot{\omega}_{ij} = 0$  for all  $i,j$  the flow is said to be *irrotational*. Rotations do not change the size or shape of an element, so they do not require the application of a stress.

As implied by the notation  $\partial u_i / \partial x_j$  ( $i, j = x, y, z$ ), the velocity vector has three components, and each of them can vary in each of the three coordinate directions. Thus, there are nine velocity derivatives:

$$\begin{array}{ccc} \frac{\partial u}{\partial x} & \frac{\partial u}{\partial y} & \frac{\partial u}{\partial z} \\ \frac{\partial v}{\partial x} & \frac{\partial v}{\partial y} & \frac{\partial v}{\partial z} \end{array}$$

$$\frac{\partial w}{\partial x} \quad \frac{\partial w}{\partial y} \quad \frac{\partial w}{\partial z}.$$

This is sometimes called the *velocity derivative tensor*. The velocity derivative tensor is not symmetric, as in general  $\partial u_i / \partial x_j \neq \partial u_j / \partial x_i$ . Therefore, it can be decomposed into symmetric and antisymmetric parts. The symmetric part is represented by Equation (9.21), and the anti-symmetric part by Equation (9.22).

### Logarithmic strain

In Equation (9.16) we defined strain by:

$$\dot{\varepsilon} = \text{Lim}_{\ell \rightarrow 0} \frac{\Delta\ell}{\ell}$$

where  $\ell$  is the initial length of a line and  $\Delta\ell$  is the elongation of that line. This definition is suitable for small (infinitesimal) strains. However, when calculating strains or strain rates from measurements, the total strain is normally not infinitesimal. This is, in part, because deformations must be large enough to exceed the uncertainty in the measurement method.

If strains are infinitesimal, we can replace  $\Delta\ell$  with  $d\ell$ . The total strain is then the sum of the infinitesimal strains, or:

$$\varepsilon = \sum_{\ell=\ell_0}^{\ell=\ell_1} \frac{d\ell}{\ell} = \int_{\ell_0}^{\ell_1} \frac{d\ell}{\ell}$$

where  $\ell_0$  is the initial length of the line and  $\ell_1$  is its final length. Integrating yields:

$$\varepsilon = \ln \frac{\ell_1}{\ell_0} \tag{9.23}$$

or in terms of rates:

$$\dot{\varepsilon} = \frac{1}{\Delta t} \ln \frac{\ell_1}{\ell_0} \tag{9.24}$$

where  $\Delta t$  is the time interval between measurements. This is known as logarithmic strain.

### General equations for transformation of strain in two dimensions

Our next objective is to develop an expression for the strain rate in an arbitrary direction,  $\theta$ . To simplify the equations, we restrict the analysis to the case of plane strain. We will then take the derivative of this expression and set it equal to zero to find the directions in which  $\dot{\varepsilon}(\theta)$  is maximum and minimum (the *principal strain rates*). Finally we will look at the implications of this in terms of the flow law.

Let us examine the elongation of line  $\bar{O}P$  in Figure 9.9a. The line has an initial length,  $\ell$ , and makes an angle,  $\theta$ , with the  $x$ -axis. The line is stretched to a final

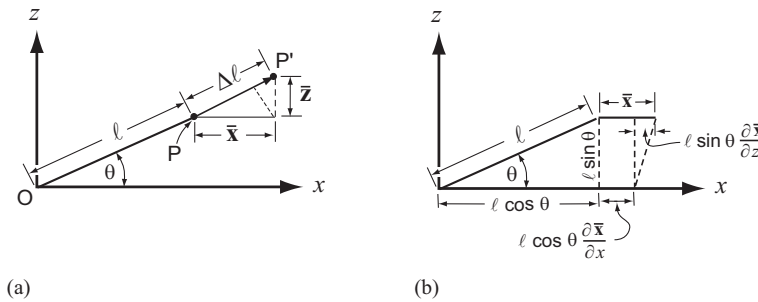


**Figure 9.9** (a) Components of strain of a line of initial length,  $\ell = \overline{OP}$ , and final length,  $\ell' = \overline{OP'}$ , and (b) details of the shear component of the strain.

length,  $\overline{OP'}$ , through a displacement with components  $\bar{x}$  and  $\bar{z}$  in the  $x$ - and  $z$ -directions, respectively. The elongation is given by (Figure 9.9a):

$$\Delta\ell = \bar{x} \cos \theta + \bar{z} \sin \theta. \quad (9.25)$$

The displacement,  $\bar{x}$ , is a consequence of strain parallel to the  $x$ -axis and a shear strain which results in tilting of any line that is initially normal to the  $x$ -axis (Figure 9.9b), thus:

$$\bar{x} = \ell \cos \theta \frac{\partial \bar{x}}{\partial x} + \ell \sin \theta \frac{\partial \bar{x}}{\partial z}. \quad (9.26a)$$

The origin of the two terms on the right hand side may be clarified by reference to Figures 9.7 and 9.8, respectively. Similarly:

$$\bar{z} = \ell \sin \theta \frac{\partial \bar{z}}{\partial z} + \ell \cos \theta \frac{\partial \bar{z}}{\partial x}. \quad (9.26b)$$

Substituting Equations (9.26) into Equation (9.25) yields:

$$\Delta\ell = \ell \cos^2 \theta \frac{\partial \bar{x}}{\partial x} + \ell \sin^2 \theta \frac{\partial \bar{z}}{\partial z} + \ell \left( \frac{\partial \bar{x}}{\partial z} + \frac{\partial \bar{z}}{\partial x} \right) \cos \theta \sin \theta.$$

Finally, dividing by  $\ell$ ; noting that  $\lim_{\ell \rightarrow 0} (\Delta\ell/\ell) = \epsilon(\theta)$ , the strain along the length of line  $\overline{OP}$ ; and using Equations (9.17) and (9.18a) to express the derivatives in terms of strains yields:

$$\epsilon(\theta) = \epsilon_{xx} \cos^2 \theta + \epsilon_{zz} \sin^2 \theta + 2\epsilon_{xz} \cos \theta \sin \theta.$$

With the trigonometric identities used earlier (page 258), this becomes:

$$\epsilon(\theta) = \frac{\epsilon_{xx} + \epsilon_{zz}}{2} + \frac{\epsilon_{xx} - \epsilon_{zz}}{2} \cos 2\theta + \epsilon_{xz} \sin 2\theta. \quad (9.27)$$

Strain rates can be obtained by taking the derivative with respect to time. Equation (9.27) is a useful relation for obtaining normal strains or strain rates in an arbitrary direction,  $\theta$ , when values in the coordinate directions  $x, z$  are known.

To obtain the maximum and minimum values of  $\dot{\epsilon}(\theta)$ , the principal strain rates, we proceed as before (Equations 9.3) to take the derivative with respect to  $\theta$ , set it to zero, and solve for  $\theta$ , thus:

$$\tan 2\theta_{sr} = \frac{2\dot{\epsilon}_{xz}}{\dot{\epsilon}_{xx} - \dot{\epsilon}_{zz}}. \quad (9.28)$$

The two solutions for  $\theta$  are the directions in which the strain rate is a maximum and minimum. The magnitudes of the principal strain rates can be obtained as we did for the principal stresses (Equation 9.4).

### Condition that principal axes of stress and strain rate coincide

In calculating the stress and velocity fields in a glacier in Chapter 10, we will need to assume that the principal axes of stress and strain rate coincide. Let us explore the consequences of this condition.

We found earlier (Equation 9.3b) that the angle which the principal stresses make with the  $x$ -coordinate may be obtained from:

$$\tan 2\theta_{stress} = \frac{2\sigma_{zx}}{\sigma_{xx} - \sigma_{zz}} = \frac{2\sigma'_{zx}}{\sigma'_{xx} - \sigma'_{zz}}.$$

Note that it does not matter whether we use deviatoric or total stresses here.

The condition that the principal axes of stress and strain rate coincide is  $\theta_{stress} = \theta_{sr}$ , or at any given point in the medium:

$$\frac{2\sigma'_{zx}}{\sigma'_{xx} - \sigma'_{zz}} = \frac{2\dot{\epsilon}_{zx}}{\dot{\epsilon}_{xx} - \dot{\epsilon}_{zz}}.$$

The only way to satisfy this condition in the general case is to let:

$$\dot{\epsilon}_{zx} = \lambda\sigma'_{zx}; \quad \dot{\epsilon}_{xx} = \lambda\sigma'_{xx}; \quad \dot{\epsilon}_{zz} = \lambda\sigma'_{zz}$$

where  $\lambda$  is a scalar; that is, its value at the particular point in the medium is independent of the direction in which the stress is acting. However,  $\lambda$  may vary from one point to another in the medium, so  $\lambda = \lambda(x, y, z)$ .

The fact that  $\lambda$  is a scalar implies that the deforming material is isotropic and incompressible. Thus, under a given stress, it will deform at the same rate, regardless of the direction in which the stress is applied. Obviously, this is an approximation in a material such as ice, that first has an hexagonal crystal structure, and secondly can develop a fabric with a preferred orientation. [If the material were compressible, a compressive deviatoric stress in, say, the  $x$ -direction,  $\sigma'_{xx}$ , would cause more deformation than the corresponding tensile deviatoric stress in the  $y$ -direction (which must equal  $\sigma'_{yy}$  in magnitude in plane strain). Thus,  $\lambda$  would differ between the two directions.]

We generalize this assumption to three dimensions and formalize it by writing:

$$\dot{\varepsilon}_{ij} = \lambda \sigma'_{ij} \quad (9.29)$$

remembering that:

$$\dot{\varepsilon}_{ij} = \frac{1}{2} \left( \frac{\partial u_i}{\partial x_j} + \frac{\partial u_j}{\partial x_i} \right) \quad (9.30)$$

and:

$$\sigma'_{ij} = \sigma_{ij} - \frac{1}{3} \delta_{ij} \sigma_{kk}.$$

Because the stress and strain rate in the flow law are defined in terms of either the effective or the octahedral stress and strain rate, we can write out the first few terms of the effective strain rate and substitute Equation (9.29) into the right hand side, as follows:

$$\begin{aligned} \dot{\varepsilon}_e^2 &= \frac{1}{2} \left( \dot{\varepsilon}_{xx}^2 + \dot{\varepsilon}_{xy}^2 + \dot{\varepsilon}_{xz}^2 + \dots \right) = \frac{1}{2} \left( \lambda^2 \sigma'_{xx}^2 + \lambda^2 \sigma'_{xy}^2 + \lambda^2 \sigma'_{xz}^2 + \dots \right) \\ &= \frac{\lambda^2}{2} \left( \sigma'_{xx}^2 + \sigma'_{xy}^2 + \sigma'_{xz}^2 + \dots \right) = \lambda^2 \sigma_e^2. \end{aligned}$$

Dropping the subscript e for convenience (and also because the flow law can be written in terms of either the effective or the octahedral stress and strain rate), we obtain:

$$\dot{\varepsilon} = \lambda \sigma = f(\sigma) \quad \text{so} \quad \lambda = \frac{f(\sigma)}{\sigma}. \quad (9.31)$$

Here,  $f(\sigma)$  is used to emphasize that, in the general case,  $\lambda$  is a function of the applied stress.

A few examples will serve to illustrate the meaning of  $\lambda$ :

- Newtonian fluid:  $\lambda = 1/\eta$ , where  $\eta$  is the Newtonian viscosity, so in this case  $\lambda$  is not a function of  $\sigma$  (see Equation 2.17).
- Power law fluid:  $\lambda = A\sigma^{n-1}$ , so  $\dot{\varepsilon} = \lambda\sigma = A\sigma^n$ .
- Perfectly plastic material: As noted earlier (Figure 9.4), in a perfectly plastic material there is no deformation below a critical stress,  $\sigma = k$ , so  $\lambda = 0$  for  $\sigma < k$ . When  $\sigma = k$ , the material deforms at a rate such that the stress does not exceed  $k$ . In other words,  $\lambda$  depends on  $\dot{\varepsilon}$ :  $\lambda = f_1(\dot{\varepsilon})$ .

In the case of the power law fluid,  $\lambda$  varies with  $\sigma$  and  $A$ , and because  $A$  is a function of temperature, density, crystal size and orientation, and perhaps other factors,  $\lambda$  varies with these properties as well.

Combining Equations (9.29), (9.30), and (9.31), writing  $\dot{\varepsilon}$  in terms of velocity derivatives, and using the summation convention, we now have the following relation between individual components of the stress and strain rate tensors:

$$\frac{1}{2} \left( \frac{\partial u_i}{\partial x_j} + \frac{\partial u_j}{\partial x_i} \right) = \frac{f(\sigma)}{\sigma} \sigma'_{ij}. \quad (9.32a)$$

This represents nine equations, only six of which are independent. Together with Equation (9.15):

$$\frac{\partial \sigma_{ij}}{\partial x_i} + \rho g_j = 0 \quad (9.32b)$$

which represents an additional three equations, we have nine independent equations which can be solved for the three normal stresses, three shear stresses, and three velocities. Our objective in Chapter 10 will be to do this, but to simplify the problem, we will confine our attention to plane strain.

## SUMMARY

In this chapter, we have reviewed some elementary principles of continuum mechanics, with a particular focus on those principles needed to understand much of the classical as well as the modern literature on glacier flow.

In the first part of the chapter, we defined stress and showed that if we know the stresses in one coordinate system, we can calculate them in another system rotated with respect to the first. This allowed us to calculate the direction and magnitude of the maximum and minimum normal stresses, the *principle stresses*. We did the calculation in two dimensions, but the extension to three dimensions is straightforward, though tedious. We found that shear stresses vanish in coordinate systems chosen with axes aligned parallel to the principle stresses.

The orientation and magnitude of the principle stresses is a property of the stress field and not of the orientation of the axes. Thus, there are certain combinations of the stresses that must be independent of the orientation of the axes: the *invariants* of the stress tensor. Glen's flow law for ice is based on the second of these invariants. This is logical because it is invariant, and also because the von Mises yield criterion can be expressed in terms of this invariant. Recent experimental data have validated this approach.

In the second part of the chapter, we derived the stress equilibrium or momentum balance equations.

In the third part, we defined strain and derived equations for calculating strains or strain rates in coordinate systems rotated with respect to one another. These equations are similar to those for transformation of stress. As with stresses, we introduced the concept of *principle strain rates*.

Finally, we showed that if a material is isotropic and incompressible, the principle axes of stress and strain rate coincide. Ice is clearly not isotropic and incompressible, but this approximation has proven to be a convenient starting point for calculations of glacier flow.

# 10

## Stress and velocity distribution in an idealized glacier

Let's now use Equations (9.32) to calculate stresses and velocities in an idealized glacier consisting of a slab of ice of infinite horizontal extent resting on a bed with a uniform slope. By appropriate choice of the coordinate system, the problem is thus reduced to two dimensions, or plane strain. The ice is assumed to be isotropic and incompressible. We will consider first the case of a perfectly plastic rheology. Then a more realistic non-linear flow law is used. Our discussion is based on papers of Nye (1951, 1957), which are classics in glaciology.

Although glaciers consisting of such slabs are uncommon, to say the least, there are several reasons for undertaking this calculation. First, it provides an opportunity to apply some of the material discussed in the previous chapter. Secondly, the stress distributions are representative of those which we expect to find in glaciers, and are commonly-used approximations when the required assumptions can be justified by the geometry of a problem. Thirdly, the calculations demonstrate the limitations of analytical methods in situations in which boundary conditions are complex. For calculations involving glaciers with realistic shapes, numerical models are required for all but the simplest situations. Finally, the effect of longitudinal stresses on velocity profiles is elucidated.

### Solutions for stresses and velocities in plane strain

The coordinate system to be used for the calculation is shown in Figure 10.1:  $x$  is parallel to the glacier surface in the direction of flow and  $z$  is directed downward normal to the surface. The origin is on the surface of the slab, which has a thickness  $h$ . The velocities are  $u$ ,  $v$ , and  $w$  in the  $x$ -,  $y$ -, and  $z$ -directions, respectively.

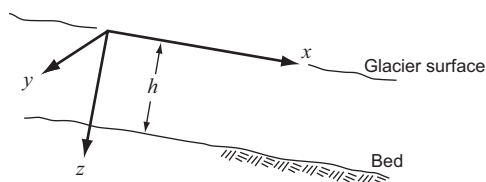


Figure 10.1 Coordinate system used in calculating stresses and velocities in plane strain.

As before, we take  $\dot{\varepsilon}_{yy}$  to be 0, so  $\sigma_{yy}' = 0$ . Therefore, as in Equations (9.12) and (9.13):

$$\sigma_{yy} = P = \frac{1}{2}(\sigma_{xx} + \sigma_{zz}). \quad (10.1)$$

Also:

$$\begin{aligned}\sigma_{xy} &= 0 \\ \sigma_{zy} &= 0. \\ v &= 0\end{aligned} \quad (10.2)$$

Equations (10.1) and (10.2) are four of the equations needed to solve for the three normal stresses, three shear stresses, and three velocities, so we need five more from Equations (9.32). These are:

$$\frac{\partial \sigma_{xx}}{\partial x} + \frac{\partial \sigma_{zx}}{\partial z} + \rho g_x = 0 \quad (10.3)$$

$$\frac{\partial \sigma_{zx}}{\partial x} + \frac{\partial \sigma_{zz}}{\partial z} + \rho g_z = 0 \quad (10.4)$$

$$\frac{\partial u}{\partial x} = \lambda \sigma'_{xx} = \lambda(\sigma_{xx} - P) = \lambda \left[ \sigma_{xx} - \frac{1}{2}(\sigma_{xx} + \sigma_{zz}) \right] = \frac{\lambda}{2}(\sigma_{xx} - \sigma_{zz}) \quad (10.5)$$

and, similarly:

$$\frac{\partial w}{\partial z} = -\frac{\lambda}{2}(\sigma_{xx} - \sigma_{zz}) \quad (10.6)$$

and

$$\frac{1}{2} \left( \frac{\partial u}{\partial z} + \frac{\partial w}{\partial x} \right) = \lambda \sigma_{zx}. \quad (10.7)$$

Note that  $\partial u / \partial x = -\partial w / \partial z$  as required by the incompressibility condition in plane strain (Equation 2.5).

Because  $\lambda = f(\sigma)/\sigma$ , we have to introduce an expression for  $\sigma$ , namely:

$$\sigma^2 = \frac{1}{4}(\sigma_{xx} - \sigma_{zz})^2 + \sigma_{zx}^2 \quad (10.8)$$

(see discussion following Equation (9.14)) which, as we have seen, can be derived from the von Mises yield criterion in plane strain, and is, in fact, the effective stress in plane strain. Still needed is an expression for  $f(\sigma)$ ; this will be based on the specific flow law chosen for any given solution.

### Stress solutions in a perfectly plastic medium

Suppose our slab is composed of perfectly plastic “ice.” Suppose, further, that accumulation and ablation are occurring on the surface of the slab, but that it is

in a steady state so the profile does not change. Thus, it must be deforming to accommodate the addition or loss of mass. In order to avoid a discontinuity at depth, the deformation must extend throughout the slab. Furthermore, in a deforming perfectly plastic material, the stress must reach but cannot exceed the yield stress,  $k$  (Chapter 9). Therefore,  $\sigma = k$  everywhere.

Because either accumulation or ablation are occurring,  $u$  must either increase or decrease, respectively, along the slab. Thus, a small uniform longitudinal strain rate is present. Near the bed, however, deformation is principally by simple shear. In a perfectly plastic material any tendency toward an increase in stress above  $k$  is absorbed by more rapid deformation. Thus,  $\dot{\varepsilon}_{zx} \rightarrow \infty$  at the bed, and  $\dot{\varepsilon}_{zx}$  becomes the dominant term in  $\dot{\varepsilon}$  (or  $\dot{\varepsilon}_e$ ). Consequently,  $\sigma_{zx}$  is the dominant term in  $\sigma$  (Equation 10.8), and  $\sigma_{zx}$  must approach  $\sigma (= k)$  at the bed. Therefore, we adopt the following boundary conditions:

$$\sigma_{zx} = -k \quad \text{on } z = h \text{ (bed)}$$

$$\sigma_{zx} = 0, \quad \sigma_{zz} = 0 \quad \text{on } z = 0 \text{ (surface)}.$$

Here  $\sigma_{zz}$  and  $\sigma_{zx}$  are 0 at the surface because atmospheric pressure is a hydrostatic pressure that can be neglected and because there can be no traction on a free surface, respectively. Note that, because the drag exerted on the ice by the bed is in the negative  $x$ -direction,  $\sigma_{zx}$  is set to  $-k$  on the bed. Because  $\sigma_{zx}$  is independent of  $x$  on the bed, we seek a solution in which  $\sigma_{zx}$  is independent of  $x$  everywhere.

The following solution is contained in a manuscript by J. F. Nye that he kindly provided to the author, and is used with his permission. We take the derivative of Equation (10.3) with respect to  $z$  and of Equation (10.4) with respect to  $x$ , thus:

$$\begin{aligned} \frac{\partial^2 \sigma_{xx}}{\partial z \partial x} + \frac{\partial^2 \sigma_{zx}}{\partial z^2} &= 0 \\ \frac{\partial^2 \sigma_{zz}}{\partial x \partial z} + \frac{\partial^2 \sigma_{zx}}{\partial x^2} &= 0. \end{aligned} \tag{10.9}$$

As  $\sigma_{xx}$  and  $\sigma_{zz}$  are continuous functions, the order of differentiation can be reversed in the first of these equations. Subtracting then yields:

$$\frac{\partial^2}{\partial x \partial z} (\sigma_{xx} - \sigma_{zz}) = \left( \frac{\partial^2 \sigma_{zx}}{\partial x^2} - \frac{\partial^2 \sigma_{zx}}{\partial z^2} \right). \tag{10.10}$$

Substituting for  $(\sigma_{xx} - \sigma_{zz})$  from Equation (10.8) and setting  $\sigma = k$ , as noted above, we find:

$$\pm \frac{\partial^2}{\partial x \partial z} \left( 2\sqrt{k^2 - \sigma_{zx}^2} \right) = \left( \frac{\partial^2 \sigma_{zx}}{\partial x^2} - \frac{\partial^2 \sigma_{zx}}{\partial z^2} \right). \tag{10.11}$$

Making use of the condition that  $\sigma_{zx}$  is independent of  $x$  allows us to simplify this to:

$$\frac{\partial^2 \sigma_{zx}}{\partial z^2} = 0 \quad (10.12)$$

which has the solution:

$$\sigma_{zx} = c_1 z + c_2. \quad (10.13)$$

To satisfy the boundary condition  $\sigma_{zx} = 0$  on  $z = 0$ , we find that  $c_2 = 0$ . The boundary condition  $\sigma_{zx} = -k$  on  $z = h$  then yields  $c_1 = -k/h$ . Thus the solution for  $\sigma_{zx}$  becomes:

$$\sigma_{zx} = -\frac{kz}{h}. \quad (10.14)$$

In other words, the shear stress varies linearly with depth.

Using this solution for  $\sigma_{zx}$  in Equations (10.3) and (10.4) yields:

$$\frac{\partial \sigma_{xx}}{\partial x} = \frac{k}{h} - \rho g_x$$

$$\frac{\partial \sigma_{zz}}{\partial z} = -\rho g_z$$

which integrate to:

$$\begin{aligned} \sigma_{xx} &= \frac{kx}{h} - \rho g_x x + f_1(z) \\ \sigma_{zz} &= -\rho g_z z + f_2(x). \end{aligned} \quad (10.15)$$

where  $f_1(z)$  and  $f_2(x)$  are functions that are dependent only upon  $z$  and  $x$ , respectively, so that  $\partial f_1(z)/\partial x = 0$  and  $\partial f_2(x)/\partial z = 0$ . They are analogous to the constants of integration in Equation (10.13), and must be evaluated with the use of the boundary conditions. Substituting these solutions for  $\sigma_{xx}$ ,  $\sigma_{zz}$ , and  $\sigma_{zx}$  back into Equation (10.8), the yield criterion, and rearranging terms we obtain:

$$\frac{kx}{h} - \rho g_x x + f_1(z) + \rho g_z z - f_2(x) = \pm 2\sqrt{k^2 - \frac{k^2 z^2}{h^2}}$$

which is true for all  $x$  and  $z$  because, as noted, the yield criterion must be met throughout the slab. Thus, collecting the terms in  $x$  on the left hand side and those in  $z$  on the right results in:

$$\frac{kx}{h} - \rho g_x x - f_2(x) = -\rho g_z z \pm 2k\sqrt{1 - \left(\frac{z}{h}\right)^2} - f_1(z) = c. \quad (10.16)$$

Because the left hand side is a function of  $x$  alone and the right hand side is a function of  $z$  alone, the two sides can be equal to each other in the general case only if each, individually, is equal to the same constant,  $c$ , as shown. We can thus solve

Equation (10.16) for  $f_2(x)$  in terms of  $c$ , and for  $f_1(z)$  in terms of  $c$ . These solutions are then inserted in Equations (10.15) to yield:

$$\begin{aligned}\sigma_{xx} &= \frac{kx}{h} - \rho g_x x - \rho g_z z \pm 2k\sqrt{1 - \left(\frac{z}{h}\right)^2} - c \\ \sigma_{zz} &= -\rho g_z z + \frac{kx}{h} - \rho g_x x - c.\end{aligned}\quad (10.17)$$

Making use of the boundary condition  $\sigma_{zz}=0$  on  $z=0$  in the second of Equations (10.17) gives:

$$c = \frac{kx}{h} - \rho g_x x = x\left(\frac{k}{h} - \rho g_x\right).$$

As this must hold for all  $x$ , it is clear that  $k/h - \rho g_x$  must equal 0, and therefore  $c$  must also be 0. Thus:

$$\frac{k}{h} = \rho g_x.$$

This implies that the block must have some critical thickness,  $h=k/\rho g_x$ . Using these results in Equations (10.17), and repeating Equation (10.14) allows us to write the complete stress solutions thus:

$$\begin{aligned}\sigma_{xx} &= -\rho g_z z \pm 2k\sqrt{1 - \left(\frac{z}{h}\right)^2} \\ \sigma_{zz} &= -\rho g_z z \\ \sigma_{zx} &= -\frac{kz}{h}.\end{aligned}\quad (10.18)$$

As a check on these solutions, they may be substituted back into the yield criterion, Equation (10.8), to show that  $\sigma = k$ .

A plot (Figure 10.2) will serve to illustrate the solutions. Scaling  $\sigma_{zz}$  by  $k$  ( $= \rho g_x h$ ) and noting that  $g_x = g \sin \alpha$  and  $g_z = g \cos \alpha$ , where  $\alpha$  is the slope of the bed (and surface), results in:

$$\frac{\sigma_{zz}}{k} = -\frac{z}{h} \frac{\cos \alpha}{\sin \alpha}.$$

So  $\sigma_{zz}$  is 0 at the surface and it decreases linearly with depth. In plotting Figure 10.2,  $\alpha$  was chosen such that  $\tan \alpha = 1/5$  so that  $\sigma_{zz} = -5k$  on  $z = h$  (Figure 10.2). Similarly,  $\sigma_{xx} = \pm 2k$  on  $z = 0$  and since  $\sigma_{xx} = \sigma_{zz}$  on the bed,  $\sigma_{xx} = -5k$  there. In this case, however, the distribution with depth is elliptical. Finally,  $\sigma_{zx}$  also decreases linearly with depth to  $-k$  on the bed.

The deviatoric stresses can also be calculated. Noting that:

$$P = \frac{1}{2}(\sigma_{xx} + \sigma_{zz}) = -\rho g_z z \pm k\sqrt{1 - \left(\frac{z}{h}\right)^2}$$

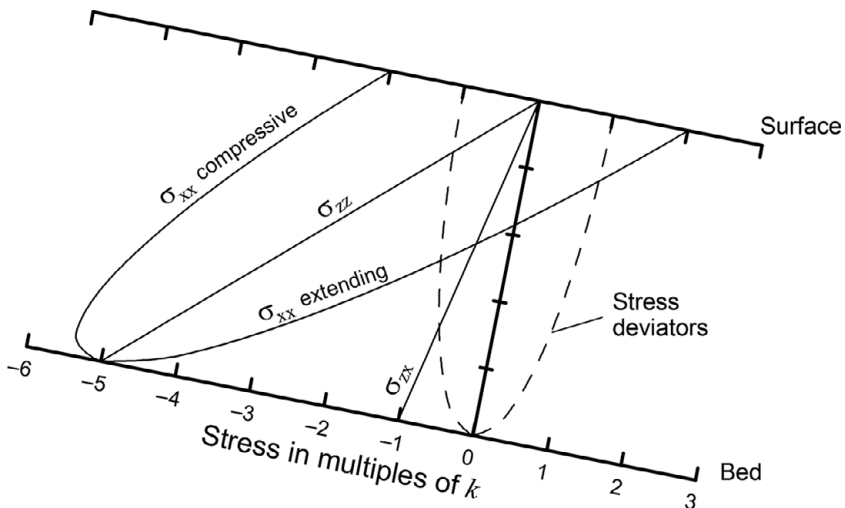


**Figure 10.2** Depth variation of stress in a deforming slab of material with a perfectly plastic rheology. The slab is of uniform thickness and density, and is resting on a bed with a uniform slope. (Modified from Nye, 1951, Figure 2c. Reproduced with permission of the author and the Royal Society of London)

we find that:

$$\begin{aligned}\sigma'_{xx} &= \sigma_{xx} - P = \pm k \sqrt{1 - \left(\frac{z}{h}\right)^2} \\ \sigma'_{zz} &= \sigma_{zz} - P = \mp k \sqrt{1 - \left(\frac{z}{h}\right)^2}\end{aligned}\quad (10.19)$$

so  $\sigma'_{xx}$  is  $\pm k$  at the surface and decreases to 0 at the bed, as shown by the dashed lines describing a semi-ellipse in Figure 10.2. As required by continuity,  $\sigma'_{zz} = -\sigma'_{xx}$ ; that is, if our medium is homogeneous, isotropic, and incompressible, as assumed, a deformation in the  $x$ -direction,  $\dot{\epsilon}_{xx}$ , caused by a stress,  $\sigma'_{xx}$ , must be accompanied by an equal deformation of opposite sign,  $\dot{\epsilon}_{zz}$ , in the  $z$ -direction, and this requires a stress equal to  $\sigma'_{xx}$ , but in the opposite direction.

Negative or compressive deviatoric stresses in the  $x$ -direction result in longitudinal compression, and this flow regime is thus referred to as *compressive flow*. Similarly, positive deviatoric stresses in the  $x$ -direction result in what is called *extending flow*. The former is characteristic of ablation zones of glaciers, where melt must be replaced by upward flow of ice, and the latter is characteristic of accumulation zones.

It is also of interest to examine the orientation of the principal stresses and of the maximum shear stresses. In Chapter 9 (Equation 9.3b) we found that:

$$\tan 2\theta = \frac{2\sigma_{zx}}{(\sigma_{xx} - \sigma_{zz})}$$

so:

$$\theta = \frac{1}{2} \tan^{-1} \frac{-2kz/h}{\pm 2k \sqrt{1 - (\frac{z}{h})^2}} = \frac{1}{2} \tan^{-1} \left( \mp \frac{z}{\sqrt{h^2 - z^2}} \right).$$

On  $z = 0$ ,  $\theta = 0^\circ$  or  $90^\circ$  and on  $z = h$ ,  $\theta = 45^\circ$  or  $135^\circ$ . Thus at the surface, the principal stresses are parallel and normal to the surface, and at the bed, they make an angle of  $45^\circ$  or  $135^\circ$  with the bed. The former could also be deduced from the fact that there is no shear traction on a free surface, so the stresses parallel and normal to this surface are principal stresses. The orientation of the planes of maximum shear stress may be found by differentiating Equation (9.2) with respect to  $\theta$  and setting the result equal to 0, thus:

$$\theta_{ss \text{ max}} = \frac{1}{2} \tan^{-1} \left( \pm \frac{\sqrt{h^2 - z^2}}{z} \right).$$

In this case,  $\theta_{ss} = \pm 45^\circ$  at the surface and  $0^\circ$  or  $90^\circ$  at the bed. (Thus, the planes of maximum shear stress make an angle of  $45^\circ$  with respect to the principal stresses.) At any intermediate depth there are two solutions for  $\theta_{ss \text{ max}}$  that are  $90^\circ$  apart. Thus, the loci of the zones of maximum shear stress are as shown in Figure 10.3. This is what is known as the *slip line field* for the particular stress configuration.

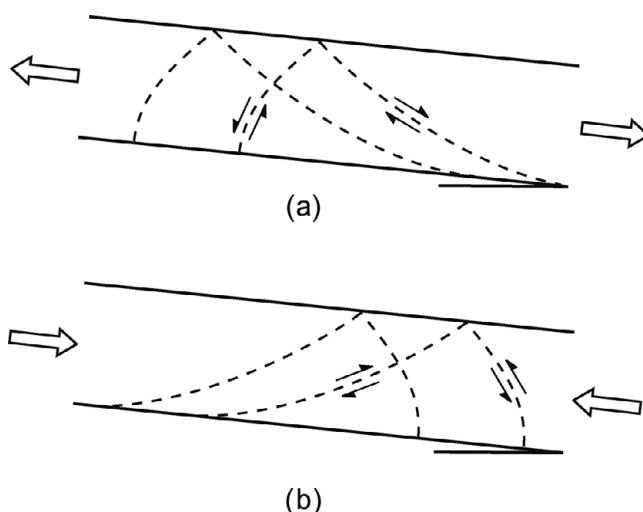


**Figure 10.3** Slip line fields in a deforming slab of material with a perfectly plastic rheology. (a) Extending flow, and (b) Compressive flow. (Modified from Nye, 1951, Figure 5)

## Velocity solutions in a perfectly plastic medium

We now use the stress solutions, Equations (10.18), to obtain solutions for the velocities from Equations (10.5) through (10.7). From Equations (10.5) and (10.6) we obtain:

$$\begin{aligned}\frac{\partial u}{\partial x} &= -\frac{\partial w}{\partial z} = \frac{\lambda}{2}(\sigma_{xx} - \sigma_{zz}) \\ &= \pm \lambda k \sqrt{1 - \left(\frac{z}{h}\right)^2}\end{aligned}\quad (10.20)$$

and from Equation (10.7):

$$\frac{\partial u}{\partial z} + \frac{\partial w}{\partial x} = 2\lambda\sigma_{xz} = -2\lambda \frac{kz}{h}. \quad (10.21)$$

Let's first examine the applicable boundary conditions. The stress solutions are valid only for the thickness  $h = k/pg_r$ . Therefore, we seek a velocity solution that will maintain this thickness. Because there is accumulation,  $b_n$  (or ablation,  $-b_n$ ) at the surface, we know that:

$$w = b_n \quad \text{on } z = 0$$

$$w = 0 \quad \text{on } z = h.$$

We will now show that  $\partial w / \partial x = 0$ . The stresses are independent of  $x$ , and the material is the limiting case of a purely viscous material in which stresses determine strain rates. Therefore, the strain rates must be independent of  $x$ . In particular,  $\partial w / \partial z$  is independent of  $x$ , so:

$$\frac{\partial}{\partial x} \left( \frac{\partial w}{\partial z} \right) = 0$$

or, as  $w$  must be continuous in  $x$  and  $z$  (so the order of differentiation can be reversed):

$$\frac{\partial}{\partial z} \left( \frac{\partial w}{\partial x} \right) = 0.$$

Therefore,  $\partial w / \partial x = \text{const}$ , independent of  $z$ . Then, because  $\partial w / \partial x = 0$  on the upper and lower boundaries from the boundary conditions,  $\partial w / \partial x = 0$  everywhere.

Equation (10.21) now becomes:

$$\frac{\partial u}{\partial z} = -2\lambda \frac{kz}{h}. \quad (10.22)$$

Combining Equations (10.20) and (10.22) to eliminate  $\lambda$  yields:

$$\begin{aligned}\frac{\partial u}{\partial z} &= \pm \frac{2(kz/h)}{k\sqrt{1 - (z/h)^2}} \frac{\partial w}{\partial z} \\ &= \pm \frac{2z}{\sqrt{h^2 - z^2}} \frac{\partial w}{\partial z}.\end{aligned}\quad (10.23)$$

Differentiating with respect to  $x$  and again making use of the fact that  $w$  is continuous in  $x$  and  $z$  so the order of differentiation can be reversed, gives:

$$\begin{aligned}\frac{\partial^2 u}{\partial x \partial z} &= \pm \frac{2z}{\sqrt{h^2 - z^2}} \frac{\partial^2 w}{\partial x \partial z} \\ &= \pm \frac{2z}{\sqrt{h^2 - z^2}} \frac{\partial}{\partial z} \left( \frac{\partial w}{\partial x} \right) \\ &= 0\end{aligned}$$

where the last equality stems from the fact that  $\partial w / \partial x = 0$ . Thus, from Equation (10.20), differentiating with respect to  $z$ , we obtain:

$$\frac{\partial^2 u}{\partial z \partial x} = -\frac{\partial^2 w}{\partial z^2} = 0 \quad (10.24)$$

which has the solution:

$$w = c_1 z + c_2.$$

Using the first boundary condition,  $w = b_n$  on  $z = 0$ , yields  $c_2 = b_n$ , whereupon the second boundary condition,  $w = 0$  on  $z = h$ , yields  $0 = c_1 h + b_n$ . The solution for the velocity in the  $z$ -direction thus becomes:

$$w = b_n \left( 1 - \frac{z}{h} \right). \quad (10.25)$$

Thus,  $w$  varies linearly with depth. We discussed this in Chapter 5 (Equation 5.21) and will analyze it in greater detail later.

Using this solution for  $w$  in Equation (10.20) we obtain:

$$\frac{\partial u}{\partial x} = -\frac{\partial w}{\partial z} = \frac{b_n}{h} \quad (10.26)$$

and from Equation (10.23):

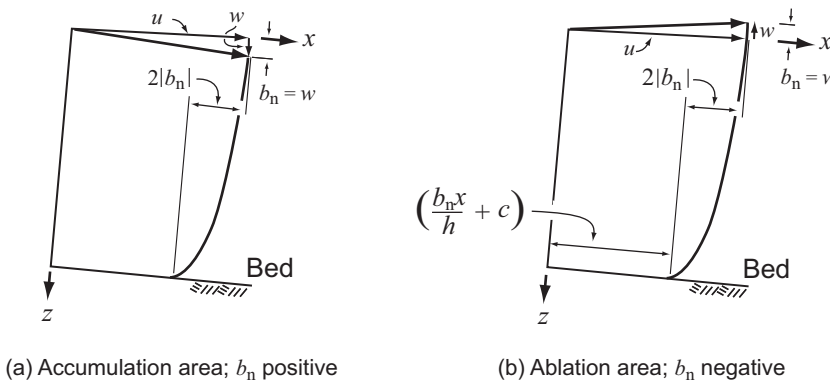
$$\frac{\partial u}{\partial z} = \mp \frac{2z}{\sqrt{h^2 - z^2}} \frac{b_n}{h}. \quad (10.27)$$

In the coordinate system we have chosen,  $\sigma_{zx}$  is negative for positive  $z$ . Therefore  $\dot{\varepsilon}_{zx}$ , and hence in Equation (10.27),  $\partial u / \partial z$ , must be negative so that a negative stress produces a negative strain rate. (In other words, the horizontal velocity must decrease with depth). Thus, when  $b_n$  is positive in Equation (10.27) we use the upper sign, and conversely. Equation (10.27) thus becomes:

$$\frac{\partial u}{\partial z} = -2 \frac{|b_n|}{h} \frac{z}{\sqrt{h^2 - z^2}}. \quad (10.28)$$

Integrating Equation (10.26) yields:

$$u = \frac{b_n x}{h} + f(z)$$

(a) Accumulation area;  $b_n$  positive(b) Ablation area;  $b_n$  negative**Figure 10.4** Velocity solutions for a deforming slab of material with a perfectly plastic rheology.

where, as in Equation (10.15),  $f(z)$  represents some function of  $z$  alone. Taking the derivative of this with respect to  $z$ , substituting the result into Equation (10.28), and integrating gives<sup>1</sup>:

$$f(z) = 2 \frac{|b_n|}{h} \sqrt{h^2 - z^2} + c.$$

Thus, the solution for the velocity in the  $x$ -direction is:

$$u = \frac{b_n x}{h} + 2 \frac{|b_n|}{h} \sqrt{h^2 - z^2} + c. \quad (10.29)$$

These velocity solutions are illustrated in Figure 10.4. On  $z = 0$ ,  $u = \frac{b_n x}{h} + 2|b_n| + c$ , and  $w = b_n$ , while on  $z = h$ ,  $u = \frac{b_n x}{h} + c$ , and  $w = 0$ . Thus, evidently,  $\frac{b_n x}{h} + c$  is the "sliding" speed. Note that Equation (10.29) implies that the ice must be free to slide on the bed at a speed determined by  $b_n$ , and independent of  $\sigma_{zx}$  and bed roughness.

If, on the contrary, the sliding speed were presumed to be a function of  $\sigma_{zx}$  and bed roughness, the distribution of stress and hence of  $w$  could not be independent of  $x$ , and the ice mass would not remain a uniform slab. A reasonable presumption is that the sliding speed would not increase sufficiently rapidly with  $x$ , and that conservation of mass would then require that the ice thickness increase upglacier, leading to a convex surface profile. Depending on the degree of convexity and the consequent change in ice thickness, such a profile would offer the potential for increasing  $\sigma_{zx}$  downglacier. This would provide the required increase in mass flux.

Note that between any two vertical sections,  $x_1$  and  $x_1 + \Delta x$ ,  $u$  increases by  $b_n \Delta x / h$ , which would be the increase in mean velocity required to transmit the additional flux,  $b_n \Delta x$ , downglacier – the balance velocity that we discussed in Chapter 5.

<sup>1</sup> The integration may be carried out with the substitution  $u = h^2 - z^2$ , whence  $du = 2z dz$ .

If there is no accumulation or ablation,  $b_n = 0$ , so  $u = c$  and  $w = 0$  throughout the block. In this case there is no internal deformation. All movement is confined to sliding. The yield criterion is then satisfied only at the bed and  $\sigma_{xx}$  can take any value between the limits shown in Figure 10.2.

This elegant solution for stresses ties together our discussions of mass balance and balance velocity in Chapter 3, of the differences in flow between the accumulation and ablation areas and the resulting concept of emergence velocities in Chapter 5, and of the orientation of principal stresses at the surface and bed in Chapter 9.

### Stress and velocity solutions for a non-linear material

Let us now relax the assumption that the material with which we are dealing is perfectly plastic, and instead allow it to have a non-linear rheology, as is the case with real ice. We will still consider a slab of infinite extent and uniform thickness resting on a bed with a uniform slope. The stress equations are not changed, so the solutions for the stresses (Equations 10.18) remain basically the same. However, now  $\sigma$  does not have a limiting value,  $k$ , the yield stress, so some changes must be made.

As before (Equations 10.18), we note that  $\sigma_{xx} \rightarrow \sigma_{zz}$  on the bed, as both are dominated by the hydrostatic pressure. As  $\sigma \gg 0$  at the bed, it is clear from Equation (10.8) that  $\sigma \approx \sigma_{zx} \gg (\sigma_{xx} - \sigma_{zz}) \approx 0$  there. Again, this emphasizes that deformation at the bed is largely by simple shear. Thus  $\sigma_{zx} \rightarrow \sigma$  on the bed, so we replace  $k$  with  $\sigma$  in Equations (10.18). In other words, while we still require that  $\sigma$  and  $\sigma_{zx}$  be uniform (independent of  $x$ ) on the bed, we do not require that they are necessarily equal to some specific value, as in a yield stress. In general, of course,  $\sigma_{zx}$  is likely to increase with the budget gradient (Figure 3.7), as flow rates must then be higher. In addition, we make use of the fact that  $k/h = \rho g_x$  from the discussion following Equation (10.17). With these changes, the stress solutions become:

$$\begin{aligned}\sigma_{xx} &= -\rho g_z z \pm 2\sqrt{\sigma^2 - (\rho g_x z)^2} \\ \sigma_{zz} &= -\rho g_z z \\ \sigma_{zx} &= -\rho g_x z.\end{aligned}\tag{10.30}$$

As before, the upper sign is for extending, and the lower for compressive flow.

In order to evaluate  $\sigma_{xx}(z)$ , we need to know how  $\sigma$  varies with depth,  $z$ . This will emerge in the course of obtaining the velocity solutions.

To solve for the velocities, we start by combining the stress solutions with Equations (10.5) through (10.7) to obtain:

$$\begin{aligned}\frac{\partial u}{\partial x} &= -\frac{\partial w}{\partial z} = \frac{\lambda}{2}(\sigma_{xx} - \sigma_{zz}) = \pm \lambda \sqrt{\sigma^2 - (\rho g_x z)^2} \\ \frac{1}{2} \left( \frac{\partial u}{\partial z} + \frac{\partial w}{\partial x} \right) &= \lambda \sigma_{xz} = -\lambda \rho g_x z.\end{aligned}\tag{10.31}$$

As before (discussion preceding Equation 10.22), because  $w = 0$  on the lower boundary, and because  $w$  must thus be independent of  $x$  everywhere to avoid discontinuities,  $\partial w / \partial x = 0$  everywhere. Thus, using the arguments outlined in Equations (10.22–10.24) we obtain, as before:

$$w = c_1 z + c_2. \quad (10.32)$$

The boundary conditions now are not as clear as they were earlier because the thickness may change with time. Thus  $w \neq b_n$  on  $z = 0$ .

From the first of Equations (10.31) and from Equation (10.32) we have:

$$\frac{\partial w}{\partial z} = c_1 = -\frac{\partial u}{\partial x}. \quad (10.33)$$

Therefore, again from the first of Equations (10.31):

$$c_1 = \mp \lambda \sqrt{\sigma^2 - (\rho g_x z)^2}. \quad (10.34)$$

Using this to eliminate  $\lambda$  in the second of Equations (10.31) yields:

$$\frac{\partial u}{\partial z} = \pm 2\rho g_x z \frac{c_1}{\sqrt{\sigma^2 - (\rho g_x z)^2}}. \quad (10.35)$$

As  $\lambda$  is defined by  $\dot{\epsilon}_{ij} = \lambda \sigma'_{ij}$ , it must be positive if positive stresses are to produce positive strain rates. To ensure that this is the case, we give  $c_1$  the values  $\mp r$  where  $r$  is a positive constant. From Equation (10.33) it is clear that  $r$  is the longitudinal strain rate. Equation (10.33) thus becomes:

$$\frac{\partial u}{\partial x} = \pm r.$$

The solution for  $w$  is now:

$$w = \mp r z + c_2.$$

Applying the boundary condition  $w = 0$  on  $z = h$ , we get  $c_2 = \pm rh$ , so:

$$w = \mp r(z - h) = \pm rh \left(1 - \frac{z}{h}\right). \quad (10.36)$$

Thus,  $w$  again varies linearly with depth as in the perfectly plastic case, despite the variation in  $\sigma$  with depth. This is implicit in the fact that the longitudinal strain rate is independent of depth, which in turn results from the fact that stresses must be independent of  $x$  in a slab on a uniform slope [see discussion following Equation (10.21);  $\partial u / \partial x = -\partial w / \partial z$  and by Equation (10.24),  $\partial w / \partial z = \text{constant}$ ].

To obtain  $u$ , integrate Equation (10.35) (with Equation 10.34), thus:

$$u = -2g_x \int_0^z \lambda \rho z \, dz + f(x). \quad (10.37)$$

Setting the derivative of this with respect to  $x$  equal to  $\pm r$ , and integrating gives  $f(x) = \pm rx + c$ . Combining this with Equation (10.37) and using the boundary condition  $u = u_0$  at  $x = z = 0$  yields:

$$u = \pm rx - 2g_x \int_0^z \lambda \rho z \, dz + u_0. \quad (10.38)$$

The velocity,  $u_s$ , at the surface ( $z = 0$ ) is  $\pm rx + u_0$ . Here  $u_0$  is the velocity at the origin,  $x = 0$ , and  $rx$  is the increase (or decrease) in velocity between the origin and the point in question as a result of longitudinal straining. In a real glacier,  $r = r(x)$ , so one would have to integrate over  $x$  to obtain  $u_s$  in this way. In practice, we would be more likely to simply take  $u_s$  as known. Accordingly, we will replace  $\pm rx = u_0$  with  $u_s$  in Equation (10.38).

To proceed further, we must assume a flow law; as before, we use  $\dot{\epsilon} = \lambda\sigma = A\sigma^n$  with  $A$  and  $n$  constant, independent of  $x$  and  $z$ . Hence,

$$\lambda = A\sigma^{n-1} \quad (10.39)$$

and Equation (10.38) becomes (assuming that  $\rho$  is independent of depth):

$$u = u_s - 2A\rho g_x \int_0^z \sigma^{n-1} z \, dz. \quad (10.40)$$

To integrate this,  $\sigma$  must be expressed in terms of  $z$ . From Equation (10.34) with  $c_1 = \mp r$ :

$$\lambda = \frac{r}{\sqrt{\sigma^2 - (\rho g_x z)^2}} = A\sigma^{n-1}.$$

Rearranging, this becomes:

$$z = \frac{\sqrt{\sigma^{2n} - (r/A)^2}}{\rho g_x \sigma^{n-1}} \quad (10.41)$$

whence:

$$\frac{dz}{d\sigma} = \frac{n\sigma^{2n-1}}{\rho g_x \sigma^{n-1} \sqrt{\sigma^{2n} - (r/A)^2}} - (n-1) \frac{\sqrt{\sigma^{2n} - (r/A)^2}}{\rho g_x \sigma^{2(n-1)}} \sigma^{n-2},$$

so

$$dz = \left[ \frac{n\sigma^n}{\rho g_x \sqrt{\sigma^{2n} - (r/A)^2}} - (n-1) \frac{\sqrt{\sigma^{2n} - (r/A)^2}}{\rho g_x \sigma^n} \right] d\sigma. \quad (10.42)$$

When  $z = 0$ , the numerator in Equation (10.41) must equal 0, so  $\sigma^{2n} = (r/A)^2$ , or  $\sigma = (r/A)^{1/n}$ . Thus, Equation (10.40) is to be integrated from  $(r/A)^{1/n}$  to  $\sigma$ . With  $z$  from Equation (10.41) and  $dz$  from Equation (10.42), Equation (10.40) becomes:

$$\begin{aligned}
 u &= u_s - 2A\rho g_x \int_{(r/A)^{1/n}}^{\sigma} \frac{\sqrt{\sigma^{2n} - (r/A)^2}}{\rho g_x} \left[ \frac{n\sigma^n}{\rho g_x \sqrt{\sigma^{2n} - (r/A)^2}} - (n-1) \frac{\sqrt{\sigma^{2n} - (r/A)^2}}{\rho g_x \sigma^n} \right] d\sigma \\
 &= u_s - \frac{2A}{\rho g_x} \int_{(r/A)^{1/n}}^{\sigma} \left[ \sigma^n + (n-1) \left( \frac{r}{A} \right)^2 \sigma^{-n} \right] d\sigma.
 \end{aligned}$$

Carrying out the integration yields:

$$u(z) = u_s - \frac{2}{\rho g_x(n+1)} \left[ A\sigma^{n+1} - \frac{(n+1)r^2\sigma^{1-n}}{A} + \frac{nr^{(1+\frac{1}{n})}}{A^{1/n}} \right] \quad (10.43)$$

which, together with Equation (10.41), provides the desired solution for  $u$  in terms of  $z$ . Expressing  $u$  explicitly in terms of  $z$  is awkward. Rather, one assumes a value of  $\sigma$ , and uses it to calculate the depth  $z$  to that  $\sigma$  and the velocity at that depth.

When  $r=0$ , these equations reduce to:

$$u(z) = u_s - \frac{2A}{\rho g_x(n+1)} \sigma^{n+1}$$

and

$$z = \frac{\sigma^n}{\rho g_x \sigma^{n-1}} = \frac{\sigma}{\rho g_x}.$$

Thus:

$$u(z) = u_s - \frac{2A}{n+1} (\rho g_x)^n z^{n+1}$$

which is the same as Equation (5.6). A fundamental assumption made in the derivation of Equation (5.6) should now be more meaningful: namely that all strain rates other than shear strain parallel to the bed,  $\dot{\varepsilon}_{zx}$ , were negligible. In deriving Equation (10.42) we added only one additional strain rate,  $\dot{\varepsilon}_{xx}$  ( $= r$ ), yet the complexity of the solution increased significantly.

Now that we have an expression relating  $\sigma$  and  $z$ , we can plot stress distributions from Equations (10.30). This is done in Figure 10.5 for a glacier with a longitudinal strain rate of  $0.1 \text{ a}^{-1}$  resting on a bed with a slope of 0.1. As in the perfectly plastic case (Figure 10.2),  $\sigma_{zz}$  and  $\sigma_{zx}$  vary linearly with depth, while  $\sigma_{xx}$  varies non-linearly and is also double valued. Furthermore, for any given depth  $\sigma$  is a function of  $n$  (Equation 10.41). That is, if  $z$  is specified (along with  $r$ ,  $A$ ,  $\rho$ , and  $g_x$ ), the value of  $\sigma$  will depend on  $n$ . Thus,  $\sigma_{xx}$  varies with  $n$ . For  $n = 1$ ,  $\sigma$  (Equation 10.41) and hence  $\sigma_{xx}$  (first of Equations 10.30) decrease linearly with depth. As  $P$  [ $= \frac{1}{2}(\sigma_{xx} + \sigma_{zz})$ ] also decreases linearly with depth with the same constant of proportionality,  $\rho g_z$ ,  $\sigma'_{xx}$  becomes independent of depth. As  $n$  becomes large, the solution for  $\sigma_{xx}$  converges on the elliptic distribution obtained earlier (Figure 10.2). In the limiting case, as  $n \rightarrow \infty$ ,  $\sigma^{2n}$  becomes much greater than  $(r/A)^2$  (Equation 10.41) so  $z \rightarrow \sigma/\rho g_x$ . On the bed,

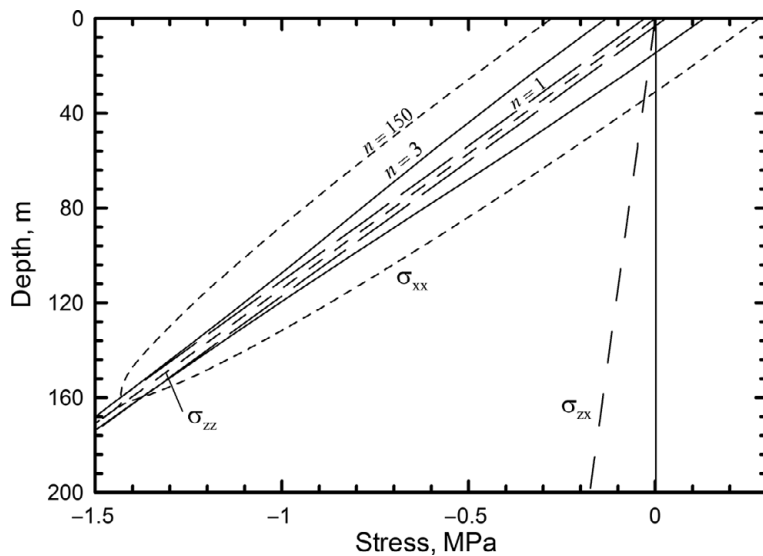


**Figure 10.5** Depth variation of stress in an ice sheet with a power law rheology. The ice sheet consists of a slab of uniform thickness and density resting on a bed with a slope of 0.1. The distribution of  $\sigma_{xx}$  is given by the pairs of curves labeled with values of  $n$ . The distributions of  $\sigma_{zz}$  and  $\sigma_{zx}$  are the same for all  $n$ . Calculations use  $n = 3$ ,  $A = 357 \text{ MPa}^{-n} \text{ a}^{-1}$ , and  $r = 0.1 \text{ a}^{-1}$ . As  $n \rightarrow \infty$ , the thickness of the ice sheet is limited to  $h = 1/\rho g_x A^{1/n}$  (see text), which in this case is  $\sim 160 \text{ m}$ .

$\sigma_{zx} \gg (\sigma_{xx} - \sigma_{zz})$  because  $\sigma_{xx} \approx \sigma_{zz}$ , both of which are dominated by  $P$ . Thus,  $\sigma \rightarrow \sigma_{zx}$  (Equation 10.8), so from the flow law,  $\dot{\varepsilon}_{zx} = A\sigma^{n-1}\sigma_{zx} \cong A\sigma_{zx}^{-n}$ . Because  $\dot{\varepsilon}_{zx}$  cannot be allowed to go either to 0 or to  $\infty$ ,  $\sigma_{zx} \rightarrow A^{-1/n}$ . Thus, the thickness in this case is  $h = 1/(\rho g_x A^{1/n})$ . Note that  $\sigma_{zx} = A^{-1/n}$  is not dimensionally consistent, so  $\sigma_{zx} = A^{-1/n}$  numerically only.

Further insight may be gained by considering the case when  $\sigma = 0$ . If  $r \neq 0$ ,  $z$  becomes indefinite. This is because, although  $\sigma_{zx} = 0$  at the surface,  $\sigma = \frac{1}{2}\sigma_{ij}\sigma_{ij} > 0$  there. Thus, when there is longitudinal strain, there is no place in the slab where  $\sigma = 0$ .

Two velocity profiles calculated from Equations (10.41) and (10.43) are shown in Figure 10.6. One profile is calculated with  $r = 0$ , and the other with  $r = 0.1 \text{ a}^{-1}$ . In the calculation,  $u_s$  is adjusted to yield  $u_b = 20 \text{ m a}^{-1}$  in both cases. One might initially think that the higher speed represented by the dashed profile in Figure 10.6 was a consequence of longitudinal stretching. However,  $r$  is a positive constant (so a negative value of  $r$  cannot be entered in Equation 10.43) and  $\partial u / \partial x = \pm r$ . Thus, the solid profile is applicable to compressive flow as well as extending flow. This is because the magnitude of the increase in  $\sigma$ , and hence in  $\lambda$ , resulting from the addition of a longitudinal stress, is independent of whether the longitudinal stress is compressive or extending. As  $\lambda$  increases so does  $\dot{\varepsilon}_{ij}$  for any given  $\sigma_{ij}$  (Equation 9.29). Specifically,  $\dot{\varepsilon}_{zx}$  ( $= \partial u / \partial z$ ) increases, regardless of whether  $\sigma_{xx}$  is positive or negative.

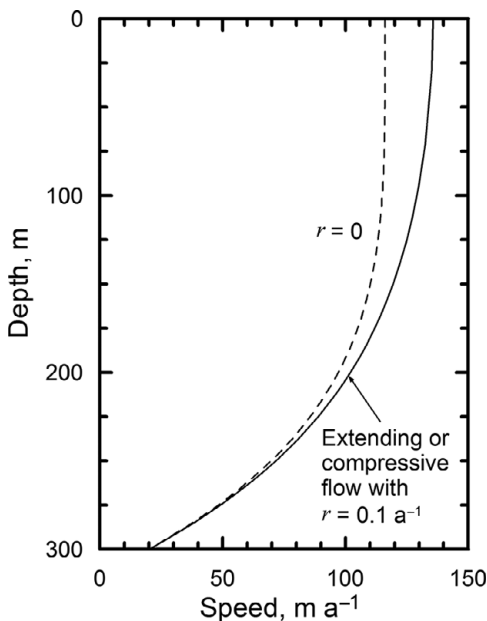


**Figure 10.6** Velocity profiles, calculated from Equations (10.41) and (10.43), in a glacier consisting of an infinite slab of ice, 300 m thick, resting on a bed with a slope of 0.046 and sliding with a speed,  $u_b$ , of 20 m  $a^{-1}$ . Calculations use  $n = 3$  and  $A = 357 \text{ MPa}^{-n} a^{-1}$ , and two different values of  $r$ , as shown.

## Comparison with real glaciers

Real glaciers are not slabs of ice of uniform thickness, nor are they perfectly plastic. Thus, it is relevant to consider what aspects of the solutions we have obtained are applicable in reality.

Consider first the result that  $\sigma_{zz}$  and  $\sigma_{zx}$  vary linearly with depth. Such a linear variation is often assumed in studies of real glaciers and is a reasonable approximation in many situations.

In addition we found that, in general, flow is extending in accumulation areas and compressive in ablation areas. This is because  $\partial u / \partial x \propto b_n$  (if the glacier is not too far from a steady state), and  $\sigma \propto r (= |\partial u / \partial x|)$  for any given depth (because the numerator in Equation (10.41) must remain constant for a given  $z$ ). Thus, as  $|\sigma_{xx}|$  varies directly with  $\sigma$  (Equation 10.30), it also varies directly with  $b_n$ , being positive when  $b_n$  is positive and conversely. In an actual glacier, however, longitudinal stresses also depend on factors such as the curvature of the longitudinal surface profile and the rate of change in thickness. Thus, it is not productive to try to calculate longitudinal stresses in a real glacier with the use of the theory presented here.

The physical processes by which the longitudinal strain rate is adjusted to balance  $b_n$  can be visualized qualitatively. If, in some location,  $\partial u / \partial x$  is too large so that thinning by extension exceeds thickening by accumulation, the profile will tend to become concave, and this will have a tendency to decrease  $\partial u / \partial x$ .

Also relevant to real glaciers is the effect of longitudinal stress on velocities. Clearly, longitudinal compression should result in upward vertical velocities, and conversely. The linear decrease in  $w$  with depth, however, is an artifact of our slab model (see discussion following Equation 10.36), although it is an approximation that is commonly used in calculations, as we noted in Chapter 5. In reality,  $\partial w/\partial z$  is lower than predicted by the linear approximation near the surface and increases toward the bed (Figure 5.9). With respect to vertical profiles of  $u$ , longitudinal stresses, whether extending or compressive, increase the effective stress, so they increase  $\partial u/\partial z$  throughout the profile. This may be particularly evident near a glacier surface where  $\sigma_{zx}$  is small so  $\dot{\varepsilon}_{zx}$  would be negligible were it not for the contribution of  $\sigma_{xx}$  to  $\sigma$ . We will find in Chapter 12, however, that certain peculiarities of measured deformation profiles cannot be explained in this way.

---

## SUMMARY

In this chapter, we have shown that Equations (9.32) can be solved for the three components of the velocity vector and nine components of the stress tensor in certain simple situations. Our solutions were for a slab of infinite horizontal extent resting on a bed with a uniform slope. We first obtained a solution for a perfectly plastic material ( $n \rightarrow \infty$ ), and found that the thickness of the slab was constrained by the yield strength of the material. We then obtained solutions for a non-linear material which are more relevant to real glaciers.

We found that  $\sigma_{zz}$  and  $\sigma_{zx}$  vary linearly with depth, which is probably a reasonable initial assumption in calculations concerning many real glaciers. We also found that longitudinal stresses should be extending in accumulation areas and compressive in ablation areas, although the magnitude of the longitudinal stress is not well constrained by our simple model.

Vertical velocities vary linearly with depth for the idealized situation that we studied and, although this is commonly used as a first approximation (e.g. Equation 6.15), in real glaciers  $\partial w/\partial z$  likely decreases with depth (Figure 5.9). Horizontal velocities decrease non-linearly with depth, as we found in Chapter 5. In this chapter, however, we were able to investigate the effect of longitudinal stresses on the velocity profile, and found that either longitudinal extension or longitudinal compression will increase  $\partial u/\partial z$ , leading to higher velocities.

# 11

## Numerical modeling

On several occasions when we've encountered problems that could not be solved readily by analytical methods, we have referred to results from numerical models. In Chapters 5 and 10 we found, in fact, that analytical solutions to problems of glacier flow could be obtained only when the problems were quite simple. The two numerical methods that are most commonly used in modeling are the finite-difference and finite-element methods. More recently, finite-volume methods have been developed, and people are experimenting with less physically-based techniques.

The analytical methods of calculus are based on taking the limit as intervals over which functions are evaluated are allowed to shrink toward zero. In finite-difference, finite-element, and finite volume models, in contrast, we let these intervals remain finite and assume that the functions describing the variation of parameters across them can be replaced by constants, by linear functions, or by low-order polynomials. The resulting equations turn out to be much simpler than the original differential equations, but because the domain of interest is now broken into many small intervals, one must do a large number of repetitive calculations to obtain a solution for the entire domain. Computers are thus required for all but the simplest numerical calculations. Moreover, the numerical solutions are not necessarily as accurate as analytical ones.

In this chapter, we first describe elementary numerical integration. This leads into some straightforward finite-difference calculations that can be carried out with the use of a spreadsheet or a short computer program. We'll then discuss more advanced techniques used in finite-difference models and in finite-element and finite-volume models. The numerical details of these models are beyond the scope of this book, but some can be implemented with the use of open-source software. Finally, we'll discuss some relatively new forays into non-deterministic or statistical models, and conclude with a few examples illustrating the use of models.

### Goals of modeling

“Solving” a mathematical problem analytically usually means finding values for one or more unknown quantities. This is true, also, of solutions using numerical

models. In typical problems with several unknowns, for example, numerical models are commonly used to explore the universe of physically-reasonable values of the unknowns, and to thus determine which combinations give satisfactory agreement with observations. An example is a study of a temperature profile measured in a borehole that penetrated the Greenland ice sheet at Dye 3, where the ice is 2037 m thick (Dahl-Jensen and Johnsen, 1986). The three unknowns, or free variables, were the Pleistocene accumulation rate, Pleistocene surface temperature, and geothermal heat flux. It was found that these could be constrained to lie, respectively, between 33 and 75% of the present accumulation rate,  $-30$  and  $-35^{\circ}\text{C}$  ( $12^{\circ}\text{C}$  below the present mean annual temperature), and  $31$  and  $45 \text{ mW m}^{-2}$ . If the model took all significant processes into consideration and did so accurately, these values are “solutions” for the three unknowns. More precise solutions are not possible because equally good matches to the observed temperature profile can be obtained with several combinations of these three parameters within the above limits.

Statistical models in which thousands of possible combinations of the unknown quantities are explored are also being tested. Combinations yielding unrealistic solutions or solutions that do not agree with observation are discarded, and the means of the values of the unknowns in the retained solutions are considered to be reasonable estimates of the actual values. These mean values provide a basis for extrapolation into the future.

The observations that one seeks to match need not necessarily be quantitative measurements. An exciting approach that is being used with increasing frequency and sophistication is the use of observations of the distribution of glacial landforms to constrain models of vanished ice sheets and, in turn, to support hypotheses regarding the origin of the landforms. Moraines obviously provide information on the extent of an ice sheet, and some glacial landforms, as we have discussed, appear to require a certain basal thermal regime. Combinations of model parameters that yield ice sheets of this size and with this basal temperature distribution are thus more likely to represent reality.

## Numerical integration

Consider a differential equation of the form:

$$\frac{d\varphi}{dx} = f(x)$$

with the solution:

$$\varphi = \int_0^X f(x) dx. \quad (11.1)$$

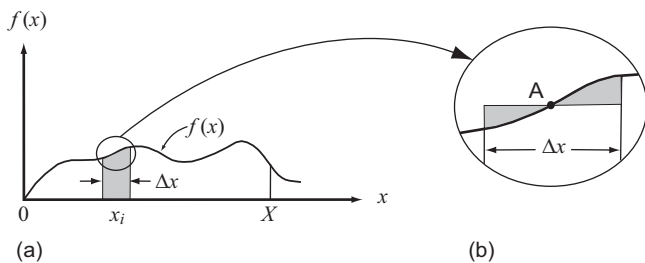


**Figure 11.1** (a) Illustration of a numerical integration to obtain the area under a curve. (b) Detail of the circled area in (a). See text for discussion.

If  $f(x)$  is the curve shown in Figure 11.1a, for example,  $\varphi$  is the area under the curve between 0 and  $X$ . If the function  $f(x)$  can be integrated analytically,  $\varphi$  is easily obtained. However, if  $f(x)$  cannot be integrated analytically we can still carry out the integration numerically. (Numerical integration is sometimes called *quadrature*.) To do this, first divide the interval  $0 \rightarrow X$  into  $n$  segments of equal length,  $\Delta x$ , and then evaluate the sum:

$$\varphi = \sum_{i=1}^n f(x_i) \Delta x. \quad (11.2)$$

This sum can be obtained by evaluating  $f(x)$  at the midpoint of every interval  $\Delta x$ , multiplying by  $\Delta x$ , and adding the results. The shaded area in Figure 11.1a would be one such product  $f(x)\Delta x$ . This procedure makes use of the fact that an integral is the limit as  $\Delta x \rightarrow 0$  of the summation in Equation (11.2).

A common alternative to this is to evaluate  $f(x)$  at the beginning and end of every interval,  $\Delta x$ , and then multiply  $\Delta x$  by the average of these two values. Because this approximates the shaded area as a trapezoid, it is called *trapezoidal integration*.

Neither solution for  $\varphi$  is exact. To see why this is the case, consider Figure 11.1b, which is an enlargement of the circled area in Figure 11.1a. The point labeled “A” is  $f(x)$  at the midpoint of the interval  $\Delta x$ . The product  $f(x)\Delta x$  overestimates the area under the curve in the interval  $\Delta x$  by the size of the shaded area to the left of A, and underestimates it by the size of the shaded area to the right of A. In this particular instance, the latter is larger, so the area under the curve is underestimated. The magnitude of the final error will depend upon the sum of these individual errors. The smaller the intervals  $\Delta x$ , the closer the numerical solution will be to the exact solution.

More sophisticated techniques for numerical integration are also available. For example, the shape of a curve between two points may be approximated by a polynomial (Irons and Shrive, 1987, pp. 64–67). This technique, sometimes called *Gaussian quadrature*, produces highly accurate results with fewer calculations, but the details are beyond the scope of this chapter.

## Finite-difference models

Finite-difference modeling is basically an extension of numerical integration. The defining characteristic of the finite-difference method is that gradients in a parameter are approximated by obtaining values of the parameter at grid points and dividing by the distance between the grid points.

A simple example is the calculation of a temperature profile in the ablation area of a glacier. The relevant equation is:

$$\frac{d\theta}{dz} = \beta_o e^{\zeta^2 z^2} \quad (11.3)$$

(Equation 6.29), in which  $\beta_o$  and  $\zeta$  are known, but which cannot be integrated analytically. We start out, as before, by dividing the profile into  $n$  parts of equal height  $\Delta z$ . Then, choosing as  $z$  the midpoint of the interval  $\Delta z$  immediately above the bed, we calculate  $\beta_o e^{\zeta^2 z^2}$ . Alternatively, we could use the values of  $z$  at the bed and at the top of the interval  $\Delta z$  and then average the two values. Either approach yields an approximation of the average temperature gradient,  $d\theta/dz$ , through the interval  $\Delta z$ . Multiplying this by  $\Delta z$  gives an estimate of how much the temperature changes over this interval. As  $\beta_o$  is negative, the gradient will be negative, so the temperature at the top of the interval  $\Delta z$  will be colder than that at the bed. Thus, subtracting this from an assumed temperature at the bed gives an estimate of the temperature at the top of the interval  $\Delta z$ . Analytically, the equations for the second approach are:

$$\frac{\theta_{i+1} - \theta_i}{\Delta z} = \beta_o \left( \frac{e^{\zeta^2 z_{i+1}^2} + e^{\zeta^2 z_i^2}}{2} \right)$$

so

$$\theta_{i+1} = \theta_i + \frac{\beta_o}{2} \left( e^{\zeta^2 z_{i+1}^2} + e^{\zeta^2 z_i^2} \right) \Delta z. \quad (11.4)$$

Note that  $z = 0$  is at the bed (Figure 6.4), so  $\beta_o$  is the basal boundary condition.

Equation (11.4) is easy to solve repetitively, but it still incorporates the assumption that  $w$  varies linearly with depth (Equation 6.15). Alternatively, we could avoid this assumption by starting with Equation (6.14):

$$0 = \kappa \frac{d^2\theta}{dz^2} - w \frac{d\theta}{dz}. \quad (11.5)$$

Equation (11.5) is one-dimensional inasmuch as  $\theta$  and  $w$  vary only with  $z$ . It can be written as:

$$\kappa \frac{d\beta}{dz} = w \frac{d\theta}{dz}. \quad (11.6)$$

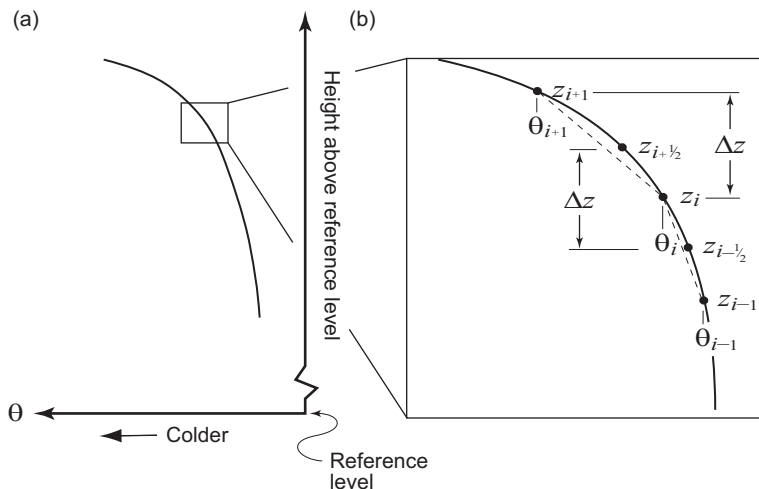


**Figure 11.2** (a) Part of a temperature profile in the ablation area of a glacier. (b) Detail of area in (a) showing definitions of subscripts used in Equations (11.7). Light dashed lines show approximations to temperature gradients at  $z_{i+1/2}$  and  $z_{i-1/2}$ .

Then, to calculate the change in  $\beta$  over  $\Delta z$ , we need  $\beta$  at both the bottom and the top of the interval. Thus, if we take the interval extending from  $z_{i-1/2}$  to  $z_{i+1/2}$  (Figure 11.2),  $\beta_{i-1/2}$  is  $(\theta_i - \theta_{i-1})/\Delta z$  and  $\beta_{i+1/2}$  is  $(\theta_{i+1} - \theta_i)/\Delta z$ . Because we need both  $\theta_{i-1}$  and  $\theta_{i+1}$  to calculate  $d\beta/dz$ , we need to calculate  $d\theta/dz$  over  $2\Delta z$ . Thus, in finite difference form, Equation (11.6) becomes:

$$\kappa \left[ \frac{1}{\Delta z} \left( \frac{\theta_{i+1} - \theta_i}{\Delta z} - \frac{\theta_i - \theta_{i-1}}{\Delta z} \right) \right] = w_i \left[ \frac{1}{2\Delta z} (\theta_{i+1} - \theta_{i-1}) \right]$$

or solving for  $\theta_i$ :

$$\theta_i = \frac{1}{2} (\theta_{i+1} + \theta_{i-1}) - w_i \frac{\Delta z}{4\kappa} (\theta_{i+1} - \theta_{i-1}). \quad (11.7)$$

With Equation (11.7) one can use non-linear variations in  $w$  with depth such as Equations (5.24) or (5.25). However, when  $\theta_i$  is being calculated,  $\theta_{i+1}$  is not known so one must set up a system of simultaneous equations in order to solve the problem.

A rather similar problem is to calculate changes in a temperature profile through time as the climate, and hence the surface temperature changes. To simplify the problem, let's just consider seasonal changes so we can restrict the domain to the upper 20 m or 30 m of the glacier, and thus neglect advection and strain heating. The appropriate differential equation is then:

$$\kappa \frac{\partial^2 \theta}{\partial z^2} = \frac{\partial \theta}{\partial t} \quad (11.8)$$

(Equation 6.30). This is now a two-dimensional problem in which  $\theta$  varies with both depth and time. Proceeding as above, Equation (11.8) can be rewritten in finite-difference form as:

$$\kappa \left[ \frac{1}{\Delta z} \left( \frac{\theta_{i+1} - \theta_i}{\Delta z} - \frac{\theta_i - \theta_{i-1}}{\Delta z} \right) \right] \Delta t = \Delta \theta. \quad (11.9)$$

To continue, we need a profile to serve as an initial condition at time  $t = t_0$ . From this profile we can get  $\theta_{i-1}$ ,  $\theta_i$ , and  $\theta_{i+1}$  and then solve Equation (11.9) for  $\Delta \theta$ . This is the amount that the ice between  $z_{i-1/2}$  and  $z_{i+1/2}$  warmed or cooled during the time interval  $\Delta t$ . Once we have done this calculation for every depth interval,  $\Delta z$ , we will have the temperature profile at time  $t_0 + \Delta t$ , and a new calculation for the next time step can be initiated.

To clarify the physics involved, consider the profile in the inset of Figure 11.2 to be part of the temperature profile of interest. This profile may have been measured, calculated during an earlier time step, or assumed. The temperature gradient,  $\Delta \theta / \Delta z$ , at  $z_{i+1/2}$  is larger than that at  $z_{i-1/2}$ , so more heat will be conducted out through the top of the volume of height  $\Delta z$  than is conducted in through the bottom. Thus the ice will become cooler during the time step. [With the coordinates shown in Figure 11.2, both  $\beta_{i-1/2}$  and  $\beta_{i+1/2}$  are negative, so as  $\beta_{i+1/2}$  is larger,  $\Delta \theta$  is negative.]

To model seasonal variations in the temperature profile, the boundary condition at the surface must be changed appropriately at the beginning of each time step. For example, if the initial profile was measured on January 1 and we choose a time step of 0.02 year (or 7.3 days), the boundary condition at the surface for the next iteration should be the temperature (measured or estimated) 7.3 days later. If the temperature variation at the surface is sinusoidal, the solution should closely approximate that given by Equation (6.31) after a number of iterations. However, the present solution has added versatility, inasmuch as accumulation or ablation can be simulated by adding or subtracting increments of thickness,  $\Delta z$ , at appropriate time steps.

Care must be taken in selecting  $\Delta t$  and  $\Delta z$  in such problems. The finite-difference solution is said to converge (or be stable) if it approaches the exact solution as  $\Delta t$  and  $\Delta z \rightarrow 0$ . Our solution will converge if:

$$0 < \frac{\kappa \Delta t}{\Delta z^2} < \frac{1}{2} \quad (11.10)$$

(Carnahan *et al.*, 1969, p. 432; Irons and Shrive, 1987, p. 95). Thus, if  $\Delta z = 1$  m and  $\kappa = 37.5 \text{ m}^2 \text{ a}^{-1}$ ,  $\Delta t$  would have to be less than about 1/75 of a year, or  $\sim 5$  days. If the integration had to span centuries or millennia and  $\Delta z$  could not be increased, a very long calculation would be necessary. When solutions do not converge, they are commonly wildly unrealistic.

Finite-difference techniques can also be used to integrate the momentum equation, but simplified versions of the momentum equation can be integrated analytically (Equations 5.6 and 10.43 are examples), and versions including longitudinal stresses and varying ice thickness require more advanced techniques, outlined below. Thus, we have focused on the energy balance equation in these examples.

Because analytical solutions are not available for a large number of differential equations of importance in science and engineering, considerable effort has gone into refining the techniques we have just outlined, and study of these techniques is now a major subfield of applied mathematics. As might be anticipated, the primary goals of this effort have been to improve the stability and accuracy of the solutions without necessitating ever finer grid spacing. A few common approaches are outlined next.

### Implicit methods

Equations like Equation (11.9), which use  $\theta_{i-1}$ ,  $\theta_i$ , and  $\theta_{i+1}$  from a temperature profile at time  $t_1$  to calculate the profile at time  $t_2$  are known as *explicit* forms of the finite-difference equation. One could also write Equation (11.9) with  $\theta_{i-1}$ ,  $\theta_i$ , and  $\theta_{i+1}$  defined as being the temperatures at time  $t_2$  which are, as yet, unknown. This is known as an *implicit* form. In this approach, equations must be written for all  $n$  points in the profile, and the equations then solved simultaneously for all the  $\Delta\theta_i$ . The temperatures at time  $t_2$  are then obtained by adding these  $\Delta\theta_i$  to the temperatures at the respective grid points at time  $t_1$ . This approach has the advantage of being unconditionally stable so larger time steps can be used. Solution of the equations is actually not as daunting as it may seem, as most contain only three unknowns, and those at the top and bottom, where the boundary conditions are applied, contain only two. The resulting equation matrix is a tridiagonal matrix with non-zero cells only on the diagonal and on the sub- and superdiagonals immediately adjacent to the diagonal. Efficient routines for solving such matrices are readily available.

A variation on this is the *Crank-Nicolson* method. In this approach, the gradients used in Equation (11.9) are the averages of the gradients at times  $t_1$  and  $t_2$ . Because gradients at time  $t_2$  are used, this is still an implicit method and requires solution of a system of equations. However, the equations are only slightly more complicated than those using just the gradients at time  $t_2$ , and the increase in accuracy is substantial (Carnahan *et al.*, 1969, p. 451).

### Alternating direction schemes

One way to avoid stability problems in explicit methods is to use alternating direction schemes. In such schemes, using the problem of Equation (11.8) as an example, one first calculates  $\Delta\theta$  starting at the surface and progressing downward,

and then calculates  $\Delta\theta$  for the next time step, starting at the lower boundary and progressing upward. In the downward direction,  $\beta_{i-\frac{1}{2}}$  for time  $t_2$  is calculated from the temperatures from time  $t_1$ , and  $\beta_{i+\frac{1}{2}}$  is calculated from temperatures at time  $t_2$ , thus:

$$\kappa \left[ \frac{1}{\Delta z} \left( \frac{\theta_{i+1,t_2} - \theta_{i,t_2}}{\Delta z} - \frac{\theta_{i,t_1} - \theta_{i-1,t_1}}{\Delta z} \right) \right] \Delta t = \theta_{i,t_2} - \theta_{i,t_1} \quad (11.11a)$$

where the second subscript is the time step. This may be compared with Equation (11.9). Here,  $\theta_{i+1,t_2}$  is known from the calculation at the previous depth, so this equation may be solved directly for  $\theta_{i,t_2}$ , yielding:

$$\theta_{i,t_2} = \frac{1}{1 + \kappa \Delta t / \Delta z^2} [\kappa \Delta t / \Delta z^2 (\theta_{i+1,t_2} - \theta_{i,t_1} + \theta_{i-1,t_1}) + \theta_{i,t_1}].$$

In the upward direction, calculating temperatures for time step  $t_3$ , the appropriate equation is:

$$\kappa \left[ \frac{1}{\Delta z} \left( \frac{\theta_{i+1,t_2} - \theta_{i,t_2}}{\Delta z} - \frac{\theta_{i,t_3} - \theta_{i-1,t_3}}{\Delta z} \right) \right] \Delta t = \theta_{i,t_3} - \theta_{i,t_2}. \quad (11.11b)$$

Now  $\theta_{i,t_2}$  and  $\theta_{i+1,t_2}$  are known from time step  $t_2$ , and  $\theta_{i-1,t_3}$  is known from the calculation at depth  $i-1$ . This scheme, known as the Saul-yev alternating direction procedure (Carnahan *et al.*, 1969, p. 451), is explicit because calculations at any depth and time can be made using a single equation. It is also unconditionally stable.

I used the Saul-yev procedure to model temperature profiles in Barnes Ice Cap (Hooke *et al.*, 1980). The study was motivated by temperature measurements in boreholes that suggested a recent warming at the surface and a systematic down-glacier increase in the temperature gradient at the bed. To model these profiles, I simplified Equation (6.13) to two dimensions, thus:

$$\frac{\partial \theta}{\partial t} = \kappa \frac{\partial^2 \theta}{\partial z^2} - u \frac{\partial \theta}{\partial x} - w \frac{\partial \theta}{\partial z} + \frac{Q}{\rho C}, \quad (11.12)$$

and then expressed it in finite difference form. The modeling suggested that temperatures at the glacier surface, after a cooling in the early 1940s, had increased 0.1–0.5°C over the past few decades. The increase in gradient at the bed appeared to be a consequence of a warming of ~2°C about 250 years ago, near the end of the Little Ice Age. Use of an unconditionally stable finite difference scheme greatly reduced the computer time needed for the calculations.

Other explicit unconditionally stable procedures, some of which also utilize alternating direction schemes, are available, as are implicit alternating direction methods (Carnahan *et al.*, 1969, pp. 541–543). Some of these are readily extended to two and three dimensions.

## Non-dimensionalization

In writing computer code for finite-difference schemes, it should be evident from Equations (11.4) to (11.11) that the code will be much simpler if the units of *spatial discretization* (subdividing the domain into many small discrete units) are of equal size. Thus,  $\Delta z$  should not change with depth. If the problem at hand involves a substantial part of an ice sheet, say along a flowline that is broken into columns of width  $\Delta x$ , each of which is then subdivided into depth increments,  $\Delta z$  (Figure 11.3), it is clearly impossible to keep both the number of depth increments and their size,  $\Delta z$ , constant from one column to the next. To avoid problems of this type, modelers commonly normalize the depth by dividing by the thickness. Thus a point at a depth,  $z$ , of 600 m in an ice sheet that is  $H = 1000$  m thick, will be at a normalized depth,  $z^*$ , of 0.6. The columns then all have a non-dimensional thickness,  $H^*$ , of 1.0, and if they are each subdivided into 20 equal depth increments, all increments will have a non-dimensional thickness of  $H^*/20$ . Non-dimensionalization or *scaling* of lengths in this way generally requires scaling of the other parameters in the equations.

Such scaling greatly simplifies the mathematics in many situations. However, results from such computations have to be restated in dimensional form before most of us can derive useful physical insights from them.

## Shallow ice approximation and higher order models

Early numerical models of ice sheets use what is known as the *shallow ice approximation*. While the shallow ice approximation was first introduced in glaciology by Fowler and Larson (1980) and in slightly different form by Hutter (1981), our discussion is based on Hutter (1983, p. 256ff). This approximation makes use of the fact that the horizontal extent of an ice sheet is large compared with its thickness. Longitudinal derivatives of stress, velocity, and temperature are thus small compared with vertical derivatives.

If the wavelengths of major undulations in the surface and bed topography are relatively long, so the surface and bed elevations are slowly varying functions of  $x$ , the longitudinal coordinate can be scaled using the relation  $\xi = \mu x$ , where  $\mu$  is small. One logical possibility is to take  $\mu$  as the ratio of the mean thickness to the horizontal extent of the ice sheet. The vertical coordinate is not changed. With this

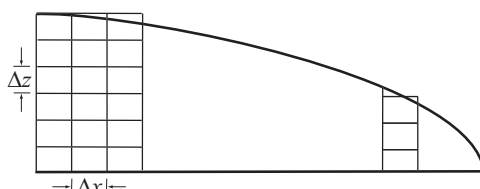


**Figure 11.3** Illustration of problems encountered with a finite-difference discretization of an ice sheet along a flowline.

scaling,  $\mu$  is introduced into the momentum and energy balance equations and into the continuity equation, and into the boundary conditions, resulting in terms like  $\mu \frac{\partial \sigma_{xx}}{\partial \xi}$ ,  $\mu \frac{\partial \theta}{\partial \xi}$ , and  $\mu^2 \frac{\partial^2 \theta}{\partial \xi^2}$ . If all terms involving  $\mu$  are then neglected and the resulting equations are solved, the solution is referred to as the zeroth-order solution. In this solution, the stress and velocity fields are calculated as if the ice sheet were a slab of uniform thickness, and the basal shear stress turns out to be  $\rho g h \alpha$ . Longitudinal stress gradients are, therefore, not included. This is the shallow ice approximation.

If terms involving  $\mu$  are included in the solution, the result is called a first-order solution. Longitudinal stress gradients are included in this solution, and a flow law that includes a linear term at low stresses is necessary to avoid a singularity in these stresses at the surface. This is the solution used in most existing finite-difference models of ice sheets. As might be expected from the above, a solution including terms in  $\mu^2$  is called a second-order solution. In modeling ice shelves, longitudinal stress effects first appear in second order solutions. Solutions including  $\mu$  or higher powers of  $\mu$  are called *higher-order solutions*.

### Full Stokes models

The continuity, momentum-balance, and energy-balance equations were derived independently by an Englishman, George Stokes, and a Frenchman, Claude-Louis Navier, in 1822, and are called the Navier-Stokes equations. The full momentum-equations include inertial forces (the force you feel when sprayed by a garden hose) and compressibility, and are thus quite complicated. However, in problems of glacier flow inertial forces and compressibility can be neglected, and the Navier-Stokes equations reduce to our Equations (2.5), (6.11), and (9.15). Numerical solutions that satisfy all of these equations simultaneously in either two or three dimensions are called full-Stokes solutions (Pattyn *et al.*, 2008).

### Finite-element models

The finite element method is another way of obtaining an approximate solution to the governing equations. In finite-element as in finite-difference models, the domain of interest is broken up into a large number of small elements. In early applications of finite-element models to glaciological problems the elements were quadrilaterals, but commercial packages now in use commonly have higher-order element geometries. The corners of elements are called nodes. Unlike finite-difference models, in a finite-element model there is no advantage in making all of the elements rectangular and the same size.

As before, parameters are assumed to be constant over the elements or to vary in some simple way. In finite-element calculations, however, use is made of the fact that the relevant differential equations can be expressed in a form consisting of a

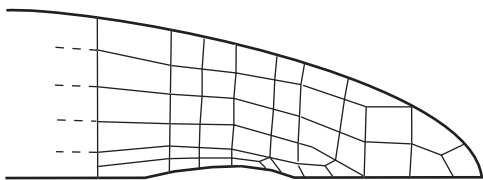


**Figure 11.4** A possible finite-element discretization of a tapered glacier margin, showing the flexibility of the finite-element method to accommodate such geometries.

sum of integrals. A solution method, called the method of weighted residuals, then guarantees that the resulting approximate solution will be the best possible solution mathematically obtainable with a given element configuration.

While initially more complicated to understand, finite-element formulations have been shown to be generally numerically more stable than finite-difference formulations (Strang and Fix, 1973). Furthermore, element shapes can be adjusted to conform to boundaries that would be awkward to model with rectangular elements (Figure 11.4). Finally, element size can be reduced in areas of low gradients and increased in areas of high gradients, as near the bed (Figure 11.4), thus increasing accuracy without increasing computation time. Complex, non-uniform, and variable boundary conditions are also easier to include in finite-element models.

Once a domain is discretized, stress or velocity conditions are specified at boundary nodes and equations are written relating stresses and velocities at interior nodes to each other, to the mean stress in the element, and to the stresses or velocities at the boundaries. As usual, the basic equations being solved are those for conservation of momentum, mass, and energy (Equations 9.15, 2.5, and 6.11, respectively). Glen's flow law is normally used. For the simplest models used in two-dimensional plain strain calculations, this procedure yields approximately  $2N + M$  equations, where  $N$  is the number of nodes and  $M$  is the number of elements. Typical problems today may involve thousands of elements and nodes. Although the number of equations to be solved simultaneously is large, the number of unknowns in each equation is small, so efficient routines for solving sparse matrices can be used. Owing to the non-linearity of the flow law, the set of equations is non-linear and an iterative solution is necessary. A trial solution is given initially, and this is corrected to obtain an improved solution at each iteration.

The two most common types of finite-element model are two-dimensional flow-band models and map-plane models. In flow-band models, the model domain extends along a flowline, which may be curvilinear, and is bounded at the top by the glacier surface and at the base by the bed or, in the case of some models that include temperature calculations, by a surface at some depth in the substrate. The domain is considered to be of unit thickness perpendicular to the flowline. Some models permit one to specify a transverse strain rate, and thus become quasi-three dimensional. A few are fully three dimensional (Hanson, 1995).

In map-plane models (Fastook and Chapman, 1989), the domain is bounded by the surface and the bed and by lateral boundaries which may be flowlines, a glacier margin, a divide, or an arbitrary transverse boundary in the glacier across which a mass flux is specified. Unlike flow-band models, map-plane models do not require prior knowledge of the direction of flow. Although many map-plane models are called three-dimensional, they are actually quasi-three dimensional inasmuch as the basic elements are columns extending through the ice mass, and parameters such as velocity are averaged over the column. The models are thus said to be *vertically integrated*. In such models, some terms of the stress tensor are replaced by assumptions in the core of the model, and variations with depth are then obtained later by, for example, using equations like Equations (5.16) and (5.18) to calculate  $u(z)$  from  $\bar{u}$ .

## Finite-volume models

The finite volume method (e.g. Peiró and Sherwin, 2005) is a method for obtaining a full-Stokes solution without resorting to higher-order approximations. In finite-volume models, the model space (glacier) is divided into a large number of small *control volumes*. As in finite-element models, the size and shape of the control volumes can be varied, allowing considerable flexibility in adapting to domains of irregular shape. Although these are called “volumes,” the method can be applied to two as well as three dimensional problems. The volumes are contiguous, so a flux of mass or energy across a particular face of one volume equals the flux into the adjacent volume across the corresponding face. Thus, mass and energy are conserved. Using the standard conservation of momentum and energy equations, one can write integral equations for the fluxes over each control volume. These integrals are then converted into integrals of the fluxes over the respective faces of the control volumes. Finally, this system of equations is solved for the fluxes at the centroids of each control volume. Approximations are involved in evaluating the integrals, so the solution is not exact.

Finite-volume and finite-element methods both use *integrals* over the boxes defined by the grid. The key difference between them is that the former focuses on fluxes at the centroids of the control volumes, while the latter focuses on velocities and stresses at the nodes defining the element. Finite difference methods, on the other hand, use *differences* between the grid points that define the elements.

## Coupling thermal and mechanical models

Because the viscosity parameter,  $A$ , is dependent on temperature and, conversely, the temperature distribution depends on the flow field through the advective terms in the energy balance equation, a complete model of a polar glacier or ice sheet must

include calculations of both the flow field and the temperature distribution. It is not practical to combine these two calculations, so they must be done iteratively. First a flow field is determined, given an assumed or previously calculated temperature field. Then the temperature distribution is modeled and used as input to the next flow calculation. Time stands still during this iterative procedure. Once convergence is achieved, so the difference between successive solutions from one iteration to the next is within certain prescribed limits, the surface profile can be updated by multiplying the calculated surface velocities and prescribed mass balance rate by the time step. An updated temperature boundary condition at the surface can then be specified, and a new calculation started.

When energy balance and momentum balance models are coupled in this way, the result is commonly called a *thermomechanical model*.

## Initial conditions and forcing

In our earlier discussions of boundary value problems, the boundary values we specified were vertical velocities at the surface (Chapter 5), temperatures and temperature gradients (Chapter 6), or stresses and velocities (Chapter 10). In all of these examples, the solutions we sought were steady-state solutions, so all time derivatives were 0.

In many modeling studies, time dependent solutions are desired. Indeed, one of the strengths of numerical modeling is that we can study the evolution of a complex system through time – a goal that is only rarely achievable with analytical solutions (Equation 6.31 is such an exception). In time-dependent models it is necessary to specify conditions at time  $t = 0$ , called *initial conditions*, and also, in most cases, the temporal evolution of some of these conditions, usually those at the glacier surface. The latter is frequently referred to as the *forcing*. We have already encountered an example of an initial condition earlier in this chapter, in discussing the solution to Equation (11.8).

The choice of initial conditions depends on the extent of our knowledge of those conditions. If there is no well-defined condition from which to start the integration, it can be started with an unrealistic situation such as a temperature profile that varies linearly with depth or an ice sheet with a parabolic profile. This approach is particularly appropriate in problems involving cyclical changes, such as seasonal changes in temperature at the surface or changes in climate driven by variations in Earth's orbit – the Milankovitch cycles. The model would then be run through several cycles until the solution at a given point in a cycle is essentially identical to that at the same point in the previous cycle. One can then conclude that the model has “forgotten” the unrealistic initial conditions. This procedure is commonly referred to as a *spin up* of the model. The final solution can then be saved for use as an initial condition in a subsequent run.

Alternatively, one can start with a known condition at some time in the past. For example, a model of cycles of ice sheet growth and decay could use a condition of no ice sheet as an initial condition, or a two-dimensional flowline model could use a glacier surface profile measured 20 or 30 years ago. In the latter case, the model could be validated by comparing the final profile with one measured recently. The model might then be run into the future to predict the effects of various climate-change scenarios.

As just noted, forcing a time-dependent model usually involves varying the boundary conditions at the surface in some prescribed way. Boundary conditions at the bed or along an upstream or downstream boundary might also be varied, but more frequently these will be calculated within the model as part of the solution. Relevant conditions at the surface are usually precipitation and temperature. These may be estimated from empirical relations, such as a relation between mean annual temperature and the Milankovitch cycles, or may be calculated in another model, such as a global climate model (GCM). If the output from an ice-sheet model is used as input for a time step in a GCM, the output of which is then used for the next time step in the ice-sheet model, the models are said to be *coupled*.

## Validation

Once a model has been programmed and appears to be giving reasonable results, it must be *validated* to ensure that there are no subtle errors that affect the results significantly, but not so much as to make them obviously unrealistic. A common way to initiate the validation process is to set parameters in the model in such a way that the model duplicates a situation for which there is an analytical solution. For example, if  $\partial\theta/\partial t$ ,  $u$ , and  $Q$  are set to zero in Equation (11.12) and  $w$  is assumed to be downward and to decrease linearly with depth, the model should reproduce the Robin (1955) solution (Equation 6.24). In flow models, the deformation of an infinite slab of ice on a uniform slope (Equation 10.43) is a good choice. Of course, once these comparisons have been made, there is still the question of whether coding of some of the terms neglected in the validation test, such as  $u(\partial\theta/\partial x)$  in Equation (11.12) is correct. The modeler will have to be more imaginative to find independent ways to test these algorithms. One possibility is to compare the output with that of similar models developed totally independently, as discussed next.

## Sensitivity testing and tuning

Because the parameters used to define the boundary conditions, initial conditions, and forcing are rarely known precisely, modelers normally test the sensitivity of their models by varying these parameters within reasonable limits. Suppose, for

example, that the most likely temperature boundary condition for a particular model is  $-5^{\circ}\text{C}$ , and suppose further that it is unlikely that the correct boundary temperature is lower than  $-7^{\circ}\text{C}$  or higher than  $-1^{\circ}\text{C}$ . The modeler then might run the model with all three temperatures to see if the conclusions changed when the extreme temperatures are used. If the conclusions are unchanged, the model is said to be *robust* against a reasonable range of temperature boundary conditions. Such tests are called *sensitivity tests*.

If there are  $N$  parameters that are only known approximately and if the maximum likely, minimum likely, and most probable values of all combinations of the parameters are to be tested, the total number of tests will be  $3^N$ . If  $N > 3$ , such a task becomes daunting.

In a similar vein, models are often *tuned* so that they reproduce observed characteristics of a glacier. For example, in the model of the Barnes Ice Cap temperature profiles discussed above (Equation 11.12), the surface temperature,  $\theta_s$ , under which the profiles were presumed to have developed prior to the most recent warming, and the longitudinal gradient,  $\partial\theta/\partial x$  were only loosely constrained by field measurements. Thus, the model was tuned by adjusting these parameters until the model profiles matched the lower parts of the measured profiles well. Then step increases of various sizes in  $\theta_s$  were tested until the upper parts of the profiles were modeled reasonably well. Tuning can be viewed either as: (1) a way of solving for unknowns that cannot be evaluated analytically, as mentioned earlier (p. 291–292), or (2) a necessary step if the model is going to be used to explore the consequences of future changes.

## Intercomparison of models

Because of the large number of ice sheet models being developed, each employing slightly different approaches and each subject to inadvertent programming errors, a group of modelers has developed a set of benchmark experiments for comparison of models. All of the models solve the momentum and energy balance equations and the continuity equation.

In the first such study (Huybrechts and Payne, 1996), one experiment utilized a square domain, 1500 km on a side, with grid points at 50 km spacing. Initially there was no ice sheet in the domain. A radially-symmetric mass balance pattern was specified, as were the flow law constants  $n$  and  $A$ , and other relevant parameters such as  $\rho$ ,  $g$ , and  $\kappa$ . Because the specified mass balance pattern was radially symmetric and constant with time, the models, when stepped through time, eventually produced a steady-state circular ice sheet.

An intercomparison of eleven finite difference models done using this test found that most of the differences among them were inconsequential. The only

significant difference was between models using a mass flux parameterization that conserves mass but required short time steps to achieve stability and models that did not conserve mass, but had the advantage of allowing longer time steps. For example, in 3-dimensional models the means and standard deviations of the thicknesses of the model ice sheets at the divide were  $2997 \pm 7.4$  m and  $2959 \pm 1.3$  m for these two types of model, respectively (Huybrechts and Payne, 1996, Table 5). An exact solution, obtained by integrating the mass balance function analytically, produced an ice sheet that was 20 km smaller in radius, and consequently somewhat thinner (2952 m), but with a 50 km grid spacing models could not come any closer to this analytical solution.

A second study (Payne *et al.*, 2000) compared results from ten thermomechanical models. The ice sheet modeled was again circular, and all models predicted a central zone in which the ice sheet was frozen to the bed surrounded by an outer zone in which the base was at the pressure melting point. This time, however, results of the comparison were somewhat less consistent, inasmuch as the area of the inner cold zone varied among the models from 13% to 42% of the total area. Furthermore, when the surface temperature at the center of the ice sheet was  $-50^{\circ}\text{C}$ , an instability appeared in all but one of the models. This instability is believed to be related to the positive feedback from velocity to frictional heat generation and thence to temperature. The models were otherwise consistent in their predictions of the area and volume of the ice sheet, and the thickness and basal temperature at the divide.

In a third intercomparison, Pattyn *et al.* (2008) compared 28 models, 11 of which were finite difference, 9 finite element, 1 finite volume, 1 analytical, and 7 that used other approaches. Fourteen of the models were higher order, and 13 were full-Stokes. A principal objective of the study was to compare models that included longitudinal stress gradients. Agreement among the models was good in all cases, but was especially good among the models employing the full-Stokes solutions and between those models and an analytical solution. The ability of these models to simulate ice flow in regions of appreciable longitudinal stress gradient represents an important advance. Still needed, however, are better techniques for handling abrupt changes in basal sliding speed.

The tests developed by these modelers are an invaluable tool. Both new models and existing ones that are being refined can be tested against these benchmark experiments to expose errors in reasoning or programming.

## Non-deterministic models

Heretofore, we've focused on models based on solutions to exact differential equations describing physical processes that are understood reasonably well. A major

drawback of these modeling efforts is that fundamental physical processes at the boundaries are often not understood well enough and may be unknowable. This is a problem that more powerful numerical methods can't solve. Thus, without more experimental and observational data, further refinement of present numerical modeling approaches may not be productive.

In the past two decades, glaciologists have begun experimenting with models based on semi-empirical or statistical techniques. While these techniques may eventually lead to a better understanding of boundary conditions, so far they have been applied primarily to other glaciological problems.

### Semi-empirical models

Semi-empirical models use empirical data to constrain some parameters of a statistical model. Models relating glacier surface area to volume are an example. Chen and Ohmura (1990) used this approach to study changes in volume of Alpine glaciers over the century prior to the 1970s, and Bahr *et al.* (1997) and Bahr *et al.* (2009) used it to estimate volumes of alpine glaciers and their potential contribution to sea level. We'll explore Bahr's model further later.

### Monte Carlo models

The central idea behind the Monte Carlo method is to use randomness to solve a deterministic problem. The method is useful when several key variables vary independently and deterministic approaches are highly non-linear. One establishes the distribution of probable values of each variable and then solves the problem, deterministically, a large number of times, each time choosing, at random, a different value for each variable from these probability distributions. Unrealistic solutions are discarded and mean values of the variables used in the remaining ones are considered to be likely solutions.

Monte Carlo methods have been used in glaciology to explore uncertainty in basal sliding speed and shear traction based on a known surface velocity field (Chandler *et al.*, 2006), in surface mass balance modeling (Machguth *et al.*, 2008), and to predict the course of the ongoing rapid retreat of Columbia Glacier, a tidewater glacier in Alaska (Colgan *et al.*, 2012). The latter is discussed below.

## Examples

Let us now examine a few modeling projects that have been undertaken. The examples chosen utilize different types of models with differing objectives. They are intended to be illustrative only, and by no means an overview of the literature.

## Role of permafrost in ice sheet dynamics and landform evolution

For decades, glacial geologists have speculated on the effects that bed conditions have on ice sheet profiles and ice dynamics (e.g. Matthews, 1974; Fisher *et al.*, 1985) and on the relation between basal thermal conditions and glacial landforms (e.g. Moran *et al.*, 1980; Attig *et al.*, 1989; Mooers, 1990). Models of increasing sophistication have been used to study these effects. Here we discuss a time-dependent modeling effort by Cutler *et al.* (2000), using a flow-band finite-element model.

The modeled domain was a ~1700 km flow band extending from James Bay in Canada across the eastern end of Lake Superior and down the axis of the Green Bay lobe in Wisconsin to a Late Glacial Maximum terminal moraine and beyond. This flow band was chosen because ice-wedge casts and similar features demonstrate that permafrost was present along the margin in Wisconsin, and the modeling team wanted to estimate the thickness and upglacier extent of the submarginal permafrost zone. Their ultimate goal was to investigate the role that permafrost may have played in the development of certain landforms.

The model domain was broken into ~100 columns with 50 nodes in the ice and 75 nodes in the substrate – a total of nearly 9000 nodes when the ice sheet extended to the terminal moraine. The particular model run discussed here began at 55 ka, with ice already covering the first 275 km of the flowline, and ran to 21 ka, the Late Glacial Maximum. Time steps were 25 years. The model was forced with a mass balance pattern that depended on mean annual temperature and precipitation, and on the daily temperature range. Including the temperature range was essential in order to ensure some melting when the mean daily temperature was still a few degrees below freezing. Temperature and precipitation were specified at the margin and were assumed to decrease in specified ways with increasing elevation and latitude along the ice sheet surface. The variation in margin temperature with time was based on well-dated paleoclimate studies (Figure 11.5a). Included in the model was a routine for keeping track of the amount of meltwater produced by subglacial melt and lost by flow through subglacial aquifers. The viscous energy dissipated by this groundwater flow was added to the geothermal flux.

Results of the model run are shown in Figure 11.5b–e. Figure 11.5b shows profiles of the ice sheet at eight times between 48 and 21 ka, and Figure 11.5c shows the length of the flow line as a function of time and of changes in substrate with distance from the divide. The abrupt decrease in thickness of the ice sheet at distances greater than about 900 km from the divide (Figure 11.5b) is a consequence of the transition in the bed from crystalline rocks to a deformable substrate at 30 ka (Figure 11.5c). Basal sliding was allowed only over the latter and only when the bed was at the pressure melting point. With sliding, the balance velocity (Equation 5.1) is reached with thinner ice and a lower driving stress ( $\rho gh\alpha$ ). Note the progressive isostatic depression of the bed as the ice advances (Figure 11.5b) and the acceleration of the advance over the soft deformable bed (Figure 11.5c). Figures 11.5d and e

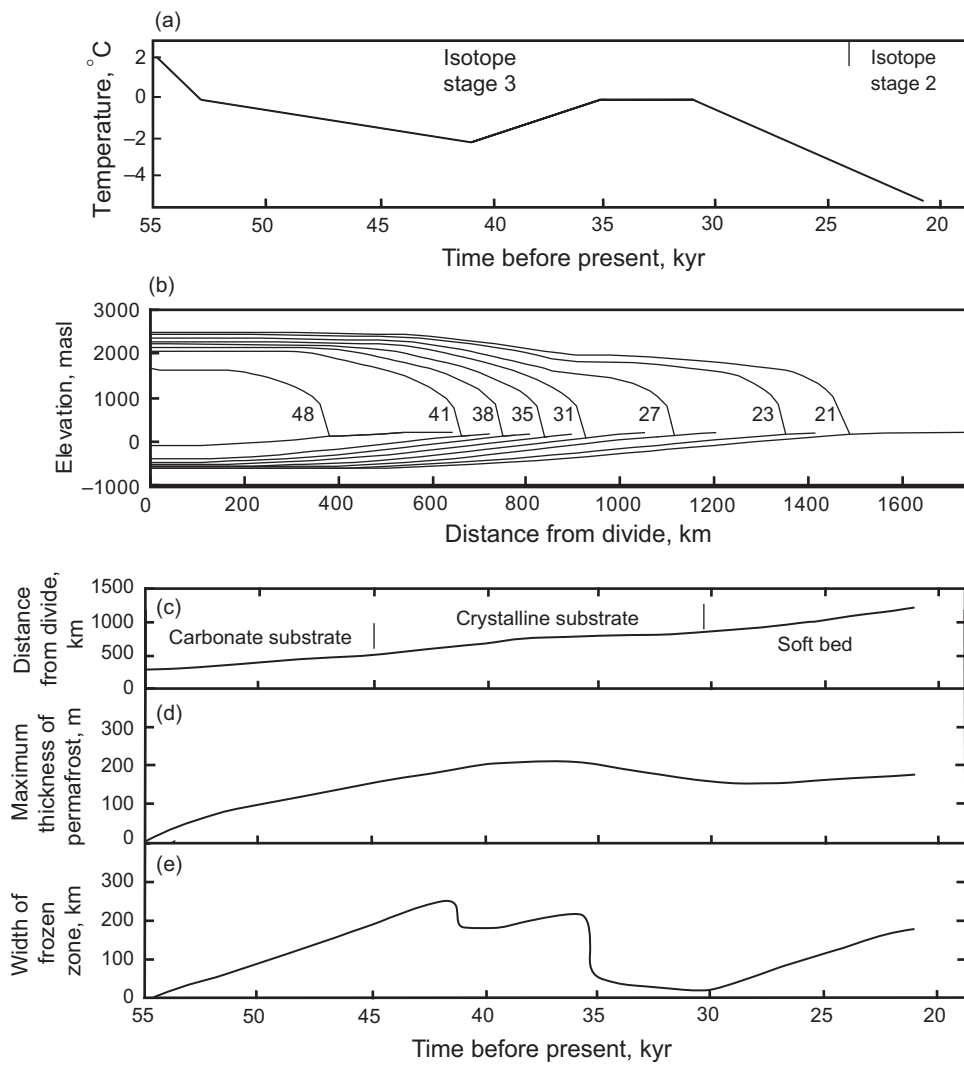


**Figure 11.5** Model of a flowline down the axis of the Green Bay-lobe of the Laurentide Ice Sheet.

(a) Temperature specified at the margin from 55 to 20 ka. (b) Profiles of the ice sheet at eight times between 48 and 21 ka (numbers to left of curves). (c) Location of margin as a function of time. (d) Maximum thickness of permafrost. (e) Width of submarginal frozen zone measured upglacier from margin along the flowline. (Redrawn from Cutler *et al.*, 2000, Figures 3, 9, and 11. Used with permission of the authors and the International Glaciological Society)

show the maximum thickness of the permafrost and the width (measured along the flowline) of the submarginal frozen zone (see Figure 6.19). The increase in maximum thickness between 55 and 40 ka is a response to the cooling climate (Figure 11.5a). The subsequent decrease from about 35 to 30 ka (Figure 11.6d) is a delayed reaction to the climatic amelioration that began at 40 ka. The permafrost is thickest when the glacier margin first reaches a given place on the landscape. As the

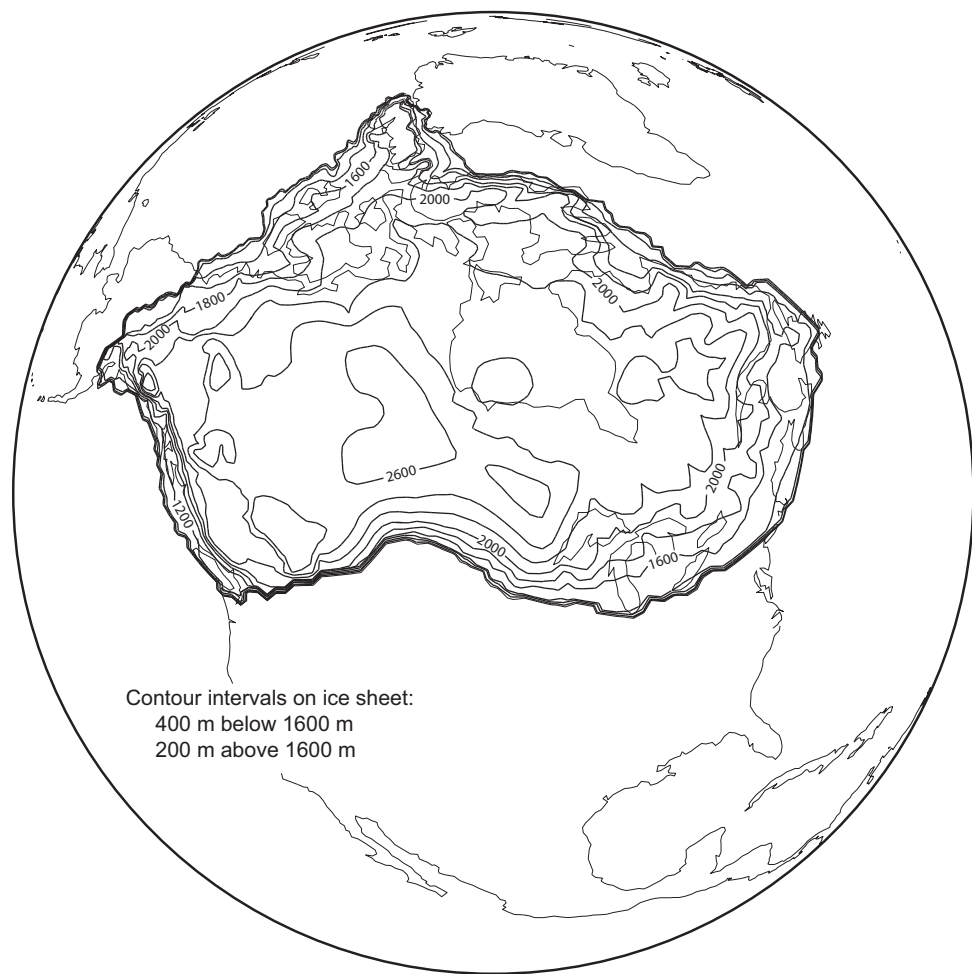


**Figure 11.6** Surface topography of the Laurentide ice sheet at 20 ka calculated with a thermomechanical model that included a basal sliding routine. (Modified from Marshall *et al.*, 2000, Figure 9b. Used with permission of the authors and the International Glaciological Society)

ice cover thickens and insulates the site from the climate, the permafrost thins and its upglacier edge thaws. Thus, the width of the permafrost zone reflects the combined effects of an increase in width as the ice sheet advances over permafrost and a decrease in width as the upglacier edge thaws. Changes in width thus result from both changes in rate of advance and changes in climate: the decrease in rate of advance at ~41 ka (Figure 11.5c) results in a decrease in width ~6 ky later (Figure 11.5e), and the increase in rate of advance at ~30 ka results in an increase in width with little delay. The abrupt ~70 km decrease in width at ~42 ka is puzzling, but both it and the abruptness of the decrease at 35 ka suggest that at the upglacier edge there may have been a wide zone of relatively thin permafrost that disappeared nearly simultaneously.

Cutler *et al.* (2000) reach three basic conclusions from this study:

- Permafrost persists for time spans of order  $10^2$ – $10^3$  years beneath an advancing ice margin.
- The maximum width of the submarginal permafrost zone is of order  $10^2$  km.
- Submarginal permafrost severely inhibits drainage of basal meltwater, leading to high subglacial water pressures.

Although the dimensions of the permafrost layer (as well as many other model results) are sensitive to the values of the parameters used to define the climate, substrate characteristics, and sliding speed, these results appear to be robust; all tested values of the parameters yield a modeled Late Glacial Maximum (LGM) ice sheet with a wide, persistent frozen toe. A caveat is that in their sensitivity studies, Cutler *et al.* varied only one input parameter at a time. Their conclusion would be stronger if they had varied two or more parameters simultaneously in a direction to minimize the width of the frozen zone.

The probable existence of such a frozen margin during the LGM has several geomorphic implications:

- As the width of the frozen margin decreases, rather abrupt releases of stored subglacial water are likely. This supports the authors' hypothesis, and that also of Hooke and Jennings (2006), that the tunnel valleys found along the LGM margin in Wisconsin (p. 247–248) were formed by such drainage.
- High subglacial water pressures are likely, so landforms associated with deforming beds are to be expected. Bands of drumlins upglacier from the presumed zone of frozen bed in Wisconsin (Attig *et al.*, 1989) are consistent with this, inasmuch as a mobile substrate appears to be an essential requirement for drumlin formation (Patterson and Hooke, 1995).
- Thrust features formed by the mechanism discussed in Chapter 6 (Figure 6.19) are expected and, indeed, are found in Wisconsin (Attig *et al.*, 1989).
- Large proglacial lakes like those that formed between the advancing ice margin and the southern shores of Lakes Michigan and Erie would have inhibited formation of submarginal permafrost. This, combined with higher marginal temperatures in more southerly latitudes, may explain why features such as drumlins, thrust features, and tunnel valleys are rare or absent south of these lakes. It may also explain why the ice lobes that filled these lakes extended further south.

While glacial geologists had speculated that permafrost might persist for some time under the margins of advancing continental ice sheets (e.g. Mickelson, 1987), numerical modeling such as that carried out by Cutler *et al.* (2000) provides a much firmer theoretical basis for this speculation.

## Siple dome

Price *et al.* (2007b) used a full-Stokes finite-volume flow-band model to study changes in ice thickness and flow of Siple dome (Figures 5.20 and 13.5b) in Antarctica during the late Pleistocene and Holocene. A 1004 m borehole to the bed near the divide yielded an ice core with an accurate age-depth profile. Data on the present ice fabric and texture and on the surface temperature history based on stable isotope measurements were obtained from the core. The present accumulation rate is  $120 \text{ mm a}^{-1}$ . The number of bubbles per cubic centimeter at pore close off (the bubble-number density) varies with temperature and the overburden firn load (Spencer *et al.*, 2006), and as the temperature is known from the stable isotope data, measurement of the bubble-number density in samples of the core yielded an estimate of the accumulation-rate history over the past 30 ky (Spencer, 2005). Radio echo profiles showed internal layers, presumed to be isochrones, and total ice thickness. A prominent Raymond bump (Figure 5.13 and p. 102–103) is present. The present temperature profile and the geothermal flux were obtained from temperature measurements in the borehole.

Enhancement factors were estimated based on the present fabric and texture and on experiments on the relation between stress configuration and deformation rate (Wang and Warner, 1999);  $E$  was allowed to vary both spatially and with time. Prior to 20 ka it was assumed to be  $\sim 1$  everywhere, while at present, it is thought to vary from 0.1 at depth beneath the divide to 5 in Pleistocene ice on the flanks.

The model domain extended 20 km on either side of the divide and, for the energy balance, 1500 m into the bedrock. By varying the ice flux out of the domain on either side of the divide through time, the ice sheet could be forced to thicken or thin, and the divide to migrate. Wind scouring at the divide was also varied (from 1.2 to  $5 \text{ mm a}^{-1}$ ). The goal was to match the observed temperature, age, and surface profiles, and the amplitude of the Raymond bump. The ultimate objective was to better understand the role of ice streams in controlling the stability of the ice sheet.

The model that best fit the profiles and Raymond bump was one in which the divide region thinned 350 m between 15 and 14 ka, and the divide migrated to its present position in the last 3 ky. The thinning is inferred to be a consequence of activation of one or both of the ice streams that bound the dome (Figures 5.20 and 13.5b). This would draw down the ice surface on either side of the dome, thus increasing the flow rates on the flanks and the longitudinal strain rate across the dome. The timing of the thinning coincides with a marked increase in sea level, meltwater pulse 1A (Fairbanks, 1989), that is believed to have occurred at  $\sim 14.5$  ka. The obvious inference is that the rise in sea level caused retreat of the grounding line and this reinvigorated the ice stream(s).

This is clearly topical: global warming is presently accelerating melting worldwide, leading to an increase in the rate of sea level rise. The rising sea level increases the speed of ice streams that then draw down the interiors of the Greenland and

Antarctic ice sheets, increasing the rate of sea level rise in a positive feedback. The present northward migration of the divide may be a lingering effect of a period of activity of Kamb ice stream which lies to the south of the dome and became effectively stagnant ~130 years ago (Retzlaff and Bentley, 1993).

The complexity of physical processes affecting glacier behavior, and the lengths to which one must go to constrain as many variables as possible in order to obtain a solution for those that are less well known, is demonstrated well by this example.

### Three dimensional models of ice sheets

Recently, glaciologists have put considerable effort into modeling entire ice sheets like those in Greenland and Antarctica. The results of some of these models have already been presented in Figures 5.2, 6.16, and 6.17. Armed with models that closely reproduce the characteristics of these modern ice sheets, one can examine the conditions under which past ice sheets expanded to lower latitudes, or predict the behavior of present ice sheets under various scenarios for climate change in the future.

An interesting application of a three-dimensional thermomechanical finite-difference model of a continental ice sheet is that of Marshall *et al.* (2000), who studied the Laurentide ice sheet. The model run starts at 122 ka, and is forced by a paleoclimate scenario based on a global climate model tuned with ice core records. With an enhancement factor of 6, apparently applied to the full thickness of the ice sheet, and without basal sliding, the model simulates the modern Greenland ice sheet well, and is in close agreement with other benchmark models of Greenland. However, when it is then used to model the Laurentide ice sheet, it produces an LGM ice mass with a volume of  $36.3 \times 10^6 \text{ km}^3$ , whereas studies of moraines, LGM sea level, and post-glacial isostatic recovery suggest that the actual volume was only  $\sim 22.5 \times 10^6 \text{ km}^3$ . To try to bring the calculated volume into better agreement with that observed, Marshall *et al.* first added a calving routine. With reasonable calving rates, this reduced the volume only modestly. Higher calving rates led to inconsistencies with the known ice sheet extent in Hudson Bay and Hudson Strait. They then added a sliding routine but did not retain the calving algorithm. This reduced the volume to  $29.1 \times 10^6 \text{ km}^3$  and resulted in an ice sheet extent that was in reasonable agreement with observations of glacial geologists (Figure 11.6). A further reduction in calculated ice volume could have been achieved by increasing the enhancement factor or by reducing precipitation in the climate forcing, but these options were not explored quantitatively.

Marshall *et al.*'s (2000) need for an enhancement factor as high as 6 in their Greenland model probably reflects: (1) sliding, which occurs in Greenland but is not allowed in their model, and (2) the presence of strong single-maximum crystal fabrics that are observed in ice deep in the ice sheet. Paterson (1991) has argued that impurities, common in Pleistocene ice, may be responsible for the strong fabrics.

Impurities inhibit grain boundary migration, resulting in smaller crystals, and the smaller crystals recrystallize readily, leading to strong preferred orientations.

That Pleistocene ice is soft was first detected in borehole deformation studies on Barnes Ice Cap (Hooke, 1973b). Later it was documented in similar studies on Devon (Patterson, 1977) and Agassiz (Fisher and Koerner, 1986) ice caps, and then in Greenland (Dahl-Jensen and Gundestrup, 1987). Modeling the present Greenland Ice Sheet by applying an enhancement factor of 6 to the entire ice mass is equivalent to modeling it with a much higher enhancement factor applied only in the Pleistocene ice. This is consistent with borehole deformation experiments on Barnes Ice Cap that have yielded enhancement factors of 17 to 18 in this ice (Hooke and Hanson, 1986).

Longitudinal stretching during the Holocene has thinned this layer of soft Pleistocene ice. In the early Holocene it would have been thicker, but whether it was as soft as it is today is unknown. However, it does seem reasonable to suggest that the appropriate enhancement factor for the Laurentide ice sheet could have been higher than 6. Other modelers have also found that relatively high enhancement factors were required to model the accepted volume of this ice sheet (Huybrechts and T'Siobbel, 1995; Tarasov and Peltier, 1999).

In conclusion, the Laurentide ice sheet can be modeled successfully if algorithms for sliding and calving are included, if the likely softness of Pleistocene ice is incorporated, and if the Pleistocene climate is assumed to have been somewhat drier than the Holocene climate. Marshall *et al.* (2000) do not pursue combinations of these effects, arguing sensibly that the physics of the calving and sliding processes are not known well enough. Sliding, for example, depends on pore water pressures in the substrate, and pore water pressures, in turn, depend upon basal temperatures and the efficiency of the basal drainage system. Models of the basal drainage system are even more tenuous than those of calving, and, as noted above, basal temperature distributions are not modeled consistently.

In short, we can choose between viewing the glass as half empty or half full. We have a long way to go to write calving and sliding algorithms that are well-supported by physics. On the other hand, the models have already revealed important characteristics of the Laurentide ice sheet and of ice in it.

### Glacier volumes and sea level

To estimate glacier volumes from their surface areas, Bahr *et al.* (1997) used a statistical model supported by empirical data. The surface area is  $w \cdot x$ , where  $w$  and  $x$  are the glacier's mean width and length. Similarly, the volume is  $w \cdot h \cdot x$ , where  $h$  is the mean thickness. Now define the characteristic values  $[w]$ ,  $[h]$ , and  $[x]$  to be representative means of  $w$ ,  $h$ , and  $x$  in a population consisting of a large number of glaciers. Thus,  $[V] \propto [w] [h] [x]$  and  $[S] \propto [w] [x]$ . Our objective now is to obtain a relation between  $[V]$  and  $[S]$ .

A common approach in engineering and physics is to take variables of potential importance in a problem and assemble them into groups of dimensionless

parameters. Common dimensionless parameters in fluid mechanics, for example, are the Reynolds and Froude numbers. In 1914 Edgar Buckingham introduced the use of the symbol “ $\pi$ ” for dimensionless parameters, and the theory has come to be known as the Buckingham  $\pi$  theorem (Buckingham, 1914). If a functional relationship involves a number of variables and  $N$  fundamental units (such as length, mass, or time), the  $\pi$ -theorem states that the relation can be rewritten in terms of  $N$  fewer arguments that are non-dimensional ratios of the original variables (Schmidt and Housen, 1995). One tenant of the  $\pi$ -theorem is that, if there is a relation among  $N + 1$  variables involving  $N$  independent dimensional units, the relation can be expressed in terms of a power-law dependence on a single non-dimensional parameter. Accordingly, a relation between  $[w]$  and  $[x]$ , two variables with one dimensional unit (length), might be expected to take the form  $[w] \propto [x]^q$ . Then:

$$[V] \propto [h][x]^{1+q} \quad \text{and} \quad [S] \propto [x]^{1+q}. \quad (11.13)$$

Length and width data from  $\sim 30,000$  Eurasian glaciers suggest that  $q \approx 0.6$  (Bahr *et al.*, 1997).

Because surface area and volume have dimensions of length squared and length cubed, respectively, a dimensional analysis can relate  $[V]$  to  $[S]$  by multiplying the latter by a quantity with dimensions of length. Bahr *et al.* (2015) note that glacier thickness is an obvious choice because surface area already contains measures of width and length. However, to account for side drag, the centerline thickness must first be multiplied by a shape factor,  $S_f$ , thus:

$$[V] \propto [S][S_f][h]. \quad (11.14)$$

As is evident from its definition (p. 90), when  $S_f$  is small it scales as the ratio of width to thickness (Bahr *et al.*, 1997, equation 12). Therefore:

$$[V] \propto [S] \frac{[w]}{[h]} [h] \quad (11.15)$$

(Bahr *et al.* (2015) emphasize, however, that on very wide glaciers and ice caps where  $S_f \rightarrow 1$ , a different derivation is required.) Noting that  $[w] \propto [S]/[x]$  and inserting the second of Equations (11.13) into Equation (11.15) then yields:

$$[V] \propto [S][S][S]^{\frac{-1}{1+q}} = [S]^{\frac{2q+1}{q+1}}.$$

Making use of the empirical value of  $q$ , 0.6, this becomes:

$$[V] \propto [S]^{1.375}. \quad (11.16a)$$

This relation agrees exceptionally well with measurements of  $V$  and  $S$  on 144 alpine glaciers in Europe, North America, central Asia, and the Arctic, which give:

$$V = 0.032 S^{1.36} \quad (11.16b)$$

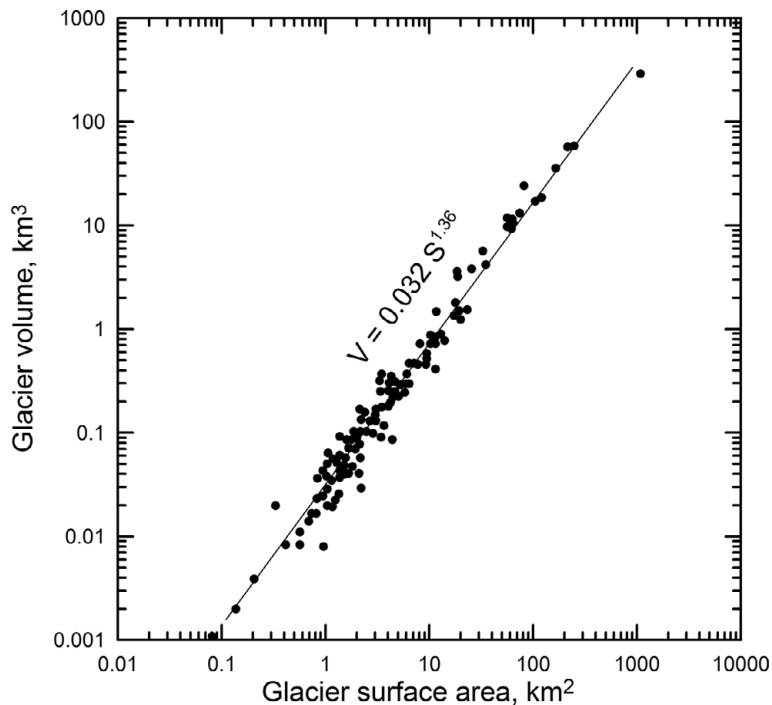


**Figure 11.7** Relation between surface areas and volumes of alpine glaciers. Volume measurements are based on reliable echo soundings done in the late 20th century. (Redrawn from Bahr *et al.*, 1997, Figure 1. Used with permission of the authors and the American Geophysical Union)

(Figure 11.7). It is also consistent with an exponent of  $1.379 \pm 0.066$  derived from a data set consisting of 103 glaciers in the Altai and Tien Shan mountains in Asia (Macheret *et al.*, 1988, cited by Bahr *et al.*, 1997). Vaughan *et al.* (2013, p. 342) used it to estimate rates of sea level rise over the past century in the 2013 IPCC report.

Bahr *et al.* (2009) also use this model to estimate future sea level rise. In a slightly different approach to this problem than theirs, let's take the derivative  $dV/dS$  of Equation (11.16b), multiply by  $dS$ , divide the left side by  $V$  and the right side by  $V$ 's equivalent,  $0.032 S^{1.36}$ , and interpret  $dV$  and  $dS$  as finite increments,  $\Delta V$  and  $\Delta S$ . This yields:

$$\Delta V = 1.36 \frac{V}{S} \Delta S. \quad (11.17)$$

To estimate  $\Delta S$ , Bahr *et al.* (2009) note that, empirically, the mean accumulation area ratio on glaciers with balanced mass budgets is  $0.57 \pm 0.01$ , but between 1997 and 2006 the worldwide average was only 0.44. Thus, present accumulation areas appear to be too small to support the glaciers; if present climate conditions persist the glaciers should eventually shrink by an amount  $\Delta S$ . Let  $S_n$  and  $S_{an}$  be

the area of a glacier and of its accumulation area now, and  $S_n - \Delta S$  be the area after equilibrium has been re-established. Then  $S_{an} = 0.44S_n = 0.57(S_n - \Delta S)$ . Thus,  $\Delta S = 0.23S_n$ . Equating  $S_n$  with  $S$  in Equation (11.17) yields:  $\Delta V = 0.31 V$ . The present volume,  $V$ , of the world's glaciers (excluding ice caps and ice sheets) is  $\sim 250 \pm 20 \times 10^3 \text{ km}^3$  (Bahr *et al.*, 2009), so  $\Delta V = 77.5 \pm 6.2 \times 10^3 \text{ km}^3$ . The area of the world's oceans is  $3.62 \times 10^8 \text{ km}^2$ , so once glaciers have come into equilibrium with the present climate, sea level will have risen  $214 \pm 17 \text{ mm}$ . The time scale for this adjustment is not determined by this approach, but alpine glaciers tend to adapt to changes in climate on time scales of decades (Chapter 15), so most of this sea level rise is likely to occur by 2100, at a rate somewhat in excess of  $\sim 2 \text{ mm a}^{-1}$ . Bahr *et al.* suggest that adding to this the contributions from ice caps (but not ice sheets) and from future climate warming will roughly double the rate. For comparison, the total rate of sea level rise at present, including contributions from ice sheets and from thermal expansion of the oceans, is estimated to be  $> 3.2 \text{ mm a}^{-1}$  (Church *et al.*, 2013).

The simplicity of Equation (11.16a) is deceptive. Bahr *et al.* (2015) emphasize that considerable care must be taken in applying it, and that many invalid applications can be found in the literature.

### Retreat of Columbia Glacier

Columbia Glacier is a tidewater glacier in Alaska that began to retreat from its Holocene terminal moraine (see Figure 3.9) in 1983. Tidewater glaciers may be chaotic entities, inasmuch as small changes in some conditions may lead to large changes, both in numerical models and in Nature, in their behavior. Colgan *et al.* (2012) wanted to predict the future behavior of Columbia Glacier, and chose to do so with the use of a Monte Carlo simulation.

In a Monte Carlo simulation, one selects values, at random, of certain unknown parameters from physically realistic distributions and uses these in a deterministic model of the problem under investigation. Physically unrealistic solutions are discarded, and the remaining solutions are analyzed statistically. The parameters Colgan *et al.* varied were: (i) the extent and magnitude of basal sliding; (ii) the elevation of the equilibrium line, using a random variation superimposed on a long term warming trend at a rate that also varied randomly; (iii) the maximum specific  $\dot{b}$  in the accumulation area (see Figure 3.4); and (iv) a randomly varying calving face height, with all ice seaward of the point where this height occurred assumed to have been lost by calving. The upper and lower bounds of these several parameters were based on observational evidence.

To predict the behavior of the glacier, Colgan *et al.* (2012) made 20,000 runs of a finite volume model that included longitudinal stress coupling. Each run used a different combination of these variables, and started with a 500 year spin up. If, at the end of this spin up, the model did not reproduce the observed ice thickness in

1978 to within  $\pm 100$  m or the observed terminus position to within  $\pm 2$  km, the run was discarded. This eliminated 16,978 of the runs. Then they continued the run for another 100 years, and discarded 353 runs in which the glacier had not started to retreat by that time. This filtering eliminated possible combinations of initial conditions that did not reproduce observed behavior, leaving 2669 useful runs.

The mean result from these 2669 runs was considered to be a reasonable estimate of the likely behavior of Columbia Glacier over the next century. This mean result suggested that the mass budget of the glacier will probably finally become balanced once again in  $\sim 2020$ , at which time the retreat will stop. The ensuing period of stability will continue until at least 2100. If this interpretation is correct, Columbia glacier will not contribute to sea level rise after  $\sim 2020$ . Other tidewater glaciers may react differently, of course.

Monte Carlo approaches of this type may provide better estimates of uncertainty than physically-based models because, when systems are highly non-linear, standard linear error propagation is unlikely to yield a realistic estimate of uncertainty.

---

## SUMMARY

In this chapter we first reviewed the two main physically-based numerical modeling techniques commonly used in glaciology, the finite-difference and finite-element techniques, and a third, the finite volume technique, that may become more common in the future. We then considered some statistical approaches. For simple problems, finite-difference models can be implemented with a spreadsheet or simple computer program. Finite-element, finite-volume, and finite-difference solutions of more complex problems require more sophisticated computer programs. While numerical details of these advanced techniques are beyond the scope of this book, we have introduced some of the vocabulary commonly associated with them. At the time of this writing, the power of numerical models has exceeded our understanding of some of the fundamental processes involved, particularly at the bed and at calving faces, thus limiting the value of additional refinements.

Owing to their complexity, numerical models can easily have flaws that result in realistic but incorrect predictions. Parts of models can often be tested against analytical solutions before the model as a whole is applied to problems without such solutions. Output of models of entire ice sheets can be compared with benchmarks. The latter tests have shown that current models generally do well at predicting the size and shape of an ice sheet, but relatively subtle differences among the models result in significant differences in solutions for basal temperature distribution, and in particular in the fraction of the bed that is at the pressure melting point.

In the last part of the chapter, we explored several applications of models to problems of glaciological and geomorphological significance. In the first, a finite-element model predicted that when an ice sheet advances over permafrost, a frozen margin of appreciable width is likely to develop and to persist for centuries or millennia. Certain landforms have been interpreted as being a consequence of such a frozen margin. The second explored the late Pleistocene and Holocene history of Siple dome and found that draw down of the dome may have coincided with a major rise in sea level at ~14.5 ka that likely activated ice streams on one or both sides of the dome. Then, we discussed a finite-difference model of the Laurentide ice sheet and found that with certain reasonable assumptions, relatively good agreement probably could be obtained between the ice volume calculated by the model and that determined from moraines, sea level records, and isostatic rebound. The results pointed, however, to the need for a better quantitative understanding of sliding, calving, and the development of basal drainage systems, and of climate history, while at the same time they constrained the ranges of these parameters that will yield agreement between model and probable reality. Finally we reviewed two statistical models, one of which used a relation between glacier surface area and volume to predict components of future sea level rise, and the second used Monte Carlo methods to predict the future course of retreat of Columbia glacier.

# Applications of stress and deformation principles to classical problems

In this chapter, we will study some glaciologically significant problems for which an appreciation of the material presented in Chapters 9 and 10 is required. Our objective is not to provide a comprehensive overview of theoretical developments in glaciology, but rather to solidify the gains made in these preceding two chapters by applying the principles developed therein. In the course of this discussion, the student will be introduced to some definitive studies, frequently referenced in the glaciological literature.

Let's first consider the problem of closure of a cylindrical borehole, in part because this is relevant to our earlier discussion of glacier hydrology. Then we'll investigate efforts to calculate basal shear stresses using a force balance model, followed by study of longitudinal coupling. Finally, the problem of using borehole deformation experiments to obtain estimates of the values of the parameters in the flow law will round out the chapter.

## Collapse of a cylindrical hole

The first problem we address is that of the closure of a cylindrical hole in ice. This problem was studied by Nye (1953) in the context of using rates of closure of ice tunnels to estimate the constants in Glen's flow law, and our development is based on Nye's paper. More recently, the theory has been used to analyze two problems in water flow at the base of a glacier: (1) the closure of a cylindrical water conduit, and (2) leakage of water into or away from a subglacial conduit. We used the first of these analyses in Chapter 8 (Equation 8.4).

Our approach is very similar to that used in Chapter 10 to obtain stresses and velocities in a "glacier" consisting of a slab of ice resting on a bed with a uniform slope, except that in this case we use a cylindrical coordinate system (Figure 12.1). We first reduce the problem to one of plane strain by setting it up so that there is no strain parallel to the axis of the hole. This reduces the number of unknowns from nine – the three components of the velocity vector and six independent components of the stress tensor – to five (three principal stresses and two velocities). Expressions for the stresses and strain rates are then obtained and inserted into the momentum

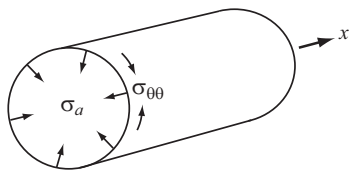


**Figure 12.1** Stresses on the wall of a cylindrical hole in a weightless medium.

and continuity equations. Finally, we use a constitutive relation between stress and strain rate, Glen's flow law, to obtain the desired solution.

Consider, first, the closure of a hole of radius  $a$  in an infinite weightless medium (Figure 12.1). Once the solution to this problem is obtained, we will modify it to apply to a real glacier. On the surface of the hole, at  $r = a$ , an internal tension,  $\sigma_a$ , is (somehow) applied. Eventually, this stress will be equated with that resulting from the difference between the pressure in the ice and that in the hole.

As there is no deformation in the  $x$ -direction,  $\dot{\epsilon}_{xx} = \lambda\sigma'_{xx} = 0$ . Thus,

$$\sigma'_{xx} = 0 = \sigma_{xx} - \frac{1}{3}(\sigma_{rr} + \sigma_{\theta\theta} + \sigma_{xx})$$

or

$$\sigma_{xx} = \frac{1}{2}(\sigma_{rr} + \sigma_{\theta\theta}). \quad (12.1)$$

The mean stress thus becomes

$$P = \frac{1}{3}\sigma_{kk} = \frac{1}{3}\left[\frac{3}{2}(\sigma_{rr} + \sigma_{\theta\theta})\right]$$

so

$$\sigma'_{rr} = \frac{1}{2}(\sigma_{rr} - \sigma_{\theta\theta}) \quad (12.2)$$

and

$$\sigma'_{\theta\theta} = -\frac{1}{2}(\sigma_{rr} - \sigma_{\theta\theta}). \quad (12.3)$$

This gives us expressions for the three deviatoric stresses and the mean stress.

Because the hole wall cannot support shear tractions, shear stresses in the  $\theta$ - and  $x$ -directions in the medium away from the hole are zero. Therefore,  $\sigma_{rr}$ ,  $\sigma_{\theta\theta}$ , and  $\sigma_{xx}$  are principal stresses. The effective stress is then

$$\sigma^2 = \frac{1}{2}2\left[\frac{1}{4}(\sigma_{rr} - \sigma_{\theta\theta})^2\right]$$

or

$$\sigma = \frac{1}{2}\sigma_{ij}\sigma_{ij} = \frac{1}{2}|\sigma_{rr} - \sigma_{\theta\theta}|. \quad (12.4)$$

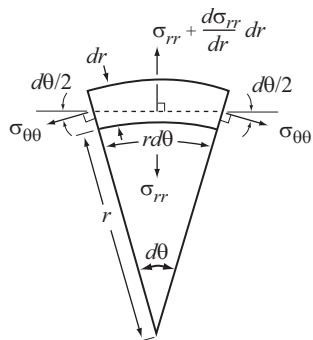


Figure 12.2 Stresses on a segment of the wall of a cylindrical hole.

Let us now obtain another relation between  $\sigma_{rr}$  and  $\sigma$  by considering the condition for stress equilibrium. From Figure 12.2, using the approximation  $\tan\left(\frac{d\theta}{2}\right) \approx \frac{d\theta}{2}$ , we have

$$\sigma_{rr}(rd\theta) - \left(\sigma_{rr} + \frac{d\sigma_{rr}}{dr} dr\right)(r + dr)d\theta + 2\sigma_{\theta\theta}dr\frac{d\theta}{2} = 0.$$

Cancelling like terms of opposite sign, dividing by  $dr d\theta$ , and ignoring the term still containing a differential yields

$$r \frac{d\sigma_{rr}}{dr} + \sigma_{rr} - \sigma_{\theta\theta} = 0$$

or, using Equation (12.4)

$$\frac{d\sigma_{rr}}{dr} + \frac{2\sigma}{r} = 0. \quad (12.5)$$

The radial stress,  $\sigma_{rr}$ , goes to 0 at infinity. Thus, Equation (12.5) may be integrated:

$$\int_{\sigma_{rr}}^0 d\sigma_{rr} = - \int_r^\infty \frac{2\sigma}{r} dr$$

or

$$\sigma_{rr} = \int_r^\infty \frac{2\sigma}{r} dr. \quad (12.6)$$

In order to integrate Equation (12.6), we must express  $r$  in terms of  $\sigma$ . We will do this by determining the velocity field, and hence  $\dot{\epsilon}$ , and inserting a flow law. Let  $u$  be the velocity in the radial direction. Other velocities vanish owing to the radial symmetry and the absence of deformation in the  $x$ -direction. Conservation of mass requires that the mass flux through two concentric cylindrical surfaces

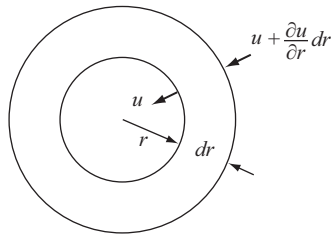


**Figure 12.3** Radial velocity field around a cylindrical hole.

with radii  $r$  and  $r+dr$  (Figure 12.3) must be the same in an incompressible medium. Thus, we have

$$2u\pi r = 2 \left( u + \frac{du}{dr} dr \right) \pi(r+dr)$$

which may be simplified, thus:

$$\frac{du}{dr} = -\frac{u}{r} \quad (12.7)$$

and integrated to yield

$$\ln u = -\ln r + \ln c.$$

Because we obtained this without referring to the direction of  $u$ , a minus sign is now inserted to indicate that  $u$  is in the negative  $r$ -direction. Thus,

$$u = -\frac{c}{r}.$$

So  $u$  is directed toward the hole and is a maximum on the hole wall, at  $r=a$ . It decreases to 0 at  $r=\infty$ .

From its definition in terms of velocity derivatives (Equations 9.21), we see that

$$\dot{\varepsilon}_{rr} = \frac{\partial u}{\partial r}$$

so from Equation (12.7):

$$\dot{\varepsilon}_{rr} = -\frac{u}{r}$$

and by continuity, since  $\dot{\varepsilon}_{xx}=0$ ,

$$\dot{\varepsilon}_{\theta\theta} = -\dot{\varepsilon}_{rr} = \frac{u}{r}.$$

The effective strain rate is thus:

$$\dot{\varepsilon}^2 = \frac{1}{2} \dot{\varepsilon}_{ij} \dot{\varepsilon}_{ij} = \frac{1}{2} \left( 2 \frac{u^2}{r^2} \right).$$

As  $u = -c/r$ , this becomes:

$$\dot{\varepsilon} = \frac{c}{r^2}. \quad (12.8)$$

We can retain the generality of the solution a little longer before inserting a flow law. Because  $\dot{\varepsilon} = f(\sigma)$ , we have

$$f(\sigma) = \frac{c}{r^2}. \quad (12.9)$$

To obtain  $r$  in terms of  $\sigma$ , note that (using Equation 12.9):

$$\frac{df(\sigma)}{d\sigma} = \frac{df(\sigma)}{dr} \frac{dr}{d\sigma} = -\frac{2c}{r^3} \frac{dr}{d\sigma}.$$

Again using Equation (12.9) to eliminate  $c$ :

$$\frac{df(\sigma)}{d\sigma} = -\frac{2}{r} f(\sigma) \frac{dr}{d\sigma}$$

so:

$$dr = -\frac{r df(\sigma)}{2 f(\sigma)}.$$

Substituting this into Equation (12.6) yields

$$\sigma_{rr} = -\int \frac{2\sigma r}{r} \frac{df(\sigma)}{2 f(\sigma)} = -\int \frac{\sigma}{f(\sigma)} df(\sigma). \quad (12.10)$$

It's now necessary to make use of a flow law, specifically Glen's flow law, to obtain an analytical expression for the functional relation in Equation (12.9), thus:

$$\dot{\varepsilon} = f(\sigma) = A\sigma^n = \frac{c}{r^2} \quad (12.11)$$

whence, differentiating:

$$df(\sigma) = A n \sigma^{n-1} d\sigma.$$

With the use of these last two relations, Equation (12.10) becomes:

$$\sigma_{rr} = \int_0^\sigma \frac{\sigma}{A\sigma^n} A n \sigma^{n-1} d\sigma = \int_0^\sigma n d\sigma$$

so,

$$\sigma_{rr} = n\sigma. \quad (12.12)$$

In other words, the radial stress at any distance  $r \geq a$  from the hole wall is simply  $n$  times the effective stress. One cannot help but be impressed by the simplicity and elegance of this result, considering the effort required to obtain it. Unfortunately,

real life is rarely so conveniently uncomplicated. Furthermore, we still have some way to go before obtaining relations that can be applied to real glaciers.

In preparation for relaxing the assumption that the medium is weightless, let us now scale this solution to the normal stress,  $\sigma_a$ , on the hole wall. Using the last equality in Equation (12.11) we obtain:

$$\sigma_{rr} = n \left( \frac{c}{Ar^2} \right)^{1/n} \text{ and at } r = a \quad \sigma_a = n \left( \frac{c}{Aa^2} \right)^{1/n}$$

whence:

$$\frac{\sigma_{rr}}{\sigma_a} = \left( \frac{a}{r} \right)^{2/n}. \quad (12.13)$$

Solutions for the remaining stresses can now be written similarly, as follows: From Equations (12.4) and (12.12):

$$\sigma = \frac{1}{2} (\sigma_{rr} - \sigma_{\theta\theta}) = \frac{1}{2} (n\sigma - \sigma_{\theta\theta})$$

whence, transposing and again using the last equality in Equation (12.11):

$$\sigma_{\theta\theta} = (n - 2)\sigma = (n - 2) \left( \frac{c}{Ar^2} \right)^{1/n}$$

so:

$$\frac{\sigma_{\theta\theta}}{\sigma_a} = \frac{n - 2}{n} \left( \frac{a}{r} \right)^{2/n}. \quad (12.14)$$

Then, from Equations (12.1), (12.13), and (12.14):

$$\frac{\sigma_{xx}}{\sigma_a} = \frac{1}{2} \left( \frac{\sigma_{rr}}{\sigma_a} + \frac{\sigma_{\theta\theta}}{\sigma_a} \right) = \frac{1}{2} \left[ \left( \frac{a}{r} \right)^{2/n} + \frac{n - 2}{n} \left( \frac{a}{r} \right)^{2/n} \right]$$

so,

$$\frac{\sigma_{xx}}{\sigma_a} = \frac{n - 1}{n} \left( \frac{a}{r} \right)^{2/n}. \quad (12.15)$$

Finally, from Equations (12.4), (12.13), and (12.14):

$$\frac{\sigma}{\sigma_a} = \frac{1}{2} \left( \frac{\sigma_{rr}}{\sigma_a} - \frac{\sigma_{\theta\theta}}{\sigma_a} \right) = \frac{1}{2} \left[ \left( \frac{a}{r} \right)^{2/n} - \frac{n - 2}{n} \left( \frac{a}{r} \right)^{2/n} \right].$$

Thus,

$$\frac{\sigma}{\sigma_a} = \frac{1}{n} \left( \frac{a}{r} \right)^{2/n}. \quad (12.16)$$

We can now relax the assumption that the medium is weightless. Suppose we have a horizontal hole at atmospheric pressure at a depth  $h_o$  in a real glacier. The

hydrostatic pressure in the glacier is  $\mathcal{P} = \rho gh$ , and around the hole it is  $\mathcal{P} = \rho gh_o$ . Note that  $\mathcal{P}$  is not equal to the mean stress,  $P$  ( $= \frac{1}{3}\sigma_{kk}$ ). If  $h_o \gg a$ ,  $\mathcal{P}$  will be nearly uniform around the hole. We have not previously specified the magnitude of  $\sigma_a$ , so let us now write Equations (12.13) through (12.16) with  $\sigma_a = \mathcal{P}$ . Because  $\mathcal{P}$  is hydrostatic, let us also add a compressive stress,  $-\mathcal{P}$ , to the solutions. This is valid because a hydrostatic pressure influences all of the stresses equally, and therefore does not affect the local differences among the stresses given by Equations (12.13) through (12.16). The resulting equations are:

$$\sigma_{rr} = \mathcal{P} \left( \frac{a}{r} \right)^{2/n} - \mathcal{P} = \mathcal{P} \left[ \left( \frac{a}{r} \right)^{2/n} - 1 \right] \quad (12.17a)$$

$$\sigma_{\theta\theta} = \frac{n-2}{n} \mathcal{P} \left( \frac{a}{r} \right)^{2/n} - \mathcal{P} = \mathcal{P} \left[ \frac{n-2}{n} \left( \frac{a}{r} \right)^{2/n} - 1 \right] \quad (12.17b)$$

$$\sigma_{xx} = \frac{n-1}{n} \mathcal{P} \left( \frac{a}{r} \right)^{2/n} - \mathcal{P} = \mathcal{P} \left[ \frac{n-1}{n} \left( \frac{a}{r} \right)^{2/n} - 1 \right] \quad (12.17c)$$

$$\sigma = \frac{1}{2} (\sigma_{rr} - \sigma_{\theta\theta}) = \frac{\mathcal{P}}{n} \left( \frac{a}{r} \right)^{2/n} \quad (12.17d)$$

and the mean stress is:

$$\begin{aligned} \frac{1}{3} \sigma_{kk} &= \frac{\mathcal{P}}{3} \left[ \left( \frac{a}{r} \right)^{2/n} - 1 + \frac{n-2}{n} \left( \frac{a}{r} \right)^{\frac{2}{n}} - 1 + \frac{n-1}{n} \left( \frac{a}{r} \right)^{\frac{2}{n}} - 1 \right] \\ &= \mathcal{P} \left[ \frac{n-1}{n} \left( \frac{a}{r} \right)^{\frac{2}{n}} - 1 \right]. \end{aligned} \quad (12.17e)$$

Now, the stress causing closure is no longer a hypothetical traction on the inside of the hole,  $\sigma_a$ . Rather it is the real hydrostatic stress in the medium. Note that the stresses  $\sigma_{ii}$  ( $i = x, r, \theta$ ) decrease to  $-\mathcal{P}$  (i.e. compressive) at large distances from the hole, while  $\sigma \rightarrow 0$ .

It is easy to show that the corresponding deviatoric stresses are:

$$\sigma'_{rr} = -\sigma'_{\theta\theta} = \frac{\mathcal{P}}{n} \left( \frac{a}{r} \right)^{\frac{2}{n}} \quad (12.18a)$$

$$\sigma'_{xx} = 0. \quad (12.18b)$$

That  $\sigma'_{rr} = -\sigma'_{\theta\theta}$  and  $\sigma'_{xx} = 0$  are a consequence of our assumption of plane strain.

Setting  $r = a$  in Equations (12.17a-d) we obtain the stresses on the hole wall:

$$\sigma_{rr} = 0$$

$$\sigma_{\theta\theta} = -\frac{2\mathcal{P}}{n}$$

$$\sigma_{xx} = -\frac{\mathcal{P}}{n}$$

$$\sigma = \frac{\mathcal{P}}{n}. \quad (12.19)$$

### Tunnel and borehole closure

These relations have been used, together with measurements of the rate of closure of a tunnel or borehole, to determine values of the constants  $n$  and  $A$  in the flow law. To do this, it is necessary to incorporate the relations into the flow law. Deviatoric stresses are thus required. Because we are interested in closure, only  $\sigma'_{rr(r=a)}$  is needed. Thus, from Equations (9.29) and (10.39):

$$\dot{\varepsilon}_{rr} = A\sigma^{n-1}\sigma'_{rr} \quad (12.20a)$$

so from Equation (12.18a) with  $r=a$ , noting that  $\sigma_{r=a} = \mathcal{P}/n$ :

$$\dot{\varepsilon}_{rr(r=a)} = A\left(\frac{\mathcal{P}}{n}\right)^{n-1}\frac{\mathcal{P}}{n}. \quad (12.20b)$$

Because  $\dot{\varepsilon}_{rr(r=a)} = -u_a/a$  where  $u_a$  is the closure rate, we obtain

$$-\frac{u_a}{a} = A\left(\frac{\mathcal{P}}{n}\right)^n. \quad (12.21)$$

To use Equation (12.21) to estimate the constants in the flow law, one needs values of  $u_a$ ,  $a$ , and  $\mathcal{P}$  at two or more places. Inserting values for two such places in Equation (12.21) would yield two equations with two unknowns ( $n$  and  $A$ ). With three or more sets of data, it is useful to plot  $\log \dot{\varepsilon}$  against  $\log \mathcal{P}$  as is done for some tunnel-closure experiments in Figure 12.4.

Some caution is required, however. In tunnel closure studies, for example, pegs are normally inserted in the tunnel walls and closure is measured by determining the change in distance between the heads of pegs on opposite sides of the tunnel. In this case, particularly in temperate glaciers, the point at which the pegs are actually gripped by the ice may be some distance back in the wall. Furthermore, such tunnels are rarely if ever circular in cross section. Thus, the correct value of  $a$  must be guessed.

In borehole closure studies, closure rates are measured with calipers, so determining the appropriate value of  $a$  is not a problem. However, the time interval between measurements is often fairly large, and a substantial amount of closure may occur between measurements. In this case, approximating  $u_a$  by  $\Delta a/\Delta t$  is likely to yield a poor estimate (Paterson, 1977). It is better to use the temporal mean value of  $u_a/a$ , which is, by the definition of a mean:

$$\overline{\dot{\varepsilon}_a} = -\frac{1}{\Delta t} \int_{t_1}^{t_2} \frac{u_a}{a} dt.$$

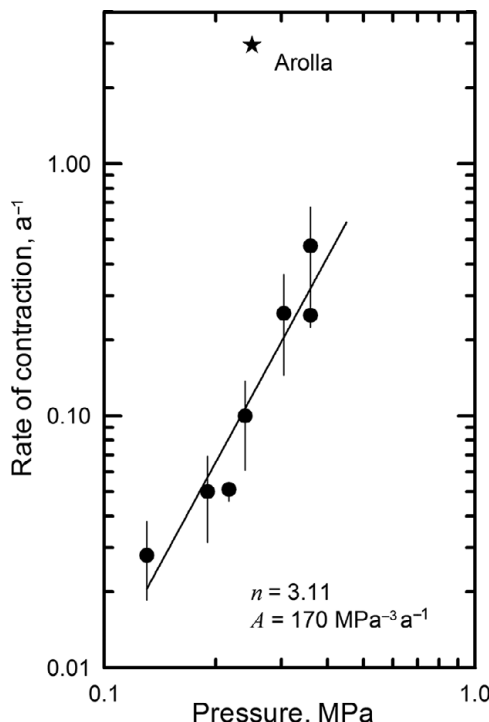


Figure 12.4 Rate of contraction,  $u_a$ , of tunnel sections plotted against overburden pressure, P. (Replotted from Nye, 1953, Figure 1. Reproduced with permission of the author and The Royal Society of London)

Noting that  $u_a = da/dt$ , this becomes (see Equation 9.24):

$$\bar{\varepsilon}_a = -\frac{1}{\Delta t} \int_{t_1}^{t_2} \frac{1}{a} \frac{da}{dt} dt = -\frac{1}{\Delta t} \ln \frac{a_2}{a_1}.$$

Some results from four borehole closure studies are presented in Figure 12.5 (open circles) along with data on the variation of  $A$  with temperature from a large number of other laboratory and field experiments.

It is instructive to look at the results in Figures 12.4 and 12.5 in somewhat greater detail. In Figure 12.4, it will be noted that several of the sets of tunnel closure data fall along a line with  $n = 3.11$  and  $A = 170 \text{ MPa}^{-3} a^{-1}$ . This value of  $A$  is plotted as  $\square$  in Figure 12.5; it is quite consistent with other data from temperate ice. However, the point representing data from an ice tunnel in Glacier d'Arolla falls well above the line in Figure 12.4. The d'Arolla tunnel is at the base of an ice fall. Owing to the contribution of longitudinal stresses,  $\sigma$  is likely significantly higher than  $P/n$  here, and, as observed, one would thus expect the actual closure rate to be higher than that calculated using  $(P/n)^{n-1}$  to approximate  $\sigma^{n-1}$  in Equation (12.20a).

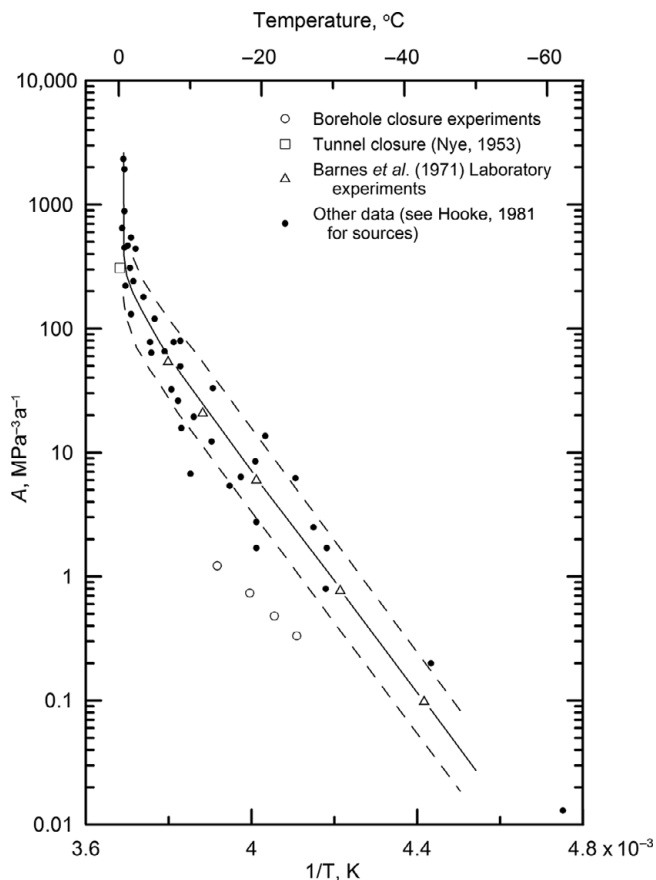


**Figure 12.5** Values of  $A$  from various experiments in which the minimum strain rate was measured or estimated. Effective stresses and strain rates were used in calculating  $A$ . Straight part of solid line is based on Barnes *et al.* (1971) data. Dashed lines are values of  $A$  that would give strain rates half or double those on the solid line.

The problem with the borehole closure rates, which seem to be too low and therefore yield values of  $A$  that appear to be too low in Figure 12.5, is different. Here, we speculate that the crystallographic fabric in the ice is adjusted to a stress regime in which the dominant deviatoric stress is simple shear normal to the axis of the hole. Such a fabric would have an effective enhancement factor  $< 1$ , thus inhibiting closure.

### Subglacial water conduits

In Chapter 8 we applied Equation (12.21) to closure of subglacial water conduits. As noted there, problems arise when one attempts to estimate closure rates of semicircular conduits, owing to drag on the bed. Even more profound difficulties arise in attempting to estimate closure rates of broad low conduits, as stresses in the ice are

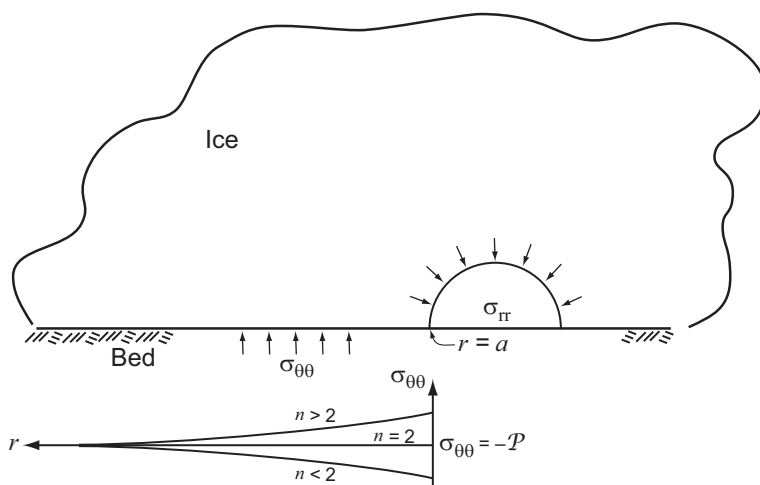


**Figure 12.6** Stresses around a semicircular conduit.  $\sigma_{rr}$  is extending and  $\sigma_{\theta\theta}$  is compressive (hence the minus sign on  $P$ ). The variation in  $\sigma_{\theta\theta}$  away from the tunnel is shown schematically. For  $n > 2$ ,  $\sigma_{\theta\theta}$  is less compressive than  $P$ , and conversely.

no longer symmetrically distributed about the conduit. Here, we look into two other problems of interest: (i) the role of stresses parallel to conduits, and (ii) normal stresses on the bed at the boundaries of a semicircular conduit, and in particular, the gradient in these stresses outward from the conduit (Figure 12.6).

As was the case with the tunnel in glacier d'Arolla, stresses parallel to a water conduit are commonly not negligible; there are shear stresses in ice surrounding the conduit, and there may be appreciable longitudinal stresses. Thus, again the effective stress,  $\sigma$ , may be appreciably larger than suggested by Equation (12.17d), resulting in a comparable increase in  $\dot{\epsilon}_{rr}$  (Equation 12.20a). Then, to maintain a steady state with  $u = m$  and  $Q$  held constant,  $P_w$  would have to increase, decreasing  $P_c$  and increasing  $r$ . So conduits would tend to be larger! The higher  $P_w$  would then also be likely to increase  $u_b$  (Meyer *et al.*, 2016).

The second problem was studied by Weertman (1972). If pressures are higher adjacent to the conduit, water in a film at the ice–bed interface will be forced away from the conduit, and conversely.

The significance of this problem lies in its application to water flow beneath polar ice sheets. Several authors have suggested that for conduits to exist beneath such ice masses in the absence of water inputs from the glacier surface, there must be an influx of water from adjacent parts of the bed (Walder, 1982; Weertman and Birchfield, 1983; Alley, 1989a; Ng, 2000a). The problem of the existence of such conduits is fundamental; where they are present, subglacial water pressures are probably lower than otherwise. Thus, any attempt to explain, for example, the fast flow of ice streams hinges upon an understanding of the nature of the subglacial hydraulic system.

The relevant stress in this problem is  $\sigma_{\theta\theta}$ . Thus, let us start with the expression for  $\sigma_{\theta\theta}$  in Equation (12.14). Note that in so doing, we tacitly assume that the bed is flat and slippery so that shear stresses do not impede movement of ice inward toward the tunnel. The appropriate value for  $\sigma_a$ , the “traction” causing closure, is now the difference between the pressure in the ice and that in the water in the conduit,  $\Delta P$ . As before, we add a pressure,  $-\mathcal{P}$ , everywhere to account for the weight of the ice. With these adjustments we have:

$$\sigma_{\theta\theta} = \frac{n-2}{n} \Delta P \left( \frac{a}{r} \right)^{\frac{2}{n}} - \mathcal{P}. \quad (12.22)$$

Note that  $\sigma_{\theta\theta}$  is negative, or compressive, as  $\mathcal{P}$  always exceeds the first term on the right.

When  $n = 2$ , the first term on the right is equal to 0, so  $\sigma_{\theta\theta} = -\mathcal{P}$ . When  $n \neq 2$ ,  $\sigma_{\theta\theta} \rightarrow -\mathcal{P}$  as  $r \rightarrow \infty$ . Over some large distance,  $R$ , from the conduit, the integral of  $\sigma_{\theta\theta}$  over  $r$  must support the weight of the glacier, so:

$$\int_0^a P_w dr + \int_a^R \left( \frac{n-2}{n} \Delta P \left( \frac{a}{r} \right)^{\frac{2}{n}} - \mathcal{P} \right) dr = -\rho g h R$$

where  $P_w$  is the water pressure in the conduit. Carrying out the integration and solving for  $\mathcal{P}$  yields:

$$\mathcal{P} = \frac{1}{R-a} \left[ \rho g h R + P_w a + \frac{n-2}{n} \Delta P \left( a^{\frac{2}{n}} R^{\frac{n-2}{n}} - a \right) \right].$$

If there is no conduit, so  $a = 0$ ,  $\mathcal{P} = \rho g h$  as expected. As  $R$  becomes large,  $(R-a) \approx R$  so:

$$\mathcal{P} = \rho g h + \frac{a}{R} P_w + \frac{n-2}{n} \Delta P \left[ \left( \frac{a}{R} \right)^{\frac{2}{n}} - \frac{a}{R} \right].$$

Now, noting that  $a/R$  is small,  $\mathcal{P}$  is slightly higher than  $\rho g h$ , thus compensating for the tunnel pressure which is less than  $\rho g h$ . For larger  $n$ , the difference is larger because  $\sigma_{\theta\theta}$  is less compressive near the conduit (Figure 12.6).

Returning now to the question of water flow on the bed adjacent to a semicircular conduit, we take the derivative of  $\sigma_{\theta\theta}$  with respect to  $r$  along the bed, thus:

$$\frac{d\sigma_{\theta\theta}}{dr} = -\frac{2}{n} \left( \frac{n-2}{n} \right) \Delta P \left( \frac{a}{r} \right)^{\frac{2}{n}-1}. \quad (12.23)$$

If  $n > 2$ , as might be expected,  $d\sigma_{\theta\theta}/dr$  is negative. Thus  $\sigma_{\theta\theta}$  decreases, or becomes more negative, or more compressive, away from the tunnel (Figure 12.6). In this case, water in a film will be forced toward the conduit, enhancing discharge in it. However, when one considers coupling of stresses, particularly where there is a shear stress on the bed or in the overlying ice parallel to the conduit, the situation is not so simple. In this case, water flow may be away from the tunnel (Weertman, 1972, pp. 299–300; Meyer *et al.*, 2016).

The physical reason for the change in behavior of  $d\sigma_{\theta\theta}/dr$  with  $n$  is not obvious. We might expect that if a cavity is introduced at the base of a glacier, compressive stresses adjacent to the cavity would increase in order to support that part of the weight of the glacier that is no longer supported by the bed under the cavity. However, toward the tunnel  $u$ , and hence  $\dot{\epsilon}_{tr}$ , increase and this requires an increase in  $\sigma'_{rr}$ . The way in which the stress field is modified to satisfy this requirement, and hence the way in which the pressure on the bed is redistributed, depends upon  $n$ . A more intuitive explanation of this effect is elusive.

### Calculating basal shear stresses using a force balance

To a first approximation, the basal drag can be estimated from  $\tau_b = \rho g h \alpha$  (or  $\tau_b = S_f \rho g h \alpha$  in a valley glacier). However, if longitudinal forces are unbalanced,  $\tau_b$  may be either greater or less than  $\rho g h \alpha$ . For example, in Figure 12.7, the body force,  $\rho g h$ , has a downslope component,  $\rho g h \alpha$ . In addition, there are longitudinal forces  $F_u$  and  $F_d$ . If  $F_u > F_d$ , as suggested by the lengths of the arrows in the figure,  $\tau_b$  will clearly have to be greater than  $\rho g h \alpha$  in order to balance forces parallel to the bed, and conversely. We now explore this effect in greater detail.

Because our goal is to calculate the drag exerted on the glacier by the bed, the momentum balance equations (Equation 9.32b) are the obvious starting point for the analysis. The coordinate system to be used is shown in Figure 12.8. The  $x$ -axis is horizontal and in the direction of flow, and the  $z$ -axis is vertical. Writing out the

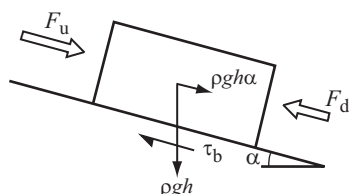


**Figure 12.7** Longitudinal forces on a segment of a glacier on a sloping bed. If  $F_u > F_d$  the basal drag will be greater than  $\rho g h \alpha$ , and conversely.

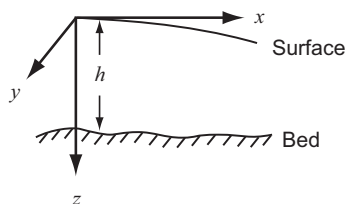


**Figure 12.8** Coordinate system used in force balance analysis.

momentum balance equations in the  $x$ - and  $z$ -directions, remembering that  $\sigma'_{ij} = \sigma_{ij} - \delta_{ij}P$ , leads to:

$$\frac{\partial\sigma'_{xx}}{\partial x} + \frac{\partial\sigma_{yx}}{\partial y} + \frac{\partial\sigma_{zx}}{\partial z} + \frac{\partial P}{\partial x} = 0 \quad (12.24a)$$

and

$$\frac{\partial\sigma_{xz}}{\partial x} + \frac{\partial\sigma_{yz}}{\partial y} + \frac{\partial\sigma'_{zz}}{\partial z} + \frac{\partial P}{\partial z} = -\rho g. \quad (12.24b)$$

The procedure now will be to solve Equation (12.24b) for  $P$ , substitute the result into Equation (12.24a), and integrate over the depth to obtain  $\sigma_{zx}$  ( $z=h$ ) ( $= \tau_b$ ).

To solve Equation (12.24b) for  $P$ , separate variables and integrate over depth  $z$ :

$$\int_0^z dP = - \int_0^z \frac{\partial\sigma_{xz}}{\partial x} dz - \int_0^z \frac{\partial\sigma_{yz}}{\partial y} dz - \int_0^z \partial\sigma'_{zz} dz - \int_0^z \rho g dz$$

or, noting that  $P=0$  at the surface:

$$P(z) = - \int_0^z \frac{\partial\sigma_{xz}}{\partial x} dz - \int_0^z \frac{\partial\sigma_{yz}}{\partial y} dz - \sigma'_{zz}(z) + \sigma'_{zz}|_{z=0} - \rho g z.$$

Now take the horizontal derivative, assuming that  $\partial\sigma'_{zz}/\partial x|_{z=0}$  is negligible and noting that  $dz/dx = \alpha$ , and substitute the result into Equation (12.24a), thus:

$$\frac{\partial\sigma'_{xx}}{\partial x} + \frac{\partial\sigma_{yx}}{\partial y} + \frac{\partial\sigma_{zx}}{\partial z} - \int_0^z \frac{\partial^2\sigma_{xz}}{\partial x^2} dz - \int_0^z \frac{\partial^2\sigma_{yz}}{\partial x \partial y} dz - \frac{\partial\sigma'_{zz}}{\partial x} - \rho g \alpha = 0. \quad (12.25)$$

Equation (12.25) is in terms of stresses at any given level,  $z$ , in the glacier, whereas we are interested in summing the stresses over depth to obtain  $\tau_b$ . Thus, as just noted, we integrate over depth:

$$\int_0^h \left( \frac{\partial\sigma'_{xx}}{\partial x} - \frac{\partial\sigma'_{zz}}{\partial x} \right) dz + \int_0^h \frac{\partial\sigma_{yx}}{\partial y} dz + \int_0^h d\sigma_{zx} - \iint_0^h \left( \frac{\partial^2\sigma_{xz}}{\partial x^2} + \frac{\partial^2\sigma_{yz}}{\partial x \partial y} \right) dz dz - \rho gh \alpha = 0. \quad (12.26)$$

Clearly,  $\sigma_{zx}$  ( $z=h$ ) ( $= \tau_b$ ) will be obtained from integrating the third term, and the last term is the familiar  $\rho gh \alpha$ . Some simplification is obviously desirable, however.

The double integral term in Equation (12.26), also sometimes referred to as the T-term, is difficult to interpret physically. In two dimensions, Budd (1969, p. 116) has shown that it can be approximated by:

$$\iint_0^h \frac{\partial^2\sigma_{xz}}{\partial x^2} dz dz \cong \frac{1}{6} \left[ \rho g \frac{\partial^2}{\partial x^2} (\alpha h^3) \right]. \quad (12.27)$$

Van der Veen and Whillans (1989 (and several other authors cited therein)) argue that this term is related to “bridging” effects, in which the pressure on the bed varies spatially owing to the influence of bed irregularities and, particularly, cavity formation. Because ice is “soft,” they suggest that these bridging effects should be small compared with the average normal pressure. Thus, they neglect the T-term in force-balance calculations, and we shall follow their lead in this respect. They acknowledge, however, that the “physical implications” of doing so are “not conceptually straightforward.”

Turning to the first term in Equation (12.26),  $\sigma'_{zz}$  can be eliminated by noting that the incompressibility condition,  $\dot{\varepsilon}_{xx} + \dot{\varepsilon}_{yy} + \dot{\varepsilon}_{zz} = 0$  together with Equation (9.29), leads to  $\sigma'_{xx} + \sigma'_{yy} = -\sigma'_{zz}$ . In addition, because  $\sigma_{zx}$  would be zero on a free horizontal surface, and is only slightly different from zero on the gently sloping glacier surface, the third term in Equation (12.26) is the desired basal drag,  $\tau_b$ , as just noted. With these modifications, Equation (12.26) becomes:

$$\int_0^h \frac{\partial}{\partial x} (2\sigma'_{xx} + \sigma'_{yy}) dz + \int_0^h \frac{\partial \sigma_{yx}}{\partial y} dz + \tau_b - \rho g h \alpha = 0. \quad (12.28)$$

To get an intuitive sense for this relation, consider a situation in which  $\sigma'_{xx}$  and  $\sigma_{yx}$  are independent of depth and  $\sigma'_{yy}$  is negligible. Then Equation (12.28) reduces to:

$$\rho g h \alpha - \tau_b = 2 \frac{\partial \sigma'_{xx}}{\partial x} h + \frac{\partial \sigma_{yx}}{\partial y} h. \quad (12.28a)$$

In two dimensions ( $\sigma_{yx} = 0$ ), this equation says that if the driving stress,  $\rho g h \alpha$ , exceeds the drag provided by the bed,  $\tau_b$ , the stretching rate ( $\dot{\varepsilon}_{xx} \propto \sigma'_{xx}$ ) will increase downglacier ( $\partial \sigma'_{xx} / \partial x > 0$ ) and conversely. The second term on the right takes shear stresses on the valley sides into consideration.

Our objective now is to express Equation (12.28) in a form that will allow evaluation of  $\tau_b$  from strain rate measurements at the glacier surface. To this end, we note that, because  $\lambda = A \sigma^{n-1}$  (Equation 10.39), the flow law can be written:

$$\dot{\varepsilon}_{ij} = A \sigma^{n-1} \sigma'_{ij} = A^{\frac{1}{n}} \dot{\varepsilon}^{\frac{n-1}{n}} \sigma'_{ij}$$

(Equation 2.17). Inserting this in Equation (12.28), reversing the order of differentiation and integration, and rearranging terms yields:

$$\tau_b = \rho g h \alpha - \frac{\partial}{\partial x} \int_0^h \frac{1}{\dot{\varepsilon}} \left( \frac{\dot{\varepsilon}}{A} \right)^{\frac{1}{n}} (2\dot{\varepsilon}_{xx} + \dot{\varepsilon}_{yy}) dz - \frac{\partial}{\partial y} \int_0^h \frac{1}{\dot{\varepsilon}} \left( \frac{\dot{\varepsilon}}{A} \right)^{\frac{1}{n}} \dot{\varepsilon}_{yx} dz + 0. \quad (12.29)$$

Van der Veen and Whillans (1989) developed a numerical procedure to carry out this integration over depth,  $z$ . However, for simple applications we can assume that strain rates are independent of depth, and express Equation (12.29) in finite difference form, thus:

$$\tau_b = \rho gh\alpha - \frac{1}{\dot{\varepsilon}} \left( \frac{\dot{\varepsilon}}{A} \right)^{\frac{1}{n}} \left\{ \left[ \frac{(2\dot{\varepsilon}_{xx} + \dot{\varepsilon}_{yy})h|_{\text{dwn}} - (2\dot{\varepsilon}_{xx} + \dot{\varepsilon}_{yy})h|_{\text{up}}}{\Delta x} \right] - \left[ \frac{\dot{\varepsilon}_{yx}h|_{\text{rgt}} - \dot{\varepsilon}_{yx}h|_{\text{lft}}}{\Delta y} \right] \right\}. \quad (12.30)$$

Here, the symbols  $|_{\text{dwn}}$ ,  $|_{\text{up}}$ ,  $|_{\text{rgt}}$ , and  $|_{\text{lft}}$  refer, respectively, to the downglacier and upglacier ends, and to the left and right sides (looking downglacier), of a “block” of the glacier of length  $\Delta x$  and width  $\Delta y$ . The second term on the right represents the contribution to  $\tau_b$  of an imbalance in forces on the ends of the block, while the third represents the contribution of forces on the sides.

An example of an application of this procedure is provided by an experiment conducted on Storglaciären, Sweden (Hooke *et al.*, 1989). Some stakes on the glacier surface (Figure 12.9) were surveyed frequently between 1982 and 1985 to determine velocities (Figure 12.10). The pattern of stakes was such that longitudinal and transverse strain rates could be calculated at the upglacier and downglacier ends of the “blocks” labeled **A** and **B** in Figure 12.9, and shear strain rates could be calculated along the sides. Results of the calculations for six time periods are shown in Table 12.1. One time period represents mean winter conditions;  $\tau_b$  was then  $-82$  kPa beneath block **A** and  $-92$  kPa beneath block **B**. The other five time periods were those during which high velocity events occurred (Figure 12.10). During these events,  $\tau_b$  was reduced an average of nearly 30% beneath block **A**. Beneath block **B** the change in  $\tau_b$  was more variable, but significant increases occurred during two events.

Study of the patterns of changes suggests that acceleration of block **A** was, in every case, accompanied by an increase in magnitude of Term 2 (the second term on the right in Equation 12.30). From the strain rate data, it can be seen that at the upglacier end of the block,  $\dot{\varepsilon}_{xx}$  became less compressive, and in two cases, even extending, while at the downglacier end it became more compressive in all but one case. Thus, the accelerations were not due to either push from upglacier or pull from downglacier. The clear implication is that this pattern of changes in strain rate was a result of a reduction in resistive drag at the bed, presumably induced by increases in water pressure.

In the case of block **B**, the strain-rate data indicate that the marked change in Term 2 reflects push from upglacier and, in the case of the June 1984 event, pull from downglacier. This combination of push and pull resulted in higher strain rates in the basal ice, and hence, owing to the proportionality between stress and strain rate, in higher basal drag.

Because we assumed that strain rates are uniform over the sides and ends of the blocks, and also owing to other uncertainties in the calculations, the values of  $\tau_b$  obtained are only estimates. However, as the errors are probably of comparable magnitude and sign in all calculations, the direction and approximate magnitude of the *changes* in  $\tau_b$  are probably reliable. These calculations thus help us understand

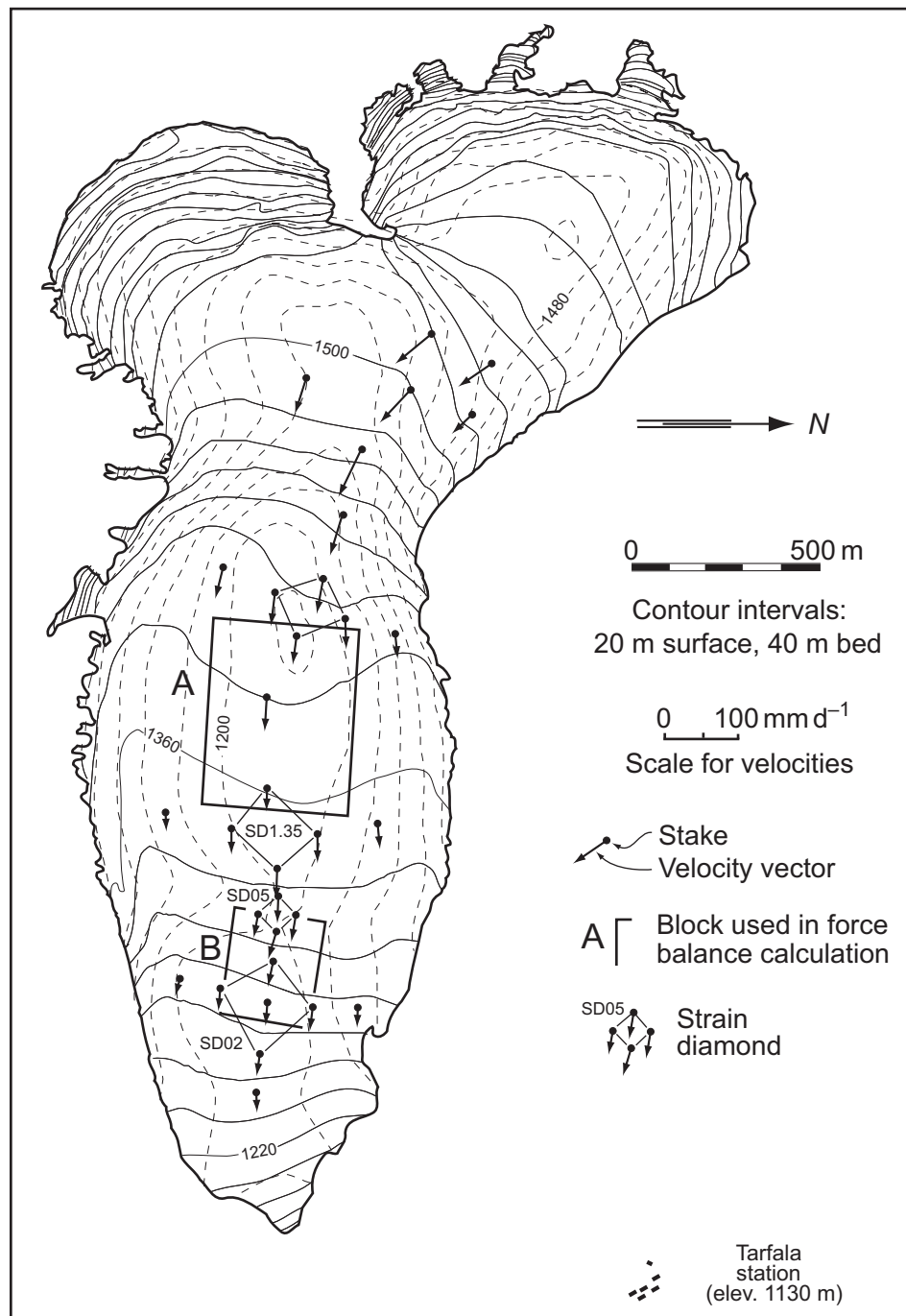


**Figure 12.9** Map of Storglaciären showing generalized surface and bed topography (solid and dashed contours, respectively), locations of stakes used for velocity measurements, velocities, and blocks used in force balance calculations. (Data from Hooke *et al.*, 1989, Figure 1a. Base map courtesy of Peter Jansson)

**Table 12.1** Force balance calculations

Time	$\dot{\varepsilon}_{xx}$ (up) $a^{-1}$	$\dot{\varepsilon}_{xx}$ (dwn) $a^{-1}$	Term 2 * kPa	Term 3 * kPa	$\tau_b$ , kPa	$\Delta\tau_b$ , %
Block A						
Winter	-0.016	-0.004	1	-34	-82	-
July 1983	0.001	-0.005	-25	-38	-52	-37
July 1983	-0.006	-0.011	-17	-36	-62	-24
May 1984	-0.008	-0.018	-19	-38	-58	-29
June 1984	0.001	-0.002	-26	-40	-49	-40
June 1985	-0.010	-0.007	-7	-38	-69	-16
Block B						
Winter	0.006	-0.008	-28	-25	-92	-
July 1983	Data incomplete					
July 1983	Data incomplete					
May 1984	0.000	-0.053	-23	-31	-91	-1
June 1984	-0.002	0.037	40	-15	-170	+84
June 1985	-0.002	-0.002	9	-25	-129	+40

$\rho gh\alpha$  was 115 kPa beneath block A and 145 kPa beneath block B.

\* Terms 2 and 3 are the second and third terms on the right hand side of Equation (12.30), the longitudinal and transverse terms, respectively.

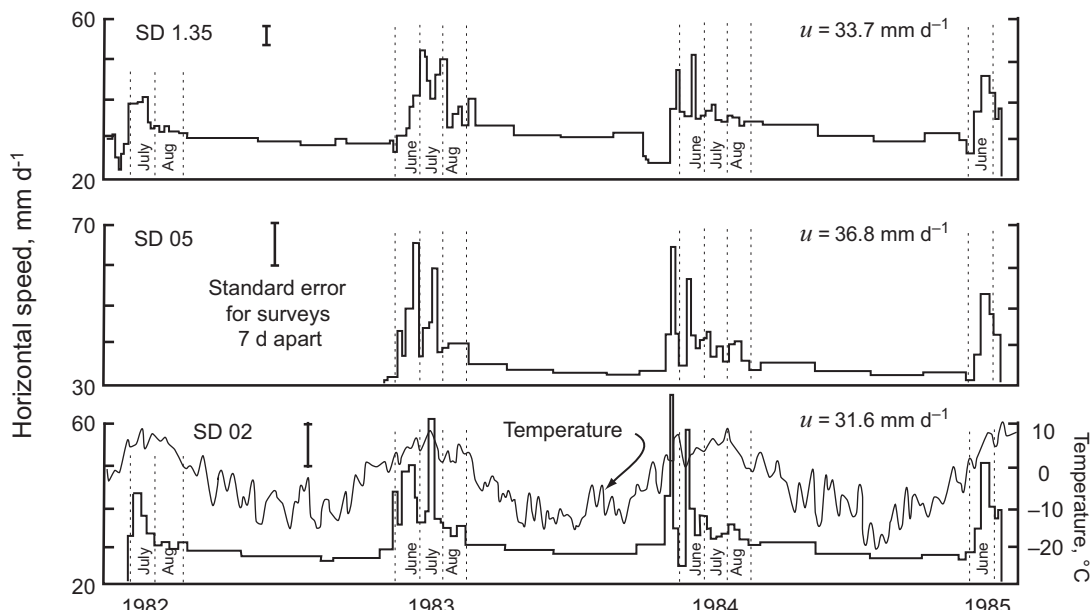


**Figure 12.10** Time series of mean horizontal velocities of the three strain diamonds (SD) shown in Figure 12.9. Velocities are averages of those of the four (or five) stakes in each diamond. Mean daily temperature, smoothed using a 5-day running mean, is shown in the bottom panel. (Modified from Hooke *et al.*, 1989, Figure 3a. Reproduced with permission of the International Glaciological Society)

the mechanisms by which the accelerations took place in these instances. Through such analyses, we can gain insight into spatial and temporal variations in factors controlling the velocity of a glacier.

## Longitudinal coupling

Our straightforward application of the flow law to calculate velocity profiles and the depth-averaged velocity (Equations 5.16 and 5.18) ignores longitudinal stress gradients such as those we just examined. If one uses local values of  $h$  ( $= H$  in Equations 5.16 and 5.18) and  $\alpha$  to calculate  $u_s$ , the longitudinal variation obtained may differ wildly from the actual one (Figure 12.11). To avoid this, it is commonly recommended that one use a surface slope averaged over a distance corresponding to one or more ice thicknesses in such calculations.

This problem has been studied in greater detail by Budd (1968, 1970), Collins (1968), Nye (1969b), Hutter (1981), Whillans and Johnsen (1983), and in a series of four papers by Barclay Kamb and Keith Echelmeyer, of which we will focus on one (Kamb and Echelmeyer, 1986). In plane strain,  $\sigma'_{yy} = \sigma'_{xy} = \sigma'_{yx} = 0$ , so Equation (12.28) becomes:

$$2 \int_b^s \frac{d\sigma'_{xx}}{dx} dz + \tau_b - \rho g h \alpha = 0$$

in which the limits of integration are now taken to be from the bed to the surface and, as  $\sigma'_{xx}$  varies only in the  $x$ -direction, the derivatives are no longer partial.

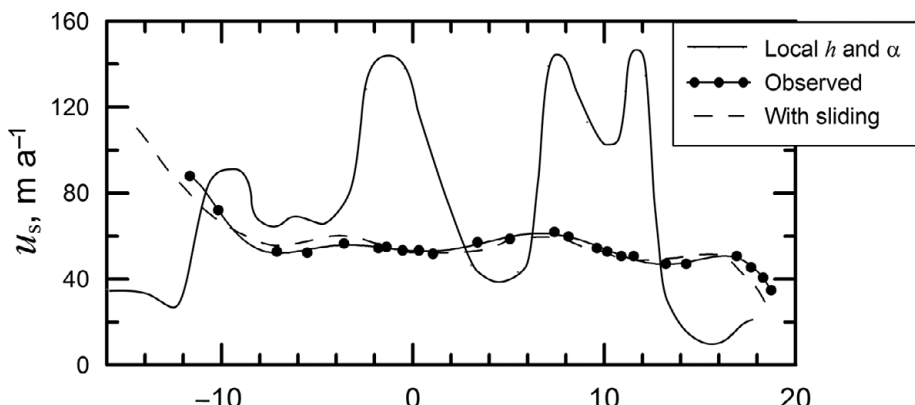


**Figure 12.11** Longitudinal variation in  $u_s$  on Blue Glacier, Washington, USA (see Figure 14.8 for map of glacier). Light solid line shows  $u_s$  calculated from local values of  $h$  and  $\alpha$ . Heavy solid line and dots show observed  $u_s$ . Dashed line shows calculated variations using longitudinal averaging of  $h$  and  $\alpha$ , and including sliding. (Modified from Kamb and Echelmeyer, 1986, Figure 11. Reproduced with permission of the International Glaciological Society)

Reversing the order of differentiation and integration in the first term and noting that the depth-averaged longitudinal stress is, by definition:

$$\bar{\sigma}'_{xx} = \frac{1}{h} \int_b^s \sigma'_{xx} dz$$

yields:

$$2 \frac{d}{dx} (h \bar{\sigma}'_{xx}) + \tau_b - \rho g h \alpha = 0. \quad (12.31)$$

Using the flow law we can write (see Equation 9.29 and discussion following Equation 9.31):

$$\sigma'_{xx} = 2\eta \frac{\partial u}{\partial x} \quad \text{where } 2\eta = \frac{1}{\lambda} = \frac{1}{A\sigma^{n-1}}. \quad (12.32)$$

Kamb and Echelmeyer now introduce a depth-averaged viscosity,  $\bar{\eta}(x)$ , which is related to the velocity gradient,  $d\bar{u}/dx$ , by:

$$\bar{\eta} \frac{d\bar{u}}{dx} = \frac{1}{h} \int_b^s \eta(z) \frac{\partial u}{\partial x} dz. \quad (12.33)$$

In the absence of sliding, Equation (5.19) becomes:

$$\bar{u} = \frac{2A}{n+2} h (S_f \rho g h \alpha)^n = c h \tau_b^n \quad (12.34)$$

in which  $c$  is a constant. Using Equations (12.32), (12.33), and (12.34) in Equation (12.31) yields:

$$4 \frac{d}{dx} \left[ h \bar{\eta}(z) \frac{d\bar{u}}{dx} \right] + \left[ \frac{\bar{u}}{ch} \right]^{\frac{1}{n}} - \rho g h \alpha = 0. \quad (12.35)$$

Kamb and Echelmeyer call this the *non-linear longitudinal flow coupling equation*. They linearize it by considering a datum state in which  $\alpha = \alpha_o$  and  $h = h_o$ , and perturbations from that datum state,  $\delta\alpha$  and  $\delta h$ , so  $\alpha = \alpha_o + \delta\alpha$  and  $h = h_o + \delta h$ . The flow perturbation resulting from these perturbations in  $\alpha$  and  $h$  is:  $v = \frac{\bar{u} - \bar{u}_o}{\bar{u}_o}$ . Here,  $\bar{u}_o$  is the depth-averaged velocity in a glacier consisting of a uniform slab of ice with constant  $h$  and  $\alpha$ , and  $\bar{u}$  is the actual depth-averaged velocity at  $x$ , given the variable  $h$  and  $\alpha$  in the vicinity of  $x$ . Using these,  $(\bar{u}/h)^{1/n}$  in the second term in Equation (12.35) becomes:

$$\left[ \frac{\bar{u}}{h} \right]^{\frac{1}{n}} = \left[ \frac{\bar{u}_o}{h_o} \right]^{\frac{1}{n}} \left[ 1 + \frac{1}{n} \left( v - \frac{\delta h}{h_o} \right) \right]. \quad (12.36)$$

{To show this, express  $[\bar{u}/h]^{\frac{1}{n}}$  in a Taylor series,  $f(x) = f(a) + f'(a)(x - a) + \dots$ , where  $f(x)$  is  $[\bar{u}/h]^{\frac{1}{n}}$ ,  $a$  is the datum state ( $\bar{u}_o/h_o$ ), and  $f'$  is the first derivative, and

make use of the fact that since the perturbation is infinitesimal,  $\delta h \ll h$ .} Then, using this in Equation (12.35) and noting that  $\bar{u} = \bar{u}_o(v + 1)$  so  $d\bar{u}/dx = \bar{u}_o(dv/dx)$ , and that  $\bar{u}_o = ch_o\tau_b^n$  (Equation 12.34), Equation (12.35) becomes:

$$4\bar{u}_o \frac{d}{dx} \left[ h\bar{\eta} \frac{dv}{dx} \right] + \tau_b \left[ \frac{h_o}{u_o} \right]^{\frac{1}{n}} \left[ \frac{u_o}{h_o} \right]^{\frac{1}{n}} \left[ 1 + \frac{1}{n} \left( v - \frac{\delta h}{h_o} \right) \right] - \rho g h \alpha = 0.$$

As  $\tau_b = \tau_o = \rho g h_o \alpha_o$ , this becomes:

$$4\bar{u}_o \frac{d}{dx} \left[ h\bar{\eta} \frac{dv}{dx} \right] + \tau_o + \frac{\tau_o}{n} v - \frac{\rho g \alpha_o}{n} \delta h = \rho g h \alpha.$$

Taking the derivative in the first term, multiplying by  $n/\tau_o$ , and defining  $\delta(h\alpha) = h\alpha - h_o\alpha_o$  yields:

$$\frac{4n\bar{u}_o}{\tau_o} \left[ h\bar{\eta} \frac{d^2v}{dx^2} + \frac{dv}{dx} \frac{d(h\bar{\eta})}{dx} \right] + v = \frac{n\delta(h\alpha)}{h_o\alpha_o} + \frac{\delta h}{h_o}.$$

Now defining:  $l = \sqrt{4n\bar{u}_o h\bar{\eta}/\tau_o}$ , making use of the fact that  $h\alpha \approx h_o\alpha_o$ , noting that, from basic calculus,  $d \ln(x) = \frac{dx}{x}$ , and defining:

$$2\gamma = l \frac{d}{dx} \ln(h\bar{\eta}) = l \frac{1}{h\bar{\eta}} \frac{d(h\bar{\eta})}{dx}$$

we obtain:

$$l^2 \frac{d^2v}{dx^2} + 2\gamma l \frac{dv}{dx} + v = n\delta \ln(h\alpha) + \delta \ln(h) = \delta \ln(\alpha^n h^{n+1}). \quad (12.37)$$

Kamb and Echelmeyer (1986) refer to this as the *linearized longitudinal flow-coupling equation*, and call  $l$  the *longitudinal coupling length*. To illustrate the role of  $l$ , they solve Equation (12.37) for the simplified case in which  $l$  is constant, independent of  $x$ , and  $\gamma$  can be neglected. The solution is:

$$\frac{\bar{u}(x) - \bar{u}_o}{\bar{u}_o} = \int_{-\infty}^{\infty} \delta \ln(\alpha^n h^{n+1}) W(x') dx'. \quad (12.38)$$

Here,  $\delta \ln(\alpha^n h^{n+1}) = \ln(\alpha^n h^{n+1}) - \ln(\alpha_o^n h_o^{n+1})$ ,  $x'$  is a location some distance,  $|x' - x|$ , from  $x$  (Figure 12.12b), and  $W(x') = \frac{\epsilon}{2l} e^{-\frac{|x'-x|}{l}}$ . In the term  $\ln(\alpha^n h^{n+1})$ ,  $\alpha$  and  $h$  are evaluated at  $x'$ .  $W(x')$  is a weighting function (Figure 12.12a) that causes locations further from  $x$  to have exponentially less influence on  $\bar{u}(x)$ .  $\epsilon$  is chosen such that  $\int_{-2l}^{2l} W dx = 1$ .

---

\* This is identical to Kamb and Echelmeyer's Equation (13), apart from some differences in sign attributable to the fact that our z-axis is directed downward whereas theirs is directed upwards.

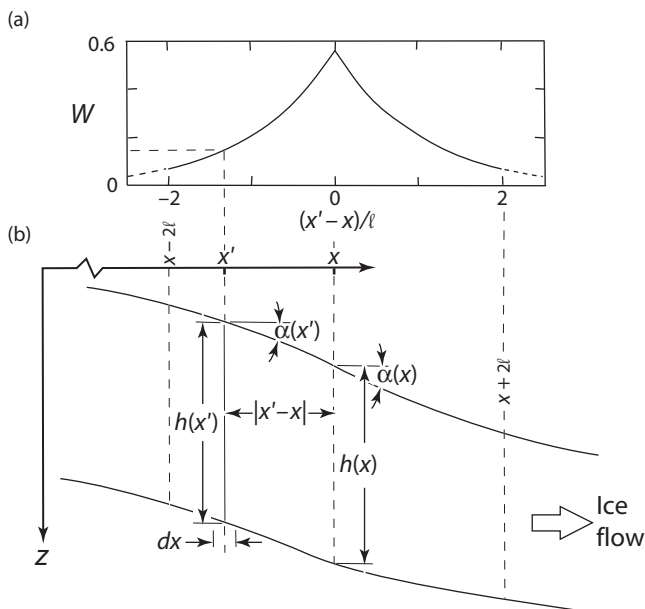


**Figure 12.12** (a) Weighting function used in longitudinal averaging in Figure 12.11. (b) Graphical depiction of Equation 12.38. ((a) is modified from Kamb and Echelmeyer, 1986, Figure 2. Reproduced with permission of the International Glaciological Society)

Equation (12.38) says that the depth-averaged velocity at location  $x$  is affected by the sum of effects at locations  $x'$ . The integration, extending from  $-\infty$  to  $\infty$ , is obviously impractical on a glacier of finite length, but owing to the exponential decay of  $W$  with increasing  $x'$ , the effect of perturbations in excess of  $2l$  from  $x$  can be neglected, so the integration can be limited to the interval  $-2l$  to  $2l$ .

To compare their theory with field data from Blue Glacier, Kamb and Echelmeyer (1986) choose a location  $x$  on the glacier and divide the section of the glacier between  $x - 2l$  and  $x + 2l$  into a number of segments of length  $dx$  (Figure 12.12b). They then evaluate  $\alpha$  and  $h$  at the midpoint of each segment, calculate  $\delta \ln(\alpha^n h^{n+1})$  for that  $x$ , multiply it by the appropriate value of  $W$  ( $\sim 0.16$  for the example  $x'$  in Figure 12.12a), and then sum the values for all segments (multiplied by  $dx'$ ). They find that they can get a fairly good match to the observed velocities if they let  $l = l(x)$  and allow  $u_b \neq 0$  (Figure 12.11).

Two characteristics of this solution merit emphasis: (i) the flow is influenced by perturbations in *both* slope and thickness, as one might well imagine would be mechanically reasonable, and (ii) the influence at  $x$  drops off exponentially with distance from  $x$ . These characteristics contrast with the common practice of using *only* slope, and of simply averaging it over a distance equivalent to one or more ice thicknesses.

## Analysis of borehole-deformation data

Our next example is drawn from the work of Shreve and Sharp (1970) and deals with the analysis of inclinometry data collected in boreholes that are undergoing deformation. In the simplest case, we might assume that at depth  $d$ ,  $\sigma_{zx} = S_f \rho g d \alpha$ , and that successive measurements of the inclination of a borehole would give  $\partial u / \partial z$ . Then  $\dot{\epsilon}_{zx} = \frac{1}{2} (\partial u / \partial z + \partial w / \partial x)$  and, if the deformation is entirely simple shear,  $\partial w / \partial x = 0$ . Thus, measurements of the change in inclination at several depths would permit a (double log) plot of  $\sigma_{zx}$  versus  $\dot{\epsilon}_{zx}$  and, if other stresses and strain rates were negligible, the slope and intercept of the resulting line could be used to obtain  $n$  and  $A$ , respectively. Such an approach would be valid if the borehole were in a slab of ice of uniform thickness and infinite horizontal extent on a constant slope. In other cases, non-zero vertical velocities and (or) longitudinal strain rates could result in errors.

Figure 12.13 illustrates the effect of the longitudinal strain rate on a borehole. In a zone of longitudinal extension, the inclination of a hole that is inclined with respect to the direction of extension will increase, and conversely, even if there is no shear strain. Nye (1957) realized this and made a correction for this effect in his reanalysis of the Jungfraufirn borehole experiment. However, it was Shreve (Shreve and Sharp, 1970) who undertook the first complete study of the problem.

We start by looking at the difference in velocity between two points in a borehole from the point of view of motion of the ice. This is what we want to determine from the inclinometry measurements. The axes are as shown in Figure 12.14. Direction cosines describing the orientation of the borehole are  $\ell_i$  ( $i = x, y, z$ ), and  $d\lambda$  is an increment of length along the hole. Two points in the hole a distance  $d\lambda$  apart will be separated from one another by distances  $\ell_i d\lambda$  in the  $i$ -direction (Figure 12.15). The

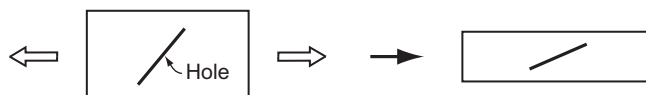


Figure 12.13 Effect of extending longitudinal strain on an inclined borehole.

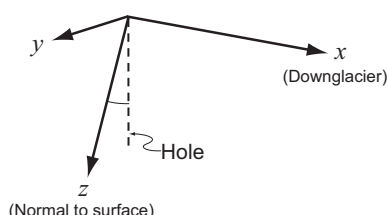
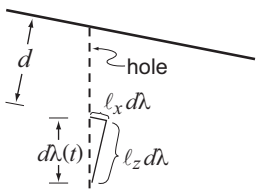
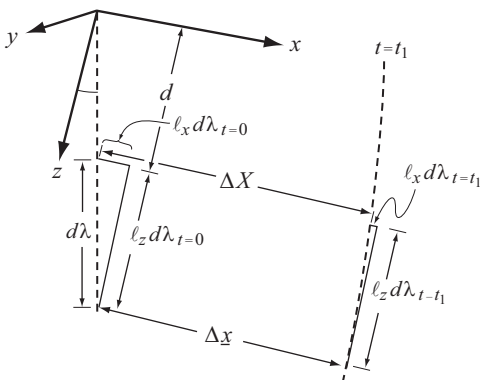


Figure 12.14 Coordinate system used for analysis of borehole deformation.



**Figure 12.15** Distance between two points in a borehole expressed in terms of the direction cosines of the hole.



**Figure 12.16** Deformation of a section of a borehole through time.

difference in the  $u_i$  velocity at depth  $(d + \ell_z d\lambda)$  and that at depth  $d$  is  $du_i^\lambda$ . This is given by

$$du_i^\lambda = \ell_x \frac{\partial u_i}{\partial x} d\lambda + \ell_y \frac{\partial u_i}{\partial y} d\lambda + \ell_z \frac{\partial u_i}{\partial z} d\lambda.$$

The first term on the right is the change in  $u_i$  as a result of moving a distance  $\ell_x d\lambda$  in the  $x$ -direction, and so forth. Using the summation convention, this can be written:

$$du_i^\lambda = \ell_j \frac{\partial u_i}{\partial x_j} d\lambda. \quad (12.39)$$

Now consider motion of the borehole at a constant elevation above some datum. We again consider the difference in velocity between points a distance  $d\lambda$  apart (Figure 12.16). In time  $\Delta t$  a point at depth  $d$  moves a distance  $\Delta X$ , and a point at depth  $(d + \ell_z d\lambda)$  moves a distance  $\Delta x$ . The inclinometry measurements, when combined with an accurate survey of the motion of the hole top, provide us with these distances. If  $\Delta u^\lambda$  is the difference in velocity between the two points, we have:

$$\Delta u^\lambda \Delta t = \Delta X - \Delta x = u_{(d)} \Delta t + [\ell_x d\lambda_{t=t_1} - \ell_x d\lambda_{t=0}].$$

where  $u = u_x$ , the  $x$ -component of the velocity, and  $u_{(d)}$  is the value of  $u$  at depth  $d$ . The quantity in brackets represents the length  $\Delta x$ ; that is, it is the length  $\Delta X$  plus the

displacement, in the  $x$ -direction, of the upper point with respect to the lower one at time  $t = t_1$  minus this displacement at time  $t = 0$  (Figure 12.16). Including the changes in  $\ell_x d\lambda$  in the  $y$ - and  $z$ -directions, allowing for a change in  $\ell_x d\lambda$  with time (unsteady flow), and expressing the result in differential form yields

$$du^\lambda \Delta t = \frac{\partial \ell_x d\lambda}{\partial x} u \Delta t + \frac{\partial \ell_x d\lambda}{\partial y} v \Delta t + \frac{\partial \ell_x d\lambda}{\partial z} w \Delta t + \frac{\partial \ell_x d\lambda}{\partial t} \Delta t.$$

Here, the derivative with respect to  $x$  in the first term on the right is the change of  $\ell_x d\lambda$  over a short distance in the  $x$ -direction, and  $u \Delta t$  gives the magnitude of this distance, and so forth. Dividing by  $\Delta t$  and using the summation convention, we obtain

$$du_i^\lambda = u_j \frac{\partial \ell_i d\lambda}{\partial x_j} + \frac{\partial \ell_i d\lambda}{\partial t} = \frac{D}{Dt} (\ell_i d\lambda) \quad (12.40)$$

where  $D/Dt$  is the substantial or Lagrangian derivative (see Equation 6.12).

Equations (12.39) and (12.40) are both expressions for  $du_i^\lambda$ , the difference in velocity between two points a distance  $d\lambda$  apart along the hole, so equating them yields

$$\ell_j \frac{\partial u_i}{\partial x_j} d\lambda = \frac{D}{Dt} (\ell_i d\lambda) = \ell_i \frac{D}{Dt} d\lambda + \frac{D \ell_i}{Dt} d\lambda. \quad (12.41)$$

We would like to divide by  $d\lambda$  to eliminate it from the first and last terms, but first we need an expression for  $D(d\lambda)/Dt$ . To obtain this, multiply both sides by  $\ell_i$ :

$$\ell_i \ell_j \frac{\partial u_i}{\partial x_j} d\lambda = \ell_i \ell_i \frac{D}{Dt} d\lambda + \ell_i \frac{D \ell_i}{Dt} d\lambda.$$

Because the sum of the squares of the direction cosines is unity,  $\ell_i \ell_i = 1$ . Thus, the last term on the right becomes:

$$\ell_i \frac{D \ell_i}{Dt} = \frac{1}{2} \frac{D}{Dt} (\ell_i \ell_i) = \frac{1}{2} \frac{D}{Dt} (1) = 0.$$

Thus,

$$\frac{D}{Dt} d\lambda = \ell_i \ell_j \frac{\partial u_i}{\partial x_j} d\lambda. \quad (12.42)$$

Equations (12.41) and (12.42) can be combined to yield the desired expression. However, we need to be careful of the subscripts when doing this. Expanding Equation (12.41) for  $i=x$  (so  $u_x = u$ ) and dividing by  $d\lambda$  yields

$$\ell_x \frac{\partial u}{\partial x} + \ell_y \frac{\partial u}{\partial y} + \ell_z \frac{\partial u}{\partial z} = \frac{1}{d\lambda} \ell_x \frac{D}{Dt} d\lambda + u \frac{\partial \ell_x}{\partial x} + v \frac{\partial \ell_x}{\partial y} + w \frac{\partial \ell_x}{\partial z} + \frac{\partial \ell_x}{\partial t}. \quad (12.43)$$

Because the inclination of the borehole at any given time is a function of  $z$  alone,  $\partial \ell_x / \partial x = \partial \ell_x / \partial y = 0$ . Expanding the right hand side of Equation (12.42), using the

result to replace the term involving  $D(d\lambda)/Dt$  in Equation (12.43), and rearranging terms, we obtain:

$$\begin{aligned} \ell_x \frac{\partial u}{\partial x} + \ell_y \frac{\partial u}{\partial y} + \ell_z \frac{\partial u}{\partial z} - \ell_x \ell_x \ell_x \frac{\partial u}{\partial x} + \ell_x \ell_x \ell_y \frac{\partial u}{\partial y} + \ell_x \ell_x \ell_z \frac{\partial u}{\partial z} \\ - \ell_x \ell_y \ell_x \frac{\partial v}{\partial x} + \ell_x \ell_y \ell_y \frac{\partial v}{\partial y} + \ell_x \ell_y \ell_z \frac{\partial v}{\partial z} \\ - \ell_x \ell_z \ell_x \frac{\partial w}{\partial x} + \ell_x \ell_z \ell_y \frac{\partial w}{\partial y} + \ell_x \ell_z \ell_z \frac{\partial w}{\partial z} = w \frac{\partial \ell_x}{\partial z} + \frac{\partial \ell_x}{\partial t}. \end{aligned} \quad (12.44)$$

Using the summation convention, this can be written as

$$\ell_k \frac{\partial u_i}{\partial x_k} - \ell_i \ell_j \ell_k \frac{\partial u_j}{\partial x_k} = w \frac{\partial \ell_i}{\partial z} + \frac{\partial \ell_i}{\partial t}$$

or even more compactly as

$$(\delta_{ij} - \ell_i \ell_j) \ell_k \frac{\partial u_j}{\partial x_k} = w \frac{\partial \ell_i}{\partial z} + \frac{\partial \ell_i}{\partial t}. \quad (12.45)$$

Because  $i$  is not repeated in any of the terms in Equation (12.45), this equation represents three separate equations (for  $i=x, y, z$ ). However, only two of these equations are independent because only two of the direction cosines are independent.

Thus, for studies of the flow law, although  $\partial u/\partial z$  is clearly one of the most important velocity derivatives, measurements of the rate of tilting of the borehole do not give it directly, contrary to what might be one's initial thought. However, if the inclination of a hole is known at two separate times, and if seven of the nine velocity derivatives in Equation (12.44) can be measured or estimated, Equations (12.45) can be solved for the two remaining velocity derivatives, of which  $\partial u/\partial z$  is one. Equations (12.45) are exact, but approximations have to be made in calculating the  $\ell_i, \partial \ell_i/\partial z$ , and  $\partial \ell_i/\partial t$  from observational data that are obtained at discrete points in time and space.

In one approach to this problem in a field experiment on Barnes Ice Cap (Hooke and Hanson, 1986), strain nets around the tops of the boreholes were used to determine  $\partial u/\partial x$ ,  $\partial v/\partial y$ ,  $\partial w/\partial x$ ,  $\partial w/\partial y$ , and  $\dot{\epsilon}_{xy}$  at the surface, and these were assumed to decrease with depth in proportion to the measured decrease in  $u$  with depth. Then  $\partial w/\partial z = -\partial u/\partial x - \partial v/\partial y$  by continuity (Equation 2.5), and  $\partial v/\partial x = 2\dot{\epsilon}_{xy} - \partial u/\partial y$  by definition (Equation 2.6a).  $\partial u/\partial y$  was obtained from measured  $u$  at the surface and the curvature of the flowline.  $\partial u/\partial z$  and  $\partial v/\partial z$  were then calculated from Equations (12.45).

Sensitivity studies suggest that this solution does not depend strongly on the assumptions. The most important term is  $\partial \ell_i/\partial t$ . In places where the inclination of the borehole changes abruptly,  $w \partial \ell_i/\partial z$  also becomes important. In experiments on other glaciers, the results might be more sensitive to some of the other velocity

derivatives, and hence to any assumptions made in obtaining them. However, Dahl-Jensen and Gundestrup (1987), in an analysis of a deep borehole at Dye 3 in Greenland, found that the flow approximated plane strain and that  $\partial u/\partial x$ ,  $w$ , and  $\partial \ell_i/\partial z$  were small enough that neglecting them resulted in errors of <2%.

A weakness of approaches like this is that some assumption must be made about the depth dependence of many of the velocity derivatives. In an ideal world, one would have three boreholes in a triangular array, so these velocity derivatives could be measured directly.

Further insight into Equation (12.45) can be realized by considering the situation in plane strain. Assuming incompressible flow and a uniform longitudinal strain rate,  $r$ , that is independent of depth, we then have  $\partial u/\partial x = -\partial w/\partial z = r$ ,  $\partial w/\partial x = 0$ ,  $\ell_x = \sin \theta$ ,  $\ell_z = \cos \theta$ , and  $\ell_y = 0$ , where  $\theta$  is the inclination of the borehole from the vertical. Equation (12.45) then reduces to

$$\frac{\partial u}{\partial z} = \frac{\partial}{\partial t} \tan \theta - 2r \tan \theta + w \frac{\partial}{\partial z} \tan \theta. \quad (12.46)$$

The first term on the right is the obvious one, involving a change in inclination of the borehole with time. The second is the one illustrated in Figure 12.13 and discussed earlier. The third is an advection effect. In an area of non-zero vertical velocity, a section of a borehole at depth  $z_2$ , measured with respect to some constant datum, and with inclination  $\ell_{i(d=z_2)}$  will, at the end of a time interval  $\Delta t$ , be at, say, depth  $z_1$  (Figure 12.17). If the initial inclination of the borehole at depth  $z_1$  was different from  $\ell_{i(d=z_2)}$ , our measurements would show that the inclination at depth  $z_1$  had changed, and this would be true even if  $\partial u/\partial z$  were 0. This is why  $w\partial \ell_i/\partial z$  becomes important in places where the borehole inclination changes rapidly with depth, as just mentioned.

The borehole deformation experiment on Barnes Ice Cap mentioned above was used to estimate the flow law parameters,  $n$  and  $A$ . Four boreholes, located approximately along a flowline, were drilled and inclinometry data were obtained from them over a period of up to 4 years. Figure 12.18 shows the location of two of the holes. Figure 12.19 shows the deformation profiles from these holes and profiles of  $\partial u/\partial z$  calculated from Equations (12.45).

The deformation profile in hole T061 ends at the top of a zone of white ice (Figure 12.18), while that in hole T0975 is largely in this white ice. Oxygen isotope

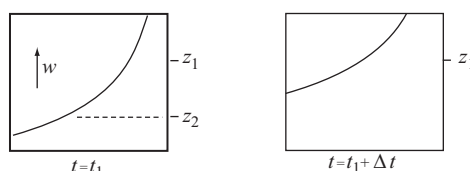
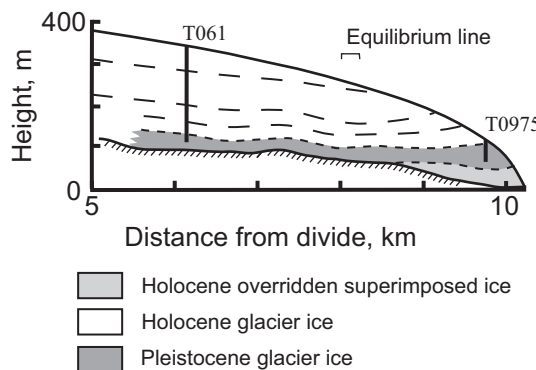


Figure 12.17 Effect of vertical advection on borehole inclination.



**Figure 12.18** Longitudinal section along the downglacier half of a flowline on Barnes Ice Cap showing boreholes T061 and T0975. The deformed superimposed ice near the margin was overridden during an advance of the glacier (see Figure 5.17). (After Hooke and Hanson, 1986, Figure 2. Reproduced with permission of Elsevier Science)

data demonstrate that this ice is of Pleistocene age (Hooke and Clausen, 1982). The ice is white because it contains abundant air bubbles that reduce its density to  $\sim 870 \text{ kg m}^{-3}$ . The density of the overlying blue ice is  $\sim 920 \text{ kg m}^{-3}$ . The high concentration of air bubbles is likely a result of two processes:

1. When the climate warmed at the end of the Pleistocene, meltwater percolation increased, and ice lenses formed. These lenses trapped air in the underlying porous firn.
2. As basal meltwater escaped into the underlying permeable bedrock, air may have been left behind in a physical fractionation process.

As noted in Chapter 11 (p. 313–314), it is commonly found that such Pleistocene ice is softer than Holocene ice, apparently because impurities lead to smaller grain sizes that then develop strong single-maximum fabrics (Paterson, 1991). The high shear strain rate implied by the dotted extrapolation of the deformation profile in hole T061 in Figure 12.19a is indicative of this weakening. The value of  $A$  obtained for this ice from the deformation profile in hole T0975 is  $1000 \text{ MPa}^{-3} \text{ a}^{-1}$  (at  $-10.1^\circ\text{C}$ ), which is much higher than those ranging from 40 to  $80 \text{ MPa}^{-3} \text{ a}^{-1}$  in the overlying blue Holocene ice in hole T061 and also much higher than other experimental values at this temperature (Figure 12.5).

Also of interest are the values of a parameter  $\Lambda$ , defined by (see Equations 2.17 and 9.29)

$$2\Lambda = \frac{1}{\lambda} = \frac{\sigma'_{zx}}{\dot{\varepsilon}_{zx}} = \frac{1}{\dot{\varepsilon}} \left( \frac{\dot{\varepsilon}}{A} \right)^{1/n}. \quad (12.47)$$

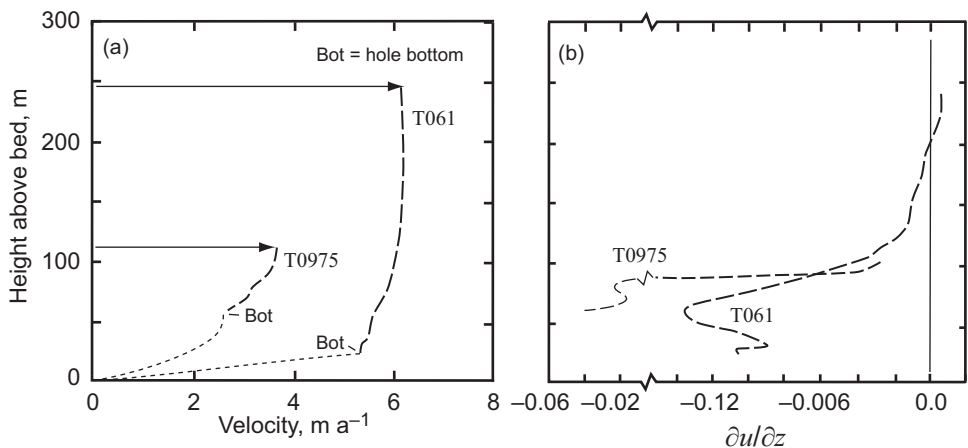


**Figure 12.19** (a) Velocity profiles in boreholes T061 and T0975; and (b)  $\partial u / \partial z$  as a function of depth. (After Hooke and Hanson, 1986, Figure 3. Reproduced with permission of Elsevier Science)

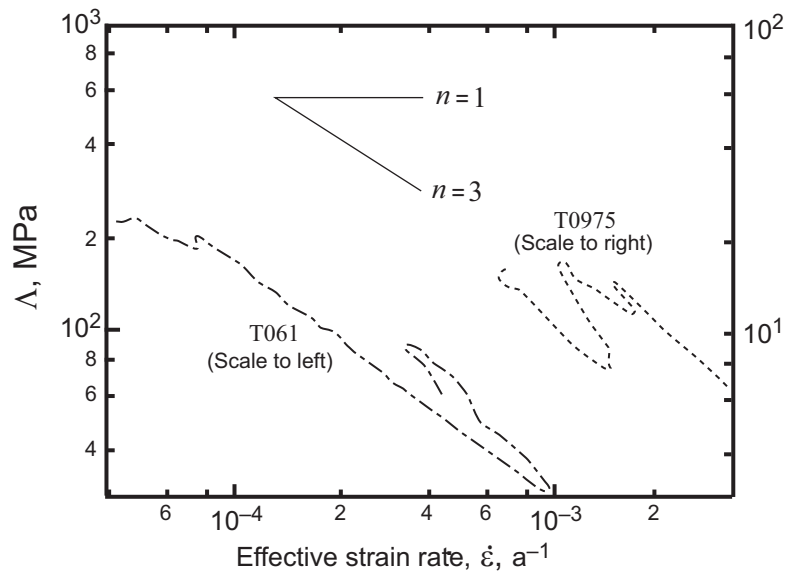


**Figure 12.20** Effective strain rate,  $\dot{\varepsilon}$ , plotted against  $\Lambda$  for the lower parts of holes T061 and T0975. Depth increases from upper left, following the lines. Reversals in trends reflect hardening of ice in zones where ice fabric is changing. (After Hooke and Hanson, 1986, Figure 4. Reproduced with the kind permission of Elsevier Science)

$\dot{\varepsilon}_{zx}$  is obtained from the velocity derivatives using Equation (9.21), while  $\sigma_{zx}$  is estimated with the use of

$$\sigma_{zx} = \rho g h \alpha - \frac{\partial}{\partial x} \int_0^z \frac{1}{\dot{\varepsilon}_e} \left( \frac{\dot{\varepsilon}_e}{A} \right)^{\frac{1}{n}} (2\dot{\varepsilon}_{xx} + \dot{\varepsilon}_{yy}) dz + T \quad (12.48)$$

which is derived from Equation (12.26) in much the same way that we derived Equation (12.29), except that we now retain the  $T$  term and also assume that changes in the transverse direction are negligible in an ice cap. Equation (12.27) was used to evaluate the  $T$  term. If  $A$  and  $n$  are constant, as might be expected,  $\Lambda$  should vary inversely with  $\dot{\epsilon}$ . The awkward fact is that near the surface, where  $\dot{\epsilon}_{zx}$  is low,  $\Lambda$  is independent of  $\dot{\epsilon}$  (Hooke and Hanson, 1986, Figure 4a). This problem is not unique to Barnes Ice Cap; Raymond (1973) also found that  $\Lambda$  was independent of  $\dot{\epsilon}$  near the surface of Athabasca Glacier.

Somewhat deeper in the glacier the situation improves, and  $\Lambda$  decreases steadily with increasing  $\dot{\epsilon}$  (Figure 12.20). Here, Equation (12.47) could be used to determine the values of  $A$  mentioned above.

---

## SUMMARY

In this chapter we've studied four classical problems in glacier mechanics: closure of cylindrical holes, calculation of force balances, longitudinal stress coupling, and deformation of boreholes. As examples of applications of these, we discussed problems such as the flow of water to, from, and in subglacial conduits, the mechanics of summer accelerations of glaciers, the distance over which  $\alpha$  must be averaged when calculating velocity profiles, and the extraction of flow-law parameters from borehole deformation data. From these examples, we gained insights into the dynamic and kinematic behavior of glaciers. These, however, were secondary objectives.

The primary objective of the chapter was to help students develop facility with the mathematics of stress and deformation as applied to problems in glacier mechanics. Such analyses are complicated because multiple stresses, strains, and strain rates are involved, and even more so because the strains in which we are interested are a consequence of deviatoric, not total stresses. In many cases, once the physics of a problem have been formulated, prescribed mathematical procedures must be followed before a result with clear physical significance reappears. Students who have mastered the material in this chapter will be able to understand many papers in the glaciological literature that would otherwise be impenetrable.

# 13

## Ice streams and ice shelves

Ice streams and ice shelves have been mentioned in previous chapters. Let's now take a closer look at these features.

Ice streams (and some outlet glaciers) merge into ice shelves. The ice shelves exert back stresses that impede this flow. When ice shelves thin or collapse, these back stresses are reduced or eliminated, the ice streams and outlet glaciers accelerate, and the transfer of inland ice to the sea increases. Ice streams are widely distributed around the margin of Antarctica and are also present in Greenland. As many of those in West Antarctica extend far inland, nearly to local ice divides (Rignot *et al.*, 2011), the West Antarctic Ice Sheet could be drawn down rapidly if they accelerated. This could raise sea level by as much as a few meters over the next century.

Ice shelves thin and collapse when increasing atmospheric and ocean temperatures cause melting on their top and bottom surfaces and at their seaward edges. Thus, ice shelves and ice streams will play a central role in determining the effect of climate warming on sea level.

### The grounding zone

Ice streams merge with ice shelves in the *grounding zone*, a zone within which the ice is alternately floating and grounded as tides raise and lower sea level. Sediment is delivered to the grounding zone by subglacial streams and possibly also in a layer of deforming till. The sediment forms a grounding-zone wedge (Figure 13.1), a delta-like feature, tens of meters in thickness and kilometers in extent (parallel to ice flow), with a modest distal slope formed by prograding sediment gravity flows (Dowdeswell and Fugelli, 2012). Stratigraphy in wedges is chaotic, as tidal fluctuations superimposed on continued ice flow alternately lift the ice, providing accommodation space for more deposition, and let it settle back onto the bed, deforming the deposited sediment. Deposition occurs at rates of order  $10^2 \text{ m}^3 \text{ a}^{-1}$  per meter width (normal to ice flow) (Anandakrishnan *et al.*, 2007). Channels crossing the wedge are occasionally detected in seismic profiles. The grounding zone has been described as the triple-point between glaciology, geology, and oceanography.

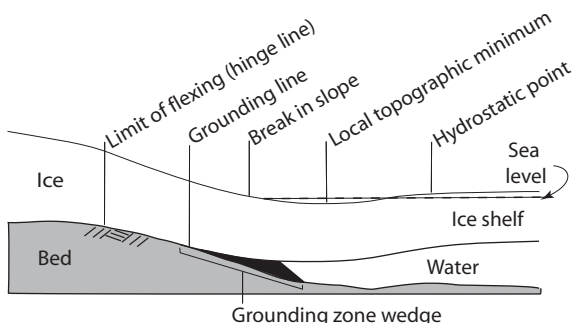


**Figure 13.1** Characteristic features of a grounding zone. (Adapted from Fricker *et al.*, 2009)

On a glacier surface within the grounding zone, two boundaries can be recognized and two topographic features may be identifiable. The innermost boundary is the hinge line or limit of tidal flexing (Figure 13.1). The hinge line is commonly identified from repeated passes of satellites that use various forms of laser altimetry to measure changes in elevation of the ice surface through a tidal cycle. Rignot (1998) thinks this boundary can be located to within  $\pm 1.3$  km, with most of the uncertainty due to tidally-induced migration of the boundary.

In 1912, as Amundsen crossed what we now recognize as the grounding line of Ross Ice Shelf, he heard loud cracking noises associated with the formation of new surface crevasses, a couple of centimeters wide (Amundsen, 1912). These crevasses are sometimes referred to as *strand cracks* (Padman *et al.*, 2018). They are a consequence of the tidal flexing.

Further seaward there may be a topographic break in slope and then a local topographic minimum. The former results from the abrupt decrease in basal traction as the ice becomes ungrounded. The latter occurs when an ice slab flowing down a sloping bed plunges below the buoyancy level for a short distance before buoyancy forces driving ice creep have time to restore hydrostatic equilibrium (Vaughan, 1995). Alternatively (or in addition), the topographic minimum may reflect concentrated sub-ice-shelf melting, as discussed later.

The seaward limit of the grounding zone is the hydrostatic point, the place where the ice shelf first comes into hydrostatic equilibrium with the sea. This may be identified by comparing the elevation of the ice surface measured by satellite laser altimetry with that calculated from radio-echo sounding measurements of ice thickness, assuming buoyancy.

The grounding zone is, thus, a diffuse belt, sinuous in plan view, within which the traction exerted by the bed on the overlying ice gradually diminishes. A break in slope and a local topographic minimum may occur within the grounding zone, but breaks in slope can also occur landward of the limit of flexing or seaward of the

hydrostatic point (Fricker and Padman, 2006; Fricker *et al.*, 2009). The limit of ice floatation, or grounding *line*, shifts back and forth with the tide. The horizontal extent of this fluctuation depends on the tidal amplitude and the bed slope, and can exceed a kilometer.

At the scale of an ice sheet, a grounding zone a few kilometers wide is essentially a line, and it is frequently referred to as such, both herein and in the literature.

## Ice streams

Ice streams may be tens of kilometers wide and hundreds of kilometers long. They are found both in bedrock valleys and in relatively featureless gently-sloping ice plains underlain by nothing more remarkable than shallow linear depressions, the boundaries of which may or may not coincide with the boundaries of the ice streams (Shabtaie and Bentley, 1988; Retzlaff *et al.*, 1993). Pine Island and Thwaites glaciers are in the former category, while the ice streams of the Siple Coast in West Antarctica fall into the latter (Figure 13.2). Some ice streams are fed by long

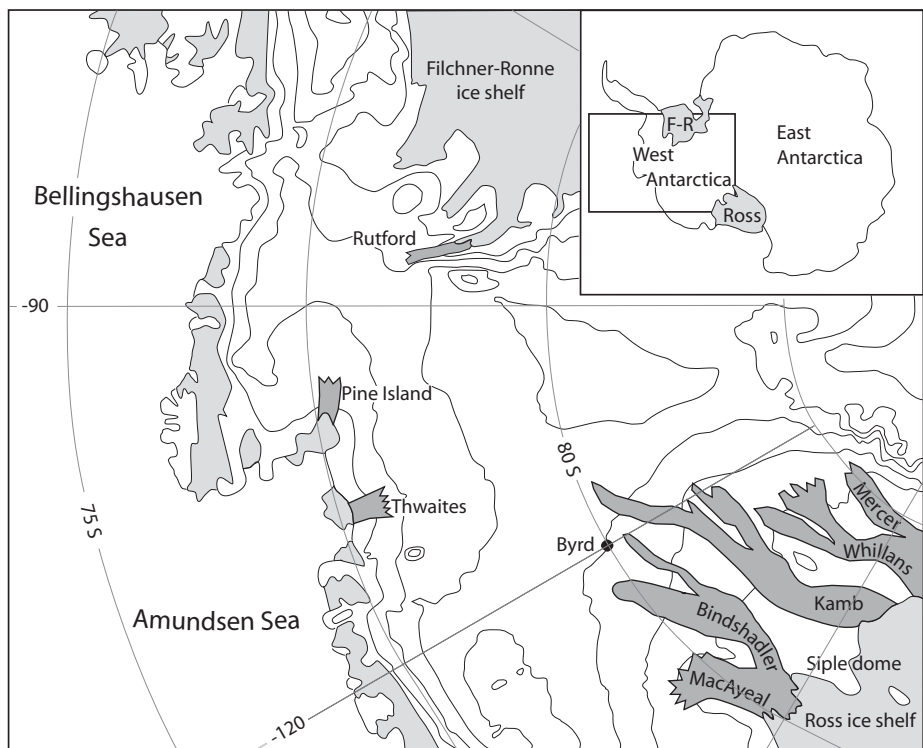


**Figure 13.2** Map of part of Antarctica showing the Siple Coast ice streams, Pine Island and Thwaites glaciers, and Rutford Ice Stream.

tributaries, typically 10–20 km wide, with lower flow rates and higher driving stresses (Joughin *et al.*, 1999; Hulbe *et al.*, 2000).

Active ice streams move at speeds of hundreds of meters per year. Their fast flow is due to enhanced basal sliding, which implies the presence of liquid water. The bed beneath some of the Siple Coast ice streams is known to consist of weak water-saturated till (Engelhardt and Kamb, 1997), but conditions at the bases of ice streams in bedrock valleys are less well known. Clarke and Echelmeyer (1996) interpret seismic reflection records as indicating that Jakobshavn Isbræ, an outlet glacier from the Greenland Ice Sheet, is underlain by compacted non-deforming till, but Smith *et al.* (2007) interpret seismic records from Rutford Ice Stream (Figure 13.2) as indicative of water-saturated deformable till.

Driving stresses,  $\rho g h \alpha$ , on ice streams are generally low. Whereas driving stresses on typical valley glaciers or ice caps are 60–100 kPa, those on Pine Island Glacier and Whillans Ice Stream are 23 kPa (Scott *et al.*, 2009), and 15 kPa (Whillans and van der Veen, 1997), respectively, although that on MacAyeal Ice Stream is 50 kPa (MacAyeal *et al.*, 1995). Force balance analyses (MacAyeal *et al.*, 1995; Whillans and van der Veen, 1997) and inverse analyses based on surface velocities and elevations (Joughin *et al.*, 2004) confirm that most of the resistance to flow of these ice streams is provided by side drag.

The surfaces of ice streams are marked by longitudinal stripes that show up spectacularly on satellite imagery (Figure 13.3). Gudmundsson *et al.* (1998) have shown that these stripes are likely generated by perturbations at the bed. In their theory, the perturbation must have a spatial extent comparable to the ice thickness, and may be in the form of either a hill or hollow in the bed, or of an unusually sticky or slippery spot. The sliding speed must also be high compared with the rate of internal deformation. In the lee of a hill on the bed, for example, a depression develops in the ice surface. This is much like the depression one sees in the water surface in the lee of a slightly-submerged boulder in a stream bed. In an ice stream such a depression will be formed as long as the hill persists, and will be advected a long distance down-glacier. Conversely, in the lee of a hollow in the bed, a ridge develops in the surface and it too is advected downglacier.

At the distal ends of ice streams, there is commonly a region called an *ice plain*. Surface slopes on ice plains are intermediate between those on active ice streams (order  $10^{-2}$ ) and those on ice shelves (order  $10^{-4}$ ) (Bindschadler *et al.*, 2003b). Driving stresses are very low; on Whillans Ice Plain the driving stress is only 2.6 kPa (Bindschadler *et al.*, 2003b).

Testimony to the likely presence of ice streams in the Laurentide Ice Sheet during the Wisconsin glaciation is provided by large, long flutes, called *megascale lineations* (Figure 13.4). These flutes are composed of till and were molded by ice flowing rapidly over a wet bed. Winsborrow *et al.* (2004) find evidence for at least 34 ice streams around the margin of the Laurentide Ice Sheet. Most are along the

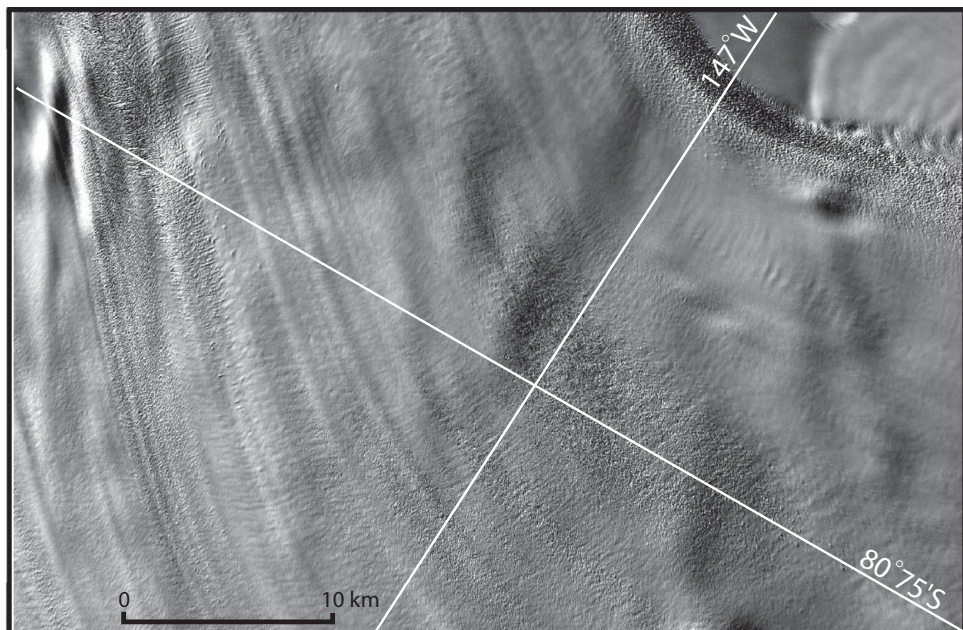


**Figure 13.3** Landsat 8 image of margin of Bindschadler Ice Stream showing prominent lineation produced by ridges and troughs that parallel ice flow. (Courtesy of William Sneed)

northern margin of the ice sheet in the Canadian Arctic Archipelago. One major one apparently discharged ice through Hudson Strait and may have drawn down the ice sheet rapidly and repeatedly, resulting in the formation of layers of ice-rafted detritus, called Heinrich layers, present in sediments throughout the North Atlantic Ocean (MacAyeal, 1993a, 1993b). On the southern margin of the ice sheet, geomorphic features in central Canada and studies of till in Iowa (Hooyer and Iverson, 2002) suggest the possibility of streaming flow feeding the Des Moines lobe of Minnesota and Iowa (Patterson, 1997).

Ice streams were also active in Antarctica during the last glacial maximum. Swath bathymetry of the ocean floor off the northern end of the Antarctic Peninsula has revealed a set of megascale lineations, 100 km long and up to 20 km wide, that extends most of the way across the continental shelf (Canals *et al.*, 2000).

### Ice streams of the Siple Coast

Owing to their perceived potential for catastrophic draw down of the West Antarctic Ice Sheet and to their enigmatic character, being confined between shear margins with little if any relation to subglacial topography, the ice streams of the Siple Coast (Figure 13.2) have been studied intensively. Initially these ice streams were identified, unimaginatively, by letters: Ice Stream A, Ice Stream B, and so forth.

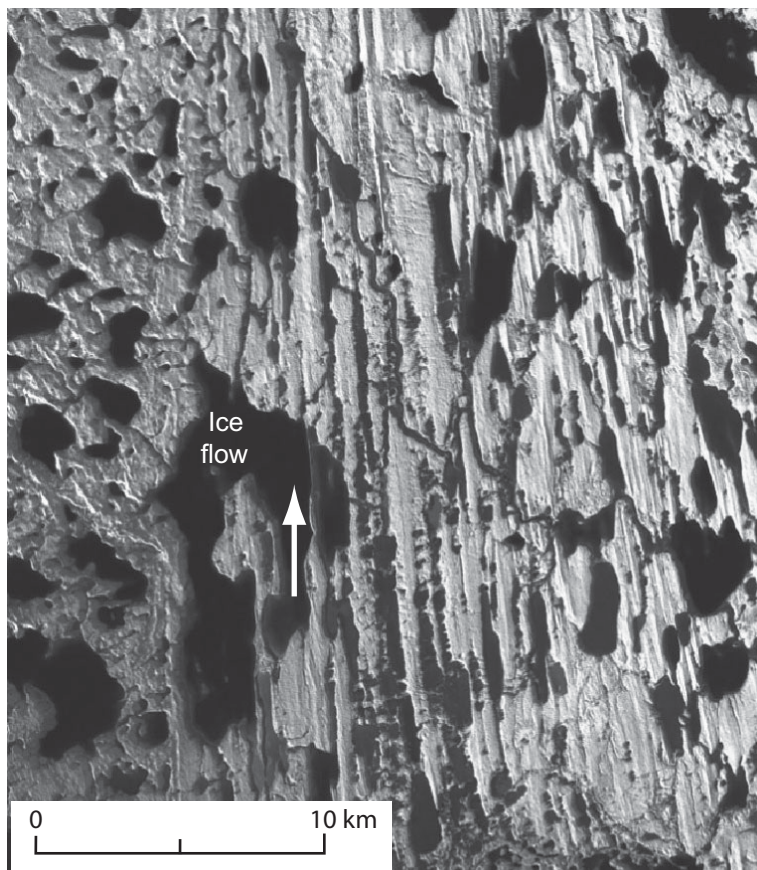


**Figure 13.4** Landsat TM image of the boundary of M'Clintock Channel paleo ice stream on Victoria Island, arctic Canada. The western (left) side of the image shows topography formed beneath slow moving ice bounding the ice stream. (see Clark and Stokes (2001) for further details. Image courtesy of C. D. Clark)

In 2001 the Advisory Committee for Antarctic Names renamed Ice Stream B in honor of Ian Whillans, who died that year. In 2003 they recognized five other glaciologists who have made significant contributions to our understanding of these features. Ice Streams A and C–F were named after the late John Mercer, the late Barclay Kamb, Bob Bindschadler, Doug MacAyeal, and the late Keith Echelmeyer, respectively, and a tributary to Whillans Ice Stream, formerly known as Ice Stream B2, was named in honor of Kees van der Veen.

The Siple Coast ice streams are bordered by topographically higher areas. These are commonly referred to as “*ridges*,” although there is rarely a distinct change in slope across the shear margin, and their topographic relief is commonly modest (Retzlaff *et al.*, 1993). The gently-sloping flanks of the ridges drive ice flow toward the ice streams.

Whillans Ice Stream is the best studied. Extensive velocity and strain rate measurements have been made on it, radar profiles have elucidated its internal structure and that of the bounding ridge, and boreholes have penetrated it, permitting measurement of subglacial water pressure and sampling of the subglacial material.

Speeds on the lower part of Whillans Ice Stream reached  $\sim 825 \text{ m a}^{-1}$  in the early 1990s, and appeared to have been roughly constant since 1985 (Whillans and van der Veen, 1993). By 2004, however, they had decreased  $\sim 10\%$  (Joughin *et al.*, 2005). MacAyeal Ice Stream was flowing at a rate of  $\sim 360 \text{ m a}^{-1}$  in 1987 (Bindschadler and Scambos, 1991). The lower part of Kamb Ice Stream, on the other hand, was essentially stagnant in the early 1990s, but more on that later. These measurements reveal the varied and remarkably dynamic character of ice stream flow.

In contrast, ice velocities in the ridges on either side of Whillans Ice Stream are only  $1\text{--}20 \text{ m a}^{-1}$ , and the motion is generally toward the adjacent ice stream (Whillans *et al.*, 1987, Raymond *et al.*, 2001) rather than parallel to it. Thus, velocity gradients across the lateral boundaries are high, resulting in the intensely crevassed marginal shear zones, kilometers in width, by which Whillans Ice Stream was first recognized – during the 1969–1970 austral summer.

Despite thicknesses approaching 1000 m, surface slopes of Siple Coast ice streams are so low that driving stresses are only 10–20 kPa. These driving stresses do not differ appreciably from those in the ridges. Thus, differences in driving stress cannot account for the great difference in speed. Rather, conditions at the bed are inferred to be responsible. Seismic studies during the 1983–1984 field season suggested that Whillans Ice Stream was underlain by water-saturated till (Blankenship *et al.*, 1986), and boreholes through the ice stream in 1988 confirmed this (Engelhardt *et al.*, 1990). Water pressures at the ice-till interface are very close to the overburden pressure; they either decouple the ice from the bed, allowing it to slide rapidly, or weaken the clay-rich till, allowing it to deform, or both.

Radar stratigraphy has been useful in elucidating some of the changes in flow rates. Smooth layering (right side of Figure 13.5a) implies lack of deformation. Chaotic layering (km 10 in Figure 13.5a) reflects intense deformation such as might be expected in an ice stream shear margin. A gently-undulating wavy pattern (left side of Figure 13.5a) is commonly found beneath relict ice streams, perhaps reflecting buried stripes.

These characteristic signatures can be used to deduce the history of changes in the flow field. The radar profile in Figure 13.5a crosses a “scar” on the east flank of Siple Dome. The scar is visible in high resolution satellite imagery (Figure 13.5b). The chaotic pattern of Figure 13.5a is beneath the scar. To the northeast of the scar, layering is gently undulating. Where the scar reaches the Ross Ice Shelf a faint trace of it continues out onto the ice shelf (Figure 13.5b). These two characteristics suggest that the ice northeast of the scar is part of a relict ice stream. Apparently, a branch of Kamb Ice Stream, or perhaps the entire ice stream, once flowed east of

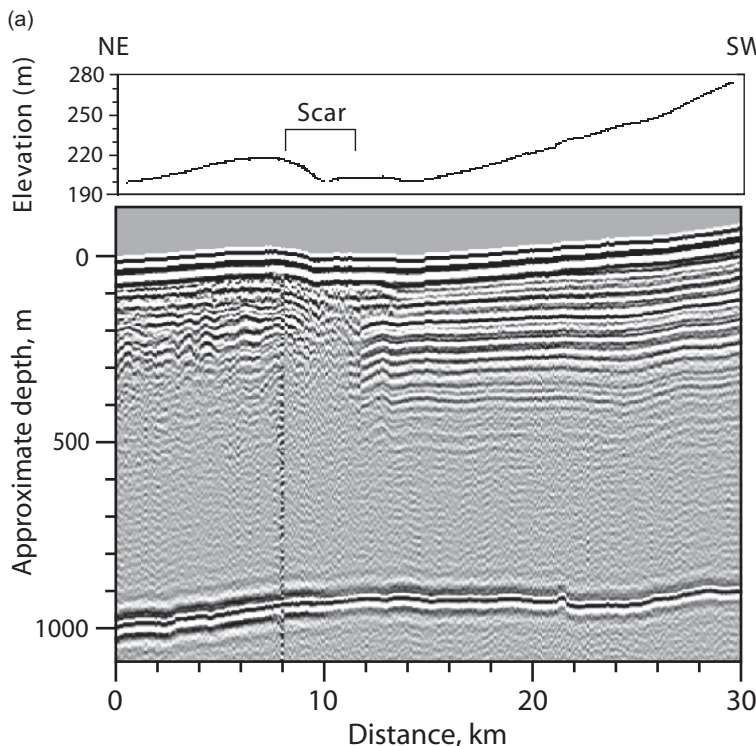


**Figure 13.5** (a) Radar profile and surface elevation across the “scar” east of Siple Dome. The profile is along the short traverse on the N side of Siple Dome in (b). The vertical disturbance at km 8 is an artifact produced by a temporary break in the antenna (from Jacobel *et al.*, 1996). Reproduced with permission of the author and the American Geophysical Union. (b) MODIS image of Siple dome and the lower end of Kamb Ice Stream showing ice streams, modern grounding line, and line of radar profile in (a). (T. Haran *et al.*, <http://nsidc.org/data/nsidc-0280.html>)

Siple Dome (Jacobel *et al.*, 1996). At the surface in the radar profile in Figure 13.5a the stratigraphy is not disturbed, indicating that ice-stream flow had ceased by the time this ice was deposited as snow. Based on an accumulation rate measured on Siple Dome, the base of the undisturbed layering is estimated to be ~1300 years old. Beneath this undisturbed layering and above the intensely deformed layering in the scar, there is moderately-deformed layering, estimated to represent ~400 years of accumulation. This is interpreted as representing slowing of the ice-stream flow. The branch of Kamb Ice Stream south of Siple Dome may have been active prior to this slowdown, or its development may have “captured” the flow northeast of the dome.

Radar traverses across the margin of the now nearly stagnant Kamb ice stream on the south side of Siple Dome reveal subparallel linear zones of crevasses buried beneath several meters of snow. The crevasses mark shear zones from a time when the ice stream was active. Based on the thickness of the snow cover over the



**Figure 13.5 (cont.)**

crevasses and the accumulation rate, it is estimated that the outermost shear zone became inactive ~500 years ago. Thereafter the margin moved inward in a series of steps, with the lower 250 km of the ice stream finally becoming inactive ~150 years ago (Jacobel *et al.*, 2000). About 200 km upstream, however, crevasses are less deeply buried, and the ice stream seems to have been inactive for only ~30 years (Retzlaff and Bentley, 1993). Tributaries to it are still flowing at  $50 \text{ m a}^{-1}$ . Thus, a wave of stagnation appears to be propagating upstream from the shelf.

The reasons for temporal changes like these constitute one of the great mysteries of ice stream behavior. Currently it is thought that they are a consequence of shifts in the basal drainage system that resulted in changes in water pressure at the bed (Retzlaff and Bentley, 1993).

### Ice streams of the Amundsen Sea

Pine Island and Thwaites glaciers are two fast-flowing glaciers draining into the Amundsen Sea (Figure 13.2). Pine Island glacier is effectively an ice stream in a bedrock valley. A deep channel underlies the fast-flowing core of Thwaites glacier (Rignot *et al.*, 2014).

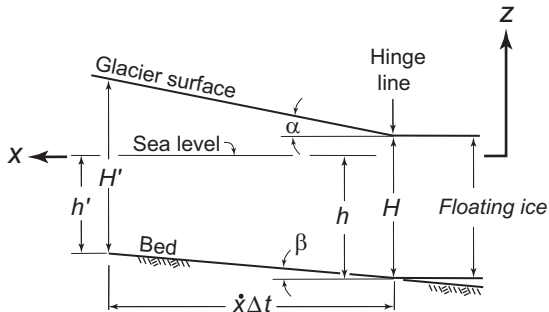


**Figure 13.6** Sketch illustrating calculation of ice thinning rate as grounding line retreats at a rate  $\dot{x}$ .  $H'$  and  $h'$  are the right- and left-hand sides of Equation (13.2), respectively, after a retreat of  $\dot{x}\Delta t$ .

Between 1992 and 1996, the hinge line (or limit of flexing) along the central 15 km of Pine Island glacier retreated at a rate of  $0.63 \pm 0.23 \text{ km a}^{-1}$  (Park *et al.*, 2013). In subsequent years the retreat accelerated, roughly linearly, to  $1.79 \pm 0.87 \text{ km a}^{-1}$  in 2010.

Knowing the hinge-line retreat rate,  $\dot{x}$ , and the slopes of the ice surface,  $\alpha$ , and bed,  $\beta$ , one can estimate the rate at which a glacier must be thinning at the hinge line (Thomas and Bentley, 1978). Let the origin be at sea level, with the  $x$ -axis pointing upglacier, so  $\dot{x}$  is positive when the hinge line is retreating and  $\alpha$  and  $\beta$  are positive when the ice surface and bed are inclined downglacier (Figure 13.6). For hydrostatic equilibrium at the hinge line at time  $t = t_1$ ,

$$h = -H\rho_i/\rho_{sw} \quad (13.1)$$

where  $H$  and  $h$  are, respectively, the ice thickness and elevation of the bed at the hinge line, and  $\rho_i$  and  $\rho_{sw}$  are the densities of ice and seawater. As the bed is below sea level,  $h$  is a negative quantity. At time  $t = t_1 + \Delta t$ ,  $h' = -H'\rho_i/\rho_{sw}$ . Using Figure 13.6 to evaluate  $h'$  and  $H'$ , and recognizing that  $\alpha$  and  $\beta$  are normally small, we have:

$$(h + \dot{x}\Delta t\beta) = -(H + \dot{x}\Delta t\alpha - \dot{x}\Delta t\beta + \dot{H}\Delta t)\frac{\rho_i}{\rho_{sw}}. \quad (13.2)$$

Substituting Equation (13.1) for  $h$  in Equation (13.2) yields:

$$\dot{H} = -\dot{x}\left[\alpha - \beta\left(1 - \frac{\rho_{sw}}{\rho_i}\right)\right]. \quad (13.3)$$

In the case of Pine Island glacier,  $\alpha \approx 0.0045$  and  $\beta \approx -0.011$ , so inserting  $\rho_i = 900 \text{ kg m}^{-3}$ ,  $\rho_{sw} = 1028 \text{ kg m}^{-3}$ , and  $\dot{x} = 0.63 \pm 0.23 \text{ km/a}$  yields a mean  $\dot{H}$  between 1992 and 1996 of  $-1.8 \pm 0.7 \text{ m a}^{-1}$ . As snow and ice were accumulating on the glacier surface, this thinning must have been due to melting at the base. Rignot (1998) estimates that an increase in the ocean temperature of only  $0.1^\circ\text{C}$  could account for the basal melt rate driving this hinge line retreat. Fourteen years

later, with the hinge line 16 km further inland and a steeper ice surface slope, the thinning rate had increased to  $-11.6 \pm 1.1 \text{ m a}^{-1}$  (Park *et al.*, 2013).

Satellite measurements of the ice velocity across the hinge lines of Thwaites and Pine Island glaciers in 1996 yield a combined ice flux of  $234 \pm 3 \text{ km}^3 \text{ a}^{-1}$  (Rignot, 2008). Accumulation over the two drainage areas, estimated from a climate model, was  $\sim 192 \pm 27 \text{ km}^3 \text{ a}^{-1}$ . Thus, the two glaciers combined had a negative mass balance of  $43 \pm 28 \text{ km}^3 \text{ a}^{-1}$ . By 2000, the ice flux had increased to  $258 \pm 4 \text{ km}^3 \text{ a}^{-1}$ , and by 2006 to  $285 \pm 4 \text{ km}^3 \text{ a}^{-1}$ . As there is no evidence of any change in accumulation, this implies a negative balance of  $\sim 93 \pm 29 \text{ km}^3 \text{ a}^{-1}$  in 2006, equivalent to  $0.23 \pm 0.07 \text{ mm a}^{-1}$  of sea level rise.

Pine Island, Thwaites, and some of the other glaciers draining into the Amundsen Sea rest on beds that deepen inland. Thus, as we discussed in Chapter 3 (p. 38–39), they are potentially unstable. Small perturbations that move the grounding line inland could trigger rapid, irreversible retreat, and thus initiate collapse of the West Antarctic Ice Sheet, perhaps eventually raising global mean sea level as much as 3 m (Bamber *et al.*, 2009). This possibility has been studied with the use of a 3-D computer model (Feldmann and Levermann, 2015). With presently-observed melt rates at the hinge lines of glaciers terminating in the Amundson Sea, the model predicted modest, reversible retreat for the next 60 years. Thereafter the system became unstable, and the retreat was not stopped by any topographic features. After 3–5 ky, sea level had risen 2 m, and after 10 ky the marine-based ice of West Antarctica was totally gone, replaced by an ice shelf.

### Ice stream shear margins

The shear margins bordering ice streams of the Siple Coast are enigmatic; the rules governing their locations are not understood, yet they control the width and velocity of the ice stream. The high velocities of active ice streams are clearly due to reduced drag at the bed, but what determines how the total resistance to flow is partitioned between basal drag and side drag? Clearly:

$$\rho HWg\alpha = \tau_b W + 2\tau_s H \quad (13.4)$$

where  $H$  and  $W$  are the thickness and width of the ice stream,  $\tau_b$  is the basal drag, and  $\tau_s$  is the side drag. Efforts have been made to use strain-rate measurements in the shear margin in force-balance calculations to determine  $\tau_s$  and in that way calculate  $\tau_b$  (See pp. 332–338). However, it is expected that ice in the shear margins will be softened by development of a preferred c-axis fabric and by strain heating, so the temperature and enhancement factor to use in the flow law in the force-balance calculations is uncertain.

Echelmeyer *et al.* (1994) were able to match an observed velocity profile in a shear margin of Whillans Ice Stream (Figure 13.7b) with a temperature of  $-15^\circ\text{C}$  and enhancement factor,  $E$ , of  $\sim 10$ , which gave  $110 < \tau_s < 180 \text{ kPa}$ . This implied that

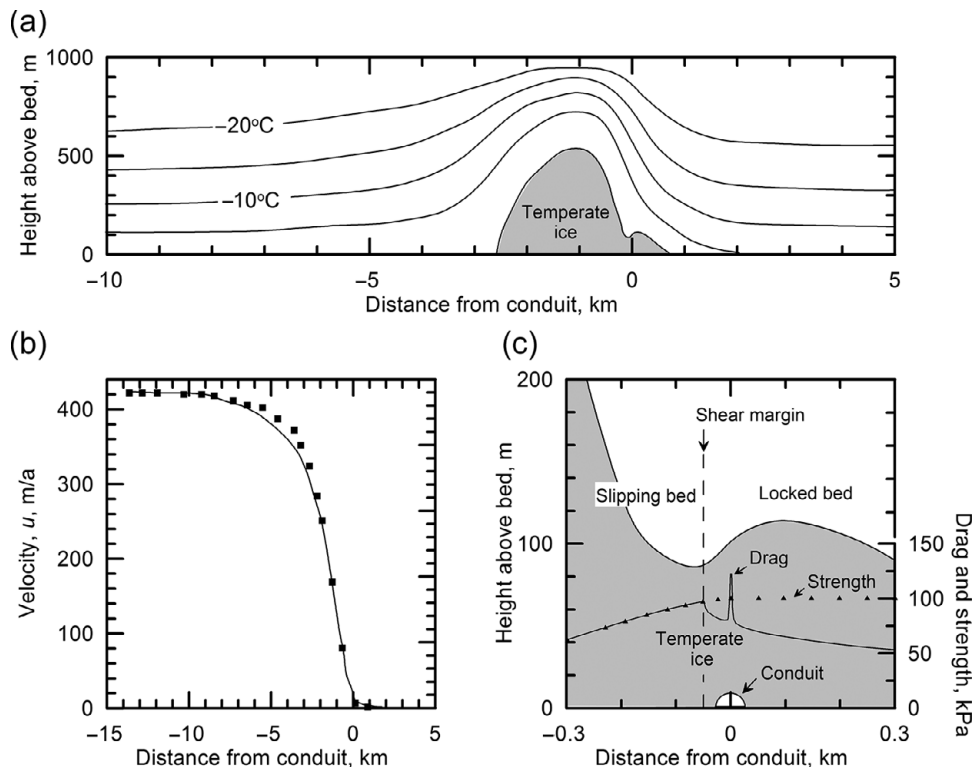


**Figure 13.7** (a) Thermomechanical numerical model of the extent of temperate ice (shaded) in a shear margin. (b) Calculated variation in longitudinal ice velocity,  $u$ , with distance from the conduit (line) compared with values measured by Echelmeyer *et al.* (1994) (dots). (c) Detail of area around conduit in panel (a).  $\blacktriangle$  = strength of the subglacial till (which increases from 20 kPa (not shown) beneath the center of the ice stream). Thin solid line is drag exerted on the bed by the ice (right axis). Conduit is not to scale. Temperatures in panels (a) and (c) are relative to the pressure melting point. (from Perol *et al.*, 2015, Figures 5 and 6. Reproduced with permission of the authors and the American Geophysical Union)

drag provided by the bed absorbed roughly half of the driving stress. Jackson and Kamb (1997), however, sampled ice from a depth of 300 m in the same shear margin and subjected the sample to a laboratory deformation test conducted at the *in situ* temperature of  $-22^{\circ}\text{C}$ , and with the sample oriented in such a way as to mimic the *in situ* stress configuration. The sample had a two-maximum fabric like that in Figure 4.12c. The laboratory strain rate implied an enhancement factor of only 1–2. As the ice was 950 m thick at this location, strain heating or fabric development in deeper ice may not have been adequately considered in the respective calculations.

Whillans and van der Veen (1997) undertook a similar study of three cross sections on Whillans and van der Veen ice streams, using lateral velocity profiles derived from repeated aerial photogrammetry. They found that  $80 < \tau_s < 250$  kPa and  $0 < \tau_b < 7$  kPa. Side drag thus supported between half and virtually all of the driving stress. Their velocity profiles suggested an  $E$  of only 1.2.

Minchew *et al.* (2018) analyzed the longitudinal evolution of fabric and temperature along the shear margins of Rutford Ice Stream, a 2000 m thick ice stream that flows into the Filchner-Ronne Ice Shelf (Figure 13.2). They used satellite imagery that yielded detailed velocities with spatial resolution of  $\sim 100$  m and uncertainties  $< 20$  mm d $^{-1}$ . By assuming that  $\tau_b/\tau_d$  was independent of  $x$  and that  $\tau_s = 0$  at the center of the ice stream, they were able to estimate  $\tau_s(y)$ . Then, knowing  $\dot{\varepsilon}(x)$  in the shear margin from the imagery, they calculated  $E\bar{A}$ , where  $\bar{A}(x)$  is a depth-averaged value. Based on laboratory experiments of Jacka and Budd (1989), they assumed that, within a few kilometers of the beginning of streaming flow, the ice fabric would have evolved to a steady state. This allowed them to estimate  $\bar{A}(x)$ . Then using a thermomechanical model integrated over depth, they again calculated appropriate values of  $\bar{A}(x)$  and found that the two estimates agreed reasonably well if they chose  $6 \leq E \leq 10$ . Finally, from  $\bar{A}(x)$  and the known surface temperature they calculated temperature-depth profiles at various points along the shear margin, finding that the temperature increased monotonically downglacier as the shear strain rate increased, but never reached the melting point. (In ice streams with warmer surface temperatures or higher shear strain rates the melting point may be reached.)

This wide range of estimated values of  $E$  in shear margins is not reassuring.

### Migration of shear margins

In addition to shifting abruptly, as we discussed earlier, ice stream shear margins can also migrate. Satellite imagery of Whillans ice stream, for example, shows that the northern shear margin migrated outward at an average rate of  $\sim 140$  m a $^{-1}$  between 1963 and 1992 (Bindschadler and Vornberger, 1998). If only one margin is moving, the rate of migration can be described, kinematically, by:

$$\frac{\partial W}{\partial t} = v_e - v \quad (13.5)$$

where  $W$  is the width of the ice stream,  $v$  is the speed with which ice outside the ice stream is moving toward the shear margin, and  $v_e$  is the rate at which this ice is entrained into the ice stream (Raymond *et al.*, 2001). Along the south margin of Whillans ice stream, GPS (Global Positioning System) measurements yield  $v \approx 1$  m a $^{-1}$ . Estimates of  $v_e$  there vary. Harrison *et al.* (1998) obtained  $v_e \approx 9.7 \pm 1.1$  m a $^{-1}$  based on temperature profiles in some boreholes, Echelmeyer and Harrison (1999) obtained  $v_e \approx 7.3 \pm 1.5$  m a $^{-1}$  at nearly the same place based on lateral shifting of the profile of longitudinal surface velocity (Figure 13.7b), and Hamilton *et al.* (1998) estimated  $5 < v_e < 28$  m a $^{-1}$  based on curvature of arcuate crevasses. Thus, there,  $\partial W/\partial t$  appears to be outward at a rate of order  $10^1$  m a $^{-1}$ .

### Stability of shear margins

The high velocity gradients across shear margins imply that the bed changes rapidly from soft and deforming to firm and rigid. We know that the bed beneath Whillans

Ice Stream is at the pressure melting point, and it is generally accepted, supported by calculated temperature profiles (Jacobson and Raymond, 1998), that the ice some distance outside of shear margins is likely frozen to the bed. We would like to know the extent to which this boundary is stable against small perturbations.

At the base of an ice stream the heat available for melting ice,  $q_m$ , is:  $\tau_b u_b + G - K\beta_o$ . Here  $\tau_b u_b$  is frictional heating (Equation 6.34),  $G$  is the geothermal heat flux,  $K$  is the thermal conductivity of ice, and  $\beta_o$  is the temperature gradient in the ice, so  $K\beta_o$  is the heat conducted away from the interface upward into the ice. Jacobson and Raymond (1998) visualize two competing processes that may be involved:

- (i) Beneath the central part of an ice stream,  $q_m$  is generally positive owing to the high  $u_b$ . However, in the vicinity of a shear margin  $u_b$  decreases. Thus, this source of heat decreases, and at the same time heat loss to the cold ice outside the shear margin increases. Some of the water at the bed may then begin to freeze, drawing water out of the pore spaces in the till and stiffening the bed. This would move the shear margin inward.
- (ii) Strain heating in the shear margin may raise the ice temperature to the melting point in a narrow zone extending a few hundred meters upward from the bed (Figure 13.7a). This heating would extend laterally into the slowly-moving ridge ice; it would also result in high shear strain rates at the bed and possibly melting there. In this case the shear margin could migrate outward.

For reasonable combinations of  $G$ , accumulation rate, and surface temperature, Jacobson and Raymond (1998) find that a delicate balance between these two processes can exist when the ice stream speed is in the neighborhood of  $100 \text{ m a}^{-1}$ , but this is an unstable equilibrium. If the speed increases, their calculations suggest that the margin would move outward, and conversely (see also Schoof, 2012). There is, however, a possible stabilizing effect: Outward movement of a shear margin could steepen the surface slope of the ridge, thus increasing inward flow of cold ice and counteracting the strain heating process.

In subsequent analyses, Suckale *et al.* (2014) and Perol *et al.* (2015) suggested that, if the influx of ice across the shear margin is not too high, frictional heating may produce enough meltwater to result in development of a subglacial drainage conduit (at  $y = 0$  in Figure 13.7c). A water filled cavity, 1.6 m high, possibly such a conduit, was encountered at the bottom of a borehole in one of the shear margins of Kamb Ice Stream (Vogel *et al.*, 2005). As the water pressure in such a conduit would be lower than the pressure in the ice, the pore water pressure in the subglacial till on either side of the conduit would be lower than elsewhere, strengthening the bed (line labeled "Strength" in Figure 13.7c). However, the drag exerted on the bed by the ice (line labeled "Drag" in Figure 13.7c), which equals the strength of the till where slipping is occurring, drops below the strength at the shear margin. The broadened zone over which basal drag then acts decelerates the ice, decreasing the stress

concentration on the locked portion of the bed and stabilizing the margin. To compensate for the zero drag over the conduit itself, the drag increases abruptly along the channel banks, possibly resulting in some till deformation there.

To summarize, we know that shear margins have changed abruptly in the past and that some are apparently migrating slowly today. Under some conditions small perturbations may destabilize them, but in other situations there may be processes, perhaps involving subglacial water conduits, that tend to stabilize them.

### Stability of ice streams

As we've noted, the stress supported by the bed beneath some ice streams is very small. Thus, one might expect that the occurrence of streaming flow would be sensitive to conditions at the bed. Tulaczyk *et al.* (2000b) and Raymond (2000) have studied this question. They focus on the melt rate,  $m$ , at the bed, which is given by:

$$m = \frac{q_m}{L\rho_i} = \frac{\tau_b u_b + G - K\beta_o}{L\rho_i}. \quad (13.6)$$

Over short time spans,  $G$  and  $\beta_o$  are effectively constant at any given location. Thus, let's look at  $\tau_b u_b$ .

One expects that  $u_b = f(\tau_b)$ . Tulaczyk *et al.* assume that this functional dependence takes the form:

$$u_b = \left( \frac{\tau_d - \tau_b}{\tau_d} \right)^n \left( \frac{W/2}{H} \right)^{n+1} u_d \quad (13.7)$$

where  $\tau_d$  is the driving stress, and  $u_d$  ( $= u_s - u_b$ ; Equation 5.16b) is the rate of internal deformation. The stress difference,  $\tau_d - \tau_b$  is a measure of  $\tau_s$ ; as  $\tau_b$  decreases, more of the resisting stress is transferred to  $\tau_s$  and  $u_b$  increases. At four cross sections on Whillans Ice Stream where  $W$ ,  $H$ ,  $\tau_d$ , and  $u_b$  ( $= u_s - u_d$ ) are known, the data are consistent with Equation (13.7) and suggest that  $\tau_b \sim 1$  kPa.

In Figure 13.8, Equations (13.6) and (13.7) are used to plot  $m$  against  $\tau_b$  for two values of  $G$  and a  $\beta_o$  of  $0.04^\circ\text{C m}^{-1}$ , conditions approximating those at the bed in the mid-reaches of Whillans Ice Stream. There is a maximum in  $\tau_b u_b$  at  $\tau_b = \frac{1}{4}\tau_d$ . [This can be verified by multiplying Equation (13.7) by  $\tau_b$  and setting the derivative of  $\tau_b u_b$  with respect to  $\tau_b$  equal to 0, assuming  $n = 3$ .] This represents the maximum possible shear heating.

A steady state water balance exists when  $m = d_r$ , where  $d_r$  is the rate of loss of meltwater, either by drainage along the bed or by advection in the deforming till layer. Let this state be represented by the horizontal dashed line in Figure 13.8. Points **A** and **B** represent the two possible steady state situations with  $G = 60 \text{ mW m}^{-2}$ . A decrease in  $m$  (or increase in  $d_r$ ) will decrease lubrication of the bed and thus increase  $\tau_b$  and decrease  $u_b$ , and conversely.

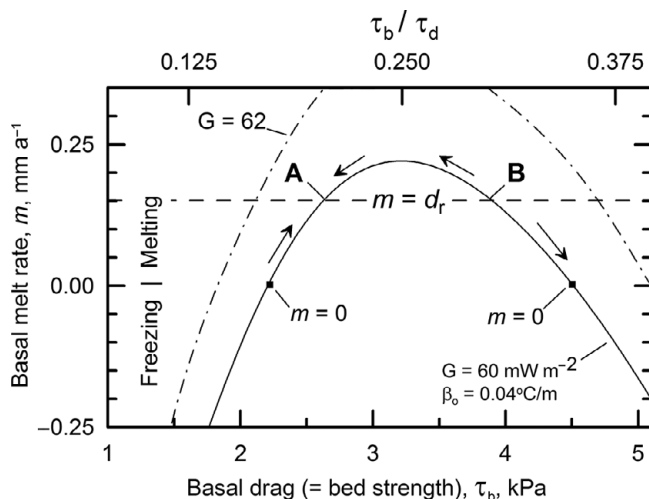


**Figure 13.8** Variation of basal melt rate with basal drag and geothermal flux for a cross section of Whillans ice stream. (Modified from Tulaczyk *et al.* 2000b, Figure 6 Reproduced with permission of the author and the American Geophysical Union)

Consider the consequences of a perturbation that increases  $\tau_b$  by an amount  $\delta\tau_b$  when the steady-state is represented by **A**. The key to understanding the effect of this perturbation is to remember that  $G$  and  $\beta_o$  are fixed (by the location on the bed), so any change in  $\tau_b$  will be accompanied by a change in  $m$  along the  $G = 60 \text{ mW m}^{-2}$  line (determined by Equations 13.6 and 13.7). Thus, the increase in  $\tau_b$  increases  $m$ . (In other words, if one worked through Equations 13.6 and 13.7 for this situation, one would find that the effect of the increase in  $\tau_b$  was greater than that of the decrease in  $u_b$ , so  $\tau_b u_b$  increased, increasing  $m$ .) This increases lubrication of the bed, thus decreasing  $\tau_b$  and driving the system back toward **A**, restoring the equilibrium at **A**. Conversely, a decrease in  $\tau_b$  when the system is at **A** would tend to decrease  $m$ , thus increasing  $\tau_b$  and again restoring the equilibrium at **A**.

Now consider a perturbation in  $\tau_b$  when the system is at the state represented by **B**. Here, a slight increase in  $\tau_b$  decreases  $m$  (so the effect on  $\tau_b u_b$  of the decrease in  $u_b$  apparently exceeds that of the increase in  $\tau_b$ ). The decrease in  $m$  results in less lubrication and a further increase in  $\tau_b$ , driving the system to the right, away from **B**. Ultimately this results in a frozen bed and a shut-down of the ice stream. Conversely, a slight decrease in  $\tau_b$  from the equilibrium at **B** increases  $m$ , decreasing  $\tau_b$  further and driving the system back toward **A**. Thus **B** is an unstable equilibrium state; any perturbation while at this state sets up forces driving the system further from it.

Thus, there appear to be two stable states, one in which the bed is frozen and one, at **A**, in which it is at the melting point,  $m = d_r$ , and  $\tau_b < \frac{1}{4}\tau_d$ . This low  $\tau_b$  implies that beds of steady-state ice streams should be porous and relatively weak.

Raymond (2000) has considered an alternative situation in which a change in  $m$  changes  $d_r$  by changing the thickness of the water layer,  $\delta$ , separating the ice from the till. An increase in  $m$  increases  $\delta$  and hence  $d_r$ . He defines two possible states. In the first, the increase in  $\delta$  increases  $u_b$  more than it decreases  $\tau_b$  so  $m$  increases, and conversely. He refers to this state as *drainage limited* because, if the rate of increase in drainage matches that in  $m$ , the situation is stable; otherwise it is unstable. In the second state, the increase in  $\delta$  decreases  $\tau_b$  more than it increases  $u_b$ , so  $m$  decreases. He refers to this as *production limited*. This state is always stable.

Also meriting consideration are the relative magnitudes of  $\tau_b u_b$ ,  $G$ , and  $K\beta_o$ . If  $\tau_b u_b > K\beta_o$ , no geothermal heat is necessary to maintain pressure melting conditions at the bed. This appears to be the case beneath Bindschadler, Kamb, and MacAyeal ice streams (Raymond, 2000). However, if  $\tau_b u_b < K\beta_o$ , geothermal heat is required to maintain sliding. This seems to be the case beneath Whillans ice stream. Indeed, at the lower end of Whillans ice stream the required value of  $G$  is close to the measured value, suggesting that freezing may be occurring there. This could account for a deceleration of this part of the ice stream documented by Bindschadler and Vornberger (1998).

In some cases, water input from upglacier may be crucial for maintaining a stable state. Consider a unit area of the bed, say  $1 \text{ km}^2$ . Clearly,  $d_r = q_{\text{out}} - q_{\text{in}}$  where  $q_{\text{out}}$  and  $q_{\text{in}}$  are the water fluxes into the control area on its upglacier side and out of it on its downglacier side. If  $q_{\text{in}}$  decreases without a corresponding decrease in  $q_{\text{out}}$ ,  $\delta$  will decrease, thus increasing  $\tau_b$ . If  $|\delta\tau_b| > |\delta u_b|$ ,  $\tau_b u_b$  will increase, thus increasing  $m$  to compensate for the decrease in  $q_{\text{in}}$ . However, if the decrease in  $q_{\text{in}}$  is large enough, the increase in  $m$  may not be sufficient to compensate for it. In this case, the ice stream could shut down. Thus, Retzlaff and Bentley's (1993) speculation that the shutdown of Kamb ice stream might be due to changes in subglacial drainage in the area where Kamb and Whillans ice streams are close together (Figure 13.2) seems well founded.

The bottom line is that ice streams are likely quite sensitive to basal hydraulic conditions, and we really don't have a good understanding of the physical processes occurring at this interface.

## Ice shelves

Ice shelves are important because they buttress outlet glaciers and ice streams, slowing their movement and thus reducing the rate at which inland ice is discharged into the sea. Yet, as noted in Chapter 3, they are prone to collapse. The  $1600 \text{ km}^2$  Larsen A shelf on the east side of the Antarctic Peninsula collapsed in 39 days in 1995, and the  $3250 \text{ km}^2$  Larsen B shelf followed suit in 41 days in 2002. Following the collapse of the Larsen ice shelves, the speeds of outlet glaciers

increased 2–6-fold, resulting in thinning of these glaciers at rates of 10–75 m a<sup>-1</sup> and rapid retreat of their grounding lines (Rott *et al.*, 2002; Scambos *et al.*, 2004).

Gradual propagation of cracks parallel to a shelf front can also separate enormous icebergs from ice shelves at a more measured rate. On July 12, 2017 a ~5800 km<sup>2</sup> slab separated from Larsen C along a crack that had been developing for more than a decade (O’Leary and Luckman, 2017).

Let’s first discuss stresses and strain rates in ice shelves, and then consider calving, bottom melting, and transfer of elastic signals across the shelves.

### Creep of ice shelves

The problem of ice shelf flow is unique because  $\tau_b$  is low beneath the distal parts of grounded glaciers tributary to shelves, and goes to zero beneath the shelf itself. Herein, we consider only the latter case. Weertman (1957b) was the first modern glaciologist to study this problem, and our approach follows his initially, but then incorporates some important modifications introduced by Thomas (1973).

The coordinate system to be used is shown in Figure 13.9. The origin is at sea level and within the ice mass. The z-axis is vertical and positive upward. As before (Figure 13.6),  $H$  is the thickness of the shelf, and  $h$  is the depth of the bottom below sea level. Inland, the surface rises gradually and the base drops further below sea level, so  $H$  and  $h$  both increase. As long as the ice shelf does not become grounded, however, we assume that hydrostatic equilibrium is maintained; therefore, assuming a constant density and thus ignoring any low density snow and firn at the surface,  $h\rho_{sw} = H\rho_i$ .

At the risk of being repetitive, it is convenient, once again, to write out the stress equilibrium equation in the z-direction:

$$\frac{\partial\sigma_{xz}}{\partial x} + \frac{\partial\sigma_{yz}}{\partial y} + \frac{\partial\sigma_{zz}}{\partial z} + \rho_i g = 0. \quad (13.8)$$

Our objective is to obtain an expression for  $\sigma'_{xx}$ , and then to use the flow law to solve for  $\dot{\varepsilon}_{xx}$ .

Because shear stresses are zero at the bed and surface, it is reasonable to assume that  $\sigma_{xz} = \sigma_{zx} = \sigma_{yz} = \sigma_{zy} = 0$ . This means that velocities and strain rates are

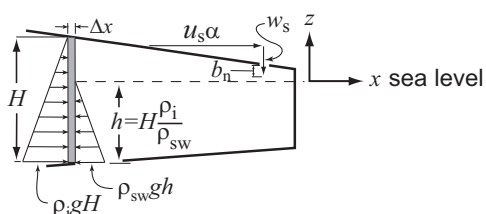


**Figure 13.9** Coordinate system and parameters used in discussion of floating ice shelves.

independent of  $z$ . We'll also ignore atmospheric pressure as it affects all parts of the system equally. Thus,  $\sigma_{zz} = 0$  at the ice surface. Equation (13.8) can now be integrated from some depth in the ice shelf,  $z$ , to the surface,  $H - h$ :

$$\int_{\sigma_{zz}}^0 d\sigma_{zz} = -\rho_i g \int_z^{H-h} dz$$

to yield:

$$\sigma_{zz} = \rho_i g ((H - h) - z). \quad (13.9)$$

Note that at depths greater than  $(H - h)$ ,  $z$  is negative. Thus,  $\sigma_{zz}$  is simply the hydrostatic (or cryostatic) pressure at depth  $((H - h) - z)$ .

Suppose field measurements at some point give:

$$\dot{\varepsilon}_{yy} = \eta \dot{\varepsilon}_{xx} \quad \text{and} \quad \dot{\varepsilon}_{xy} = v \dot{\varepsilon}_{xx}.$$

Then, from the first of these and the incompressibility condition:

$$\dot{\varepsilon}_{zz} = -(1 + \eta) \dot{\varepsilon}_{xx}. \quad (13.10)$$

Both  $\eta$  and  $v$  are functions of  $x$  and  $y$ , but because strain rates are independent of  $z$ ,  $\eta$ , and  $v$  are also independent of  $z$ . Thus, to the extent that ice can be approximated as an isotropic material,  $\dot{\varepsilon}_{ij} = \lambda \sigma'_{ij}$ , and we have:

$$\sigma'_{yy} = \eta \sigma'_{xx}, \quad \sigma'_{xy} = v \sigma'_{xx}, \quad \text{and} \quad \sigma'_{zz} = -(1 + \eta) \sigma'_{xx}.$$

From the last of these expressions, converting to total stresses, we obtain

$$\sigma'_{xx} - \sigma'_{zz} = \sigma'_{xx} + (1 + \eta) \sigma'_{xx} = (\sigma_{xx} - P) - (\sigma_{zz} - P)$$

or:

$$\sigma'_{xx} = \frac{\dot{\varepsilon}_{xx}}{\lambda} = \frac{\sigma_{xx} - \sigma_{zz}}{2 + \eta}. \quad (13.11)$$

When  $\eta = 0$ , this expression reduces to one that often appears in analyses in plane strain. It can be derived, for example, from Equations (10.18) and (10.19).

Let's consider the implications of this relation:  $\sigma_{zz}$  varies linearly with depth (Equation 13.9), but  $\dot{\varepsilon}_{xx}$  is independent of depth. However, the temperature of an ice shelf is normally well below 0°C at the surface and close to the pressure melting point at the base, so  $A$  (and  $\lambda$ ), and thus  $\sigma'_{xx}$ , also vary strongly with depth (Figure 12.5). Thus,  $\sigma_{xx}$  varies with depth in a way that is not intuitively obvious. We circumvent this problem by seeking an expression for  $\dot{\varepsilon}_{xx}$  in terms of the depth-integrated values of  $A$  and  $\sigma_{xx}$ .

We proceed by determining the total force per unit width. To do this, integrate Equation (13.11) (with Equation 13.9 for  $\sigma_{zz}$ ) from the base,  $b$ , to the surface,  $s$ :

$$\begin{aligned}
\int_b^s \sigma'_{xx} dz &= \frac{1}{2 + \eta} \left[ \int_b^s \sigma_{xx} dz - \int_{-h}^{H-h} \rho_i g (H - h - z) dz \right] \\
&= \frac{1}{2 + \eta} \left[ \int_b^s \sigma_{xx} dz - \rho_i g \left( Hz - hz - \frac{z^2}{2} \Big|_{-h}^{H-h} \right) \right] \\
&= \frac{1}{2 + \eta} \left[ \int_b^s \sigma_{xx} dz + \rho_i g \frac{H^2}{2} \right]
\end{aligned}$$

or defining:

$$F = - \int_b^s \sigma_{xx} dz$$

yields:

$$\int_b^s \sigma'_{xx} dz = \frac{1}{2 + \eta} \left[ \rho_i g \frac{H^2}{2} - F \right]. \quad (13.12)$$

$F$  is the force per unit length ( $\text{N m}^{-1}$ ) opposing movement of a vertical section, of unit width normal to the flow direction, of the ice shelf. Shear from valley sides or from a grounded section of the ice shelf some distance downflow from the grounding line would be such forces.

We now need to use the flow law to express the left hand side of Equation (13.12) in terms of strain rates. First, the effective stress is:

$$\begin{aligned}
\sigma &= \left[ \frac{1}{2} \sigma_{ij} \sigma_{ij} \right]^{1/2} \\
&= \left[ \frac{1}{2} \left( \sigma_{xx}'^2 + \sigma_{yy}'^2 + \sigma_{zz}'^2 + 2\sigma_{xy}'^2 \right) \right]^{1/2} \\
&= \left[ \frac{1}{2} (1 + \eta^2 + 1 + 2\eta + \eta^2 + 2v^2) \sigma_{xx}'^2 \right]^{1/2} \\
&= (1 + \eta + \eta^2 + v^2)^{1/2} |\sigma'_{xx}|
\end{aligned}$$

Thus, from the flow law:

$$|\dot{\epsilon}_{xx}| = A (1 + \eta + \eta^2 + v^2)^{\frac{n-1}{2}} |\sigma'_{xx}|^n$$

in which the sign of  $\dot{\epsilon}_{xx}$  is determined by that of  $\sigma'_{xx}$ . The next steps are simpler if we follow Thomas (1973) and use the alternate form of the flow law  $\dot{\epsilon} = \frac{\sigma^{n-1}}{B^n} \sigma'_{ij}$  so  $A = 1/B^n$ . Then, taking  $n = 3$  (so we can drop the absolute value signs) and rearranging:

$$\sigma'_{xx} = \frac{\dot{\epsilon}_{xx}^{1/n}}{(1 + \eta + \eta^2 + v^2)^{(n-1)/2n}} B.$$

As strain rates are assumed to be independent of  $z$ , Equation (13.12) now becomes:

$$\int_b^s \sigma'_{xx} dz = \frac{\dot{\varepsilon}_{xx}^{1/n}}{(1 + \eta + \eta^2 + v^2)^{(n-1)/2n}} \int_b^s B dz = \frac{1}{2 + \eta} \left[ \rho_i g \frac{H^2}{2} - F \right]. \quad (13.13)$$

Because  $B$  varies with depth, we define a depth-averaged values of  $A$  and  $B$  by:

$$\bar{B} = \bar{A}^{-\frac{1}{n}} = \frac{1}{H} \int_b^s B dz.$$

We also define  $\theta$  by:

$$\theta = \frac{(1 + \eta + \eta^2 + v^2)^{\frac{n-1}{2}}}{(2 + \eta)^n}.$$

Solving for  $\dot{\varepsilon}_{xx}$  now yields:

$$\dot{\varepsilon}_{xx} = \theta \bar{A} \left[ \rho_i g \frac{H}{2} - \frac{F}{H} \right]^n. \quad (13.14)$$

Note that  $\rho_i g H / 2$  is the mean cryostatic pressure ( $\text{N m}^{-2}$ ) on the left side of the shaded element in Figure 13.9.

To proceed further, we need to evaluate  $F$ , the force per unit length opposing motion. We do this for two special situations. In the first, the ice shelf is free to expand in both the  $x$ - and  $y$ -directions, and movement is restrained by seawater pressure,  $F_w$ , only. Then,  $\eta = 1$  and

$$F_w = - \int_{-h}^0 \rho_w g z dz = \rho_w g \frac{h^2}{2}.$$

Here,  $\rho_i g h / 2$  is the mean hydrostatic pressure on the right side of the shaded element in Figure 13.9, and  $h$  is the water depth so  $\rho_i g h^2 / 2$  is the force ( $\text{N per m width normal to the flow}$ ) exerted by sea water on this element. Making use of the condition of hydrostatic equilibrium,  $\rho_w h = \rho_i H$ , yields:

$$F_w = \rho_i g \left( \frac{\rho_i}{\rho_w} \right) \frac{H^2}{2}$$

and Equation (13.14) becomes:

$$\dot{\varepsilon}_{xx} = \theta \bar{A} \left[ \frac{\rho_i g}{2} \left( H - H \frac{\rho_i}{\rho_w} \right) \right]^n.$$

The term in the inner brackets on the right hand side is simply  $H - h$ , so this becomes

$$\dot{\varepsilon}_{xx} = \theta \bar{A} \left[ \frac{\rho_i g (H - h)}{2} \right]^n. \quad (13.15)$$

As the right hand side is always positive, strain rates will always be extending. Note that the surface slope does not appear in this solution; thus, even an iceberg with a horizontal surface will deform. This solution does not apply very near an ice front, however, where bending moments are present.

Let's compare this expression with that developed in Chapter 5 (Equation 5.3 with  $\sigma_{zx}$  given by Equation 5.2c) for  $\dot{\varepsilon}_{xx}$  at the bed of a land-based glacier in the absence of significant longitudinal strain:

$$\dot{\varepsilon}_{xx} = A(\rho_i g H \alpha)^n.$$

With  $n = 3$  and noting that  $H - h = \left(1 - \frac{\rho_i}{\rho_w}\right)H \approx 0.1H$  and that  $\theta = 1/9$  when  $\eta = 1$ ,  $v = 0$ , Equation (13.15) becomes:

$$\dot{\varepsilon}_{xx} = A(0.024\rho_i g H)^3. \quad (13.16)$$

Thus, the driving stress ( $\rho_i g H$ ) in an ice shelf is comparable to that in a land-based ice sheet with the same thickness and mean value of  $A$ , and with a (moderately steep) surface slope of  $\approx 0.024$ .

The second example is that of an ice shelf between approximately parallel valley walls. In this case,  $F = F_w + \bar{\tau}_s H$ , where  $\bar{\tau}_s H$  ( $N m^{-1}$ ) is the mean shear force per unit length,  $\Delta x$ , on the valley sides. Utilizing the expression for  $F_w$  just obtained,  $\dot{\varepsilon}_{xx}$  becomes:

$$\dot{\varepsilon}_{xx} = \bar{A}\theta \left[ \frac{\rho_i g (H - h)}{2} - \bar{\tau}_s \right]^n. \quad (13.17)$$

If  $\bar{\tau}_s$  is sufficiently large,  $\dot{\varepsilon}_{xx}$  can now be negative, or compressive.

Mean measured values of  $\dot{\varepsilon}_{xx}$ ,  $h$ , and  $H$  are available for sections of length  $\Delta x$  on Thwaites and Pine Island glaciers and Rutford Ice Stream (Table 13.1). If we take  $\eta = v = 0$  at the centerlines of these roughly 2-D glaciers, and choose a reasonable value for  $\bar{A}$  ( $7 \text{ MPa}^{-3} \text{a}^{-1}$  at  $\sim -18^\circ\text{C}$  (Figure 12.5)), we can use these measurements in Equation (13.17) to solve for  $\bar{\tau}_s$ . Thwaites Glacier ends in a floating ice tongue mélange extending  $>100$  km into the ocean; there,  $\bar{\tau}_s \approx 89 \text{ kPa}$ . Pine Island Glacier, in contrast, ends in a 70 km ice shelf confined between a valley wall on one side and a valley wall and adjacent ice shelf on the other, resulting in  $\bar{\tau}_s \approx 757 \text{ kPa}$ . Rutford Ice Stream is confined by valley walls on both sides; there  $\bar{\tau}_s \approx 948 \text{ kPa}$ . The latter two values are quite high compared with the estimates of  $\bar{\tau}_s$  in the shear margins of the Siple Coast ice streams, and also compared with typical values of  $\tau_b$  on valley glaciers ( $50 < \tau_b < 150 \text{ kPa}$ ) (see p. 90). This reflects the enormous driving stresses forcing large volumes of ice through these narrow outlet channels.

Let's look further at  $\tau_s$ . Suppose that  $a$  is the distance from the centerline of an ice shelf to the valley wall. If  $\bar{\tau}_s$  is the depth-averaged drag on a valley wall, then  $\bar{\tau}_s H$  ( $N m^{-1}$ ) is the drag force the valley wall exerts on the ice per unit length along the direction of flow. This force must balance forces acting in the direction of flow over

**Table 13.1** Calculation of  $\tau_s$  for Pine Island and Thwaites glaciers and Rutford Ice Stream

	Rutford	Pine Island <sup>1</sup>	Thwaites <sup>2</sup>
Data			
$H$ , m	1650	1077	1162
$h$ , m	1469	959	1034
$\dot{\varepsilon}_{xx}$ , $a^{-1}$	-0.002	-0.01	0.1
Calculations			
Back pressure from water, kPa <sup>3</sup>	816	532	574
Strain rate term, kPa <sup>4</sup>	-132	-235	485
	-----	-----	-----
$\tau_s$ , kPa	948	757	89

<sup>1</sup> Rignot (2001); <sup>2</sup> Stephenson and Doake (1982); <sup>3</sup>  $\rho_i g(H-h)/2$ ; <sup>4</sup>  $(\dot{\varepsilon}_{xx}/(\bar{A}\theta))^{1/n}$

the half-width of the ice shelf. In the absence of basal drag, it is reasonable to assume that any vertical slice of unit width extending through the ice shelf and oriented parallel to the direction of flow will be restrained equally by this side drag. Thus, any such slice will experience a drag of  $\bar{\tau}_s H/a$  per unit length along the direction of flow. Noting that  $\bar{\tau}_s$  is a negative quantity, as it is directed in the up-flow direction (Figure 13.9), the total resisting force per unit of ice stream width is:

$$F_s = - \int_x^L \bar{\tau}_s \frac{H(x)}{a} dx. \quad (13.18)$$

Here,  $x$  is the coordinate position where the calculation is being made, and  $L$  is the  $x$ -coordinate of the edge of the shelf.

Equation (13.18) says that  $F_s$  increases with distance upglacier from the shelf edge. It is less on a wide glacier (larger  $a$ ) because more of the shear is taken up within the ice rather than on the valley wall. Thus, from Equation (13.17), noting that  $\tau_s = F_s/H$ ,  $\dot{\varepsilon}_{xx}$  must commonly change from positive or extending near the shelf edge to compressive further inland. This is the reverse of the normal situation in a grounded glacier, in which compressive flow is the rule in the ablation area and extending flow in the accumulation area. With extending flow near the shelf edge,  $w_s$  will be downward or negative in our coordinate system (Figure 13.9), and  $u_s\alpha$  will be quite low (and also negative) as  $\alpha$  is typically small on ice shelves. Then, since a steady-state can exist only if  $b_n = -w_s + u_s\alpha$  (Figure 13.9), it is clear that  $b_n$  must normally be positive. This means that ice shelves with ablation zones near the shelf edge should be uncommon, as is, in fact, the case. Furthermore, if the mass balance near the shelf edge is positive, it must also be positive at higher elevations further inland. Thus, if  $F_s$  ever becomes large enough to make  $\dot{\varepsilon}_{xx}$  compressive near the

shelf edge, the ice shelf would increase in thickness unstably until it became grounded. The exception, of course, would be if bottom melting compensated for the accumulation on the surface; this, as we shall see, is the case for Pine Island and probably for Thwaites glaciers.

### Calving of ice shelves

Although there is no drag on the undersurface of ice shelves, calving of ice shelves is similar to that of grounded tidewater glaciers, inasmuch as both are affected by melting of the calving face below sea level and by lack of water pressure above the waterline (see pp. 34–36). Let's first look at the stresses, following an analysis by Reeh (1968).

Because the hydrostatic pressure at an ice front is applied below the waterline while the cryostatic pressure is applied throughout the thickness of an ice shelf (Figure 13.10a), there is a torque or bending moment,  $M$ , tending to pull the top of the ice shelf forward. Taking the origin of our coordinate system now at the base of the ice shelf (Figure 13.10a) (so  $h$  is now positive), this moment is:

$$M = \int_0^H \sigma_{xx} z \, dz$$

at the shelf front. The longitudinal stress,  $\sigma_{xx}$ , is:

$$\sigma_{xx} = \rho_i g(H - z) - \rho_{sw} g(h - z) \quad z < h$$

$$\sigma_{xx} = \rho_i g(H - z) \quad h < z < H.$$

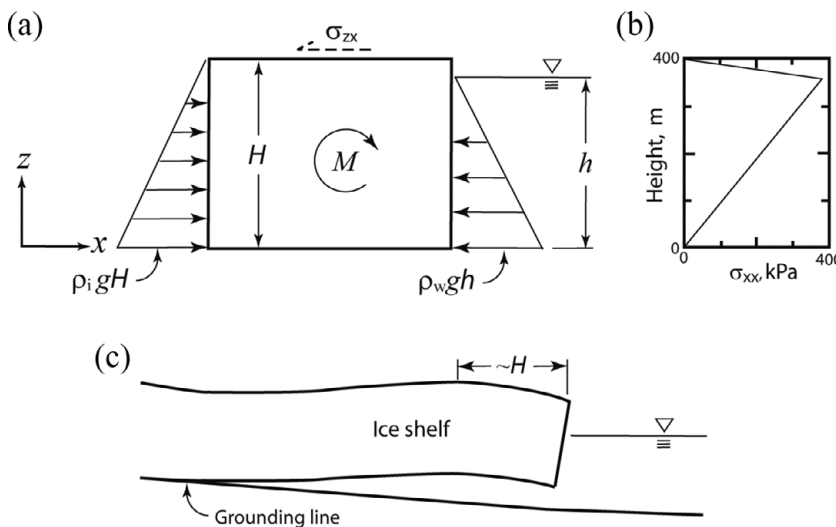


**Figure 13.10** (a) Forces on the floating tongue of an ice shelf. (b)  $\sigma_{xx}$  at the ice front. (c) Bending of shelf caused by torque in (a).

Thus, neglecting any creep resulting from these stresses:

$$M = g \int_0^h (\rho_i Hz - \rho_i z^2 - \rho_{sw} hz + \rho_{sw} z^2) dz + \rho_i g \int_h^H (Hz - z^2) dz.$$

As  $\rho_i H = \rho_{sw} h$ , the first and third terms in the first integrand cancel each other. Carrying out the integration yields:

$$M = \frac{g}{6} (\rho_i H^3 - \rho_{sw} h^3).$$

For an ice shelf 400 m thick with  $\rho_i = 917 \text{ kg m}^{-3}$  and  $\rho_{sw} = 1028 \text{ kg m}^{-3}$ ,  $M = 19,600 \text{ MPa m}^2$ . To put this in perspective, on the surface of an ice block 400 m long, a shear traction of 122 kPa would be necessary to balance such a torque. This is represented by the dashed arrow in Figure 13.10. The deformation would thus be equivalent to that in a 400 m thick glacier on a slope of 0.034. Perhaps more relevant is the magnitude of  $\sigma_{xx}$  at the waterline: 388 kPa (Figure 13.10b). As  $\sigma_{xx}$  is 0 at the surface and base, such a stress would result in bulging of the calving face at the waterline, forming an overhang, and promoting calving of relatively small sections of the face. This is consistent with the pattern of velocities at the calving face of a grounded tidewater glacier calculated with a finite element model (Hanson and Hooke, 2000). The calving rate, however, would be significantly less than that of a grounded tidewater glacier because ice shelf ice is cold and relatively unfractured, and thus stronger.

The torque results in bending the shelf (Figure 13.10c), resulting in an upward deflection that reaches a maximum about one ice thickness from the ice front (Reeh, 1968). For our 400-m thick shelf the deflection would be  $\sim 5 \text{ m}$ . This is where tensile stresses reach a maximum, so Reeh thought fracturing would be likely here, creating icebergs with widths comparable to the thickness of the shelf.

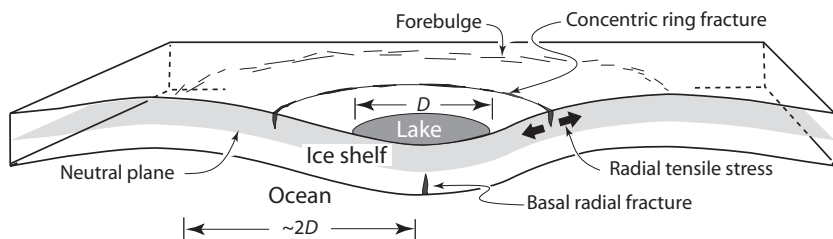
Enormous icebergs, however, with widths of tens of kilometers, have become separated from the fronts of some ice shelves. Two examples, mentioned in Chapter 3, are a  $\sim 4600 \text{ km}^3$  iceberg which broke off from the Ross Ice Shelf in April 2000 and a  $\sim 6000 \text{ km}^3$  slab that separated from Larsen C ice shelf on July 12, 2017 (Hogg and Gudmundsson, 2017). Others dating from as far back as 1968 are reported by Swithinbank (1969) and Lazzara *et al.* (2008). The cracks that eventually result in these icebergs typically take a decade or more to develop (Lazzara *et al.*, 2008). The one that separated the iceberg from Larsen C was first recognized in the late 2000s. In 2014 it began to advance across the ice shelf episodically, in 20-km bursts, leading to final failure in 2017 (Hogg and Gudmundsson, 2017).

The processes leading to separation of such massive icebergs are not well understood. The cracks generally parallel the ice front and are thus normal to the tensile stresses characteristic of ice shelves (Equation 13.15). They may be initiated at points of weakness (Lazzara *et al.*, 2008) and propagated due to the enhancement

of such tensile stresses at crack tips. It is also not clear whether these calving events are part of a normal fluctuation in extent of the ice shelf, such that another such event will not occur until flow of ice into the shelf balances that just lost, or whether they represent a more-or-less permanent reduction in size of the shelf. There is no evidence that they are related to climate warming (Lazzara *et al.*, 2008).

In contrast, climate warming is almost certainly responsible for the rapid collapse of the Larsen B and Larsen C ice shelves in 1995 and 2002, respectively. Rapid retreat of several ice shelves along the Antarctic Peninsula began in the 1970s and 1980s, a period during which air temperatures increased (Scambos *et al.*, 2003). When the mean annual temperature rises above  $\sim -5^{\circ}\text{C}$  a considerable amount of melting occurs during the summer. Thus, in the decade before the collapse of Larsen B, thousands of small lakes formed on the glacier surface during the melt season (Glasser and Scambos, 2008). As an ice shelf resembles a thin elastic plate, water in even a small lake depresses the ice. Around lakes with diameters,  $D$ ,  $< \sim 1\text{ km}$ , a forebulge develops  $\sim 2D$  km from the lake's center (Figure 13.11a) (Banwell *et al.*, 2013). If the lake is more than a few meters deep, the resulting tensile stresses are sufficient to produce concentric crevasses about halfway to the crest of the forebulge and radial crevassing in the bottom of the ice shelf immediately beneath the lake (Figure 13.11a). During the lifetime of the lake, melting at its bottom thins the

(a)



(b)

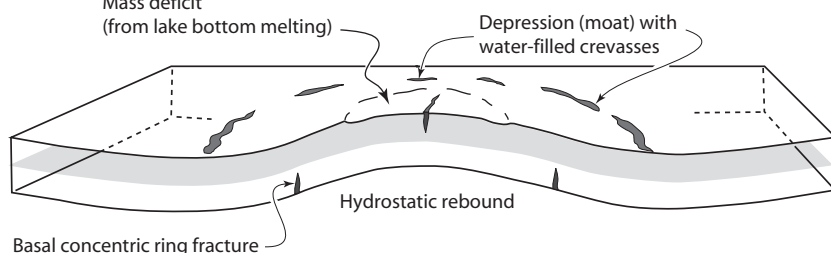


**Figure 13.11** Sketches showing: (a) a forebulge and crevassing around a lake on an ice shelf, and (b) a dome or doline resulting from drainage of such a lake. (After Banwell *et al.*, 2013. Modified in consultation with A. Banwell and D. MacAyeal. Reproduced with permission of the authors and the American Geophysical Union)

shelf. Thus, when such a lake drains, the thinned “plate” rebounds, forming a low dome with a depression at its center and surrounded by a shallow depression formed by the collapsed forebulge. Complementary fractures of similar geometry may then develop in the opposite surfaces of the shelf (Figure 13.11b). Propagation of both the surface and basal crevasses is facilitated by repeated filling and draining of the lake and by filling of the surface crevasses with water. Overlapping of areas of crevasse formation from neighboring lakes creates a dense pattern of crevasses. Banwell *et al.* argue that if one such lake fails suddenly by drainage through a crevasse, stresses in its vicinity will be modified, inducing surrounding lakes to drain. This results in an outward propagating front of lake drainage. The dense pattern of crevasses produces ice blocks that are high relative to their width and length. Such blocks are unstable and capsize, and in so doing push neighboring blocks apart (MacAyeal *et al.*, 2003). This causes the observed rapid dispersal of shelf fragments. In short, the connection between climate warming and the collapse of Larsen A and B is robust, and Banwell *et al.* provide a rational explanation for the rapidity of the collapses and for the multitude and small size of the resulting fragments.

## Processes at the bases of ice shelves

### Circulation and diffusion

Water circulates beneath ice shelves (Figure 13.12). Either or both of two *thermohaline circulation* processes may be involved in this circulation. In the first, dense saline seawater moves inward under a shelf along the seabed. This flow is particularly strong in situations in which the seabed slopes downward toward the grounding line. Near the grounding line the water rises to the base of the shelf and, if its temperature is above the local pressure melting temperature, as is commonly the case, it initiates melting, or *thermal erosion*. As ice shelves typically thin outward, the bottom slopes upward toward the ice front. The lower density brackish water resulting from the thermal erosion flows outward along this upward-sloping base, reinforcing the convection. This is a form of *free convection*.

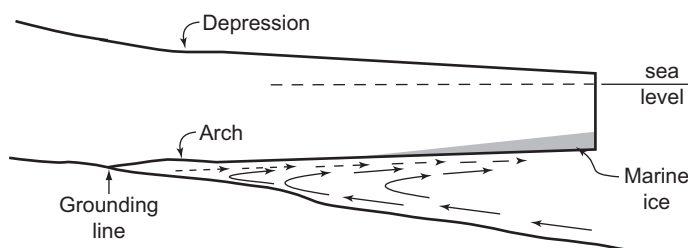


**Figure 13.12** Longitudinal section showing circulation of water beneath an ice shelf, a broad arch in the base resulting from basal melting just downflow from the grounding line, a resulting depression in the surface above the cavity, and a zone of brackish ice resulting from freezing of seawater. Solid and dashed arrows represent seawater and brackish or freshwater, respectively. The amplitudes of the arch and the depression are exaggerated.

The second process involves subglacial freshwater emerging at a grounding line. This water is typically less dense than the water into which it merges, so it also rises along the upward-sloping sub-ice-shelf surface, entraining potentially warmer seawater along the way. If warm enough, this brackish water can also erode basal ice, increasing the outward flux of low density water. This is a form of *forced convection*.

The temperature of any outward-flowing water derived from thermal erosion will be the pressure melting temperature at the point where melting occurred. As this water rises along the shelf base, it must warm to remain at the increasing pressure melting temperature; it does so by selective freezing, forming frazil ice and releasing the heat of fusion (Robin, 1979). Outward from the grounding line, the temperature gradient in the ice shelf also increases, albeit only slightly, because the surface and basal temperatures remain nearly constant while the ice thins. Both of these processes favor accretion of mildly saline marine ice on the shelf base toward the ice front (Figure 13.12). Marine ice is, indeed, commonly encountered at the bottoms of boreholes in these locations (Morgan, 1972; Robin, 1979; Holland *et al.*, 2009). The freezing increases the salinity of the remaining outwardly-flowing water. Once this residual water, now warmed, becomes sufficiently saline, it may sink and recirculate inland along the sea floor, and is thus available to melt more ice near the grounding line in a self-perpetuating process (Lewis and Perkin, 1983, 1986).

Tidal forcing appears to be important in controlling the amount of circulation. Numerical modeling (Makinson *et al.*, 2011) suggests that in the absence of tidal forcing, circulation beneath Filchner-Ronne ice shelf would be halved. This would result in a 67% reduction in the melt rate and an 83% reduction in the amount of refreezing! The net melt would be halved. The modeling reproduced other independent estimates of the amount and distribution of melting rather well, giving some confidence in these results.

Diffusive processes are more complicated because both heat and salinity can diffuse; hence the name: *double diffusion*. The molecular diffusivity for heat, however, is two orders of magnitude higher than that for salinity. Several mechanisms have been proposed for a type of double diffusion, called *diffusive convection* (Radko, 2013, p. 189). Let's look at one that is readily visualized and that could occur in the grounding zone. The upward-sloping base of an ice shelf will be at an effectively constant pressure melting temperature, but some distance *horizontally* (along a plane of equipotential) outward from the base the temperature may be higher. Thus, a lateral temperature gradient is present. Suppose the salinity of the far-field water increases uniformly with depth. The saline solution near the ice will be cooler, and because its temperature is  $<4^{\circ}\text{C}$ , its density will be lower. It will thus rise along the ice surface. As it rises, it loses salinity slowly but cools more rapidly. It also encounters far-field water with lower salinity, and hence lower density. When it reaches a level at which its density nearly matches the density of the far-field water it spreads horizontally. This can result in multiple

layers with step-like increases in salinity between layers called a *double-diffusive staircase* (Kranenborg and Dijkstra, 1998).

In situations in which mixing by tidal forcing or by incoming subglacial water is relatively weak, such double-diffusive staircases may develop beneath ice shelves. Such seems to be the case beneath George VI Ice Shelf where Kimura *et al.* (2015) found at least four layers, ranging from 1 m to 3 m in thickness. Temperature and salinity were constant within a layer, but increased abruptly with depth between layers. In the grounding zone beneath Ross Ice Shelf, Begeman *et al.* (2018) also found a ~1 m thick layer of cold freshwater, and measured temperature and salinity gradients suggestive of a double-diffusive staircase. If widespread, Begeman *et al.* think this stratification could limit melting in the grounding zone to  $<0.1 \text{ m a}^{-1}$ . Double-diffusive staircases could also develop in front of near-vertical calving faces if the farfield water was appropriately stratified and other circulation suppressed.

### Melting

Rignot (1998) calculated the amount of bottom melting along the shelf fronting Pine Island Glacier. He used satellite observations to determine the surface elevation,  $z$ , and velocity,  $v$ , at various places along the shelf, and calculated the ice thickness,  $H$ , at these locations, assuming hydrostatic equilibrium. The ice flux,  $Q$ , through a cross section of width,  $W$ , is then:  $Q = vHW$ . He found that the flux decreased systematically downflow from the grounding line. As snow was accumulating on the tongue, the decrease could not be attributed to surface melting, so it had to be due to basal melting. Consistent with the free convection process described above, the melt rate was highest near the grounding line, and decreased outward. In the first 20 km from the grounding line it exceeded  $50 \text{ m a}^{-1}$ ! Warm Circumpolar Deep Water was apparently being guided to the grounding line from the shelf edge by a landward-deepening trough in the sea floor (Schodlok *et al.*, 2012).

Such thermal erosion near a grounding line can produce a broad arch in the base of a shelf. To preserve hydrostatic equilibrium, a depression then develops in the shelf surface above the arch (Figure 13.12). The sinking of the surface results in “synclines” in internal layering just downflow from grounding lines. Catania *et al.* (2006, 2010) imaged such features, some up to 200 m deep and 4 km wide, in radar profiles across the grounding zone of Ross Ice Shelf (Figure 13.13). The amplitude of the synclines increases with depth, and the deepest layers are truncated at the base of the shelf. Both characteristics are consistent with formation by concentrated basal thermal erosion.

Such synclinal structures are formed only under transient conditions, lasting a few centuries. Over longer time periods the distal edge of the syncline is advected away from the grounding line, a process that would obscure its geometry (Catania *et al.*, 2010). Surface lineations and stratigraphic signatures marking locations of former grounding lines can, however, persist for several hundred years.

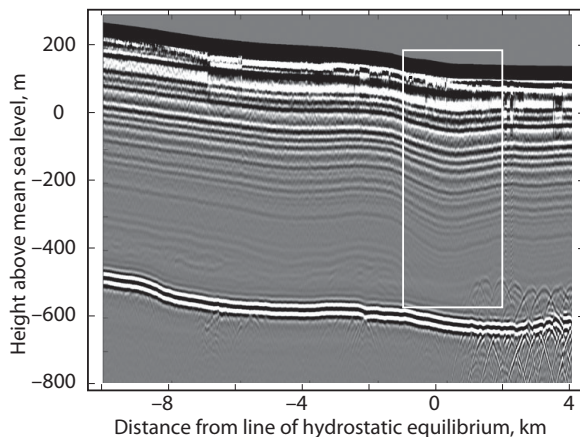


**Figure 13.13** Radar profile across the grounding line at the distal end of Kamb Ice Stream. Ice flow is from left to right. White box brackets syncline. (From Catania *et al.*, 2010, Figure 2b. Reproduced with permission of the author and the International Glaciological Society)

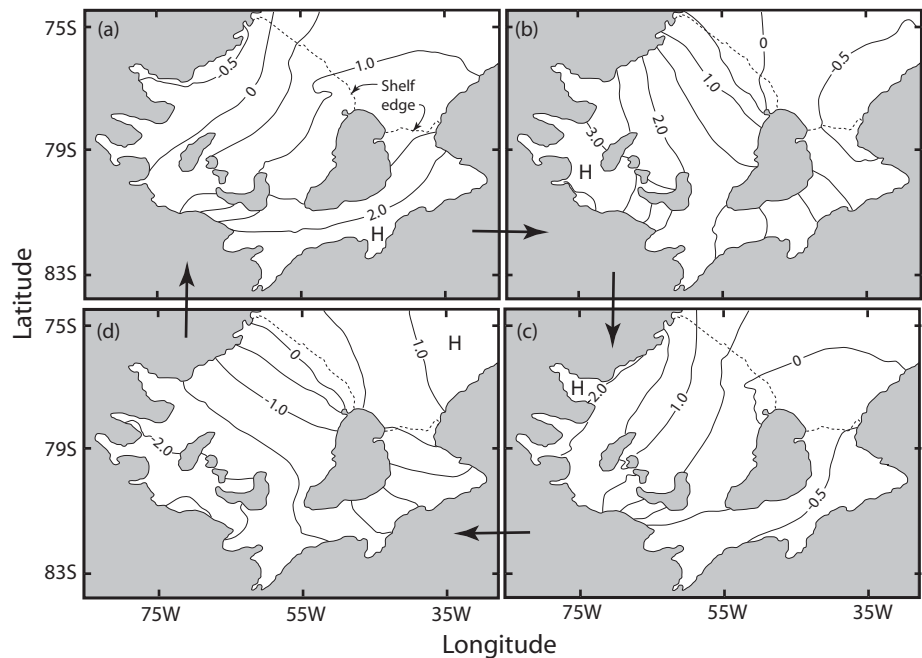
### Ice streams, ice shelves, and ocean tides

Ocean tides exert buoyant forces on ice shelves. These forces raise and lower the ice in synchrony with the tidal cycle, and thus alter the effective normal stress on the bed in the grounding zone. As an ice shelf behaves like a rigid beam, this alternately increases and decreases the slope of its surface, and thus alters the driving stress. Ice shelves and the distal ends of ice streams react to these influences, but differently in different places.

The tidal wave is quite different from what one might expect standing on a coastline and watching the water level rise and fall. As a wave approaches the Ronne Ice Shelf through the Weddell Sea, for example, it is deflected to the left by the Coriolis effect. It thus piles up against the coast of East Antarctica (Figure 13.14) and, beneath the ice shelf, it travels clockwise around the inner boundary of the shelf, raising first the southeast side (Panel a), then the southwest side (Panel b), and then the northwest side (Panel c). Such a wave, driven by the Coriolis effect and guided by coastlines, is called a *Kelvin wave*. While the tidal range at the inner edge of the ice shelf reaches 7 m during spring tides, the height at the center of the shelf front does not change. Such a zero-amplitude point is called an *amphidrome*.

Outward tilting of the shelf results in a gravitational stress in addition to the longitudinal stress provided by the imbalance between the cryostatic pressure in the ice and the hydrostatic pressure at the ice front. As this additional stress varies diurnally with the tide, and as the ice is cold ( $\sim -20^\circ\text{C}$ ), deformation is expected to be almost purely elastic (Gudmundsson, 2007; Makinson *et al.*, 2012).

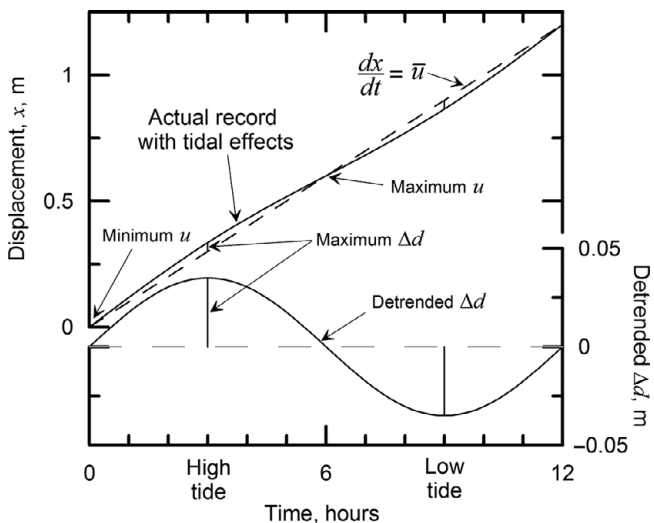
On an ice shelf, suppose a GPS station moves seaward at a mean velocity,  $\bar{u}$ , represented by the slope,  $dx/dt$ , of the dashed line in the time–distance plot in



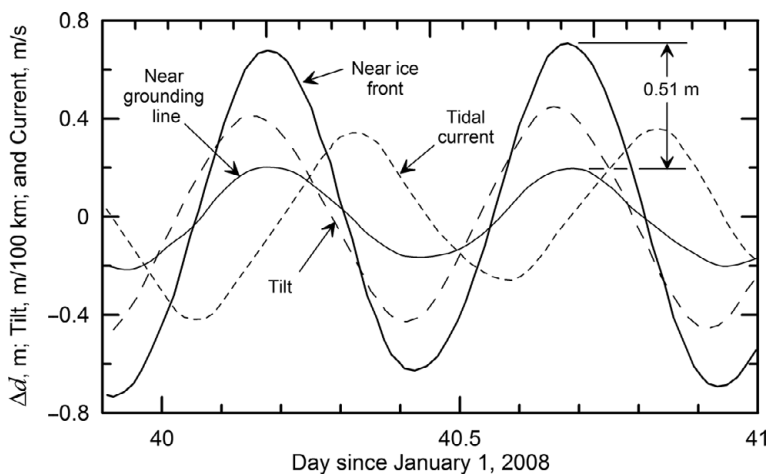
**Figure 13.14** The central Ronne Ice Shelf is almost a flat plain tilted by the tide. The contours in the four panels show the height (m) of the tide under and in front of the shelf at intervals of  $\sim 3$  hours, progressing clockwise, during the 12-hour semidiurnal cycle. The heights shown are deviations from the mean surface. H marks the location of high tide in each panel. The approximate shelf edge in 2012 is labelled in panel (a). (Based on illustration drafted by Keith Makinson – Personal communication, January 2018)

Figure 13.15. Superimposed on this are oscillations due to the tidal effects. During a rising tide, when the shelf is being tilted seaward, elastic stretching increases the velocity so the slope of the time–distance curve is steeper than the mean, and conversely. Let's define  $\Delta d$  as the difference between the actual location of the station and the location it would have had if moved with the mean velocity (Figure 13.15). The maximum  $\Delta d$  occurs at high and low tides, but the maximum and minimum velocities occur at mid-tide. As  $\Delta d$  is typically small compared with the total movement, the time distance record is usually detrended by subtracting  $\bar{u}$  and plotting  $\Delta d$  on an expanded scale, as shown at the bottom of Figure 13.15.

Records of  $\Delta d$  at two GPS stations on Ronne Ice Shelf are shown in Figure 13.16 (solid lines), together with the tilt of the shelf between the two stations (long dashed line), and the tidal current beneath the shelf (short dashed line). The station locations were recorded at 5-minute intervals. One of the stations was near the grounding line and the other was near the shelf edge. The stations were 389 km apart. The magnitudes of  $\Delta d$  reflect velocity variations that are up to  $\pm 300\%$  of the mean velocity. The maximum differences in  $\Delta d$  between the two stations are  $\sim 0.45$  m, with the larger  $\Delta d$  at the station near the ice front.



**Figure 13.15** Displacement of a hypothetical GPS station as a result of the mean flow speed (dashed line) of an ice shelf upon which are superimposed oscillations due to tidal effects. Detrended  $\Delta d$  is at the bottom.



**Figure 13.16** Records, over one day in January, 2008, of  $\Delta d$  at two GPS stations on the Ronne Ice Shelf, of the tilt of the shelf surface between the two stations, and of the tidal current. Positive tidal current is toward the shelf front. (Adapted from Makinson *et al.*, 2012, Figure 3. Reproduced with permission of the author and the American Geophysical Union)

If a gently-sloping rigid plate of length  $L$  and density  $\rho_i$  is anchored at its upslope end, the stress applied to an element of length  $dx$  a distance  $x$  from the upslope end is  $\sigma_{xx} = \rho_i g \alpha(L - x)$ , where  $\alpha$  is the slope of the plate (Figure 13.17). The elastic elongation of the element  $dx$  is  $(\sigma_{xx}/E)dx$ , where  $E$  is the elastic modulus (4.8 GPa; Brunt and MacAyeal, 2014). The total elongation over the length of the plate is then:

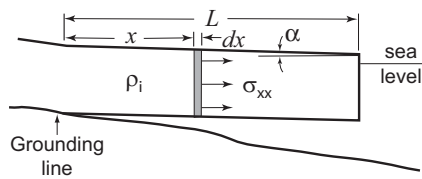


**Figure 13.17** Gravitation stress,  $\sigma_{xx}$ , on a cross section of an ice shelf, modeled as a parallel-sided plate, a distance  $L - x$  from the plate edge. The plate is tilted through an angle  $\alpha$  (by tidal action).

$$\varepsilon = \frac{\rho_i g \alpha}{E} \int_0^L (L - x) dx = \frac{\rho_i g \alpha L^2}{E} \frac{1}{2}. \quad (13.19)$$

Ronne Ice Shelf is tilted seaward at 0.4 m/100 km at high tide and landward by the same amount at low tide (Figure 13.16). Thus, with  $L = 389$  km, we find that  $\varepsilon = 0.56$  m. This is remarkably close to the measured maximum differences in  $\Delta d$  between the two stations: ~0.5 m (Figure 13.16). Importantly, Equation (13.19) predicts that  $\varepsilon$  should increase with  $L$ , which is consistent with the common observation that  $\Delta d$  tends to increase toward shelf edges.

GPS records sufficiently detailed to resolve variations at tidal periods have now been made at numerous points on the Antarctic coast. In most cases, the variations are similar to those in Figure 13.16, but on Whillans Ice Plain that is not the case (Figure 13.18). GPS stations there exhibit *stick-slip* motion. Periods of negligible movement lasting 6–18 hours are interspersed with abrupt displacements at rates of ~1 m hr<sup>-1</sup> and lasting 10–30 minutes. In the case shown in Figure 13.18b, the first and third slip events occurred near the end of high tide, and the second and fourth near the midpoint of the falling tide. Bindschadler *et al.* (2003a) suggest that continued flow of ice from upglacier during periods of quiescence at the site of the observations results in buildup of stress at the interface between the ice and the subglacial till. Eventually the stress exceeds the strength of the till, which may simultaneously be weakening somewhat owing to the decrease in effective normal pressure ( $N_e$ ) as the tide rises (e.g. Equation 7.16). This leads to failure and an abrupt slip event. The stress then starts to build up again, but this time more rapidly owing to a tensile stress as the tide falls seaward of the grounding line, tilting the ice plain seaward. This shortens the time to the next slip event (Winberry *et al.*, 2014).

Slip is likely to result in dilation of the till. Dilation can strengthen till by sucking water into the increasing void space, and thus increasing  $N_e$  (Iverson, 2010). In the case of Whillans Ice Plain, however, the permeability of the till is sufficient to offset this effect, and dilation weakens the till. The strength drop can be as much as 0.35 kPa (Winberry *et al.*, 2009). During quiescent intervals,  $N_e$  increases and the till consolidates, strengthening it again.

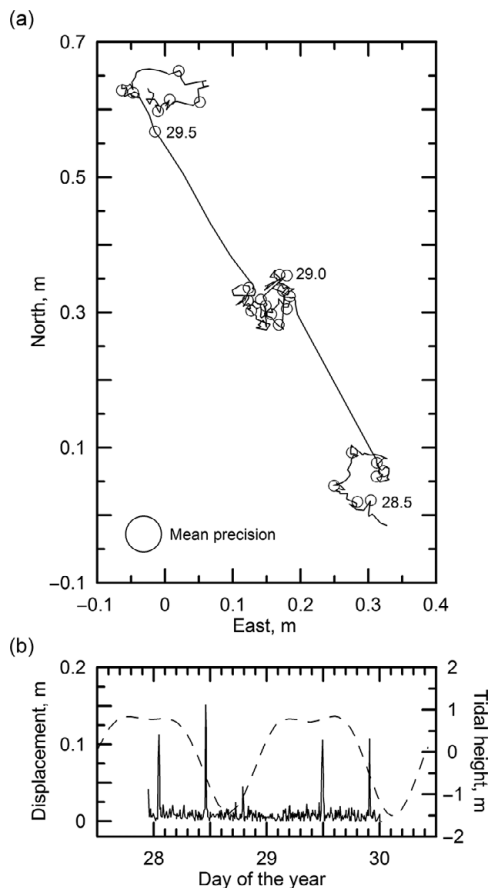


**Figure 13.18** (a) Displacement of a GPS station on Whillans Ice Plain over 30 hours in January 1999. Positions were recorded every 5 minutes. Circles show positions every hour. Numbers are day of the year. (b) Solid line is horizontal displacement between successive 5-minute positions. Dashed line is modeled tidal height. The record is from a time period close to a spring tide. (From Bindschadler *et al.* (2003b). Reproduced with permission of the International Glaciological Society)

Semidiurnal oscillations have also been documented on Rutford Ice Stream, but there they are superimposed on the fortnightly oscillations between neap and spring tides (Figure 13.19a) (Gudmundsson, 2011; Rosier *et al.*, 2015). These latter oscillations result from a resonance between the lunar semidiurnal tide, M<sub>2</sub>, with a period of 12.42 hrs and the solar semidiurnal tide, S<sub>2</sub>, with a period of 12.00 hrs.

GPS data show that the horizontal displacement of the ice stream is out of phase with the diurnal tidal cycle (Figure 13.19c). A falling tide somewhat seaward of the grounding line increases the surface slope of the ice stream, accelerating it (elastically on the time scale of a semidiurnal tidal signal), and conversely. Gudmundsson (2011) was able to simulate this behavior rather well with a numerical model using a

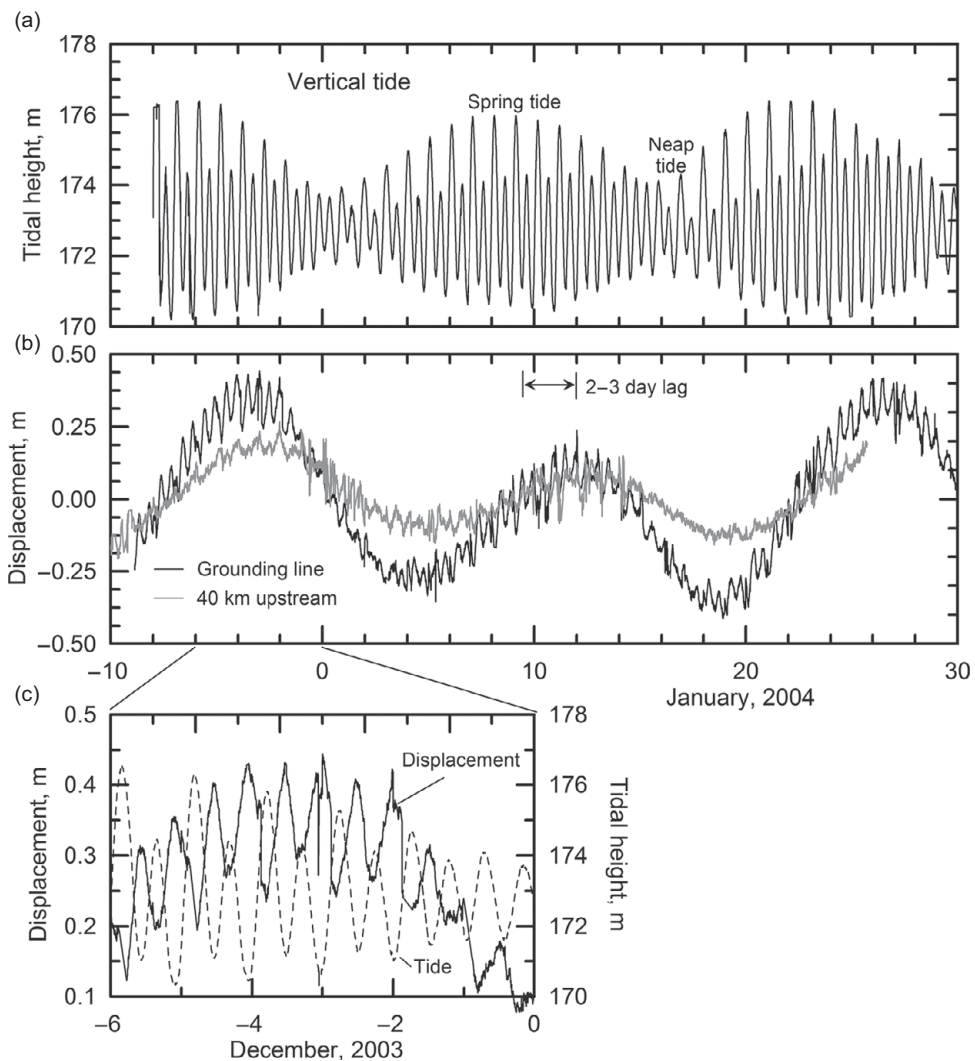


**Figure 13.19** (a) Fortnightly tidal signal from a point ~20 km downglacier from the grounding line of Rutford Ice Stream; (b) time series of detrended displacements at GPS stations near the grounding line and 40 km upstream from the grounding line; and (c) detail of tidal signal and displacements. (Data acquired by H. Gudmundsson and provided by S. Rosier (written communication, February, 2018))

non-linear law relating  $u_b$  (sliding plus till deformation) to  $\tau_b$  and forced with the M2 and S2 tidal signal a few kilometers seaward of the grounding line.

The GPS data, together with extensive satellite data (Minchew *et al.*, 2017), show that the ice stream accelerates on the rising limb of the fortnightly oscillation and decelerates on the falling limb, but with a lag of 2–3 days (compare Figures 13.19a and b); it appears to be responding to the integrated effect of the changing tidal amplitude. The accelerations are present from 10 km downglacier from the

grounding line to up to 50 km upglacier from it. Minchew *et al.* attribute the acceleration to decoupling of the ice from the bed near the bases of the shear margins. As tidal heights increase on the build up to spring tides, these grounding zones migrate outward, increasing the effective width of the ice stream, and hence its speed, and conversely.

In subsequent simulations, Rosier *et al.* (2015) found that the surface speed was unexpectedly sensitive to small variations in basal water pressure. He noted that oscillations many kilometers upglacier from the grounding line implied a highly conductive drainage system. Such a system might consist of a number of fairly large conduits that quickly transmitted pressure fluctuations upstream, whence the fluctuations diffused outward through the till, affecting  $N_e$  over a substantial part of the bed. A cubic dependence of  $u_b$  on  $\tau_b$  was necessary to properly model the upstream decrease in the response. An interesting implication of this study is the possibility that observations of tidally-forced oscillations in displacement at a glacier surface may tell us a lot about the subglacial drainage system.

---

## SUMMARY

In this chapter we first discussed ways to locate the grounding line. Then, focusing first on ice streams on the Siple coast, where the ice streams are embedded in slowly-moving ice, we found that ice stream boundaries may change and ice streams may shut down. Former boundaries can be identified in radar profiles by chaotic stratigraphy, often beneath surface scars. We then found that the high velocity of some ice streams, despite their low driving stresses, was due to weak coupling with the bed. The primary support for these ice streams is in the shear margins. However, the locations of shear margins of active ice streams on the Siple coast appear to be sensitive to variations in strain heating and in the influx of ice from the bordering uplands. The ice streams, themselves, are sensitive to the melt rate at the bed and to the thickness of the water layer there. Slight variations in either can cause the ice stream to shut down. Then we discussed the fact that ice streams debouching into the Amundsen Sea are thinning and their grounding lines retreating. If this continues, a point may be reached when the West Antarctic Ice Sheet collapses, albeit over a few kiloyears. Finally, we noted that megascale glacial lineations provided convincing evidence that ice streams were present in the Laurentide Ice Sheet.

In our discussion of ice shelves, we started by studying a theoretical model that gave insights into forces restraining their motion. Then we looked first at the separation of gigantic icebergs from shelf fronts and found that they could not be

explained by the bending torque at the shelf front, and secondly at the collapse of the Larsen ice shelves, apparently due to fracturing caused by elastic deformation as lakes on the shelf surface were repeatedly filled and drained. Beneath ice shelves, circulation of “warm” ocean water commonly results in thermal erosion near the grounding line and accretion of ice nearer the shelf front, thus accounting for thick sections of marine ice found beneath some shelves. Finally, we looked at how both diurnal and fortnightly tides affect ice shelves, reducing the coupling with the bed and alternately stretching and compressing them elastically.

# 14

## Finite strain and the origin of foliation

Suppose one were to drop a sphere of silly putty into the accumulation area of a glacier. As the sphere became buried deeper and deeper in the glacier, it would be deformed by the flow. Because the accumulation area is normally an area of longitudinal extension and vertical compression, it would become an ellipsoid, elongated in the direction of flow and compressed vertically. If there were also significant transverse compression it would become a prolate ellipsoid, whereas if there were transverse extension, it would become oblate. Figure 14.1 illustrates, schematically, how the shape of the sphere would change as it passed through the glacier.

Our objective in this chapter is to discuss the cumulative deformation experienced by ice as it is advected through a glacier, and to show the relation between this deformation and the banded structure, called *foliation*, that is so characteristic of glaciers.

### The strain ellipse

The ellipsoid we have just discussed is called the strain ellipsoid or, in two dimensions, the strain ellipse. Following normal convention, we will denote the greatest, intermediate, and shortest principal semi-axes of the ellipsoid by subscripts 1, 2, and 3, and the directions of these axes by  $X$ ,  $Y$ , and  $Z$ , respectively. These axes rotate with respect to our fixed  $x$ ,  $y$ ,  $z$  coordinate system as the strain ellipsoid rotates (Figure 14.2). The lengths of the axes of the ellipsoid are a measure of the strain it has experienced. As in Equation (9.16) we define the strain by:

$$e = \frac{\ell - \ell_o}{\ell_o} = \frac{\ell}{\ell_o} - 1. \quad (14.1)$$

If  $\ell_o$ , the radius of the initial sphere, is taken as 1, then  $\ell_i = 1 + e_i$  is the length of the  $i$ th semi-axis of the ellipsoid (Figure 14.2). From Equation (9.23) the logarithmic strain is then:

$$\varepsilon_i = \ln \frac{\ell_i}{\ell_o} = \ln (1 + e_i). \quad (14.2)$$

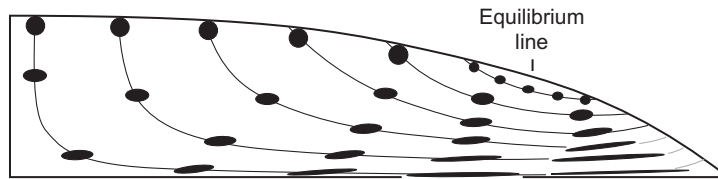


**Figure 14.1** Schematic illustration of deformation experienced by an initially spherical object as it passes through a glacier. (From Hooke and Hudleston, 1978, Figure 3B. Reproduced with permission of the International Glaciological Society)

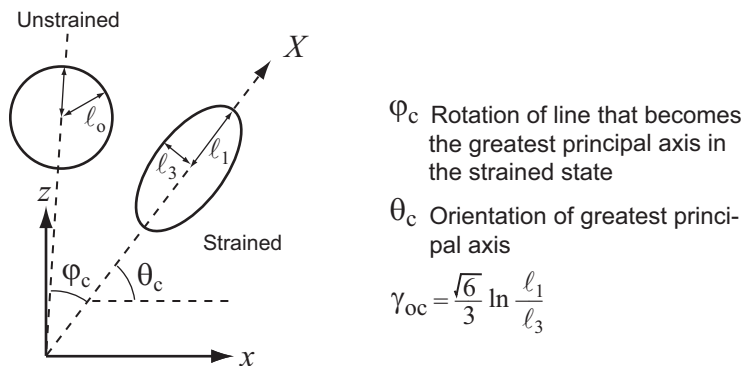


**Figure 14.2** Sketch showing parameters used to describe, in two dimensions, the cumulative strain experienced by an initially circular object. (Modified from Hooke and Hudleston, 1980, Figure 8C).

Let us now take  $\ell_i / \ell_j$  ( $i, j = 1, 2, 3$ , and  $i \neq j$ ) as a measure of the strain in the  $i, j$  plane. Then:

$$\varepsilon_i - \varepsilon_j = \ln \frac{\ell_i}{\ell_j}. \quad (14.3)$$

A useful measure of the magnitude of the *total strain* experienced by the ellipsoid is then:

$$\bar{\gamma}_{oc} = \frac{2}{3} \left[ (\varepsilon_1 - \varepsilon_2)^2 + (\varepsilon_2 - \varepsilon_3)^2 + (\varepsilon_3 - \varepsilon_1)^2 \right]^{1/2}. \quad (14.4)$$

$\bar{\gamma}_o$  is called the natural octahedral unit shear (Nadai, 1950, p. 115) and the additional subscript c denotes cumulative. (“Natural” in this context is a reference to the appearance of the natural logarithm in the expressions for  $\varepsilon_i$ , not to a contrast with some “artificial” counterpart.)

In plane strain with  $\varepsilon_2 = 0$  and  $\varepsilon_1 = -\varepsilon_3$ , the intermediate or Y-axis of the ellipsoid will be transverse to the flow and thus parallel to the y-axis of the fixed coordinate system. Equation (14.4) can then be simplified and combined with Equation (14.2) to yield:

$$\bar{\gamma}_{oc} = \frac{2\sqrt{6}}{3}\varepsilon_1 = \frac{2\sqrt{6}\ell_1}{3\ell_0}. \quad (14.5)$$

As  $\varepsilon_1 = -\varepsilon_3$  we can eliminate  $\ell_0$  by setting  $i = 1$  and  $j = 3$  in Equation (14.3), thus:

$$\bar{\gamma}_{oc} = \frac{\sqrt{6}}{3} \ln \frac{\ell_1}{\ell_3}. \quad (14.6)$$

## Simple and pure shear

As we've discussed previously (Figure 4.13), when a two-dimensional object is deformed by a compressive stress parallel to the  $z$ -axis and an extensional stress parallel to the  $x$ -axis, the deformation is known as *pure shear* (Figure 14.3a), whereas if it is deformed by a shear stress,  $\sigma_{zx}$ , parallel to the  $x$ -axis, the deformation is known as *simple shear* (Figure 14.3b). In Figure 14.3a the axis of maximum shortening is clearly parallel to the  $z$ -axis, and the axis of maximum extension is parallel to the  $x$ -axis. This is also true of the *instantaneous stretching axes*, or axes along which the maximum and minimum normal strain rates occur during any infinitesimal strain. *Material lines* (lines of physical points in the deforming material) that are initially parallel to the instantaneous stretching axes remain parallel to these axes. The strain is thus *irrotational*, and the deformation is said to accumulate *coaxially*.

In contrast, in simple shear the instantaneous stretching axes are always at  $\pm 45^\circ$  to the direction of shear ( $\theta_{in} = 45^\circ$  where the subscript "in" refers to instantaneous or infinitesimal; Figure 14.3b). However, the axis of maximum extension will be at  $45^\circ$  only after the first infinitesimal increment of strain. In the next increment, the initial axis of maximum extension will be rotated slightly. This axis is parallel to a material line that started at an angle greater than  $45^\circ$  to the  $x$ -axis and that has been rotated through the  $45^\circ$  position to an angle less than  $45^\circ$ . This is most easily

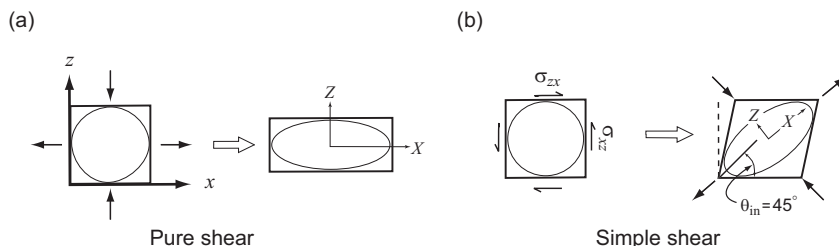


**Figure 14.3** Sketches illustrating (a) pure and (b) simple shear. Note the orientation of the axes of the ellipsoid,  $X$  and  $Z$ , relative to the coordinate axes  $x$  and  $z$ .

visualized if one considers very large strains, as in the lower right part of Figure 14.1. The material line that became the nearly-horizontal axis of maximum extension in this case started off nearly vertical. Because material lines rotate through the axes of instantaneous stretching (which are *non-material lines*) the deformation in simple shear is *rotational* and *non-coaxial*.

In either simple or pure shear there are always two lines that are initially perpendicular and that are still perpendicular after deformation. These lines coincide with the directions of maximum extension (or elongation) and shortening in the deformed state. These are called the *principal axes of strain*.

## Parameters describing cumulative deformation

Although  $\bar{\gamma}_{oc}$  describes the deformation of the original sphere, it does not describe either its rotation or its final orientation. For that we need two additional parameters,  $\theta$  and  $\varphi$  (Figure 14.2);  $\varphi_c$  is *the angle through which the material line that becomes a principal axis in the strained state has rotated*, and  $\theta_c$  is *the angle that the greatest principal axis makes with the x-axis*. Again, the subscript c denotes cumulative.

In the pure shear of Figure 14.3a, the axis of maximum elongation, the X-axis of the ellipsoid, is horizontal, both for infinitesimal strains and for cumulative strain over a long period of time. Thus,  $\theta_c$  is 0, and because the X-axis does not rotate,  $\varphi_c$  is also 0. In contrast, in simple shear as in Figure 14.3b, the X-axis is at  $45^\circ$  to the shear direction for any infinitesimal increment of strain. However, during any such increment, the line that became the X-axis will have rotated slightly from its previous orientation, so  $\varphi_c$  is slightly greater than 0 and  $\theta_c$  slightly less than  $45^\circ$ . As the strain accumulates,  $\varphi_c$  increases toward  $90^\circ$  (but it will never actually become  $90^\circ$ ) and  $\theta_c$  will approach  $0^\circ$ . The reader may wonder why  $\varphi_c \rightarrow 90^\circ$  when the X-axis after the first increment of strain was inclined at  $45^\circ$ . The answer lies in the phrase, “... the rotation of the line that *becomes* the principal axis ...” After very large shear strains, the line that becomes the X-axis will be the one that started out nearly vertical.

As one would expect from consideration of velocity profiles like those in Figure 10.6, pure shear dominates near the glacier surface where  $\partial u / \partial x$  and  $\partial w / \partial z$  are large compared with  $\partial u / \partial z$ , and conversely, simple shear dominates near the bed where  $\partial u / \partial z$  becomes large compared with  $\partial u / \partial x$  and  $\partial w / \partial z$ . Immediately beneath the divide,  $\partial u / \partial z = 0$  at all depths, so pure shear extends all the way to the bed. Across the equilibrium line, the flow gradually changes from extending to compressive, so both  $\partial w / \partial z$  and  $\partial u / \partial x$  go through maxima and begin to decrease. Here, the ratio of simple shear to pure shear increases, despite the small  $\partial u / \partial z$  in the upper part of the glacier.

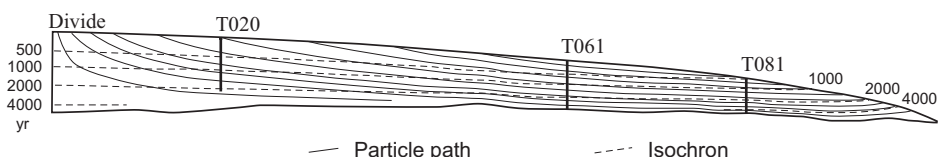
## Calculating cumulative strain

In order to calculate the cumulative strain in a glacier, one first must know the velocity field. One then calculates the path that a particle of ice would follow through the glacier and velocity derivatives at discrete points along the path. To obtain the incremental strain as the ice moves from one point to the next, strain rates are then calculated from the velocity derivatives and multiplied by the time needed for this movement (Ramsay and Graham, 1970, equations 7–10). Finally, these incremental strains are added to get the cumulative strain.

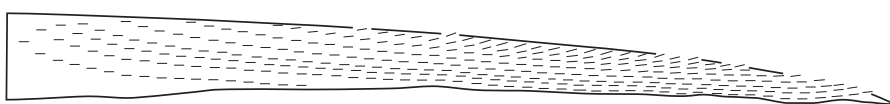
Hudleston (Hudleston and Hooke, 1980) made such a calculation using a comprehensive set of data on surface velocities and mass balance along a flow line on Barnes Ice Cap. To estimate horizontal velocities at depth, he used measured surface velocities and adjusted the value of  $A$  in Equation (5.7) to get zero velocity on the bed, where the temperature is well below the melting point. Rather than use measured vertical velocities, he used the mass balance data to estimate the long-term steady-state vertical velocity at the surface, and assumed that it decreased linearly with depth. Transverse strain rates are small, so he assumed that they could be neglected.

The results of his calculations are shown in Figures 14.4 and 14.5. By following particles starting at nine points in the accumulation area, he first mapped nine

(a) Particle paths and isochrons



(b) Direction of maximum cumulative extension



(c) Cumulative strain magnitude,  $\bar{\gamma}_{oc}$

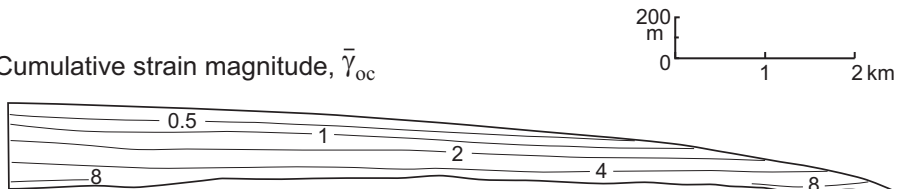


**Figure 14.4** (a) Isochrones and particle paths calculated from velocity field as described in the text.

(b) Orientation of maximum cumulative extension direction shown at 200 m intervals along the particle paths in (a). (c) Contours of  $\bar{\gamma}_{oc}$ . (From Hudleston and Hooke, 1980, Figures 6 and 7. Reproduced with permission of Elsevier Scientific Publishing)

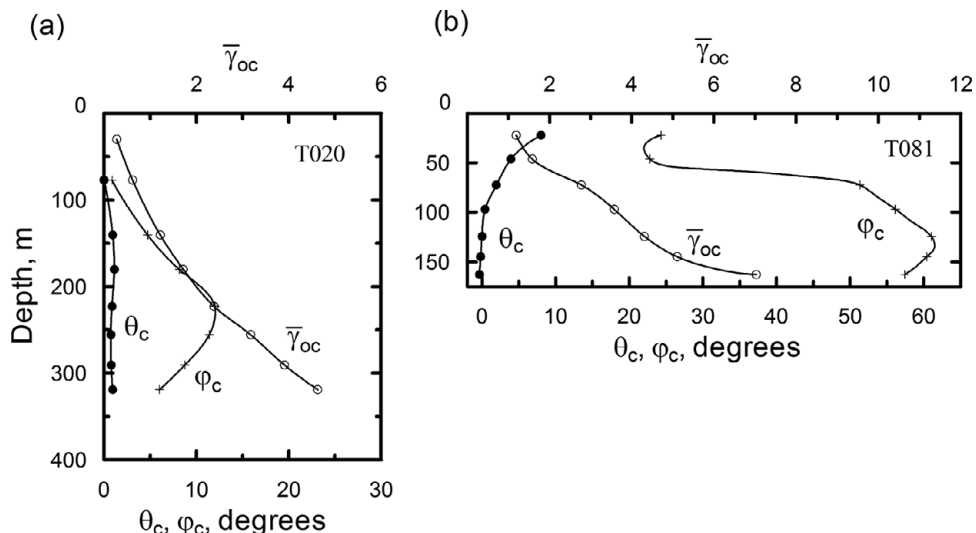


**Figure 14.5** Calculated variation of  $\bar{\gamma}_{oc}$ ,  $\theta_c$ , and  $\varphi_c$  with depth at locations, shown in Figure 14.4, of Barnes Ice Cap boreholes (a) T020 and (b) T081. (From Hooke and Hudleston, 1980, Figures 8a and 9a. Reproduced with permission of the International Glaciological Society)

flowlines (Figure 14.4a). He then calculated the orientations of the axes of maximum cumulative extension ( $X$ -axes: Figure 14.4b). Noteworthy in this figure is the fact that these axes are nearly parallel to the bed throughout most of the glacier. The increased upglacier dip at the surface near and downglacier from borehole T061 is a consequence of the increase in the ratio of simple shear to pure shear as the equilibrium line is approached. As just noted, in simple shear the axis of maximum elongation dips  $45^\circ$  initially; with increasing deformation it is gradually rotated toward parallelism with the plane of the shear.

The cumulative strain magnitude,  $\bar{\gamma}_{oc}$ , is shown in Figure 14.4c. These numbers do not appear significant until one realizes that  $\bar{\gamma}_{oc}$  is proportional to the natural logarithm of the axial ratio of the strain ellipse. Thus,  $\bar{\gamma}_{oc} = 8$ , found in the most distal basal ice, corresponds to an elongation of  $\sim 18,000:1$ . A 1 m cube would be stretched into a 1 m wide ribbon 134 m long and 7.5 mm thick!

Figure 14.5 shows the variation of  $\bar{\gamma}_{oc}$ ,  $\theta_c$ , and  $\varphi_c$  with depth in boreholes T020 and T081 (Figure 14.4a). Because the dominant strain pattern at T020, particularly in the upper part of the glacier, is nearly pure shear with vertical compression and longitudinal extension, the axis of maximum cumulative extension is nearly horizontal. Thus,  $\theta_c$  remains close to 0. On the other hand,  $\varphi_c$  is 0 at the surface and initially increases gradually with depth as  $\partial u / \partial z$  increases. However, with increasing depth in the glacier, the ice arriving at T020 has passed through a larger and larger region dominated by pure shear. Thus,  $\varphi_c$  reaches a maximum ( $\sim 12^\circ$ ) at a depth of  $\sim 240$  m and then decreases at greater depth.

The pattern at the site of borehole T081 is different in several respects. Because this hole is in the upper part of the ablation area, ice at the surface accumulated some strain as it moved from higher in the glacier. Thus,  $\bar{\gamma}_{oc} > 0$  at the surface. With increasing depth, the ice has traveled a greater distance and accumulated more strain so  $\bar{\gamma}_{oc}$  increases to about 7, representing an axial ratio of over 5000. Because ice near the surface has experienced a modest amount of mixed simple and pure shear,  $\theta_c \approx 10^\circ$  and  $\varphi_c \approx 25^\circ$  here. With increasing depth,  $\varphi_c$  first increases, reaching a maximum at a depth of  $\sim 120$  m and then decreases, reflecting the early history of pure shear that this deeper ice experienced.

To further quantify the influence of the early history of pure shear, Hudleston calculated  $\varphi_c$  for a particle of ice that experienced a total strain,  $\bar{\gamma}_{oc}$ , of 3.75 entirely by simple shear (Hooke and Hudleston, 1980). In this case,  $\varphi_c$  is  $80^\circ$  and increases toward  $90^\circ$  as  $\bar{\gamma}_{oc}$  increases further. For comparison, in holes T020 and T081 the actual rotations at this strain magnitude are  $9^\circ$  and  $57^\circ$ , respectively. (Locate the depths at which  $\bar{\gamma}_{oc} = 3.75$  in Figure 14.5a and b and then find  $\varphi_c$  at those depths.)

Let us now use our understanding of cumulative strain to study the origin of foliation.

## Components of foliation

Glaciers commonly appear to be banded (e.g. Figures 5.18 and 8.8). The banding is penetrative; that is, the bands are cross sections of layers in the ice. Banding is most prominent in the ablation area once the winter snow has melted. Here, it is commonly referred to as foliation, a term used to describe the repetitive layered structure of metamorphic rocks. (Ice is an inorganic material with an ordered crystalline structure so it is a mineral, and a glacier is a monomineralic rock. In the ablation area of a glacier the ice has undergone intense deformation so it is metamorphic. Thus, referring to this banding as foliation is fully appropriate.) Usually, the banded appearance results from layering defined by variations in bubble or dirt content, though elongate bubbles and, in some instances, elongate crystals may contribute, as may differences in crystal size on surfaces “weathered” by radiation.

Banding may also be seen in crevasse walls in the accumulation area, although it has a very different appearance and most people would correctly refer to it as annual layering or sedimentary stratification.

Both sedimentary stratification and foliation in glaciers are normally subparallel to the nearest bounding surface, be it the bed, the surface, or the valley walls. However, in the lower part of the ablation area, foliation defined by variations in dirt content typically dips gently to steeply upglacier (Figure 14.6a). This has given rise to the mistaken impression that some folia are shear planes along which debris was (somehow) carried to the surface. This is rarely the case.

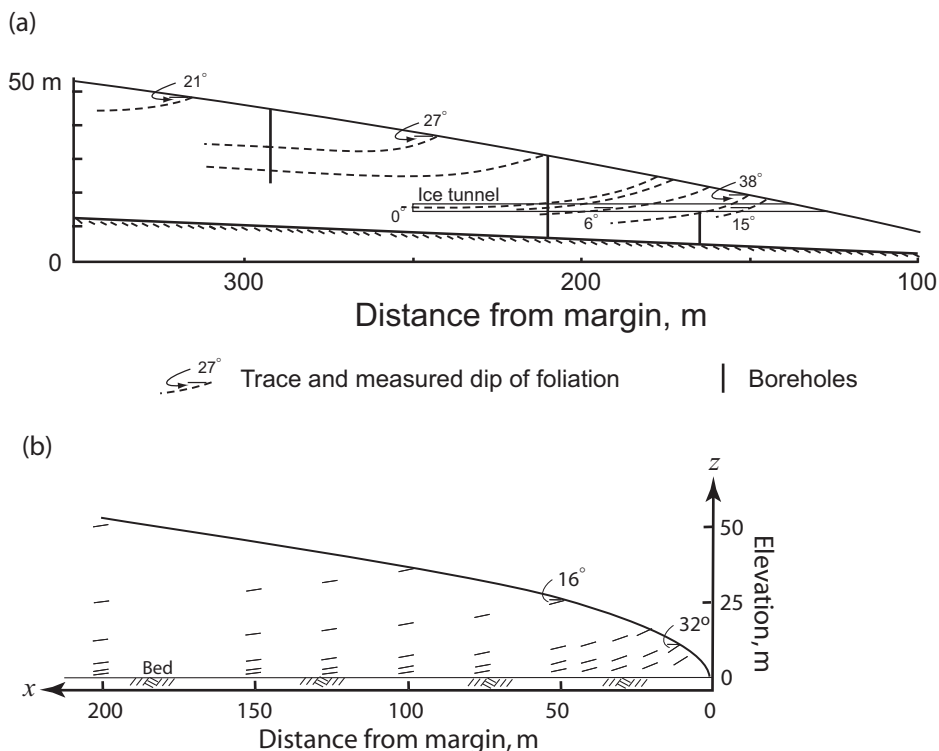


**Figure 14.6** (a) Cross section of the margin of Barnes Ice Cap showing dips of foliation planes measured on the ice surface and in a tunnel excavated in the margin. Dashed lines show traces of foliation planes inferred from measured dips and core stratigraphy. (b) Calculated foliation attitudes in the margin of an idealized perfectly plastic glacier with a parabolic surface profile. See text for explanation.

The most conspicuous foliation is the end product of subjecting inhomogeneities of any origin to cumulative stretching and shearing by strains such as those discussed in the first part of this chapter. After such straining, the origin of the initial inhomogeneity is not likely to be obvious. Suppose, for example, that the 1 m cube we mentioned earlier were a Michelangelo sculpture in a material with a rheology similar to that of ice. Would we recognize it after it had become a ribbon 135 m long and 7.5 mm thick? Perhaps we could identify the material, but certainly not the original handsome shape.

So what are the inhomogeneities that result in this foliation? The most obvious is the sedimentary stratification seen in crevasse walls in the accumulation area. This stratification is defined, in part, by variations in grain size, particularly near the base of an annual layer where depth hoar forms. In addition, wind-blown dust picked up from snow-free ground during the melt season commonly discolors the surface of annual layers, and percolating meltwater may spread out and refreeze along horizons defined by variations in snow density, forming relatively

bubble-free lenses. Rockfalls from valley walls may form local layers of debris that become incorporated into this stratigraphy. Gland-shaped bodies of bubble-free ice may also form from refreezing of percolating meltwater (p. 20). From the pattern of ellipses in Figure 14.1 and elongation directions in Figure 14.4b, it is clear that these inhomogeneities will be stretched longitudinally and compressed vertically. This deformation accentuates the original layering. By the time the inhomogeneities reappear low in the ablation area, they will bear little resemblance to the original sedimentary stratification or glandular structures. It is after such inhomogeneities have been deformed beyond ready recognition that the structure is properly called foliation.

Another major component of foliation is crevasse fillings. Snow blows into crevasses during the winter, and meltwater may saturate this snow during the summer. When the crevasse gets moved into a location, or rotated into an orientation, such that stresses across it are compressional, it closes and this filling gets squashed. A band is thus formed that cross cuts either sedimentary layering or foliation derived from such layering. If the crevasse-filling snow is saturated with water, it is likely to form a band of clear blue ice. Initially, the cross-cutting relation is obvious and the origin of the filling can be properly identified, even if it crosscuts foliation of unidentifiable origin. However, once the filling has been squashed further, rotated to near parallelism with other foliation, and stretched, its origin will be less obvious. Careful observers, however, may still be able to detect the cross-cutting relation.

In basal ice, debris is an important component of foliation. As we have discussed, there are various mechanisms by which debris may become entrained in basal ice – the refreezing part of the regelation cycle, freeze-on by the mechanisms discussed by Robin (Figure 7.6) or in areas where temperature gradients in basal ice lead to local refreezing (Figure 6.11), entrainment in frazil ice in overdeepenings (Figure 8.36), and so forth. In all situations, the resulting layers are parallel to the bed or valley walls, and are in areas subject to high rates of simple shear. The precise origin of the layers is hard to determine before they become deformed, and after shearing the task is usually hopeless, although chemical and isotopic signatures may help (Souchez and Lorrain, 1978).

For the most part, the inhomogeneous distribution of bubbles and dirt particles that define foliation is largely primary, inherited from the sedimentary stratification, crevasse fills, and basal debris-incorporation processes. However, both bubbles and dirt particles can migrate under a temperature gradient (Shreve, 1967; Stehle, 1967; Römkens and Miller, 1973). Bubbles migrate because molecules sublime from the warmer wall and condense on the cooler wall. Dirt particles migrate because a film of liquid water surrounds the particle, and solutes in this film, being most concentrated on the cold side of the particle, diffuse to the warm side causing melting there (and refreezing on the cold side). Thus, in both cases, migration is

toward the warmer temperatures. The speed of migration is expected to be proportional to the magnitude of the temperature gradient, although this has only been verified in the case of air bubbles. Migration speeds, although  $<\sim 20 \text{ mm a}^{-1}$  for bubbles and  $<\sim 200 \text{ mm a}^{-1}$  for dirt grains, are high enough to be significant. Temperature gradients, however, don't vary appreciably over short distances, so all particles or bubbles might be expected to move the same amount. On the other hand, differences in speed, perhaps due to differences in bubble or particle size or to interference among particles, might lead to segregation.

Solid particles and deformable spheres in viscous media also tend to migrate toward regions of low velocity gradient (Goldsmith and Mason, 1961; Bhattacharji, 1967; Husband *et al.*, 1994). In cold ice, shear strain rates in folia with modest to high dirt concentrations are likely to be stiffer than clean ice (Hooke *et al.*, 1972), so particles may migrate toward these folia.

In addition, Azuma *et al.* (2012) found that bubbles in ice were “caught and swept” along by migrating grain boundaries as grains were annealed and grew larger. Kamb (1972) and Pfeffer (1992) have documented formation of lenses of clear ice, a couple of centimeters in thickness and decimeters in length, formed under transient conditions of high compressive stress lasting only a few days. Hudleston (2015) speculates that bubbles may have been swept out of the bubble-free lenses ice by migrating grain boundaries.

These migration processes likely modify the distribution of bubbles and dirt particles in ice, and thus contribute to the visual appearance. They may either accentuate or blur primary characteristics such as depth hoar or ice lenses. However, they are largely local, and thus do not, alone, form glacier-scale folia like those in Figure 5.18. They, or similar processes, do form small scale foliation features such as the longitudinal foliation in Figure 14.7.

Because foliation, once formed, is advected passively, it reflects the cumulative deformation the ice has undergone. It thus contains a wealth of information about this deformation.

### Longitudinal septa

Intense deformation may occur where ice from two or more accumulation basins converges to form a trunk glacier. In their study of Blue Glacier (Figure 14.8), Allen *et al.* (1960) referred to the resulting foliation pattern as a *longitudinal septum* (or informally in the field as *gesundheit strasse*). Although the upflow extension of the septum was covered by firn, they thought it likely formed downflow from a rock bastion that separated two 300-m high ice falls. A trench formed in the lee of the bastion, and they supposed that snow accumulating in the trench was strongly compressed by the high angle at which flow from Ice fall B converged with that from Ice fall A (Figure 14.8), resulting in a near vertical foliation. In addition, the glacier surface slope downflow from Ice fall A was appreciably steeper than that

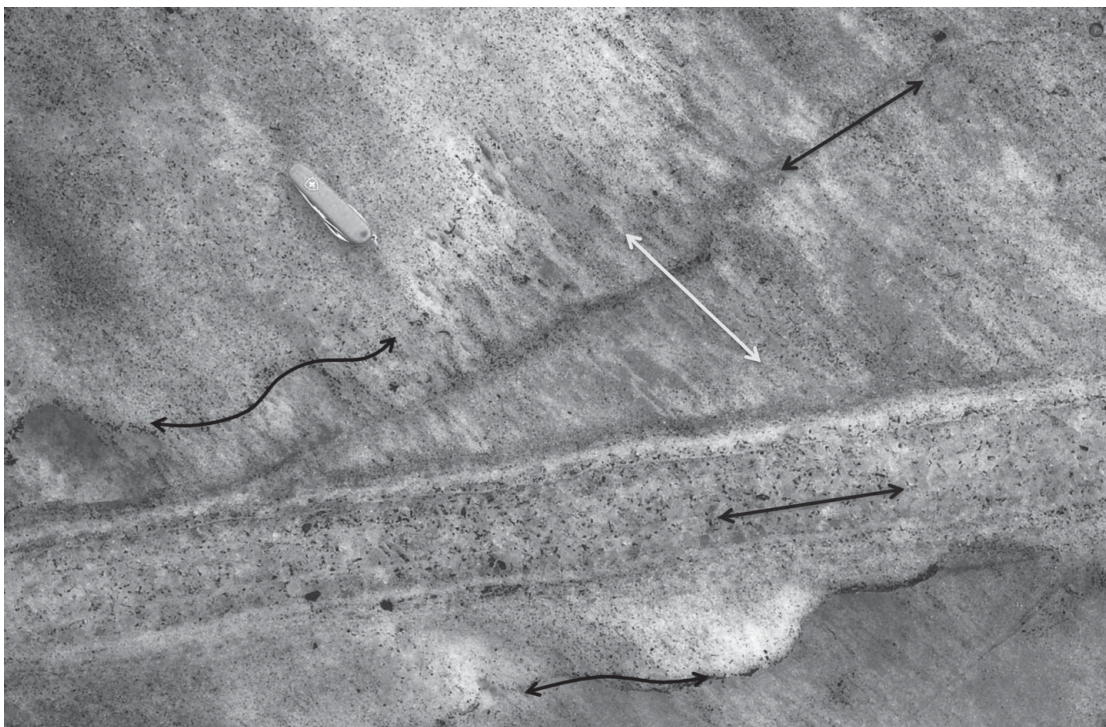


**Figure 14.7** A subtle near-vertical longitudinal foliation (straight white arrow and knife) is normal to primary stratification (wavy black arrows). Also in the image are two veins infilling fractures (straight black arrows). (Figure 16d from Hudleston (2015). Reproduced with the permission of the author and Elsevier Scientific Publishing)

downflow from Ice fall B, and was thus moving faster. This shear likely accentuated foliation in the septum in and just below the junction.

Ice flowing past such a bastion commonly erodes it, so longitudinal septa are commonly marked by medial moraines, although that is not the case in Figure 14.8.

### Folds in foliation

Folds in foliation are a record of deformation. Most folds, particularly large ones, are similar folds, or ones in which the bounding surfaces of the folded layer are essentially identical in shape, and the thickness of the layer varies, becoming thinner on the flanks where it has been stretched (Figure 14.9a). In parallel folds, on the other hand, the folded layer maintains a constant thickness and the boundaries are not similar (Figure 14.9b). Parallel folds are formed when a compressive force is applied parallel to bedding and the bedding buckles. Such folds, called *buckle folds*, form when there is a viscosity contrast between the beds. Stiff dirty layers, centimeters in thickness, occasionally form small scale buckle folds in cold ice (Hudleston, 2015), but otherwise viscosity contrasts of sufficient magnitude to form such folds are rare in glaciers.

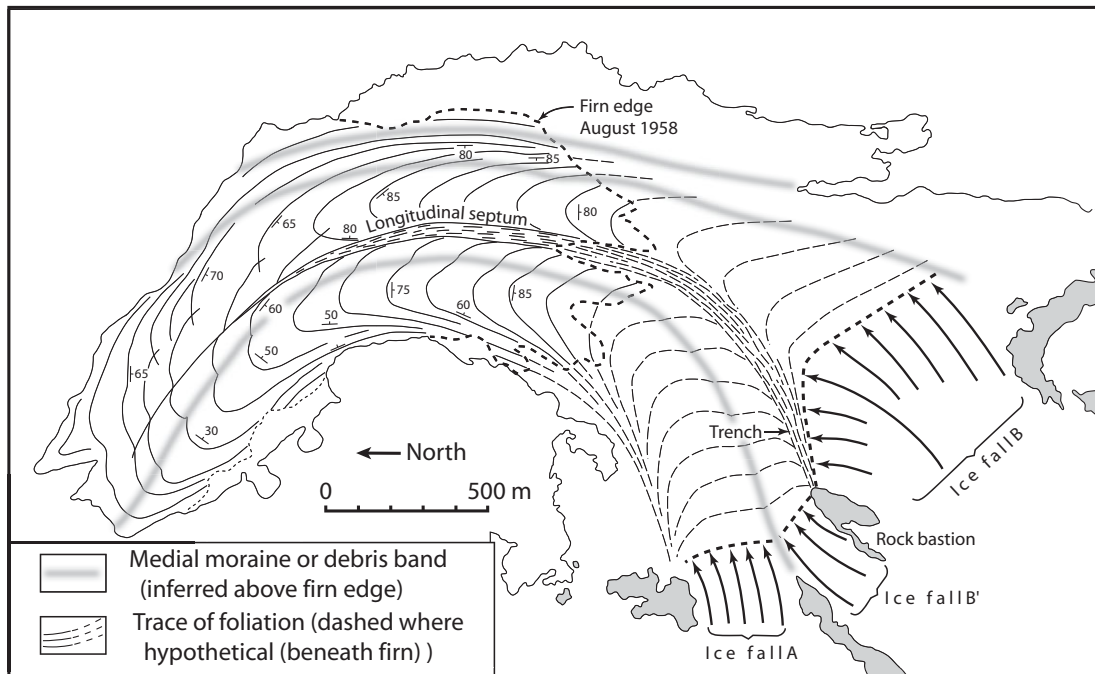


**Figure 14.8** Map of Blue Glacier, Washington, USA, showing traces of foliation and longitudinal septum. Ice falls A and B originate from separate accumulation basins. Strike and dip symbols show a pair of nested-spoon structures, one from each accumulation basin. (Redrawn from Figure 1 of Kamb (1959). Reproduced with permission of the author and the American Geophysical Union. Strike and dip symbols from Allen *et al.* (1960), Figure 7.)

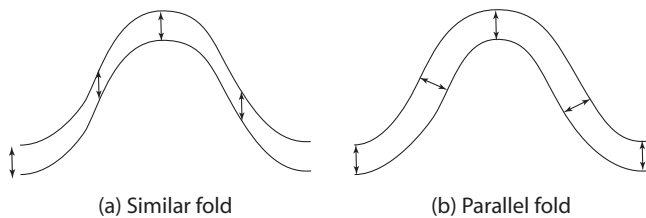


**Figure 14.9** (a) A similar fold. (b) A parallel fold. Double-headed arrows in both panels are the same length.

Similar folds may form in glaciers by several different processes. The most dramatic are those delineated by medial moraines formed when a tributary glacier surges into a trunk glacier (Figure 14.10). Drag along the valley side deforms such folds as they are transported passively downglacier. Such folds are diagnostic of surging, and if the velocity of the trunk glacier is known, the spacing between folds can be used to estimate the recurrence interval of the surges.

Similar folds also form in the foliation of valley glaciers when sedimentary stratification, originating in a wide accumulation area, undergoes transverse



**Figure 14.10** Similar folds in foliation defined by medial moraines, Yanert glacier, Alaska, August 13, 1961. The tributary glacier in the upper right is a surging glacier. Each time it surges, the left lateral moraine of Yanert Glacier is punched outward. Subsequent flow carries this bulge downglacier and deforms it. Three old surges, of gradually diminishing size, are outlined by the moraines. A fourth surge may be in progress. (Image by Austin Post. University of Washington Libraries PH Coll 734.AD-108. Used with permission)

compression as it is advected downglacier into a narrower tongue. If the annual layers in the accumulation area were strictly planar and of uniform thickness and composition, such transverse compression would simply thicken them uniformly. However, as we saw earlier (p. 100–101), transverse profiles in the accumulation area are normally concave upward, so the sedimentary stratification is “born” synclinal. As it is advected toward the terminus and transverse strain rates become compressive, the syncline’s amplitude is accentuated. Longitudinal strain rates also become compressive in the ablation area, so  $\partial w/\partial x$  is positive. Foliation in the central part of the glacier is thus tilted upglacier (as analyzed in greater detail later (p. 404–406). These two processes result in the characteristic nested spoon shape of the foliation in the tongues of many valley glaciers.

A different process is inferred to be responsible for the nested-spoon structure in Blue Glacier (Figure 14.8). There, crevasses in the ice falls are filled with snow; intense compression at the bases of the ice falls is then believed to result in a near-vertical transverse foliation. As this foliation is advected downglacier,  $\partial u/\partial z$  shear tilts it downglacier, decreasing its dip (Figure 14.8). The change in dip is consistent with the variation in  $\partial u/\partial z$  with depth in a borehole (Allen *et al.*, 1960). Near the terminus, however,  $\partial w/\partial x$  likely begins to steepen the dip again.

Isoclinal similar folds that plunge upglacier were found in the longitudinal septum of Blue Glacier. They were likely born synclinal as sedimentary layering in the trench and then tightened into isoclinal folds by compression there.

### Isoclinal folds generated by changes in flow regime

Folds can also be nucleated over irregularities in the bed by changes in the flow regime. Recumbent folds in the marginal zone of Barnes Ice Cap (Figure 14.11) were



**Figure 14.11** Recumbent fold in foliation in basal ice of Barnes Ice Cap.

likely formed in this way. Hudleston (1976) explored this possibility with a numerical model (Figure 14.12). As the flow is nearly two dimensional, he assumed that the variation in  $u$  with depth was adequately described by Equation (5.6) with the surface slope averaged over a distance equal to the local ice thickness, and that

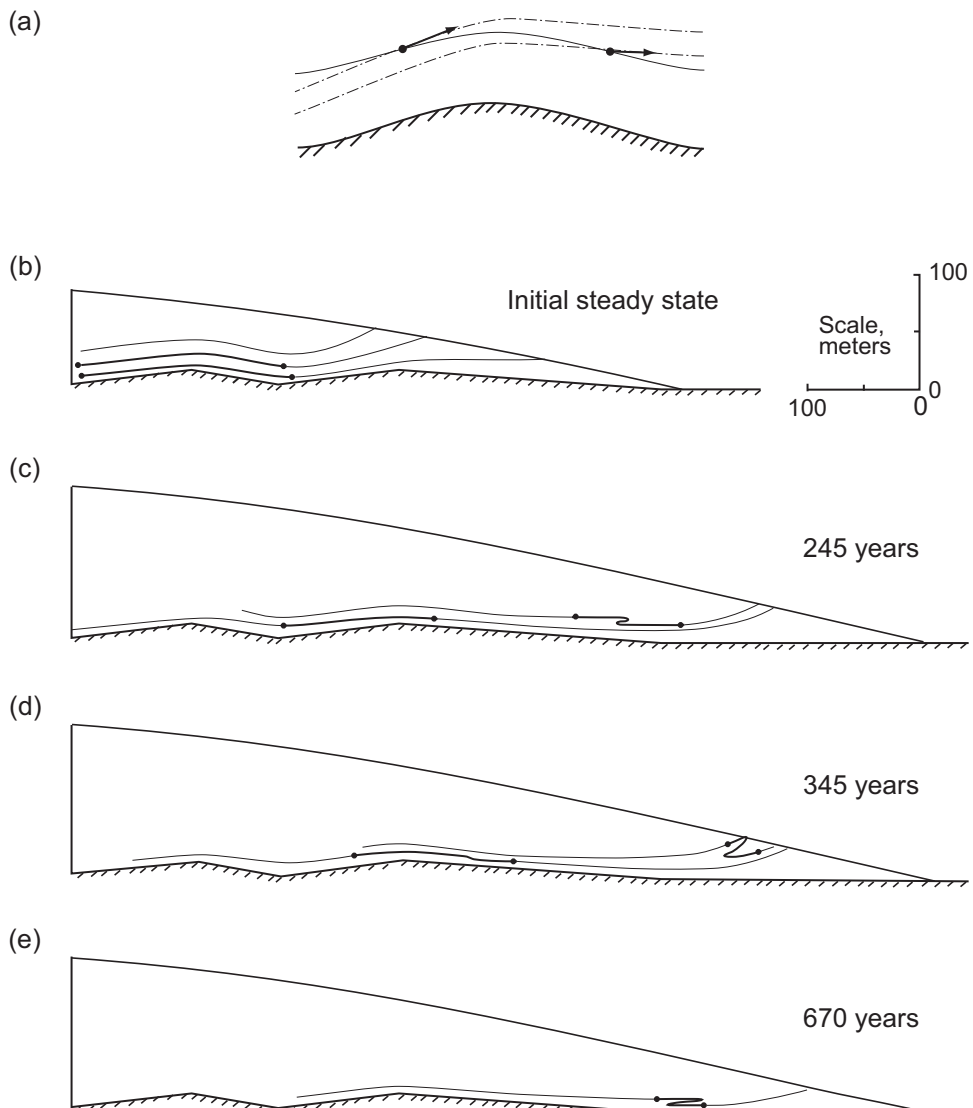


**Figure 14.12** Generation of recumbent folds as a result of a glacier advance. (a) Sketch showing one of several possible changes in velocity vectors that would result in a fold. (b) Initial steady state geometry. Foliation is assumed to have developed parallel to the three particle paths shown. Heavier parts of paths, between dots, are followed downflow in panels (c) through (e). (c) Situation after a ~200 m advance lasting 30 model years followed by a new steady state lasting 245 model years. (d) and (e) Situation 345 and 670 model years after establishment of the new steady state. (Compiled from Hudleston, 1976, Figures 7 and 8. Reproduced with the permission of the author and the Geological Society of America).

$w(z) = - \int_b^s \frac{\partial u}{\partial x} dz$  with the boundary condition  $w = 0$  at the bed. With this velocity field, he could calculate particle paths.

As an initial condition, Hudleston assumed that foliation some distance from the margin had developed over a period of many years under a stable flow regime, and thus would be nearly parallel to the bed and to particle paths in the ice (Figure 14.12b). He then let the glacier advance 200 m, followed by a new steady state. Such an advance (or retreat) of a glacier changes the velocity vector at any given point because the ice thickness and surface slope change. In this case, the change in the velocity field was such that velocity vectors became inclined upward with respect to the previous particle path (Figure 14.12a), so points on a foliation plane on the stoss side of a bump were moved upward with respect to more distal points on that same foliation plane. These upglacier points are thus moved to a level where  $u$  is higher, so they gradually overtake more distal parts of the foliation plane. If the distance to the margin is sufficient, this results in a recumbent fold with a subhorizontal axis transverse to the flow direction (Figure 14.12c–e). Such folds are common in the bubbly white Pleistocene ice in the marginal zone of Barnes Ice Cap; they may have been initiated by the Little Ice Age advance discussed earlier (Figure 5.17). Note that while the folds are seeded over a bump in the bed, they do not become apparent until the ice has moved some distance toward the margin. Folds developed in higher foliation planes reach the margin first, and are somewhat more open (Figure 14.12d and e). After a sufficiently long time without further changes in regime, all such folds will melt out, and this record of the regime change will vanish.

Folding could also result from migration of a divide beneath which a Raymond bump had formed. Once the divide was sufficiently far from the bump and the flow had become unidirectional (rather than symmetrical as it is beneath the divide), the velocity gradient would deform annual layering into a recumbent fold.

Wolovick *et al.* (2014) have suggested another mechanism for generating large-scale folds. Suppose the bed of an ice sheet is at the pressure melting point over some distance and then becomes frozen. Plug flow ( $\bar{u} = u_b$ ) prevails in the thawed region, but  $u_b \rightarrow 0$  abruptly at the transition. This deflects velocity vectors upward, and over a distance of a few tens of kilometers the velocity profile transitions to one described by Equation (5.6) with  $u_b = 0$  (Figure 14.13a). Wolovick *et al.* then introduce, in their numerical model, a perturbation in the water flux into the warm-based zone. This increases  $u_b$ , thus increasing compression at the transition and increasing the upward velocity,  $w$ . Basal foliation is thus bowed upward into an anticlinal fold, and the temperature gradient in the basal ice is reduced. The latter traps heat at the bed, increasing melting and thus also increasing  $u_b$  up-flow from the transition. The increase in melting causes the boundary between thawed and frozen bed to migrate downflow and also increases the extending strain rate

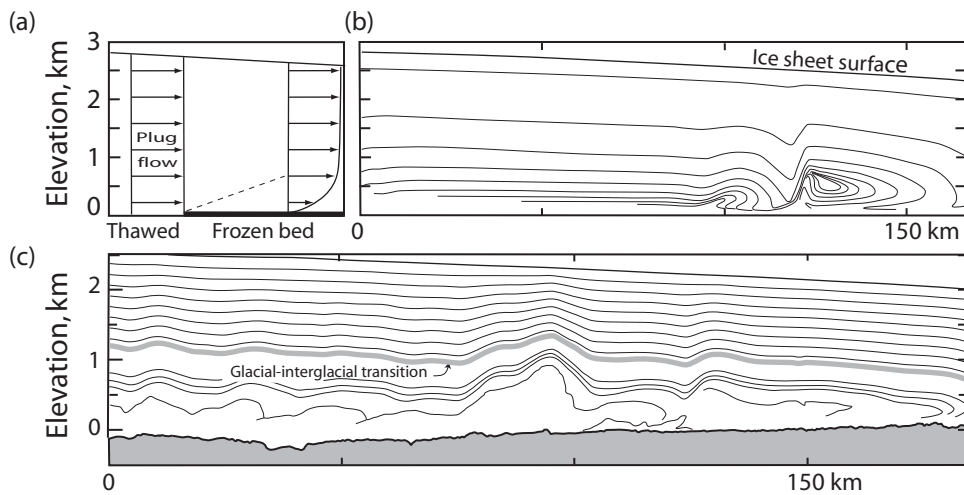


**Figure 14.13** (a) Change in velocity profile at transition from a thawed to a frozen bed in an ice sheet; (b) computer simulation 9 ky after perturbation in water flux, as described in text; (c) interpretation of a radar image from northern Greenland depicting basal units and associated deformation. In panels (b) and (c) light lines are foliation defined by sedimentary stratification, and vertical exaggeration is 15x. (Redrafted from Wolovick *et al.*, 2014, Figures 1 and 4d. Reproduced with the permission of the author and the American Geophysical Union)

somewhat up-flow, bringing cold ice to the bed. Under the right circumstances, this cold ice freezes to the bed, resulting in an isolated zone of warm-based ice that then travels down-flow. In this way, Wolovick *et al.* develop folds extending through half the ice-sheet thickness (Figure 14.13b). Their model folds are rather similar to folds observed in radar profiles in both Greenland and Antarctica (Figure 14.13c).

Glaciers advance and retreat, they rest on irregular beds, divides migrate, and basal water fluxes change. Thus, we should expect folding in basal ice to be common. Indeed, oxygen isotope profiles from the 3000 m GRIP and GISP 2 cores through the Greenland Ice Sheet are quite similar to a depth of 2750 m, but in the basal 250 m the correlation breaks down (Grootes *et al.*, 1993). Similar discrepancies were found in the lowest 10 m of two 299 m cores, taken 27 m apart, on Devon Ice Cap (Paterson *et al.*, 1977), and in the lowest 12 m of three cores, within 2 km of each other, from Agassiz Ice Cap (Fisher, 1987). A likely explanation for the lack of correlation in deeper ice in these cores is folding, although boudinage (Hudleston, 2015, pp. 18–29) is also possible.

Tight folds with steeply plunging axes are found along valley sides. These can be produced by two processes. Valley sides are irregular, so the process shown in Figure 14.12 is clearly one. On a smaller scale, however, deformation in the vicinity of crevasses can also produce folds by another mechanism described by Hudleston (1989). When a crevasse opens at a high angle across a planar feature that is parallel to a valley side, the feature is offset both longitudinally and laterally

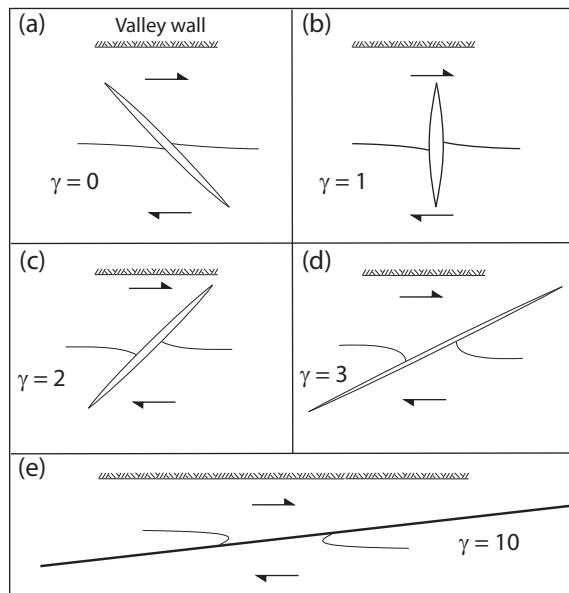


**Figure 14.14** Development of a flanking fold. (a) Crevasse opens, breaking a foliation plane. (b) After shear strain of  $\gamma = 1$ , the crevasse is normal to valley side and the foliation plane is offset both longitudinally and laterally. (c and d) with continuing shear strain and owing to the increase in  $u$  outward from the valley side, the foliation plane is folded and displaced to form a flanking structure – a double hook-shaped fold. By  $\gamma = 2$ , the crevasse has filled with snow and refrozen meltwater. The fracture trace at  $\gamma = 10$  is truncated. (From Hudleston, 2015, Figure 28. Reproduced with the permission of the author and Elsevier Scientific Publishing)

(Figure 14.14a). The component of opening that is normal to the valley side bends the planar feature slightly. As deformation continues, this slight lateral bend is exploited by the increase in  $u$  outward from the valley wall,  $\partial u / \partial y$ , and after strain to  $\gamma = 10$  a double hook-shaped fold has formed (Figure 14.14e). Note that sense of offset (left lateral) is opposite to that of shear (right lateral) and opposite to the drag implied by the folds.

### Foliation in the marginal zones of ice caps and ice sheets

We noted, above, that foliation in glacier margins has often been mistaken for “shear planes.” Shear planes would be parallel to planes of maximum shear stress. Here, we demonstrate that the upglacier dip of the foliation at a glacier surface bears only a coincidental, not a genetic relation to directions of maximum shear stress. We do this for an idealized glacier with a steady-state surface profile described by  $h = \sqrt{cx}$  where  $x$  is the distance upglacier from the margin and  $c$  is a constant. The ablation rate,  $b_n$ , is constant over  $x$ .

As before (Figures 14.4 and 14.5), the first task is to determine the velocity field. Then that velocity field is used to see how foliation that is nearly parallel to the bed some distance from the margin is deformed as it is passively advected to the margin.

Because the glacier is in a steady state, conservation of mass requires that:

$$b_n x = -\bar{u} \sqrt{cx} \quad (14.7)$$

where  $\bar{u}$  is the depth-averaged horizontal velocity. Because  $\frac{\partial u}{\partial x} + \frac{\partial w}{\partial z} = 0$ , substituting  $\bar{u}(x)$  from Equation (14.7) and integrating yields:

$$w = -\frac{b_n}{2\sqrt{cx}} z. \quad (14.8)$$

Knowing both  $u$  and  $w$ , we can calculate a path for an element of ice starting at  $(x_o, z_o)$ , where  $x_o$  is some distance from the margin, and  $z_o$  is slightly above the bed. As  $u = dx/dt$ , Equation (14.7) can be integrated to yield:  $x = \left(x_o^{1/2} + \frac{b_n}{2\sqrt{c}} t\right)^2$ . Combining this with Equation (14.8) to eliminate  $x$ , remembering that  $w = dz/dt$ , and integrating yields:

$$z = z_o \left(\frac{x_o}{x}\right)^{1/2}. \quad (14.9)$$

Now consider a foliation plane in this element of ice. At  $(x_o, z_o)$  the plane will have a small upglacier dip,  $\beta_o$ , with respect to the particle path. This is because  $\theta_c$  is always greater than 0 under steady-state conditions. We wish to compute its dip when the element reaches the glacier surface. The element is subjected to longitudinal compression and vertical extension which will change the inclination of any line that is not parallel to the direction of compression or extension (Figure 12.13). In addition, at any fixed height,  $z$ , above the bed,  $w$  increases toward the margin as  $h$  ( $= \sqrt{cx}$ ) decreases (Equation 14.8). Therefore, the shear strain  $\partial w / \partial x$  will also increase the upglacier inclination of the plane. The problem thus strongly resembles the deformation of a borehole (Chapter 12), except that now the “hole” is nearly horizontal, not vertical, and the primary shear to which it is subjected is  $\partial w / \partial x$ , not  $\partial u / \partial z$ . Consequently, Equation (12.46) is applicable in the form:

$$\frac{\partial \beta}{\partial t} = \frac{\partial w}{\partial x} + 2\beta \frac{\partial w}{\partial z} - u \frac{\partial \beta}{\partial x}. \quad (14.10)$$

To express  $\beta$  in terms of  $x$  alone, we obtain  $\partial w / \partial x$  and  $\partial w / \partial z$  from Equation (14.8). Then using the chain rule,  $\frac{\partial \beta}{\partial t} = \frac{\partial \beta}{\partial x} \frac{\partial x}{\partial t} = \bar{u} \frac{\partial \beta}{\partial x}$ , and Equation (14.9), we obtain a first-order linear ordinary differential equation:

$$\frac{\partial \beta}{\partial x} + \frac{\beta}{2x} - \frac{z_o x_o^{1/2}}{8x^{5/2}} = 0 \quad (14.11)$$

which has the solution (e.g. Sokolnikoff and Redheffer, 1958, pp. 23–24):

$$\beta = \sqrt{\frac{x_o}{x}} \left[ \beta_o + \frac{z_o}{8} \left( \frac{1}{x_o} - \frac{1}{x} \right) \right]. \quad (14.12)$$

$\beta_o$  is negative in our coordinate system, indicating an upglacier dip. As  $x_o > x$  in this system,  $\beta$  is also negative.

Dips of foliation planes at different positions in the margin of such an idealized glacier, calculated using Equation (14.12), are plotted in Figure 14.6b. The surface profile used is a good approximation for that in the margin of Barnes Ice Cap. The initial dip of the foliation,  $\beta_0$ , was upglacier and  $2.5^\circ$  steeper than the flow paths. Six elements of ice, starting at different heights above the bed at  $x_0 = 1250$  m, were followed along paths defined by  $u(x)$  and  $w(x, z)$ , and the dips of foliation planes contained in the elements were determined at various points along the way. A rapid increase in dip near the surface is clearly shown. This analytical result is consistent with the dip of the isoclinal fold reaching the surface after 345 years in Hudleston's numerical model (Figure 14.12d), and also with foliation attitudes measured at the surface and in an ice tunnel in the margin of Barnes Ice Cap (Figure 14.6a).

Foliation attitudes calculated from Equation (14.12) are sensitive to the choice of  $\beta_0$  as well as other parameters, so detailed comparison between the calculated and observed attitudes is not warranted. The important point is that passive deformation of foliation that is nearly parallel to the bed some distance from the margin can account for observed dips at the surface near the margin. Furthermore, because shear stresses vanish on a free surface, the planes of maximum shear stress dip  $45^\circ$  up- and downglacier relative to the surface (Figure 10.3). Observed foliation attitudes (Figure 14.6; Allen *et al.*, 1960; Hooke, 1970, among others) bear no such consistent relation to planes of  $\sigma_{S\max}$ .

---

## SUMMARY

In this chapter, we've reviewed the fundamentals of finite strain and showed that three quantities are needed to describe the cumulative change in shape and orientation of a hypothetical sphere of ice as it is squeezed and stretched while being advected through a glacier or ice sheet. These are the natural octahedral unit shear,  $\bar{\gamma}_{oc}$ , which is a measure of the total strain; the orientation of the  $X$ -axis of the strain ellipse with respect to the  $x$ -axis of the coordinate system,  $\theta_c$ ; and the rotation of the line that eventually becomes the  $X$ -axis in the strained state,  $\varphi_c$ . With increased deformation,  $\bar{\gamma}_{oc}$  increases and  $\theta_c$  approaches 0 as the  $X$ -axis approaches parallelism with particle paths or flow lines. However,  $\varphi_c$  may remain substantially less than  $90^\circ$  if the ice experiences a long early history of nearly pure shear.

Inhomogeneities in the ice such as sedimentary stratification, crevasse fillings, meltwater glands and lenses, and debris-rich layers become buried, stretched longitudinally, and squeezed vertically during flow in the accumulation zone. By the time

these features are re-exposed in the ablation area, their origin is normally difficult or impossible to determine. The result is then properly called foliation. Once a foliation has developed, it may be enhanced with further strain and deformed as it is passively advected toward the margin.

A surge of a tributary, a change in flow regime, or displacement by a marginal crevasse may lead to folding of foliation.

# 15

## Response of glaciers to climate change

Changes in climate, or more specifically in temperature and precipitation, affect the meteorological component of mass balance ( $\dot{B}_m$ ; Equation 3.1). We've seen that negative perturbations in  $\dot{B}_m$  can cause a tidewater glacier to retreat from its terminal moraine, initiating dramatic retreat of the terminus (p. 34–36), and that an increase in melting on the surface of an ice shelf can lead to its collapse (Figure 13.11). Similarly, climatically induced ocean warming can thin an ice shelf, instigating irreversible retreat of its grounding line (p. 360). In this chapter, however, we'll focus on the details of adjustments to perturbations in  $\dot{B}_m$  when such rapid dynamical changes (p. 23) are not involved. Glaciers then react to changes in climate by expanding or contracting at more measured rates.

If the climate of a region were to remain constant for a long time, several decades or even centuries, the geometry of ordinary glaciers would adjust so that the specific net balance was everywhere equal to the local emergence or submergence velocity. The integral of the specific net balance over the glacier,  $B_n = \int b_n dA$ , would then be zero, and the glacier would be in a steady state. Climate does change, however, so this is an ideal that may occasionally be approached but rarely, if ever, reached. The change may involve changes in precipitation, in temperature, in radiation balance, or most likely in all three (see Chapter 3). From the perspective of a glacier, though, the net effect is to change the amount and the spatial distribution of accumulation and melt. This leads to discrepancies between the specific net balance and the local emergence or submergence velocity (p. 96–97), and hence to changes in glacier geometry.

In most situations, the principal adjustment that takes place is a change in the glacier's length or size. A negative mass balance, maintained over a period of years, results in retreat. As the glacier retreats to higher elevations or more northerly latitudes, the size of the ablation area decreases so the summer balance becomes more positive until it equals (in magnitude) the winter balance. The net balance then returns to zero.

## Feedback processes

Let's first discuss some feedback processes that can influence the way in which a polar glacier adjusts to climatic change, but which we will not consider in detail. One such process was discussed by Lliboutry (1970). A change in temperature has an immediate effect on the mass balance, but it also has a delayed effect on the flow owing to the temperature dependence of the flow law. An increase in temperature, for example, may increase ablation. The resulting decrease in net balance causes the glacier to thin. Then, as the temperature change gradually penetrates into the glacier, the flow rate increases. Because this increases the mass flux to the terminus relative to the input of ice upglacier, it results in further thinning in a positive feedback. The thinning leads to further warming at the glacier surface owing to the increase in temperature with decreasing elevation.

It is well to keep in mind, however, that if the climate is sufficiently cold, increases in temperature may actually increase the winter balance, as the atmosphere is then able to hold more moisture in the vapor state. For example, studies of the volume of air in bubbles in a core from Byrd Station in West Antarctica (Figure 13.2) suggest that, as the Pleistocene gave way to the Holocene and the climate warmed, the ice sheet there thickened by ~250 m (Raynaud and Whillans, 1982). As the warm wave penetrated deeper into the ice sheet and the flow rate increased, however, the ice sheet began to thin (Alley and Whillans, 1991). Thus, in this case, the processes did not reinforce one another. Measurements of strain rate and mass balance along a 160 km strain network upglacier from Byrd Station suggest that the thinning continued until at least 1974 (Whillans, 1977).

Superimposed on these influences is the normal increase in  $b_n$  with elevation. Owing to this increase, perturbations that result in thickening or thinning of a glacier are effectively amplified. This positive feedback is known as the *Böðvarsson effect* (Böðvarsson, 1955).

In large ice masses yet another delayed response is superimposed on these positive feedback loops: the response of Earth's crust to the ice load. As an ice sheet grows, the crust is depressed isostatically. Because the response of the crust is slow, the crust may continue to subside long after the ice sheet mass has roughly stabilized. The continued subsidence lowers the surface elevation of the ice sheet, resulting in warming and possibly initiating one of the positive feedbacks just discussed. Where the bed becomes depressed below sea level, any continued depression of the crust may lead to a rise in relative sea level and to buoyancy forces that greatly increase flow speeds.

Numerical models are commonly used to study these complex interrelated feedback processes, each of which has its own time scale.

## Pleistocene climate

Let's now take a look at climatic changes that are known to have occurred in the past – those associated with the Pleistocene glaciations. Advances and retreats of ice sheets during the Pleistocene were modulated by variations in solar insolation at high latitudes, occasioned by periodicities in Earth's orbit – the so-called Milankovitch cycles (Hays *et al.*, 1976). During the early Pleistocene, variations in the tilt of Earth's axis with a periodicity of 41,000 years correlate well with proxy measures of ice volume derived from deep sea sediment cores (Figure 15.1a). About 900,000 years ago, however, the periodicity in ice volume gradually changed to 100,000 years, which is roughly the time scale on which Earth's orbit changes in eccentricity. This latter correlation is puzzling because changes in eccentricity have a quite modest influence on insolation. The correlation could be fortuitous, but it seems more likely that there are positive feedbacks, as yet unidentified, that amplified the eccentricity signal.

Superimposed on the last of these 100,000 year cycles are 25 sharp oscillations in temperature, first identified in Greenland ice cores by Willy Dansgaard and Hans Oeschger (Dansgaard *et al.*, 1993). These are called Dansgaard–Oeschger or D-O events. Four are shown in Figure 15.1b. Each starts with an abrupt warming of

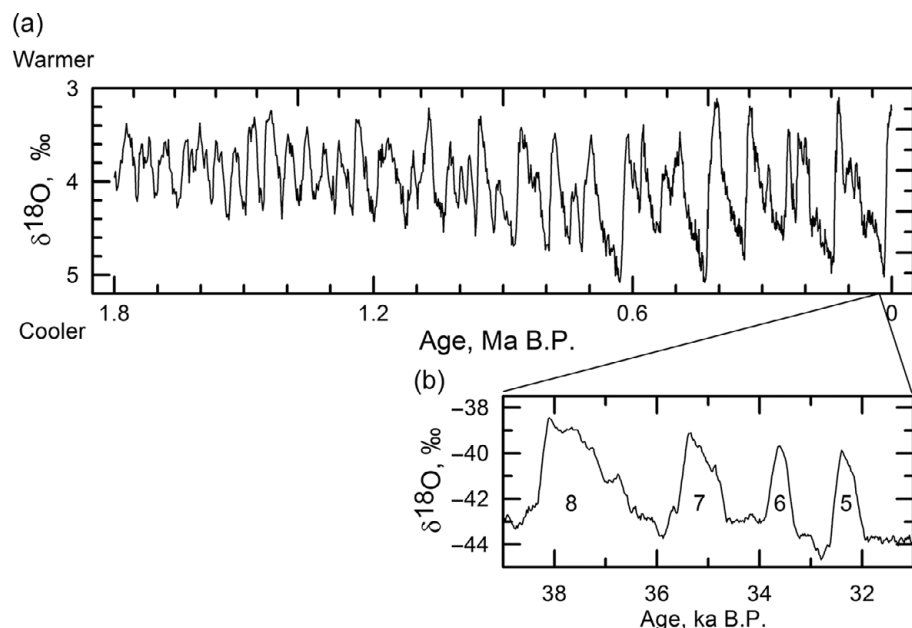


**Figure 15.1** (a) Variations in  $\delta^{18}\text{O}$  over the past 1.8 Ma showing change from 41 ka periodicity to 100 ka periodicity at ~0.9 Ma. (b) Dansgaard–Oeschger cycles 8-5 in the Greenland Ice Sheet Project (NGRIP) core. ((a) From Lisiecki and Raymo, 2005, Figure 4a. Reproduced with permission of the authors and the American Geophysical Union; (b) From GICC05)

several degrees in only a few decades. The warming is then followed by gradual cooling over a few hundred years. The mean duration of a D–O event is slightly less than 1500 years, or a multiple thereof. While this may reflect a physically significant periodicity, a study based on new time scales for the cores suggests that the recurrence interval is indistinguishable from random (Ditlevsen *et al.*, 2007). In any case, neither variations in Earth's orbit nor those in solar irradiance vary on this time scale, so the mechanism must be internal to the climate–ice sheet system.

The Dansgaard–Oeschger events are likely related in some way to the Atlantic meridional overturning circulation, or AMOC. At present, the Gulf Stream transports warm saline water northeastward from the Caribbean to the Barents Sea, between Norway and Iceland. The water evaporates as it moves northward, increasing its salinity, and also cools. In the Barents Sea its increased salinity and lowered temperature make it dense enough to sink. Thence it flows southward at depth. The AMOC transports huge amounts of heat northward, so any process that weakens it cools the North Atlantic and conversely.

Cycles with a recurrence interval similar to that of the D–O events appear to have continued into the Holocene, albeit with reduced amplitude (Bond *et al.*, 1997). The well-known Younger Dryas (12.5 ka), the 8.2 ka cooling episode, and the Little Ice Age (1.4 ka) are examples of the associated cold snaps. Others occurred at intervals of  $1.4 \pm 0.4$  ky.

Despite not knowing what causes these oscillations, we are continuing to pump CO<sub>2</sub> and CH<sub>4</sub> into the atmosphere, driving the climate into uncharted territory. On the Antarctic Peninsula the synchronicity of glacier responses has been steadily increasing over the Holocene; now 140 tidewater glaciers there are retreating simultaneously, reflecting a unified response to climate change (Minzoni *et al.*, 2017). At the end of the Pleistocene, in contrast, only a few glaciers responded synchronously. With luck, we won't pass a tipping point, provoking an abrupt change that somehow amplifies the present warming trend.

## Response of a temperate glacier

Let's now look in greater detail at how a glacier adjusts to changes in mass balance. Such changes lead, initially, to changes in thickness of the glacier which influence its speed. They also have an immediate effect on the terminus, causing it to advance or retreat as the ablation rate is either decreased or increased, respectively. The changes in thickness propagate and diffuse down the glacier, and thus control the way in which the glacier profile adjusts to the new mass balance conditions. They affect the rate at which ice is transferred from the accumulation area to the ablation area. These changes in mass flux eventually reach the terminus, reinforcing the advance or retreat already underway there.

We will find that the total time required for adjustment depends, quite logically, on the volume of ice that must be gained or lost in order to reach a new steady state. Thus, years can elapse before the terminus gets the message that something has happened higher on the glacier, and decades may pass before the glacier comes close to fully adjusting to the changes.

Suppose  $b_h(x)$  increases, becoming more positive in the accumulation area and less negative in the ablation area. Initially, this leads to an increase in thickness (as well as some advance of the terminus). Suppose further that the longitudinal strain rate is extending in the accumulation area, as is normally the case. Over the course of a year, this extension, operating on a block of ice of thickness  $h$ , results in thinning by an amount  $\Delta h$  (Figure 15.2a). In Figure 15.2a, conservation of mass requires that  $\Delta h \cdot x \cong (h - \Delta h) \cdot \Delta x$ , so ignoring second order terms,  $\Delta h \cong h \cdot (\Delta x / x)$ . Thus, as the glacier grows thicker,  $\Delta h$  increases. After many years,  $\Delta h$  becomes large enough to absorb most of the increased accumulation, and the glacier approaches a new steady state. We shall see, however, that the time required for full adjustment is theoretically infinite.

The situation is quite different if the longitudinal strain rate is compressive, as is normally the case in ablation areas:  $\Delta h$  is still proportional to  $h$ , but now, because both the longitudinal strain rate *and* the change in mass balance cause the glacier to become thicker (Figure 15.2b),  $\Delta h$  increases each year, unstably. Thus, in the absence of some mitigating effect, a new steady state would never be reached. This contrast in behavior between accumulation and ablation areas, however, leads to kinematic waves which restore stability.

These kinematic waves are not dynamic waves like waves on a water body. Dynamic waves are a consequence of inertial forces. Because velocities are low in glaciers, inertial forces are negligible in comparison with gravitational and viscous forces. Kinematic waves, on the other hand, are a consequence of a conservation law. On a glacier, it is mass (or volume at constant density) that is conserved, and the type of kinematic wave in which we are interested is a wave of constant ice flux. Kinematic waves move through a medium at a speed that is different from the speed of the medium itself.

Kinematic waves on glaciers arise from the fact that if the ice flux into an element of a glacier of length  $dx$  is greater than the flux out of it, the glacier becomes thicker.

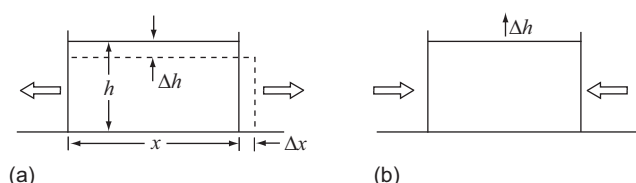


**Figure 15.2** Sketch illustrating why adjustment toward a new steady state is: (a) stable where flow is extending, and (b) unstable where flow is compressive.

Because both the ice velocity and the ice flux in the thicker ice are greater than in the thinner ice on either side of it, the resulting wave moves faster than the ice. (For comparison, waves of denser traffic on a highway are also a form of kinematic wave. In this case, cars catching up to a wave from behind are forced to slow down, while those finally making their way through the wave can accelerate again. Thus, in this case, the wave speed is less than the speed of the individual cars.) Mass could also be conserved if the ice in  $dx$  became denser, in which case the kinematic wave would not necessarily have a wave form. However, owing to the low compressibility of ice, kinematic waves on glaciers do tend to have a wave form.

Numerical modeling experiments suggest that kinematic waves on glaciers are likely to be long and low, and that the increases in velocity and thickness associated with them should rarely exceed  $\sim 10\%$  of the unperturbed values (van de Wal and Oerlemans, 1995). Thus, they will be difficult to detect in the field. Larger waves have been observed in the field, but these are probably a consequence of changes in other factors, such as  $u_b$ , that may be unrelated to perturbations in mass balance.

## Elementary kinematic wave theory

Let's now develop these ideas analytically, following an analysis by Nye (1960). We'll consider a slab of ice on a slope,  $\beta(x)$ , with thickness,  $h(x,t)$ , and surface slope,  $\alpha(x,t)$  (Figure 15.3). We'll assume that  $\partial h / \partial x$  is small and that the slab is of infinite extent in the horizontal direction normal to the  $x$ -axis. The surface slope is related to the bed slope by:

$$\alpha = \beta - \frac{\partial h}{\partial x}. \quad (15.1)$$

(Note that, if  $h$  decreases downglacier, as in Figure 15.3,  $\partial h / \partial x$  is negative, so  $\alpha > \beta$ .)

Consider conservation of mass in an element of a glacier of length  $dx$  (Figure 15.4). For convenience, we'll express mass fluxes in terms of the equivalent volumes of ice, based on a standard density. Ice flows into the element at a rate,  $q(x, h, \alpha, t)$ , and out of it at a rate,  $q + \frac{\partial q}{\partial x} dx$ . Here,  $q$  is the flux per unit of glacier width, and thus has the dimensions  $\text{m}^3 \text{ a}^{-1} \text{ m}^{-1}$ . In addition, there is accumulation at a rate  $b dx$ . If more ice accumulates in the element, or flows into it than leaves it, the

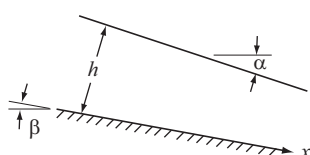


Figure 15.3 Glacier model used in analysis of kinematic waves.

glacier increases in thickness at a rate  $(\partial h / \partial t)$ , so the increase in volume of ice in the element is  $(\partial h / \partial t) dx$ . Thus:

$$q - \left( q + \frac{\partial q}{\partial x} dx \right) + bdx = \frac{\partial h}{\partial t} dx$$

or, simplifying:

$$\frac{\partial q}{\partial x} + \frac{\partial h}{\partial t} = b. \quad (15.2)$$

Because  $q$  is a function of  $h$  and  $x$ , the functional dependence expressed by Equation (15.2) leads to a general class of motions in flow systems: namely kinematic waves (Lighthill and Whitham, 1955). Our objective next is to gain some appreciation for the nature of such waves on glaciers.

Let's begin by considering wave speed. Suppose we multiply both sides of Equation (15.2) by  $(\partial q / \partial h)_x = c$ , so  $c$  is the change in flux resulting from a change in thickness at point  $x$ , thus:

$$c \frac{\partial q}{\partial x} + \frac{\partial q}{\partial h} \frac{\partial h}{\partial t} = bc \quad \text{or} \quad c \frac{\partial q}{\partial x} + \frac{\partial q}{\partial t} = bc. \quad (15.3)$$

Equation (15.3) is known as the kinematic wave equation;  $c$  has the dimensions  $\text{m}^3 \text{ a}^{-1} \text{ m}^{-1}/\text{m} = \text{m a}^{-1}$ . Thus, it is a speed. In fact, it is the celerity (or speed) of the wave.

To gain some appreciation for the implications of Equation (15.3), consider the hypothetical example in Figure 15.5. The ice flux into a 100 m long section of the

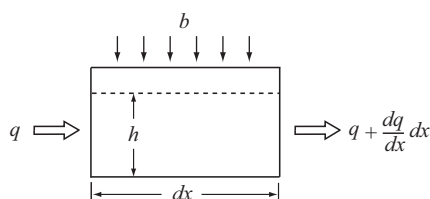


**Figure 15.4** Contributions to the change in mass in an element of a glacier of length  $dx$ .

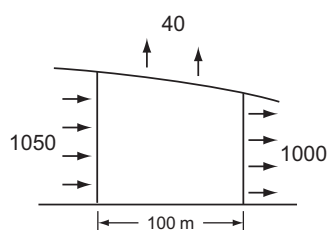


**Figure 15.5** Numerical interpretation of Equation (15.3).

glacier is  $1050 \text{ m}^3 \text{ a}^{-1} \text{ m}^{-1}$ , while that out is  $1000 \text{ m}^3 \text{ a}^{-1} \text{ m}^{-1}$ . The section is in the ablation area and the ablation rate is  $-0.4 \text{ m a}^{-1}$ , or  $-40 \text{ m}^3 \text{ a}^{-1} \text{ m}^{-1}$  over the length of the section. Thus, more ice is entering the section than leaving it, and the glacier is increasing in thickness. With Equation (15.3) we can calculate the rate of increase in mass flux,  $\partial q/\partial t$ , resulting from this increase in thickness as follows: The flux gradient,  $\partial q/\partial x$ , over the section is  $-50 \text{ m}^3 \text{ a}^{-1} \text{ m}^{-1}/100 \text{ m}$  or  $-0.5 \text{ m a}^{-1}$ . Suppose  $c = 200 \text{ m a}^{-1}$ . Then  $c\partial q/\partial x$  is  $-100 \text{ m}^3 \text{ a}^{-1} \text{ m}^{-1}$  and  $bc$  is  $-80 \text{ m}^3 \text{ a}^{-1} \text{ m}^{-1}$  so  $\partial q/\partial t$  is  $20 \text{ m}^3 \text{ a}^{-1} \text{ m}^{-1}$ . In other words, owing to the increase in thickness and the resulting increase in speed, the mass flux increases by  $20 \text{ m}^3 \text{ a}^{-1} \text{ m}^{-1}$ .

The relationship among  $q$ ,  $h$ ,  $\bar{u}$ , and  $c$  is illustrated in Figure 15.6, in which  $q$  is plotted against  $h$ . Because of the non-linearity of the flow law, we expect  $q$  to increase nonlinearly with  $h$ , as shown. The mean speed,  $\bar{u}$ , of a glacier with a thickness and ice flux given by the values of  $q$  and  $h$  at point P in the figure is  $\bar{u} = q/h$ . This is represented by the slope of the dashed line connecting P with the origin. However, the speed,  $c$ , of a kinematic wave is  $(\partial q/\partial h)_P$ , which is the slope of a line drawn tangent to the  $q-h$  curve at point P. In other words, as mentioned earlier, the speed of the kinematic wave is appreciably larger than the mean speed of the glacier.

To get a sense of how much faster the kinematic wave moves, consider the case of a glacier moving entirely by internal deformation such that (from Equation 5.19):

$$\bar{u} = \frac{2A}{n+2} (S_f \rho g \alpha)^n h^{n+1}.$$

As  $q = \bar{u}h$ , we have:

$$q = \frac{2A}{n+2} (S_f \rho g \alpha)^n h^{n+2} \quad (15.4)$$

so:

$$c = \frac{\partial q}{\partial h} = 2A(S_f \rho g \alpha)^n h^{n+1} = (n+2)\bar{u} \quad (15.5)$$

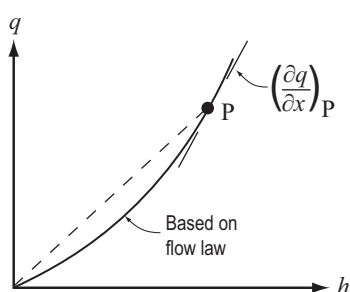


**Figure 15.6** Relation between mean speed of a glacier and speed of a kinematic wave.

or with  $n \cong 3$ :

$$c \cong 5\bar{u}. \quad (15.6)$$

In other words, the kinematic wave moves with a speed that is roughly five-times the depth-averaged velocity of the glacier. This relation applies, rigorously, only to infinitesimal waves. Waves of finite amplitude may have higher speeds.

### Analysis of the effect of a small change in mass balance using a perturbation approach

Let us now, following Nye (1960, pp. 561–562), use perturbation techniques to study the change in thickness with time after a small change in mass balance. Consider the situation in which the specific mass balance is shown by the solid line in Figure 15.7. We will refer to this situation as the “0” or *datum* or *equilibrium* state, and analyze the effect of small perturbations from this state such as those represented by the dashed lines in the figure. For example, during a cold or unusually snowy year the mass balance may be increased everywhere by an amount  $b'(x, t)$ , so we have:

$$b(x, t) = b_0(x) + b'(x, t).$$

Note that  $b_0$  is a function only of  $x$ ; it does not vary with time because the datum state is a steady state. Other properties of the datum state are  $q_0(x, h, \alpha)$ ,  $h_0(x)$ , and  $\alpha_0(x)$ . In the perturbed state these become  $q = q_0 + q'$ ,  $h = h_0 + h'$ , and  $\alpha = \alpha_0 + \alpha'$ . Substituting these into Equation (15.2) yields:

$$\frac{\partial}{\partial x}(q_0 + q') + \frac{\partial}{\partial t}(h_0 + h') = b_0 + b'. \quad (15.7)$$

Now write Equation (15.2) in terms of the datum state, thus:

$$\frac{\partial q_0}{\partial x} + \frac{\partial h_0}{\partial t} = b_0.$$

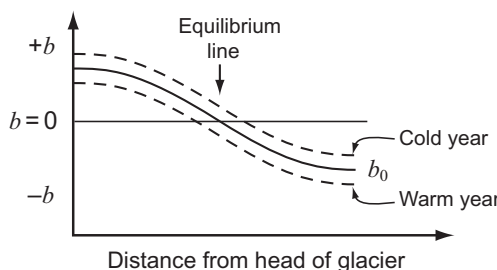


**Figure 15.7** Perturbations in mass balance from an equilibrium state,  $b_0$ .

Subtracting this from Equation (15.7) yields:

$$\frac{\partial q'}{\partial x} + \frac{\partial h'}{\partial t} = b'. \quad (15.8)$$

(Note, in passing, that because  $h_0$  is a property of the datum state,  $\partial h_0 / \partial t = 0$ .)

At any position,  $x$ ,  $q$  varies with  $h$  and  $\alpha$  so we can write:

$$dq = \frac{\partial q}{\partial h} dh + \frac{\partial q}{\partial \alpha} d\alpha.$$

For small perturbations,  $dq = q'$ ,  $dh = h'$ , and  $d\alpha = \alpha'$ , so:

$$q' = \frac{\partial q}{\partial h} h' + \frac{\partial q}{\partial \alpha} \alpha'. \quad (15.9)$$

We've already identified  $\partial q / \partial h$  with the celerity of a kinematic wave,  $c$ , or in the datum state:  $(\partial q / \partial h)_0 = c_0$ . Now we similarly define  $D_0 = (\partial q / \partial \alpha)_0$ . Thus, in the datum state, Equation (15.9) becomes:

$$q' = c_0 h' + D_0 \alpha'. \quad (15.10)$$

This relation is valid only for small perturbations. Were we interested in larger perturbations, terms involving  $h'^2, h'^3, \dots, \alpha'^2, \alpha'^3, \dots$  would have to be included. Thus, our approach is referred to as a *linearized theory*.

Equations (15.8) and (15.10) are a pair of simultaneous differential equations that can be solved for the change in ice flux,  $q'$ , and thickness,  $h'$ , resulting from a perturbation,  $b'_n$ , in net balance. Substituting  $q'$  from Equation (15.10) into Equation (15.8) yields:

$$\frac{\partial c_0}{\partial x} h' + c_0 \frac{\partial h'}{\partial x} + \frac{\partial D_0}{\partial x} \alpha' + D_0 \frac{\partial \alpha'}{\partial x} + \frac{\partial h'}{\partial t} = b'_n. \quad (15.11)$$

Returning to Equation (15.1) we see that in the datum and perturbed states, respectively:

$$\alpha_0 = \beta - \frac{\partial h_0}{\partial x} \quad \text{and} \quad \alpha_0 + \alpha' = \beta - \frac{\partial(h_0 + h')}{\partial x}. \quad (15.12)$$

Subtracting the first of these expressions from the second:  $\alpha' = -\partial h' / \partial x$ . Substituting this into Equation (15.11) yields, after some rearranging:

$$\begin{array}{l} \frac{\partial h'}{\partial t} = b' - \frac{\partial c_0}{\partial x} h' - \left( c_0 - \frac{\partial D_0}{\partial x} \right) \frac{\partial h'}{\partial x} + D_0 \frac{\partial^2 h'}{\partial x^2}. \\ \text{(i)} \quad \text{(ii)} \quad \text{(iii)} \quad \text{(iv)} \end{array} \quad (15.13)$$

As (Nye, 1960, p. 562) noted, the terms in this equation have the following meanings:

- (i) This term shows that  $h'$  increases at a rate given by the perturbation in accumulation.

- (ii) This term results in an exponential decrease or increase in the rate of change of  $h'$  as we will show below.
- (iii) This term represents a kinematic wave of constant  $h'$  which moves with a speed  $(c_0 - \partial D_0 / \partial x)$  in the  $+x$  direction. Note that both  $c_0$  and  $\partial D_0 / \partial x$  have dimensions  $\ell \cdot t^{-1}$ .
- (iv) This term represents diffusive (note the second derivative) damping of the perturbation  $h'$ ;  $D_0$  is the diffusivity.

To study term (ii), we'll now solve Equation (15.13) for a simple case in which diffusion is neglected. Then we'll investigate the role of diffusion.

### Solution for a small part of a glacier with uniform longitudinal strain rate and without diffusion

Consider a situation in which a glacier is initially in a steady state with an accumulation rate  $b_0$  (Nye, 1960, p. 563). Then the accumulation rate increases abruptly by an amount  $b'$  to  $b = b_0 + b'$ , and remains at this increased level indefinitely. Suppose  $\partial c_0 / \partial x$  is independent of  $x$  on this glacier. From Equations (15.5) we see that:

$$\frac{\partial c_0}{\partial x} \simeq (n+2) \frac{\partial \bar{u}_0}{\partial x} \quad (15.14)$$

where  $\partial \bar{u}_0 / \partial x$  is the longitudinal strain rate,  $r_0$ , so this corresponds to a situation in which the longitudinal strain rate is uniform in the  $x$ -direction. Thus,  $h'$  is independent of  $x$ , so  $\partial h' / \partial x = 0$ . This means that the increase in thickness is uniform over the glacier. Let  $\gamma_0 = \partial c_0 / \partial x$ .

With these simplifications, Equation (15.13) becomes:

$$\frac{dh'}{dt} = b' - \gamma_0 h'. \quad (15.15)$$

Separating variables we obtain:

$$\int_0^{h'} \frac{dh'}{b' - \gamma_0 h'} = \int_0^t dt.$$

Integration yields:

$$h' = \frac{b'}{\gamma_0} (1 - e^{-\gamma_0 t}). \quad (15.16)$$

If  $\gamma_0$  is positive, corresponding to a positive longitudinal strain rate such as we expect in an accumulation area,  $h'$  asymptotically approaches the value  $b'/\gamma_0$  (Figure 15.8). In other words, after a very long time, the glacier will have increased

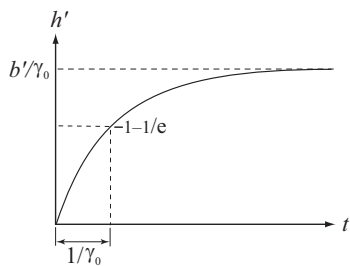


**Figure 15.8** Asymptotic adjustment of a glacier toward a new steady state,  $b'/\gamma_0$ , following a perturbation in accumulation rate,  $b'$ , in an area of extending flow.  $1/\gamma_0$  is the response time.

in thickness by this amount. This is the situation described earlier and illustrated in Figure 15.2a.

The quantity  $1/\gamma_0$ , which has the dimensions of time, is known as the time constant for this change. This is sometimes associated with the “response time” of a glacier, or the length of time required for a glacier to respond to a change in climate. When  $t = 1/\gamma_0$ ,  $(1-e^{-\gamma_0 t}) = (1-1/e) = 0.63$  so  $h'$  is a little less than two-thirds of the way to the new equilibrium state. This is commonly called the e-folding time. Mathematically (Equation 15.16), it is clear that the new equilibrium state is never reached. Thus, it would be meaningless to try, instead, to define the response time as the total time required to attain a new steady state.

From Equation (15.14) we see that  $1/\gamma_0 \cong 1/(5r_0)$ . In other words, in this simple model the response time is inversely proportional to the longitudinal strain rate. Typical longitudinal strain rates for Storglaciären, Barnes Ice Cap, and the Antarctic Ice Sheet are  $0.015 \text{ a}^{-1}$ ,  $0.005 \text{ a}^{-1}$ , and  $0.00005 \text{ a}^{-1}$ , respectively. Thus, the response time of Barnes Ice Cap might be expected to be 3-times as long as that of Storglaciären, and that of the Antarctic Ice Sheet, 100-times as long as Barnes Ice Cap. While these multiples are not unrealistic, it turns out that  $1/(5r_0)$  seriously underestimates the actual response time. We’ll see below that this is because diffusion has been neglected.

If  $\gamma_0$  is negative, corresponding to longitudinal compression as would be typical in an ablation zone, there is an obvious problem. Equation (15.16) then predicts that  $h'$  will increase exponentially with time. Thus, a new steady state is never even approached. This is the situation which we discussed in connection with Figure 15.2b.

Clearly, it is not possible to have the upper part of a glacier increasing in thickness slowly and stably while the lower part is increasing rapidly and unstably. In the absence of diffusion, Nye (1960) suggests that the initial response in the ablation area would, indeed, be unstable. At any location, however, stability would be restored when a kinematic wave, initiated in the vicinity of the equilibrium line

and propagating down glacier, reached that location. With diffusion, however, such an unstable response may never develop.

## Effect of diffusion

Diffusion occurs whenever fluxes are proportional to gradients. In the present case, the flux,  $q$ , is proportional to the slope (or gradient),  $\alpha$ . Where  $\alpha$  is largest, on the downslope side of a wave,  $q$  is highest. Conversely,  $q$  is lowest on the upslope side of the wave. Thus, the flux into the wave is diminished and that out of it is enhanced. This tends to decrease the amplitude and increase the wavelength of the wave.

As in the case of  $c$  (or  $c_0$ ) (Equation 15.5), an analytical expression for  $D_0$  can be obtained by differentiating  $q$  with respect to  $\alpha$ , thus:

$$D_0 = \left( \frac{\partial q}{\partial \alpha} \right)_0 = \left( \frac{2n}{n+2} \right) A (S_f \rho g)^n h^{n+2} \alpha^{n-1} = \frac{nq}{\alpha}$$

or with  $n \cong 3$ :

$$D_0 \cong \frac{3\bar{u}h}{\alpha}. \quad (15.17)$$

In other words, diffusion will be most significant where the glacier is thick, the speed high, and the slope low.

We can't probe this dependence more thoroughly at the level of the treatment herein. However, Nye (1963, pp. 442–445) has shown that diffusion decreases the rate of thickening, a result that is intuitively logical. As a result, the response time can increase by as much as or more than an order of magnitude.

## A novel approach to response times

Jóhannesson *et al.* (1989) took an alternative approach to response times. They identify three possible natural time scales that might be used in the analysis of glacier responses:

$$\tau_C = \frac{\ell_0}{\overline{c}_0} \quad \left[ \frac{m}{m \text{ a}^{-1}} \right] \quad (15.18a)$$

$$\tau_D = \frac{\ell_0^2}{\pi^2 D_0} \quad \left[ \frac{m^2}{m^2 \text{ a}^{-1}} \right] \quad (15.18b)$$

$$\tau_V = \frac{V_1}{b' \ell_0} \quad \left[ \frac{m^3 m^{-1}}{m \text{ a}^{-1} m} \right]. \quad (15.18c)$$

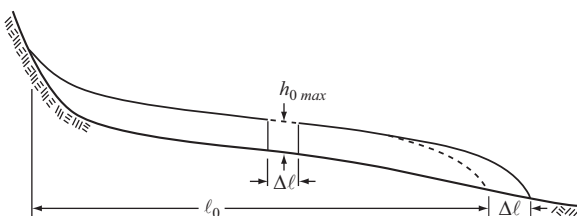


**Figure 15.9** Geometrical interpretation of  $\tau_V$ . During an advance,  $\Delta\ell$ , the mass that must be added to a glacier is approximately  $\Delta\ell h_{0\ max}$ .

Here,  $\ell_0$  is the length of the glacier in the datum state,  $\tau_C$  and  $\tau_D$  are the time constants for propagation and diffusion,\* respectively, of a disturbance over the length of the glacier, and  $V_1$  is the total change (per unit width) in glacier volume an infinite amount of time after a perturbation that adds a volume of ice,  $b'\ell_0$ , to the glacier every year. In effect, all of these are measures of the time required to establish the general shape of the new surface profile. As the glacier adjusts, the size of any disturbance decreases, so the rate of propagation or diffusion also decreases, asymptotically approaching an equilibrium state. Therefore, as with  $1/\gamma_0$ ,  $\tau_C$  and  $\tau_D$  are measures of the time required for the processes to proceed about two-thirds of the way to completion. Similarly, as we'll show below,  $\tau_V$  is the time required for accumulation (or loss) of about two-thirds of  $V_1$ .

Jóhannesson *et al.* (1989) find that  $\tau_V$  is usually appreciably longer than  $\tau_C$  or  $\tau_D$ . This means that perturbations in ice thickness are spread out over the glacier by propagation and diffusion rather quickly in comparison with the time needed for accumulation of the additional mass. Clearly, then,  $\tau_C$  and  $\tau_D$  are questionable measures of the response time, as a glacier cannot be considered to have adjusted some specified fraction of the way to a new equilibrium state until the necessary additional mass has accumulated (or been lost).

Jóhannesson *et al.* (1989) have developed a simple geometrical argument to estimate  $\tau_V$ . Consider the situation in Figure 15.9 in which an advance of a glacier by an amount  $\Delta\ell$  is illustrated graphically by cutting the glacier at its point of maximum thickness and sliding the lower part forward by  $\Delta\ell$ . The increase in volume of the glacier is then  $\sim\Delta\ell \cdot h_{0\ max}$ . Detailed numerical modeling suggests that this is a good approximation to the response of a real glacier when the dynamical properties of the glacier are the same in the initial and final state, and thus influence the initial and final profiles in the same way.

Eventually the annual mass gain resulting from the perturbation,  $b'\ell_0$ , will equal the annual mass loss by ablation over the new part of the glacier,  $\Delta\ell$ , thus:

\*The  $\pi^2$  term in Equation (15.18b) comes from the Fourier solution of the diffusion equation (T. Jóhannesson, written communications, dated November 7 and 14, 1996).

$$b'\ell_0 = b_t \Delta\ell \quad (15.19)$$

where  $b_t$  is the (negative of the) net balance rate at the terminus. Then:

$$V_1 = \Delta\ell h_{0 \text{ max}} = \frac{b'\ell_0 h_{0 \text{ max}}}{b_t}. \quad (15.20)$$

Whence, from Equation (15.18c):

$$\tau_V = \frac{h_{0 \text{ max}}}{b_t}. \quad (15.21)$$

Thus,  $\tau_V$  can be estimated, quite easily, from knowledge of the thickness of the glacier and the net balance rate at the terminus.

We mentioned above that  $\tau_V$  is a time constant in the same sense that  $1/\gamma_0$  is. Let's now demonstrate this. Immediately after a permanent perturbation in balance rate,  $b'$ , the rate at which additional mass is acquired by the glacier,  $dV/dt$ , is  $B' = \bar{b}'\ell_0$ . However, as the glacier becomes longer [by an amount  $\delta\ell(t)$ ], some of the additional annual input is lost through ablation in the new part of the terminus region. Thus:

$$\frac{dV}{dt} = B' - b_t \delta\ell(t).$$

Now from Equation (15.20) or Figure 15.9,  $\delta\ell(t) \cong V(t)/h_{0 \text{ max}}$ , where  $\delta\ell$  is the amount the glacier has lengthened by time  $t$  after the perturbation, and  $V(t)$  is the increase in volume up to that time. Thus:

$$\frac{dV}{dt} = B' - \frac{b_t}{h_{0 \text{ max}}} V.$$

Comparing this with Equation (15.15), it is clear that  $h_{0 \text{ max}}/b_t$  is analogous to  $1/\gamma_0$ .

When calculating  $\tau_V$  in practice, Equations (15.19) to (15.21) need to be generalized to three dimensions. For example, we can write Equation (15.19) as:

$$\bar{b}'A_0 = b_t \cdot W_t \cdot \Delta\ell \quad (15.22)$$

where  $A_0$  is the initial area of the glacier and  $W_t$  is the width of the terminus. Then if  $W_c$  is the width of the central part of the glacier,  $V_1 = \bar{h}_{0 \text{ max}} W_c \Delta\ell$  where  $\bar{h}_{0 \text{ max}}$  is a mean thickness over this central part. Recognizing that  $b'A_0$  is the 3D equivalent of  $b'\ell_0$ , Equation (15.18c) now becomes:

$$\tau_V = \frac{\bar{h}_{0 \text{ max}}}{b_t} \cdot \frac{W_c}{W_t}. \quad (15.23)$$

For purposes of illustration, let's put some realistic numbers into some of these equations. The ablation rate on the lower part of the tongue of Storglaciären averages  $\sim 1.3 \text{ m a}^{-1}$ , the mean thickness over the central region of the glacier is between 100 and 150 m,  $W_c$  is  $\sim 800 \text{ m}$ , and the  $W_t$  is  $\sim 700 \text{ m}$ , so using Equation

(15.23),  $\tau_V$  is  $\sim 110$  years. Numerical modeling (Brugger, 2007) suggests a comparable volume response time,  $\sim 125$  years, while field observations suggest that about two-thirds of Storglaciären's retreat from its Little Ice Age maximum position, which it reached in 1910, took place in  $\sim 45$  years (Holmlund, 1987). The difference between the two estimates of  $\tau_V$  and the more rapid response observed is likely a consequence of two factors: (1)  $b_t$  was probably higher (more negative) when the glacier extended to lower elevations, and (2) the change from Little Ice Age conditions was hardly a small perturbation.

### Two problems with $\tau_V$

Harrison *et al.* (2003) point out two possibly significant effects that are not incorporated in Equation (15.23). First, the normal increase in  $b_n$  with elevation, the Böðvarsson effect, is ignored. Owing to this increase, perturbations that result in thickening or thinning of a glacier are effectively amplified, potentially leading to significant underestimates of the response time. In extreme cases, this could lead to unstable (or runaway) growth or shrinkage of a glacier as, for example, if thickening of the glacier increased  $b_n$  more than advance of the terminus to a lower elevation in the same time period increased ablation. Secondly, they argue that one must take into consideration the likelihood that the glacier is not in a steady-state prior to any given perturbation in mass balance. A negative mass balance, for example, may have thinned the glacier, reducing its volume, but terminus retreat may not have reduced the area enough to bring it into balance with the lower flow rates resulting from the thinning. The second of these problems is particularly important, and limits our ability to apply these models to observed glacier fluctuations.

Harrison *et al.* (2003) develop theoretical approaches to these problems, but find their theory nearly impossible to apply because they need precise measurements of glacier area, volume, and balance rate at three or more times over a period of years, and such data are rarely available.

### A three stage model

Roe and Baker (2014) have extended the Jóhannesson *et al.* (1989) model in an interesting way. They note that mass redistribution by advection and diffusion is much more effective in the interior than at the margin. They therefore suggest thinking of there being three stages in the adjustment of a glacier to a perturbation in mass balance (Figure 15.10). In the first stage, a perturbation  $b'$  results in thickening or thinning of the interior of the glacier. The perturbation is assumed to be permanent, and to be uniform over the glacier. (For simplicity, we will consider a longitudinal flow band of unit width along which there has been a positive perturbation, resulting in thickening.) The thickening,  $h'_1$ , drives an increase in flux,  $q'_1$ , into a terminus region (region ② in Figure 15.10) of length,  $\delta\ell$ , that is short compared with the total length of the glacier,  $\ell_0$ , but otherwise of unspecified

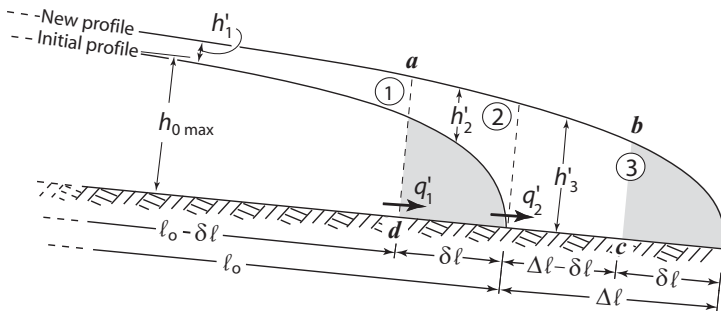


**Figure 15.10** Schematic illustration of the transition from an initial profile of length  $\ell_0$  to a new profile of length  $\ell_0 + \Delta\ell$  in three stages. (After Roe and Baker, 2014, Figure 6)

length. The subscript on  $q$  refers to the region, and the prime denotes a perturbation. In the second stage,  $q'_1$  causes an increase in thickness,  $h'_2$ , in region ②, and this drives an increase in flux,  $q'_2$  into region ③. In the third stage,  $q'_2$  causes the glacier terminus to advance a distance,  $\Delta\ell$ .

In the first stage, the interior of the glacier increases in volume by an amount,  $b'_1(\ell_0 - \delta\ell)$ , but also loses mass owing to the flux,  $q'_1$ . Thus, the change in volume is:

$$\frac{dV'_1}{dt} = b'_1(\ell_0 - \delta\ell) - q'_1. \quad (15.24a)$$

As  $\delta\ell \ll \ell_0$ , we can approximate  $V'_1$  by  $h'_1\ell_0$ . We'll also assume that  $q'_1$  can be approximated by  $h'_1\ell_0/\tau_1$ , where  $\tau_1$  is the time scale over which an increase in thickness drives an increase in  $q'_1$ . Then Equation (15.24a) becomes:

$$\ell_0 \frac{dh'_1}{dt} = b'_1\ell_0 - \frac{h'_1\ell_0}{\tau_1}.$$

Dividing by  $\ell_0$  and rearranging yields:

$$\frac{dh'_1}{dt} + \frac{h'_1}{\tau_1} = b'_1. \quad (15.25a)$$

In the second stage, the change in volume in region ②, neglecting ablation on the surface is:

$$\frac{dV'_2}{dt} = q'_1 - q'_2. \quad (15.24b)$$

As in region ①,  $V'_2 = h'_2\delta\ell$  and we'll assume that  $q'_2$  can be approximated by  $h'_2\delta\ell/\tau_2$ , so  $V'_2 = \tau_2 q'_2$ . Then Equation (15.24b) becomes:

$$\frac{dq'_2}{dt} + \frac{q'_2}{\tau_2} = \frac{h'_1\ell_0}{\tau_1\tau_2}. \quad (15.25b)$$

As in Figure 15.9, Roe and Baker think of the lower half of the glacier as being slid forward a distance,  $\Delta\ell$ , so the two shaded regions in Figure 15.10 are the same size.

Because  $h'_1 \ll h_{0 \text{ max}}$ , we see that  $h'_3 \cong h_{0 \text{ max}}$ . Therefore,  $V'_3 \cong \Delta\ell h_{0 \text{ max}}$ . Then, noting that the mass fluxes in and out of region 3 are  $q'_2$  and  $\Delta\ell b_t$  respectively, we have in the third stage:

$$\frac{dV'_3}{dt} = h_{0 \text{ max}} \frac{d\Delta\ell}{dt} = q'_2 - \Delta\ell b_t. \quad (15.24c)$$

Consistent with the definitions of  $\tau_1 (= V'_1/q'_1)$  and  $\tau_2 (= V'_1/q'_2)$  as time scales on which changes in volume drive the fluxes  $q'_1$  and  $q'_2$ , respectively, we define  $\tau_3$  by

$\tau_3 = \frac{\Delta\ell h_{0 \text{ max}}}{b_t \Delta\ell} = \frac{V'_3}{b_t \Delta\ell}$ , so Equation (15.24c) becomes:

$$\frac{d\Delta\ell}{dt} + \frac{\Delta\ell}{\tau_3} = \frac{q'_2}{h_{0 \text{ max}}}. \quad (15.25c)$$

Note the similarity between Equations (15.25a, b, c) and Equation (15.2). These three equations qualitatively characterize three overlapping stages of glacier adjustment. Roe and Baker now argue that there should be only one underlying time scale for glacier adjustment. Indeed, if the profile changes self-similarly (Figure 15.10),  $\tau_1 \approx \tau_3$ , and if the volume-flux relationship is the same in each segment,  $\tau_1 \approx \tau_2$ . Therefore, we set  $\tau_1 = \tau_2 = \tau_3$ . Roe and Baker further show that these time scales equal  $\tau_V/\sqrt{3}$ . Dividing  $\tau_V$  by  $\sqrt{3}$  brings Roe and Baker's heuristic model into exact agreement with solutions based on integration of Equation (15.8). It also results in a time constant that is appreciably longer than  $\tau_V$ , which may explain why values of  $\tau_V$  calculated from Equation (15.21) commonly underestimate the response time based on field measurements.

As the two shaded regions in Figure 15.10 are the same size, the volume  $abcd$  is equivalent to  $\Delta\ell h_{0 \text{ max}}$  in Jóhannesson *et al.*'s (1989) model (Figure 15.9).

If we write Equations (15.25) in finite difference form (e.g. Equation (15.25a) becomes:  $h'_{1,t_2} - h'_{1,t_1} = b'\Delta t - h'_1 \Delta t / \tau_1$ ) and integrate them numerically to obtain  $h$ ,  $q$ , and  $\Delta\ell$  as functions of  $t$  (normalized by  $\tau_V$ ), the asymptotic approaches of  $h$ ,  $q$ , and  $\Delta\ell$  to equilibrium are expressed in the sigmoidal shapes of the curves, and the lags of  $q$  behind  $h$  and of  $\Delta\ell$  behind  $q$  are clear from the offsets of the curves (Figure 15.11). These lags occur because each stage of the adjustment process depends on the previous stage and during each stage there is a lag between the perturbation and the response. Note that the e-folding time for  $\Delta\ell$  is  $\sim 2\tau_V$ . This is because the three stages of adjustment are sequential, so although each is  $= \tau_V/\sqrt{3}$ , the total is  $> \tau_V$ , and this explains why observed and modeled response times are commonly longer than  $\tau_V$ .

## Numerical modeling of glacier responses

In the absence of analytical solutions to Equation (15.13), glaciologists have resorted to numerical modeling. Such models are not restricted to infinitesimal

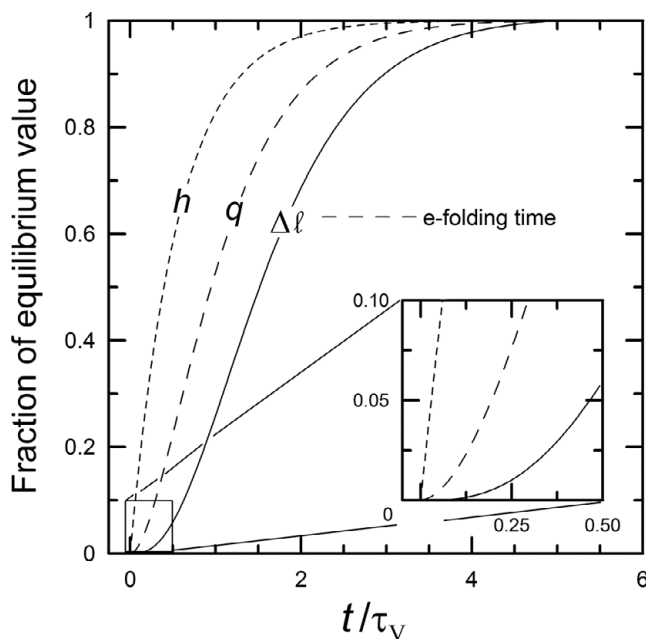


**Figure 15.11** Changes in glacier thickness,  $h$ , mass flux,  $q$ , and length,  $\Delta\ell$ , with time after a perturbation in mass balance. (After Roe and Baker, 2014, Figure 7).

perturbations, so one can retain non-linear effects which are neglected in linearized theories. Furthermore, one can use glacier shapes and mass balance patterns based on field measurements on a particular glacier.

A good example is a model of Hintereisferner in the Austrian Alps by van de Wal and Oerlemans (1995). First the authors calculated a surface profile that would be in equilibrium with a certain mass balance rate,  $b_0(x)$  (Figure 15.12a). Then they increased the mass balance rate by  $0.5 \text{ m a}^{-1}$  for one year. This could represent the situation during an unusually positive balance year (see the curve labeled “+” in Figure 3.4 or that labeled “Cold year” in Figure 15.7). The following year, the net budget was returned to its normal value. Figure 15.12b shows the increase in thickness as a function of distance from the head of the glacier at various times after the perturbation. After 2 years, a wave has formed with its crest  $\sim 3 \text{ km}$  from the head, or about a kilometer upglacier from the equilibrium line. The change in thickness is larger than  $0.5 \text{ m}$  because ice from a broad upper part of the accumulation area is funneled into a narrower glacier tongue. By the sixth year, the crest is a little more than  $4 \text{ km}$  from the head, representing a wave speed of about  $300 \text{ m a}^{-1}$ . For comparison, the depth-averaged velocity over this part of the glacier is a little under  $50 \text{ m a}^{-1}$ . In addition, the wave has been damped and lengthened by diffusion. With time, diffusion continues to smooth the wave, the surface in the accumulation area sinks back toward its original level, and the surface in the

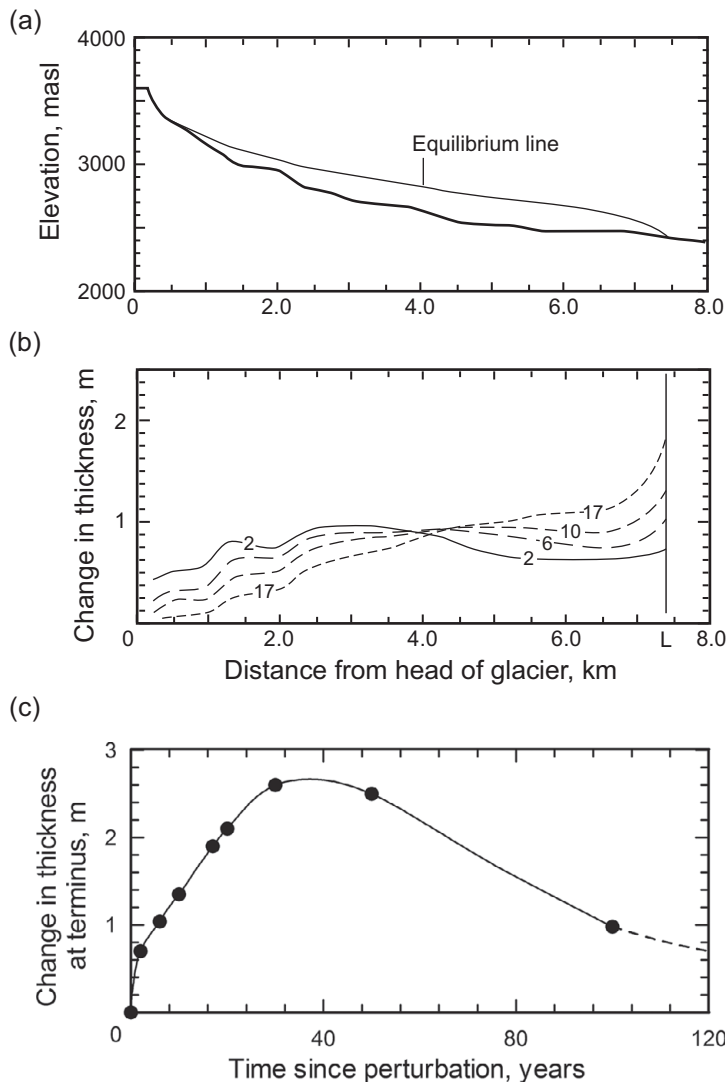


**Figure 15.12** Response of Hintereisferner to a perturbation in mass balance. (a) Longitudinal profile of Hintereisferner in a stable state. (b) Changes in thickness resulting from a 0.5 m increase in mass balance,  $b'$ , at time  $t=0$  and lasting one year. Times are in years. (c) Change in thickness at the terminus as a function of time after the perturbation. ((a) and (b) are reproduced from van de Wal and Oerlemans, 1995, Figures 7a and 9b, with permission of the authors and the Journal of Glaciology; (c) is calculated from data in their Figures 9b and 9c)

ablation area, particularly at the terminus, rises sharply. In Figure 15.12c it will be seen that the terminus begins to collapse back to its original form after about 30 years, but that a significant thickening remains there after 100 years!

The Hintereisferner modeling experiment serves to emphasize that kinematic waves on glaciers are likely to be long and low, as mentioned earlier. Thus,

sophisticated survey techniques are required to detect them in the field. In addition, the modeling suggests that the wave speed is  $\geq 6$ -times the depth-averaged velocity,  $\bar{u}$ , rather than  $\cong 5\bar{u}$  as suggested by Equation (15.6). Van de Wal and Oerlemans (1995) think that this may be due to changes in the longitudinal strain rate which are included in the numerical model, but which are not taken into consideration in the linear model. Such changes are likely to affect the  $q-h$  relation. Finally, the response at the terminus is stable, as shown in Figure 15.12c.

In another modeling experiment, Roe and O'Neal (2009) studied the effect of random fluctuations in climate on the lengths of valley glaciers on Mount Baker in the Pacific Northwest, USA. They first obtained climate data spanning 75 years from a nearby weather station. Statistical tests showed that there was no correlation from one year to the next in either annual precipitation or melt season temperature, nor was there any correlation between these two parameters. In other words, both records were indistinguishable from normally-distributed white noise. However, both records showed periods of precipitation or temperature that were persistently either higher or lower than the mean. Roe and O'Neal then used these records to generate an artificial record of normally-distributed annual mass balances for the glaciers, and used this to drive a numerical model of a glacier comparable in size to those on Mount Baker. The model is a finite difference solution to Equation (15.2) using Equation (15.4) for  $q$ . The striking result (Figure 15.13) is that under conditions of *statistically constant climate*, the random fluctuations in temperature and precipitation led to sequences of years during which the mass balance was persistently either sufficiently positive or

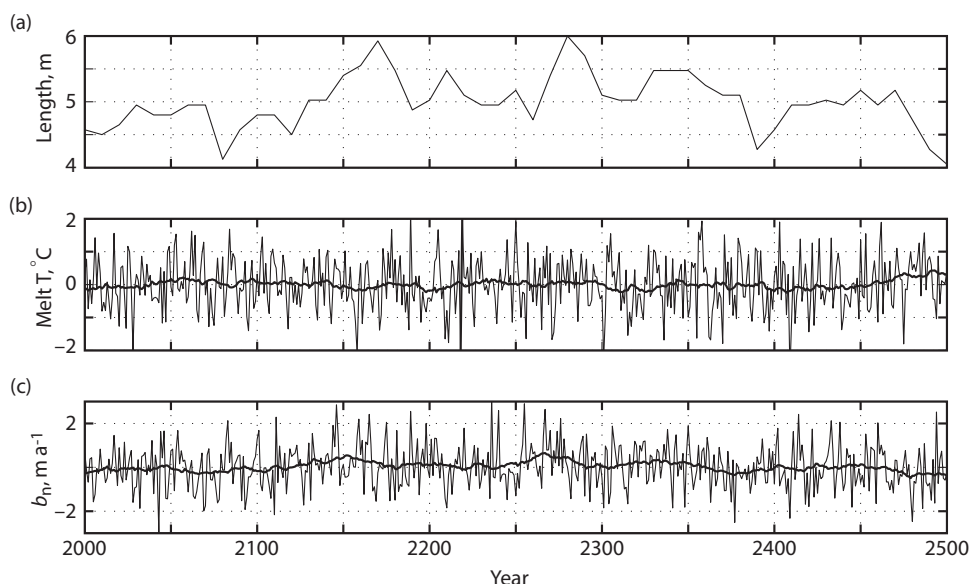


**Figure 15.13** (a) Glacier length variations over a 500 year model time span driven by uncorrelated stochastic variations in: (b) temperature and (c) accumulation. (After Roe and O'Neal, 2009, Figure 6. Reproduced with permission of the authors and the Journal of Glaciology)

sufficiently negative to drive changes in length of  $\pm 1$  km on a glacier with an average length of 5 km! The modeled variations were consistent with known variations in lengths of glaciers on Mount Baker. Such statistical fluctuations in glacier length may explain why dates on moraines thought to be contemporaneous sometimes differ significantly. They also imply that caution must be exercised when invoking climatic explanations for sequences of closely-spaced moraines.

## Comparison with observation

### Greenland ice sheet

A kinematic wave is inferred to have moved down Rink glacier, an outlet glacier in west-central Greenland, in 2012 (Adhikari *et al.*, 2017). During that summer, a summer of intensive melt, a continuously-monitored GPS station on bedrock near the margin of the glacier and  $\sim 25$  km inland from its terminus moved  $\sim 7$  mm northeastward, away from the terminus. During the ensuing winter, it moved part-way back to the southwest.

Adhikari *et al.* infer that the northeastward movement of the station reflected elastic rebound of the crust due to thinning in the glacier's terminal region (at a rate of 7 m per month). They think the thinning initiated a kinematic wave that moved down from the accumulation area at a rate of  $200\text{--}250 \text{ m d}^{-1}$  (10 times the surface speed). The wave thickened the tongue, depressing the crust once again, and resulting in the southwesterly movement of the GPS station during the winter.

### Nisqually Glacier

Nisqually Glacier on Mt. Rainier in Washington state, USA, retreated several hundred meters during the first part of the twentieth century. However, the net budget turned generally positive between 1942 and 1951 (Figure 15.14a). [In fact, the retreat rate of many temperate alpine glaciers in the Northern Hemisphere decreased during this time period, and some actually advanced. This is a nice example of the effect of such a sequence of positive balance years on glacier length modeled by Roe and O'Neal (2009) (Figure 15.13).] The terminus of Nisqually Glacier, on the other hand, continued to retreat during this time (Figure 15.14b); it was still responding to negative mass budgets of the early twentieth century. The total retreat between 1918 and 1960 was  $\sim 1000$  m.

In the late-1940s, a wave of thickening was detected  $\sim 1500$  m upglacier from the terminus, and this wave was tracked down glacier until it reached the terminus in about 1959 (lower part of Figure 15.14b). The wave was presumably a response to the positive mass budgets of the 1940s. The progress of the wave was documented by surveys, conducted almost annually, of the average elevation of the glacier surface along three transverse profiles (Figure 15.15a). At Profile 3, which is 2.7 km from the mid-twentieth-century terminus, thickening began in about 1945.

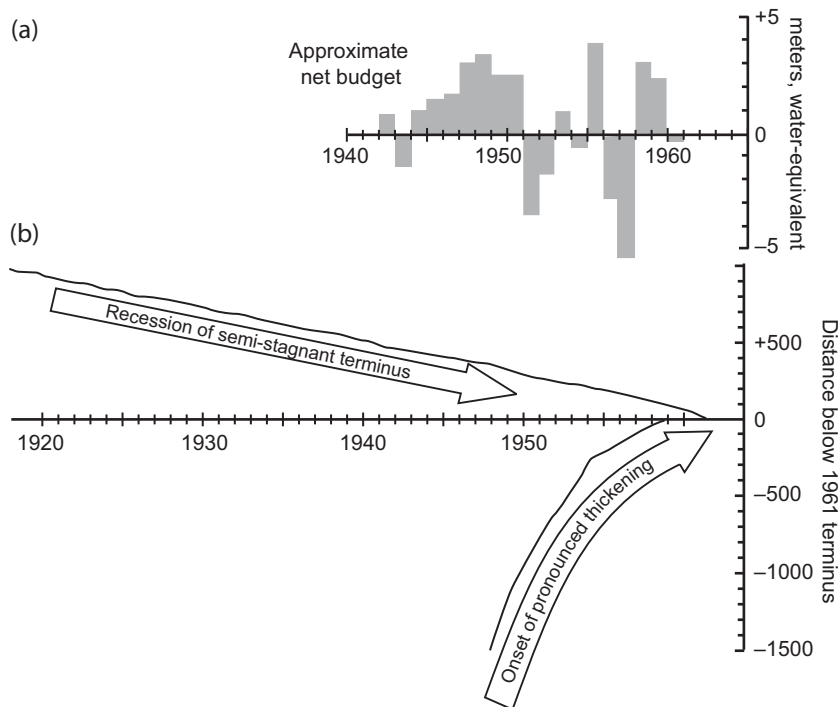


**Figure 15.14** (a) Approximate net budget of Nisqually Glacier between 1918 and 1961, and (b) recession of the terminus from 1920 to 1961 and advance of a wave of pronounced thickening between 1948 and 1959. (Reproduced from Meier, 1965, Figure 8 with permission of the author).

Profile 2 is 1.6 km from the terminus; thickening there began in 1949. The wave reached Profile 1, 0.8 km from the terminus, in 1955. In Figure 15.15b the ice surface slope, surface elevation, and velocity at Profile 2 are shown as functions of time. As noted earlier, this is probably not a pure kinematic wave as the changes in thickness and velocity are rather large. Thus, some other mechanisms, such as an increase in longitudinal compression due to an increase in sliding speed on the upper part of the glacier, were probably involved.

The change in velocity in Figure 15.15b can be compared with that predicted by Equation (5.7) with  $u_b = 0$ :

$$u_s = \frac{2A}{n+1} (\rho g \alpha)^n h^{n+1}. \quad (15.26)$$

To do this, we take the differential of Equation (15.26) and divide the result by Equation (15.26) to yield:

$$\frac{du_s}{u_s} = n \frac{d\alpha}{\alpha} + (n+1) \frac{dh}{h}. \quad (15.27)$$

Despite the approximations inherent in Equations (15.26) and (15.27) and in estimating the values of the parameters in Equation (15.27) from the field data, the

(a)



(b)

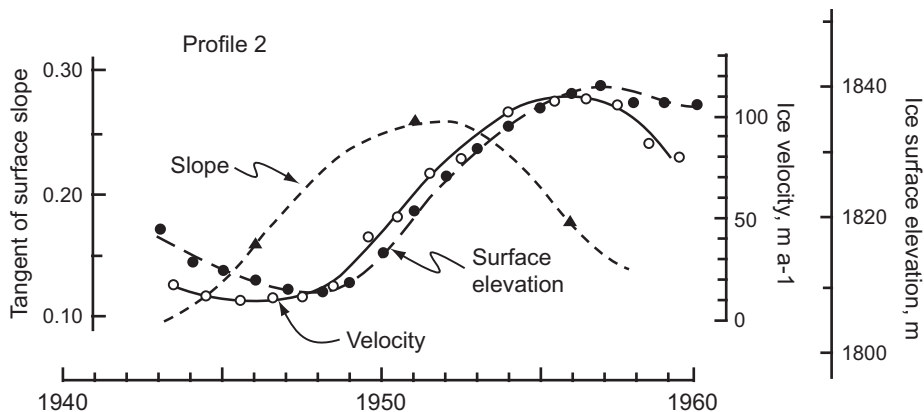


**Figure 15.15** (a) Variation in ice surface elevation on three transverse profiles on Nisqually Glacier, 1931–1960. (b) Variations in ice surface elevation, velocity, and surface slope at Profile 2, 1943–1960. ((a) is from Johnson, 1960, Figure 2; (b) is from Meier, 1965, Figure 4. Reproduced with permission of the authors)

calculated  $du_s$  is surprisingly close to that observed. (The numerical computations are left as an exercise for the reader: Problem 15.2.)

## SUMMARY

We began this chapter by looking at some feedbacks. Changes in temperature affect mass balance on short time scales and glacier flow on longer time scales, and these

cause changes in glacier surface elevation which, in turn, may affect mass balance in a positive feedback. Other positive feedbacks occur between mass balance, glacier surface elevation, and isostatic adjustment of the crust. We then reviewed evidence for changes in the Laurentide Ice Sheet during the Pleistocene. Dansgaard–Oeschger cycles punctuated the last glacial episode, the Wisconsinan. Some of these events apparently occurred quite abruptly. Their causes are still imperfectly understood, but changes in ocean circulation and climate are likely involved.

We then reviewed Nye's classic kinematic wave theory for predicting the response of a glacier to changes in mass balance, and solved the resulting linearized equation (Equation 15.13) for a simplified situation neglecting diffusion. Largely because it neglects diffusion, this solution predicts response times that are, in general, too short. Nevertheless, evidence from real glaciers is consistent with at least two of the conclusions from Nye's theory: that the most visible response is at the terminus, and that the time constant for this response is years, decades, or even centuries.

Jóhannesson *et al.* (1989) suggested three alternative time scales for adjustment. Their time scales for propagation and diffusion of a disturbance over a glacier,  $\tau_C$  and  $\tau_D$ , provide measures of the time required for the glacier to adjust its shape (but not size) to changed conditions. Their volume time scale,  $\tau_V$ , on the other hand, utilizes a conservation of mass argument: after a change in  $b_n$  a glacier will be either too large or too small, and thus not in equilibrium with the changed conditions. It takes time for the surplus or deficit in mass balance to bring about the necessary change in volume. Thus, the volume time scale is more consistent with “response times” based on observation, and indeed with those based on numerical modeling. Roe and Baker (2014) parse this response into three overlapping stages: (i) a perturbation in mass balance results in changes in thickness in the interior of a glacier which (ii) drive changes in flux to the terminus which, in turn, (iii) drive changes in glacier length. Owing to the delayed response at the terminus, their response time is somewhat longer than  $\tau_V$ .

Numerical modeling suggests that kinematic waves such as those which Nye envisioned should form on glaciers, but they are likely to be long and low, and the increase in ice velocity within them, small. Thus, they will be difficult to detect. Additional factors, such as major changes in conditions at the bed, are probably responsible for impressive waves that have been documented by some field observations. Diffusive processes dampen kinematic waves relatively rapidly, so unstable responses (Figure 15.3b) do not occur in areas of compressive flow.

# 16

## Ice core studies

Over the past few decades our understanding of changes that have occurred, over millennia, in atmospheric and oceanic chemistry and circulation patterns, and in their causes, has improved dramatically. Much of this progress has been based on records preserved in ice cores. The cores must be retrieved from higher parts of accumulation areas where surface melting is negligible because meltwater percolating through a snow pack garbles the stratigraphic sequence and also homogenizes the chemistry. Some of the ice core records are proxies for paleotemperature. Others provide insights into the composition of the paleoatmosphere. Still others can be used to identify sources of air masses, and hence hint at paths air masses may have followed in getting to the site of deposition, and at changes in these paths – or changes in atmospheric circulation – through time. Some document human activities. In this chapter we'll diverge a bit from the main focus of this book, glacier mechanics, and discuss the types of records preserved in ice cores and their interpretation in terms of climatic phenomena.

To retrieve cores, a number of deep drilling projects have been undertaken in Greenland and Antarctica (Jouzel, 2013). Among these are the European Greenland Ice Core Project (GRIP), and one ~200 km further north, called North GRIP or NGRIP, and two American Greenland Ice Sheet Projects (GISP) and (GISP2). GISP2 and NGRIP reached bedrock in 1993 and 2003, respectively, at depths of 3054 m and 3085 m. The stratigraphic record in the GISP2 core was disturbed by folding below ~2200 m, but a reasonably accurate time scale can be reconstructed back to 128.5 ka. NGRIP bottomed in ice dated to 123 ka.

In Antarctica, accumulation rates are lower so cores cover a longer time span, but at lower resolution. Two important Antarctic cores are one from the Russian station at Vostok and one from Dome C (Figure 6.15). The Vostok core reached 3350 m in 1993, and was deepened nearly two decades later, reaching subglacial Lake Vostok in 2012 at >3650 m. The Dome C core reached the bed at 3260 m in 2005. Ice at 3310 m in the Vostok core has an estimated age of 420 ka, and that at the base of Dome C is slightly older than 800 ka.

Initial processing of cores is done in “science trenches” excavated in the firm immediately adjacent to the drill rig. In this natural cold laboratory, core segments can be studied as soon as they are brought to the surface. During GISP2,

for example, each core segment was cut lengthwise. One part was microtomed to obtain a smooth, uniform surface, placed on a light table, and viewed with transmitted light to facilitate logging of visual stratigraphy (Meese *et al.*, 1997). Other measurements that do not require high-tech laboratory equipment, such as electrical conductivity, were also made on this half. The other half was archived for later chemical and isotopic analysis in laboratories throughout the world.

## Laboratory techniques

In early studies, the commonly-contaminated outer part of a core had to be carefully removed under clean or ultra clean conditions. The inner part was then analyzed. Some analyses required as much as 0.1–0.2 m of core per sample.

Modern studies usually use a technique called *continuous flow analysis*. A core is set on a hot plate, on end, and melted continuously. Meltwater from the outer part of the core is routed to a mass spectrometer to measure ratios of stable isotopes of oxygen, hydrogen, argon, and nitrogen. Contamination is not a problem in these analyses. Water from the inner, clean part of the core can be passed through an ion chromatograph to determine concentrations of major ions (Cole-Dai *et al.*, 2006), routed to an inductively-coupled plasma mass spectrometer (ICP-MS) for analysis of up to 32 trace elements (McConnell *et al.*, 2002), or collected in vials for later study (Osterberg *et al.*, 2006). Variations in the abundances of many trace elements can be measured at the ppb level and in some cases at the ppq level (1 part in  $10^{15}$ !). Depth resolutions of ~10 mm are achieved with this technique.

Alternatively, a laser can be used to ‘blast’ ions off a core. The ions are then analyzed with the ICP-MS (Sneed *et al.*, 2015). This laser ablation (acronym: LA-ICP-MS) approach yields a resolution of ~0.10 mm, and can thus resolve individual storms (Figure 16.1c). However, it takes a day to analyze ~1/2 m of core, so it is practical only for selected detailed studies.

## Carbon dioxide

$\text{CO}_2$  is of particular interest because it is a greenhouse gas, and to understand climate change we need to know how it has varied through time as ice sheets waxed and waned. The concentration of  $\text{CO}_2$  in air bubbles in ice reflects that in the atmosphere from which the bubbles were isolated. Developing laboratory techniques for measuring the concentration in the bubbles presented a special challenge, however, because  $\text{CO}_2$  is present in the ice lattice as well as in air bubbles (Berner *et al.*, 1980), and some of that in the ice lattice may come from dust or from decomposition of organic material. There was concern that oxidation or carbonate-acid reaction (Raynaud, 2012) might release  $\text{CO}_2$  from the latter sources,

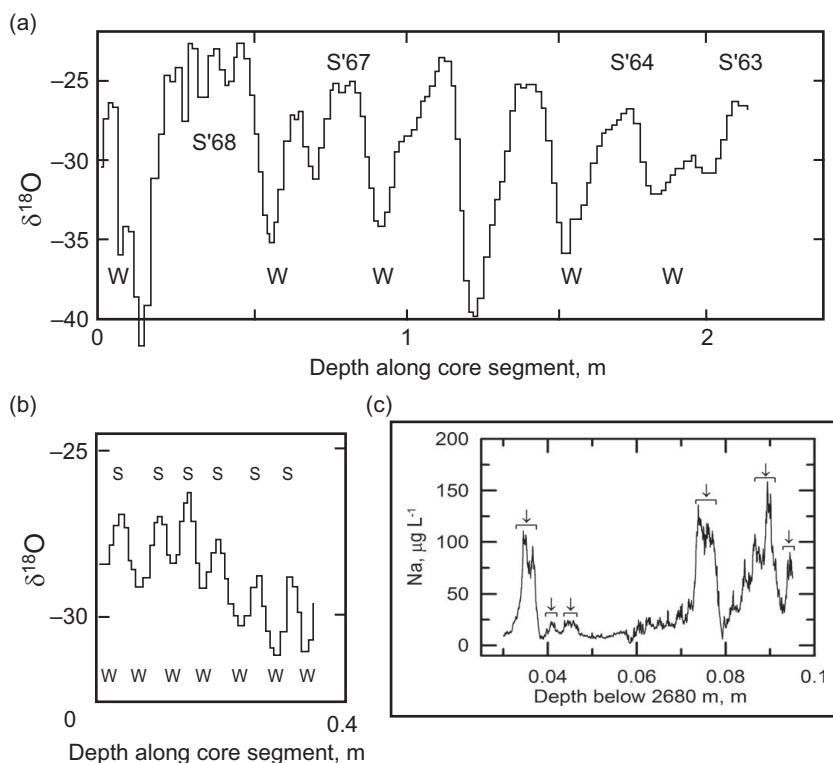


**Figure 16.1** (a) and (b)  $\delta^{18}\text{O}$  variations in the Camp Century, Greenland, ice core. (a) Ice from 1963–1968. (b) Ice that is ~8300 years old, and in which seasonal variations can still be detected. (c) Laser ablation mass spectrometry analysis of Na in ice that is ~86,000 years old from the Greenland Ice Sheet Project (GISP2) core. Arrows and brackets identify peaks interpreted to be annual layers defined by spring input of Na. Other data (Meese *et al.*, 1997) suggest that some of the less prominent peaks are also spring peaks. The mean thickness of annual layers is ~5 mm!. ((a and b) adapted from Johnsen *et al.*, 1972. Reproduced with permission of the authors and *Nature*; (c) adapted from Snead *et al.*, 2015, Figure 5. Reproduced with permission of the authors and the *Journal of Glaciology*)

contaminating air in the bubbles (Berner *et al.*, 1980). Also troubling was the possibility that diffusion might seriously modify the signal.

Initial attempts to measure  $\text{CO}_2$  in ice cores produced erratic results, justifying the concern. After years of experimentation, however, it was found that the  $\text{CO}_2$  in bubbles could be isolated by crushing ice at temperatures well below freezing and trapping the gas released (Delmas *et al.*, 1980; Moor and Stauffer, 1984), a process referred to as *dry extraction*. Contamination from the ice lattice can also be minimized by focusing on ice from Antarctica in which there is relatively little dust and organic material. Finally, measurements of the diffusivity demonstrated that even in old ice, smoothing by diffusion is not of sufficient magnitude to affect the record significantly (Ahn *et al.*, 2008).

The reliability of dry extraction was demonstrated by comparing concentrations of CO<sub>2</sub> in ice from Siple Dome (Figure 6.15), obtained by dry extraction, with those in the atmosphere measured at Mauna Loa over the last half of the twentieth century (Siegenthaler and Oeschger, 1987). In older ice, the similarity of measurements in multiple cores gives considerable confidence in the technique (Neftel *et al.*, 1988).

### Electrical conductivity measurements

The electrical conductivity of ice in a core can be detected readily in the field, and provides a useful measure of the concentrations of nitrate (NO<sub>3</sub><sup>-</sup>) and sulfate (SO<sub>4</sub><sup>2-</sup>). A pair of brass electrodes is drawn along a flat surface exposed on the side of a core (Hammer, 1980). A potential of ~1250 volts is applied across the electrodes, which are 10 mm apart. The electrodes are moved rapidly (>20 mm s<sup>-1</sup>), as the conductivity of the ice begins to decrease soon after the potential is applied. They are also moved in a zig-zag path to minimize the influence of bubbles and other causes of poor contact. The induced current is a measure of the conductivity.

## Establishing a time scale for a core

A crucial step in ice core studies is establishing an accurate time scale so that the relative timing of climate events observed in different cores can be determined. Because layers of snow deposited in an accumulation area are gradually stretched and thinned as they are buried, one cannot determine the age of a layer by simply dividing its depth by the annual accumulation rate (expressed in meters of ice equivalent). Depth hoar (an early fall accumulation) or dust (a spring deposit) are readily detected visually, however, so one can count annual layers downward from the surface. This is done in the field, while logging the visual stratigraphy, in order to get a preliminary estimate of the age of ice in a core. Once detailed chemical data become available, this initial count is refined using seasonal variations in stable isotope ratios and in concentrations of some ions. Radiogenic dates and volcanic ash layers of known age provide further checks.

Although counting layers is tedious, and resolving discrepancies resulting from missing peaks and double peaks is time consuming and sometimes subjective, one can often date ice up to several thousand years old quite accurately in this way. Computer algorithms have been written to automate this process (Taylor *et al.*, 2004; Winstrup, 2016). Statistical algorithms in these programs provide objective estimates of not only the age but also of the uncertainty in the timescale as a function of depth.

Once layers have been stretched significantly, some will be missed, or will be misinterpreted as consisting of two layers. Thus, in older ice or in locations with low accumulation rates, other, less precise approaches must be used.

Let's now discuss these techniques in somewhat greater detail.

### Visual layer counting

Depth hoar layers and layers with appreciable concentrations of dust are readily observed on the light table in a science trench. In the GISP2 core, depth hoar layers could be identified to a depth of 1678 m (11.65 ka), covering the entire Holocene (Meese *et al.*, 1997). At greater depths, thinning of the layers together with a lower Pleistocene accumulation rate made identification more difficult. However, as discussed further below, increases in dust in the atmosphere, particularly in the spring, resulted in annual cloudy bands in the ice, allowing visual stratigraphy to be extended to 2430 m (~50 ka) (Alley *et al.*, 1997).

### Oxygen and deuterium isotopes

Molecules containing the lighter isotope of oxygen,  $^{16}\text{O}$ , are more likely to diffuse to a water surface and also require less energy to vaporize. Thus, they are more likely to evaporate than molecules composed of the heavier isotope,  $^{18}\text{O}$  – a process called *fractionation*. When the water vapor later condenses, molecules containing  $^{18}\text{O}$  are preferentially precipitated (another fractionation), reducing the  $^{18}\text{O}$  content of the remaining vapor still further.

The ratio of  $^{18}\text{O}$  to  $^{16}\text{O}$  in a sample of ice or water can be determined quite precisely. The result is expressed as:

$$\delta^{18}\text{O} = \frac{(^{18}\text{O}/^{16}\text{O})_{\text{sample}} - (^{18}\text{O}/^{16}\text{O})_{\text{standard}}}{(^{18}\text{O}/^{16}\text{O})_{\text{standard}}} \times 1000.$$

The present standard, dubbed VSMOW, is a water standard approximating the average composition of freshwater. Multiplying the ratio by 1000 casts  $\delta^{18}\text{O}$  in parts per thousand, or per mil. Today we can measure  $\delta^{18}\text{O}$  to  $\pm 0.1\text{\textperthousand}$  (Gupta *et al.*, 2009).

By the time an air mass reaches a glacier, multiple episodes of fractionation may have left the water in it quite depleted in  $^{18}\text{O}$ . Typical  $\delta^{18}\text{O}$  values in Antarctic ice today are between  $-30$  and  $-35\text{\textperthousand}$ . During the Late Pleistocene they were in the  $-40\text{\textperthousand}$  to  $-45\text{\textperthousand}$  range. Concurrently, selective loss of  $^{16}\text{O}$  from the ocean (or other water bodies) during evaporation leaves the remaining water enriched in  $^{18}\text{O}$ . The ocean reservoir, however, is huge, so the enrichment is small. In foraminifera from ocean sediment cores, for example,  $\delta^{18}\text{O}$  is, today, typically between  $+2$  and  $+2.5\text{\textperthousand}$ . During the Pleistocene, values ranged as high as  $+5\text{\textperthousand}$  as  $^{16}\text{O}$  became locked up in ice sheets (Lisiecki and Raymo, 2005).

When the weather is warm,  $^{18}\text{O}$  is more readily evaporated from water bodies. Thus, ice derived from summer snow has more  $^{18}\text{O}$ , and  $\delta^{18}\text{O}$  values in it are higher

(less negative) than in ice derived from winter snow. Such seasonal variations in  $\delta^{18}\text{O}$  are easily measured in ice cores (Figure 16.1a and b). This is a powerful technique for identifying annual layers. However, owing to differing distances between the vapor source and the glacier and differing amounts of precipitation in transit, air masses undergo different amounts of fractionation along the way. Storm tracks also change. This variability can result in years with no apparent summer peaks and others with more than one.

Owing to differing amounts of fractionation, the amplitude of the  $\delta^{18}\text{O}$  signal at the glacier surface can vary from place to place. At Camp Century, Greenland, it is  $\sim 15\%$ , while 600 km away and 1200 m higher, at GISP2, it is only  $\sim 4\%$ . As the ice is buried, diffusion reduces the amplitude. Thus, whereas an annual  $\delta^{18}\text{O}$  signal was readily detectable in ice  $>\sim 8300$  years old at Camp Century (Figure 16.1b), annual variations were of limited use in ice only 1000 years old at GISP2 (Meese *et al.*, 1997; J. White, written communication, February 2018). Diffusive damping is also faster when gradients are steeper, as is the case when accumulation rates are low.

Deuterium (D or  $^2\text{H}$ ) is an isotope of hydrogen that has a neutron in its nucleus in addition to the single proton. Deuterium also fractionates upon evaporation or condensation. A parameter,  $\delta\text{D}$ , is defined in much the same way as  $\delta^{18}\text{O}$ , and is also used to define annual layers (Figure 16.2d).

Fractionation processes during evaporation result in a well-defined linear relation between  $\delta\text{D}$  and  $\delta^{18}\text{O}$ . For  $\delta^{18}\text{O} < 0$ , Craig (1961) found that  $\delta\text{D} = 8 \cdot \delta^{18}\text{O} + d$ . The intercept,  $d$ , is called the deuterium excess. Normally,  $d = 10\%$ , but when analyzed in detail it has been found that it reflects the temperature, relative humidity, seasonality of precipitation, and wind speed at the source, and thus provides additional information. Temporal changes in  $d$  thus reflect differences in climate in the source area, although the exact nature of these changes may not be obvious.

Our discussion of oxygen isotopes, so far, has focused on elements in the  $\text{H}_2\text{O}$  molecule. Measurement of  $\delta^{15}\text{N}$ ,  $\delta^{40}\text{Ar}$ , and especially  $\delta^{18}\text{O}_{\text{atm}}$ , in air bubbles in the ice can also be fruitful. Precise dating is challenging, however, because firn is permeable, so air in pores is exchanged with air at the glacier surface until compaction and metamorphism finally close connections between the pores and the surface. Wind and changes in atmospheric pressure drive a “pumping” action that facilitates this exchange. The depth to pore close-off at a site depends on the accumulation rate and temperature. In different places it thus occurs at different depths, and in ice of different ages. Pore close-off may occur at depths of as much as 120 m, and the difference in age between the ice and the air in bubbles,  $\Delta\text{age}$ , can be as much as a few thousand years (Bender, 2002).  $\Delta\text{age}$  may also vary through time (Goujon *et al.*, 2003).

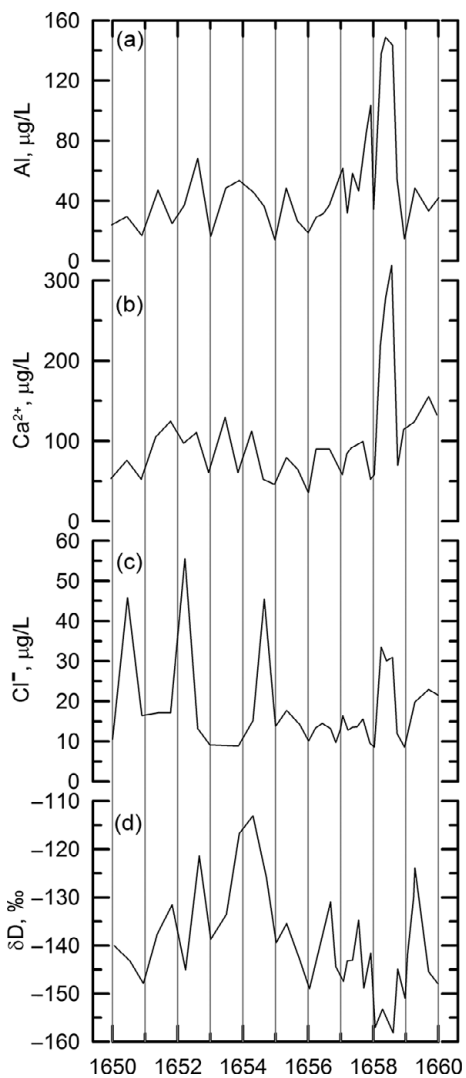


**Figure 16.2** An example of using several annually-varying parameters to date an ice core. The core is from the East Rongbuk Col on Mt. Everest. Here one can see that 1653–1655 C.E. was a challenging time period, inasmuch as there is only one Al, one  $\text{Cl}^-$ , and one  $\delta\text{D}$  peak over a time span interpreted on the basis of the  $\text{Ca}^{2+}$  record as being 2 years.  $\text{Ca}^{2+}$  and Al are inferred to be derived from dust. (After Kaspari *et al.*, 2008, Figure 2. Reproduced with permission of author and the International Glaciological Society)

It has been found that  $\delta^{18}\text{O}_{\text{atm}}$  is highly correlated with insolation variations arising from precession of the equinoxes, with a lag of 5–6 kyr. The reasons for this correlation are not well understood, but seem to be related to biospheric productivity (e.g. Landais *et al.*, 2010). Because orbital variations are well understood and dated, however, one can date ice in deep, low-resolution cores by measuring  $\delta^{18}\text{O}_{\text{atm}}$  in bubbles. This would be inappropriate, of course, if one were trying to understand the relation between climate and the orbital parameters.

Orbital variations also seem to affect the  $\text{O}_2/\text{N}_2$  ratio in air bubbles. In ice older than 190 ka in the Vostok core,  $\delta\text{O}_2/\text{N}_2$  variations track the 78°S summer insolation remarkably well (Figure 16.3) (Bender, 2002). The reasons for this, again, are not

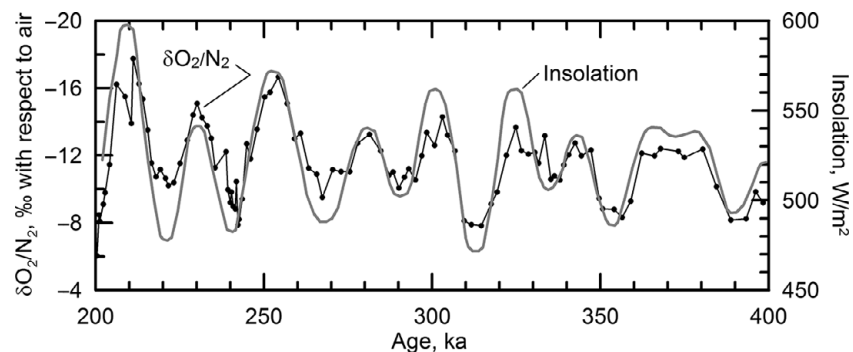


**Figure 16.3**  $\delta\text{O}_2/\text{N}_2$  record in the Vostok core and 78°S insolation ( $\text{O}_2\text{N}_2$  data from Suwa and Bender, 2008).

well understood. Apparently  $\text{O}_2$  is selectively lost, and the loss is greater, resulting in more negative  $\delta\text{O}_2/\text{N}_2$  values, when insolation is low. This technique has been used to date older parts of the Vostok (Suwa and Bender, 2008) and Dome F (Kawamura *et al.*, 2007) cores.

### Other elements

The abundances of many chemical species vary seasonally. Any soluble species that is not volatile and that does not react with other species can be useful for defining annual layering. Among these species are  $\text{Na}^+$ ,  $\text{NH}_4^+$ ,  $\text{Ca}^{2+}$ ,  $\text{Mg}^{2+}$ ,  $\text{Al}$ ,  $\text{Cl}^-$ ,  $\text{NO}_3^-$ , and  $\text{SO}_4^{2-}$  (Legrand and Mayewski, 1997).

Sodium ( $\text{Na}^+$ ) is entrained as winds detach water droplets from crests of ocean waves. Because air masses moving over oceans are routed over ice sheets more frequently in winter, Na has clear winter maxima in Greenland and Antarctica (Figure 16.1c).  $\text{Cl}^-$  also varies seasonally for the same reason (Figure 16.2c), but because HCl is also entrained in summer in some locations, the Cl signal can become damped compared with Na. Some Na and a fair amount of Ca is also derived from terrestrial sources. To distinguish these sources from the marine contributions, the concentrations of Na and Ca are compared with those expected based on the concentrations of other marine-sourced ions, particularly Cl. Any excesses are referred to as non-sea salt (nss): nssNa, nssCa.

Soluble calcium ( $\text{Ca}^{++}$ ) is derived from terrestrial sources of gypsum and from ocean spray; insoluble Ca is largely from continental dust. Al is also a good proxy for dust. Both it and insoluble Ca have distinct spring maxima in Greenland, owing to the proximity of land that is becoming free of snow but on which vegetation has yet to emerge. For the same reason,  $\text{NH}_4$  from biospheric sources also varies seasonally in Greenland. Ca and Al also peak in the late winter and spring on Mt. Everest (Figure 16.2a and b). Both ions are from local dust sources. They are much less abundant in Antarctic cores, owing to the distance from

terrestrial sources. During glacial periods, both Ca and Na from sea salt are higher despite the increase in sea ice, and thus in transport distances; this is attributed to higher wind speeds at the sea surface and to more efficient meridional transport.

Acidic molecules like nitrate ( $\text{NO}_3^-$ ) and sulfate ( $\text{SO}_4^{2-}$ ) also increase in spring and summer. Legrand and Mayewski (1997) present a good discussion of the seasonal variations of these and other chemical species in cores.

### Volcanic eruptions

Volcanic eruptions eject large amounts of  $\text{SO}_2$  and other aerosols into the atmosphere. The  $\text{SO}_2$  oxidizes, combines with water to form sulphuric acid, and is precipitated in snow. Ice layers formed from such snow are readily detected with electrical conductivity measurements (ECM), and signals from significant volcanic eruptions are generally easily distinguished from the much less pronounced seasonal oscillations. Acidity can also be detected by high-resolution continuous flow analysis (Winstrup *et al.*, 2019). The trace-element chemistry of shards extracted from ice with such acidity maxima can, in many cases, be correlated with a specific volcanic eruption of known age.

Many tephra layers contain too little sulfate to detect with ECM, and shards are too small and few to be detected visually. Such deposits are referred to as *cryptotephra*. They are sometimes found in samples collected during continuous flow analysis, and sometimes by melting selected core segments where tephra is expected (Bourne *et al.*, 2015). New techniques have been developed for mounting very small shards and analyzing them quantitatively with an electron microprobe in order to determine a source (Iverson *et al.*, 2017).

Particularly large eruptions such as that of Tambora in Indonesia in 1815 or of Toba in Sumatra at ~72 ka can be detected in both Greenland and Antarctica. The eruption of Laki in Iceland in 1783 provides a good reference horizon in Greenland. Eruptions of Erebus on the east side of McMurdo Sound are detected in many Antarctic cores. Ages based on layer counting can be adjusted when volcanic horizons of known age, like these, are available.

### $^{10}\text{Be}$

Between 39 and 43 ka there was a period of low geomagnetic field intensity, referred to as the *Laschamp event*. During this event the flux of cosmic rays reaching Earth increased, resulting in increased production of  $^{10}\text{Be}$  in the atmosphere, and in an increased flux of  $^{10}\text{Be}$  atoms to ice sheets. (nb. flux = concentration (of  $^{10}\text{Be}$  atoms in the ice)  $\times$  accumulation rate.) This increase is readily recognized in deep ice cores in both hemispheres (Figure 16.4a and b). The peaks show structure on centennial and even decadal time scales, suggesting that they are also recording periods of variable solar activity (Raisbeck *et al.*, 2007).

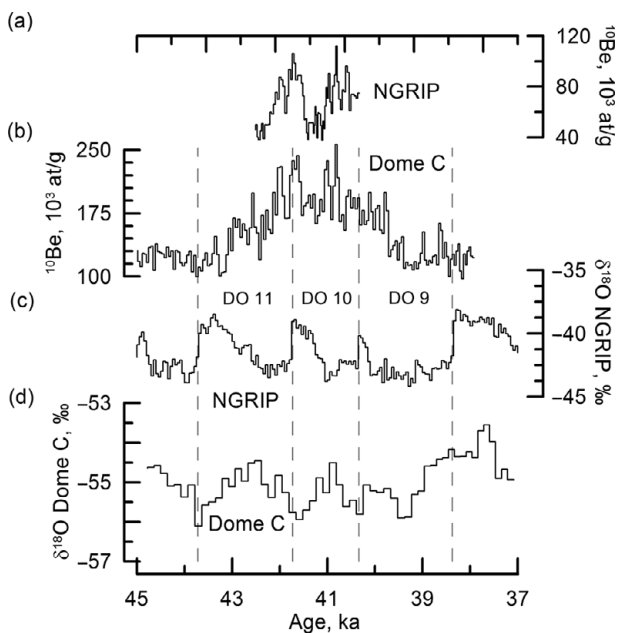


**Figure 16.4**  $^{10}\text{Be}$  concentrations between 37 and 45 ka at (a) NGRIP and (b) Dome C, and paleotemperature records based on  $\delta^{18}\text{O}$  records at (c) NGRIP and (d) Dome C. Dansgaard–Oeschger events 9–11 are shown in (c). They coincide with positive temperature excursions at Dome C, demonstrating that the Dansgaard Oeschger events were not confined to the Northern Hemisphere. ( $^{10}\text{Be}$  data from Raisbeck *et al.* (2017).  $\delta^{18}\text{O}$  records from NGRIP members (2004) and EPICA Community members (2004). Reproduced with permission of author and the European Geosciences Union)

Raisbeck *et al.* have identified a characteristic signature involving peaks at ~41 and 42 ka in both the NGRIP (Greenland) and Dome C (Antarctica) cores, and propose that this signature provides a temporal tie between the two cores. Furthermore, the  $^{10}\text{Be}$  signature spans Dansgaard–Oeschger event 10 at ~41.1–41.8 ka in the NGRIP core (Figure 16.4c) and a similar positive temperature excursion in the Dome C core (Figure 16.4d), strongly suggesting that the Dansgaard–Oeschger events reflect global, not just Northern Hemisphere climatic events. Thus the  $^{10}\text{Be}$  excursion during the Laschamp event serves not only to temporally correlate cores, but also, and perhaps more importantly, to firmly synchronize paleoclimatic records in cores from the two hemispheres.

## Dust

Dust is blown onto ice sheets in the spring after the snow has melted but before soil-stabilizing vegetation has emerged. The possibility of using dust to define annual layers was perhaps first recognized by Marshall (1959), and was verified by Thompson (1977) in studies of the Camp Century and Byrd Station ice cores, although the reason for the annual variation was not then understood. Thompson's

measurements were made laboriously on individual melted samples. Later, Ram *et al.* (1995) discovered that the intensity of light backscattered from a laser source was proportional to the mass of dust particles in the ice. Thus measurements could be made on cores in the science trench soon after they were recovered. The laser technique is able to detect dust bands that are not visible. As with most indicators of annual layering, however, storms can deposit dust at times other than spring and early summer, occasionally resulting in more than one dust peak in a year.

In Greenland, accumulation rates increased ~4-fold during the transition from the Younger Dryas to the Preboreal, while in Antarctica they decreased somewhat. Thus, to estimate the amount of dust in the atmosphere it is, as with  $^{10}\text{Be}$ , the flux to the ice sheet, not the concentration in the ice, that must be considered. During the Pleistocene, dust concentrations increased 15–20-fold in Antarctica and 30–35-fold in Greenland (Fischer *et al.*, 2007), so the increase in flux was ~30-fold in Antarctica and only 7–8-fold in Greenland. The increases during the Pleistocene are attributed to higher wind speeds, enlarged arid areas, increased erosional activity, and exposure of continental shelves.

The Sr/Nd isotopic composition of dust samples has been used to determine provenance. With the caveat that modern samples that can be used for comparison are not available from some potential source regions, such as continental shelves, it has been convincingly shown that the desert regions of China and Patagonia are the primary sources of dust in Pleistocene ice in Greenland and Antarctica, respectively (Fischer *et al.*, 2007). During the Holocene, Antarctica also received significant contributions from Australia.

The amount of dust in the atmosphere over an ice sheet depends on the quantity entrained in the source area, the rate at which it is removed by wet or dry precipitation en route to the ice sheet, and the length of the path to the site of deposition. Mayewski *et al.* (1994) speculate that high Pleistocene fluxes in Greenland likely reflect expanded high latitude atmospheric circulation, probably a consequence of the presence of the Laurentide Ice Sheet. Interestingly, dust concentrations decreased significantly during Dansgaard–Oeschger events (Meese *et al.*, 1997), apparently owing to a combination of higher snow accumulation rates and some reorganization of atmospheric circulation.

### Laser ultrasound observations of mechanical properties

A new technique for analyzing ice cores uses variations in velocity of ultrasonic waves (Mikesell *et al.*, 2017). A laser, which can be outside the cold room, is focused on the side of a core. The laser causes local thermal expansion of the ice, initiating an elastic wave. On the other side of the core a receiver laser measures the wave speed. The core is moved under the laser and wave speeds are recorded with sub-millimeter resolution. Test runs on two core segments with no visible stratigraphy revealed variations in wave speed that were in phase with annual cycles based on

chemical variations. The causes of the speed variations are not fully understood, but with further study and development the technique may provide another tool for detecting annual layers in cores.

### Radioactive isotopes

Radioactive isotopes are used for dating cores in two ways. Bomb tests in 1955 and 1963–1965 injected radioactive debris into the stratosphere, whence it was distributed globally. Upon being washed out of the atmosphere, this debris accumulated in both snow and clastic sediment. The radioactive isotopes decay by emission of high energy electrons or positrons called  $\beta$  particles. Thus, horizons containing these isotopes are readily detected in both ice and sediment cores by their unusual  $\beta$  activity. Identification of these horizons is widely used for dating cores.

Other radioactive isotopes like  $^{14}\text{C}$  trapped in air bubbles or  $^{10}\text{Be}$  and  $^{36}\text{Cl}$  in aerosols can also be used for dating in the conventional way, by measuring the amount of the isotope remaining in the ice, estimating the amount that was originally present, and knowing the half-life. As the uncertainty in such radiometric dates is significant, this approach is used, primarily, to date ice in which layer counting is not possible.

### Analytical approaches

The age of ice as a function of depth in an accumulation area can be estimated with a simple analytical model. The age is equal to the time,  $t$ , that it takes to bury the layer to depth,  $z$ . We'll use the coordinate system shown in Figure 16.5, with  $u$ ,  $v$ , and  $w$  being the velocities in the  $x$ ,  $y$ , and  $z$  directions. By definition,  $w = \frac{dz}{dt}$ , so:

$$\int_0^t w dt = \int_0^z dz. \quad (16.1)$$

Consider a situation in which  $\partial v / \partial x$  is negligible and  $\partial u / \partial x$  decreases parabolically with depth in such a way that:  $w = w_s \left( \frac{H-z}{H} \right)^2$  (Equation 5.25). At the surface,  $w_s = b_n$  where  $b_n$  is measured in meters of ice. Making these substitutions and rearranging, Equation (16.1) becomes:

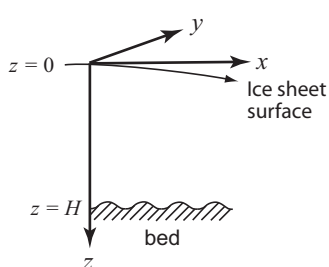


**Figure 16.5** Coordinate system used in discussing age-depth calculations.

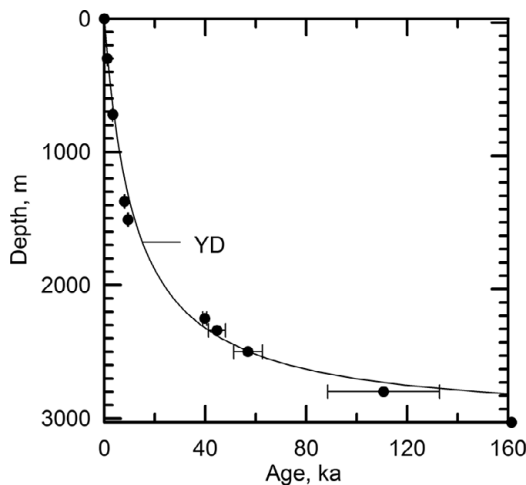


**Figure 16.6** Age of ice as a function of depth in the GISP2 core based on multiparameter analysis of the core and an analytical profile calculated using Equation (16.2), with  $b_n = 0.25 \text{ m a}^{-1}$ .

$$\int_0^t dt = \int_0^z \frac{1}{w} dz = \frac{H^2}{b_n} \int_0^z \frac{dz}{(H-z)^2}.$$

Carrying out the integration yields:

$$t = -\frac{H^2}{b_n} \left( \frac{1}{H-z} - \frac{1}{H} \right). \quad (16.2)$$

Figure 16.6 is a plot of age vs. depth in the 3030 m GISP2 core. The data points are from Meese *et al.* (1997) and are based on multiparameter analysis of the core. The analytical solution is based on Equation (16.2). The mean layer thickness at a depth of 100–104 m is 0.25 m, and this is taken as the value of  $b_n$ . The analytical solution is in remarkably good agreement with the ages based on layer counting. Actually, however, there is a sharp increase in layer thickness at a depth of 1678 m. This corresponds to the termination of the Younger Dryas, or YD, at 11.65 ka (Alley *et al.*, 1997; Meese *et al.*, 1997), and reflects higher accumulation rates during the warmer Holocene conditions.

Figure 16.6 illustrates both the value and the limitations of this simple analytical approach. The calculated profile matches observations rather well in the upper 2500 m, but seriously overestimates ages at greater depths. Furthermore, the calculation depends on having a good estimate of  $b_n$ . Such simple calculations are useful for illustrating the effect of layer thinning on age–depth relations, and might be useful in preliminary planning of a deep drilling program.

More sophisticated numerical models are also used both in planning and in analysis of completed cores, and can incorporate more relevant variables. Petit *et al.* (1999) developed a remarkably successful numerical model of the age–depth

relation in the Vostok core with only three tuning parameters,  $b_n$ , the basal melt rate, and the fraction of the surface velocity due to sliding. They tuned the model to assumed ages at two depths, 1534 and 3254 m. The assumed ages were based on deep dips in  $\delta D$  that were correlated with two well-defined marine isotope stages. The resulting ages of peaks in measured  $\delta^{18}\text{O}_{\text{atm}}$ , a proxy for atmospheric temperature, were within 3% of the ages of maxima in July insolation at 65°S.

Inverse modeling, in which one starts with a series of observations from several cores and determines the parameters of a numerical model that will reproduce those observations, is also currently used in dating deep cores with low accumulation rates (Lemieux-Dudon *et al.*, 2010). The method involves developing a background chronology for several cores based on modeling of accumulation rates, firn densification, and ice flow; on absolute ages from various measures such as those described above; and on stratigraphic links between cores. Confidence limits are placed on the various components of the chronologies. A statistical algorithm then calculates a best fit to the data supplied.

## The fruits of ice core studies

Ice core studies have contributed immensely to our understanding of climate history. Of the wealth of studies using cores to explore past climates, let's review a few that are particularly relevant to current concerns.

### Composition of the atmosphere one million years ago

Basal ice is rarely exposed at the surface in Antarctica. In some local areas, however, wind scouring inhibits snow accumulation and sublimation results in an ablation zone in which very old bubbly blue ice is exposed. One such area is in the Allan Hills, ~150 km northwest of McMurdo Sound (Figure 6.15). Ice in the Allan Hills blue ice areas has traveled less than ~20 km from the site of accumulation. Meteorites that fell in the accumulation area long ago and were buried are now being exposed in the blue ice area. This has stimulated numerous studies of this ice. Among them is an analysis of a 126-m core that reaches to within 5 m of the bed (Higgins *et al.*, 2014).

To date ice in the core, Higgins *et al.* made use of the fact that the  $^{40}\text{Ar}/^{38}\text{Ar}$  ratio in the atmosphere is gradually increasing due to outgassing from the continental crust and midocean ridges. The  $^{40}\text{Ar}$  is produced by radioactive decay of  $^{40}\text{K}$  in the crust and mantle; the rate of increase is 0.040 %/Ma (Bender *et al.*, 2008). Thus, by measuring the  $^{40}\text{Ar}/^{38}\text{Ar}$  ratio in air bubbles in old ice, one can estimate the age of the ice, albeit with a fairly large uncertainty. In the Allan Hills core, 30 analyses were made, distributed over the length of the core. In the upper part of the core, from 25 to 113 m depth, 19 analyses yielded an age of  $320 \pm 160$  ka;

in the basal 11 m, six analyses averaged  $990 \pm 110$  ka. The two core sections are likely separated by a shear zone.

Abrupt fluctuations in  $\delta D$  and  $\delta^{18}\text{O}$  over depth intervals of  $\sim 0.1$  m suggest that ice within each core segment is also stratigraphically disturbed, either by shear zones or by folding, but on a scale that did not mix ice of dramatically different ages. Thus successive measurements of a parameter with depth have no significance, but the mean and range of values within a core segment reflect conditions spanning the time interval represented by that segment. These values are of considerable interest because, as we have seen (Figure 15.1), there was a dramatic change in amplitude and period of glaciations from 40 ky cycles before  $\sim 900$  ka to 100 ky cycles since. One key to understanding this mid-Pleistocene transition is  $\text{CO}_2$ : we know that  $\text{CO}_2$  has varied in phase with glacial advances since 900 ka (Figure 16.7); was this also the case earlier? If so, were the amplitudes of the  $\text{CO}_2$  oscillations similar to those later, or were they damped, as were the glacial oscillations? Answers to these questions would clarify the role of  $\text{CO}_2$  in driving glaciations.

In the basal ice from the Allan Hills core, the amplitudes of  $\text{CO}_2$ ,  $\text{CH}_4$ , and  $\delta D$ , all of which are indicators of climate, are smaller than those during the last 800 ky, and mean values of  $\text{CO}_2$  and  $\delta D$  are shifted toward higher (warmer) values. Also, the  $\text{CH}_4/\text{CO}_2$  ratio was lower in the mid-Pleistocene, suggesting a lesser role of  $\text{CH}_4$  in modulating climate. While the former results are consistent with warmer temperatures and smaller amplitudes of glacial fluctuations in the mid-Pleistocene based on  $\delta^{18}\text{O}$  records from benthic forams (Figure 15.1), one must remember that the Allan Hills sample is relatively small and likely missed the highest and lowest values. These are, however, the first direct measurements of the composition of the atmosphere in the mid-Pleistocene.

### Past concentrations of $\text{CO}_2$ and $\text{CH}_4$ in the atmosphere

Burning of fossil fuels is steadily increasing the concentrations of carbon dioxide and methane in the atmosphere, leading to climate warming. But what role did these gases play in modulating climate during the Pleistocene? And when did human activities begin to affect the concentrations? These questions have dogged glaciologists and climate scientists for years.

Concentrations of both  $\text{CO}_2$  and  $\text{CH}_4$  closely track atmospheric temperature, recorded by  $\delta D$ , in the cores from Vostok (Petit *et al.*, 1999) and Dome C (Figure 16.7). However, owing to the difference in age between the ice and the air in bubbles ( $\Delta\text{age}$ ), it is not clear whether  $\text{CO}_2$  and  $\text{CH}_4$  lead or lag the temperature signal.

Of particular interest are the rapid warming trends, called *Terminations* ( $T_1-T_IV$  in Figure 16.7), that end ice ages. These warmings have occurred at intervals of  $\sim 100$  ky for the past  $\sim 900$  ky. The advances and retreats of ice sheets, documented by  $\delta D$  and  $\delta^{18}\text{O}$  records, are strongly correlated with changes in insolation resulting

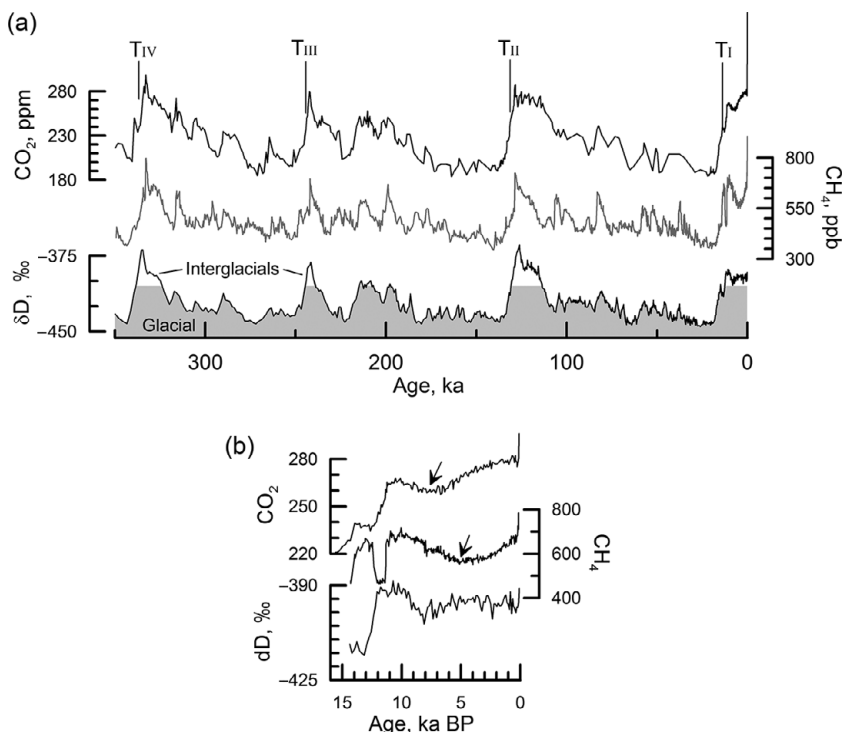


**Figure 16.7** (a) Variation of  $\text{CO}_2$ ,  $\text{CH}_4$ , and  $\delta\text{D}$  with time in the upper 350 m of the Dome C core. T = Termination, the end of an ice age. (b) Detail of  $\text{CO}_2$ ,  $\text{CH}_4$ , and  $\delta\text{D}$  variations during the past 15 ky. Arrows show where  $\text{CO}_2$  and  $\text{CH}_4$  trends deviate from trends following earlier terminations.  $\text{CO}_2$  and  $\text{CH}_4$  records end in 1900 CE. [ $\delta\text{D}$  data are from EPICA Community members (2004),  $\text{CH}_4$  data from Loulergue *et al.* (2007), and  $\text{CO}_2$  data from Lüthi *et al.* (2008)]

from secular changes in Earth's orbit – the Milankovitch cycles – particularly at the precession (19 and 23 ky) and obliquity (41 ky) periods (Hays *et al.*, 1976). The 100 ky cyclicity is reminiscent of the orbit's ellipticity period, but the effect of ellipticity on insolation is too small to have such a dramatic effect on the ice sheets. Thus, some feedback processes must be involved.

One possible feedback involves greenhouse gases. Increasing insolation would initiate both ice-sheet retreat and ocean warming. As the solubility of  $\text{CO}_2$  in the ocean is inversely proportional to temperature, a warming ocean is expected to release  $\text{CO}_2$ , which then, through the greenhouse effect, increases Earth's temperature in a positive feedback. Retreating ice also exposes wetlands which are an important source of  $\text{CH}_4$ , resulting in another positive feedback. This model implies that insolation initiates the retreat. Alternatively, there may be processes on an ellipticity time scale that release  $\text{CO}_2$  or  $\text{CH}_4$ , or both, thus initiating warming which, again through the same positive feedbacks, results in retreat of ice sheets. So it is not clear whether terminations are initiated by insolation or by release of  $\text{CO}_2$ .

Furthermore, Dansgaard–Oeschger events look like failed terminations, during which the process stopped well before full deglaciation. Why didn't feedbacks lead to full deglaciation during these perturbations?

Also of interest in Figure 16.7 are the changes in CO<sub>2</sub> and CH<sub>4</sub> following Termination I. During the preceding three terminations, both species peaked and then decreased, in some cases fairly abruptly. Following Termination I, however, both species initially decreased but then started to increase (see arrows in Figure 16.7b). Ruddiman (2003, 2007) argues that humans are responsible for these anomalous increases. The departure of CO<sub>2</sub> from the normal post-climate peak occurred at ~8 ka, when humans were first adopting agriculture and clearing the land to plant crops. The deforestation released CO<sub>2</sub> stored in trees. The departure of CH<sub>4</sub> from the normal pattern appears to correspond well with increased rice farming and animal husbandry in southeast Asia ~5 ka. Rice production involves the development of artificial wetlands, and ruminants are efficient converters of grass to CH<sub>4</sub>. Particularly fascinating is Ruddiman's demonstration that dips in CO<sub>2</sub> at three times during the past 2 ky correspond with periods of plague, when significant percentages of the population died and farms began to revert to woodlands.

### The end of the Younger Dryas

Detailed studies of the Younger Dryas–Holocene transition at 11.7 ka in the NGRIP and GISP2 cores reveal remarkable details of this climate event. Using continuous flow analysis, Steffensen *et al.* (2008) analyzed δ<sup>18</sup>O, Na<sup>+</sup>, Ca<sup>2+</sup>, dust, and *d* (deuterium excess) in the NGRIP core at subannual resolution (Figure 16.8); they also implemented an algorithm that provides a measure of the time span over which a change in a measured parameter occurred. Mayewski *et al.* (2014) conducted LA-ICP-MS analysis of Ca<sup>2+</sup> and Na<sup>+</sup> in two 50 mm segments of the GISP2 core spanning only ~6 years, albeit not consecutive, to study finer details of this YD-Holocene climate shift (Figure 16.9). In both studies, seasonal fluctuations in the measured parameters were used to define annual layer thickness,  $\lambda$ .

Of these various parameters, *d* is controlled by temperatures at the source of the moisture (see p. 438), while δ<sup>18</sup>O reflects temperatures at the core site and  $\lambda$  is a measure of accumulation there (Steffensen *et al.*, 2008), Ca ions are largely from terrestrial dust transported from Asian deserts to Greenland by zonal westerly winds, and Na is derived from ice-free marine sources (Mayewski *et al.*, 2014). Peak concentrations in Na, Ca, and dust occur during the transition from winter to spring, when storms are most frequent and intense (Whitlow *et al.*, 1992).

Across the YD-Holocene boundary *d* decreases ~2‰ in 2 years (Figure 16.8), suggesting cooling of the moisture source area by 2–4°C. A few years later  $\lambda$  roughly doubles in ~6 years, reflecting a comparable increase in accumulation rate, possibly due either to shortening of the distance to the moisture source or to

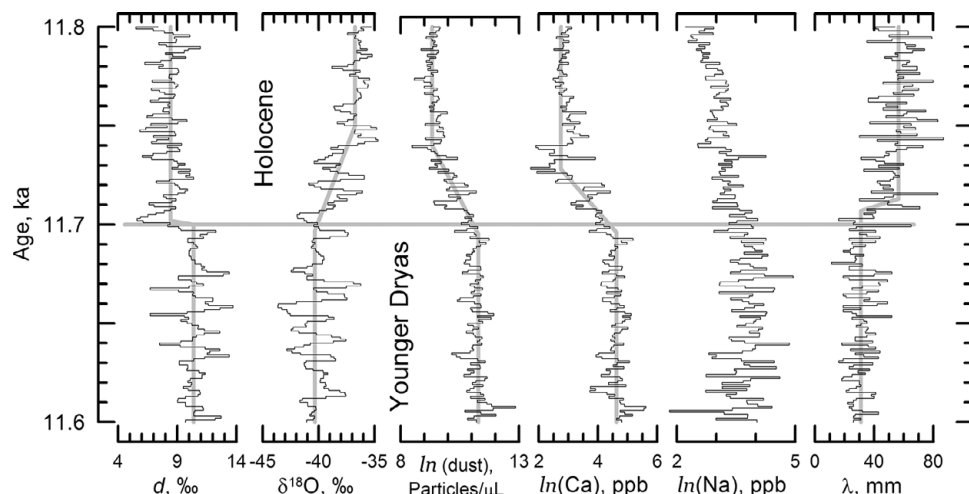


**Figure 16.8** Continuous flow analysis of  $d$ ,  $\delta^{18}\text{O}$ ,  $\text{Ca}^+$ ,  $\text{Na}^+$ , dust, and  $\lambda$  in the NGRIP core.  
(Replotted from Steffensen *et al.*, 2008, Figure 2. Reproduced with permission of the author and the American Association for the Advancement of Science)

warming that allowed the atmosphere to hold more moisture. During the initial decades of the Holocene,  $\delta^{18}\text{O}$  increases by  $\sim 3\text{\textperthousand}$  over a period of  $\sim 50$  years (Figure 16.8), implying a remarkable  $\sim 10^\circ\text{C}$  warming at the core site, and Ca and dust decrease by a factor of 5–7 over a period of 30–40 years. Na also decreases, but over a longer time span.

The only characteristic of the climate that can change over time spans as short as 2 years is atmospheric circulation. Thus, the abrupt change in  $d$  likely reflects a reorganization of atmospheric circulation such that moisture was brought to the ice sheet from a new cooler, perhaps closer and more northerly source area. The new circulation resulted in an increase in the accumulation rate over  $\sim 6$  years. The temperature at the core site ( $\delta^{18}\text{O}$ ) took a few decades to adjust. The longer-term decreases in Ca and dust could be due to a decrease in storminess, a change that is supported by a decrease in the frequency of exceptionally high peaks in the raw LA-ICP-MS data (Figure 16.9) (Mayewski *et al.*, 2014). Alternatively, Steffensen *et al.* (2008) suggest that more rain in the Asian desert regions reduced dust entrainment there.

Mayewski *et al.* call attention to the lower peak concentrations in Na and Ca in the post YD LA-ICP-MS record (Figure 16.9), and the longer periods of low concentrations between peaks. They attribute the former to a decrease in storminess, and the latter to a lengthening of the summer season. Both would represent significant changes in climate. The long-term decrease in Na may reflect such a decrease in storminess, resulting in less transport of Na to the ice sheet despite a likely decrease in sea ice extent that would shorten the transport distance.

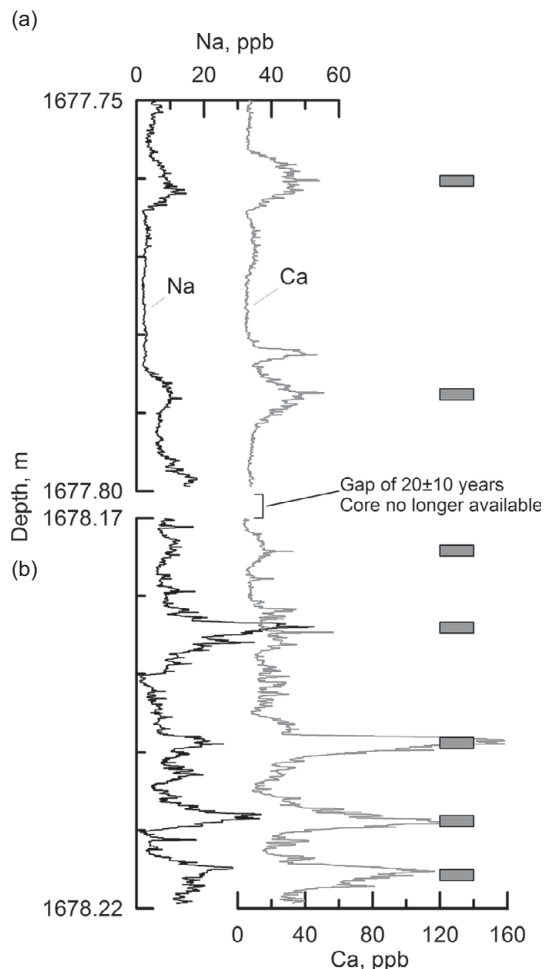


**Figure 16.9** LA-ICP-MS analysis of  $\text{Ca}^{2+}$  and  $\text{Na}^+$  in two 50 mm segments of the GISP2 core. (a) A record spanning the YD-Holocene transition. (b) A record from a period a decade or two after the beginning of the Holocene. Owing to previous studies, there is no longer any core left from the first decades of the Holocene. (After Mayewski *et al.*, 2014, Figure 3. Reproduced with permission of the author and John Wiley & Sons, Ltd)

The warming transition from the Oldest Dryas to the Bølling also appears to have occurred within 2–3 years (Alley *et al.*, 1993; Steffensen *et al.*, 2008). On the other hand, cooling transitions, such as that from the Bølling to the Younger Dryas (14.4–12.7 ka) took a few centuries (Figure 16.10). Dansgaard–Oeschger events exhibit a similar asymmetrical sawtooth pattern (Figure 16.4c). Mayewski *et al.* worry that climate changes resulting from ongoing human activities may trigger other abrupt changes with which we are ill-prepared to deal. Such changes will be hard to predict because we do not have analogs for the present climate preserved in high-resolution records.

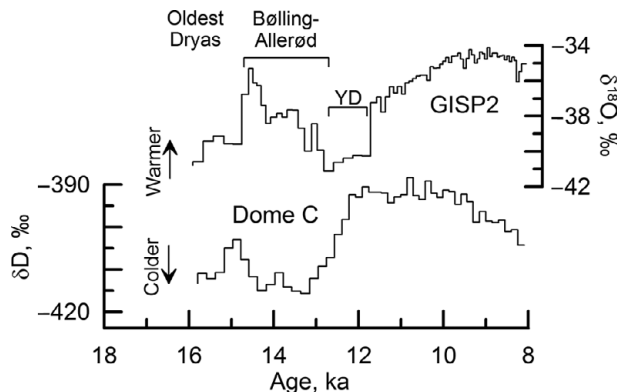


**Figure 16.10** The bipolar seesaw during the transition from the Bølling-Ållerød to the Holocene in the GISP2 and Dome C cores ( $\delta D$  data from EPICA Community members (2004).  $\delta^{18}\text{O}$  data from <ftp://ftp.ncdc.noaa.gov/pub/data/paleo/icecore/greenland/summit/gisp2/isotopes/gispd18o.txt>.

### The bipolar seesaw

When it was cold in the northern hemisphere, sea ice in the North Atlantic extended southward, inhibiting downwelling of warm saline water from the Gulf Stream. This reduced upwelling of cold bottom water in the South Atlantic. The South Atlantic thus began to warm, resulting in warming of the Antarctic continent. This can be seen in Figure 16.10. In the initial phases of the cooling from the Bølling-Ållerød to the YD in the GISP2  $\delta^{18}\text{O}$  record,  $\delta D$  records cooling at Dome C. However, well before the coldest phase of the GISP2 record, temperatures at Dome C begin to rise. This oscillation was first described by Broecker (1998), who dubbed it the *bipolar seesaw*.

The bipolar seesaw also operated during Dansgaard-Oeschger event D09 (Figure 16.4c and d). In the NGRIP record, the abrupt warming that initiates a D-O event is followed by a long slow cooling. During D09 this cooling is initially accompanied by cooling in the Dome C record but then, as the maximum cooling is approached in the NGRIP record, Dome C begins to warm up. The slight lag likely reflects the time necessary for ocean circulation to adjust to the decrease in downwelling in the North Atlantic (Stocker and Johnsen, 2003).

The seesaw did not operate during the 100 ka cycles.

### Pb in the atmosphere

The lead (Pb) content of a 72-m core from Colle Gnifetti glacier in the Swiss-Italian Alps was analyzed using high-resolution ICP-MS and dated by layer counting from 100 C.E. to 2007 C.E. (More *et al.*, 2017). Saharan dust events of known age were used as an additional constraint on the chronology, and  $^{14}\text{C}$  dating of particulate organic carbon corroborated the time scale. The key finding of the study was that Pb levels dropped below detection limits as the most devastating of the Black Death

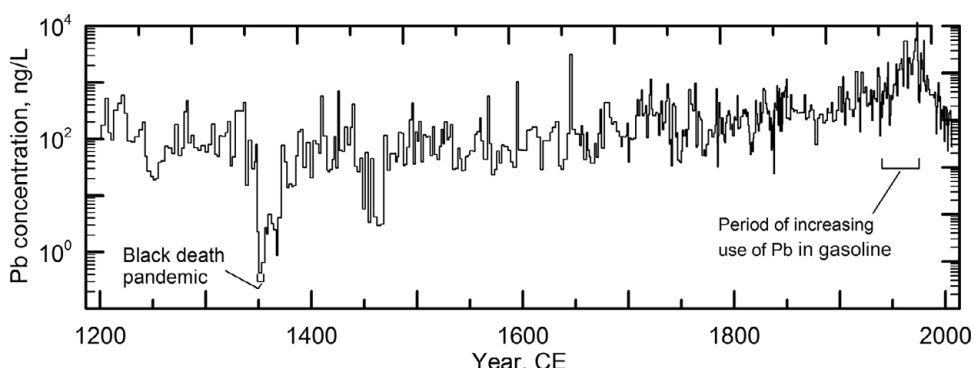


**Figure 16.11** LA-ICP-MS analysis of Pb in the Colle Gnifetti core. Note the logarithmic ordinate scale. Pb concentrations dropped abruptly when mining districts were shut down by the plague between 1349 and 1351. Pb concentrations rose between 1940 and 1995 when tetraethyl lead was used in gasoline. [data courtesy of S. Sneed. Based on More *et al.* (2017) Reproduced with permission of the author and the American Geophysical Union]

pandemics advanced across Europe between 1349 and 1351 C.E. (Figure 16.11). Seven European Pb mining districts were progressively closed as the plague evolved. The lowest Pb levels during the rest of the 2000 year period were an order of magnitude higher, yet these are the levels commonly assumed to be preindustrial natural background levels, and therefore assumed to be “safe.”

The Colle Gnifetti core also records the use of tetraethyl lead in gasoline, which started in ~1940. The dangers of lead were recognized in the 1960s, and automobile manufacturers were ordered to design engines to run on lead-free gasoline by 1975.

## SUMMARY

Glaciers and ice sheets contain a trove of information about climate, atmospheric circulation, and environmental conditions in the past. Ice cores probe this archive. The atmosphere is global, and climate is a global phenomenon with extensive teleconnections. To utilize the data from ice cores to explore these teleconnections, one must date the ice accurately.

In this chapter we first reviewed laboratory techniques used to extract information from ice cores, and then elaborated upon techniques for dating ice in the cores. Counting annual layers using visual stratigraphy or seasonal variations in chemistry is clearly the most exact, but anomalous chemistry or stratigraphy can result in missing layers or in a single layer being interpreted as two. Volcanic ash layers of known provenance and age and certain radiometric dating techniques can serve as checks on results of layer counting.

Layer counting has been used to date ice nearly 12,000 years old in areas where accumulation rates are high. In older ice or in cores from areas of low accumulation rate, diffusion and thinning of layers by longitudinal strain degrade the signal. In these cores, numerical modeling and correlation of proxy measures of insolation with variations in orbital parameters that influence insolation have been reasonably successful.

We rounded out the chapter with some examples from the multitude of studies utilizing ice cores to better understand climates and environments of the past. Of particular interest recently has been the concentration of greenhouse gasses in the atmosphere, as such gasses are responsible for ongoing climate warming. We found that a million years ago greenhouse gas levels were lower than they have been during the last 800 ky, and that both CO<sub>2</sub> and CH<sub>4</sub> track temperature closely, although owing to uncertainty in age it is not clear which was driving the changes. We also saw that the Holocene increases in CO<sub>2</sub> began when humans began clearing forests for agriculture, and those in CH<sub>4</sub> when rice farming and animal husbandry developed in southeast Asia. Then we found that significant changes in climate can occur in as little as half a decade, and are transmitted between hemispheres by atmospheric and oceanic teleconnections. Finally, we looked briefly at the record of atmospheric Pb, noting that present levels are still higher than preindustrial natural background levels.

## Problems

### Chapter 3

- 3.1 (a) Determine the changes in  $b_w$ ,  $R$ , and  $T_a$  that would, if they occurred alone, result in a 100 m increase in equilibrium line altitude. Assume a 120 d melt season, a lapse rate of  $-0.007^\circ\text{C m}^{-1}$ , and  $\partial b_w/\partial z = 1 \text{ kg m}^{-2} \text{ m}^{-1}$ .
- (b) Recalculate  $\delta T_a$  assuming that a  $1^\circ\text{C}$  increase in  $T_a$  increases  $R$  by about  $0.3 \text{ MJ m}^{-2} \text{ d}^{-1}$ .

### Chapter 4

- 4.1 Determine the activation energy for creep for the following two sets of data: All experiments were run at the same stress. Express the activation energy in  $\text{kJ mol}^{-1}$ .

Data set 1		Data set 2	
$\dot{\varepsilon}$ , $\text{a}^{-1}$	T, $^\circ\text{C}$	$\dot{\varepsilon}$ , $\text{a}^{-1}$	T, $^\circ\text{C}$
18.65	-5.5	1.33	-30.4
9.06	-9.9	0.0047	-61.0

- 4.2 (a) The temperature dependence of ice creep can be represented by an Arrhenius-type relation:

$$\dot{\varepsilon}_e = A_0 \sigma_e^n e^{-\frac{Q}{R\theta}}$$

By differentiating this with respect to  $\theta$  and expressing the result in terms of differentials, determine the fractional change in  $\dot{\varepsilon}$ ,  $d\dot{\varepsilon}/\dot{\varepsilon}$ , due to a change,  $d\theta$ , in  $\theta$ .

- (b) In a laboratory experiment run at a temperature of  $-15^\circ\text{C}$ , what would be the approximate percentage variation in  $\dot{\varepsilon}$  if the temperature were allowed to vary by  $0.5^\circ\text{C}$ ? Use  $Q = 60 \text{ kJ mol}^{-1}$ .

- 4.3 (a) Calculate a  $\sigma - \dot{\varepsilon}$  curve (log-log axes) for  $\theta = 263 \text{ K}$ ,  $d = 0.002 \text{ m}$ , and  $0.01 < \sigma < 1.3$  using the Goldsby and Kohlstedt relation  $\dot{\varepsilon} = \dot{\varepsilon}_{\text{GBS}} + \dot{\varepsilon}_{\text{disl}}$ ,

where the subscripts denote grain boundary sliding and dislocation creep, respectively. Both strain rates on the right hand side are of the form:  $\dot{\varepsilon} = A_0 \sigma_e^n \frac{1}{d^p} \exp\left(-\frac{Q}{R\theta}\right)$ . The values of the constant parameters are given in the table\* below:

	Grain boundary sliding	Dislocation creep
$A_0$	9.467E33 MPa <sup>-n</sup> a <sup>-1</sup>	1.893E36 MPa <sup>-n</sup> a <sup>-1</sup>
$Q$	192 kJ mol <sup>-1</sup>	181 kJ mol <sup>-1</sup>
$n$	1.8	4.0
$p$	1.4	0.0

\* These values of the constants are for temperatures above 258 K only.

- (b) Plot an  $n = 3$  line passing through  $\sigma = 0.25$  MPa,  $\dot{\varepsilon} = 0.043$  a<sup>-1</sup>, and spanning  $0.07 < \sigma < 3$  MPa. How well does this line cover the range in stresses likely to be found in a glacier?

- 4.4 (a) Calculate and plot the variation of crevasse depth,  $d$ , with tensile stress,  $\sigma_{xx}$ , for depths ranging from 0.5–40 m. Use  $K_{lc} = 0.16$  MPa. (You will need to assume values of  $d$  and calculate  $\sigma_{xx}$ .)  
 (b) What is the significance of the minimum in  $\sigma_{xx}$  at ~4 m depth?

## Chapter 5

- 5.1 Calculate the difference between the surface velocity and the bed velocity in a glacier 300 m thick with a surface slope of 0.046. Use  $n=3$  and  $A = 357$  MPa<sup>-3</sup> a<sup>-1</sup>. Use:

- The infinitely wide approximation,
- An approximation based on Raymond's estimate of the appropriate shape factor for Athabasca Glacier (0.58), and
- The semicircular approximation.

Which result comes closest to the values measured by Raymond on Athabasca Glacier, and why?

- 5.2 At the equilibrium line on the Barnes Ice Cap Trilateration Net, the surface velocity is  $6.7$  m a<sup>-1</sup>, the ice is 185 m thick, and the surface slope is 0.07. Using  $A = 100$  MPa<sup>-3</sup> a<sup>-1</sup> (appropriate for ice at about  $-5^\circ\text{C}$ ) and  $n = 3$ , calculate and plot a velocity profile through the ice cap. What is the basal velocity. Is your result consistent with the above ice temperature?

- 5.3 An infinitely-wide glacier has a velocity of  $1 \text{ m a}^{-1}$  at the surface and  $0.7 \text{ m a}^{-1}$  at a depth of 16 m. Determine the thickness of the glacier. Assume  $u_b = 0$  and  $n = 3$ .
- 5.4 (a) Derive an equation analogous to Equation (5.6) using Equations (4.4) and (4.5). Neglect contributions to  $\dot{\epsilon}_e$  other than  $du/dz$ .  
(b) Use this equation to calculate a velocity profile through the Greenland Ice Sheet at Camp Century. Use the constants in Table 4.1 and assume a constant temperature of  $-22^\circ\text{C}$ . The ice sheet is 1368 m thick and the surface slope is  $3.6 \times 10^{-3}$ .  
(c) Compare this profile with one calculated with the use of Equation (5.6).
- 5.5 (a) An ice sheet has a surface profile given by  $h = \sqrt{cx}$ , where  $h$  is the height in meters and  $x$  is the distance from the margin, also in meters. Differentiate this to obtain an expression for the surface slope,  $S$ . By inserting this in the expression for the basal drag,  $\tau = \rho ghS$ , show that  $\tau$  is independent of  $x$ . Obtain a numerical value for  $\tau$  if  $c = 16 \text{ m}$ .  
(b) Let the ablation rate be  $b_n \text{ m a}^{-1}$ . By equating the discharge through any cross section to the volume of ice lost by melting downglacier from that cross section, show that the average horizontal velocity in the ablation zone is:  $u = -b_n \sqrt{x/c}$ . (The minus sign indicates that  $u$  is in the  $-x$  direction.)  
(c) At  $x = 1500 \text{ m}$  the glacier flows over a bump in the bed, 0.5 m high, and quarries a cobble from the lee slope of the bump. The ice closes under the cobble, so at the start of its journey to the margin it is 0.5 m above the bed. Determine the  $x$ - and  $z$ -coordinates ( $z$  vertical) of the point where the cobble will melt out, and its time en route. Plot its path. Assume plug flow and incompressibility. Use  $b_n = 0.6 \text{ m a}^{-1}$  and  $c = 16 \text{ m}$ , and assume the ablation zone is 2 km wide. [Hint: Use the incompressibility condition,  $du/dx = -dw/dz$ , and the result from problem 5.5b to get  $w(x)$ . Then use the definition of velocity,  $u = dx/dt$ , and the initial condition,  $x_{t=0} = x_0$ , to integrate the expression for  $u$  to get  $x(t) = (\sqrt{x_0} - b_n t / (2\sqrt{c}))^2$ . Then use  $w = dz/dt$ , and the initial condition,  $z_{t=0} = z_0$  to obtain  $z(t) = z_0 \sqrt{x_0/x}$ .]  
(d) The accumulation zone in the above problem is 10 km wide (Figure P1). At the end of the Pleistocene, a mammoth dies 500 m from the divide. Determine the  $x$ - and  $z$ -coordinates of the point where he melts out, and his time en route. Assume the glacier has had a balanced budget for the last 10,000 a, and that the ablation rate is  $0.6 \text{ m a}^{-1}$  over the 2 km wide ablation zone, as before. Plot the path. [Hint: Do as in problems 5.5b and 5.5c, remembering that the horizontal velocity is now  $u = -b_n(L-x)/\sqrt{cx}$ , where  $L$  is the distance from the margin to the divide. You will encounter an integral,

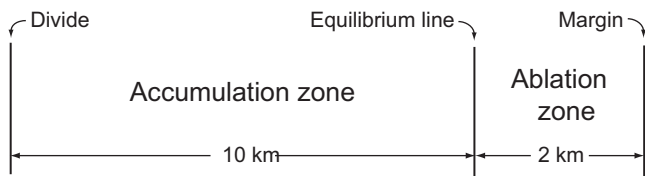


Figure P1

$\int \sqrt{x}/(L-x)dx$ , which may be transformed using  $r=L-x$  and then evaluated using the tabulated integral:

$$\int \frac{\sqrt{L-r}}{r} dr = 2\sqrt{(L-r)} + L \left( \frac{1}{\sqrt{L}} \ln \frac{\sqrt{(L-r)} - \sqrt{L}}{\sqrt{(L-r)} + \sqrt{L}} \right).$$

- (e) If the mammoth was 3 m long and, when she died, she was lying down with her tail 3 m closer to the divide than her head, determine the time required for her body to pass completely beneath the equilibrium line, and her approximate length when she is at this point in her journey.

## Chapter 6

- 6.1 Calculate and plot a temperature profile for an ice sheet that is 1368 m thick, assuming that  $\theta_s = -24^\circ\text{C}$ ,  $b_n = 0.35 \text{ m a}^{-1}$ ,  $\kappa = 37.2 \text{ m}^2 \text{ a}^{-1}$ ,  $\bar{u} = 0$ , and  $\beta_o = -0.0228^\circ\text{C m}^{-1}$ . Obtain temperatures at least at 0, 200, 500, and 900 m above the bed.

- 6.2 (a) Determine the influence of strain heating on a temperature profile by integrating the energy balance equation, simplified with the use of the following assumptions:

- Horizontal temperature gradients are negligible,
- $K = \text{constant}$ ,
- Steady state,
- Zero accumulation (or  $w_s = 0$ ), and
- $\dot{\varepsilon} = A\sigma^3$ .

(Note: This is easier if the  $z$ -axis points downward. If you retain a  $z$ -axis pointing upward, the sign of  $\beta_o$  below must be changed.)

- (b) Calculate the profile for a glacier that is 1000 m thick with:

$$\begin{aligned}\theta_s &= -35^\circ\text{C} & \rho &= 900 \text{ kg m}^{-3} & \alpha &= 0.01 \\ \beta_o &= 0.0228^\circ\text{C m}^{-1} & K &= 7.1 \times 10^7 \text{ J m}^{-1} \text{ a}^{-1} \text{ }^\circ\text{C}^{-1} & n &= 3 \\ A &= 16.0 \text{ MPa}^{-3} \text{ a}^{-1}\end{aligned}$$

Plot the bottom 200 m or so of the profile, using an expanded temperature axis so you can see the curvature.

- 6.3 Solve problem 6.2, but with the additional assumption that strain heating is negligible, and calculate the temperature at the base of this same 1000 m thick glacier. How much does strain heating increase the basal temperature?
- 6.4 (a) To get a sense of the influence of longitudinal advection, calculate and plot a temperature profile for the glacier in problem 6.1, assuming  $\bar{u} = 15 \text{ m a}^{-1}$ . Use the Column model with the values of  $\theta_s$ ,  $b_n$ ,  $\kappa$ , and  $H$ , given in problem 6.1,  $\beta_G = -0.228^\circ\text{C m}^{-1}$ ,  $K = 7.1 \times 10^7 \text{ J m}^{-1}\text{a}^{-1}\text{C}^{-1}$ ,  $\alpha = -0.01$ ,  $\lambda = -0.01^\circ\text{C m}^{-1}$ , and  $w_b = 0 \text{ m a}^{-1}$ .
- (b) Compare the result with that from problem 6.1 in detail.
- 6.5 (a) Obtain an expression for the temperature gradient and the temperature distribution in a stagnant sheet of ice of infinite horizontal extent, and thickness  $H$ . Assume that the climate has been warming at a rate of  $\dot{\theta}$ , that the interior of the glacier is warming at the same rate, and that  $K$  is independent of depth.
- (b) Plot the profile for a glacier 1000 m thick with  $\dot{\theta} = 0.001^\circ\text{C a}^{-1}$  and  $\beta_o = -0.020^\circ\text{C m}^{-1}$ . By examining the original differential equation after simplification, explain how the uniform warming rate is accomplished.

## Chapter 8

- 8.1 Water flowing along a glacier bed must warm up as the ice thins and the pressure melting point increases. Water flowing up an adverse bed slope must warm up more rapidly, as the ice is thinning more rapidly. The energy needed to warm the water comes from viscous dissipation. Determine how steep the bed slope can get, relative to the surface slope, without exceeding the amount of viscous energy available. Obtain a numerical value for the constant of proportionality between the two slopes.
- 8.2 The discharge in a horizontal subglacial conduit with a circular cross section is  $0.025 \text{ m}^3 \text{ s}^{-1}$ . The water pressure in the conduit is 1.5 MPa and the hydrostatic pressure in the adjacent ice is 2.0 MPa. The Manning roughness of the conduit is  $0.1 \text{ m}^{-1/3} \text{ s}$  and the viscosity parameter,  $A$ , is  $245 \text{ MPa}^{-3} \text{ a}^{-1}$ . Determine the pressure gradient in the conduit, the radius of the conduit, the water velocity in the conduit, and the melt rate on the conduit walls (or closure rate).
- 8.3 An esker splits as shown in (Figure P2). Stratigraphic relations suggest that the branch around the end of the ridge is younger. Explain why the esker changed course, and estimate the basal shear stress at the time of the change in course. Assume that the glacier had a parabolic profile,  $h = \sqrt{cx}$ . Assume further that water flow down the potential gradient could be maintained even though some water might be forced to refreeze to keep the temperature at the pressure melting point.

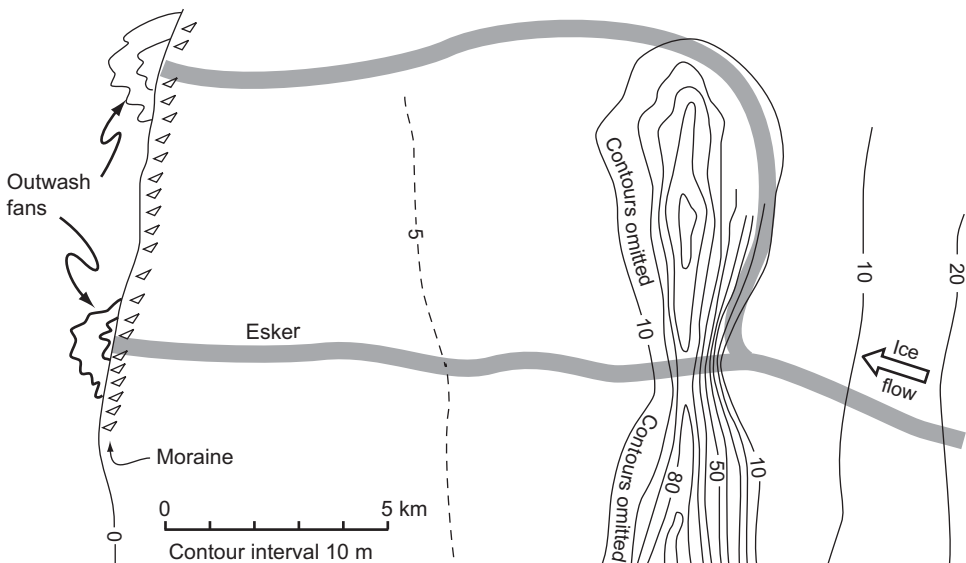


Figure P2

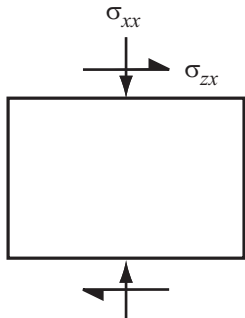
8.4 Consider a glacier with a parabolic profile,  $h = \sqrt{16x}$ , where  $x$  is the horizontal coordinate in meters and  $h$  is the surface elevation. Assume that the glacier is 2 km long and is on a horizontal bed. It is drained by a circular conduit at the bed. Calculate and plot the height of the hydraulic grade line as a function of distance from the terminus for discharges of  $0.015 \text{ m}^3 \text{ s}^{-1}$ , a winter discharge, and  $1.0 \text{ m}^3 \text{ s}^{-1}$ , a summer discharge. Use a channel Manning roughness of  $0.1 \text{ m}^{-1/3} \text{ s}$  and ice viscosity parameter,  $A = 360 \text{ MPa}^{-3} \text{ a}^{-1}$ . Assume that the conduit is at atmospheric pressure within 50 m of the margin. (The integration, which has to be carried out numerically, can be easily done in a spreadsheet.)

## Chapter 9

9.1 Using Equation (9.2) for  $\sigma_s$  in terms of  $\sigma_{xx}$ ,  $\sigma_{zz}$ , and  $\theta$ :

- Determine the angle  $\theta$  of the planes on which  $\sigma_s$  is a maximum.
- Determine the orientation of these planes relative to those on which  $\sigma_N$  is a maximum.
- Determine the normal stress,  $\sigma_N$ , on the plane on which  $\sigma_s$  is a maximum.
- Determine the magnitude of  $\sigma_{s\max}$ .

Express all answers in terms of  $\sigma_{xx}$ ,  $\sigma_{zz}$ , and  $\sigma_{zx}$ .

**Figure P3**

- 9.2 Express  $J_1$  and  $J_2$  (Equations 9.8a) in terms of  $\sigma_{xx}$ ,  $\sigma_{zz}$ , and  $\sigma_{xz}$  in two dimensions, showing that  $J_1 = 0$  and  $\sqrt{J_2}$  is given by Equation (9.5b).
- 9.3 We have shown (Chapter 6) that  $\frac{1}{2}\dot{\varepsilon}_{zx}\sigma_{xz} + \frac{1}{2}\dot{\varepsilon}_{zx}\sigma_{zx}$  is the total work done per unit time in a unit volume of ice subjected to simple shear. It is also true that  $\frac{1}{2}\dot{\varepsilon}_{xx}\sigma'_{xx}$  is the work done by a normal stress. Thus, the total work done is  $W = \frac{1}{2}\dot{\varepsilon}_{ij}\sigma'_{ij}$ . Show that, because  $\dot{\varepsilon}_{ij} = \lambda\sigma'_{ij}$ ,  $W = \dot{\varepsilon}_e\sigma'_e$ .
- 9.4 A laboratory ice deformation experiment is run using biaxial compression with applied stresses  $\sigma_1$  and  $\sigma_2$  on the faces of a cube. Stresses in the third direction are atmospheric. Strain rates are  $\dot{\varepsilon}_1$  and  $\dot{\varepsilon}_2$  in the  $\sigma_1$  and  $\sigma_2$  directions. Determine the effective stress and the effective strain rate.
- 9.5 An experimental system is designed to run tests in combined uniaxial compression and simple shear (Figure P3). Determine the effective stress and effective strain rate for this stress configuration.

## Chapter 10

- 10.1 Calculate and plot velocity profiles for an infinitely wide glacier that is 300 m thick with a surface slope of 0.046. Use  $n = 3$  and  $A = 357 \text{ MPa}^{-n} \text{ a}^{-1}$ . Calculate one profile for  $\dot{\varepsilon}_{xx} = 0.0$  and one for  $\dot{\varepsilon}_{xx} = 0.1 \text{ a}^{-1}$ . Assume a sliding velocity,  $u_b$ , of  $20 \text{ m a}^{-1}$ . Explain the difference between the profiles.

## Chapter 11

- 11.1 Calculate a temperature profile in the ablation area of a glacier in a place where the ice is 500 m thick, the vertical velocity at the surface,  $w$ , is  $0.25 \text{ m a}^{-1}$  (upward),  $\beta_o$  is  $-0.017^\circ\text{C m}^{-1}$ , and the temperature at the surface is  $-20^\circ\text{C}$ . Assume that  $w$  decreases linearly with depth.

- 11.2 Using Equation (11.9) and an initial condition in which  $\theta = -20^\circ\text{C}$  at the surface, varies linearly to  $-11^\circ\text{C}$  at a depth of 4 m, and is then independent of depth to a depth of 15 m, calculate a temperature profile for the end of June ( $t = 1/2$  year). Use  $\kappa = 16 \text{ m}^2 \text{ a}^{-1}$  and a sinusoidal variation in temperature with time at the surface, with  $\theta_r = 18^\circ\text{C}$ . The initial condition applies on January 1 ( $t=0$ ). Compare your solution to the analytical solution given by Equation (6.31). (*Hint:* you will need to use a quite small time step to avoid an instability.)

## Chapter 12

- 12.1 For comparison of borehole deformation rates, with shear stress  $\sigma_{zx}$  and shear strain rate  $\dot{\varepsilon}_{zx}$ , with deformation rates in uniaxial compression, the stress in uniaxial compression must be multiplied by  $1/\sqrt{3}$  and the strain rate by  $\sqrt{3}/2$  (Nye, 1953). Show that this is true by calculating  $\sigma_e$  and  $\dot{\varepsilon}_e$  for the two stress configurations.
- 12.2 Verify that the vertically downward forces on the top of the semi-cylinder of ice in Figure 12.6 balance the vertically upward forces on the bed when the pressure in the ice is  $P$  and the “traction” tending to close the conduit is  $\Delta P$ .
- 12.3 (a) The surface and bed profiles of the lower part of the Trilateration Net on Barnes Ice Cap can be reasonably described by:

$$z_s = 501.5 + 0.1001x - 1.15E-5x^2 + 5.44E-10x^3$$

and

$$z_b = 384 + 0.069x - 1.46E-5x^2 + 9.21E-10x^3,$$

in which  $x$  is the distance from the margin in meters. Estimate  $u(x)$  at  $x = 4$  km by carrying out the integration in Equation (12.38) numerically, from  $(x' - x)/l = -2$  to 2. Use  $x_o = 4$  km as the datum state (so what you are actually calculating is the effect of longitudinal coupling on the velocity at 4 km). Use  $2l = 1.1$  km and break the distance  $2l$  into five parts on either side of a central interval centered on  $x = 4$  km. (So there are 11 intervals, each  $dx$  is 200 m, and  $x_o = 4000$  m). To calculate  $u_o$  use  $A = 108.5 \text{ MPa}^{-3} \text{ a}^{-1}$ , and  $n = 3$ . You'll need to adjust  $\epsilon$  so  $\int_{-2l}^{2l} W dx = 1$ .

- (b) Why does  $u(x)$  differ from  $u_o$  in the direction that it does?
- 12.4 Starting with Equation (12.45), verify Equation (12.46). To do this it is necessary to use only one of Equations (12.45) (i.e. for  $i = 1$ ).
- 12.5 Starting with  $\dot{\varepsilon} = A\sigma^n$  and  $\dot{\varepsilon}_{ij} = \lambda\sigma'_{ij}$ , show that the constants  $n$  and  $A$  in Glen's flow law can be evaluated if one can determine only one component of

the stress tensor, the corresponding component of the strain rate tensor, and  $\dot{\varepsilon}$  at two or more places.  $n$  and  $A$  are determined either algebraically when there are only two points, or by plotting  $1/\lambda$  against  $\dot{\varepsilon}$  and drawing a straight line through the points. Explain.

- 12.7 Determine  $n$  and  $A$  in  $\text{MPa}^{-3} \text{ a}^{-1}$  for the following two sets of velocity derivatives.

Depth	Velocity	$x$	$y$	$z$
9.4 m	$u$	-0.004 45	0.000 00	-0.014 17
	$v$	0.000 00	0.000 13	0.003 61
	$w$	0.000 99	-0.000 40	0.004 32
12.5 m	$u$	-0.004 14	0.000 00	-0.022 96
	$v$	0.000 00	0.000 12	0.003 93
	$w$	0.000 99	-0.004 68	0.004 02

The surface slope is 0.152. Depths are in meters and velocities in  $\text{m a}^{-1}$ . The  $y$ -axis is transverse and the  $z$ -axis is normal to the surface and directed downward. Assume that gradients in  $\sigma'_{xx}$ ,  $\sigma'_{yy}$ , and  $\sigma_{yx}$  are negligible. Data are from the Barnes Ice Cap boreholes.

## Chapter 13

- 13.1 (a) Calculate temperature-depth profiles in an ice shelf at places where the ice shelf is 370 and 470 m thick. Ignore horizontal advection. The accumulation rate on the ice shelf is  $0.1 \text{ m a}^{-1}$ . The surface temperature is  $-28^\circ\text{C}$ . The water temperature beneath the ice shelf,  $T_b$ , can be calculated from:

$$T_b = -0.036 - 0.0759P - 0.0499S - 0.000112S^2$$

where  $P$  is the pressure in MPa, and  $S$  is the salinity. Use  $S = 34.39 \text{ ppt}$ . [Note that this problem is very much like that discussed on p. 120–124), except that you need to use a temperature boundary condition at the bed, not a temperature gradient condition.]

- (b) What is the mean  $dT/dz$  over the bottom 200 m of the two profiles?  
 (c) What thickness of ice could be formed annually at the base of the ice shelf if the heat of fusion were conducted upward into the ice by these temperature gradients?

## Chapter 14

- 14.1 Verify Equation (14.5).
- 14.2 Calculate  $\bar{y}_{oc}$  for the mammoth in Problem 5.5e.
- 14.3 Verify that Equation (14.11) follows from Equation (14.10) and that Equation (14.12) is a solution to Equation (14.11).

## Chapter 15

- 15.1 (a) Derive Equation (15.27).  
 (b) The ice flux per unit width is  $q = \bar{u}h$ , and if  $u_b = 0$  then  $\bar{u} = \frac{4}{5}u_s$  (Equation 5.19). Obtain an expression similar to Equation (15.27) for  $dq/q$ .
- 15.2 Using Figure 15.15:
- (a) Compare the observed change in velocity of Nisqually Glacier from 1949 to 1951 with that calculated from Equation (15.27). Use  $h \approx 80$  m.
  - (b) Estimate the change in flux,  $dq$ , and use the equation from Problem 15.1b to estimate the fractions of that change that are due to the changes in thickness and in surface slope, respectively. Then calculate  $c_0$  and  $D_0$  from their definitions, expressed in finite difference form. (Note that  $dh$ ,  $d\alpha$ , and  $dq$  need to be expressed as changes per year as  $q$ ,  $c_0$ , and  $D_0$  are in  $\text{m a}^{-1}$  and  $\text{m}^2 \text{a}^{-1}$ , respectively. Note also that  $q$ ,  $c_0$ , and  $D_0$  are defined in terms of a unit width.)
- 15.3 Consider a perturbation,  $b' = 0.1 \text{ m a}^{-1}$  on Storglaciären. Calculate  $\Delta\ell$  and  $\tau_V$ . Use the Jóhannesson *et al.* (1989) model generalized to three dimensions. The glacier area is  $3.03 \times 10^6 \text{ m}^2$ , and the ablation rate at terminus is  $1.3 \text{ m a}^{-1}$ . Other geometrical properties of the glacier can be scaled from Figures 8.14 and 12.9. Note that the topography is such that the width at the terminus would expand significantly as the glacier thickened.
- 15.4 Express Equations (15.25) in finite difference form and integrate them numerically. Plot them (as in Figure 15.11) to show the lags of  $q$  and  $\Delta\ell$ . Use  $H = 44 \text{ m}$ ,  $b' = 0.1 \text{ m a}^{-1}$ ,  $\ell_0 = 8 \text{ km}$ , and  $\tau_1 = \tau_2 = \tau_3 = 1 \text{ year}$ .

## Chapter 16

- 16.1 (a) Calculate and plot an age-depth profile for an ice sheet 2000 m thick with an accumulation rate of  $0.2 \text{ m a}^{-1}$  using Equation (16.2).  
 (b) Make the same calculation for this ice sheet assuming a linear decrease in  $w$  with depth. Plot the profile on the graph you made in part (a).  
 (c) Explain physically (not mathematically) why the two profiles differ in the way they do.

## References

- Aber, J. S., and Ber, A. (2007). *Glaciotectonism*. Developments in Quaternary Science, 6, Amsterdam: Elsevier, 246pp.
- Adhikari, S., Ivins, E. R., and Larour, E. (2017). Mass transport waves amplified by intense Greenland melt and detected in solid earth deformation. *Geophysical Research Letters*, 44, 4965–4975.
- Adhikari, S., Nakawo, M., Seko, K., and Shakya, B. (2000). Dust influence on the melting process of glacier ice: experimental results from Lirung Glacier, Nepal Himalayas. In Nakawo, M., Raymond, C. F., and Fountain, A. (eds.) *Debris-Covered Glaciers*. IAHS Publication no. 264, 43–52.
- Ahn, J., Headley, M., Wahlen, M., Brook, E. J., Mayewski, P. A., and Taylor, K. C. (2008). CO<sub>2</sub> diffusion in polar ice: observations from naturally formed CO<sub>2</sub> spikes in the Siple Dome (Antarctica) ice core. *Journal of Glaciology*, 54(187), 685–695.
- Allen, C. R., Kamb, W. B., Meier, M. F., and Sharp, R. P. (1960). Structure of lower Blue Glacier, Washington. *Journal of Geology*, 68(6), 601–625.
- Alley, R. B. (1988). Fabrics in polar ice sheets: development and prediction. *Science*, 240, 493–495.
- Alley, R. B. (1989a). Water pressure coupling of sliding and bed deformation: I. Water system. *Journal of Glaciology*, 35(119), 108–118.
- Alley, R. B. (1989b). Water-pressure coupling of sliding and bed deformation: II. Velocity-depth profiles. *Journal of Glaciology*, 35(119), 119–129.
- Alley, R. B. (1991). Deforming bed origin for the southern Laurentide till sheets? *Journal of Glaciology*, 37(125), 67–76.
- Alley, R. B. (1992). Flow-law hypotheses for ice-sheet modeling. *Journal of Glaciology*, 38(129), 245–256.
- Alley, R. B. (1993). In search of ice-stream sticky spots. *Journal of Glaciology*, 39(133), 447–454.
- Alley, R. B., and Whillans, I. M. (1991). Changes in the West Antarctic ice sheet. *Science*, 254(5034), 259–263.
- Alley, R. B., et al. (1993). Abrupt increase in Greenland snow accumulation at the end of the Younger Dryas event. *Nature*, 362(6420), 527–529.
- Alley, R. B., Gow, A. J., and Meese, D. A. (1995). Mapping c-axis fabrics to study physical processes in ice. *Journal of Glaciology*, 41(137), 197–203.
- Alley, R. B., Gow, A. J., Meese, D. A., Fitzpatrick, J. J., Waddington, E. D., and Bolzan, J. F. (1997). Grain-scale processes, folding, and stratigraphic disturbance in the GISP2 ice core. *Journal of Geophysical Research*, 102(C12), 26819–26830.
- Amundsen, R. (1912). The South Pole: an account of the Norwegian Antarctic expedition in the “Fram”, 1910–1912,

- Volumes 1 and 2, translated by A. G. Chater.
- Anandakrishnan, S., Catania, G. A., Alley, R. B., and Horgan, H. J. (2007). Discovery of till deposition at the grounding line of Whillans ice stream. *Science*, 315, 1835–1838.
- Andrews, L. C. et al. (2014). Direct observations of evolving subglacial drainage beneath the Greenland Ice Sheet. *Nature*, 514, 80–83.
- Arendt, A., Luthcke, S., Gardner, A., O’Neel, S., Hill, D., Moholdt, G., and Abdalati, W. (2013). Analysis of a GRACE global mascon solution for Gulf of Alaska glaciers. *Journal of Glaciology*, 59(217), 913–924, doi: 10.3189/2013JoG12J197.
- Ashley, G. M., Boothroyd, J. C., and Borns, H. W. Jr. (1991). Sedimentology of late Pleistocene (Laurentide) deglacial-phase deposits, eastern Maine; an example of a temperate marine grounded ice-sheet margin. *Geological Society of America Special Paper*, 261, 107–125.
- Atkinson, B. K. (1984). Subcritical crack growth in geological materials. *Journal of Geophysical Research*, 89(B6), 4077–4144.
- Atkinson, B. K., and Rawlings, R. D. (1981). Acoustic emission during stress corrosion cracking in rocks. In Simpson, D. W., and Richards, P. G. (eds.) *Earthquake Prediction. An International Review*. Ewing Series, 4. Washington, DC: American Geophysical Union, pp. 605–619.
- Attig, J. W., Mickelson, D. M., and Clayton, L. (1989). Late Wisconsin landform distribution and glacier bed conditions in Wisconsin. *Sedimentary Geology*, 62(3–4), 399–405.
- Azuma, N., Miyakoshi, T., Yokoyama, S., and Takata, M. (2012). Impeding effect of air bubbles on normal grain growth of ice. *Journal of Structural Geology*, 42, 184–193.
- Bahr, D. B., Dyurgerov, M., and Meier, M. F. (2009). Sea-level rise from glaciers and ice caps: a lower bound. *Geophysical Research Letters*, 36, L03501, doi:10.1029/2008GL036309.
- Bahr, D. B., Meier, M. F., and Peckham, S. D. (1997). The physical basis of glacier volume-area scaling. *Journal of Geophysical Research*, 102(B9), 20355–20362.
- Bahr, D. B., Pfeffer, W. T., and Kaser, G. (2015). A review of volume-area scaling of glaciers. *Reviews of Geophysics*, 53, 95–140.
- Baker, R. W. (1981). Textural and crystal-fabric anisotropies and the flow of ice masses. *Science*, 211(4486), 1043–1044.
- Baker, R. W. (1982). A flow equation for anisotropic ice. *Cold Regions Science and Technology*, 6(3), 141–148.
- Bamber, J. L., Riva, R. E. M., Vermeersen, B. L. A., and LeBrocq, A. M. (2009). Reassessment of the potential sea-level rise from a collapse of the West Antarctic ice sheet. *Science*, 324(5929), 901–903.
- Banerjee, I., and McDonald, B. C. (1975). Nature of esker sedimentation. *The Society of Economic Paleontologists and Mineralogists Special Publication* 23, 132–154.
- Banwell, A. F., MacAyeal, D. R., and Sergienko, O. V. (2013). Breakup of

- Larsen B ice shelf triggered by chain reaction drainage of supraglacial lakes. *Journal of Geophysical Research*, **40**, 1–5, doi: 10.1002/2013GL057694.
- Barnes, P., Tabor, D., and Walker, J. C. F. (1971). Friction and creep of polycrystalline ice. *Proceedings of the Royal Society of London, Series A*, **324** (1557), 127–155.
- Begeman, C. B., et al. (2018). Ocean stratification and low melt rates at the Ross ice shelf grounding zone. *Journal of Geophysical Research, Oceans*, **123**(10), 7438–7452, doi: 10.1029/2018JC013987.
- Bell, J. F. (1941). Morphology of mechanical twinning in crystals. *American Mineralogist*, **26**, 247–261.
- Beltaos, S. (2002). Collapse of floating ice covers under vertical loads: test data vs. theory. *Cold Regions Science and Technology*, **34**, 191–207.
- Bender, M. L. (2002). Orbital tuning chronology for the Vostok climate record supported by trapped gas composition. *Earth and Planetary Science Letters*, **204**, 275–289, doi: 10.1016/S0012-821X(02)00980-9.
- Bender, M. L., Barnett, B., Dreyfus, G., Jouzel, J., and Porcelli, D. (2008). The contemporary degassing rate of  $^{40}\text{Ar}$  from the solid Earth. *Proceedings of the National Academy of Science, USA*, **105**(24), 8232–8237.
- Benn, D. I. (1994). Fluted moraine formation and till genesis below a temperate valley glacier, Slettmarkbreen, Jotunheimen, southern Norway. *Sedimentology*, **41**, 279–292.
- Benn, D. I., Hulton, N. R. J., and Mottram, R. H. (2007). ‘Calving laws’, ‘sliding laws’ and the stability of tidewater glaciers. *Annals of Glaciology*, **46**, 123–130.
- Benoist, J.-P. (1979). The spectral power density and shadowing function of a glacial microrelief at the decimetre scale. *Journal of Glaciology*, **23**(89), 57–66.
- Benson, C. S. (1961). Stratigraphic studies in the snow and firn of the Greenland Ice Sheet. *Folia Geographica Danica*, **9**, 13–37.
- Benson, C. S. (1962). Stratigraphic studies in the snow and firn of the Greenland Ice Sheet. *U.S. Snow, Ice, and Permafrost Research Establishment. Research Report* 70.
- Berner W., Oeschger, H., and Stauffer, B. (1980). Information on the  $\text{CO}_2$  cycle from ice core studies. *Radiocarbon*, **22**(2), 227–235.
- Bhattacharji, S. (1967). Mechanics of flow differentiation in ultramafic and mafic sills. *The Journal of Geology*, **75**(1), 101–112.
- Biegel, R. L., Sammis, C. G., and Dieterich, J. H. (1989). The frictional properties of simulated gouge having a fractal particle distribution. *Journal of Structural Geology*, **11**(7), 827–846.
- Bindschadler, R. A., and Scambos, T. A. (1991). Satellite-image-derived velocity field of an Antarctic ice stream. *Science*, **252**(5003), 242–246.
- Bindschadler, R., and Vornberger, P. (1998). Changes in the West Antarctic Ice Sheet since 1963 from declassified satellite photography. *Science*, **279**, 689–692.
- Bindschadler, R. A., King, M. A., Alley, R. B., Anandakrishnan, S., and Padman, L. (2003a). Tidally controlled stick-slip

- discharge of a West Antarctic ice stream. *Science*, **301**, 1087–1089.
- Bindschadler, R. A., Vornberger, P. L., King, M. A., and Padman, L. (2003b). Tidally-driven stick-slip motion in the mouth of Whillans Ice Stream, Antarctica. *Annals of Glaciology*, **36**, 263–272.
- Bishop, B. C. (1957). Shear moraines in the Thule area, northwest Greenland. *U.S. Army Snow, Ice, and Permafrost Research Establishment*, Research Report **17**, 47 p.
- Björnsson, H. (1992). Jökulhlaups in Iceland: prediction, characteristics, and simulation. *Annals of Glaciology*, **16**, 95–106.
- Blankenship, D. D., Bentley, C. R., Rooney, S. T., and Alley, R. B. (1986). Seismic measurements reveal a saturated, porous layer beneath an active Antarctic ice stream. *Nature*, **322** (6074), 54–57.
- Blackburn, T., Siman-Tov, S., Coble, M. A., Stock, G. M., Brodsky, E. E., and Hallet, B. (2019). Composition and formation age of the amorphous silica coating glacially polished surfaces. *Geology*, **47**(4), 347–350.
- Bluemle, J. P., Lord, M. L., and Hunke, N. T. (1993). Exceptionally long, narrow drumlins formed in subglacial cavities, North Dakota. *Boreas*, **22**, 15–24.
- Böðvarsson, G. (1955). On the flow of ice sheets and glaciers. *Jökull*, **5**, 1–8.
- Bolduc, A. M. (1992). The formation of eskers based on their morphology, stratigraphy and lithologic composition, Labrador, Canada. PhD thesis, Lehigh University.
- Bond, G., et al. (1997). A pervasive millennial-scale cycle in north Atlantic holocene and glacial climates. *Science*, **278**(5341), 1257–1266.
- Boon, S., and Sharp, M. (2003). The role of hydrologically-driven ice fracture in drainage system evolution on an Arctic glacier. *Geophysical Research Letters*, **30**(18), doi: 10.1029/2003GL018034
- Borstad, C., Khazendar, A., Scheuchl, B., Morlighem, M., Larour, E., and Rignot, E. (2016). A constitutive framework for predicting weakening and reduced buttressing of ice shelves based on observations of progressive deterioration of the remnant Larsen B Ice Shelf. *Geophysical Research Letters*, **43**, 2027–2035.
- Boulton, G. S. (1987). A theory of drumlin formation by subglacial sediment deformation. In Menzies, J., and Rose, J. (eds.) *Drumlin Symposium*. Rotterdam: Balkema Publishers, pp. 25–80.
- Boulton, G. S., and Hindmarsh, R. C. A. (1987). Sediment deformation beneath glaciers: rheology and geological consequences. *Journal of Geophysical Research*, **92**(B9), 9059–9082.
- Bourne, A. J., et al. (2015). A tephra lattice for Greenland and a reconstruction of volcanic events spanning 25–45 Ka b2k. *Quaternary Science Reviews*, **118**, 122–141.
- Brand, G., Pohjola, V., and Hooke, R. LeB. (1987). Existence of a layer of deformable till at the base of Storglaciären, Sweden, revealed by electrical resistivity measurements. *Journal of Glaciology*, **33**(115), 311–314.
- Broecker, W. S. (1998). Paleocean circulation during the last glaciation: a bipolar

- seesaw. *Paleoceanography*, 13(2), 119–121.
- Brown, C. S., Meier, M. F., and Post, A. (1982). Calving speed of Alaska tidewater glaciers, with application to Columbia Glacier. *U.S. Geological Survey Professional Paper*, 1258-C, C1–C13.
- Brown, N. L., Hallet, B., and Booth, D. B. (1987). Rapid soft-bed sliding of the Puget glacial lobe. *Journal of Geophysical Research*, 92(B9), 8985–8997.
- Brugger, K. A. (2007). The non-synchronous response of Rabots Glaciär and Storglaciären, northern Sweden, to recent climatic change: a comparative study. *Annals of Glaciology*, 46, 275–282.
- Brunt, K. M., and MacAyeal, D. R. (2014). Tidal modulation of ice-shelf flow: a viscous model of the Ross Ice Shelf. *Journal of Glaciology*, 60(221), 500–508.
- Buckingham, E. (1914). On physically similar systems; illustrations of the use of dimensional equations. *Physical Review*, 4(4), 345–376.
- Budd, W. F. (1968). The longitudinal velocity profile of large ice masses. *Union de Géodesie et Geophysique Internationale. Association Internationnale d'Hydrologie Scientifique. Assemblée générale de Bern, 25 Sept.–7 Oct. 1967. [Commission de Neiges et Glaces.] Rapports et discussions*, pp. 58–77. (Publication No. 79 de l' Association Internationale d'Hydrologie Scientifique.)
- Budd, W. F. (1969). The dynamics of ice masses. *Australian National Antarctic Expeditions Scientific Reports*, Series A (IV) Glaciology. Publication No. 108.
- Budd, W. F. (1970). The longitudinal stress and strain-rate gradients in ice masses. *Journal of Glaciology*, 9(55), 19–27.
- Budd, W. F., and Jacka, T. H. (1989). A review of ice rheology for ice sheet modelling. *Cold Regions Science and Technology*, 16(2), 107–144.
- Budd, W. F., Jensen, D., and Radok, U. (1971). Derived physical characteristics of the Antarctic Ice Sheet. *Australian National Antarctic Expeditions Interim Reports*, Series A (IV) Glaciology. Publication No. 120.
- Butkovitch, T. R. (1954). The ultimate strength of ice. *Snow, Ice, and Permafrost Research Establishment Research Report*, 11, 12.
- Canals, M., Urgeles, R., and Calafat, A. M. (2000). Deep sea-floor evidence of past ice streams off the Antarctic Peninsula. *Geology*, 28(1), 31–34.
- Carnahan, B., Luther, H. A., and Wilkes, J. O. (1969). *Applied Numerical Methods*. New York: John Wiley and Sons, Inc.
- Carslaw, H. S., and Jaeger, J. C. (1959). *Conduction of Heat in Solids*. Oxford: Clarendon Press, 510 p.
- Catania, G. A., Conway, H., Raymond, C. F., and Scambos, T. A. (2006). Evidence for floatation or near floatation in the mouth of Kamb Ice Stream, West Antarctica, prior to stagnation. *Journal of Geophysical Research*, 111, F01005, doi: 10.1029/2005JF000355
- Catania G. A., Hulbe, C., and Conway, H. (2010). Grounding-line basal melt rates determined using radar-derived internal stratigraphy. *Journal of Glaciology*, 56 (197), 545–554.

- Chandler, D., Hubbard, A., Hubbard, B., and Nienow, P. (2006). A Monte Carlo error analysis for basal sliding velocity calculations, *Journal of Geophysical Research*, 111, F04005, doi: 10.1029/2006JF000476.
- Chandler, D. M., et al. (2013). Evolution of the subglacial drainage system beneath the Greenland Ice Sheet revealed by tracers. *Nature Geoscience*, 6, 195–198.
- Chen, J., and Ohmura, A. (1990). Estimation of alpine water resources and their change since the 1870s. *Hydrology in Mountainous regions: I. Hydrological measurements; the water cycle* (Proceedings of two Lausanne Symposia, August 1990). IAHS Publication No. 193, 127–135.
- Church, J. A., et al., (2001). Changes in sea level. In Houghton, J. T., et al. (eds.) *Climate Change 2001: The Science Basis*, Contribution of Working Group I to the Third Assessment Report of the Intergovernmental Panel on Climate Change. Cambridge: Cambridge University Press, pp. 641–693.
- Church, J. A., et al. (2013). Sea level change. In Stocker, T. F., et al. (eds.) *Climate Change 2013: The Physical Science Basis*, Contribution of Working Group I to the Fifth Assessment Report of the Intergovernmental Panel on Climate Change. Cambridge: Cambridge University Press, pp. 1137–1216.
- Clark, C. D., and Stokes, C. R. (2001). Extent and basal characteristics of the M'Clintock Channel Ice Stream. *Quaternary International*, 86, 81–101.
- Clark, P. U., and Hansel, A. R. (1989). Clast ploughing, lodgement and glacier sliding over a soft glacier bed. *Boreas*, 18(3), 201–207.
- Clarke, G. K. C. (1982). Glacier outburst floods from "Hazard Lake", Yukon Territory, and the problem of flood magnitude prediction. *Journal of Glaciology*, 28(98), 3–21.
- Clarke, G. K. C. (1976). Thermal regulation of glacier surging. *Journal of Glaciology*, 16(74), 231–250.
- Clarke, T. S., and Echelmeyer, K. (1996). Seismic-reflection evidence for a deep subglacial trough beneath Jakobshavn Isbræ, West Greenland. *Journal of Glaciology*, 43(141), 219–232.
- Clayton, L., and Cherry, J. A. (1967). Pleistocene superglacial and ice-walled lakes of west-central North America. In Clayton, L., and Freers, T. F. (eds.) *Glacial Geology of the Missouri Coteau and adjacent areas*. Grand Forks, ND: N. Dakota Geological Survey Miscellaneous Series, 30, pp. 47–52.
- Clayton, L. (1967). Stagnant-glacier features of the Missouri Coteau in North Dakota. In Clayton, L., and Freers, T. F. (eds.) *Glacial Geology of the Missouri Coteau and adjacent areas*. Grand Forks, ND: N. Dakota Geological Survey Miscellaneous Series, 30, pp. 25–45.
- Cohen, D. (2000). Rheology of ice at the bed of Engabreen, Norway. *Journal of Glaciology*, 46(155), 611–621.
- Cole-Dai, J., Budner, D. M., and Ferris, D. G. (2006). High-speed, high resolution, and continuous chemical analysis of ice core using a melter and ion chromatography. *Environmental Science and Technology*, 40, 6764–6769.

- Colgan, W., Pfeffer, W. T., Rajaram, H., Abdalati, W., and Balog, J. (2012). Monte Carlo ice flow modeling projects a new stable configuration for Columbia Glacier, Alaska, c. 2020. *The Cryosphere*, **6**, 1395–1409.
- Collins, I. F. (1968). On the use of the equilibrium equations and flow law in relating the surface and bed topography of glaciers and ice sheets. *Journal of Glaciology*, **7**(50), 199–204.
- Conway, H., Hall, B. L., Denton, G. H., Gades, A. M., and Waddington, E. D. (1999). Past and future grounding-line retreat of the West Antarctic Ice Sheet. *Science*, **286**, 280–283.
- Cook, E. R., D'Arrigo, R. D., and Briffa, K. R. (1998). A reconstruction of the North Atlantic Oscillation using tree-ring chronologies from North America and Europe. *The Holocene*, **8**, 9–17.
- Costa, J. B. (1983). Paleohydraulic reconstruction of flash-flood peaks from boulder deposits in the Colorado Front Range. *Geological Society of America Bulletin*, **94**, 986–1004.
- Craig, H. (1961). Isotopic variations in meteoric waters. *Science*, **133**, 1702–1703.
- Cuffey, K. M., and Clow, G. D. (1997). Temperature, accumulation, and ice sheet elevation in central Greenland through the last glacial transition. *Journal of Geophysical Research*, **102** (C12), 26383–26396.
- Cuffey, K. M., and Paterson, W. S. B. (2010). *The Physics of Glaciers*. Burlington, MA: Butterworth-Heinemann/Elsevier, 693pp.
- Cullather, R. I., Bromwich, D. H., and Van Woert, M. L. (1996). Interannual variations in Antarctic precipitation related to El Niño–Southern Oscillation. *Journal of Geophysical Research*, **101**(D14), 19109–19118.
- Cutler, P. M., Colgan, P. M., and Mickelson, D. M. (2002). Sedimentologic evidence for outburst floods from the Laurentide Ice Sheet margin in Wisconsin, USA: implications for tunnel-channel formation. *Quaternary International*, **90**, 23–40.
- Cutler, P. M., MacAyeal, D. R., Mickelson, D. M., Parizek, B. R., and Colgan, P. M. (2000). A numerical investigation of ice-lobe – permafrost interaction around the southern Laurentide ice sheet. *Journal of Glaciology*, **46**(153), 311–325.
- Dahl-Jensen, D., and Gundestrup, N. S. (1987). Constitutive properties of ice at Dye 3, Greenland. *International Association of Hydrological Sciences Publication 170* (Symposium at Vancouver 1987 - *The physical basis for ice sheet modelling*), 31–43.
- Dahl-Jensen, D., and Johnsen, S. J. (1986). Palaeotemperatures still exist in the Greenland ice sheet. *Nature*, **320**, 250–252.
- Dahl-Jensen, D., Mosegaard, K., Gundestrup, N., Clow, G. D., Johnsen, S. J., Hansen, A. W., and Balling, N. (1998). Past temperatures directly from the Greenland Ice Sheet. *Science*, **282**, 268–271.
- Damsgaard, A., Egholm, D. L., Beem, L. H., Tulaczyk, S., Larsen, N. K., Piotrowski, J. A., and Siegfried, M. R. (2016). Ice flow dynamics forced by water pressure variation in subglacial granular beds.

- Geophysical Research Letters*, 43, 12165–12173.
- Dansgaard, W., et al. (1993). Evidence for general instability of past climate from a 250-kyr ice-core record. *Nature*, 364, 218–220.
- Das, S. B., Joughlin, I., Behn, M. D., Howat, I. M., King, M. A., Lizarralde, D., and Bhatia, M. P. (2008). Fracture propagation to the base of the Greenland Ice Sheet during supraglacial lake drainage. *Science*, 320(5877), 778–781.
- Dash, J. G. (1995). The premelting of ice and its environmental consequences. *Reports on Progress in Physics*, 58, 115–167.
- de La Chapelle, S., Duval, P., and Baudet, B. (1995). Compressive creep of polycrystalline ice containing a liquid phase. *Scripta Metallurgica et Materialia*, 33(3), 447–450.
- Deeley, R. M., and Parr, P. H. (1914). The Hintereis Glacier. *Philosophical Magazine*, 6, 153–176.
- Delmas, R. J., Ascencio, J.-M., and Legrand, M. (1980). Polar ice evidence that atmospheric CO<sub>2</sub> 20,000 yr BP was 50% of present. *Nature*, 284(5752), 155–157.
- Demorest, M. (1941). Glacier flow and its bearing on the classification of glaciers. *Geological Society of America Bulletin*, 52(12), 2024–2025.
- Demorest, M. (1942). Glacier regimens and ice movement within glaciers. *American Journal of Science*, 240(1), 31–66.
- Desai, C. S. (2000). Evaluation of liquefaction using disturbed state and energy approaches. *Journal of Geotechnical and Geoenvironmental Engineering*, 126(7), 618–631.
- Ditlevsen, P. D., Andersen, K. K., and Svensson, A. (2007). The DO-events are probably noise induced: statistical investigation of the claimed 1470 years cycle. *Climate of the Past*, 3, 129–134.
- Donner, J. J. (1965). The quaternary of Finland. In Rankama, K. (ed.) *The Quaternary*. New York, Interscience, pp. 199–272.
- Dowdeswell, J. A., and Fugelli, E. M. G. (2012). The seismic architecture and geometry of grounding-zone wedges formed at the marine margins of past ice sheets. *Geological Society of America Bulletin*, 124(11/12), 1750–1761.
- Dunlop, P., and Clark, C. D. (2006). The morphological characteristics of ribbed moraine. *Quaternary Science Reviews*, 25, 1668–1691.
- Dunse, T., Schellenberger, T., Hagen, J. O., Käab, A., Schuler, T. V., and Reijmer, C. H. (2015). Glacier-surge mechanisms promoted by a hydro-thermodynamic feedback to summer melt. *The Cryosphere*, 9, 197–215.
- Duval, P. (1977). The role of water content on the creep rate of polycrystalline ice. In Isotopes and impurities in snow and ice. Proceedings of the Grenoble Symposium, August–September 1975, *International Association of Scientific Hydrology*, Publication, 118, 29–33.
- Duval, P., Ashby, M. F., and Anderman, I. (1983). Rate-controlling processes in the creep of polycrystalline ice. *Journal of Physical Chemistry*, 87(21), 4066–4074.

- Duval, P., and Castelnau, O. (1995). Dynamic recrystallization of ice in polar ice sheets. *Journal de Physique IV, Colloque C3*, supplement to *Journal de Physique III*, 5, C3–197–C3–205.
- Dykes, R. C., and Brook, M. S. (2010). Terminus recession, proglacial lake expansion and 21st century calving retreat of Tasman Glacier, New Zealand. *New Zealand Geographer*, 66, 203–217.
- Echelmeyer, K., and Harrison, W. D. (1999). Ongoing margin migration of Ice Stream B, Antarctica. *Journal of Glaciology*, 45(150), 361–369.
- Echelmeyer, K., and Wang, Z. (1987). Direct observation of basal sliding and deformation of basal drift at sub-freezing temperatures. *Journal of Glaciology*, 33(113), 83–98.
- Echelmeyer, K. A., Harrison, W. D., Larsen, C., and Mitchell, J. E. (1994). The role of the margins in the dynamics of an active ice stream. *Journal of Glaciology*, 40(136), 527–538.
- Ehlers, J., and Stephan, H.-J. (1979). Forms at the base of till strata as indicators of ice movement. *Journal of Glaciology*, 22(87), 345–355.
- Elsberg, D. H., Harrison, W. D., Echelmeyer, K. A., and Krimmel, R. M. (2001). Quantifying the effects of climate and surface change on glacier mass balance. *Journal of Glaciology*, 47(159), 649–658.
- Engelhardt, H., and Kamb, B. (1997). Basal hydraulic system of a West Antarctic ice stream: constraints from borehole observations. *Journal of Glaciology*, 43(144), 207–230.
- Engelhardt, H., and Kamb, B. (1998). Basal sliding of ice stream B, West Antarctica. *Journal of Glaciology*, 44(147), 223–230.
- Engelhardt, H. F., Humphrey, N., Kamb, B., and Fahnestock, M. (1990). Physical conditions at the base of a fast moving Antarctic ice stream. *Science*, 248 (4951), 57–59.
- EPICA community members. (2004). Eight glacial cycles from an Antarctic ice core. *Nature*, 429, 623–628.
- Etchecopar, A. (1977). A plane kinematic model of progressive deformation in a polycrystalline aggregate. *Tectonophysics*, 39, 121–139.
- Eyles, N., Salden, J. A., and Gilroy, S. (1982). A depositional model for stratigraphic complexes and facies superimposition in lodgement till. *Boreas*, 11(4), 317–333.
- Fagan, B. (2008). *The Great Warming*. New York: Bloomsbury Press. 282pp.
- Fairbanks, R. (1989). A 17,000-year glacio-eustatic sea level record: influence of glacial melting rates on the Younger Dryas event and deep ocean circulation. *Nature*, 232, 637–742.
- Fastook, J. L., and Chapman, J. E. (1989). A map-plane finite-element model: three modeling experiments. *Journal of Glaciology*, 35(119), 48–52.
- Fastook, J. L., and Holmlund, P. (1994). A glaciological model of the Younger Dryas event in Scandinavia. *Journal of Glaciology*, 40(134), 125–131.
- Feldmann, J., and Levermann, A. (2015). Collapse of the West Antarctic Ice Sheet after local destabilization of the Admunsen Basin. *Proceedings of the National Academy of Sciences*, 112(46), 14191–14196.

- Fischer, H., Siggaard-Andersen, M.-L., Ruth, U., Röhlisberger, R., and Wolff, E. (2007). Glacial/interglacial changes in mineral dust and sea-salt records in polar ice cores: sources, transport, and deposition. *Reviews of Geophysics*, 45, RG1002, doi: 10.1029/2005RG000192.
- Fisher, D. A. (1987). Enhanced flow of Wisconsin ice related to solid conductivity through strain history and recrystallization. *International Association of Scientific Hydrology Publication*, 170, 45–51.
- Fisher, D. A., and Koerner, R. M. (1986). On the special rheological properties of ancient microparticle-laden Northern Hemisphere ice as derived from bore-hole and core measurements. *Journal of Glaciology*, 32(112), 501–510.
- Fisher D. A., Reeh, N., and Langley, K. (1985). Objective reconstructions of the late Wisconsinan Laurentide ice sheet and the significance of deformable beds. *Géographie Physique et Quaternaire*, 39, 229–238.
- Fountain, A. G. (1989). The storage of water in, and hydraulic characteristics of, the firm of South Cascade Glacier, Washington State, U.S.A. *Annals of Glaciology*, 13, 69–75.
- Fountain, A. G., Jacobel, R. W., Schlichting, R., and Jansson, P. (2005). Fractures as the main pathways of water flow in temperate glaciers. *Nature*, 433, 618–621.
- Fountain, A. G., and Walder, J. S. (1998). Water flow through temperate glaciers. *Reviews of Geophysics*, 36(3) 299–328.
- Fowler, A. C. (2000). An instability mechanism for drumlin formation. In Maltman, A., Hambrey, M. J., and Hubbard, B. (eds.) *Deformation of Glacial Materials*. London: Geological Society, 176, pp. 307–319.
- Fowler, A. C., and Larson, D. A. (1980). On the flow of polythermal glaciers: II. Surface wave analysis. *Proceedings of the Royal Society, London*, A370, 155–171.
- Fowler, A. C., Murray, T., and Ng, F. S. L. (2001). Thermally controlled glacier sliding. *Journal of Glaciology*, 47(159), 527–538.
- Fricker, H. A., Coleman, R., Padman, L., Scambos, T. A., Bohlander, J., and Brunt, K. M. (2009). Mapping the grounding zone of Amery Ice Shelf, East Antarctica using InSAR, MODIS, and ICESat. *Antarctic Science*, 21(5), 515–532.
- Fricker, H. A., and Padman, L. (2006). Ice shelf grounding zone structure from ICESat laser altimetry. *Geophysical Research Letters*, 33, L15502, doi: 10.1029/2006GL026907.
- Fried, M. J., et al. (2015). Distributed subglacial discharge drives significant submarine melt at a Greenland tidewater glacier. *Geophysical Research Letters*, 42, 9328–9336.
- Giovinetto, M. B., and Zwally, H. J. (2000). Spatial distribution of net surface accumulation on the Antarctic ice sheet. *Annals of Glaciology*, 31, 171–178.
- Glasser, N. F., and Scambos, T. A. (2008). A structural glaciological analysis of the 2002 Larsen B ice-shelf collapse. *Journal of Glaciology*, 54(184), 3–15.
- Glasstone, S., Laidler, K. J., and Eyring, H. (1941). *The Theory of Rate Processes*. New York: McGraw-Hill.

- Glen, J. W. (1955). The creep of polycrystalline ice. *Proceedings of the Royal Society, Series A* 228(1175), 519–538.
- Glen, J. W. (1958). The flow law of ice. A discussion of the assumptions made in glacier theory, their experimental foundations and consequences. *International Association of Scientific Hydrology*, 47, 171–183.
- Glen, J. W. (1963). Contribution to the discussion. *International Association of Scientific Hydrology Bulletin*, 8(2), 68.
- Gogineni, S., Chuah, T., Allen, C., Jezek, K., and Moore, R. K. (1998). An improved coherent radar depth sounder. *Journal of Glaciology*, 44(148), 659–669.
- Gold, L. W. (1958). Some observations on the dependence of strain on stress for ice. *Canadian Journal of Physics*, 36(10), 1265–1275.
- Goldsby, D. (2009). Superplastic flow of ice relevant to glacier and ice-sheet mechanics. In Knight, P. (ed.) *Glacier Science and Environmental Change*. Oxford: Wiley-Blackwell, 527pp.
- Goldsby, D. L., and Kohlstedt, D. L. (1997). Grain boundary sliding in fine-grained Ice I. *Scripta Materialia*, 37(9), 1399–1406.
- Goldsby, D. L., and Kohlstedt, D. L. (2001). Superplastic deformation of ice: experimental observations. *Journal of Geophysical Research*, 106(B6), 11017–11030.
- Goldsby, D. L., and Kohlstedt, D. L. (2002). Reply to comment by P. Duval and M. Montagnat on “Superplastic deformation of ice: experimental observations”. *Journal of Geophysical Research*, 107(B11), 11017–11030, doi: 10.1029/2002JB001842.
- Goldsmith, H. L., and Mason, S. G. (1961). Axial migration of particles in Poiseuille flow. *Nature*, 190(4781), 1095–1096.
- Goldstein, R. M., Engelhardt, H., Kamb, B., and Frolich, R. M. (1993). Satellite radar interferometry for monitoring ice sheet motion: application to an Antarctic ice stream. *Science*, 262(5139), 1525–1530.
- Goldthwait, R. P. (1951). Development of end moraines in east-central Baffin Island. *Journal of Geology*, 59(6), 567–577.
- Goujon, C., Barnola, J.-M., and Ritz, C. (2003). Modeling the densification of polar firn including heat diffusion: application to close off characteristics and gas isotopic fractionation for Antarctica and Greenland sites. *Journal of Geophysical Research-Atmospheres*, 108(D24), 4792, doi: 10.1029/2002JD003319.
- Gow, A. J. (1969). On the rates of growth of grains and crystals in south polar firn. *Journal of Glaciology*, 8(53), 241–252.
- Gow, A. J., and Williamson, T. (1976). Rheological implications of the internal structure and crystal fabrics of the West Antarctic ice sheet as revealed by deep core drilling at Byrd Station. *Geological Society of America Bulletin*, 87, 1665–1677.
- Gravenor, C. P. (1955). The origin and significance of prairie mounds. *American Journal of Science*, 253, 475–481.
- Gravenor, C. P., and Kupsch, W. O. (1959). Ice disintegration features in western Canada. *Journal of Geology*, 67, 48–67.

- Gravenor, C. P., and Meneley, W. A. (1958). Glacial flutings in central and northern Alberta. *American Journal of Science*, 256, 715–728.
- Greve, R., Zwinger, T., and Gong, Y. (2014). On the pressure dependence of the rate factor in Glen's flow law. *Journal of Glaciology*, 60(220), 397–398.
- Griffith, A. A. (1921). The phenomena of rupture and flow in solids. *Philosophical Transactions of the Royal Society of London*, A221, 163–197.
- Griffith, A. A. (1924). Theory of rupture. *Proceedings of the First International Congress on Applied Mechanics*, Delft, 55–63.
- Grootes, P. M., Stuiver, M., White, J. W. C., Johnsen, S., and Jouzel, J. (1993). Comparison of oxygen isotope records from the GISP 2 and GRIP Greenland ice cores. *Nature*, 366, 552–554.
- Grove, J. M. (1988). *The Little Ice Age*. London: Methuen.
- Groves, G. W., and Kelly, A. (1969). Change of shape due to dislocation climb. *Philosophical Magazine*, 19, 977–986.
- Gudmundsson, G. H. (2007). Tides and the flow of Rutford Ice Stream, West Antarctica. *Journal of Geophysical Research*, 112, F04007, doi: 10.1029/2006JF000731.
- Gudmundsson, G. H. (2011). Ice stream response to ocean tides and the form of the basal sliding law. *The Cryosphere*, 5, 259–270.
- Gudmundsson, G. H., Raymond, C. F., and Bindschadler, R. (1998). The origin and longevity of flow stripes on Antarctic ice streams. *Annals of Glaciology*, 27, 145–152.
- Gupta, P., Noone, D., Galewsky, J., Sweeney, C., and Vaughn, B. H. (2009). Demonstration of high-precision continuous measurements of water vapor isotopologues in laboratory and remote field deployments using wavelength-scanned cavity ring-down spectroscopy (WS-CRDS) technology. *Rapid Communications in Mass Spectroscopy*, 23, 2534–2542.
- Haefeli, R. (1962). The ablation gradient and the retreat of a glacier tongue. In *Symposium of Obergurgl, International Association of Scientific Hydrology*, Publication 58, 49–59.
- Hallet, B. (1976a). Deposits formed by subglacial precipitation of CaCO<sub>3</sub>. *Geological Society of America Bulletin*, 87(7), 1003–1015.
- Hallet, B. (1976b). The effect of subglacial chemical processes on sliding. *Journal of Glaciology*, 17(76), 209–221.
- Hallet, B. (1979a). A theoretical model of glacial abrasion. *Journal of Glaciology*, 23(89), 39–50.
- Hallet, B. (1979b). Subglacial regelation water film. *Journal of Glaciology*, 23(89), 321–334.
- Hallet, B. (1981). Glacial abrasion and sliding: their dependence on the debris concentration in basal ice. *Annals of Glaciology*, 2, 23–28.
- Hallet, B. (1996). Glacial quarrying: a simple theoretical model. *Annals of Glaciology*, 22, 1–8.
- Hallet, B., and Anderson, R. S. (1980). Detailed glacial geomorphology of a proglacial bedrock area at Castleguard Glacier, Alberta, Canada. *Zeitschrift für Gletscherkunde und Glazialgeologie*, 16, 171–184.

- Hallet, B., Lorrain, R. D., and Souchez, R. A. (1978). The composition of basal ice from a glacier sliding over limestones. *Geological Society of America Bulletin*, **89**(2), 314–320.
- Hamilton, G. S., Whillans, I., and Morgan, P. (1998). First point measurements of ice-sheet thickness change in Antarctica. *Annals of Glaciology*, **27**, 125–129.
- Hamilton, W. C., and Ibers, J. A. (1968). *Hydrogen Bonding in Solids; Methods of Molecular Structure Determination*. New York: W. A. Benjamin.
- Hammer, C. U. (1980). Acidity of polar ice cores in relation to absolute dating, past volcanism, and radio-echoes. *Journal of Glaciology*, **25**(93), 359–372.
- Hanna, E., Cappelen, J., Fettweis, X., Huybrechts, P., Luckman, A., and Ribergaard, M. H. (2009). Hydrologic response of the Greenland ice sheet: the role of oceanographic warming. *Hydrological Processes*, **23**, 7–30.
- Hanson, B. (1995). A fully three-dimensional finite-element model applied to velocities on Storglaciären, Sweden. *Journal of Glaciology*, **41**(137), 91–102.
- Hanson, B., and Hooke, R. LeB. (2000). A model study of the forces involved in glacier calving. *Journal of Glaciology*, **46**(153), 188–194.
- Hanson, B., and Hooke, R. LeB. (2003). Buckling rate and overhang development at a calving face. *Journal of Glaciology*, **49**(167), 577–586.
- Hanson, B., Hooke, R. LeB., and Grace, E. M., Jr. (1998). Short-term velocity and water-pressure measurements down-glacier from a riegel, Storglaciären, Sweden. *Journal of Glaciology*, **44**(147), 359–367.
- Harrison, W. (1958). Marginal zones of vanished glaciers reconstructed from preconsolidation-pressure values of overridden silts. *The Journal of Geology*, **66**(1), 72–95.
- Harrison, W. D. (1972). Temperature of a temperate glacier. *Journal of Glaciology*, **11**(61), 15–29.
- Harrison, W. D., Echelmeyer, K. A., and Larsen, C. F. (1998). Measurement of temperature in a margin of Ice Stream B, Antarctica: implications for margin migration and lateral drag. *Journal of Glaciology*, **44**(148), 615–624.
- Harrison, W. D., Raymond, C. F., Echelmeyer, K. A., and Krimmel, R. M. (2003). A macroscopic approach to glacier dynamics. *Journal of Glaciology*, **49**(164), 13–21.
- Hättestrand, C., and Kleman, J. (1999). Ribbed moraine formation. *Quaternary Science Reviews*, **18**, 43–61.
- Hausmann, M. R. (1990). *Engineering Principles of Ground Modification*. New York: McGraw-Hill.
- Hays, J. D., Imbrie, J., and Shackleton, N. S. (1976). Variations in the Earth's orbit: pacemaker of the ice ages. *Science*, **194**(4270), 1121–1132.
- Hebrand, M., and Åmark, M. (1989). Esker formation and glacier dynamics in eastern Skåne and adjacent areas, southern Sweden. *Boreas*, **18**(1), 67–81.
- Higgins, J. A., et al. (2014). Atmospheric composition 1 million years ago from blue ice in the Allan Hills, Antarctica. *Proceedings of the National Academy of Science, USA*, **112**(22), 6887–6891.
- Hindmarsh, R. C. A. (1998). Drumlinization and drumlin-forming instabilities:

- viscous till mechanisms. *Journal of Glaciology*, 44(147), 293–314.
- Hobbs, P. V. (1974). *Ice Physics*. New York: Oxford Clarendon Press.
- Hock, R., and Hooke, R. LeB. (1993). Further tracer studies of internal drainage in the lower part of the ablation area of Storglaciären, Sweden. *Geological Society of America Bulletin*, 105(4), 537–546.
- Hodge, S. M., Trabant, D. C., Krimmel, R. M., Heinrichs, T. A., March, R. S., and Joshberger, E. G. (1998). Climate variations and changes in mass balance of three glaciers in western North America. *Journal of Climate*, 11, 2161–2179.
- Hoffman, M. J., et al. (2016). Greenland subglacial drainage evolution regulated by weakly connected regions of the bed. *Nature Communications*, 7(13903), doi: 10.1038/ncomms13903.
- Hogg, A. E., and Gudmundsson, G. H. (2017). Impacts of the Larsen-C ice shelf calving event. *Nature Climate Change*, 7, 540–542.
- Holland, P. R., Corr, H. F. J., Vaughan, D. G., Jenkins, A., and Skvarca, P. (2009). Marine ice in Larsen ice shelf. *Geophysical Research Letters*, 36, L11604, doi: 10.1029/2009GL038162.
- Holmlund, P. (1987). Mass balance of Storglaciären during the 20th century. *Geografiska Annaler*, 69A(3–4), 439–447.
- Holmlund, P. (1988). Internal geometry and evolution of moulin, Storglaciären, Sweden. *Journal of Glaciology*, 34(117), 242–248.
- Hong, S., Candelone, J.-P., Patterson, C. C., and Boutron, C. F. (1994). Greenland ice evidence of hemispheric lead pollution two millennia ago by Greek and Roman civilizations. *Science*, 265, 1841–1843.
- Hooke, R. LeB. (1970). Morphology of the ice-sheet margin near Thule, Greenland. *Journal of Glaciology*, 9(57), 303–324.
- Hooke, R. LeB. (1973a). Flow near the margin of the Barnes Ice Cap and the development of ice-cored moraines. *Geological Society of America Bulletin*, 84(12), 3929–3948.
- Hooke, R. LeB. (1973b). Structure and flow in the margin of Barnes Ice Cap, Baffin Island, N.W.T., Canada. *Journal of Glaciology*, 12(66), 423–438.
- Hooke, R. LeB. (1976). Pleistocene ice at the base of the Barnes Ice Cap, Baffin Island, N.W.T., Canada. *Journal of Glaciology*, 17(75), 49–60.
- Hooke, R. LeB. (1981). Flow law for polycrystalline ice in glaciers: comparison of theoretical predictions, laboratory data, and field measurements. *Reviews of Geophysics and Space Physics*, 19(4), 664–672.
- Hooke, R. LeB. (1984). On the role of mechanical energy in maintaining subglacial conduits at atmospheric pressure. *Journal of Glaciology*, 30(105), 180–187.
- Hooke, R. LeB. (1989). Englacial and subglacial hydrology: a qualitative review. *Arctic and Alpine Research*, 21(3), 221–233.
- Hooke, R. LeB. (1991). Positive feedbacks associated with the erosion of glacial cirques and overdeepenings. *Geological Society of America Bulletin*, 103(8), 1104–1108.

- Hooke, R. LeB., Alexander, E. C. Jr., and Gustafson, R. J. (1980). Temperature profiles in Barnes Ice Cap, Baffin Island, Canada, and heat flux from the subglacial terrane. *Canadian Journal of Earth Sciences*, 17(9), 1174–1188.
- Hooke, R. LeB., Calla, P., Holmlund, P., Nilsson, M., and Stroeven, A. (1989). A three-year record of seasonal variations in surface velocity, Storglaciären, Sweden. *Journal of Glaciology*, 35(120), 235–247.
- Hooke, R. LeB., and Clausen, H. B. (1982). Wisconsin and Holocene  $\delta^{18}\text{O}$  variations, Barnes Ice Cap, Canada. *Geological Society of America Bulletin*, 93(8), 784–789.
- Hooke, R. LeB., Cummings, D. I., Lesemann, J.-E., and Sharpe, D. R. (2013). Genesis of dispersal plumes in till. *Canadian Journal of Earth Sciences*, 50(8), 847–855.
- Hooke, R. LeB., Dahlin, B. B., and Kauper, M. T. (1972). Creep of ice containing dispersed fine sand. *Journal of Glaciology*, 11(63), 327–336.
- Hooke, R. LeB., and Elverhøi, A. (1996). Sediment flux from a fjord during glacial periods, Isfjorden, Spitsbergen. *Global and Planetary Change*, 12, 237–249.
- Hooke, R. LeB., and Fastook, J. (2007). Thermal conditions at the bed of the Laurentide Ice Sheet in Maine during deglaciation: implications for esker formation. *Journal of Glaciology*, 53 (183) 646–658.
- Hooke, R. LeB., Gould, J. E., and Brzozowski, J. (1983). Near-surface temperatures near and below the equilibrium line on polar and subpolar glaciers. *Zeitschrift für Gletscherkunde und Glazialgeologie*, 19(1), 1–25.
- Hooke, R. LeB., and Hanson, B. H. (1986). Borehole deformation experiments, Barnes Ice Cap, Canada. *Cold Regions Science and Technology*, 12(3), 261–276.
- Hooke, R. LeB., Hanson, B., Iverson, N. R., Jansson, P., and Fischer, U. H. (1997). Rheology of till beneath Storglaciären, Sweden. *Journal of Glaciology*, 43(143), 172–179.
- Hooke, R. LeB., and Hudleston, P. J. (1978). Origin of foliation in glaciers. *Journal of Glaciology*, 20(83), 285–299.
- Hooke, R. LeB., and Hudleston, P. J. (1980). Ice fabrics in a vertical flowplane, Barnes Ice Cap, Canada. *Journal of Glaciology*, 25(92), 195–214.
- Hooke, R. LeB., and Hudleston, P. J. (1981). Ice fabrics from a borehole at the top of the South Dome, Barnes Ice Cap, Baffin Island. *Geological Society of America Bulletin*, 92(5), 274–281.
- Hooke, R. LeB., and Iverson, N. R. (1995). Grain size distribution in deforming subglacial tills: role of grain fracture. *Geology*, 23(1), 57–60.
- Hooke, R. LeB., and Jennings, C. (2006). On the formation of tunnel valleys. *Quaternary Science Reviews*, 25(11–12), 1364–1372.
- Hooke, R. LeB., Johnson, G. W., Brugger, K. A., Hanson, B., and Holdsworth, G. (1987). Changes in mass balance, velocity, and surface profile along a flow line on Barnes Ice Cap. (1970–1984). *Canadian Journal of Earth Sciences*, 24(8), 1550–1561.
- Hooke, R. LeB., Laumann, T., and Kohler, J. (1990). Subglacial water pressures and

- the shape of subglacial conduits. *Journal of Glaciology*, **36**(122), 67–71.
- Hooke, R. LeB., and Medford, A. (2013). Are drumlins a result of a thermo-mechanical instability? *Quaternary Research*, **79**(3), 458–464.
- Hooke, R. LeB., and Pohjola, A. (1994). Hydrology of a segment of a glacier situated in an overdeepening, Storglaciären, Sweden. *Journal of Glaciology*, **40**(134), 140–148.
- Hooke, R. LeB., Pohjola, V., Jansson, P., and Kohler, J. (1992). Intra-seasonal changes in deformation profiles revealed by borehole studies, Storglaciären, Sweden. *Journal of Glaciology*, **38**(130), 348–358.
- Hooke, R. LeB., Wold, B., and Hagen, J. O. (1985). Subglacial hydrology and sediment transport at Bondhusbreen, southwest Norway. *Geological Society of America Bulletin*, **96**(3), 388–397.
- Hooyer, T. S., and Iverson, N. R. (2002). Flow mechanism of the Des Moines Lobe of the Laurentide ice sheet. *Journal of Glaciology*, **48**(163), 575–586.
- Houghton, J. T., et al. (2001). *Climate Change 2001: The Scientific Basis*. Report of the Intergovernmental Panel on Climate Change (IPCC). Cambridge: Cambridge University Press, 881pp.
- Howell, D., Behringer, R. P., and Veje, C. (1999). Stress fluctuations in a 2D granular Couette experiment: a continuous transition. *Physical Review Letters*, **82**(96), 5241–5244.
- Hudleston, P. J. (1976). Recumbent folding in the base of the Barnes Ice Cap, Baffin Island, Northwest Territories, Canada. *Geological Society of America Bulletin*, **87**(12), 1678–1683.
- Hudleston, P. J. (1989). The association of folds and veins in shear zones. *Journal of Structural Geology*, **11**(8), 949–957.
- Hudleston, P. J. (2015). Structures and fabric in glacial ice: a review. *Journal of Structural Geology*, **81**, 1–27.
- Hudleston, P. J., and Hooke, R. LeB. (1980). Cumulative deformation in the Barnes Ice Cap and implications for the development of foliation. *Tectonophysics*, **66**, 127–146.
- Hughes, T. (1992). Abrupt climate change related to unstable ice-sheet dynamics: toward a new paradigm. *Palaeogeography, Palaeoclimatology, Palaeoecology*, **97**, 203–234.
- Hulbe, C., Joughin, I., Morse, D., and Bindschadler, R. A. (2000). Tributaries to West Antarctic ice streams: characteristics deduced from numerical modelling of ice flow. *Annals of Glaciology*, **31**, 184–190.
- Hull, D. (1969). *Introduction to Dislocations*. New York: Pergamon Press.
- Humphrey, N. F., and Raymond, C. F. (1994). Hydrology, erosion and sediment production in a surging glacier: Variegated Glacier, Alaska, 1982–83. *Journal of Glaciology*, **40**(136), 539–552.
- Husband, D. M., Mondy, L. A., Ganani, E., and Graham, A. L. (1994). Direct measurements of shear-induced particle migration in suspensions of bimodal spheres. *Rheologica Acta*, **33**(3), 185–192.
- Hutchinson, J. W. (1976). Bounds and self-consistent estimates for creep of polycrystalline materials. *Proceedings*

- of the Royal Society, Series A., 348, 101–127.
- Hutter, K. (1981). The effect of longitudinal strain on the shear stress of an ice sheet. In defense of using stretched coordinates. *Journal of Glaciology*, 27(95), 39–56.
- Hutter, K. (1983). *Theoretical glaciology*. Tokyo, Japan: D. Reidel Publishing, 510pp.
- Huybrechts, Ph. (1990). A 3-D model for the Antarctic ice sheet: a sensitivity study on the glacial-interglacial contrast. *Climate Dynamics*, 5, 79–92.
- Huybrechts, Ph. (2002). Sea-level changes at the LGM from ice-dynamic reconstructions of the Greenland and Antarctic ice sheets during the glacial cycles. *Quaternary Science Reviews*, 21(1–3), 203–231.
- Huybrechts, P., de Nooze, P., and Decleir, H. (1989). Numerical modeling of Glacier d'Argentière and its historical front variations. In Oerlemans, J. (ed.) *Glacier Fluctuations and Climatic Change*. The Netherlands: Kluwer Academic, pp. 373–389.
- Huybrechts, P., Payne, T., and The EISMINT Intercomparison Group. (1996). The EISMINT benchmarks for testing ice-sheet models. *Annals of Glaciology*, 23, 1–12.
- Huybrechts, P., Steinhage, D., Wilhelms, F., and Bamber, J. (2000). Balance velocities and measured properties of the Antarctic ice sheet from a new compilation of gridded data for modelling. *Annals of Glaciology*, 30, 52–60.
- Huybrechts, P., and T'Siobbel, S. (1995). Thermomechanical modeling of northern hemisphere ice sheets with a two-level mass balance parameterization. *Annals of Glaciology*, 21, 111–117.
- Iken, A. (1981). The effect of subglacial water pressure on the sliding velocity of a glacier in an idealized numerical model. *Journal of Glaciology*, 27(97), 407–421.
- Iken, A., and Bindschadler, R. A. (1986). Combined measurements of subglacial water pressure and surface velocity of Findelengletscher, Switzerland: conclusions about the drainage system and sliding mechanism. *Journal of Glaciology*, 32(110), 101–119.
- Iken, A., and Truffer, M. (1997). The relationship between subglacial water pressure and velocity of Findelengletscher during its advance and retreat. *Journal of Glaciology*, 43(144), 328–338.
- Irons, B. M., and Shreve, N. G. (1987). *Numerical Methods in Engineering and Applied Science: Numbers are Fun*. New York: John Wiley & Sons, 248pp.
- Iverson, N. A., Kalteyer, D., Dunbar, N. W., Kurbatov, A., and Yates, M. (2017). Advancements and best practices for analysis and correlation of tephra and cryptotephra in ice. *Quaternary Geochronology*, 40, 45–55.
- Iverson, N. R. (1989). Theoretical and experimental analyses of glacial abrasion and quarrying. PhD thesis, University of Minnesota, Minneapolis, 233pp.
- Iverson, N. R. (1991a). Morphology of glacial striae: implications for abrasion of glacier beds and fault surfaces.

- Geological Society of America Bulletin*, 103, 1308–1316.
- Iverson, N. R. (1991b). Potential effects of subglacial water-pressure fluctuations on quarrying. *Journal of Glaciology*, 37(125), 27–36.
- Iverson, N. R. (1993). Regelation of ice through debris at glacier beds: implications for sediment transport. *Geology*, 21(6), 559–562.
- Iverson, N. R. (1999). Coupling between a glacier and a soft bed: II. Model results. *Journal of Glaciology*, 45(149), 41–53.
- Iverson, N. R. (2000). Sediment entrainment by a soft-bedded glacier: a model based on regelation into the bed. *Earth Surface Processes and Landforms*, 25, 881–893.
- Iverson, N. R. (2010). Shear resistance and continuity of subglacial till: hydrology rules. *Journal of Glaciology*, 56(200), 1104–1114.
- Iverson, N. R. (2012). A theory of glacial quarrying for landscape evolution models. *Geology*, 40(8), 679–682.
- Iverson, N. R., Baker, R. W., and Hooyer T. S. (1997). A ring-shear device for the study of till deformation: tests on tills with contrasting clay contents. *Quaternary Science Reviews*, 16, 1057–1066.
- Iverson, N. R., et al. (2003). Effects of basal debris on glacier flow. *Science*, 301, 81–84.
- Iverson, N. R., and Hooyer, T. S. (2004). Estimating the sliding velocity of a Pleistocene ice sheet from plowing structures in the geologic record. *Journal of Geophysical Research*, 109, F04006, doi: 10.1029/2004JF000132.
- Iverson, N. R., Hooyer, T. S., and Baker, R. W. (1998). Ring-shear studies of till deformation: coulomb-plastic behavior and distributed strain in glacier beds. *Journal of Glaciology*, 44(148), 634–642.
- Iverson, N. R., et al. (2007). Soft-bed experiments beneath Engabreen, Norway: regelation infiltration, basal slip and bed deformation. *Journal of Glaciology*, 53(182), 323–340.
- Iverson, N. R., Hooyer, T. S., and Hooke, R. LeB. (1996). A laboratory study of sediment deformation: stress heterogeneity and grain-size evolution. *Annals of Glaciology*, 22, 167–175.
- Iverson, N. R., and Iverson, R. M. (2001). Distributed shear of subglacial till due to Coulomb slip. *Journal of Glaciology*, 47(158), 481–488.
- Iverson, N. R., and Petersen, B. B. (2011). A new laboratory device for study of subglacial processes: first results on ice-bed separation during sliding. *Journal of Glaciology*, 57(206), 1135–1146, doi: 10.3189/002214311798843458.
- Iverson, N. R., and Slemmons, D. J. (1995). Intrusion of ice into porous media by regelation: a mechanism of sediment entrainment by glaciers. *Journal of Geophysical Research*, 100(B7), 10219–10230.
- Iverson, N. R., and Souchez, R. (1996). Isotopic signature of debris-rich ice formed by regelation into a subglacial sediment bed. *Geophysical Research Letters*, 23(10), 1151–1154.
- Jacka, T. H., and Budd, W. F. (1989). Isotropic and anisotropic flow relations for ice dynamics. *Annals of Glaciology*,

- 12(1), 81–84, doi: 10.3198/  
1989AoG12-1-81-84.
- Jacka, T. H., and Maccagnan, M. (1984). Ice crystallographic and strain rate changes with strain in compression and extension. *Cold Regions Science and Technology*, 8(3), 269–286.
- Jackson, M., and Kamb, B. (1997). The marginal shear stress of Ice Stream B, West Antarctica. *Journal of Glaciology*, 43(145), 415–426.
- Jacobel, R. W., Scambos, T. A., Nereson, N. A., and Raymond, C. F. (2000). Changes in the margin of Ice Stream C, Antarctica. *Journal of Glaciology*, 46 (152), 102–110.
- Jacobel, R. W., Scambos, T. A., Raymond, C. F., and Gades, A. M. (1996). Changes in the configuration of ice stream flow from the West Antarctic Ice Sheet. *Journal of Geophysical Research*, 101 (B3), 5499–5504.
- Jacobson, H. P., and Raymond, C. F. (1998). Thermal effects on the location of ice stream margins. *Journal of Geophysical Research*, 103(B9), 12111–12122.
- Jansson, E. P. (1995). Water pressure and basal sliding on Storglaciären, northern Sweden. *Journal of Glaciology*, 41(138), 232–240.
- Jenkins, A. (2011). Convection-driven melting near the grounding lines of ice shelves and tidewater glaciers. *Journal of Physical Oceanography*, 41, 2279–2294.
- Jóhannesson, T., Raymond, C. F., and Waddington, E. (1989). Time-scale for adjustment of glaciers to changes in mass balance. *Journal of Glaciology*, 35(121), 355–369.
- Johnsen, S. J., Dansgaard, W., Clausen, H. B., and Langway, C. C., Jr. (1972). Oxygen isotope profiles through the Antarctic and Greenland ice sheets. *Nature*, 235 (5339), 429–434.
- Johnson, A. (1960). Variation in surface elevation of the Nisqually glacier Mt. Rainier, Washington. *International Association of Scientific Hydrology Bulletin*, 19, 54–60.
- Johnson, W., and Mellor, P. B. (1962). *Plasticity for Mechanical Engineers*. Princeton, NJ: Van Nostrand, Ltd., 412pp. (There is also a 1973 edition, in which the relevant pages are 44–49).
- Jones, N. (1982). The formation of glacial flutings in east-central Alberta. *Proceedings - Guelph Symposium on Geomorphology*, 6, 49–70.
- Jones, S. (1982). The confined compressive strength of polycrystalline ice. *Journal of Glaciology*, 28(98), 171–177.
- Joughin, I., et al. (1999). Tributaries of West Antarctic ice streams revealed by RADARSAT interferometry. *Science*, 286, 283–286.
- Joughin, I., et al. (2005). Continued deceleration of Whillans Ice Stream. *Geophysical Research Letters*, 32, L22501, doi: 10.1029/2005GL024319.
- Joughin, I., MacAyeal, D. R., and Tulaczyk, S. (2004). Basal shear stress of the Ross ice streams from control method inversions. *Journal of Geophysical Research*, 109, B09405, doi: 10.1029/2003JB002960.
- Jouzel, J. (2013). A brief history of ice core science over the last 50 yr. *Climate of the Past*, 9, 2525–2547.

- Kamb, B. (1959). Ice petrofabric observations from Blue Glacier, Washington, in relation to theory and experiment. *Journal of Geophysical Research*, 64(11), 1891–1909.
- Kamb, B. (1965). Structure of ice VI. *Science*, 150(3693), 205–209.
- Kamb, B. (1970). Sliding motion of glaciers: theory and observation. *Reviews of Geophysics and Space Physics*, 8(4), 673–728.
- Kamb, B. (1972). Experimental recrystallization of ice under stress. In Heard, H. C., Borg, I. Y., Carter, N. L., and Raleigh, C. B. (eds.) *Flow and Fracture of Rocks*. Washington, DC: American Geophysical Union, 16, 211–241.
- Kamb, B. (1987). Glacier surge mechanism based on linked cavity configuration of the basal water conduit system. *Journal of Geophysical Research*, 92(B9), 9083–9100.
- Kamb, B. (2001). Basal zone of the West Antarctic ice streams and its role in lubrication of their rapid motion. In Alley, R. B., and Bindschadler, R. A. (eds.) *The West Antarctic Ice Sheet: Behavior and Environment*. Washington, DC: American Geophysical Union, Antarctic Research Series, 77, 157–201.
- Kamb, B., and Echelmeyer, K. A. (1986). Stress-gradient coupling in glacier flow: 1. Longitudinal averaging of the influence of ice thickness and surface slope. *Journal of Glaciology*, 32(111), 267–284.
- Kamb, B., et al. (1985). Glacier surge mechanism: 1982–1983 surge of Variegated Glacier, Alaska. *Science*, 227(4686), 469–479.
- Kamb, B., and LaChapelle, E. (1964). Direct observation of the mechanism of glacier sliding over bedrock. *Journal of Glaciology*, 5(38), 159–172.
- Kanninen, M. F., and Popelar, C. H. (1985). *Advanced Fracture Mechanics*. New York: Oxford University Press, 563pp.
- Kaspari, S., Hooke, R. LeB., Mayewski, P. A., Kang, S., Hou, S., and Qin, D. (2008). Snow accumulation rate on Qomolangma (Mt. Everest), Himalaya: synchronicity with sites across the Tibetan Plateau on 50–100 year timescales. *Journal of Glaciology*, 54 (185), 343–352.
- Kaspari, S., Mayewski, P. A., Dixon, D. A., Spikes, V. B., Sneed, S. B., Handley, M. J., and Hamilton, G. S. (2004). Climate variability in West Antarctica derived from annual accumulation rate records from ITASE Firn/ice cores. *Annals of Glaciology*, 39, 585–594.
- Kaufman, B. G., et al. (2014). Centennial-scale variability of the Southern Hemisphere westerly wind belt in the eastern Pacific over the past two millennia. *Climate of the Past*, 10, 1125–1144.
- Kawamura, K., et al. (2007). Northern Hemisphere forcing of climatic cycles in Antarctica over the past 360 000 years. *Nature*, 448, 912–916.
- Keegan, K. M., Albert, M. R., McConnell, J. R., and Baker, I. (2014). Climate change and forest fires synergistically drive widespread melt events of the Greenland Ice Sheet, Proceedings to the National Academy of Sciences, May 19, 2014, [www.pnas.org/cgi/doi/10.1073/pnas.1405397111](http://www.pnas.org/cgi/doi/10.1073/pnas.1405397111).

- Kendall, K. (1978). The impossibility of comminuting small particles by compression. *Nature*, **272**, 710–711.
- Kenneally, J. (2003). Crevassing and calving of glacial ice. PhD thesis, University of Maine, Orono, 145pp.
- Kenneally, J. P., and Hughes, T. (2006). Calving giant icebergs: old principles, new applications. *Antarctic Science*, **18**(3), 409–419.
- Ketcham, W. M., and Hobbs, P. V. (1969). An experimental determination of the surface energies of ice. *Philosophical Magazine*, **19**(162), 1161–1173.
- Kimura, S., Nichols, K. W., and Venables, E. (2015). Estimation of shelf melt rates in the presence of a thermohaline staircase. *Journal of Physical Oceanography*, **45**(1), 133–148.
- Kinosita, S. (1962). Transformation of snow into ice by plastic compression. *Low Temperature Science, A*, **20**, 131–157.
- Kirby, S. H., Durham, W. B., Beeman, M. L., Heard, H. C., and Daley, M. A. (1987). Inelastic properties of ice Ih at low temperatures and high pressures. *Journal de Physique Colloques*, **48**(C1), C1-227–C1-232.
- Kirkbride, M. P. (2011). Debris-covered glaciers. In Singh, V. P., Singh, P., and Haritashya, U. K. (eds.) *Encyclopedia of Snow, Ice and Glaciers*. Dordrecht: Springer, pp. 190–192, doi: 10.1007/978-90-481-2642-2.
- Kleman, J., and Borgström, I. (1994). Glacial landforms indicative of a partly frozen bed. *Journal of Glaciology*, **40**(135), 255–264.
- Kleman, J., and Hättestrand, C. (1999). Frozen-bed Fennoscandian and Laurentide ice sheets during the Last Glacial Maximum. *Nature*, **402**, 63–66.
- Kranenborg, E. J., and Dijkstra, H. A. (1998). On the evolution of double-diffusive intrusions into a stably stratified liquid: a study of the layer merging process. *International Journal of Heat and Mass Transfer*, **41**(18), 2743–2756.
- Kruk, N. S., Vendrame, I. F., Rocha, H. R., Chou, S. C., and Cabral, O. (2010). Downward longwave radiation estimates for clear and all-sky conditions in the Sertãozinho region of São Paulo, Brazil. *Theoretical and Applied Climatology*, **99**, 115–123.
- Kuhn, M. (1981). Climate and glaciers. *International Association of Scientific Hydrology*, **131**, 3–20.
- Kuhn, M. (1989). The response of the equilibrium line altitude to climate fluctuations: theory and observations. In Oerlemans, J. (ed.) *Glacier Fluctuations and Climatic Change*. Dordrecht: Kluwer Academic Publishers, pp. 407–417.
- Lambe, T. W., and Whitman, R. V. (1969). *Soil Mechanics*. New York: John Wiley, 553pp.
- Landais, A., et al. (2010). What drives millennial and orbital variations of  $\delta^{18}\text{O}_{\text{atm}}$ ? *Quaternary Science Reviews*, **29**, 235–246.
- Langdon, T. G. (1991). The physics of superplastic deformation. *Materials Science and Engineering*, **A137**, 1–11.
- Lawn, B. (1993). *Fracture of Brittle Solids*, 2nd ed. Cambridge: Cambridge University Press, 378pp.
- Lawson, D. E., Strasser, J. C., Evenson, E. B., Alley, R. B., Larson, G. J., and Arcane, S. A. (1998). Glaciohydraulic

- supercooling: a freeze-on mechanism to create stratified, debris-rich basal ice: I. Field evidence. *Journal of Glaciology*, 44(148), 547–562.
- Lazzara, M. A., Jezek, K. C., Scambos, T. A., MacAyeal, D. R., and van der Veen, C. J. (1999). On the recent calving of icebergs from the Ross Ice Shelf. *Polar Geography*, 23(3), 201–212.
- Lazzara, M. A., Jezek, K. C., Scambos, T. A., MacAyeal, D. R., and van der Veen, C. J. (2008). On the recent calving of icebergs from Ross Ice Shelf. *Polar Geography*, 31(1–2), 15–26.
- Legrand, M., and Mayewski, P. A. (1997). Glaciochemistry of polar ice cores: a review. *Reviews of Geophysics*, 35(3), 219–243.
- Lemieux-Dudon, B., et al. (2010). Consistent dating for Antarctic and Greenland ice cores. *Quaternary Science Reviews*, 29, 8–20.
- Leonard, K. C., Bell, R. E., and Studinger, M. (2003). The influence of subglacial topography on accumulation rates at Lake Vostok. American Geophysical Union Annual Meeting, December 7–12, 2003.
- Leonard, K. C., and Fountain, A. G. (2003). Map-based methods for estimating glacier equilibrium line altitudes. *Journal of Glaciology*, 49(166), 329–336.
- Levermann, A., Albrecht, T., Winkelmann, R., Martin, M. A., Haseloff, M., and Jougin, I. (2012). Kinematic first-order calving law implies potential for abrupt ice-shelf retreat. *The Cryosphere*, 6, 273–286.
- Lewis, E. L., and Perkin, R. G. (1983). Supercooling and energy exchange near the Arctic Ocean surface. *Journal of Geophysical Research*, 88(C12) 7681–7685.
- Lewis, E. L., and Perkin, R. G. (1986). Ice pumps and their rates. *Journal of Geophysical Research*, 91(C10) 11756–11762.
- Li, J., Jacka, T. H., and Budd, W. F. (1996). Deformation rates in combined compression and shear for ice which is initially isotropic and after the development of strong anisotropy. *Annals of Glaciology*, 23, 247–252.
- Lighthill, M. J., and Whitham, G. B. (1955). On kinematic waves, I. Flood movement in long rivers. *Proceedings of the Royal Society, Series A*, 229(1178), 281–316.
- Lile, R. C. (1978). The effect of anisotropy on the creep of polycrystalline ice. *Journal of Glaciology*, 21(85), 475–483.
- Lipenkov, V. Ya., Barkov, N. I., Duval, P., and Pimienta, P. (1989). Crystalline texture of the 2083 m ice core at Vostok station, Antarctica. *Journal of Glaciology*, 35(121), 392–398.
- Lisiecki, L. E., and Raymo, M. E. (2005). A Pleistocene-Pliocene stack of 57 globally distributed benthic  $\delta^{18}\text{O}$  records. *Paleoceanography*, 20, PA1003, doi: 10.1029/2004PA001071.
- Liu, C.-H., Nagel, S. R., Schecter, D. A., Coppersmith, S. N., Majumdar, S., Narayan, O., and Witten, T. A. (1995). Force fluctuations in bead packs. *Science*, 269(5223), 513–515.
- Liu, H., Jezek, K. C., and Li, B. (1999). Development of an Antarctic DEM database by integrating cartographic and remotely sensed data: a GIS approach. *Journal of Geophysical Research*, 104(B10), 23199–23213.

- Lliboutry, L. (1964). *Traité de Glaciologie*, Vol. 1. Paris: Masson and Co.
- Lliboutry, L. (1968). General theory of subglacial cavitation and sliding of temperate glaciers. *Journal of Glaciology*, 7(49), 21–58.
- Lliboutry, L. (1970). Ice flow law from ice sheet dynamics. Proceedings of the International Symposium on Antarctic Glaciological Exploration, Hanover, NH, 3–7 September, 1968; *International Association of Scientific Hydrology*, Publication no. 86, 216–228.
- Lliboutry, L. (1976). Physical processes in temperate glaciers. *Journal of Glaciology*, 16(74), 151–158.
- Lliboutry, L. (1979). Local friction laws for glaciers: a critical review and new openings. *Journal of Glaciology*, 23(89), 67–95.
- Lliboutry, L. (1983). Modifications to the theory of intraglacial waterways for the case of subglacial ones. *Journal of Glaciology*, 29(102), 216–226.
- Lliboutry, L. (1996). Temperate ice permeability, stability of water veins and percolation of internal meltwater. *Journal of Glaciology*, 42(141), 201–211.
- Loewe, F. (1970). Screen temperatures and 10 m temperatures. *Journal of Glaciology*, 9(56), 263–268.
- Loulgue, L., et al. (2007). New constraints on the gas age–ice age difference along the EPICA ice cores, 0–50 kyr. *Climate of the Past*, 3, 527–540.
- Luckman, A., Benn, D. I., Cottier, F., Bevan, S., Nilsen, F., and Inall, M. (2015). Calving rates at tidewater glaciers vary strongly with ocean temperature. *Nature Communications*, 6(8566), doi: 10.1038/ncomms9566.
- Lüthi, D., et al. (2008). High-resolution carbon dioxide concentration record 650,000–800,000 years before present. *Nature*, 453, 379–382.
- MacAyeal, D. R. (1993a). A low-order model of the Heinrich event cycle. *Paleoceanography*, 8(6), 767–773.
- MacAyeal, D. R. (1993b). Binge/purge oscillations of the Laurentide Ice Sheet as a cause of the North Atlantic's Heinrich events. *Paleoceanography*, 8(6), 775–784.
- MacAyeal, D. R., Bindschadler, R. A., and Scambos, T. A. (1995). Basal friction of Ice Stream E, West Antarctica. *Journal of Glaciology*, 41(138), 247–262.
- MacAyeal, D. R., Scambos, T. A., Hulbe, C. L., and Fahnestock, M. A. (2003). Catastrophic ice-shelf break-up by an ice-shelf-fragment-capsize mechanism. *Journal of Glaciology*, 49(164), 22–36.
- Macheret, Y. Y., Cherkasov, P. A., and Bobrova, L. I. (1988). Tolschina i ob'em lednikov Djungarskogo Alatau po danniy aeroradiozondirovaniya. (Thickness and volume of glaciers of the Dzhungar Mountains according to results of aero-radio-sounding). Materialy Glyatsiologicheskikh Issled. *Khronika Obsuzhdeniya*, 62, 59–71.
- Machguth, H., Purves, R. S., Oerlemans, J., Hoelzle, M., and Paul, F. (2008). Exploring uncertainty in glacier mass balance modelling with Monte Carlo simulation. *The Cryosphere*, 2, 191–204, doi: 10.5194/tc-2-191-2008.
- Makinson, K., Holland, P. R., Jenkins, A., Nicholls, K. W., and Holland, D. M. (2011). Influence of tides on melting

- and freezing beneath Filchner-Ronne Ice Shelf, Antarctica. *Geophysical Research Letters*, 38, L06601, doi: 10.1029/2010GL046462.
- Makinson, K., King, M. A., Nicholls, K. W., and Gudmundsson, G. H. (2012). Diurnal and semidiurnal tide-induced lateral movement of Ronne Ice Shelf, Antarctica. *Geophysical Research Letters*, 39, L10501, doi: 10.1029/2012GL051636.
- Mandl, G., de Jong, L. N. J., and Maltha, A. (1977). Shear zones in granular material – an experimental study of their structure and mechanical genesis. *Rock Mechanics*, 9(2-3), 95–144.
- Mantua, N. J., and Hare, S. R. (2002). The Pacific decadal oscillation. *Journal of Oceanography*, 58, 35–44.
- Marshall, E. W. (1959). Stratigraphic use of particulates in polar ice caps. *Geological Society of America Bulletin*, 70, 1643.
- Marshall, S. J., Tarasov, L., Clarke, G. K. C., and Peltier, W. R. (2000). Glaciological reconstruction of the Laurentide Ice Sheet: physical processes and modeling challenges. *Canadian Journal of Earth Sciences*, 37, 769–793.
- Martín, C., Gudmundsson, G. H., Pritchard, H. D., and Gagliardini, O. (2009). On the effects of anisotropic rheology on ice flow, internal structure, and the age-depth relationship at ice divides. *Journal of Geophysical Research*, 114 (F4), F04001, doi: 10.1029/2008JF001204.
- Massonnet, D., and Feigl, K. L. (1998). Radar interferometry and its application to changes in the Earth's surface. *Reviews of Geophysics*, 36(4), 441–500.
- Matsuda, M., and Wakahama, G. (1978). Crystallographic structure of polycrystalline ice. *Journal of Glaciology*, 21(85), 607–620.
- Matthews, J. B. (1981). The seasonal circulation of Glacier Bay, Alaska fjord system. *Estuarine, Coastal, and Shelf Science*, 12, 679–700.
- Matthews, W. H. (1974). Surface profiles of the Laurentide ice sheet in its marginal areas. *Journal of Glaciology*, 13(67), 37–43.
- Maxwell, K. D. (2002). Pacific decadal oscillation and Arizona precipitation. Available online from: <http://www.wrhh.noaa.gov/wrhq/02TAs/0208/>.
- Mayewski, P., et al. (1994). Changes in atmospheric circulation and ocean ice cover over the North Atlantic during the last 41,000 years. *Science*, 263, 1747–1751.
- Mayewski, P. A., Snead, S. B., Birkel, S. D., Kurbatov, A. V., and Maasch, K. A. (2014). Holocene warming marked by abrupt onset of longer summers and reduced storm frequency around Greenland. *Journal of Quaternary Science*, 29(1), 99–104, doi: 10.1002/jqs.2684.
- McConnell, J. R., Lamorey, G. W., Lambert, S. W., and Taylor, K. C. (2002). Continuous ice-core chemical analyses using inductively coupled plasma mass spectrometry. *Environmental Science and Technology*, 36, 7–11.
- Meese, D. A., et al. (1997). The Greenland Ice Sheet Project 2 depth-age scale: methods and results. *Journal of Geophysical Research*, 102(C12), 26411–26423.

- Meier, M. F. (1961). Mass budget of South Cascade Glacier, 1957–1960. U.S. Geological Survey Professional Paper, 424-B, 206–211.
- Meier, M. F. (1965). Glaciers and climate. In Wright Jr., H. E., and Frey, D. G. (eds.) *The Quaternary of the United States*. Princeton, NJ: Princeton University Press, 795–805.
- Meier, M. F., et al. (1994). Mechanical and hydrologic basis for the rapid motion of a large tidewater glacier: 1. Observations. *Journal of Geophysical Research*, 99(B8), 15219–15229.
- Meier, M., et al. (2007). Glaciers dominate eustatic sea-level rise in the 21st century. *Science*, 317, 1064–1067.
- Meier, M. F., and Post, A. (1987). Fast tidewater glaciers. *Journal of Geophysical Research*, 92(B9), 9051–9058.
- Meier, M. F., Rasmussen, L. A., Krimmel, R. M., Olsen, R. W., and Frank, D. (1985). Photogrammetric determination of surface altitude, terminus position, and ice velocity of Columbia Glacier, Alaska. U.S. Geological Survey Professional Paper, 1258-F, F1–F40.
- Meierbacholt, T., Harper, J., and Humphrey, N. (2013). Basal drainage system response to increasing surface melt on the Greenland Ice Sheet. *Science*, 341, 777–779.
- Mellor, M., and Testa, R. (1969). Effect of temperature on the creep of ice. *Journal of Glaciology*, 8(52), 131–145.
- Menzies, J., and Shilts, W. W. (1996). Subglacial environments. In Menzies, J. (ed.) *Past Glacial Environments—Sediments, Forms, and Techniques*. *Glacial Environments*, Vol. 2. Oxford: Butterworth-Heinemann, pp. 15–136.
- Meyer, C. R., Fernandes, M. C., Creyts, T. T., and Rice, J. R. (2016). Effects of ice deformation on Röthlisberger channels and implications for transitions in subglacial hydrology. *Journal of Glaciology*, 62(234), 750–762.
- Mickelson, D. M. (1987). Central Lowlands. In Graf, W. L. (ed.) *Geomorphic Systems of North America*. Boulder, CO: Geological Society of America, Centennial Special Volume 2, pp. 111–118.
- Mikesell, T. D., van Wijk, K., Otheim, L. T., Marshall, H.-P., and Kurbatov, A. (2017). Laser ultrasound observations of mechanical property variations in ice cores. *Geosciences*, 7(3), 47, doi: 10.3390/geosciences7030047.
- Miller, J. K. (1984). *Model for Clastic Indicator Trains in Till: Prospecting in Areas of Glaciated Terrain*. London: The Institution of Mining and Metallurgy, pp. 69–77.
- Minchew, B. M., Meyer, C. R., Robel, A. A., Gudmundsson, G. H., and Simons, M. (2018). Processes controlling the downstream evolution of ice rheology in glacier shear margins: case study on Rutford Ice Stream, West Antarctica. *Journal of Glaciology*, 64(246), 583–594.
- Minchew, B. M., Simons, M., Riel, B., and Milillo, P. (2017). Tidally induced variations in vertical and horizontal motion on Rutford Ice Stream, West Antarctica, inferred from remotely sensed observations. *Journal of Geophysical Research: Earth Surface*, 122(1), 167–190.

- Mingle, J. (2015). *Fire and Ice: Soot, Solidarity, and Survival on the Roof of the World*. New York: St. Martin's Press, 450pp.
- Minzoni, R. T., Anderson, J. B., Wellner, J. S., and Fernandez, R. (2017). Antarctic Peninsula glacier synchronicity increased during the Holocene: implications for modern recession. *Geological Society of America Annual Meeting Abstracts with Programs*, Paper 51-14.
- Mitchell, J. K. (1993). *Fundamentals of Soil Behavior*, 2nd ed. New York: John Wiley.
- Mitchell, J. K., Campanella, R. G., and Singh, A. (1968). Soil creep as a rate process. *Journal of the Soil Mechanics and Foundations Division, American Society of Civil Engineers*, 94(SM1), 231–253.
- Mitchell, J. K., and Soga, K. (2005). *Fundamentals of Soil Behavior*, 3rd ed. Hoboken, NJ: John Wiley, 577pp.
- Montagnat, M., and Duval, P. (2000). Rate controlling processes in the creep of polar ice, influence of grain boundary migration associated with recrystallization. *Earth and Planetary Science Letters*, 183, 179–186.
- Montagnat, M., and Duval, P. (2004). Dislocations in ice and deformation mechanisms: from single crystals to polar ice. *Defect and Diffusion Forum*, 229, 43–54.
- Mooers, H. D. (1989). On the formation of tunnel valleys of the Superior Lobe, Central Minnesota. *Quaternary Research*, 32, 24–35.
- Mooers, H. D. (1990). Ice marginal thrusting of drift and bedrock: thermal regime subglacial aquifers, and glacial surges. *Canadian Journal of Earth Sciences*, 27(6), 849–862.
- Moor, E., and Stauffer, B. (1984). A new dry extraction system for gasses in ice. *Journal of Glaciology*, 30(106), 358–361.
- Moore, P. L. (2014). Deformation of debris-ice mixtures. *Reviews of Geophysics*, 52, 435–467.
- Moore, P. L., Iverson, N. R., and Cohen, D. (2010). Conditions for thrust faulting in a glacier. *Journal of Geophysical Research*, 115, 15, doi: 10.1029/2009JF001307. F02005.
- More, A. F., et al. (2017). Next-generation ice core technology reveals true minimum natural levels of lead (Pb) in the atmosphere: insights from the Black Death. *GeoHealth*, 1(4), 211–219.
- Morgan, V. I. (1972). Oxygen isotope evidence for bottom freezing on the Amery Ice Shelf. *Journal of Glaciology*, 24(90), 393–394.
- Motyka, R. J., Dryer, W. P., Amundson, J., Truffer, M., and Fahnestock, M. (2013). Rapid submarine melting driven by subglacial discharge, LeConte Glacier, Alaska, U.S.A. *Geophysical Research Letters*, 40, 5153–5158, doi: 10.1002/grl.51011.
- Motyka, R. J., Hunter, L., Echelmeyer, K. A., and Connor, K. (2003). Submarine melting at the terminus of a temperate tidewater glacier, LeConte Glacier, Alaska, U.S.A. *Annals of Glaciology*, 36, 57–65.
- Moran, S. R., Clayton, L., Hooke, R. LeB., Fenton, M. M., and Andriashuk, L. D. (1980). Glacier bed landforms of the

- prairie region of North America. *Journal of Glaciology*, 25(93), 457–476.
- Morse, D. L., Waddington, E. D., and Steig, E. J. (1998). Ice age storm trajectories from radar stratigraphy at Taylor Dome, Antarctica. *Geophysical Research Letters*, 25(17), 3383–3386.
- Müller, F. (1962). Zonation in the accumulation area of the glaciers of Axel Heiberg Island, N.W.T., Canada. *Journal of Glaciology*, 4(33), 302–318.
- Murozumi, M., Chow, T. J., and Patterson, C. (1969). Chemical concentrations of pollutant lead aerosols, terrestrial dusts and sea salts in Greenland and Antarctic snow strata. *Geochimica et Cosmochimica Acta*, 33, 1247–1294.
- Nadai, A. (1950). *Theory of Flow and Fracture of Solids*, volume 1, 2nd ed. New York: McGraw Hill, 572pp.
- Nakase, A., and Kamei, T. (1986). Influence of strain rate on undrained shear strength characteristics of  $K_o$ -consolidated cohesive soils. *Soils and Foundations*, 26, 85–95.
- Nakawo, M., and Rana, B. (1999). Estimation of ablation rate of glacier ice under a supraglacial debris layer. *Geografiska Annaler*, 81A(4), 695–701.
- Neftel, A., Oeschger, H., and Stauffer, B. (1988). CO<sub>2</sub> record in the Byrd ice core 50,000–5,000 years BP. *Nature*, 331, 609–611.
- Nereson, N. A., Raymond, C. F., Waddington, E. D., and Jacobel, R. W. (1998). Migration of the Siple Dome ice divide, West Antarctica. *Journal of Glaciology*, 44(148), 643–652.
- Ng, F. S. L. (1999). A mathematical model of wide subglacial water drainage channels. In Wetlaufer, J. S., Dash, J. G., and Untersteiner, N. (eds.) *Ice Physics and the Natural Environment*. Berlin: Springer-Verlag, pp. 325–327 (NATO ASI Series I: Global Environmental Change 56).
- Ng, F. S. L. (2000a). Canals under sediment-based ice sheets. *Annals of Glaciology*, 30, 146–152.
- Ng, F. S. L. (2000b). Coupled ice-till deformation near subglacial channels and cavities. *Journal of Glaciology*, 46 (155), 580–598.
- Ng, F., and Hallet, B. (2002). Patterning mechanisms in subglacial carbonate dissolution and deposition. *Journal of Glaciology*, 48(162), 386–400.
- NGRIP members. (2004). High-resolution record of Northern Hemisphere climate extending into the last interglacial period. *Nature*, 431, 147.
- Nguyen, V. B., Darnige, T., Bruand, A., and Clement, E. (2011). Creep and fluidity of a real granular packing near jamming. *Physical Review Letters*, 107, 5.
- Nicholls, K. W., Corr, H. F. J., Stewart, C. L., Lok, L. B., Brennan, P. V., and Vaughan, D. G. (2015). A ground-based radar for measuring vertical strain rates and time-varying basal melt rates in ice sheets and shelves. *Journal of Glaciology*, 61(230), 1079–1087, doi: 10.3189/2015JoG15J073.
- Nick, F. M., van der Veen, C. J., Vieli, A., and Benn, D. I. (2010). A physically based calving model applied to marine outlet glaciers and implications for the glacier dynamics. *Journal of Glaciology*, 56 (199), 781–794.
- NSIDC. (2017). National Snow and Ice Data Center. Available online from:

- <https://nsidc.org/cryosphere/seaice/processes/albedo.html> [Accessed 15 August 2017].
- Nygård, A., Sejrup, H. P., Haflidason, H., Lekens, W. A. H., Clark, C. D., and Bigg, G. R. (2007). Extreme sediment and ice discharge from marine-based ice streams: new evidence from the North Sea. *Geology*, 35(5), 395–398.
- Nye, J. F. (1951). The flow of glaciers and ice sheets as a problem in plasticity. *Proceedings of the Royal Society of London, Series A*, 207(1091), 554–572.
- Nye, J. F. (1952a). Reply to Mr. Joel E. Fisher's comments. *Journal of Glaciology*, 2(11), 52–53.
- Nye, J. F. (1952b). Mechanics of glacier flow. *Journal of Glaciology*, 2(12), 82–93.
- Nye, J. F. (1953). The flow law of ice from measurements in glacier tunnels, laboratory experiments, and the Jungfraufirn borehole experiment. *Proceedings of the Royal Society of London, Series A*, 219(1139), 477–489.
- Nye, J. F. (1955). Comments on Dr. Lowe's letter and notes on crevasses. *Journal of Glaciology*, 2(17), 512–514.
- Nye, J. F. (1957). The distribution of stress and velocity in glaciers and ice sheets. *Proceedings of the Royal Society of London, Series A*, 239(1216), 113–133.
- Nye, J. F. (1960). The response of glaciers and ice sheets to seasonal and climatic changes. *Proceedings of the Royal Society, Series A*, 256(1287), 559–584.
- Nye, J. F. (1963). On the theory of the advance and retreat of glaciers. *Geophysical Journal of the Royal Astronomical Society*, 7(4), 432–456.
- Nye, J. F. (1965). The flow of a glacier in a channel of rectangular, elliptic, or parabolic cross section. *Journal of Glaciology*, 5(41), 661–690.
- Nye, J. F. (1969a). The calculation of sliding of ice over a wavy surface using a Newtonian viscous approximation. *Proceedings of the Royal Society of London, Series A*, 311(1506), 445–467.
- Nye, J. F. (1969b). The effect of longitudinal stress on the shear stress at the base of an ice sheet. *Journal of Glaciology*, 8(53), 207–213.
- Nye, J. F. (1970). Glacier sliding without cavitation in a linear viscous approximation. *Proceedings of the Royal Society of London, Series A*, 315 (1522), 381–403.
- Nye, J. F. (1973a). The motion of ice past obstacles. In Whalley, E., Jones, S. J., and Gold, L. W. (eds.) *The Physics and Chemistry of Ice*. Ottawa: Royal Society of Canada, pp. 387–394.
- Nye, J. F. (1973b). Water at the bed of a glacier. *IUGG-AIHS Symposium on the Hydrology of Glaciers, Cambridge, September 7–13, 1969*. International Association of Scientific Hydrology Publication 95, 189–194.
- Nye, J. F. (1976). Water flow in glaciers: Jökulhlaups, tunnels and veins. *Journal of Glaciology*, 17(76), 181–207.
- Nye, J. F., and Frank, F. C. (1973). Hydrology of intergranular veins in a temperate glacier. *IUGG-AIHS Symposium on the Hydrology of Glaciers, Cambridge, 7–13 September 1969*. International Association of Scientific Hydrology Publication, 95, 157–161.
- Nye, J. F., and Mae, S. (1972). The effect of non-hydrostatic stress on intergranular water veins and lenses in ice. *Journal of Glaciology*, 11(61), 81–101.

- O'Leary, M. O., and Christoffersen, P. (2013). Calving on tidewater glaciers amplified by submarine frontal melting. *The Cryosphere*, 7, 119–128.
- O'Leary, M. O., and Luckman, A. (2017). Larsen C calves trillion ton iceberg. Available online from: <http://www.projectmidas.org/blog/calving/>.
- Osterberg, E. C., et al. (2017). The 1200 year composite ice core record of Aleutian Low intensification. *Geophysical Research Letters*, 44, 7447–7454.
- Osterberg, E. C., Handley, M. J., Sneed, S. B., Mayewski, P. A., and Kreutz, K. J. (2006). Continuous sampling ice core melter system with discrete sampling for major ion, trace element, and stable isotope analyses. *Environmental Science and Technology*, 40, 3355–3361.
- Östrem, G. (1959). Ice melting under a thin layer of moraine, and the existence of ice cores in moraine ridges. *Geografiska Annaler*, 41(4), 228–230.
- Padman, L., Siegfried, M. R., and Fricker, H. A. (2018). Ocean tide influences on the Antarctic and Greenland ice sheets. *Reviews of Geophysics*, 56, 142–184, doi.org/10.1002/2016RG000546.
- Painter, T. H., Flanner, M. D., Kaser, G., Marzeion, B., VanCuren, R. A., and Abdalati, W. (2013). End of the Little Ice Age in the Alps forced by industrial black carbon. *PNAS*, 110(38), 15216–15221.
- Park, J. W., Gourmelen, N., Shepherd, A., Kim, S. W., Vaughan, D. G., and Wingham, D. J. (2013). Sustained retreat of the Pine Island Glacier. *Geophysical Research Letters*, 40, 2137–2142.
- Parker, G. (1979). Hydraulic geometry of active gravel rivers. *Journal of the Hydraulics Division, American Society of Civil Engineers*, 105(HY9), 1185–1201.
- Paterson, W. S. B. (1971). Temperature measurements in Athabasca Glacier, Alberta, Canada. *Journal of Glaciology*, 10(60), 339–349.
- Paterson, W. S. B. (1977). Secondary and tertiary creep of glacier ice as measured by borehole closure rates. *Reviews of Geophysics and Space Physics*, 15(1), 47–55.
- Paterson, W. S. B. (1991). Why ice-age ice is sometimes “soft”. *Cold Regions Science and Technology*, 20, 75–98.
- Paterson, W. S. B., et al. (1977). An oxygen isotope climatic record from the Devon Island ice cap. Arctic Canada. *Nature*, 266(5602), 508–511.
- Patterson, C. J. (1994). Tunnel-valley fans of the St. Croix moraine, east-central Minnesota, USA. In Warren, W., and Croot, C. (eds.) *Formation and Deformation of Glacial Deposits*. Rotterdam: Balkema, pp. 69–87.
- Patterson, C. J. (1997). Southern Laurentide ice lobes were created by ice streams: Des Moines lobe in Minnesota, USA. *Sedimentary Geology*, 111, 247–261.
- Patterson, C. J., and Hooke, R. LeB. (1995). Physical environment of drumlin formation. *Journal of Glaciology*, 41(137), 30–38.
- Pattyn, F., et al. (2008). Benchmark experiments for higher-order and full-Stokes ice sheet models (ISMIP-HOM). *The Cryosphere*, 2, 95–108.
- Payne, A. J., et al. (2000). Results from the EISMINT model intercomparison:

- the effects of thermomechanical coupling. *Journal of Glaciology*, 46(153), 227–238.
- Peiró, J., and Sherwin, S. (2005). Finite difference, finite element, and finite volume methods for partial differential equations. In Yip, S. (ed.) *Handbook of Materials Modeling, Volume 1: Methods and Models*. The Netherlands: Springer, pp. 1–32.
- Peltz, M. S., and Warren, C. R. (1991). Relationship between tidewater glacier calving velocity and water depth at the calving front. *Annals of Glaciology*, 15, 115–118.
- Perol, T., Rice, J. R., Platt, J. D., and Suckale, J. (2015). Subglacial hydrology and ice stream margin locations. *Journal of Geophysical Research Earth Surface*, 120, 1352–1368, doi: 10.1002/2015JF003542.
- Petit, J. R., et al. (1999). Climate and atmospheric history of the past 420,000 years from the Vostok ice core, Antarctica. *Nature*, 399, 429–436.
- Pfeffer, W. T. (1992). Stress-induced foliation in the terminus of Variegated Glacier, Alaska, U.S.A., formed during the 1982–83 surge. *Journal of Glaciology*, 38(129), 213–222.
- Philberth, K., and Federer, B. (1971). On the temperature profile and age profile in the central part of cold ice sheets. *Journal of Glaciology*, 10(58), 3–14.
- Philip, J. R. (1980). Thermal fields during regelation. *Cold Regions Science and Technology*, 3, 193–203.
- Pimienta, P., and Duval, P. (1987). Rate controlling processes in the creep of polar glacier ice. *Journal de Physique*, 48, Colloque C1, Supplement to no. 3, C1-243–C1-248.
- Pimienta, P., Duval, P., and Lipenkov, V. Ya. (1988). Mechanical behavior of ice along the 2040 m Vostok core, Antarctica. *Annals of Glaciology*, 10, 137–140.
- Piotrowski, J. A., Mickelson, D. M., Tulaczyk, S., Krzyszkowski, D., and Junge, F. W. (2001). Were deforming subglacial beds beneath past ice sheets really widespread? *Quaternary International*, 86, 139–150.
- Pohjola, V. A., and Rogers, J. C. (1997). Atmospheric circulation and variations in Scandinavian glacier mass balance. *Quaternary Research*, 47, 29–36, doi: 10.1006/qres.1996.1859.
- Pralong, A., and Funk, M. (2005). Dynamic damage model of crevasse opening and application to glacier calving. *Journal of Geophysical Research*, 110, B01309, doi: 10.1029/2004JB003104.
- Price, S. F., Conway, H., and Waddington, E. D. (2007a). Evidence for late Pleistocene thinning of Siple Dome, West Antarctica. *Journal of Geophysical Research*, 112, F03021, doi: 10.1029/2006JF000725.
- Price, S. F., Waddington, E. D., and Conway, H. (2007b). A full-stress, thermomechanical flow band model using the finite volume method. *Journal of Geophysical Research*, 112, F03020, doi: 10.1029/2006JF000724.
- Prior, D. J., et al. (2015). Making EBSD on water ice routine. *Journal of Microscopy*, 259(3), 237–256.
- Radko, T. (2013). *Double-Diffusive Convection*. Cambridge: Cambridge University Press, 342pp.

- Raisbeck, G. M., et al. (2017). An improved north-south synchronization of ice core records around the 41 kyr  $^{10}\text{Be}$  peak. *Climate of the Past*, 13, 217–229.
- Raisbeck, G. M., Yiou, F., Jouzel, J., and Stocker, T. F. (2007). Direct north-south synchronization of abrupt climate change record in ice cores using Beryllium 10. *Climate of the Past*, 3, 541–547.
- Ram, M., Illing, M., Weber, P., Koenig, G., and Kaplan, M. (1995). Polar ice stratigraphy from laser-light scattering: scattering from ice. *Geophysical Research Letters*, 22(24), 3525–3527.
- Ramanathan, V., and Carmichael, G. (2008). Global and regional climate change due to black carbon. *Nature Geoscience*, 1, 221–227.
- Ramsay, J. G., and Graham, R. H. (1970). Strain variation in shear belts. *Canadian Journal of Earth Sciences*, 7, 786–813.
- Ramseier, R. O. (1967). Self-diffusion of tritium in natural and synthetic ice monocrystals. *Journal of Applied Physics*, 36(6), 2553–2556.
- Rasmussen, E. M. (1984). El Niño: the ocean/atmosphere connection. *Oceanus*, 27(2), 5–12.
- Rasmussen, L. A., and Meier, M. F. (1982). Continuity equation model of the predicted drastic retreat of Columbia Glacier, Alaska. U.S. Geological Survey Professional Paper, 1258-F, A1–A23.
- Ratcliffe, E. H. (1962). Thermal conductivity of ice. *Philosophical Magazine*, 7, 1197–1203.
- Rathbun, A. P., Marone, C., Alley, R. B., and Anandakrishnan, S. (2008). Laboratory study of the frictional rheology of sheared till. *Journal of Geophysical Research*, 113(F2), F02020, doi: 10.1029/2007JF000815.
- Raymond, C. F. (1971). Flow in a transverse section of Athabasca Glacier, Alberta, Canada. *Journal of Glaciology*, 10(58), 55–84.
- Raymond, C. F. (1973). Inversion of flow measurements for stress and rheological parameters in a valley glacier. *Journal of Glaciology*, 12(64), 19–44.
- Raymond, C. F. (1983). Deformation in the vicinity of ice divides. *Journal of Glaciology*, 29(103), 357–373.
- Raymond, C. F. (2000). Energy balance of ice streams. *Journal of Glaciology*, 46(155), 665–674.
- Raymond, C. F., Echelmeyer, K. A., Whillans, I. M., and Doake, C. S. M. (2001). Ice stream shear margins in the West Antarctic Ice Sheet: behavior and environment. *Antarctic Research Series*, 77, 137–155.
- Raymond, C. F., and Harrison, W. D. (1975). Some observations on the behavior of liquid and gas phases in temperate glacier ice. *Journal of Glaciology*, 14 (71), 213–234.
- Raymond, C. F., and Harrison, W. D. (1988). Evolution of Variegated Glacier, U.S.A., prior to its surge. *Journal of Glaciology*, 34(117), 154–165.
- Raynaud, D. (2012). The integrity of the ice record of greenhouse gases with special focus on atmospheric CO<sub>2</sub>. *Лёд и Снег (Ice and Snow)*, 118(2), 5–14.
- Raynaud, D., Jouzel, J., Barnola, J.-M., Chappellaz, J., Delmas, R. J., and Lorius, C. (1993). The ice core record of greenhouse gases. *Science*, 259(5097), 926–934.

- Raynaud, D., and Whillans, I. M. (1982). Air content of the Byrd core and past changes in the West Antarctic Ice Sheet. *Annals of Glaciology*, 3, 269–273.
- Reeh, N. (1968). On the calving of ice from floating glaciers and ice shelves. *Journal of Glaciology*, 7(50), 215–232.
- Rempel, A. W. (2008). A theory for ice-till interactions and sediment entrainment beneath glaciers. *Journal of Geophysical Research, Earth Surface*, 113(F1), doi: 10.1029/2007JF000870.
- Retzlaff, R., and Bentley, C. R. (1993). Timing of stagnation of Ice Streams A, West Antarctica, from short-pulse radar studies of buried surface crevasses. *Journal of Glaciology*, 39(133), 553–561.
- Retzlaff, R., Lord, N., and Bentley, C. R. (1993). Airborne-radar studies: ice streams A, B and C, West Antarctica. *Journal of Glaciology*, 39(133), 495–506.
- Rignot, E. (1998). Fast recession of a West Antarctic glacier. *Science*, 281, 549–551.
- Rignot, E. (2001). Evidence for rapid retreat and mass loss of Thwaites Glacier, West Antarctica. *Journal of Glaciology*, 47(157), 213–222.
- Rignot, E. (2008). Changes in West Antarctic ice stream dynamics observed with ALOS PALSAR data. *Geophysical Research Letters*, 35, L12505, doi: 10.1029/2008GL033365.
- Rignot, E., Fenty, I., Xu, Y., Cai, C., and Kemp, C. (2015). Undercutting of marine-terminating glaciers in West Greenland. *Geophysical Research Letters*, 42, 5909–5917.
- Rignot, E., Mouginot, J., Morlighem, M., Seroussi, H., and Scheuchl, B. (2014). Widespread, rapid grounding line retreat of Pine Island, Thwaites, Smith, and Kohler glaciers, West Antarctica, from 1992 to 2011. *Geophysical Research Letters*, 41, 3502–3509.
- Rignot, E., Velicogna, I., van den Broeke, M. R., Monaghan, A., and Lenaerts, J. T. M. (2011). Acceleration of the contribution of the Greenland and Antarctic ice sheets to sea level rise. *Geophysical Research Letters*, 38, L05503, doi: 10.1029/2011GL046583.
- Rist, M. A., Sammonds, P. R., Murrell, S. A. F., Meredith, P. G., Doake, C. S. M., Oerter, H., and Matsuki, K. (1999). Experimental and theoretical fracture mechanics applied to Antarctic ice and surface crevassing. *Journal of Geophysical Research*, 104(B2), 2973–2987.
- Robin, G. deQ. (1955). Ice movement and temperature distribution in glaciers and ice sheets. *Journal of Glaciology*, 2 (18), 523–532.
- Robin, G. DeQ. (1976). Is the basal ice of a temperate glacier at the pressure melting point? *Journal of Glaciology*, 16(74), 183–195.
- Robin, G. DeQ. (1979). Formation, flow, and disintegration of ice shelves. *Journal of Glaciology*, 24(90), 259–271.
- Roe, G. H., and Baker, M. B. (2014). Glacier response to climate perturbations: an accurate linear geometric model. *Journal of Glaciology*, 60(222), 670–684.
- Roe, G. H., and O'Neal, M. A. (2009). The response of glaciers to intrinsic climate variability: observations and models of

- late-Holocene variations in the Pacific Northwest. *Journal of Glaciology*, 55(193), 839–854.
- Römkens, M. J. M., and Miller, R. D. (1973). Migration of mineral particles in ice with a temperature gradient. *Journal of Colloidal and Interface Science*, 42(1), 103–111.
- Rose, J. (1989). Glacier stress patterns and sediment transfer associated with the formation of superimposed flutes. *Sedimentary Geology*, 62, 151–176.
- Rosenberg, R. (2005). Why is ice slippery? *Physics Today*, 58(12), 50–55.
- Rosier, S. H. R., Gudmundsson, G. H., and Green, J. A. M. (2015). Temporal variations in the flow of a large Antarctic ice stream controlled by tidally induced changes in the subglacial water system. *The Cryosphere*, 9, 1649–1661.
- Röthlisberger, H. (1972). Water pressure in intra- and subglacial channels. *Journal of Glaciology*, 11(62), 177–204.
- Röthlisberger, H. (1974). Möglichkeiten und grenzen der gletscherüberwachung (Possibilities and limits of glacier surveillance). *Neuen Zürcher Zeitung*, 196, 15p.
- Röthlisberger, H., and Iken, A. (1981). Plucking as an effect of water-pressure variations at the glacier bed. *Annals of Glaciology*, 2, 57–62.
- Rott, H., Rack, W., Skvarca, P., and De Angelis, H., 2002. Northern Larsen Ice Shelf, Antarctica: further retreat after collapse. *Annals of Glaciology*, 34, 277–282.
- Ruddiman, W. F. (2003). The anthropogenic greenhouse era began thousands of years ago. *Climate Change*, 61, 261–293.
- Ruddiman, W. F. (2007). The early anthropogenic hypothesis: challenges and responses. *Reviews of Geophysics*, 45, RG4001, doi: 10.1029/2006RG000207.
- Russell-Head, D. S., and Budd, W. F. (1979). Ice-sheet flow properties derived from bore-hole shear measurements combined with ice-core studies. *Journal of Glaciology*, 24(90), 117–130.
- Sammis, C. G., King, G., and Biegel, R. (1987). The kinematics of gouge deformation. *Pure and Applied Geophysics*, 125(5), 777–812.
- Sane, S. M., Desai, C. S., Jenson, J. W., Contractor, D. N., Carlson, A. E., and Clark, P. U. (2008). Disturbed state constitutive modeling of two Pleistocene tills. *Quaternary Science Reviews*, 27, 267–283.
- Scambos, T. A., Bohlander, J. A., Shuman, C. A., and Skvarca, P. (2004). Glacier acceleration and thinning after ice shelf collapse in the Larsen B embayment, Antarctica. *Geophysical Research Letters*, 31, L18402.
- Scambos, T. A., Hulbe, C., Fahnestock, M., and Bohlander, J. (2000). The link between climate warming and break-up of ice shelves in the Antarctic Peninsula. *Journal of Glaciology*, 46(154), 516–530.
- Scambos, T. A., Hulbe, C., Fahnestock, M. A., and Bohlander, J. (2003). The link between climate warming and break-up of ice shelves in the Antarctic Peninsula. *Journal of Glaciology*, 46(154), 516–530.

- Schellenberger, T., Dunse, T., Kääb, A., Schuler, T. V., Hagen, J. O., and Reijmer, C. H. (2017). Multi-year surface velocities and sea-level rise contribution of the Basin-3 and Basin-2 surges, Austfonna, Svalbard. *The Cryosphere*, doi: 10.5194/tc-2017-5, 2017.
- Schmidt, R., and Housen, K. (1995). Problem solving with dimensional analysis. *The Industrial Physicist*, 1, 21–24.
- Schneider, N., and Cornuelle, B. D. (2005). The forcing of the Pacific Decadal Oscillation. *Journal of Climate*, 18, 4355–4373.
- Schodlok, M. P., Menemenlis, D., Rignot, E., and Studinger, M. (2012). Sensitivity of the ice-shelf/ocean system to the sub-ice-shelf cavity shape measured by NASA IceBridge in Pine Island Glacier, West Antarctica. *Annals of Glaciology*, 53(60), 156–162.
- Schoof, C. G. (2012). Thermally-driven migration of ice stream margins. *Journal of Fluid Mechanics*, 712, 552–578.
- Schoof, C. G., and Clarke, G. K. C. (2008). A model for spiral flows in basal ice and the formation of subglacial flutes based on a Reiner-Rivlin rheology for glacial ice. *Journal of Geophysical Research, Earth Surface*, 113(B5), doi: 10.1029/2007JB004957.
- Schlüson, E. M. (1999). The structure and mechanical behavior of ice. *Journal of the Minerals Metals & Materials Society*, 52(1), 21–27.
- Scott, J. B. T., Gudmundsson, G. H., Smith, A. M., Bingham, R. G., Pritchard, H. D., and Vaughan, D. G. (2009). Increased rate of acceleration on Pine Island Glacier strongly coupled to changes in gravitational driving stress. *The Cryosphere*, 2, 125–131.
- Seaberg, S. Z., Seaberg, J. Z., Hooke, R. LeB., and Wiberg, D. W. (1988). Character of the englacial and subglacial drainage system in the lower part of the ablation area of Storglaciären, Sweden, as revealed by dye-trace studies. *Journal of Glaciology*, 34(117), 217–227.
- Segall, P. (1984). Rate-dependent extensional deformation resulting from crack growth in rock. *Journal of Geophysical Research*, 89(B6), 4185–4195.
- Shabtaie, S., and Bentley, C. R. (1988). Ice-thickness map of the West Antarctic ice streams by radar sounding. *Annals of Glaciology*, 11, 126–136.
- Sharp, M. (1982). Modification of clasts in lodgement tills by glacial erosion. *Journal of Glaciology*, 28(100), 475–481.
- Shaw, J., and Freschauf, R. C. (1973). A kinematic discussion of the formation of glacial flutings. *Canadian Geographer*, 17(1), 19–35.
- Shepherd, A., et al. (2012). A reconciled estimate of ice-sheet mass balance. *Science*, 338(6111), 1183–1189.
- Shreve, R. L. (1967). Migration of air bubbles, vapor figures, and brine pockets in ice under a temperature gradient. *Journal of Geophysical Research*, 72(16), 4093–4100.
- Shreve, R. L. (1972). Movement of water in glaciers. *Journal of Glaciology*, 11(62), 205–214.

- Shreve, R. L. (1984). Glacier sliding at subfreezing temperatures. *Journal of Glaciology*, 30(106), 341–347.
- Shreve, R. L. (1985a). Esker characteristics in terms of glacier physics, Katahdin Esker system, Maine. *Geological Society of America Bulletin*, 96(5), 639–646.
- Shreve, R. L. (1985b). Late Wisconsin ice-surface profile calculated from esker paths and types, Katahdin esker system, Maine. *Quaternary Research*, 23(1), 27–37.
- Shreve, R. L., and Sharp, R. P. (1970). Internal deformation and thermal anomalies in lower Blue Glacier, Mount Olympus, Washington, USA. *Journal of Glaciology*, 9(55), 65–86.
- Shumskii, P. A. (1964). *Principles of Structural Glaciology*. New York: Dover.
- Shumway, J. R., and Iverson, N. R. (2009). Magnetic fabrics of the Douglas Till of the Superior lobe: exploring bed-deformation kinematic. *Quaternary Science Reviews*, 28, 107–119.
- Siegenthaler, U., and Oeschger, H. (1987). Biospheric CO<sub>2</sub> emissions during the past 200 years reconstructed by deconvolution of ice core data. *Tellus B: Chemical and Physical Meteorology*, 39(1–2), 140–154.
- Sigl, M., Abram, N. J., Gabrieli, J., Jenk, T. M., Osmont, D., and Schwikowski, M. (2018). 19th century glacier retreat in the Alps preceded the emergence of industrial black carbon deposition on high-alpine glaciers. *The Cryosphere*, 12, 3311–3331.
- Sih, G. C. (1973). *Handbook of Stress-Intensity Factors; Stress-Intensity Factor Solutions and Formulas for Reference*. Bethlehem, PA: Institute of Fracture and Solid Mechanics, Leigh University.
- Siman-Tov, S., Stock, G. M., Brodsky, E. E., and White, J. C. (2017). The coating layer of glacial polish. *Geology*, 45(11), 987–990.
- Smith, A. M., Murray, T., Nicholls, K. W., Makinson, K., Aðalgeirsdóttir, G., Behar, A. E., and Vaughan, D. G. (2007). Rapid erosion, drumlin formation, and changing hydrology beneath an Antarctic ice stream. *Geology*, 35(2), 127–130.
- Sneed, S. B., et al. (2015). New LA-ICP-MS cryocell and calibration technique for sub-millimeter analysis of ice cores. *Journal of Glaciology*, 61(226), 233–242.
- Sneed, W. A., Hooke, R. LeB., and Hamilton, G. S. (2008). Thinning of the south dome of Barnes Ice Cap, arctic Canada, over the past two decades. *Geology*, 36(1), 71–74.
- Sokolnikoff, I. S., and Redheffer, R. M. (1958). *Mathematics of Physics and Modern Engineering*. New York: McGraw Hill, 810pp.
- Sommerfeld, R., and LaChapelle, E. (1970). The classification of snow metamorphism. *Journal of Glaciology*, 9(55), 3–17.
- Souchez, R. A., and Lorrain, R. D. (1978). Origin of the basal ice layer from Alpine glaciers indicated by its chemistry. *Journal of Glaciology*, 20(83), 319–328.
- Spencer, M. K. (2005). Paleoclimatic change inferred through firnification processes. PhD thesis, The Pennsylvania State University, 196pp.

- Spencer, M. K., Alley, R. B., and Fitzpatrick, J. J. (2006). Developing a bubble-number density paleoclimatic indicator for glacier ice. *Journal of Glaciology*, 52(178), 358–364.
- Steffensen, J. P., et al. (2008). High-resolution Greenland ice core data show abrupt climate change happens in a few years. *Science*, 321(5889), 680–684.
- Stehle, N. S. (1967). Migration of air bubbles in ice under a temperature gradient. In Öura, H. (ed.) *Physics of Snow and Ice: International Conference on Low Temperature Science 1966 Proceedings*. Sapporo: Institute of Low Temperature Science, Hokkaido University, 1(1), 219–232.
- Stephenson, S. N., and Doake, C. S. M. (1982). Dynamic behavior of Rutford Ice Stream. *Annals of Glaciology*, 3, 295–299.
- Stevens, L. A., et al. (2015). Greenland supraglacial lake drainages triggered by hydrologically induced basal slip. *Nature*, 522, 73–76.
- Straneo, F., Heimbach, P. (2013). North Atlantic warming and the retreat of Greenland's outlet glaciers. *Nature*, 504, 36–43.
- Strang, G., and Fix, G. J. (1973). *An Analysis of the Finite-Element Method*. New York: Prentice Hall, 306pp.
- Stocker, T. F., and Johnsen, S. J. (2003). A minimum thermodynamic model for the bipolar seesaw. *Paleoceanography*, 18(4).
- Stokes, C. R., Fowler, A. C., Clark, C. D., Hindmarsh, R. C. A., and Spagnolo, M. (2013). The instability theory of drumlin formation and its explanation of their varied composition and internal structure. *Quaternary Science Reviews*, 62, 77–96.
- Stokes, C. R., Lian, O. B., Tulaczyk, S., and Clark, C. D. (2008). Superimposition of ribbed moraine on a palaeo-ice-stream bed: implications for ice stream dynamics and shutdown. *Earth Surface Processes and Landforms*, 33, 593–609.
- Stone, G. H. (1899). *The glacial gravels of Maine and their associated deposits*. U.S. Geological Survey Monograph 34, 499pp.
- Suckale, J., Platt, J. D., Perol, T., and Rice, J. R. (2014). Deformation-induced melting in the margins of the West Antarctic ice streams. *Journal of Geophysical Research: Earth Surface*, 119, 1004–1025, doi: 10.1002/2013JF003008.
- Sundal, A. V., Shepard, A., Nienow, P., Hanna, E., Palmer, S., and Huybrechts, P. (2011). Melt-induced speed-up of Greenland ice sheet offset by efficient subglacial drainage. *Nature*, 469, 521–524.
- Suwa, M., and Bender, M. L. (2008). Chronology of the Vostok ice core constrained by O<sub>2</sub>/N<sub>2</sub> ratios of occluded air, and its implication for the Vostok climate records. *Quaternary Science Reviews*, 27, 1093–1106, doi: 10.1016/j.quascirev.2008.02.017.
- Swithinbank, C. (1969). Giant icebergs in the Weddell Sea, 1967–68. *Polar Record*, 14(91), 477–478.
- Tarasov, L., and Peltier, W. R. (1999). Impact of thermomechanical ice sheet coupling on a model of the 100 kyr ice age cycle. *Journal of Geophysical Research*, 105(D4), 9517–9545.

- Taylor, K. C., et al. (2004). Dating the Siple Dome (Antarctica) ice core by manual and computer interpretation of annual layering. *Journal of Glaciology*, 50(170), 453–461.
- Taylor, L. D. (1963). Structure and fabric on the Burroughs Glacier, south-east Alaska. *Journal of Glaciology*, 4(36), 731–752.
- Tedesco, M., Doherty, S., Fettweis, X., Alexander, P., Jeyaratnam, J., and Stroeve, J. (2016). The darkening of the Greenland ice sheet: trends, drivers, and projections (1981–2100). *The Cryosphere*, 10, 477–496.
- Terzaghi, K. (1950). Mechanics of landslides. In *Application of Geology to Engineering Practice*. New York: Geological Society of America, Berkey Volume, 83–125.
- Thomas, R. H. (1973). The creep of ice shelves: theory. *Journal of Glaciology*, 12(64), 45–53.
- Thomas, R. H., and Bentley, C. R. (1978). A model for Holocene retreat of the West Antarctic Ice Sheet. *Quaternary Research*, 10, 150–170.
- Thomason, J. F., and Iverson, N. R. (2008). A laboratory study of particle ploughing and pore-pressure feedback: a velocity-weakening mechanism for soft glacier beds. *Journal of Glaciology*, 54(184), 169–181.
- Thomason, J. F., and Iverson, N. R. (2009). Deformation of the Bateson till of the Lake Michigan lobe, Laurentide ice sheet. *Journal of Glaciology*, 55(189), 131–146.
- Thompson, L. G. (1977). Variations in microparticle concentration, size distribution and elemental composition found in Camp Century, Greenland, and Byrd station, Antarctica, deep ice cores. *International Association of Hydrological Sciences Publication*, 118, 351–364.
- Tika, T. E., Vaughan, P. R., and Lemos, L. J. (1996). Fast shearing of preexisting shear zones in soil. *Géotechnique*, 46(2), 197–233.
- Tresca, M. H. (1864). Mémoire sur l'écoulement des corps solides soumis à de fortes pressions. *Comptes Rendus des Séances de l'Academie des Sciences, Paris*, 59, 754–758.
- Trevorrow, A., Budd, W. F., Jacka, T. H., and Warner, R. C. (2012). The tertiary creep of polycrystalline ice: experimental evidence for stress-dependent levels of strain-rate enhancement. *Journal of Glaciology*, 58(208), 301–314.
- Truffer, M., Echelmeyer, K. A., and Harrison, W. D. (2001). Implications of till deformation on glacier dynamics. *Journal of Glaciology*, 47(156), 123–134.
- Truffer, M., Harrison, W. D., and Echelmeyer, K. A. (2000). Glacier motion dominated by processes deep in underlying till. *Journal of Glaciology*, 46(153), 213–221.
- Tulaczyk, S. (1999). Ice sliding over weak, fine-grained tills: dependence of ice-till interactions on till granulometry. In Mickelson, D. M., and Attig, J. W. (eds.) *Glacial Processes Past and Present*. Boulder, CO: Geological Society of America Special Paper, 337, 159–177.
- Tulaczyk, S., Kamb, B., Scherer, R., and Engelhardt, H. (1998). Sedimentary processes at the base of a West Antarctic ice stream: constraints from

- textural and compositional properties of subglacial debris. *Journal of Sedimentary Research*, 68, 487–496.
- Tulaczyk, S., Kamb, W. B., and Engelhardt, H. F. (2000a). Basal mechanics of Ice Stream B, West Antarctica 1. Till mechanics. *Journal of Geophysical Research*, 105(B1), 463–481.
- Tulaczyk, S., Kamb, W. B., and Engelhardt, H. F. (2000b). Basal mechanics of Ice Stream B, West Antarctica 2. Undrained plastic bed model. *Journal of Geophysical Research*, 105(B1), 483–494.
- Tulaczyk, S., Kamb, W. B., and Engelhardt, H. F. (2001). Estimates of effective stress beneath a modern West Antarctic ice stream from till preconsolidation and void ratio. *Boreas*, 30, 101–114.
- Ussing, N. V. (1903). On Jyllands hedesletter og teorierne om deres dannelse. [On Jyllands meltwater outwash plains and theories of their origin]. *Oversigt over det Kongelige Danske Videnskabernes Selskabs Forhandlinger*, 2, 99–165.
- Vallon, M., Petit, J.-R., and Fabre, B. (1976). Study of an ice core to bedrock in the accumulation zone of an alpine glacier. *Journal of Glaciology*, 17(75), 113–128.
- Van Beaver, H. G. (1971). The significance of the distribution of clasts within the Great Pond esker and adjacent till. MS thesis, University of Maine, Orono, 61pp.
- van de Wal, R. S. W., and Oerlemans, J. (1995). Response of valley glaciers to climatic change and kinematic waves: a study with a numerical ice flow model. *Journal of Glaciology*, 41(137), 142–152.
- van de Wal, R. S. W., et al. (2015). Self-regulation of ice flow varies across the ablation area in south-west Greenland. *The Cryosphere*, 9, 603–611.
- Van der Veen, C. J. (1998). Fracture mechanics approach to penetration of surface crevasses on glaciers. *Cold Regions Science and Technology*, 27, 31–47.
- Van der Veen, C. J., and Whillans, I. M. (1989). Force budget: I. Theory and numerical methods. *Journal of Glaciology*, 35(119), 53–60.
- Van der Veen, C. J., and Whillans, I. M. (1994). Development of fabric in ice. *Cold Regions Science and Technology*, 22, 171–195.
- Vaughan, D. G. (1993). Relating the occurrence of crevasses to surface strain rates. *Journal of Glaciology*, 39 (132), 255–266.
- Vaughan, D. G. (1995). Tidal flexure at ice shelf margins. *Journal of Geophysical Research*, 100(B4), 6213–6224.
- Vaughan, D. G., Corr, H. F. J., Doake, C. S. M., and Waddington, E. D. (1999). Distortion of isochronous layers in ice revealed by ground penetrating radar. *Nature*, 398(6725), 323–326.
- Vaughan, D. G., et al. (2013). Observations: cryosphere. In Stocker, T. F., et al. (eds.) *Climate Change 2013: The Physical Science Basis*. Contribution of Working Group I to the Fifth Assessment Report of the Intergovernmental Panel on Climate Change. Cambridge: Cambridge University Press, pp. 317–382.
- Velicogna, I. (2009). Increasing rates of ice mass loss from the Greenland and

- Antarctic ice sheets revealed by GRACE. *Geophysical Research Letters*, 36, L19503, doi: 10.1029/2009GL040222.
- Vivian, R., and Bocquet, G. (1973). Subglacial cavitation phenomena under the glacier d'Argenti  re, Mont Blanc, France. *Journal of Glaciology*, 12(66), 439–451.
- Vogel, S. W., et al. (2005). Subglacial conditions during and after stoppage of an Antarctic Ice Stream: is reactivation imminent? *Geophysical Research Letters*, 32, L14502, doi: 10.1029/2005GL022563.
- von Mises, R. (1928). Mechanik der plastischen Form  nderung von Kristallen. *Zeitschrift fur Angewandte Mathematik und Mechanik*, 8, 161–185.
- Waite, A. H., and Schmidt, S. J. (1961). Gross errors in height indication from pulsed radar altimeters operating over thick ice or snow. *Institute of Radio Engineers International Convention Record*, 5, 38–53.
- Walder, J. S. (1982). Stability of sheet flow of water beneath temperate glaciers and implications for glacier surging. *Journal of Glaciology*, 28(99), 273–293.
- Walder, J. S., and Fowler, A. (1994). Channelized subglacial drainage over a deformable bed. *Journal of Glaciology*, 40(134), 3–15.
- Walder, J. S., and Hallet, B. (1979). Geometry of former subglacial water channels and cavities. *Journal of Glaciology*, 23(89), 335–346.
- Walters, R., and Meier, M. F. (1989). Variability of glacier mass balances in Western North America. In Peterson, D. H. (ed.) *Aspects of Climate Variability in the Pacific and Western Americas*. Washington, DC: American Geophysical Union, Geophysical Monograph 55, pp. 365–374.
- Walters, R. A., Joshberger, E. G., and Driedger, C. L. (1988). Columbia Bay, Alaska: an ‘upside down’ estuary. *Estuarine, Coastal, and Shelf Science*, 26, 607–617.
- Wang, W., and Warner, R. (1999). Modelling of anisotropic ice flow in Law Dome, East Antarctica. *Annals of Glaciology*, 29, 184–190.
- Warren, C. R., Glasser, N. F., Harrison, S., Winchester, V., Kerr, A., and Rivera, A. (1995). Characteristics of tide-water calving at Glaciar San Rafael, Chile. *Journal of Glaciology*, 41(138), 273–289.
- Warren, S. G., Dadic, R., Mullen, P., Schneebeli, M., and Brandt, R. E. (2012). Albedo of bare ice near the Trans-Antarctic Mountains to represent sea-glaciers on the tropical ocean of Snowball Earth. *American Geophysical Union*, Fall Meeting 2012, Abstract #U11A-06.
- Watson, E., and Luckman, B. H. (2004). Tree-ring-based mass-balance estimates for the past 300 years at Peyto Glacier, Alberta, Canada. *Quaternary Research*, 62, 9–18.
- Weertman, J. (1957a). On sliding of glaciers. *Journal of Glaciology*, 3(21), 33–38.
- Weertman, J. (1957b). Deformation of floating ice shelves. *Journal of Glaciology*, 3(21), 38–42.
- Weertman, J. (1964). Glacier sliding. *Journal of Glaciology*, 5(39), 287–303.
- Weertman, J. (1972). General theory of water flow at the base of a glacier or ice sheet.

- Reviews of Geophysics and Space Physics*, 10(1), 287–333.
- Weertman, J. (1973). Can a water-filled crevasse reach the bottom surface of a glacier? *International Association of Scientific Hydrology Publication*, 95, 139–145.
- Weertman, J. (1983). Creep deformation of ice. *Annual Reviews of Earth and Planetary Science*, 11, 215–240.
- Weertman, J., and Birchfield, G. E. (1983). Stability of sheet water flow under a glacier. *Journal of Glaciology*, 29(103), 374–382.
- Westgate, J. A. 1968. Linear sole markings in Pleistocene till. *Geological Magazine*, 105(6), 501–505.
- Whillans, I. M. (1977). The equation of continuity and its application to the ice sheet near “Byrd” Station, Antarctica. *Journal of Glaciology*, 18(80), 359–371.
- Whillans, I. M., Bolzan, J., and Shabtaie, S. (1987). Velocity of ice streams B and C, Antarctica. *Journal of Geophysical Research*, 92(B9), 8895–8902.
- Whillans, I. M., and Johnsen, S. J. (1983). Longitudinal variations in glacial flow: theory and test using data from the Byrd Station strain network, Antarctica. *Journal of Glaciology*, 29 (101), 78–97.
- Whillans, I. M., and Tseng, Y.-H. (1995). Automatic tracking of crevasses on satellite images. *Cold Regions Science and Technology*, 23(2), 201–214.
- Whillans, I. M., and van der Veen, C. J. (1993). New and improved determinations of velocity of Ice Streams B and C, West Antarctica. *Journal of Glaciology*, 39(133), 483–490.
- Whillans, I. M., and van der Veen, C. J. (1997). The role of lateral drag in the dynamics of Ice Stream B, Antarctica. *Journal of Glaciology*, 43(144), 231–237.
- Whitlow, S., Mayewski, P. A., and Dibb, J. E. (1992). A comparison of major chemical species input timing and accumulation at South Pole and Summit Greenland. *Atmospheric Environment*, 26, 2045–2054.
- Wilen, L. A., Diprinzio, C. L., Alley, R. B., and Azuma, N. (2003). Development, principles, and applications of automated ice fabric analyzers. *Microscopy Research and Technique*, 62(1), 2–18.
- Williams, R. (2017). <https://www.youtube.com/watch?v=UdqIcf6g230>
- Winberry, J. P., Anandakrishnan, S., Alley, R. B., Bindschadler, R. A., and King, M. A. (2009). Basal mechanics of ice streams: insights from the stick-slip motion of Whillans Ice Stream, Antarctica. *Journal of Geophysical Research*, 114, F01016, doi: 10.1029/2008JF001035.
- Winberry, J. P., Anandakrishnan, S., Alley, R. B., Wiens, D. A., and Pratt, M. J. (2014). Tidal pacing, skipped slips and the slowdown of Whillans Ice Stream, Antarctica. *Journal of Glaciology*, 60(222), 795–807.
- Winsborrow, M. C. M., Clark, C. D., and Stokes, C. R. (2004). Ice streams and the Laurentide Ice Sheet. *Géographie physique et Quaternaire*, 58(2–3), 269–280.
- Winski, D. A., et al. (2017). Industrial-age doubling of snow accumulation in the Alaska Range linked to tropical ocean

- warming. *Scientific Reports*, **7**, 17869, doi: 10.1038/s41598-017-18022-5.
- Winstrup, M. (2016). A hidden Markov model approach to infer timescales for high-resolution climate archives. *Proceedings of the Twenty-Eighth AAAI Conference on Innovative Applications (IAAI-16)*, July 27–31, 2014, Québec, Canada, 4053–4060.
- Winstrup, M., et al. (2019). A 2700-year annual time scale and accumulation history for an ice core from Roosevelt Island, West Antarctica. *Climate of the Past*, **15**, 751–779.
- Wiscombe, W. J., and Warren, S. G. (1981). A model for the spectral albedo of snow. I: pure snow. *Journal of Atmospheric Sciences*, **37**, 2712–2733.
- Wolovick, M. J., Creyts, T. T., Buck, W. R., and Bell, R. E. (2014). Traveling slippery patches produce thickness-scale folds in ice sheets. *Geophysical Research Letters*, **41**, 8895–8901.
- Yen, Y.-C. (1981). Review of the thermal properties of snow, ice and sea ice. *Cold Regions Research and Engineering Laboratories Report 81-10*, 27pp.
- Zwally, H. J., Abdalati, W., Herring, T., Larson, K., Saba, J., and Steffen, K. (2002). Surface melt-induced acceleration of Greenland Ice-Sheet flow. *Science*, **297**, 218–222.
- Zwally, H. J., and Giovinetto, M. B. (2000). Spatial distribution of net surface mass balance on Greenland. *Annals of Glaciology*, **31**, 126–132.
- Zwally, H. J., Li, J., Robbins, J. W., Saba, J. L., Yi, D., and Brenner, A. C. (2015). Mass gains of the Antarctic ice sheet exceed losses. *Journal of Glaciology*, **62**(230) 1019–1036.

# Index

Bold page numbers refer to pages with illustrations

- A. *See* flow law
- ablation
- effect of debris cover on, 27–28
- ablation area, 17
- basal melting beneath, 137
  - compressive flow in, 279
  - emergence velocity in, 96–97
  - foliation in, 393–406
  - lateral moraines in, 101
  - near surface temperature in, 125, 130–131
  - temperature profile in, 127, 136, 294–295
  - transverse surface profile in, 99–100
- abrasion
- production of fine material by, 176
  - rate of, 192
  - resulting in polishing, 193
- accumulation area, 17
- accumulation-area ratio, 33
- activation
- energy, 52–53
  - enthalpy, 71
  - volume, 71
- albedo
- of bare ice, 27
  - definition, 26
  - effect of black carbon on, 26–28
  - effect of debris on, 27–28
  - effect of dirt cover on, 33
  - effect on mass balance, 26–28
  - of snow, 26
- Aleutian Low, 40
- Allan Hills, 446
- Amundson Sea, 360
- angle of internal friction, 170–171
- Antarctica
- accumulation rate, 26
  - basal drag in, 141
  - basal temperatures in, 138–141, 142
  - digital elevation model of, 140
  - dust in ice, 443
  - ice streams in, 350, 352, *See also* ice streams
  - mass balance in, 34, 39, 43, 409
- Arolla ice tunnel, 328
- Athabasca glacier
- longitudinal velocity in, 91
  - sliding speed, 155
  - transverse velocity in, 100
- axes
- instantaneous stretching, 389
- principal
- in strained state, 390
  - of strain, 390
  - of stress and strain rate, 14, 271–273
- Barnes Ice Cap, 391–393
- borehole deformation studies, 346
  - foliation in margin, 394, 404–406
  - ice fabrics in, 68
  - longitudinal cross section, 347
  - near-surface temperatures in, 125
  - Pleistocene ice in, 314
  - recumbent folds in margin of, 400
  - temperature profiles in, 298
  - Thule-Baffin moraines on, 108
  - winter balance on, 31
- basal ice
- rheology of, 160–161
  - effect of sediment on, 160–161
- bed roughness, 150, 153
- controlling obstacle size, 197
  - sinusoidal beds, 154
  - white roughness, 155
- Bindschadler Ice Stream, 188
- Bingham material, 263
- bipolar seesaw, 452
- Bjerrum defects, 48
- black carbon, 26–28
- Black Rapids Glacier, 188, 190
- Blue Glacier, 155, 199, 338, 341, 396
- Böðvarsson effect, 409
- borehole
- closure of, 327
  - deformation of, 342–349
- Breiðamerkurjökull, 188–189
- bubbles
- $\Delta$ age of, 438, 447
  - $^{40}\text{Ar}/^{38}\text{Ar}$  ratio in, 446
  - in Barnes Ice Cap Pleistocene ice, 347
  - in basal ice, 160
  - blocking veins, 199
  - $^{14}\text{C}$  in, 444
  - $\text{CO}_2$  in, 434–436
  - defining foliation, 396
  - in dirty ice, 137
  - $\text{O}_2/\text{N}_2$  ratio in, 439
  - at pore close off, 312
  - in superimposed ice, 21
  - volume of air in, 409
- budget (mass)
- definition, 22
  - gradient, 32–34
  - imbalance, 33
- bullet boulders, 249
- Byrd Station
- debris in basal ice, 137

- ice fabrics, 67  
 ice temperature, 68  
 Pleistocene-Holocene transition, 409
- c-axis, 48  
 calving, 17  
   of ice shelves, 39  
   loss of ice by, 34  
   rates of, 36–38  
   of tidewater glaciers, 34–36
- Camp Century  
   debris in basal ice, 137  
    $\delta^{18}\text{O}$  variations in core, 435
- cavities, subglacial  
   effect of water pressure on, 162–163  
   formation of, 161  
   linked, 220–221  
   role in quarrying, 248–252  
   seasonal evolution of, 230–231
- cirques  
   erosion of, 252–254
- Clausius-Clapeyron slope, 7
- climate  
   continental, 33, 203  
   maritime, 33, 203
- climate change. *See also ice core studies*  
   analysis using perturbation theory, 416–418  
   anthropogenic, 2  
   during Pleistocene, 410–411  
   at end of Pleistocene, 21  
   effect on ice shelves, 39  
   effect on mass balance, 28–32  
   effect on sea level, 314–317  
   effect on temperature distribution, 143  
   instabilities in response to, 409  
   kinematic waves, 413–416  
   response of glaciers to, 408, 411–413  
   3-stage response, 423–425  
   effect of diffusion, 420  
   Green Bay Lobe, 308–311  
   modeling, 425–428  
   observations of  
    Greenland, 429  
    Nisqually glacier, 429–431
- volume response, 420–423  
 without diffusion, 418–420
- response time  
   Johannesson theory, 420–423  
   Nye theory, 419  
   Roe and Baker model, 423–425
- CO<sub>2</sub>. *See* ice core studies
- coaxial deformation, 389
- Cobol creep, 55
- cohesion, 168–169
- cold patches, 156–158
- Columbia Glacier  
   bottom melting, 39  
   retreat of, 39, 317–318
- Column model, 131–135
- compressive flow, 279
- conduits  
   closure of, 205–207  
   englacial, 204  
   equilibrium size, 205  
   on eskers, 242–243  
   melt rates in, 212  
   subglacial  
    closure of, 329–332  
    comparison of theory and field observations, 220  
    distributed, 216–217  
    efficient/inefficient, 209  
    linked cavity, 220–221, 233  
    Nye channels, 209  
    Röthlisberger channels, 209  
    shape of, 219  
    on till, 221–232  
    water pressure in  
     hard beds, 213–217  
     soft beds, 223–225  
    under cold ice, 213
- consolidation, 169–170
- controlling obstacle size, 153
- core recovery, 433–434
- Crank-Nicolson, 297
- creep  
   diffusional, 55–56  
   dislocation, 56  
   grain-boundary sliding, 56  
   primary, secondary, transient, 58
- crevassing. *See also* fracture propagation to bed, 73, 203
- critical state line, 173
- cross glide, 52
- cross slip, 57
- crystal size. *See* grain size
- cumulative strain, 388  
   calculating, 391  
   in Barnes Ice Cap, 391–393  
   parameters describing, 387–388
- cylindrical hole, closure of, 320–326
- Dansgaard-Oeschger cycles, 410
- Dawson's integral, 125, 133
- debris. *See* dirt
- debris entrainment. *See* erosion
- deformation. *See* strain
- deformation mechanism map, 68–70
- deformation mechanisms, 55–56
- del operator, 119
- depth hoar, 21
- Des Moines lobe, 173, 183, 354
- Des Moines lobe  
   till strength, 179
- Devon Ice Cap, 403
- diffusion  
   grain boundary, 55  
   self, 55  
   volume, 55
- dilation, of till, 170–171
- dirt  
   in basal ice, 138  
   in cores of ice-cored  
    moraines, 107  
   effect on albedo, 33  
   effect on ice rheology, 160  
   in foliation, 395–396  
   on ice-cored moraines, 109
- disintegration ridges, 111
- dislocation  
   climb, 57  
   cross-slip, 57  
   density of, 51, 57, 63  
   edge, 49  
   generation of, 52  
   healing of, 70  
   recovery processes, 57  
   screw, 49  
   tangles, 51, 57, 79, 160
- Dome C, 433
- doughnuts, 111

- drainage systems, subglacial  
  efficient, 209  
  inefficient, 209  
    linked cavity, 220–221  
    on till, 221–232  
    spatial and temporal  
      distribution of, 232
- drumlins, 194–196
- dry-snow  
  facies, 20  
  line, 20  
  zone, 20
- effective normal pressure, 163
- electromagnetic forces, on  
  clays, 169
- energy balance  
  in polar ice sheets, 115–120  
  advection effect, 115–116  
  conduction effect, 117–118  
  strain heating effect,  
    118–119
- energy grade line, 216
- energy of liquid–solid interface,  
  7
- Engabreen, 156, 183, 186, 218
- enhancement factor  
  in Barnes Ice Cap Pleistocene  
    ice, 313–314  
  in borehole closure, 329  
  in development of Raymond  
    bumps, 105  
  estimates of, 71–72  
  in Siple Dome, 312  
  in Whillans Ice Stream  
    margin, 360
- ENSO, 40–42
- equilibrium line, 17, 21  
  altitude, 29–31
- equipotential surfaces, 205–208
- erosion, 143, *See also* abrasion,  
  quarrying, cirques  
  by abrasion, 192  
  beside flutes, 196  
  role in drumlin formation,  
    194  
  role of cold patches, 158
- error function, 124, 125
- eskers, 238–247  
  conduits on, 242–243  
  crossing ridges, 238–239  
  esker heads, 244  
  esker nets, 244  
  Katahdin, 240
- paths, 238  
  on valley sides, 239
- sediment supply to, 240–242
- segments, alignment of,  
  244–247
- Eulerian coordinate system,  
  116  
  extending flow, 279
- fabric  
  development of, 64–65,  
    67–68  
  measurement of, 60–63  
  multiple-maximum, 67  
  single maximum, 66  
  small circle, 64
- facies, 20
- Findelengletscher, 165–166,  
  207, 230
- finite-difference modeling. *See*  
  numerical modeling
- finite-element modeling. *See*  
  numerical modeling
- firn, 17
- flow field, 81, 97–99
- flow law, 70–72  
  effect of fabric on, 71–72  
  effect of fracture on, 78–79  
  effect of grain size on, 68–71  
  effect of pressure on, 71  
  effect of temperature on, 53,  
    329  
  effect of water on, 73
- Glen's, 15
- flowlines, 97–98, 392
- flutes, 196–197
- flux, ice, 92
- foliation  
  around conduit, 211  
  folds in, 397–400  
    isoclinal, 400–404  
  in ice sheet margin, 107,  
    404–406  
  in longitudinal septa,  
    396–397  
  origin of, 393–396
- force balance, 332–338
- fracture, 73–77  
  effect on flow law, 78–79  
  fracture toughness, 75  
  linear fracture mechanics,  
    73–76
- Frank-Read source, 51
- frazil ice, 253, 377
- free energy, 19, 59, 160
- freezing at bed, 125–126, 136  
  in overdeepenings, 253  
  role in erosion, 157
- friction  
  angle of internal, 170–172  
  rock-to-rock, 197
- frictional heating  
  in basal ice, 134, 191  
  in basal ice of ice streams,  
    363  
  role in basal melting, 39  
  during surging, 235
- gas constant, 53
- Gaukler-Manning-Strickler  
  equation, 210
- geothermal heat  
  role in basal melting, 129  
  role in ice stream stability,  
    363–366  
  warming subglacial Icelandic  
    lakes, 236
- geothermal heat flux, 122  
  at Dye 3, 292  
  effect on basal melt rates,  
    125–126  
  effect on temperature  
    profiles, 127  
  topographic focusing, 137,  
    195
- GISP, GISP2, 433
- glacier  
  cirque, 5  
  classification, 5  
  outlet, 6  
  polar, 6  
  polythermal, 6  
  source of water, 2–3  
  temperate, 6  
  temperature of, 6–7, 115–122  
  tidewater, 5  
  valley, 5
- glacier volume  
  estimate from surface area,  
    317
- Glen's flow law, 15–16, 70
- glide planes, 51
- Global Positioning System, 82
- global warming, 3, 312
- Gornergletscher, 230
- grain boundary  
  impurities on, 54  
  liquid on, 7, 53

- migration, 59  
 sliding on, 56, 60  
 slip on, 51  
 grain bridges. *See* till  
 grain fracture. *See* till  
 grain nucleation, 64  
 grain size (ice), 394  
     effect of impurities on, 347  
     effect on rheology, 46, 56, 58,  
         60, 68–71  
     variation with depth, 63  
 Greenland  
     age of ice, 21  
     albedo, 26  
     basal ice, 137  
     borehole deformation, 346  
     climate history, 143, 292  
     dust in cores, 443, 449  
     folds in basal ice, 403  
     ice cores, 433  
     ice deformation, 56  
     ice-core chemistry, 441–442  
     kinematic wave, 429  
     lead in, 2  
     mass balance, 26, 34, 135,  
         443  
     modeling, 313–314  
     subglacial water, 228–231  
     superglacial lake drainage,  
         73  
     Thule-Baffin moraines in,  
         106–111  
     tidewater glaciers in, 37  
 $\delta^{18}\text{O}$ , 435, 438  
 GRIP, 433
- heat  
     advection, 115–116  
     conduction, 117–118  
     sensible, latent, 29, 236  
 heat flow unit, 122  
 heat of fusion, 125, 157, 377  
 Heinrich layers, 354  
 hill-hole pair, 144  
 Hintereisferner, 23, 31, 426,  
     427
- Holocene ice  
     rheology of, 347
- Hudson Bay, 313
- Hudson Strait, 354
- hydraulic grade line, 216, 217,  
     219
- hydraulic jacking, 162, 197
- hydroelectric power, 3, 156
- ice  
     crystal structure of, 47–48  
     dating. *See* ice core studies:  
         dating  
     electrical conductivity of, 53  
     heat capacity of, 8, 54  
     Pleistocene. *See* Pleistocene  
         ice  
     water content of, 7, 72, 161
- ice cap, 6, 8
- ice core studies. *See also* climate  
     change  
     ancient atmosphere  
     composition, 446–447  
 $\text{CO}_2$ , measurement of,  
     434–436  
     core logging  
         field, 433–434  
         laboratory, 434  
     dating, 436–446  
 $^{10}\text{Be}$ , 441–442  
 $^{18}\text{O}$  and  $\text{D}_2$ , 437–440  
     analytical methods,  
         444–446  
     chemical variations,  
         440–441  
     dust layers, 442–443  
     layer counting, 436–437  
     radioactive dating, 444  
     volcanic events, 441  
     electrical conductivity, 434,  
         436  
     Pleistocene  $\text{CO}_2$  and  $\text{CH}_4$ ,  
         447–449
- ice sheet, 6
- ice shelves, 366–378  
     bottom melting, 40, 378  
     calving of, 376  
     circulation beneath, 376–378  
     creep of, 367–373  
     effect of tides on, 379–382  
     Larsen, 39, 366, 376  
     Ross, 39
- ice stream shear margins  
     migration of, 362  
     stability of, 362–364
- ice streams, 112–113  
     characteristics of, 354  
     draining to Amundson Sea,  
         358–360  
     effect of tides on, 383–385  
     erosional capabilities of, 168  
     in Laurentide Ice Sheet, 353  
     Rutford, 371, 383
- Siple Coast, 358  
 speed, 113, 167  
     temporal changes in, 356  
 stability of, 364–366
- ice-walled lake plains, 112
- impurities  
     effect on ice rheology, 54  
     effect on sliding, 158–159
- incompressibility condition,  
     8–9
- indicator trains, 138
- invariant. *See* tensor
- irrotational deformation, 268,  
     389
- isotropic  
     material, 71  
     stress, 13
- Jakobshavn Isbræ, 353
- jökulhlaup, 218, 236–237
- Kamb Ice Stream, 313, 357,  
     358, 363, 366, 379
- Kangerlussuaq, 110
- Kelvin effect, 18
- kettled outwash plain, 244
- kinematic wave  
     description of, 412–413  
     equation, 418  
     modeling, 427  
     on Nisqually glacier, 430  
     on Rink glacier, 429  
     theory, 416
- Kronecker  $\delta$ , 261
- Lagrangian coordinate system,  
     116, 120
- Lake Vostok, 106, 433
- landscapes, relict, 145–146
- lapse rate, 30, 33
- Late Glacial Maximum, 308
- latent heat of fusion. *See* heat
- Laurentide Ice Sheet  
     demise of, 21  
     ice streams in, 353  
     model of, 310  
     modeling, 313–314  
     temperature in, 246, 309  
     tunnel valleys beneath, 247
- Law Dome, 72
- lead, in atmosphere, 452–453
- linked cavity system. *See*  
     conduits, subglacial
- liquid-solid surface energy, 7

- Little Ice Age  
 advances, 2, 40  
 initiate folds in Barnes Ice Cap, 402  
 initiate Thule-Baffin moraines, 110  
 cold snap, 411  
 effect on Alaskan tidewater glaciers, 38  
 near-surface temperature in Barnes Ice Cap, 298  
 Storglaciären retreat from, 423  
 longitudinal coupling, 338–341  
 longitudinal strain rate  
   across Siple Dome, 312  
   effect on basal temperature, 128–129  
   effect on borehole deformation, 342  
   effect on calving, 38  
   role in balancing  $b_n$ , 289  
   role in glacier response to climate change, 412, 418–420  
   in a slab, 284–288
- MacAyeal Ice Stream, 353, 356, 366  
 Manning equation, 210  
 mass balance, 22  
   Alaskan glaciers, 40  
   black carbon effect, 28  
   climate causes of, 28–32  
   dynamic, 22–23  
   effect of albedo on, 26–28  
   effect on sea level, 44  
   measuring, 23–26  
   meteorological, 22–23  
   polar ice sheets, 26  
   principles of, 22–23  
 mass, conservation of, 8–9  
 material lines, 389  
 megascale lineations, 353  
 melting  
   basal, 39–40  
   base of ice shelves, 39–40  
   of conduit walls, 205, 211  
 melting point depression, 7  
 Mer de Glace, 2  
 microcracks  
   in ice, 73  
   in rock, 248  
 Milankovitch cycles, 303  
 Mohr-Coulomb relation, 168  
 Mohr's circle, 259–260  
 momentum balance, 265–266  
 moraines  
   ribbed, 146–147  
   stoss side, 146  
   Thule-Baffin, 106–110  
 moulins, 204  
*n*, 46  
   at low stresses, 56  
 NGRIP, 433  
 Nisqually Glacier, 429–431  
 normal consolidation line, 173  
 North Atlantic oscillation, 43  
 numerical integration, 292–293  
   Crank Nicolson method, 297  
   finite difference models, 294–298  
   trapezoidal, 293  
 numerical modeling  
   finite difference models  
    alternating direction schemes, 297–298  
    implicit methods, 297  
   finite element models, 300–302  
   finite volume models, 302  
   full Stokes models, 300  
   goals of, 291–292  
   initial conditions, 303–304  
   intercomparison of models, 305–306  
   non-deterministic models, 306–307  
    Monte Carlo models, 307  
    semi-empirical models, 307  
   non-dimensionalization, 299  
   sensitivity testing, 305  
   shallow ice approximation, 299–300  
   thermomechanical models, 303  
   tuning, 305  
   validation, 304  
 Nye channels, 209  
 octahedral plane, 14  
 ore plumes, 138  
 overdeepenings  
   drainage through, 253–254  
   erosion of, 252–254  
   till in, 254  
 Pacific decadal oscillation, 43  
 Pb, in atmosphere, 452–453  
 Penobscot River, 240  
 percolation  
   facies, 20  
   zone, 20  
 perfect plasticity, 263  
 permafrost, role in glacier flow, 308–311  
 permeability  
   of glacier ice, 199  
   of till, 177, 188, 382  
 perturbation techniques  
   applied to changes in ELA, 30–31  
   applied to changes in glacier profile, 416–418  
 Peyto Glacier, 42  
 piezometric head, 216, 221  
 Pine Island glacier, 353, 358  
 plane strain, 264  
   maximum shear stress in, 265  
   stresses and velocities in non-linear material, 288  
   perfectly plastic material, 274–284  
 Pleistocene ice  
   dust in, 443  
   folds in Barnes Ice Cap, 402  
   impurities in, 313  
   isotopic ratios in, 110  
   rheology of, 314, 347  
 plowing, in till, 182–184  
 polygonization, 61, 63  
 pore close off, 20  
 precipitates, subglacial  
    $\text{CaCO}_3$ , 159  
   Si, 193  
 preconsolidation test, 173  
 premelting, 7, 53–55  
 pressure  
   effective normal, 163  
   melting point, 7  
   separation, 162  
 principal axes. See axes  
 prismatic plane, 51  
 profile  
   transverse surface, 99–101  
 pyramidal plane, 51  
 quadrature, 293  
   Gaussian, 293  
 quarrying, 248–252

- R channels, 209  
radiation  
  black body, 32  
  gradient, 33  
  solar, 26, 29  
rate-limiting processes,  
  56–57  
climb, 57–58  
definition of, 57  
drag, 57  
other slip directions, 59  
Raymond bump, 102, 103, 312  
recrystallization, 60–64  
  dynamic, 59  
  by grain growth, 63  
  by nucleation of new  
    grains, 64  
  by polygonization, 63  
migration, 64  
regelation  
  contribution to sliding,  
    150–152, 152  
  effect of impurities, 158  
into subglacial till,  
  184–186  
regelation layer, 155  
Roman lead smelting, 2  
Ross Ice Shelf, 112  
  calving from, 39, 374  
  grounding zone, 351, 378  
rotation  
  of ice crystals, 64  
  in simple shear, 267, 390  
  of strain axes, 271  
Röhlisberger channel, 223  
Rutford Ice Stream, 362  
satellite interferometry, 82  
sea level  
  effect of collapse of West  
    Antarctic Ice Sheet,  
    360  
  effect on ice streams, 312  
estimate of future rise,  
  314–317  
twentieth century rise, 3,  
  43–44  
shallow ice approximation,  
  299–300  
shape factor, 90  
shear  
  pure, 62, 64, 65, 66, 389  
  simple, 62, 65, 66, 118, 276,  
    329, 342, 389  
shear stress, basal, 84–86  
  calculation using force  
    balance, 332–338  
SI units, 5  
sintering, 19  
Siple Coast, 112  
Siple Dome, 102, 357, 436  
  modeling of, 312–313  
sliding  
  effect of cavities on, 161  
  effect of impurities on, 159  
  effect of rock-to-rock friction  
    on, 156  
  effect of water pressure on,  
    162–166  
  Nye-Kamb roughness, 154  
  by plastic flow, 152  
  by regelation, 150–152  
  speed, 154  
  stress, 149–150  
  at subfreezing temperatures,  
    193–194  
  tests of theories, 155–156  
  weaknesses of theories,  
    156–160  
slip line field, 280  
snow drifting  
  effect on budget gradient,  
    23  
  effect on velocity field,  
    105–106  
Storglaciären, 162  
  break through curves, 229  
  effect of  $N_e$  on  $u_s$ , 165, 167  
  englacial drainage in, 204  
  longitudinal cross section of,  
    219, 253  
  map of, 336  
  moulins in, 204  
  surface speed of, 230  
  till rheology, 171, 179, 181  
 $\tau_V$ , 422  
stoss side moraines, 145  
strain, 266–269  
  cumulative, in a glacier,  
    391–393  
  definition, 12  
  ellipse, 387–389  
  logarithmic, 12, 269  
  notation, 12  
  transformation of, 269–271  
strain heating, 118–119  
  in basal boundary condition,  
    132  
strain rate  
  definition, 12  
  effective, 14  
  equation for, 267  
  longitudinal. *See longitudinal*  
    strain rate  
  octahedral shear, 14  
  principal axes of, 271–273  
stratigraphy  
  radar, 101–105  
  snow, 21  
  use in dating ice, 21  
stress  
  comparison of theory with  
    measurements,  
    289–290  
  definition, 10  
  deviatoric, 13, 260–262  
  effective, 14  
  equilibrium, 265–266,  
    332–338  
  in a slab on a uniform slope,  
    274–275  
  nonlinear material,  
    284–288  
  perfectly plastic material,  
    275–280  
  non-hydrostatic, 13  
  octahedral, 14  
  principal, 14, 259  
  principal axes of, 271–273  
  sign convention, 10  
  transformation of, 256–258  
  yield, 12  
stress intensity factor, 74–76  
striations, 192–193  
summation convention, 261  
supercooling, 218, *See also*  
  frazil ice  
superimposed ice, 21  
surging, 232–236  
  drainage mechanisms, 235  
  thermal mechanisms,  
    235–236  
Svartisen Subglacial  
  Laboratory, 156, 160  
T term, 333  
temperature  
  basal in Antarctica, 138–141  
  distribution along a flowline,  
    135–137  
  mean annual near surface,  
    130–131

- temperature boundary condition  
bed, 122–123, 125–126  
surface, 124–125
- temperature profile  
ablation area, 129, 294–295  
accumulation area, 127–128  
beneath divide, 121–126  
effect of vertical velocity on, 128–129  
far from divide, 131–135  
response to climate change, 143  
seasonal variation, 295–296
- tensor  
invariants of, 260  
in plane strain, 264–265  
rank of, 11, 256  
rotation rate, 268  
strain, 12, 267  
strain rate, 12  
symmetric, 11  
velocity derivative, 268
- texture, 60, 61
- thermal conductivity  
ice, 117, 120  
rock, 151
- thermal diffusivity, 118
- thin section, 60
- thrust features, 311  
blocks, 197  
hill-hole pair, 144  
slab entrainment, 190
- Thule, Greenland, 106, 110
- Thule-Baffin moraines. *See* moraines
- Thwaites glacier, 358
- tidewater glaciers, 6, 34  
calving from, 34–36  
retreat of, in Antarctica, 411  
unstable retreat of, 38–39
- till  
consolidation of, 169–170  
Coulomb plastic behavior, 181  
deformation of, 166–172  
dilatant hardening, 177  
role of pore water, 177
- depth of deformation in, 191
- dilation of, 170–171, 178, 382
- flow law for, 178–182
- grain bridges in, 174–175
- grain fracture in, 175–176
- granulometry of, 175–176
- plowing, 182–184
- rheology of, 177–178
- sediment transport in  
deforming, 168
- strength  
failure, 168, 171  
fundamental, 171  
residual, 171  
ultimate, 171  
yield, 171
- void ratio of, 172–174
- tiltmeters, 181, 189
- transformation of snow to ice, 18, 19
- transverse till scarps, 145
- Tresca yield criterion, 262
- trimline, 90
- triple point, 7, 7
- tunnel closure, 213, 327–329
- tunnel valleys, 247–248
- uniaxial compression, 64
- units, 5
- unloading-reloading line, 173
- Urumqi Glacier No. 1, 161, 194
- Variegated Glacier, 220  
surge of, 233, 234
- veins, 6, 200  
energy balance in, 202  
water flow in, 156, 199
- velocity  
balance, 83–84  
effect of drifting on, 105–106
- horizontal  
comparison of theory and measurements, 91–92
- depth variation of, 86–88
- depth-averaged, 92
- in valley glaciers, 88–90
- measurement of, 82–83
- submergence/emergence, 96–97
- vertical  
beneath divide, 96
- variation with depth, 93–96
- velocity distribution  
comparison of theory with measurements, 289–290
- in a slab on a uniform slope  
nonlinear material, 284–288
- perfectly plastic material, 281–284
- viscoplastic material, 263
- viscous heating in water, 205, 213, 237, 246
- void ratio, 172, 177
- von Mises yield criterion, 262
- Vostok, 66, 433  
Lake Vostok, 106
- water content of ice. *See* ice
- water equivalent line, 216, 218
- water flow  
englacial, 204  
in veins, 199–202
- subglacial  
on adverse bed slopes, 218, 253  
on hard beds, 213–217  
on soft beds, 221–227
- water pressure  
during surges, 233–235  
effect of A on, 216  
effect of bed slope on, 216–218
- in conduits on till, 223–225
- in pore water  
Des Moines Lobe, 174  
near conduit, 363  
role in erosion, 144  
role in plowing, 198  
role in sliding, 314
- water table in firn, 203
- West Antarctic Ice Sheet, 42, 350  
collapse of, 360, 385  
ice streams, 354
- wet snow zone, 20
- Whillans Ice Plain, 383  
driving stress, 353  
stick-slip movement, 382
- till permeability, 382
- Whillans Ice Stream  
driving stress, 353  
grounding line wedge, 186

- shear margin, 356, 361  
  migration of, 362  
speed of, 113, 356  
stability of, 364–365  
subglacial channel spacing,  
  227  
till beneath, 167, 169–170, 356  
till deformation, 187–188
- till rheology, 179, 180  
  preconsolidation stress, 180
- yield criterion, 262–264  
  Tresca, 262  
  von Mises, 262
- yield strength, 263  
  ice, 76
- till, 171  
yield stress, 12, 263  
Younger Dryas  
  age, 21  
  change in  $b_n$  at end of, 21,  
    443, 445  
  cold snap, 411  
  end of, 449–451

